

Design of Chiral-at-Ruthenium and Chiral-at-Iron Complexes for Asymmetric Catalysis

A DISSERTATION

In

Chemistry

Presented to the Faculties of Philipps-Universität Marburg in Partial Fulfillment
of the Requirements for the Degree of Doctor of Science

(Dr. rer. nat.)

Yubiao Hong

Fujian, P. R. China

Marburg/Lahn 2021

Die vorliegende Dissertation entstand in der Zeit von Dezember 2017 bis März 2021 am Fachbereich Chemie der Philipps-Universität Marburg unter der Betreuung von Herrn Prof. Dr. Eric Meggers.

Vom Fachbereich Chemie der Philipps-Universität Marburg (Hochschulkenziffer: 1180) als Dissertation am _____ angenommen.

Erstgutachter:	Prof. Dr. Eric Meggers
Zweitgutachter:	Prof. Dr. Armin Geyer
weitere Mitglieder Prüfungskommission:	Prof. Dr. Jörg Sundermeyer
	Prof. Dr. Bernhard Roling

Tag der mündlichen Prüfung: _____

Acknowledgements

Pursuing the doctoral degree is a very unforgettable experience for me. I would like to express my gratitude to all those who helped me over the past several years.

At the very first, I would like to express my deep gratitude to Prof. Eric Meggers who has given me invaluable supervision and suggestions over the past three and half years. I have benefited tremendously from his attitude to academic research and insightful viewpoint for chemistry.

Next, I sincerely appreciate Prof. Qi Shen for introducing me to do my Ph.D. degree in the Meggers group.

Besides, I also own my appreciation to Prof. Geyer, Prof. Roling and Prof. Sundermeyer for referring my thesis and being the defense committee.

Moreover, I would like to thank all the past and current members of the Meggers group. Thanks a lot to Dr. Lili Zhang, Dr. Sabrina Höbenreich, Ina Pinnschmidt, and Andrea Tschirch for their kind help. Special thanks to Dr. Chuanyong Wang, Dr. Yu Zheng and Dr. Jie Qin for their help in my study and life from Suzhou to Marburg. Thanks a lot to Dr. Lucie Jarrige and Xiaoqiang Huang for their cooperation and help on my research and publications. Thanks a lot to Philipp Steinlandt for translating the abstract into the German version. Thanks a lot to all of group members Dr. Shipeng Luo, Dr. Qi Zhang, Dr. Naifu Hu, Dr. Guanghui Wang, Dr. Long Li, Dr. Jia Ma, Dr. Yuqi Tan, Dr. Zijun Zhou, Yvonne Grell, Erik Winterling, Chenhao Zhang, Xiang Shen, Tianjiao Cui, Feng Han, Chen-Xi Ye, Xin Nie, Marcel Hemming, Lifang Zhao, Jiahui Lin and Wenjian Zhou for their kind help and cooperation.

Furthermore, I would like to thank all the collaborators from the chemistry department and other institutes. Thanks a lot to Dr. Xiulan Xie for the NMR measurements and analysis. Thanks a lot to Dr. Klaus Harms and Sergei Ivlev for the measurement and analysis of all the single crystals.

Last but not least, I would like to extend my deep gratefulness to my family for their constant support and comfort.

Best wishes to all of you.

Publications

Publications:

Part of work has been already published

1. Y. Hong, L. Jarrige, K. Harms, E. Meggers, Chiral-at-Iron Catalyst: Expanding the Chemical Space for Asymmetric Earth-Abundant Metal Catalysis. *J. Am. Chem. Soc.* **2019**, *141*, 4569–4572.
2. Z. Zhou, S. Chen, Y. Hong, E. Winterling, Y. Tan, M. Hemming, K. Harms, K. Houk, E. Meggers, Non- C_2 -Symmetric Chiral-at-Ruthenium Catalyst for Highly Efficient Enantioselective Intramolecular $C(sp^3)$ -H Amidation. *J. Am. Chem. Soc.* **2019**, *141*, 19048–19057.
3. Y. Grell, Y. Hong, X. Huang, T. Mochizuki, X. Xie, K. Harms, E. Meggers, Chiral-at-Rhodium Catalyst Containing Two Different Cyclometalating Ligands. *Organometallics*, **2019**, *38*, 3948–3954.
4. L. Li, F. Han, X. Nie, Y. Hong, S. Ivlev, E. Meggers, Complementing Pyridine-2,6-bis(oxazoline) with Cyclometalated N-Heterocyclic Carbene for Asymmetric Ruthenium Catalysis. *Angew. Chem. Int. Ed.* **2020**, *59*, 12392–12395.
5. Y. Tan, Z. Zhou, Y. Hong, S. Ivlev, S. M. Chen, K. N. Houk, E. Meggers, Intramolecular $C(sp^3)$ -H Bond Oxygenation through Transition Metal Acylnitrenoids. *Angew. Chem. Int. Ed.* **2020**, *139*, 4322–4325.

Abstract (English)

This thesis is deals with the development of new types of octahedral chiral-at-ruthenium and chiral-at-iron complexes. The chiral-at-iron complexes were investigated for applications in asymmetric catalysis.

In the first section, we introduce a new type of racemic and non-racemic octahedral ruthenium complexes where the metal center is cyclometalated by two 7-alkyl-1,7-phenanthrolium ions, giving chelating pyridylidene remote N-heterocyclic carbene ligands. The octahedral coordination sphere is incorporating two additional acetonitriles and the dicationic complexes are complemented by two hexafluorophosphate counterions. The racemic complexes are synthesized in a C_2 -symmetric geometry. Resolution of racemic complexes with a chiral sulfinamide auxiliary, followed by treating with TFA, results in non- C_2 -symmetric chiral-at-ruthenium complexes. Single crystal X-ray analysis showed that one of the bidentate ligands underwent a reorganization within the ligand sphere. Depending on the helical twist of the bidentate ligands, the metal center can adopt either a Λ or Δ metal-centered configuration. These chiral-at-ruthenium complexes are stable and enantiomeric enriched as confirmed by ^1H NMR and CD spectroscopy. Furthermore, the *trans*-effect of the pyridylidenes in this family of ruthenium complexes is investigated by crystallographic analysis, indicating the stronger electron-donating ability of pyridylidenes in comparison to pyridyl donors, as well as imidazol-2-ylidenes in related complexes.

In the second section, the first example of a chiral-at-iron complex for asymmetric catalysis is described, which is exclusively constructed with achiral bidentate and monodentate ligands and the iron ion serves as the stereogenic center. The *cis*-geometric coordination consists of two N-(2-pyridyl) imidazol-2-ylidene ligands and two acetonitrile ligands. Two acetonitrile ligands are labilized due to a strong electron donating imidazolylidene ligand in *trans*-position and hence promotes asymmetric transition metal catalysis. This is demonstrated with an enantioselective Cannizzaro reaction (96% yield, 89% ee) and an asymmetric Nazarov cyclization (89% yield, >20:1 d.r., 83% ee).

A highly enantioselective and diastereoselective transformation catalyzed by this new class of chiral-at-iron catalysts is developed by introduction of high steric crowding around the catalytic site. An iron complex bearing bulky 2,6-diisopropylphenyl moieties at the imidazolylidene ligands, proved to be the best catalyst for inverse electron demand hetero-Diels-Alder cycloadditions of β,γ -unsaturated α -

ketoester with enol ethers, providing 3,4-dihydro-2*H*-pyrans in high yields with excellent diastereoselectivities (up to 99:1 dr) and excellent enantioselectivities (up to 99:1 er). An electron rich vinyl azide is also cyclized to the corresponding product with excellent diastereoselectivity (95:5 d.r.) and enantioselectivity (95% ee).

Zusammenfassung (Deutsch)

Der Fokus dieser Arbeit bestand hauptsächlich aus der Synthese und Charakterisierung von neuartigen oktaedrischen Ruthenium- und Eisenkomplexen mit ausschließlich metallzentrierter Chiralität (*chiral-at-metal*-Komplexe). Die Eisenkomplexe wurden auf Anwendungen in der asymmetrischen Katalyse untersucht.

Im ersten Abschnitt wird eine neue Art von racemischen und nicht-racemischen oktaedrischen Rutheniumkomplexen vorgestellt, bei denen das Metallzentrum von zwei 7-Alkyl-1,7-Phenanthrolium-Liganden koordiniert ist, wodurch chelatisierende Pyridyliden-*N*-heterocyclische Carbenliganden erhalten wurden. Die oktaedrische Koordinationssphäre besteht zudem aus zwei Acetonitril-Liganden und der dikationischen Komplex ist mit zwei Hexafluorophosphat-Gegenionen ergänzt. Die racemischen Komplexe wurden in einer C_2 -symmetrischen Geometrie synthetisiert, wohingegen die Trennung der Enantiomere mit einem chiralen Sulfinamid-Auxiliar und die anschließende Behandlung mit TFA zu nicht C_2 -symmetrischen chiralen Rutheniumkomplexen führte. Einkristall-Röntgenanalyse zeigte, dass es zu einer Isomerisierung kam. Abhängig von der helikalen Verdrehung der zweizähligen Liganden kann das Metallzentrum entweder eine Λ - oder Δ -Konfiguration annehmen. Diese chiralen Rutheniumkomplexe waren stabil und enantiomerenangereichert, was durch $^1\text{H-NMR}$ - und CD-Spektroskopie bestätigt wurde. Darüber hinaus wurde der *trans*-Effekt der Pyridyliden-Liganden in diesen Komplexen durch kristallographische Analyse untersucht, die die stärkeren elektronenschiebenden Eigenschaften von Pyridylidenen im Vergleich zu Pyridyl-Donoren sowie zu Imidazol-2-yliden in analogen Komplexen bestätigen.

Im zweiten Abschnitt dieser Arbeit wird das erste Beispiel eines chiralen *chiral-at-metal* Katalysators beschrieben, der ausschließlich aus achiralen bidentaten und monodentaten Liganden aufgebaut ist und dessen Eisenatom als Stereozentrum dient. Die *cis*-Anordnung der bidentaten Liganden besteht aus zwei *N*-(2-Pyridyl)imidazol-2-yliden-Liganden und zwei Acetonitril-Liganden, die aufgrund der stark elektronenschiebenden Imidazolyliden-Liganden in *trans*-Position eine hohe Labilität aufweisen, was asymmetrische Lewisäurekatalyse an diesen Stellen erleichtert. Dies wurde mit einer enantioselektiven Cannizzaro-Reaktion (96% Ausbeute, 89% *ee*) und einer asymmetrischen Nazarov-Cyclisierung (89% Ausbeute, >20:1 d.r.,

83% *ee*) gezeigt.

Weiterhin wurde erstmalig eine hochgradig enantio- und diastereoselektive Transformation gezeigt, die durch einen *chiral-at-iron* Komplex katalysiert wurde, der keine chiralen Liganden enthält. Der Vorteil dieses neuen *chiral-at-iron* Katalysator-Designs besteht aus der Einführung sterisch anspruchsvoller Gruppen in der Nähe des katalytisch aktiven Zentrums, was für eine verbesserte Stereoselektivität von entscheidender Bedeutung ist. Ein Eisen-Komplex, der große 2,6-Diisopropylphenyl-Reste an den Imidazolyliiden-Liganden trägt, erwies sich als bester Katalysator für eine Hetero-Diels-Alder-Cycloaddition mit inversem Elektronenbedarf von β,γ -ungesättigten α -Ketoestern mit Enolethern. Die dabei gebildeten 3,4-Dihydro-2*H*-Pyrane konnten in hohen Ausbeuten mit hervorragenden Diastereoselektivitäten (bis zu 99:1 d.r.) und hervorragenden Enantioselektivitäten (bis zu 99:1 e.r.) erhalten werden. Ein elektronenreiches Vinylazid wurde ebenfalls zu dem entsprechenden Produkt mit ausgezeichneter Diastereoselektivität (95:5 d.r.) und Enantioselektivität (95% *ee*) cyclisiert.

Table of Contents

Acknowledgements	I
Publications	III
Abstract (English)	IV
Zusammenfassung (Deutsch)	VII
Table of Contents	IX
Chapter 1: Introduction	1
1.1 Complexes with 2-Imidazolylidene and Pyridylidene Ligands	1
1.1.1 Octahedral Iron Complexes with N-(2-Pyridyl)-Based Imidazol-2-Ylidene Ligands	2
1.1.2 Complexes Containing the Pyridylidene Ligands with N-Donors	12
1.2 Well-established Chiral Octahedral Iron Complexes for Asymmetric Catalysis	18
1.2.1 Chiral Bipyridine-Based Catalysts	19
1.2.2 Chiral N4-Based Catalysts	20
1.2.3 Chiral PNNP-Based Iron Catalysts	27
1.2.4 Chiral PNP-Based Catalysts	34
1.3 Aim of work	35
1.3.1 Synthesis and Characterization of Chiral-at-Ruthenium Complexes Containing Pyridylidene Ligands	36
1.3.2 Chiral-at-Iron Catalyst: Expanding the Chemical Space for Asymmetric Earth- Abundant Metal Catalysis	37
Chapter 2: Synthesis and Characterization of Chiral-at-Ruthenium Complexes with Pyridylidene Ligands	47
2.1 Catalyst Design	47
2.2 Synthesis and Characterization of Racemic Ruthenium Complexes	49
2.2.1 Ruthenium Complex with 3'-Methyl 2,3'-Bipyridinium Ligand	49
2.2.2 Ruthenium Complex with 7-Methyl 1,7-Phenanthroline Ligand	52
2.2.3 Ruthenium Complex with Modified 1,7-Phenanthroline Ligands.....	54
2.3. Synthesis and Characterization of Non-Racemic Ruthenium Complexes	59
2.3.1 Synthesis and Characterization of Λ/Δ -rNHCRu2*	59
2.3.2 Synthesis and Characterization of Λ/Δ -rNHCRu4*	63
2.4 Stability of Enantiomerically Enriched Ruthenium Complexes	64
2.5 Trans-Influence of Octahedral Pyridylidene Ruthenium Complexes	66
2.5.1 <i>Trans</i> -Effect of Pyridylidene versus 2-Imidazolylidene and Pyridine Ligands.....	66
2.5.2 <i>Trans</i> -Effect of Pyridylidene Ligands with Different Substituents	67
2.6 Conclusion	68
Chapter 3	71

3.1 Chiral-at-Iron Catalysts: Expanding the Chemical Space for Asymmetric Earth-Abundant Metal Catalysis.....	71
3.1.1 Catalyst Design	71
3.1.2 Synthesis of Chiral-at-Iron Catalyst	72
3.1.3 Characterization of the Iron Catalysts	75
3.1.4 Stability Study of Iron Catalyst	77
3.1.5 Iron-Catalyzed Enantioselective Intramolecular Cannizzaro Reaction	78
3.1.6 Iron-Catalyzed Asymmetric Intramolecular Nazarov Cyclization	80
3.1.7 Conclusion	81
3.2 Chiral-at-Iron Catalyst for Highly Enantioselective and Diastereoselective Hetero-Diels-Alder Reaction	82
3.2.1 Catalysts Design	82
3.2.2 Synthesis and Characterization of New Iron Complexes	83
3.2.3 Iron-Catalyzed Asymmetric Oxa-Diels-Alder Cycloadditions	87
3.2.4 Racemization Study	94
3.2.5 Conclusion	96
Chapter 4: Summary and Outlook.....	102
4.1 Summary	102
4.2 Outlook	106
Chapter 5: Experimental Part	108
5.1 Materials and Methods.....	108
5.2 Synthesis and Characterization of Chiral-at-Ruthenium Complexes with Pyridylidene Ligands.....	110
5.2.1 Synthesis of Ligands	110
5.2.2 Synthesis of Racemic Ruthenium Complexes.....	114
5.2.3 Synthesis of Non-Racemic Ruthenium Complexes	117
5.2.4 Single Crystal X-Ray Diffraction Studies	120
5.3 Chiral-at-Iron Catalyst: Expanding the Chemical Space for Asymmetric Earth-Abundant Metal Catalysis.....	132
5.3.1 Synthesis of Imidazolium Ligands	132
5.3.2 Synthesis of Iron Complex <i>Rac-FeH</i>	132
5.3.3 Synthesis of Iron Complex <i>Rac-Fe1</i>	133
5.3.4 Synthesis of Non-Racemic Iron Complexes	134
5.3.5 Iron-Catalyzed Enantioselective Intramolecular Cannizzaro Reaction	136
5.3.6 Iron-Catalyzed Asymmetric Nazarov Cyclization	137
5.3.7 Single Crystal X-Ray Diffraction Study	138
5.4 Chiral-at-Iron Catalyst for Highly Enantioselective and Diastereoselective Hetero-Diels-Alder Reaction	140
5.4.1 Synthesis of Imidazolium Ligands	140
5.4.2 Synthesis of Racemic Iron Complexes.....	144
5.4.3 Synthesis of Non-Racemic Iron Complexes	147

5.4.4 Synthesis of Substrates.....	152
5.4.5 Typical Procedure for Iron-catalyzed Asymmetric Oxa-Diels-Alder Reaction....	156
5.4.6 Experimental and Characterization Data of the Products.....	156
5.4.7 Assignment of Absolute and Relative Configurations	170
5.4.8 CD Spectra of Chiral-at-Iron Complexes.....	173
5.4.9 Single Crystal X-Ray Diffraction.....	178
Chapter 6: Appendices	190
6.1 List of Abbreviations.....	190
6.2 List of Schemes.....	191
6.3 List of Figures.....	193
6.4 List of Tables.....	196
6.5 List of Octahedral Transition Metal Complexes	197
6.6 List of Organic Compounds.....	197
6.7 Enantiomeric Excess for Catalytic Reactions.....	200
6.8 List of NMR Spectra of New Metal Complexes	231
6.9 List of NMR Spectra of New Organic Compounds	291
Statement.....	321
Curriculum Vitae.....	322

Chapter 1: Introduction

The work of this thesis is mainly focused on design and synthesis of new chiral-at-metal complexes with N-heterocyclic carbene (NHC) ligands, involving a new class of chiral-at-ruthenium with pyridylidene ligands and chiral-at-iron complexes with N-(2-pyridyl) substituted imidazol-2-ylidene ligands. The latter served as Lewis acid catalysts for asymmetric transformations including the Cannizzaro reaction, Nazarov cyclization reaction and inverse electron demand hetero-Diels-Alder reaction. Therefore, the theoretical part will introduce the background of the following two topics.

1.1 Complexes with 2-Imidazolylidene and Pyridylidene Ligands

For a long time, N-heterocyclic carbenes are generally treated as fragile species until Arduengo reported the isolation and characterization of the first stable free N-heterocyclic carbene, 1,3-di(1-adamantyl)imidazol-2-ylidene, which can be crystallized under oxygen and moisture free conditions.¹ This discovery demonstrated that free NHCs are not always unstable species. Since Herrmann and co-workers set a fundamental work on the synthesis of NHC-metal catalysts in 1995,² the use of NHCs as ancillary ligands has experienced intense development in organometallic chemistry and homogeneous catalysis.^{3,4} Compared to phosphorus and nitrogen ligands, NHCs are stronger σ -donors and π -acceptors and therefore result in stable and electron-rich complexes.^{4b,4c,5} In addition to classical Arduengo-type imidazole-2-ylidene NHCs, libraries of additional NHC derivatives with different heterocyclic scaffolds have been elevated, such as five-membered imidazolinylidene, 1,2,3-triazolylidenes, pyrazolylidenes, oxazolylidenes, thiazolylidenes, isoxazolylidenes and tetrazolylidenes and six-membered pyridylidenes as well as fused benzimidazolylidenes.^{3,4} These NHCs can be commonly divided into three types: normal (*n*NHCs), abnormal (*a*NHCs) or mesoionic (MICs), and remote (*r*NHCs).^{4h} For example, in the five-membered imidazolylidene series, C2-carbenes are normal because they have all-neutral resonance forms while C4 or C5-carbenes only have mesoionic forms representing an *a*NHCs/MICs. In addition to *n*NHCs and *a*NHCs, *r*NHCs which have a carbene center nonadjacent to any heteroatoms are often found in six-membered pyridylidenes. In this class, both C3 and C4-carbenes are considered as *r*NHCs. The former are

also termed *a*NHCs while the latter belong to *n*NHCs.

In this section, we aim to describe the complexes with 2-imidazolylidene and pyridylidene ligands, which can be specifically divided into two topics: (1) octahedral iron complexes with N-(2-pyridyl)-based imidazol-2-ylidene ligands; (2) complexes containing the pyridylidene ligands with N-donors.

1.1.1 Octahedral Iron Complexes with N-(2-Pyridyl)-Based Imidazol-2-Ylidene Ligands

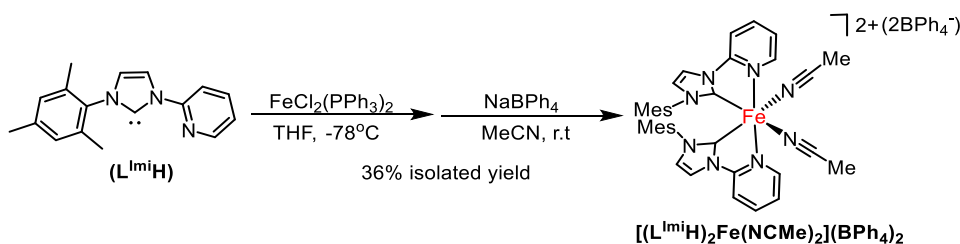
2-Imidazolylidenes are the most widely used NHC ligands for transition metals due to their stability, coordination versatility and availability of suitable precursors. The generally high stability of this type of free carbenes is most likely thanks to the excessive heteroatom stabilization, which is caused by the presence of two nitrogen atoms in the adjacent positions to the carbene center.¹

The use of 2-imidazolylidenes with additional nitrogen donors, particularly N-(2-pyridyl)-substituted ligands, has drawn much attention.³ Such ligands do not only furnish enhanced stability by the chelate effect,⁶ but can adjust the steric and electronic properties of their complexes either by modifying the substituents at the pyridine rings or by modulating the imidazole skeleton. In comparison to the N-(2-pyridyl)-based imidazol-2-ylidene complexes of noble metals,³⁻⁵ iron complexes in this regard have become widespread only at the beginning of this century.⁷ Common methods to access carbene-iron complexes are introduced. The most common way is through the reaction of appropriate metal precursors or metal salts with free carbenes, which can be generated by the deprotonation of imidazolium salts with a strong base.⁷ They also can be directly prepared by the metalation of basic iron precursors, such as $\text{Fe}[\text{N}(\text{SiMe}_3)_2]_2$,⁸ with imidazolium salt. Alternatively, the formation of carbene-iron complexes through transmetalation between the appropriate iron sources and silver carbene intermediates has recently attracted some attention.⁹ Despite the growing interest in the area of 2-imidazolylidene iron chemistry, there remains less attention on the use of these ligands in octahedral iron complexes and their application.

(1) Bidentate imidazol-2-ylidene ligands

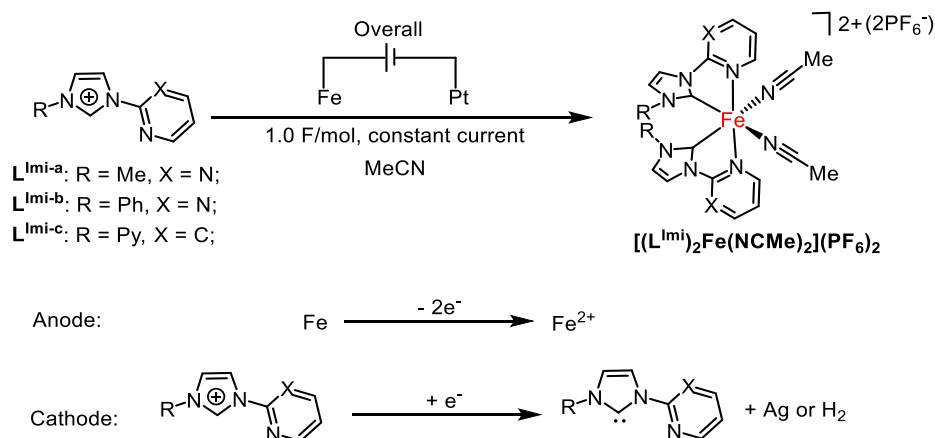
In the use of bidentate N-(2-pyridyl)-based imidazole-2-ylidene ligands, Hahn and co-workers set a precious example in 2008. A C_2 -symmetric octahedral iron complex,

$[(L^{ImiH})_2Fe(NCMe)_2](BPh_4)_2$, where L^{ImiH} = 1-mesityl-3-(pyridine-2-yl)-1H-imidazol-2-ylidene, was synthesized in two successive steps, applying $[FeCl_2(PPh_3)_2]$ and N-mesityl-N'-pyridyl-imidazol-2-ylidene (L^{ImiH}) in a ratio of 1:2, followed by anion metathesis (Scheme 1). The iron center was coordinated with two achiral bidentate ligands and two labile acetonitrile ligands in *cis*-topology. Moreover, the intramolecular π - π interactions were present between each of pyridyl ring and mesityl ring on a neighboring molecular in the crystal structure, which further stabilized the constitution of this complex. However, the authors did not consider any catalytic properties at that time.¹⁰

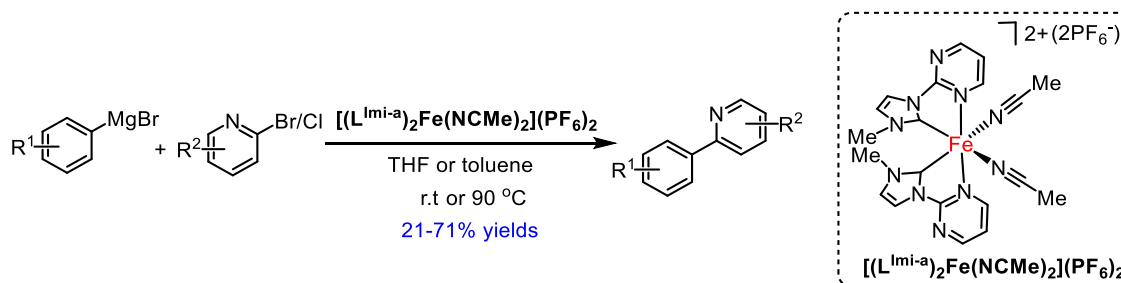


Scheme 1. Synthesis of bis(pyridyl-imidazol-2-ylidene)-iron complex via $[FeCl_2(PPh_3)_2]$ and free NHC.

Later in 2012, Chen et al. reported a facile method for the preparation of such kind of octahedral iron complexes by the electrochemical reaction. The advantage of this procedure was without required the air and water sensitive iron precursors or strong base. As shown in Scheme 2, the electrolysis of iron plate with silver-NHC intermediate or imidazolium salt to give after passing through 1.0 F/mol of electricity at a constant current corresponding iron complex in good yield. It was worth noting that the electrolysis process was successfully applied to the synthesis of pyrimidine-based 2-imidazolylidene iron complexes.¹¹ The successful extension of their catalytic activity in Kumada cross-coupling reactions of aryl or alkyl halides with Grignard reagents was demonstrated in the same year. The coupling products were obtained in low to moderate yields (21-71% yields) (Scheme 3).¹²

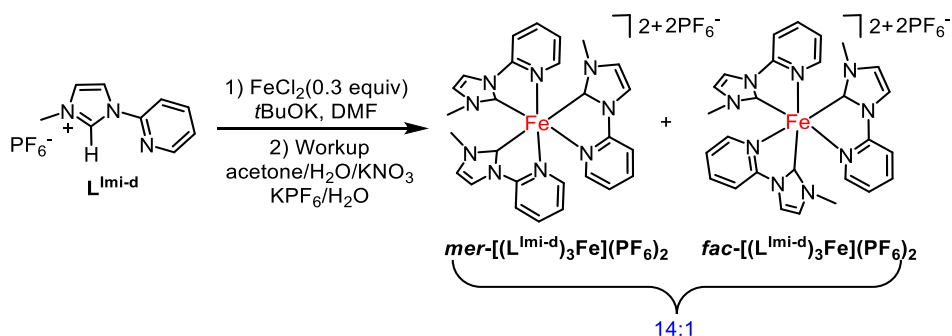


Scheme 2. Synthesis of bis(pyridyl-imidazol-2-ylidene) iron complexes via electrolysis of iron element and silver-carbene complexes.



Scheme 3. Iron-catalyzed Kumada cross-coupling reactions.

In 2018, Francés-Monerris and Monari described the synthesis of the tris-(pyridyl-imidazol-2-ylidene) iron complexes by using imidazolium salt, FeCl_2 and a strong base *t*BuOK in dry DMF under nitrogen. The iron complex was isolated as an inseparable mixture of both *mer*- $[(\text{L}^{\text{Imi-d}})_3\text{Fe}](\text{PF}_6)_2$ and *fac*- $[(\text{L}^{\text{Imi-d}})_3\text{Fe}](\text{PF}_6)_2$ isomers in a ratio of 14:1 (Scheme 4).¹³

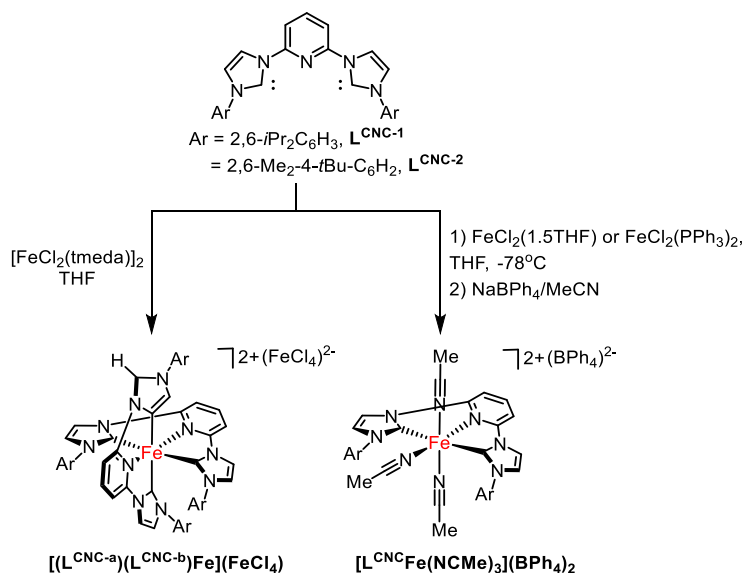


Scheme 4. Synthesis of tris-(pyridyl-imidazol-2-ylidene) iron complex.

(2) Tridentate imidazol-2-ylidene ligands

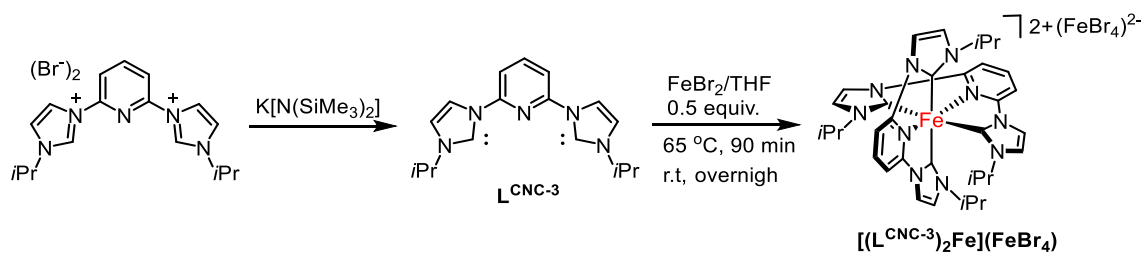
Reports on the synthesis of the octahedral iron complex bearing N-(2-pyridyl)-substituted imidazol-2-ylidene first appeared in 2004 by Danopoulos et al. The reaction of pincer

bis(arylimidazolylidene)pyridine with iron precursors in the THF, allowed for the synthesis of a small range of six-coordinate Fe^{II} complexes. As shown in Scheme 1, the reaction starting from FeCl₂(1.5THF) or FeCl₂(PPh₃)₂ in THF with ligands at -78 °C led to the formation of stable tris-acetonitrile iron complexes [L^{CNC}Fe(NCMe)₃](BPh₄)₂ after anion exchange with NaBPh₄, in which the pincer ligands were approximately coplanar. However, replacement of iron starting material by [FeCl₂(TMEDA)]₂ yielded the inert bis-tridentate iron complexes [(L^{CNC-a})(L^{CNC-b})Fe](FeCl₄), composing of one symmetrical coordination by two C2-metallated NHC rings and one unsymmetrical bonding by two NHC rings metallated at C2 and C5 (Scheme 5).⁸



Scheme 5. Synthesis of octahedral bis(arylimidazolylidene)pyridine iron complexes.

In contrast, Gibson and co-workers reported the synthesis of another octahedral iron complex [(L^{CNC-3})₂Fe](FeBr₄) with two pincer ligands, bearing isopropyl substituents, coordinated in the chelating C₂-symmetric mode to the metal center (Scheme 6).⁷ These complexes lack solubility in common organic solvents which might be responsible for the less attention on the investigation of their catalytic properties.



Scheme 6. Synthesis of C₂-symmetric octahedral bis(carbene)pyridine iron complex.

Very recently, the group of Polarz presented an interesting report on an amphiphilic Fe(II) catalyst $[(L^{CNC-4})_2Fe](Cl)_2$ bearing a long chain 4-dodecylphenyl substituent at the pyridine ring for atom transfer radical polymerization (ATRP) of methyl methacrylate (MMA). However, the polydispersity index (PDI) was high in a range of 1.9-2.0 (Figure 1).¹⁴

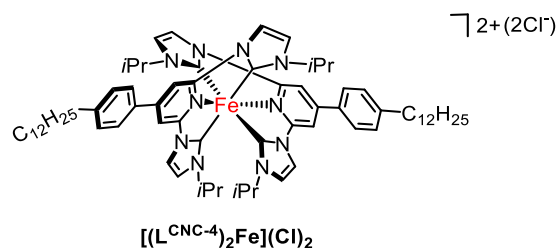


Figure 1. Amphiphilic bis(carbene)pyridine Fe(II) catalyst.

In addition, it was found that this kind of octahedral iron complexes can be designed to explore their photophysical and photovoltaic property.¹⁵⁻¹⁷ For instance, individual work was reported by Gros et al.¹⁵ and Bauer et al.¹⁷ by using such iron complexes as the photosensitizers (Figure 2).

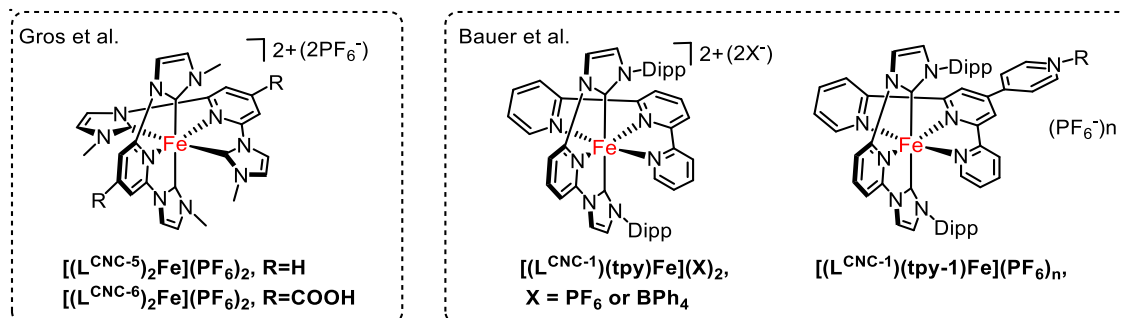
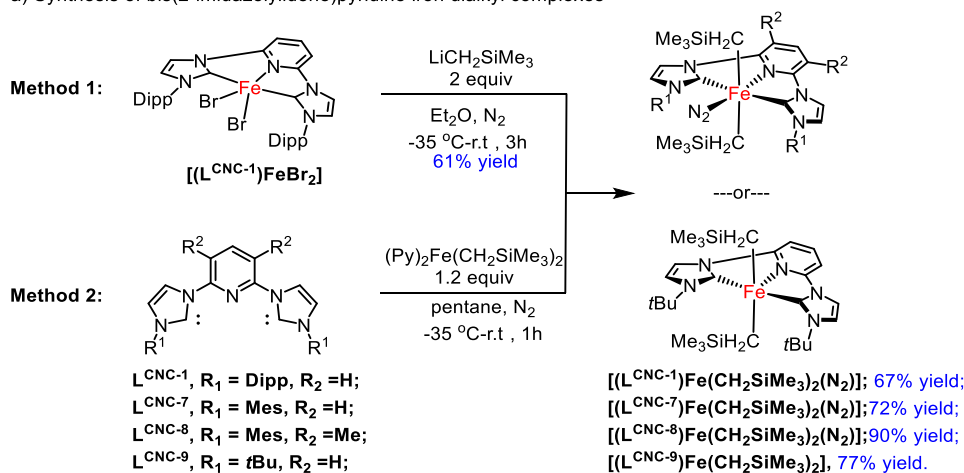


Figure 2. Iron-based photosensitizers.

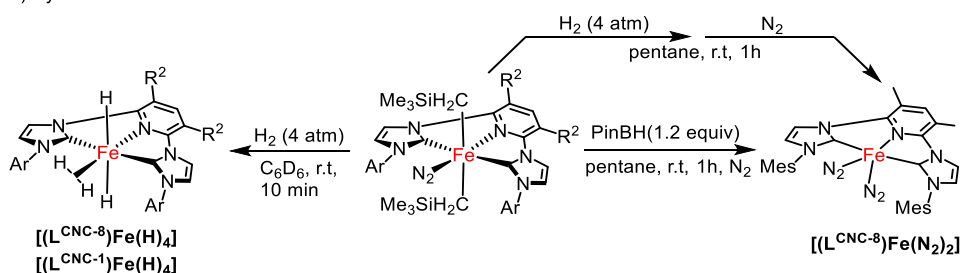
From the same pre-ligand, bis(2-imidazolylidene)pyridine iron dialkyl complexes were also reported by Chirik and co-worker in 2019.¹⁸ The corresponding iron complexes, $[L^{CNC}Fe(CH_2SiMe_3)_2(N_2)_n]$ ($n = 0$ or 1), were synthesized by addition reaction of well-defined $(py)_2Fe(CH_2SiMe_3)_2$ to free CNC carbenes (Scheme 7a, method 1). An alternative route was developed by alkylation of the iron dihalide complex like $[L^{CNC-1}FeBr_2]$ using $LiCH_2SiMe_3$. In the case of the iron complexes of the type $[(L^{CNC})Fe(CH_2SiMe_3)_2(N_2)]$ bearing aryl-substituted CNC ligands, the X-ray diffraction analysis proved the octahedral geometry around the metal center with the two CH_2SiMe_3 moieties in trans position and one dinitrogen ligand located trans

to pyridyl ring. However, with *tert*-butyl-substituted CNC ligands, iron complex $[(L^{CNC-9})Fe(CH_2SiMe_3)_2]$ was afforded as a distorted trigonal bipyramidal geometry lacking dinitrogen ligand (Scheme 7a, method 2). When the octahedral iron complexes $[(L^{CNC-1})Fe(CH_2SiMe_3)_2(N_2)]$ and $[(L^{CNC-8})Fe(CH_2SiMe_3)_2(N_2)]$ were treated with H_2 , the dealkylation reaction ensued, and the high yields of corresponding iron hydride $[(L^{CNC})Fe(H)_4]$ complexes were obtained and acted as catalysts for hydrogen isotope exchange between the deuterated benzene solvent and H_2 . Furthermore, the dialkyl complex $[(L^{CNC-8})Fe(CH_2SiMe_3)_2(N_2)]$ was also shown to successively converted to the related five-coordinated $[(L^{CNC-8})Fe(N_2)_2]$ derivative. (Scheme 7b).

a) Synthesis of bis(2-imidazolylidene)pyridine iron dialkyl complexes



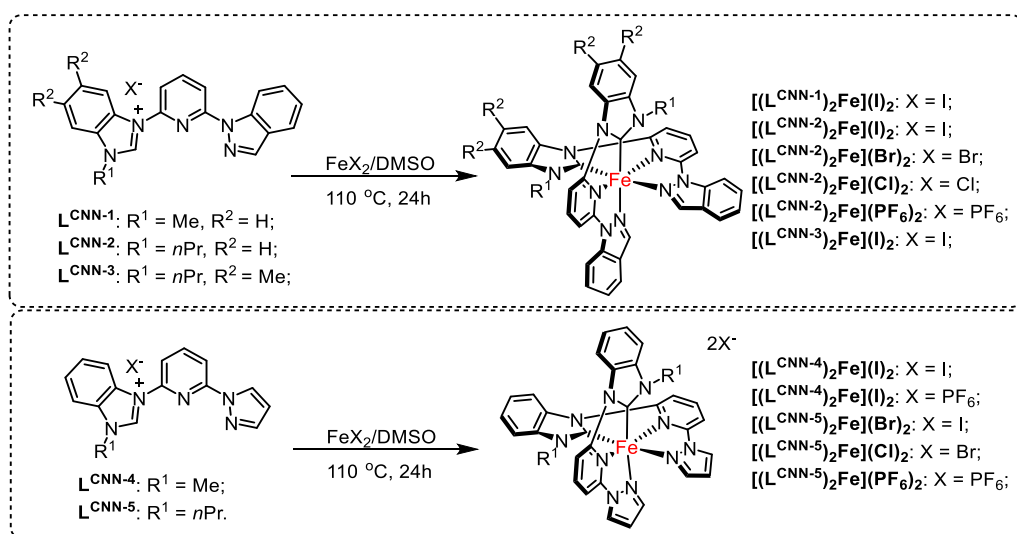
b) Synthesis of related CNN-iron derivatives



Scheme 7. Synthesis of bis(arylimidazolylidene)pyridine iron dialkyl complexes and their derivatives.

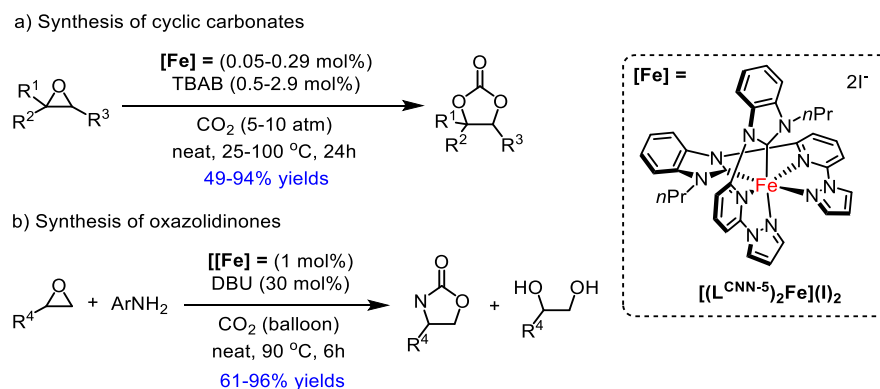
Back in 2017, Dai and Liu reported a family of diamagnetic iron complexes $[(L^{CNN})_2Fe](X)_2$ bearing unsymmetrical pyridine-bridged pincer-type imidazolylidene ligands, prepared from the corresponding starting iron dihalide complex (FeX_2 , $X = \text{I}, \text{Br}, \text{Cl}$) and imidazolium salts in dimethyl sulfoxide (DMSO) at 110°C under a nitrogen atmosphere (Scheme 8). A single-crystal X-ray study showed that $[(L^{CNN-5})_2Fe](I)_2$ was a nearly octahedral

complex and the whole molecule was formed by a symmetry coordination.¹⁹



Scheme 8. Synthesis of a family of CNN-pincer iron complexes.

These iron complexes can be employed in the cycloaddition of CO_2 to epoxides. The more promising results were performed by using $[(\text{L}^{\text{CNN-5}})_2\text{Fe}](\text{I})_2$ as the catalyst, featuring an *n*-propyl substituent at the NHC ring and the pyrazolyl group at the pyridyl ring. The corresponding cyclic carbonate products were obtained in moderate to high yields (49-94% yields) at 25–80 °C with excellent selectivity over polymerization (Scheme 9a). In addition, the iron catalyst can be easily recycled six times without significant loss of activity by simple filtration.¹⁹ Moreover, this methodology was compatible with various cis-fatty acid-derived epoxides.²⁰ Finally, the same authors further extended this protocol for the synthesis of oxazolidinones from epoxides and CO_2 in the presence of anilines, the cyclic products were obtained in moderate to excellent yields (Scheme 9b).²¹



Scheme 9. CNN-pincer iron-catalyzed cycloaddition of CO_2 to epoxides.

The experimental study suggested that the catalyst most likely served as both Lewis acid and nucleophilic species by a dissociated NHC moiety. Thus, the proposed mechanism might first go through the formation of an iron dihalide intermediate $[(L^{CNN})FeX_2]$ and a free CNN ligand which would activate the CO_2 to yield an imidazolium carboxylate **A**. This $[(L^{CNN})FeX_2]$ further bonded to epoxides to form intermediate **B**, which then attracted by halide to convert an iron alkoxide species **C**. The transfer carboxylation of **A** toward **C** to produce the iron carboxylate complex, followed by intramolecular SN_1 or SN_2 substitution to release the corresponding cyclic carbonates and regenerate the $[(L^{CNN})FeX_2]$ and free CNN ligand (Figure 3).¹⁹

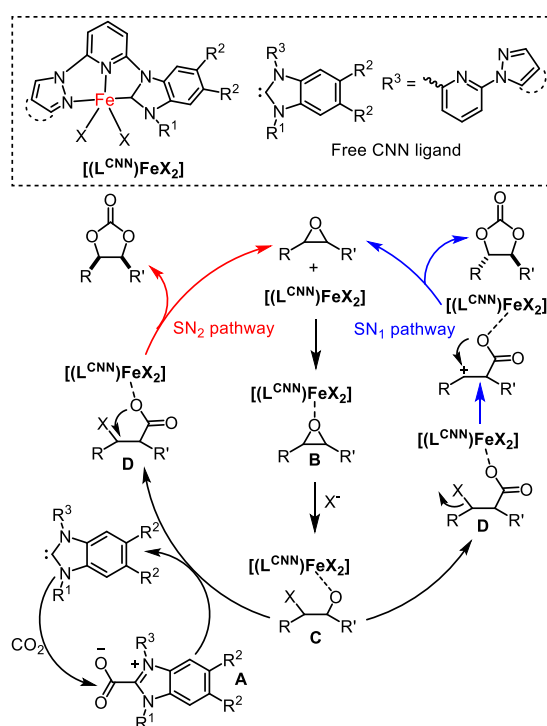
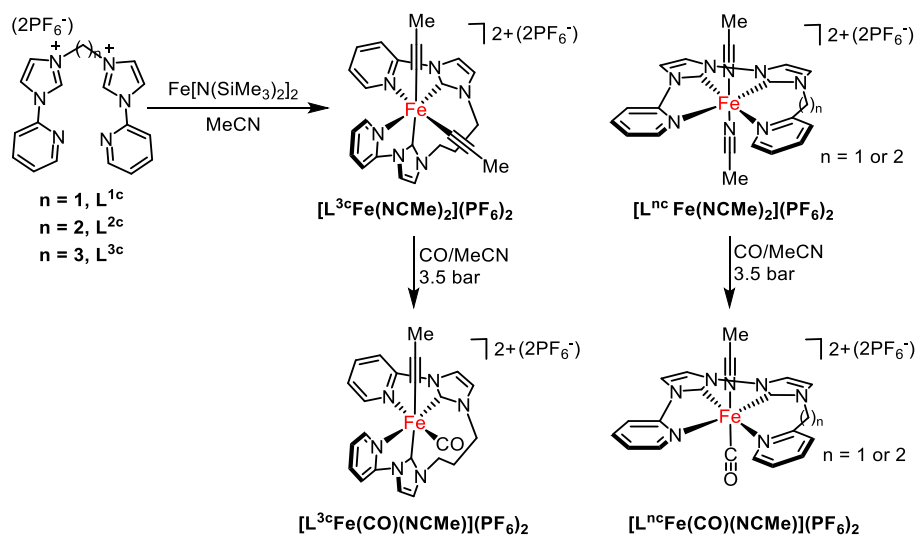


Figure 3. Proposal mechanism of iron-catalyzed cycloaddition of epoxides to CO_2 .

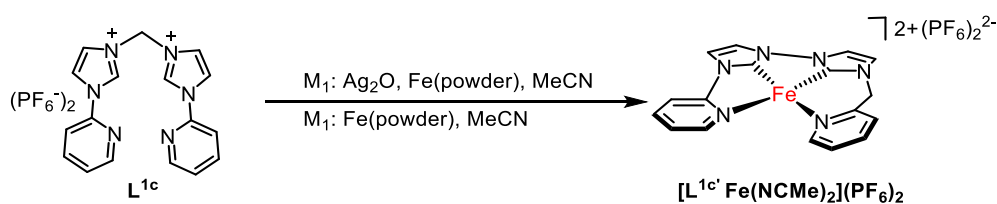
(3) Tetradentate imidazol-2-ylidene ligands

Further work reported by Herrmann and Kühn in 2012 involved the synthesis of a novel class of octahedral trans or cis-bis(acetonitrile) iron(II) complexes with tetradentate NCCN ligand linking the alkylene units. The related iron complexes can be easily afforded by the aminolysis of dicationic ligand and $Fe[N(SiMe_3)_2]_2$ (or $Fe(HMDS)_2$) in acetonitrile at $-35\text{ }^\circ\text{C}$ in 90-93% yields. As illustrated in Scheme 10, the geometric coordination was strongly dependent on the alkylene bridged units. As a result, the (CH_2) - and $(CH_2)_2$ -bridged ligands

brought about the trans-positioned acetonitriles iron complexes $[\text{L}^{1c}\text{Fe}(\text{NCMe})_2](\text{PF}_6)_2$ and $[\text{L}^{2c}\text{Fe}(\text{NCMe})_2](\text{PF}_6)_2$, having a nearly planar geometry of the NCCN ligand, whereas in the $(\text{CH}_2)_3$ -bridged NHC iron complexes $[\text{L}^{3c}\text{Fe}(\text{NCMe})_2](\text{PF}_6)_2$, two cis-oriented acetonitrile ligands were trans to imidazole ring and pyridyl ring, respectively, resulting in a sawhorse-binding mode. The reactivity of the iron complexes were next evaluated by the exposure of its acetonitrile solution to a carbon monoxide atmosphere, which led to a clean substitution of one acetonitrile ligand. The diamagnetic iron products $[\text{L}^{\text{NCCN}}\text{Fe}(\text{CO})(\text{NCMe})](\text{PF}_6)_2$ were isolated in quantitative yields. As for $[\text{L}^{3c}\text{Fe}(\text{CO})(\text{NCMe})](\text{PF}_6)_2$, the added CO ligand was preferred trans to pyridyl ring owing to the difference in the ground state free energies of two possible isomers.²² It should be noted that Chen and co-workers in 2009 first reported the synthesis of the iron complex using the (CH_2) -bridged NCCN ligand. The iron complex can be obtained by the one-pot reaction of ligand, Ag_2O and iron powders or alternative to ligand and iron powders under air. Compared to the work by Kühn et al., the X-ray diffraction analysis only showed a 14-valence-electron iron complex with a square-planar geometry (Scheme 11).⁹

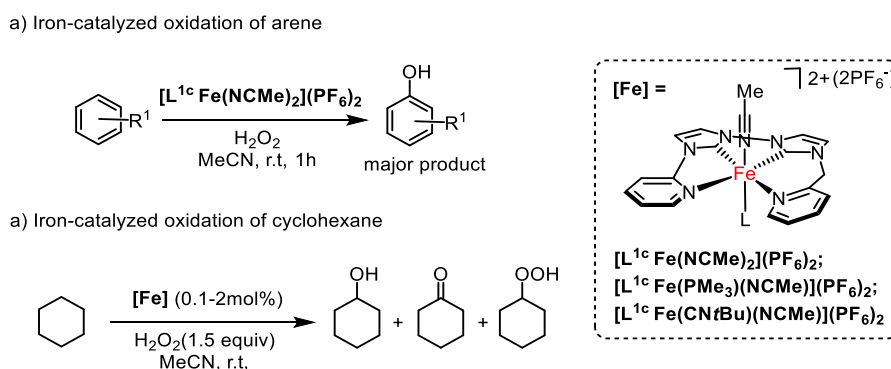


Scheme 10. Synthesis of NCCN-iron complexes via $\text{Fe}(\text{HMDS})_2$ precursor and imidazolium salts.



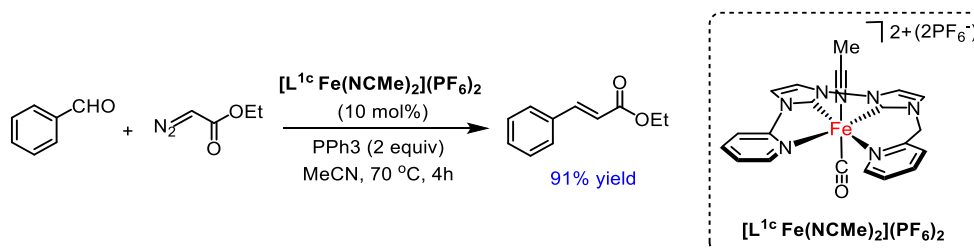
Scheme 11. Synthesis of NCCN-iron complex via imidazolium salt and iron powders.

In a subsequent report, the air and moisture stable iron complex $[\text{L}^{\text{1c}}\text{Fe}(\text{NCMe})_2](\text{PF}_6)_2$ was tested for the hydroxylation of benzene, toluene and other more electron-rich substrates like p-xylene and 1,2,4-trimethylbenzene (TMB) using aqueous H_2O_2 as oxidant at 25 °C under air atmosphere. High to excellent selectivities for corresponding phenols and benzoquinones were observed, albeit the conversion were low (Scheme 12a).²³ In addition, this catalyst was demonstrated to be active for the oxidation reaction of typically inert cyclohexane, the catalytic activity can be improved by using $[\text{L}^{\text{1c}}\text{Fe}(\text{CNtBu})(\text{NCMe})](\text{PF}_6)_2$ bearing a bulky isonitrile axial ligand as a catalyst (Scheme 12b).²⁴



Scheme 12. NCCN-Fe-catalyzed oxidation of (a) arene. (b) cyclohexane.

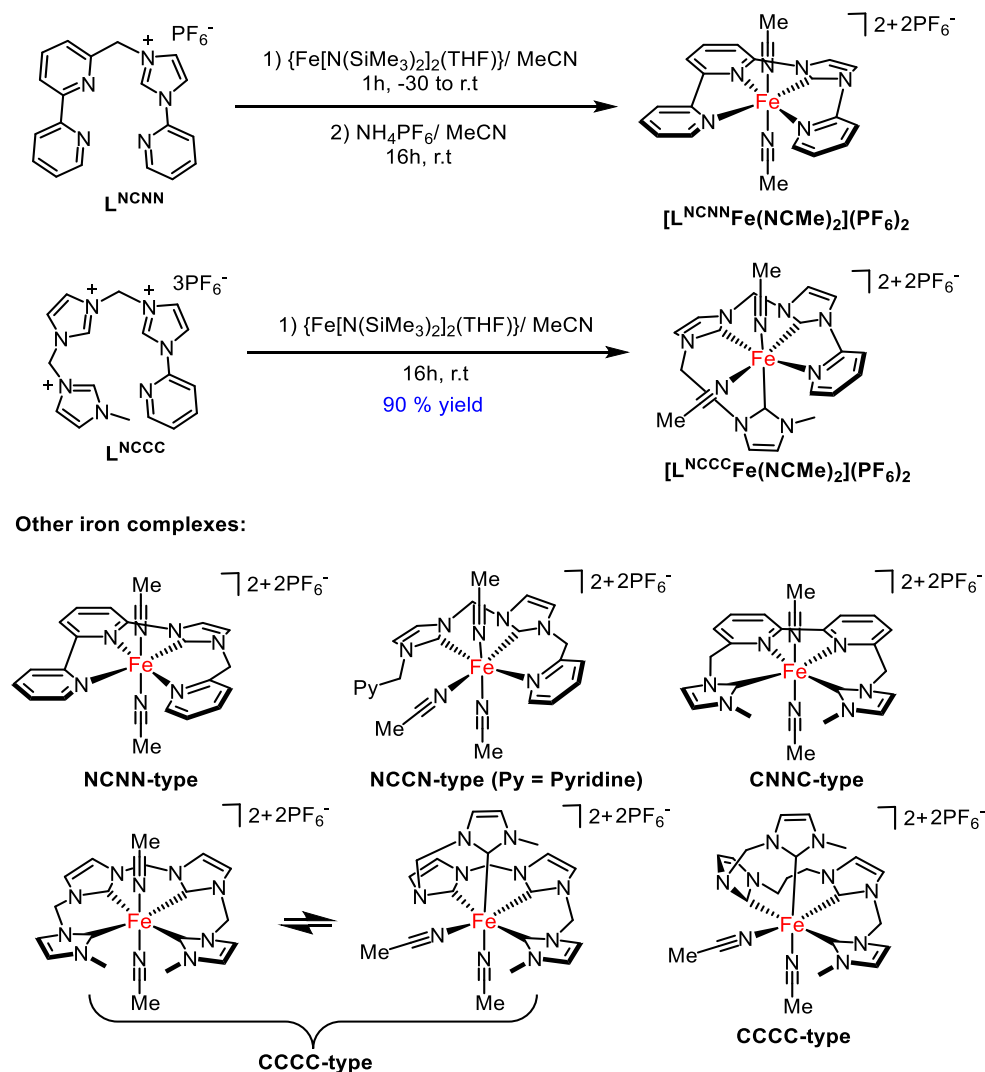
In 2016, the same authors described the catalytic activity of iron complex $[\text{L}^{\text{1c}}\text{Fe}(\text{NCMe})_2](\text{PF}_6)_2$ towards Wittig olefination of ethyl diazoacetate (EDA) and benzaldehyde in the presence of PPh_3 . Under an optimized condition, the resulted yield of E-ethyl cinnamate was 91% with excellent E-selectivity (>94%) (Scheme 13).²⁵



Scheme 13. NCCN-Fe-catalyzed Wittig reaction.

In the same area, Kühn et al. further designed other types of tetradentate ligands for the study of the influence of NHC and pyridine donors on the redox behavior of their iron complexes. The reaction of $\{\text{Fe}[\text{N}(\text{SiMe}_3)_2]_2(\text{THF})\}$ with tetradentate NHC ligands including mono-NHC (NCNN), di-NHCs (NCCN or CNNC), tri-NHCs (NCCC) and poly-NHCs (CCCC)

in acetonitrile, allowed for the synthesis of a small scope of octahedral Fe(II) complexes. Structural analysis of these complexes revealed that the coordination modes also relied upon the linkage of ligands. Finally, cyclic voltammetry (CV) experiments of $[\text{LFe}(\text{NCMe})_2](\text{PF}_6)_2$ complexes proved that the number of NHC donors impacted the major influence on redox potentials, in which the half-cell potentials exhibited a good linear correlation and followed the order of $\text{CCCC} > \text{tri-NHCs} > \text{di-NHCs} > \text{mono-NHC}$ (Scheme 10).²⁶



Scheme 14. Octahedral iron complexes based on tetradentate NHC ligands.

1.1.2 Complexes Containing the Pyridylidene Ligands with N-Donors

As another type of neutral donors, pyridylidenes attracted less attention due to the relatively restrict synthetic protocol along with lower stability compared to imidazolylidenes. Pyridylidene complexes are formally normal if metalated at C2, are abnormal and remote when metalated at C3, and are normal and remote in case metalated at C4, which leads to generally

stronger donor properties and therefore exhibits the potentially high catalytic activity. The first pyridylidene transition-metal complex was reported by Stone in 1974, who described the synthesis of pyridylidene iridium and rhodium complexes via the oxidative addition of 4-chloropyridinium salt to Ir/Rh(0) carbonyl precursors.²⁷ Since then, chemists started turning their attention to this field. The common methods for the preparation of pyridylidene complexes are the oxidative addition of low valent transition metals like Ir, Rh,²⁷ Pd,²⁸ Ni,^{28a,b,e} or Pt²⁹ with halopyridium salts²⁷⁻³⁰ and on the quaternization of non-coordinated nitrogen of cyclometalated metal complexes³¹⁻³³. Another synthetic approach is the metalation reaction of the metal precursors or metal salts with free carbenes intermediate in situ generated by deprotonation of functionalized pyridiniums with strong bases³⁴. The metalation reaction by C-H bond activation of pyridiniums with the metal source has been proved to be the more attractive and versatile method owing to the availability of starting material and without the requirement of the relatively toxic and dangerous strong base.³⁵⁻³⁹ However, much of the work has been focused on the investigation of simply monodentate pyridine or quinoline derived NHC complexes, pyridylidene complexes bearing a C,N-chelating system and their applications are less explored.

Watts et al.⁴⁰ reported that coordination of 2,2'-bipyridine (bpy) to an iridium chloride in the presence of NaOMe yielded the corresponding abnormal pyridylidene iridium complex. However, the molecular structure, containing three bipyridine ligands with the carbon atom of one bpy bonding to the metal center, was finally defined by X-ray diffraction analysis by Serpone (Figure 4)³⁵.

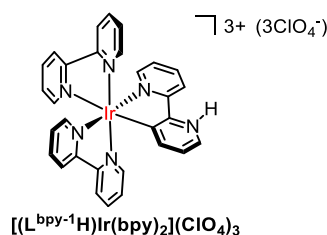
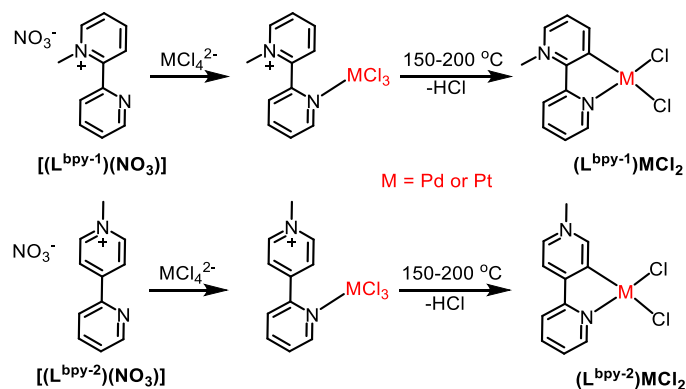


Figure 4. First C,N-chelating abnormal pyridylidene complex.

Wimmer and co-workers described a more promising method to reach such a system. Individual addition of N'-methyl-2,2'-bipyridinium $[(L^{bpy-1})(NO_3)]$ and N'-methyl-2,4'-bipyridinium $[(L^{bpy-2})(NO_3)]$ to tetrachloropalladate or tetrachloroplatinate precursor to give four monodentate cyclometalated complexes, which were converted to the corresponding

pyridylidene complexes $(L^{bpy})MCl_2$ through the elimination of HCl at 150-200 °C in aqueous solutions or the solid state (Scheme 15). However, the electron-donating properties of these complexes failed to further reveal passably due to their poor solubility in common solvents.³⁶



Scheme 15. Synthesis of abnormal C,N-chelating pyridylidene palladium and platinum complexes.

In 1995, Constable and Thompson reported the first example of the terpyridinium-derived N,N,C-chelating ruthenium complex $[(L^{tpy-1}H)Ru(tpy)](PF_6)_2$ where the cyclometalated pyridyl ring of ligand was protonated on the non-coordinated nitrogen atom (Figure 5).⁴¹

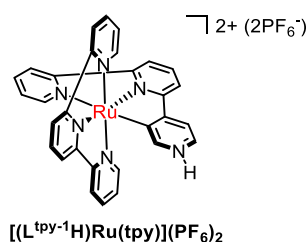
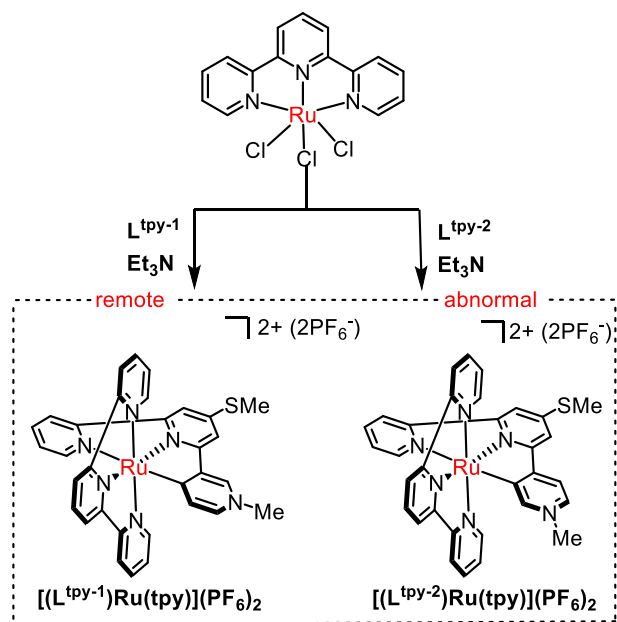


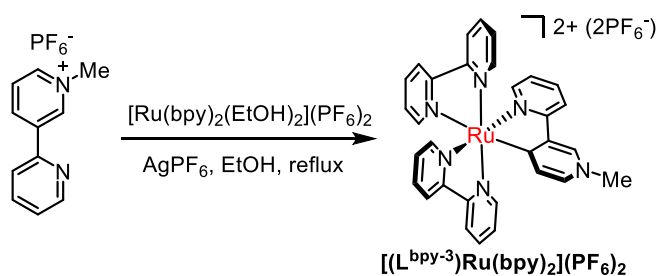
Figure 5. First terpyridinium-derived N,N,C-chelating ruthenium complex.

Following this work, Tanaka and co-workers described the synthesis and characterization of several terpyridinium-derived N,N,C- and N,C,N-chelating ruthenium complexes³⁷, including the first case of remote-type pyridylidene complex^{37a}. The corresponding complex $[(L^{tpy-2})Ru(tpy)](PF_6)_2$, which had a quaternized N-Me unit at the para-position of the bonded carbon atom, was afforded by the reaction of N''-methyl-4'-methylthio-2,2':6',3''-terpyridinium salt (L^{tpy-2}) with well-defined $[Ru(tpy)Cl_3]$ (Scheme 16, left). These authors also prepared and studied the electronic behavior of an analogous abnormal complex $[(L^{tpy-3})Ru(tpy)](PF_6)_2$ for comparison (Scheme 16, right).^{37a} The ¹³C NMR and CV studies indicated that the higher carbene character in the $[(L^{tpy-2})Ru(tpy)](PF_6)_2$ relative to that of the $[(L^{tpy-3})Ru(tpy)](PF_6)_2$.



Scheme 16. Synthesis of remote or abnormal pyridylidene ruthenium complexes.

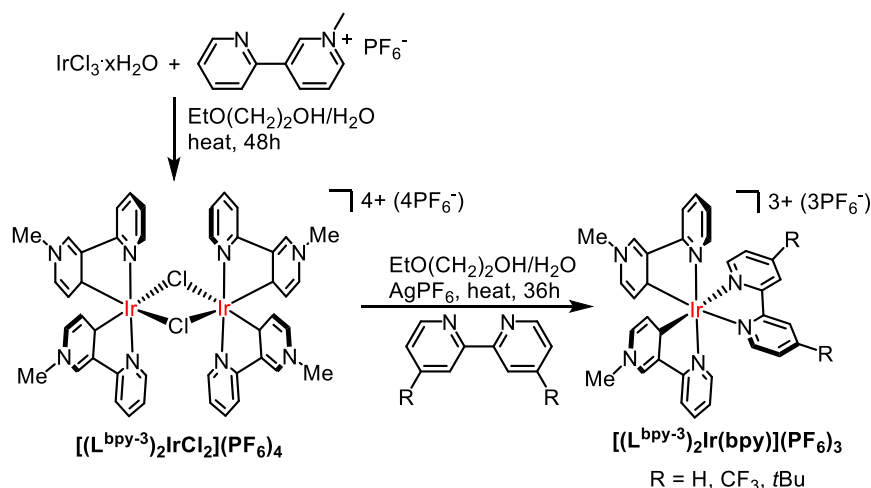
Later in 2005, the same authors reported the preparation of a similar remote-type octahedral ruthenium complex comprising of two bpy and one bidentate pyridyl-substituted pyridylidene ligands. The ligand *N*'-methyl-2,3'-bipyridinium salt ($\text{L}^{\text{bpy}-3}$) could easily coordinate to ready prepared $[\text{Ru}(\text{bpy})_2(\text{EtOH})_2](\text{PF}_6)_2$ to generate the desired complex $[(\text{L}^{\text{bpy}-3})\text{Ru}(\text{bpy})_2](\text{PF}_6)_2$ with high regioselectivity (Scheme 17).^{37c} The preferential metal-pyridylidene structure in $[(\text{L}^{\text{tpy}-2})\text{Ru}(\text{tpy})](\text{PF}_6)_2$ and $[(\text{L}^{\text{bpy}-3})\text{Ru}(\text{bpy})_2](\text{PF}_6)_2$ might be caused by a combination of the shielding effect by methyl substituent for the ortho positions and electronic favorite for C4 metalation.



Scheme 17. Highly selective synthesis of the normal and remote pyridylidene ruthenium complex.

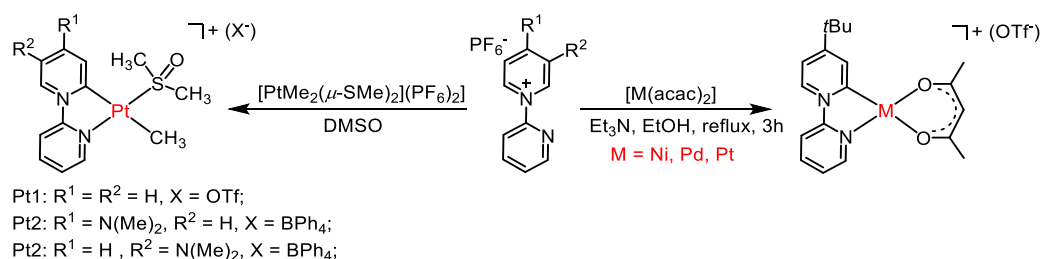
The same regioselectivity of the C-H metalation was found in the work of Coe, who presented a series of bis(*r*NHC)iridium complexes with the same bidentate ligand. Interestingly, the coordination of the $\text{L}^{\text{bpy}-3}$ to IrCl_3 hydrate rendered a cyclometalated chloride-bridged dimer,

which was allowed to transform to $[(L^{bpy-3})_2Ir(bpy)](PF_6)_3$ upon the elimination of chloride in the presence of silver hexafluorophosphate ($AgPF_6$) (Scheme 18). In these complexes, two 2-(pyridyl)-pyridylidene ligands provided a pseudo-octahedral coordination at the Ir center, where the pyridylidene rings lied in a cis topology.³⁹ⁿ



Scheme 18. Highly selective preparation of bis(*r*NHC)iridium complexes.

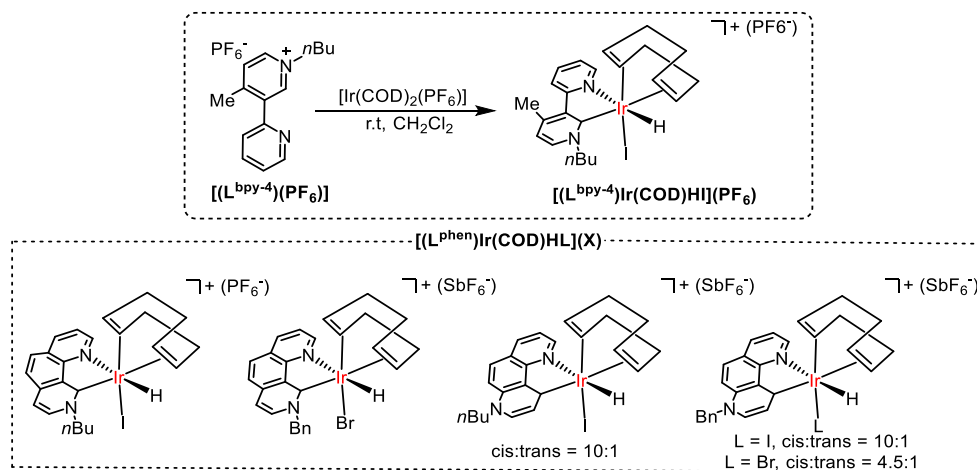
To reach the regioselectivity for C2-metallation, Bercaw and co-workers designed a type of pyridine functionalized bidentate pyridylidene ligands where the chelating donor site was installed on the functional group that is used for pyridine N-quaternization. As displayed in Scheme 19, the reaction of the N-(2-pyridyl)-pyridinium salts with metal precursors were allowed for the synthesis of a small range of normal pyridylidene complexes.³⁸



Scheme 19. Synthesis of C2-metallated pyridylidene complexes.

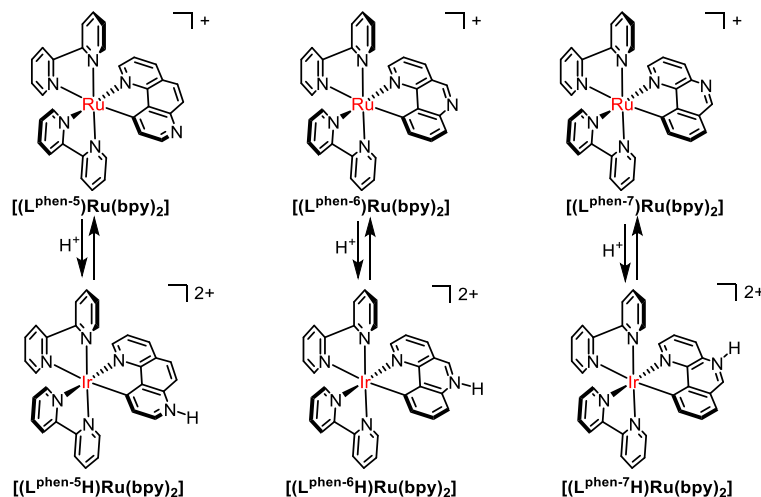
Another strategy to improve the regioselectivity was reported by Li and colleagues, which involved the use of pyridylidene ligands with blocking groups for the synthesis of the iridium(III) complexes that only contained normal or remote pyridylidene, respectively. C-H metalation of N'-n-butyl-4'-methyl-2,3'-bipyridinium salt $[(L^{bpy-4})(I)]$ with the $[Ir(COD)_2](PF_6)$ exclusively yielded an isomer $[(L^{bpy-4})Ir(COD)HI](PF_6)$ (Scheme 20, top). This route was

alternatively applied to the preparation of $[(L^{\text{phen}})\text{Ir}(\text{COD})\text{HL}](\text{X})$ hydrides based on 9-*n*Bu-1,9-phenanthroline ($L^{\text{phen-1}}$), 9-Bn-1,9-phenanthroline ($L^{\text{phen-2}}$), 7-*n*Bu-1,7-phenanthroline ($L^{\text{phen-3}}$) and 9-Bn-1,9-phenanthroline ($L^{\text{phen-4}}$) ligands (Scheme 20, bottom).^{39c}



Scheme 20. Highly selective synthesis of normal or remote pyridylidene iridium(III) complexes.

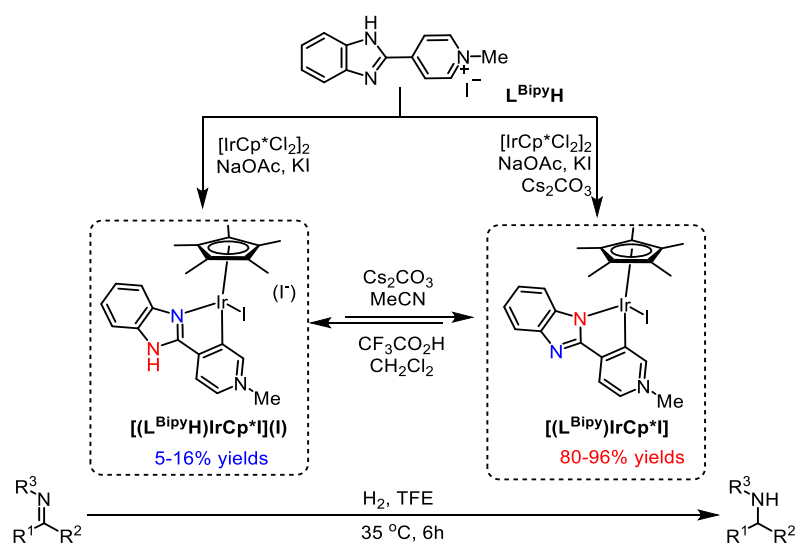
As mentioned above, quaternization of cyclometalated complexes has also been successfully utilized for the preparation of C,N-chelating pyridylidene complexes. For instance, Ehara et al. have addressed a small scope of ruthenium complexes bearing 1,5-phenanthroline, 1,6-phenanthroline, 1,7-phenanthroline ligands, which were prepared by reversible protonation of non-coordinated nitrogen of related cyclometalated ruthenium complexes (Scheme 21).³¹¹



Scheme 21. Synthesis of pyridylidene complexes via protonation of cyclometalated precursors.

To the best of our knowledge, only one example of (benzimidazole-2-yl)-pyridylidene complex was reported by Choudhury in 2016, representing another type of C,N-chelating

complexes. The 4-(1H-benzimidazol-2-yl)-1-methylpyridinium salt (L^{BipyH}) was composed of a neutral imine donor for directing cyclometalation with $[IrCp^*Cl_2]_2$. The generated corresponding iridium complex $[(L^{BipyH})IrCp^*I](I)$ contained an NH unit that underwent reversible deprotonation to yield $[(L^{Bipy})IrCp^*I]$ complex with an anionic amido-type Ir-N bond, which can be directly formed from starting iridium precursor and ligand in the presence of Cs_2CO_3 . This amido-Ir complex was demonstrated to be a more efficient catalyst for the catalytic hydrogenation of imine than its parent complex (Scheme 22).^{39o}



Scheme 22. Benzimidazole-pyridylidene iridium complexes for the hydrogenation of imine.

1.2 Well-established Chiral Octahedral Iron Complexes for Asymmetric Catalysis

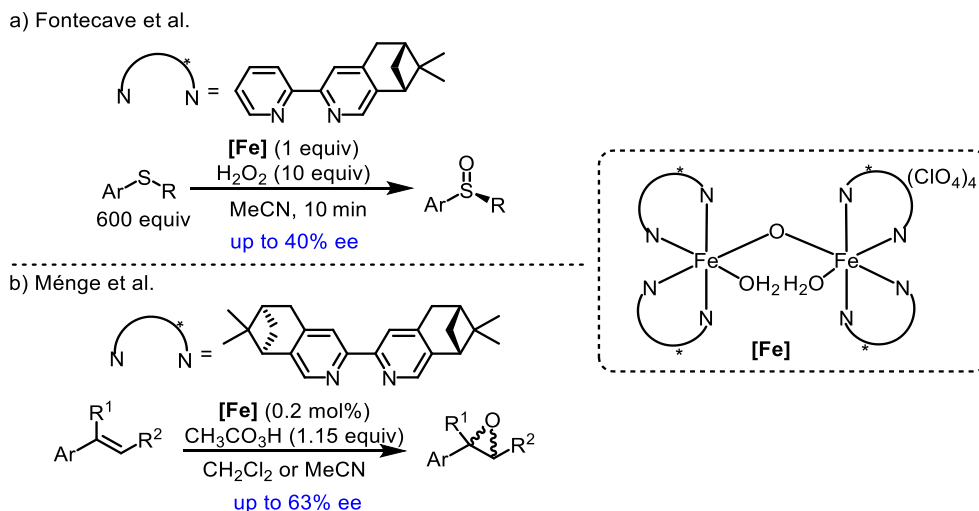
Over the past decades, the chemistry of asymmetric transition metal catalysis has implemented a remarkable development. In this respect, chiral transition metal catalysts based on precious metals like platinum, iridium, osmium, palladium, rhodium, and ruthenium have been established to be efficient for a wide range of asymmetric reactions. However, these noble metals are too expensive and generally rather toxic and thus bring a great challenge in terms of the applications of precious-metals catalysis in biological, pharmaceutical and agrochemical industries.⁴²⁻⁴⁵ Iron, the fourth most common element in the Earth's crust, has recently attracted increasing attention due to its low cost and low toxicity, the latter allowing high concentrations (>1300 ppm) of this metal in marketed drugs and other applications.^{46,47} In addition, iron complexes can be assembled with carbon-, nitrogen-, oxygen-, or phosphorus-based ligands.⁴⁸ Such a character along with several oxidation states of iron in a range of -2 - +6 make iron

complexes sustainable and promising catalysts for many types of asymmetric reactions.⁴⁹ Since the initial discovery of Groves and Myers in 1983, the design and application of chiral iron catalysts have been achieved significant growth.⁵⁰ However, controlling the diverse reactivity of iron complexes is difficult, since the complicated electronic states including both low- and high-spin states.⁵¹ As a result, the number of well-defined iron catalyst systems, especially for chiral octahedral iron catalysts, are still limited in comparison to those of precious metal systems.

This section mainly describes the advances made in the enantioselective transformation catalyzed by well-established chiral octahedral iron catalysts, including chiral bipyridine-based catalysts, chiral N4-based catalysts, chiral PNNP-based catalysts and chiral PNP-based catalysts.

1.2.1 Chiral Bipyridine-Based Catalysts

One of the first examples of a well-defined chiral non-racemic octahedral iron complex was reported by Fontecave et al. around 1997. In this oxo-bridged dinuclear architecture, as shown in Scheme 23a, each ferric center was coordinated with two chiral bipyridine ligands ((-)-4,5-pinene-2,2'-bipyridine) composing one bridged O atom and H₂O ligand. This iron complex was successfully employed for the asymmetric sulfide oxidation in the presence of hydrogen peroxide, although the enantioselectivities were low (< 40% ee).⁵² Later in 2007, a similar diiron complex reported by Ménge et al., bearing bis(4,5-pinene-2,2'-bipyridine), was used to catalyze enantioselective the epoxidation of alkenes, yielding corresponding epoxides with unsatisfying enantioselectivities (< 63% ee) (Scheme 23b).⁵³



Scheme 23. Chiral oxo-bridged dinuclear iron-catalyzed asymmetric catalysis.

Yamamoto and co-workers discovered that the enantioselectivities of epoxidations catalyzed by iron complexes of the bipyridine family can be improved by introducing chiral binaphthyl and bulky 3,5-dimethylphenyl substituents at the 1,10-phenanthroline ring. The reaction was performed by using the catalyst in situ generated from chiral ligand and iron salt. Although the single crystal study of the iron-ligands coordination only showed a pseudooctahedral C_2 -symmetric diastereomer, in which two cis-coordinated chiral phenanthroline ligands were complemented by one acetonitrile and two OTf ligands with one counterion (Figure 6), the actual structure of catalyst in the reaction medium was still unclear and therefore not further discussed here.⁵⁴

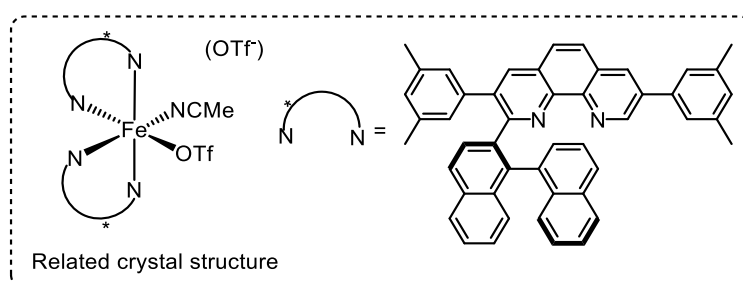


Figure 6. Octahedral iron complex based on chiral 1,10-phenanthroline ligands.

1.2.2 Chiral N₄-Based Catalysts

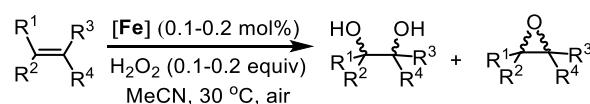
Another type of this area are chiral N₄-based iron complexes, which can be easily modified by changing both the chiral amino groups and the pyridine moieties of aminopyridine ligands and therefore represent an advantageous alternative to porphyrin-based iron complexes in the

field of catalysis.

An early example of enantioselective N₄-based iron catalysis was reported by Que and co-workers in 2001 and involved first example of an iron-catalyzed asymmetric cis-dihydroxylation of alkenes. Chiral iron(II) complexes, [α -(L^{N₄₋₁})Fe(OTf)₂] and [β -(L^{N₄₋₁})Fe(OTf)₂], were utilized as the catalysts and H₂O₂ as the oxidant, gave corresponding diol-products in low to high enantioselectivities.⁵⁵ In order to improve the enantioselectivity of this reaction, a series of catalysts were next synthesized and evaluated. Compared to the [α -Fe(L^{N₄₋₂})(OTf)₂] and [α -Fe(L^{N₄₋₃})(OTf)₂] as well as previous β -Fe(L^{N₄₋₁})(OTf)₂ catalysts (L^{N₄₋₂} = 1,1'-bis(pyridin-2-ylmethyl)-2,2'-bipyrrolidine, L^{N₄₋₃} = 1,1'-bis(quinolin-2-ylmethyl)-2,2'-bipyrrolidine), the [α -Fe(L^{N₄₋₄})(OTf)₂] exhibited the more efficient not only cis-diol selectivity, but also asymmetric induction with up to 97% ee. This was most likely due to a more crowded ligand field of α -substituents and the more rigid bipyrrolidine backbone, the latter bringing about a superior cis- α topology (Scheme 24a).⁵⁶

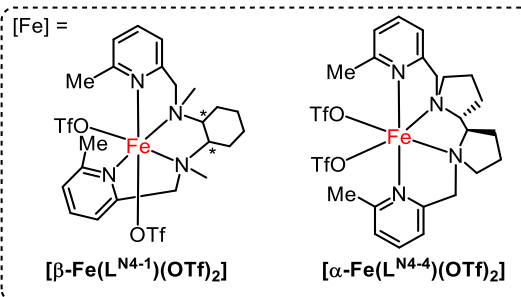
In parallel to the above catalytic system, Che et al. also demonstrated that the cis-diols could be conveniently observed by an iron-catalyzed dihydroxylation of alkenes applying H₂O₂ as an oxidant and reaction in MeOH at -27 °C. The catalyst [α -(L^{N₄₋₅})Fe(OTf)₂] showed good tolerance for a wide range of (*E*)-alkenes and terminal alkenes, efficiently affording the related products in gratifying yields (68-99%) and enantioselectivities (82->99% ee). However, for the reaction of (*Z*)-alkenes, the enantioselectivities were low to moderate (23-83% ee) with moderate yields (53-81%). Based on their experiments, including ¹⁸O-labeling, UV/Vis, electron paramagnetic resonance (EPR) spectroscopy, ESI-MS analyses, and Density functional theory (DFT) calculations studies, the authors revealed the participation of a chiral [Fe^{III}-OOH] active species in the enantioselective formation of the two C-O bonds (Scheme 24b).⁵⁷

a) Que et al.

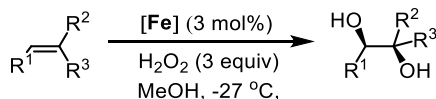


$[\text{Fe}] = [\beta\text{-Fe}(\text{L}^{\text{N}4\text{-}1})(\text{OTf})_2]$:
5.5:1 - 11.2:1; 3-82% ee

$[\text{Fe}] = [\alpha\text{-Fe}(\text{L}^{\text{N}4\text{-}4})(\text{OTf})_2]$:
13:1 - >75:1; 68-97% ee

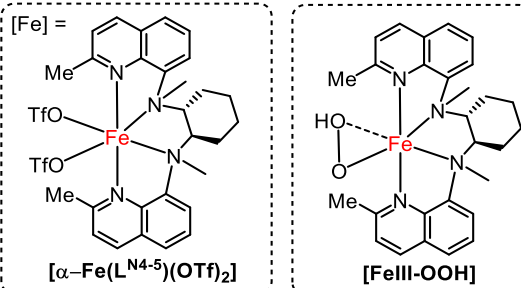


b) Che et al.



(E)-alkenes and terminal alkenes:
68-99% yields and 82->99% ee

(Z)-alkenes:
53-81% ee; 23-83% ee

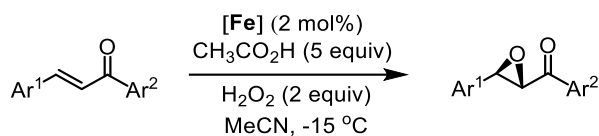


Scheme 24. Chiral N4-Fe-catalyzed asymmetric *cis*-dihydroxylation.

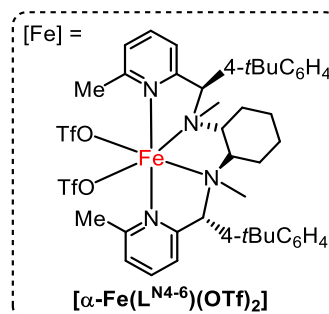
In another context, Sun and co-workers in 2011 reported that the iron complex $[\alpha\text{-}(\text{L}^{\text{N}4\text{-}6})\text{Fe}(\text{OTf})_2]$ could smoothly promote the epoxidation of a variety of chalcones in the presence of hydrogen peroxide and acetic acid in 52-90% yields and moderate ee values (74-87% ee) (Scheme 25a). However, this protocol remained a limited substrate scope employing only with the α,β -enones.⁵⁸

Later in 2012, Talsi et al. reported a similar reaction for several alkenes using $[\alpha\text{-}(\text{L}^{\text{N}4\text{-}2})\text{Fe}(\text{OTf})_2]$ as the catalyst, hydrogen peroxide (H_2O_2) as oxidant and carboxylic acid as an additive. The best results were afforded with more sterically demanding 2-ethylhexanoic acid (EHA) (98% yield and 86% ee) (Scheme 25b, for catalyst on the left).⁵⁹ In a further example, they developed an oxo-bridged Fe(III) dimer $[\alpha\text{-}(\text{L}^{\text{N}4\text{-}7})\text{Fe}(\text{OH})_2](\text{OTf})_4$ as a catalyst and 2-ethylhexanoic acid as co-ligand for epoxidation of chalcone, producing the desired epoxide in 73% yield and 84% ee with H_2O_2 as an oxidant while 78% yield and 82% ee with tert-butyl hydroperoxide ($t\text{BuO}_2\text{H}$) (Scheme 25b, for catalyst on the right).⁶⁰

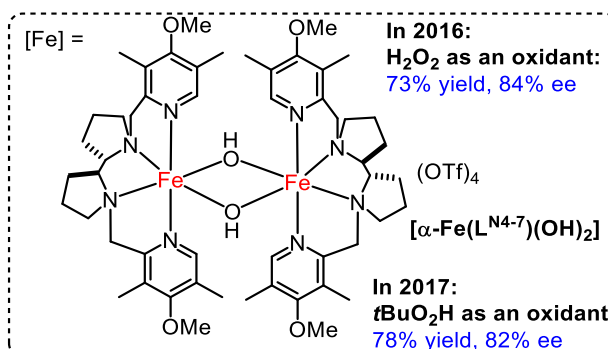
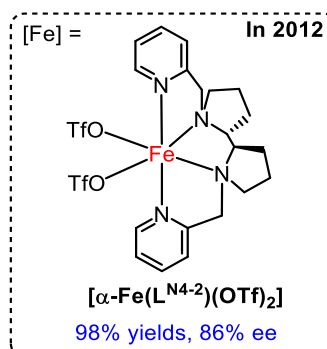
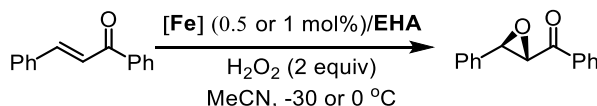
a) Sun et al.



52-90% yields, 74-87% ee

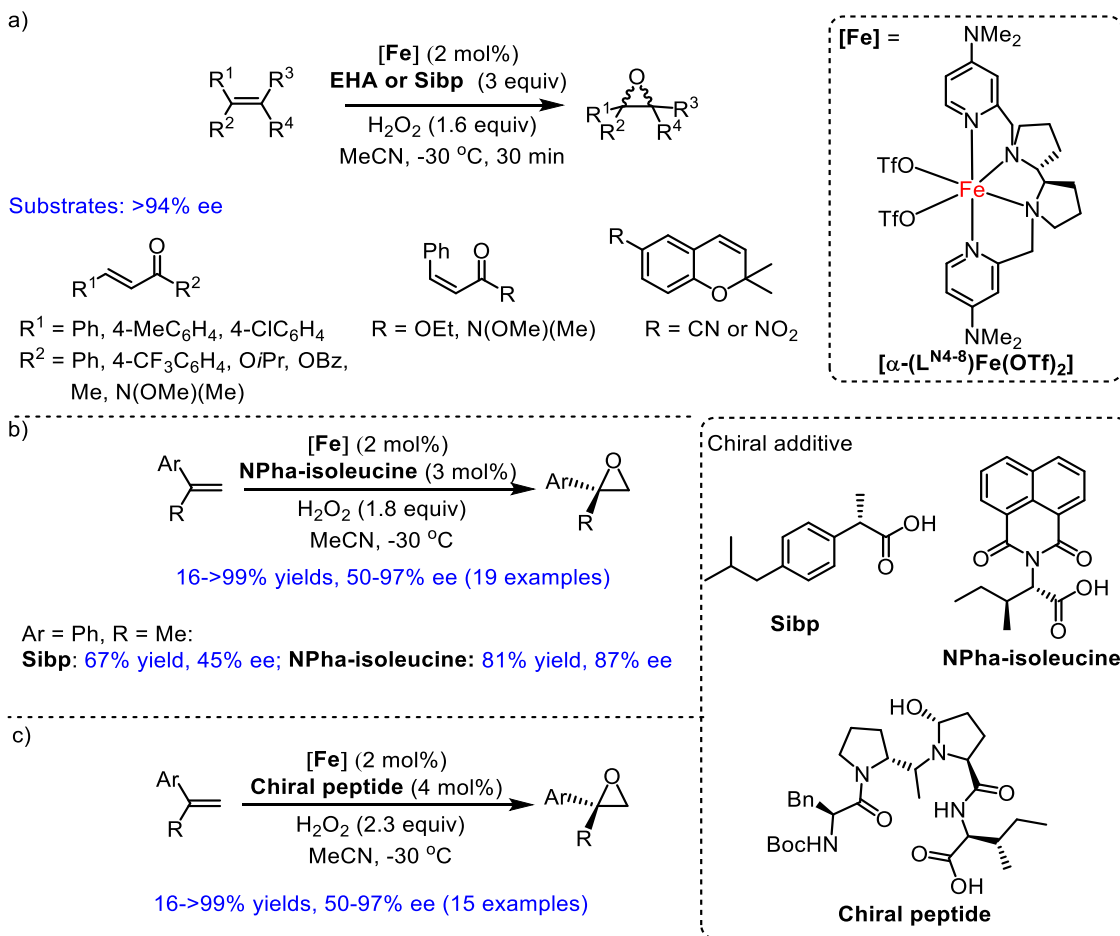


b) Talsi et al.

**Scheme 25.** Chiral N₂Py₂-Fe/organic acid-catalyzed asymmetric epoxidation of α,β -enones.

Costas and co-workers have made great contributions towards the highly enantioselective epoxidation of both activated and non-activated alkenes. The yields and enantioselectivities of epoxidations catalyzed by the N₄-iron family, developed in 2013, could be enhanced by presenting electron-donating substituents at the pyridine moieties of the N₄ ligand.⁶¹ The better results were achieved with complexes $[\alpha\text{-}(\text{L}^{\text{N}4\text{-}7})\text{Fe}(\text{OTf})_2]$ and $[\alpha\text{-}(\text{L}^{\text{N}4\text{-}8})\text{Fe}(\text{OTf})_2]$, bearing 3,5-dimethyl-4-methoxypyridyl and N,N-dimethylaminopyridyl rings, respectively. The latter combined with an additive of EHA or S-ibuprofen (Sibp), displaying generally high enantioselectivities of more than 94% ee for most of the substrates (Scheme 26a).^{61a} Notably, the reaction of challenging series of α -alkyl-substituted styrenes catalyzed by $[\alpha\text{-}(\text{L}^{\text{N}4\text{-}8})\text{Fe}(\text{OTf})_2]$ with a bulkier chiral additive N-Naphthalic anhydride (NPha) isoleucine and H₂O₂ in the acetonitrile at -30 °C led to corresponding epoxides in low to excellent yields (16-→99%) with moderate to remarkable enantioselectivities (50-97% ee) (Scheme 26b).^{61b} Further work in this area developed in 2017 resulted in a more effective process combining a chiral peptide co-ligand and the $[\alpha\text{-}(\text{L}^{\text{N}4\text{-}8})\text{Fe}(\text{OTf})_2]$ catalyst. The corresponding epoxides were afforded in

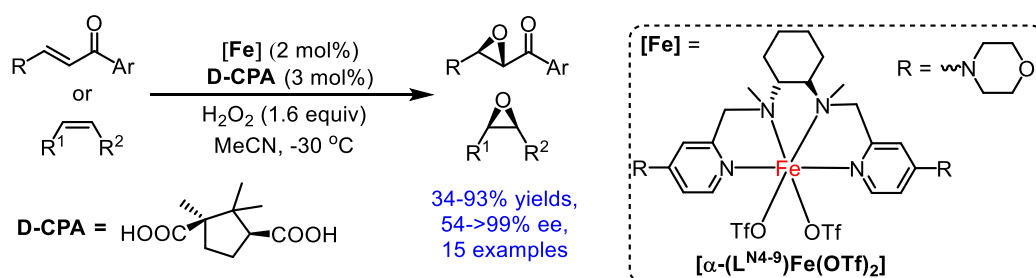
moderate to quantitative yields (66-99%) with moderate to very good enantioselectivities (64-92% ee) (Scheme 26c).⁶²



Scheme 26. $\text{N}_2\text{Py}_2\text{-Fe}$ /organic acid-catalyzed enantioselective epoxidation.

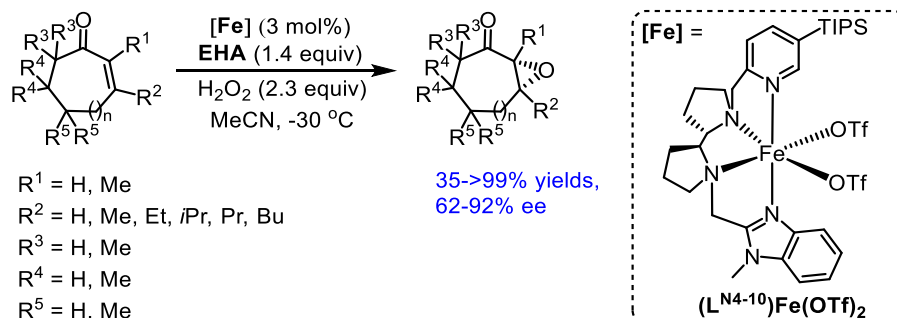
Sun and co-workers extended this method by introducing a new catalytic system combined with iron complex $[\alpha\text{-(L}^{\text{N4-9}}\text{)Fe(OTf)}_2]$, featuring morpholinyl rings on the pyridine moieties, and chiral additive D-(+)-camphoric acid (**D-CPA**). The epoxidations of α,β -unsaturated ketones having different electronic characters on the phenacyl or phenyl groups of alkenes proceeded in comparable yields (34-93% yield) and moderate to outstanding enantioselectivities (54->99% ee) (Scheme 27).⁶³ Apparently, the asymmetric inductions were impacted by donor properties of the amino-pyridine ligand and the structure of the carboxylic acid. The involved investigation was developed by Talsi and others based on EPR spectroscopy studies and catalytic data. The iron complexes constructing a ligand with donor substituents or the carboxylic acid with tertiary α -carbon atoms exhibited generally small g-factor anisotropy and generated an active oxo-iron $[\text{Fe(IV)=O}]$ species in the reaction, which ensured higher

enantioselectivity in the epoxidation of electron-deficient olefins.^{59,60}



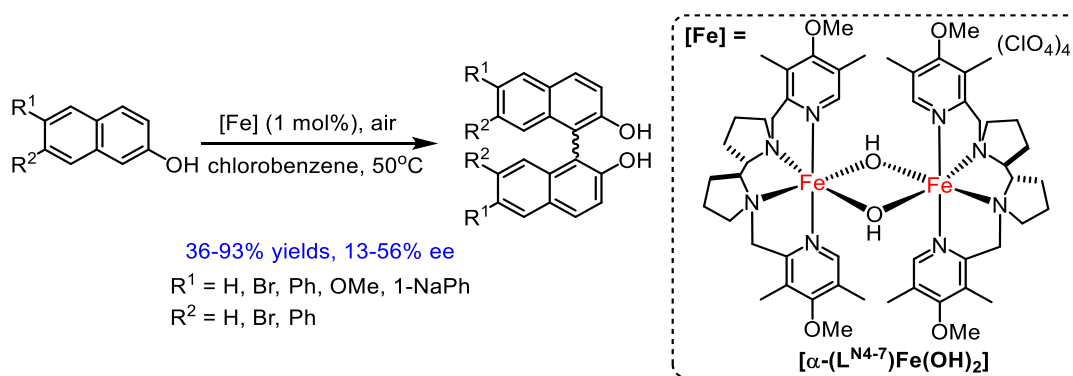
Scheme 27. $\text{N}_2\text{Py}_2\text{-Fe/D-CPA}$ -catalyzed enantioselective epoxidation.

Costa and co-workers also described the synthesis and catalytic application of a class of C_1 -symmetric iron complexes. The catalytic activity was subsequently evaluated in the enantioselective epoxidation of challenging cyclic α,β -enones. The iron complex $[\alpha\text{-}(\text{L}^{\text{N}4\text{-}10})\text{Fe}(\text{OTf})_2]$, composing a triisopropylsilyl (TIPS) substituted picoline, an N-methyl benzimidazole ring, and a chiral bipyrrolidine group, established to be the best catalyst, leading to corresponding epoxides in moderate to excellent yields and enantioselectivities (35->99% yields, 62-92% ee) (Scheme 28).⁶⁴



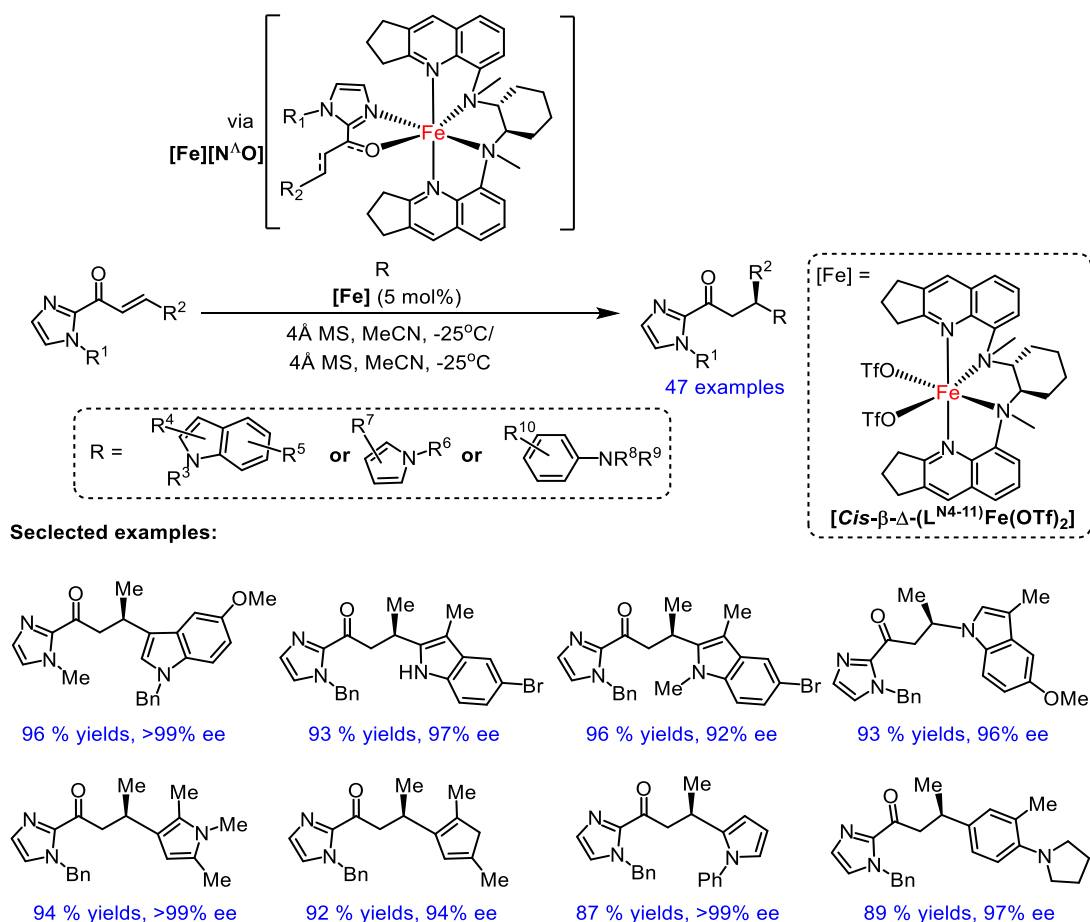
Scheme 28. C_1 -symmetric iron catalyst/EHA-catalyzed enantioselective epoxidation of challenging cyclic α,β -enones.

In another area, Bryliakov and co-workers disclosed an example of asymmetric aerobic-coupling of substituted 2-naphthols in the presence of catalytic amounts $[\alpha\text{-}(\text{L}^{\text{N}4\text{-}7})\text{Fe}(\text{OH})_2](\text{ClO}_4)_4$ as the catalyst and air as a green oxidant in chlorobenzene at $50\text{ }^\circ\text{C}$ to give chiral BINOLs in good yields (36-93%) although with low enantioselectivities (13-56% ee) (Scheme 29).⁶⁵



Scheme 29. $\text{N}_2\text{Py}_2\text{-Fe}$ -catalyzed asymmetric coupling of 2-naphthols.

Very recently, chiral iron complexes containing N_4 ligands were exploited to promote the Friedel-Crafts alkylation of indoles, pyrroles and N,N -disubstituted anilines with 2-acyl imidazoles by Che and co-workers. A series of chiral N_2Py_2 ligands were allowed to prepare the corresponding high spin iron complexes. Here, the chiral ligand coordinated to the iron, which generated an octahedral scaffold and at the same time induced a stereogenic metal center. It was demonstrated that $[\text{cis-}\beta\text{-}\Delta\text{-(L}^{\text{N}4\text{-}11}\text{)Fe(OTf)}_2]$ bearing fused cyclopentane moieties on the quinoline rings was the best catalyst and could catalyze the reactions delivering the related products in high yields and enantioselectivities (87-98% yields, 95-99% ee). The proposed catalytic cycle began with chelation-activation between 2-acyl imidazoles and iron complex to give $[\text{Fe}][\text{N}^{\text{A}}\text{O}]$ intermediate. Enantioselective addition of nucleophile into $[\text{Fe}][\text{N}^{\text{A}}\text{O}]$ provided the final product and released the active iron catalytic species (Scheme 30).⁶⁶



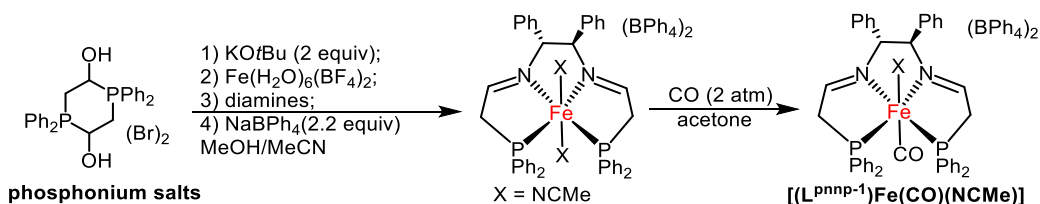
Scheme 30. Iron-catalyzed alkylation reactions.

1.2.3 Chiral PNNP-Based Iron Catalysts

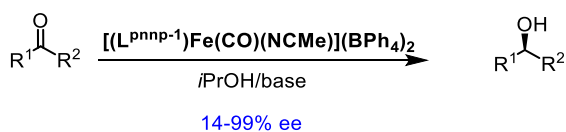
Recently, chiral PNNP compounds including bis(imine)diphosphine, bis(amine)diphosphine or imine(amine)diphosphine have been realized as one of the important ligands for precious transition metals, especially for ruthenium⁶⁷, in asymmetric catalysis. The first example of the catalytic application of the well-established octahedral chiral PNNP-based iron complex was developed by Morris and co-workers in 2009. The reaction of phenyl substituted phosphonium salts, base (*t*BuOK), iron precursor $[\text{Fe}(\text{H}_2\text{O})_6(\text{BF}_4)_2]$ and 1,2-diphenylethane-1,2-diamine in MeOH/MeCN to provide C_2 -symmetric iron complex [*trans*- $\text{L}^{\text{PNNP-1}}\text{Fe}(\text{NCMe})_2](\text{BPh}_4)_2$. For the preparation of the carbonyl iron complex, [*trans*- $\text{L}^{\text{PNNP-1}}\text{Fe}(\text{CO})(\text{NCMe})](\text{BPh}_4)_2$ was synthesized by ligands exchange reaction of [*trans*- $\text{L}^{\text{PNNP-1}}\text{Fe}(\text{NCMe})_2](\text{BPh}_4)_2$ under a CO atmosphere in the acetone (Scheme 31a). The catalytic activity of this carbonyl catalyst was screened in the asymmetric transfer hydrogenation (ATH)

of acetophenone derivative in the presence of isopropanol and base at 22 °C. The reduction of the ketones proceeded with low to excellent enantioselectivities (14-99% ee) (Scheme 31b).⁶⁸

a) Synthesis of bis(imine)diphosphine iron complex

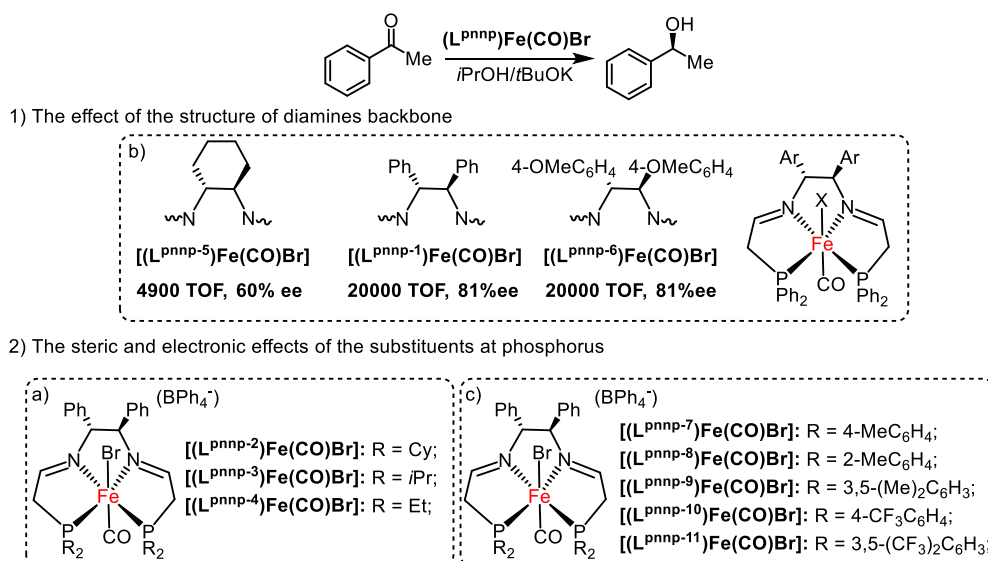


b) Iron-catalyzed ATH reaction



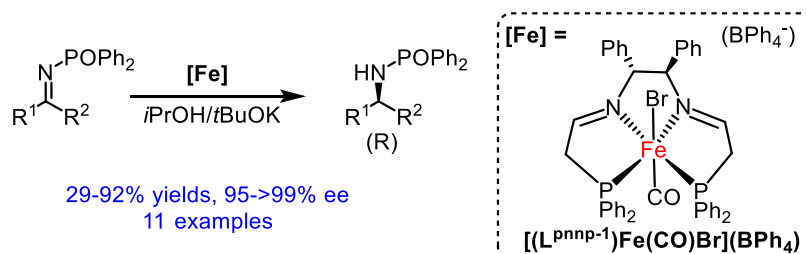
Scheme 31. Synthesis and catalytic application of bis(imine)diphosphine iron complex.

As an extension, iron bromide complexes $[(L^{pnnp})Fe(CO)Br](BPh_4)$ featuring different alkyl group on the phosphorus atoms, were allowed for template synthesis and tested their reactivity. However, only $[(L^{pnnp-4})Fe(CO)Br](BPh_4)$ could produce the (*R*)-1-phenylethanol with 60% ee (Scheme 32a).⁶⁹ Meanwhile, the effect of the structure of the diamine backbone was studied. The iron complexes $[(L^{pnnp-1})Fe(CO)Br](BPh_4)$ and $[(L^{pnnp-5})Fe(CO)Br](BPh_4)$, bearing the 1,2-diphenylethylenediamine and 1,2-bis(4-methoxyphenyl)ethylenediamine, proved to be the better catalysts compared to $[(L^{pnnp-4})Fe(CO)Br](BPh_4)$, leading to desired product in high TOF (20000) and enantioselectivities (81 and 82% ee, respectively) (Scheme 32b).⁷⁰ They next shifted their attention to the aryl substituent at the phosphine units of PNNP ligand. Replacing the phenyl group (L^{pnnp-1}) with a 3,5-dimethylphenyl group (L^{pnnp-9}) provided the ATH product with 30000 h⁻¹ TOF and 90% ee, which elucidated to be a most active catalyst (Scheme 32c).⁷¹



Scheme 32. Chiral bis(imine)diphosphine-Fe-catalyzed ATH reactions

Later in 2012, they further explored the activity of this type of iron catalysts in the reduction of imines. More promising are the results for the same reaction catalyzed by $[(L^{pnnp-1})Fe(CO)Br](BPh_4^-)$, which afforded the reduced amine in low to high yields with the ee in the range of 95% to >99% (Scheme 33).⁷²



Scheme 33. Chiral bis(imine)diphosphine-Fe-catalyzed ATH reaction of imines.

The detailed experimental and computational mechanistic studies and suggested that the catalytic cycle in these reactions might be incited by an active iron amide and iron hydride intermediates. The postulated mechanism started with C–H activation of $[(L^{pnnp})Fe(CO)Br]$ by isopropoxide to give an iron amide species $[Fe-N]$ and isopropanol as well as related acetone. Hydride addition of isopropanol toward this one imine linkage of the bis(imine)diphosphine ligand of the imide species generated an iron hydride intermediate $[HFeNH]$, which subsequently reacted with ketones to produce the corresponding alcohols and regenerated the iron amide species. These active intermediates could be trapped with hydrogen chloride in ether to provide imine(amine)diphosphine complex $[(L^{NNH})Fe(CO)Cl]$, which was demonstrated to

be a more active catalyst than $[(L^{pnnp})Fe(CO)Br]$ (Figure 7).⁷¹

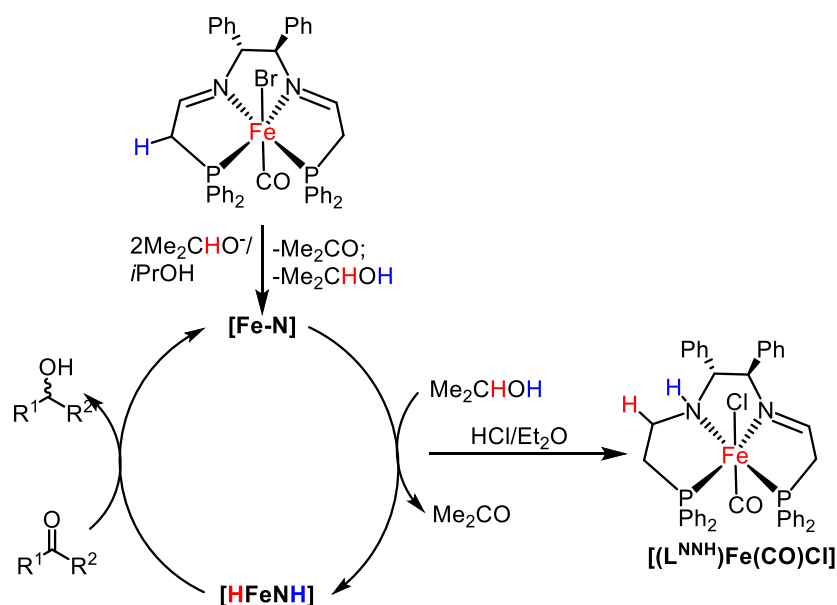


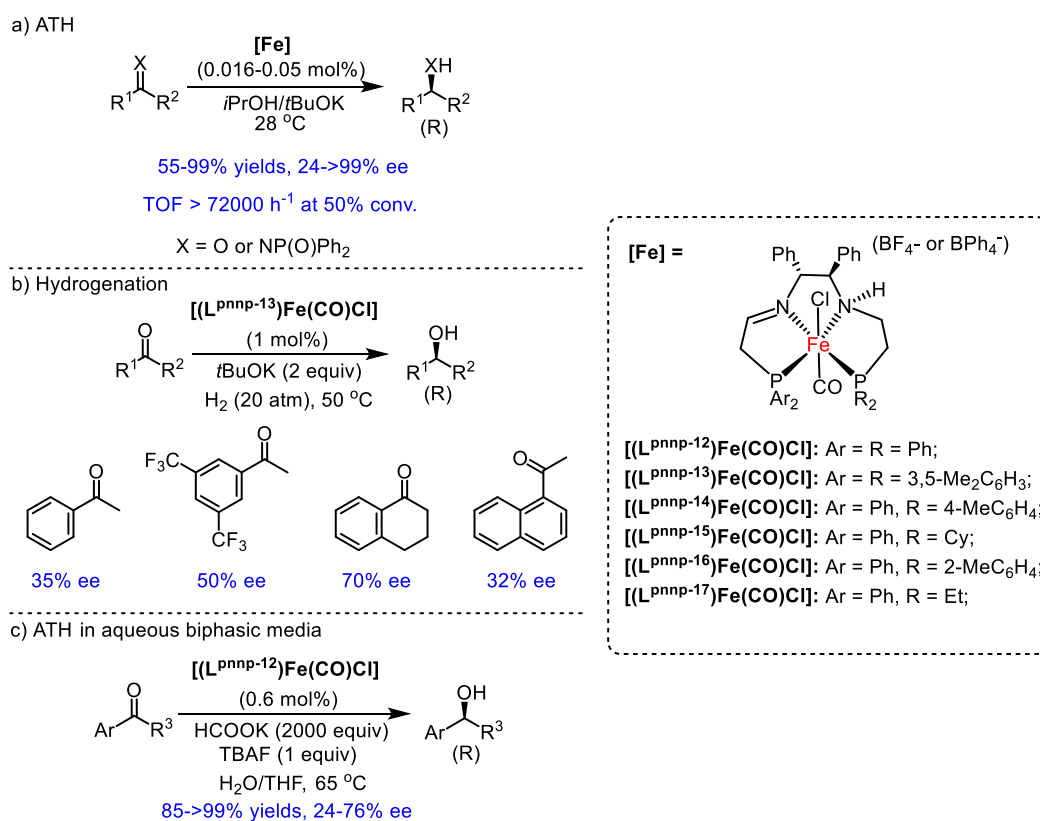
Figure 7. Proposed mechanism of bis(imine)diphosphine-Fe-catalyzed ATH reaction of ketones.

Based on their successful mechanistic study, later in 2013, the same authors described the synthesis of a novel unsymmetrical chiral amine(imine)diphosphine iron complex, containing an N–H moiety in the tetradentate ligand, with the hope for improvement concerning activity and asymmetric induction. As shown in Scheme 34a, three iron complexes, $[(L^{pnnp-12})Fe(CO)Cl]$ - $[(L^{pnnp-14})Fe(CO)Cl]$, were performed for enantioselective transfer hydrogenation of ketones and imines. The rate of conversion at $28^\circ C$ was higher than those reported bis(imine)diphosphine complexes, which provided the turnover frequencies (TOF) of up to $720,000 h^{-1}$ at 50% conversion. The desired alcohol products were obtained in moderate to excellent yields (55-99%) with low to excellent enantioselectivities (24->99% ee). Notably, the previous hypothesis of the catalytic mechanism was clarified by the spectroscopic detection of iron hydride and amide intermediates.⁷³

Their further work demonstrated that the iron catalyst, $[(L^{pnnp-13})Fe(CO)Cl]$, could be applied not only in ATH reactions but also the asymmetric hydrogenation of ketones in the presence of the base under the hydrogen atmosphere (10-20 atm). Under this process, chiral alcohols were obtained with low to moderate enantioselectivities (29-70% ee).⁷⁴ Later, related iron complexes $[(L^{pnnp-15})Fe(CO)Cl]$ - $[(L^{pnnp-17})Fe(CO)Cl]$ were prepared to evaluate the role

of steric effects of the phosphine. The catalysts $[(L^{pnnp-15})Fe(CO)Cl]$ and $[(L^{pnnp-16})Fe(CO)Cl]$, supporting more sterically hindered groups (Cy and 2-MeC₆H₄ compared to Et), resulted in effective asymmetric induction (Scheme 34b).⁷⁵

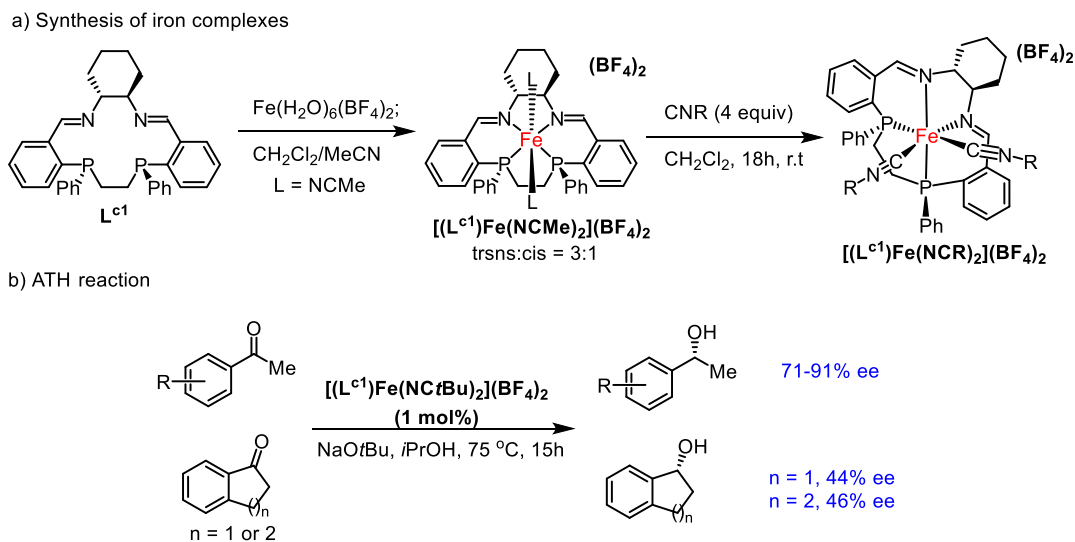
It was found that, as for the proton and hydride source, the water/potassium formate replacing the isopropanol/*t*BuOK could also promote ATH reactions. Under aqueous biphasic media (H₂O/THF = 1:1) at 65 °C, the corresponding chiral alcohols were obtained (85->99%) in the presence of 0.6 mol% $[(L^{pnnp-12})Fe(CO)Cl]$ and a phase transfer catalyst like TBAF in excellent yields, although the enantioselectivities were low to moderate (24-76% ee) (Scheme 34c).⁷⁶



Scheme 34. Chiral amine(imine)diphosphine iron-catalyzed transformation. (a) ATH. (b)Hydrogenation. (c) ATH in aqueous biphasic meida.

Earlier in 2014, Mezzetti group reported the synthesis of other PNNP-based iron catalysts and their catalytic application in enantioselective transfer hydrogenation of ketones.⁷⁷ The coordination of $[Fe(H_2O)_6](BF_4)_2$ precursor with a macrocycle PNNP diamine ligand, afforded the diamagnetic bis-(acetonitrile) complex $[L^cFe(MeCN)_2](BF_4)_2$. The bis-(acetonitrile) complex next reacted with different isocyanides to provide a small library of stable

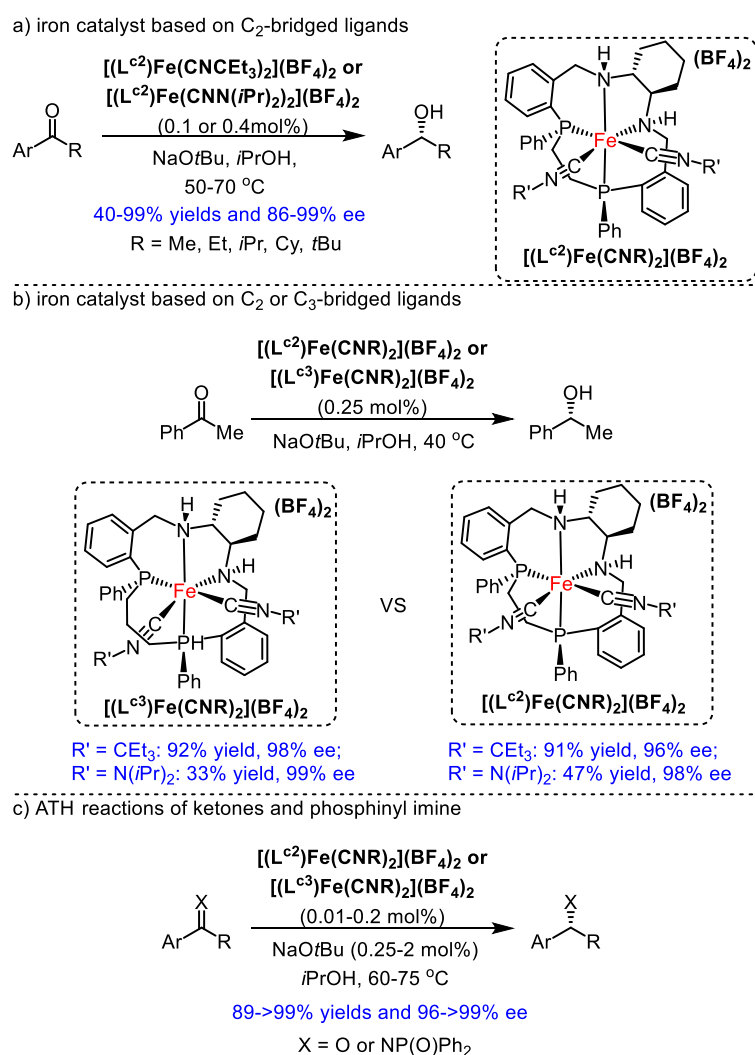
bis(isonitrile)-iron catalysts, in which the Λ -[*cis*- β -(L^{c1})Fe(CNR)₂](BF₄)₂ were separated as the major isomers (*cis* : *trans* \approx 93:7) (Scheme 35a). The iron catalyst [Λ -*cis*- β -(L^{c1})Fe(CN*t*Bu)₂](BF₄)₂ was chosen as the best catalyst of choice and reduced a range of aromatic ketones with high to excellent enantioselectivities (71-91% ee) in the presence of NaO*t*Bu (4 mol%). However, the reaction of cyclic aromatic ketones only provided the reduced product with moderate enantioselectivities (44% and 46% ee) (Scheme 35b).



Scheme 35. Synthesis and catalytic application of bis(imine)diphosphine iron complexes.

Further improvements in these iron-catalyzed asymmetric transfer hydrogenation achieved by the same authors in 2015 and concerned with the use of the new generation of sterically demanding catalysts composing the diamine PNNP ligands and bulkier substituents of isonitrile ligands, such as CNCEt₃ or CNN(*i*Pr)₂.⁷⁸ Using a low catalytic amount of [*cis*- β -(L^{c2})Fe(CNCEt₃)₂](BF₄)₂ or [*cis*- β -(L^{c2})Fe(CNN(*i*Pr)₂)₂](BF₄)₂ (0.1 or 0.4 mol%), this reduced process in isopropanol of a broad scope of aryl alkyl ketones was highly enantioselective to give the related alcohol products, in a range of 86% to 99% ee, in the presence of 1 mol% of NaO*t*Bu at 50, 60, or 70 °C. The higher reaction temperature and catalyst loading was required to afford the prominent enantioselectivities (97-98% ee) for the reaction of ketones formulating second or tertiary alkyl groups (R = *i*Pr, Cy, *t*Bu) (Scheme 36a).^{78a} It was worth mentioning that another type of iron catalysts [*cis*- β -(L^{c3})Fe(CNR)₂](BF₄)₂, bearing C₃-linker diamine ligands, could also be individually separated as the single isomers in the presence of catalytic amount of 1,8-diazabicyclo[5.4.0]undec-7-ene (DBU) and yielded the (R)-

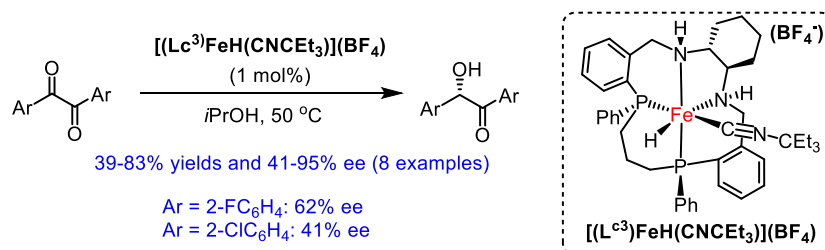
phenylethanol incomparable activities and enantioselectivities with those of C₂-bridge complexes $[\text{cis-}\beta\text{-(L}^{\text{c}2}\text{)Fe(CNR)}_2\text{]}\text{(BF}_4\text{)}_2$ (Scheme 36b).^{78b} These complexes were further demonstrated to be highly efficient catalysts for the reaction of some ketones including one example of phosphinyl imine (89→99% yields and 96→99% ee). For example, the catalyst $[\text{cis-}\beta\text{-(L}^{\text{c}3}\text{)Fe(CNCET}_3\text{)}_2\text{]}\text{(BF}_4\text{)}_2$ could provide the (R)-phenylethanol without any erosion of yield and enantioselectivity (91.8% yield and 96.3% ee) with a significantly low catalyst loading of 0.01 mol% and lower quantities of NaOtBu (0.25 mol%) and reaction in isopropanol at 60 °C (Scheme 36c).⁷⁹



Scheme 36. Iron-catalyzed asymmetric transfer hydrogenation of ketones or imines.

In contrast to the iron-catalyzed ATH reactions via the participation of the base, Mezzetti, and De Luca reported an intriguing example of the reduction of benzyls under a base-free process using an iron hydride isonitrile complex as a catalyst. Under these processes,

corresponding chiral benzoin products were obtained in both moderate to high yields and enantioselectivities using catalytic amounts of $[(Lc^3)FeH(CNCEt_3)](BF_4)$ (1 mol%) and isopropanol as a hydrogen source at 50 °C. Compared to the unsubstituted benzoin substrate, the benzoin substrates with ortho substituents led to related products with much lower enantioselectivities ranging from 41% to 62% ee (Scheme 37).⁸⁰



Scheme 37. Iron-catalyzed enantioselective transfer hydrogenation of benzoin.

In addition, Zirakzadeh and Kirchner explored another kind of PNNP-iron catalysts containing homochiral ferrocene moieties at the ligand backbone, which were distinctive to those featuring the chirality at the bridge of ligands. These catalysts could facilitate the asymmetric transfer hydrogenation of several ketones, albeit both the activities and enantioselectivities were low (16-44% yields, <20% ee) (Figure 8).⁸¹

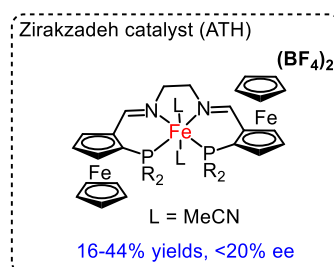


Figure 8. Chiral ferrocene-based bis(imine)diphosphine iron catalyst.

1.2.4 Chiral PNP-Based Catalysts

In a similar vein, Morris et al. also demonstrated that another type of PNP-based, (imine)diphosphine or (amine)diphosphine, iron complexes could be successfully applied for the enantioselective hydrogenation of aryl alkyl ketones, leading to resulted chiral alcohols in low to excellent yields with good enantioselectivities (Figure 9).^{82,83}

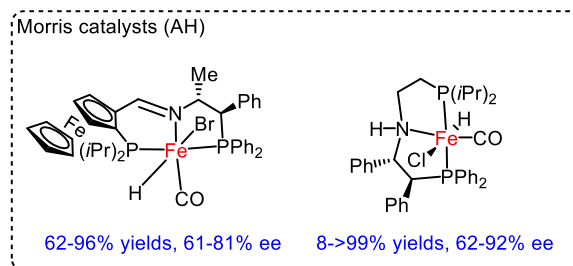


Figure 9. PNP-based iron catalysts.

1.3 Aim of work

Chemists have been fascinated with asymmetric transition metals catalysis for more than 50 years. The Nobel Prize to Knowles, Noyori, and Sharpless for their contributions to asymmetric hydrogenation and oxidation in 2001 demonstrates that asymmetric transition-metal catalysis is widely used in organic chemistry research. Much of the work in this area has been performed by using chiral transition metal catalysts that contain carefully modified chiral organic ligands.⁸⁴ Recently, an alternative to this modular chiral-ligand-plus-metal design had emerged in which chiral transition metal catalysts exclusively consist of achiral ligands.^{85,86} In this approach, the essential overall chirality formally originates from a stereogenic metal center (Figure 10a). Depending on the helical twist of the achiral ligands, the metal center can adopt either a left- (Λ enantiomer) or right-handed (Δ enantiomer) propeller. Proof-of-principle for such chiral-at-metal catalysts, which are synthetically accessible via auxiliary-mediated resolution, has been demonstrated recently for the metals iridium,⁸⁷ rhodium,^{88,89} and ruthenium^{90,91} by Meggers and others (Figure 10b). Importantly, such kind of chiral-at-metal complexes has been applied and provided excellent catalytic activity and stereoselectivity for a broad range of asymmetric catalysis, including asymmetric Lewis Acid catalysis,⁸⁵⁻⁹¹ asymmetric photoredox catalysis,⁹² asymmetric electrocatalysis,⁹³ and asymmetric C-H functionalization reaction.⁹⁴ These outcomes can be considered as a synergistic interplay of the electronic and steric features of achiral ancillary ligands of the catalysts and the nature of their stereogenic metals. Hence, it is encouraged to explore new chiral-at-metal catalysts based on benefit ligands for new catalytic reactions. Furthermore, developing less costly and less toxic earth-abundant metal catalysts to replace and complement the precious metal catalysts is greatly desirable.

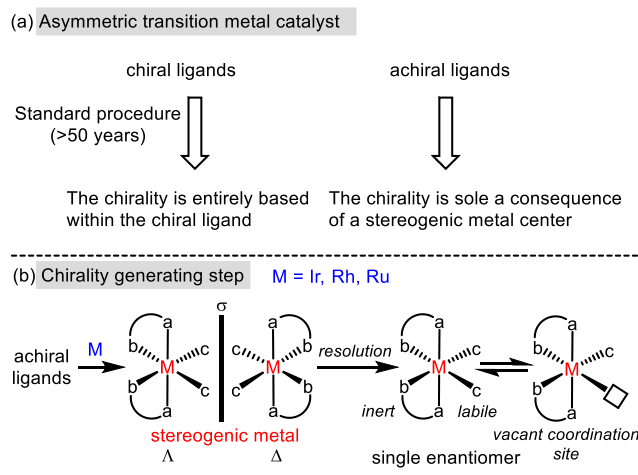


Figure 10. Asymmetric transition metal catalyst. (a) Design from chiral ligands versus achiral ligands. (b) Metal-centered chirality exclusively.

1.3.1 Synthesis and Characterization of Chiral-at-Ruthenium Complexes Containing Pyridylidene Ligands

Pyridylidenes, where the carbene center is stabilized by only one heteroatom, have attracted less attention because of the much higher electron density and relatively lower stability.^{3,4} As the direct consequence, there are still rather limited examples of pyridylidene complexes. Furthermore, limited strategies available for the metalation of much less acidic C-H bond of pyridiniums remain an additional challenge.^{39c} However, chemists such kind of ligands are stronger σ -donors and better π -acceptors than the more common Arduengo-type imidazolylidene ligands, which result in a more electron-rich metal center.^{28a,39h,95} One can imagine that the enhanced σ -donor properties of pyridylidenes may be ideal for promoting labilization of a trans ligand for further catalytic applications. Ruthenium complexes have been known for their versatile catalytic properties and are less costly than other platinum-group metals. These characteristics make them a class of especially promising catalysts. Over the past few years, the Meggers group has developed a new class of chiral-at-ruthenium complexes based on N-(2-pyridyl)-based imidazol-2-ylidene ligands (Figure 11, on the left), providing highly efficient catalytic property in asymmetric catalysis. The high catalytic activities of such robust chiral-at-ruthenium complexes can be considered as a result of the strong σ -donating and weak π -accepting characters of the bidentate imidazol-2-ylidene ligand. Given these aspects, the author of this thesis is interested in developing a novel family of chiral-at-ruthenium

complexes that contain pyridylidene ligands (Figure 11, on the right).

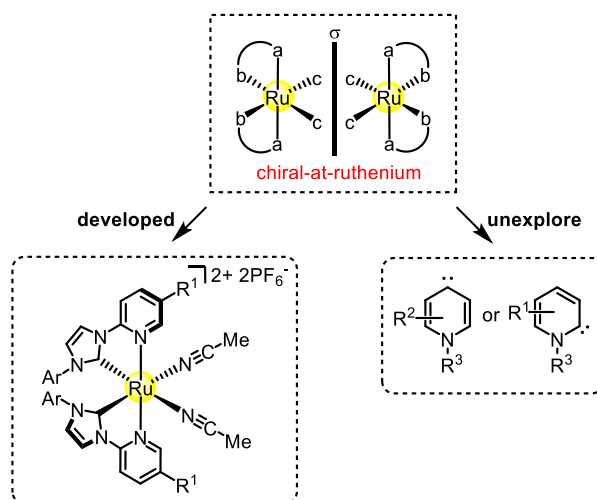


Figure 11. Aim 1: Design chiral-at-ruthenium complexes from 2-imidazolyliidene versus pyridylidene ligands.

1.3.2 Chiral-at-Iron Catalyst: Expanding the Chemical Space for Asymmetric Earth-Abundant Metal Catalysis

As mentioned above, octahedral chiral-at-metal catalysts based on precious metals (Ir/Rh/Ru) have been demonstrated recently as powerful structural scaffolds for large numbers of asymmetric reactions by Meggers group and others. In contrast, the design of reactive chiral-at-metal alternatives based on earth-abundant metals, which have sustainable and benign benefits, is rare.⁹⁶ The weaker coordination between ligands and 3d in comparison to 4d and 5d transition metals may account for unsuccessful exploration. Meanwhile, it is an unresolved challenge to combine a configurationally inert metal stereocenter with a reactive metal center in a single earth-abundant transition metal catalyst. The design strategy is especially appealing for its combination of sustainability (base metals)⁹⁷ and simplicity (achiral ligands). More importantly, it is expected that without the requirement for chiral structural motifs in the ligand sphere untapped opportunities emerge for the design of earth-abundant metal complexes with new electronic properties and structural architectures that were expected to provide distinct catalytic properties for applications in academia and industry. The author of this thesis plans to further design and synthesize chiral-at-iron complexes based on 2-imidazolyliidene ligands and investigate their catalytic application (Figure 12).

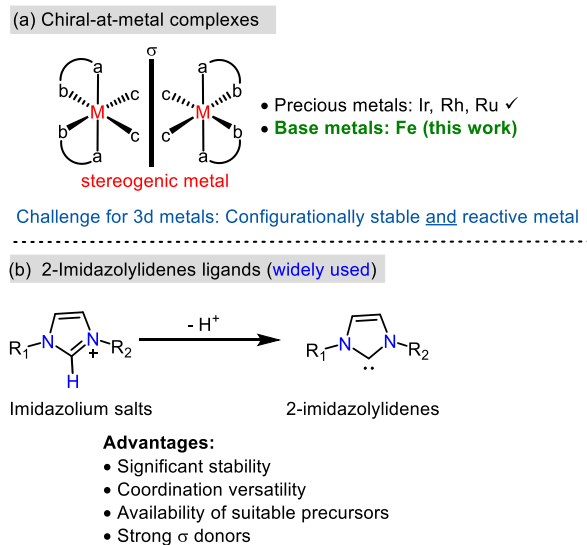


Figure 12. Aim 2: Design and synthesis of chiral-at-iron catalyst.

References

- 1 J. Arduengo, R. L. Harlow, M. Kline, *J. Am. Chem. Soc.* **1991**, *113*, 361–363.
- 2 (a) W. A. Herrmann, M. Alison, J. Fischer, C. Kocher, G. R. J. Artus, *Angew. Chem. Int. Ed. Engl.* **1995**, *34*, 2371–2374. (b) W. A. Herrmann, M. Alison, J. Fischer, C. Kocher, G. R. J. Artus, *Chem.-Eur. J.* **1996**, *2*, 772–780.
- 3 For Books of N-Heterocyclic Carbene catalysts: (a) In *N-Heterocyclic Carbenes: From Laboratory Curiosities to Efficient Synthetic Tools*; Diez-Gonzalez, S., Ed.; Catalysis Series; The Royal Society of Chemistry: Cambridge, UK, **2011**. (b) In *N-Heterocyclic Carbenes in Transition Metal Catalysis and Organocatalysis*; Cazin, C. S. J., Ed.; Springer: Dordrecht, Netherlands, **2011**. (c) In *N-Heterocyclic Carbenes: From Laboratory Curiosities to Efficient Synthetic Tools*, 2nd ed.; Diez-Gonzalez, S., Ed.; Catalysis Series; The Royal Society of Chemistry: Cambridge, UK, **2017**.
- 4 For Reviews of N-Heterocyclic Carbenes: (a) D. Bourissou, O. Guerret, F. P. Gabbai, G. Bertrand, *Chem. Rev.* **2000**, *100*, 39–92. (b) E. Peris, R. H. Crabtree, *Coord. Chem. Rev.*, **2004**, *248*, 2239–2246. (c) C. M. Crudden, D. P. Allen, *Coord. Chem. Rev.*, **2004**, *248*, 2247–2273. (d) P. L. Arnold, S. Pearson, *Coord. Chem. Rev.*, **2007**, *251*, 596–609. (e) O. Köhl, *Coord. Chem. Rev.*, **2009**, *253*, 2481–2492. (f) A. J. Arduengo, G. Bertrand, *Chem. Rev.*, **2009**, *109*, 3209–3210. (g) O. Schuster, L. Yang, H. G. Raubenheimer, M. Albrecht,

- Chem. Rev.* **2009**, *109*, 3445–3478. (h) R. H. Crabtree, *Coord. Chem. Rev.* **2013**, *257*, 755–766. (i) M. Soleilhavoup, G. Bertrand, *Acc. Chem. Res.* **2015**, *48*, 256–266. (j) M. Soleilhavoup, G. Bertrand, *Acc. Chem. Res.* **2015**, *48*, 256–266. (k) Á. Vivancos, C. Segarra, M. Albrecht, *Chem. Rev.* **2018**, *118*, 9493–9586. (l) E. Peris, *Chem. Rev.* **2018**, *118*, 9988–10031. (m) N. U. Din Reshi, J. K. Bera, *Coord. Chem. Rev.* **2020**, (doi.org/10.1016/j.ccr.2020.213334).
- 5 (a) W. A. Herrmann, *Angew. Chem., Int. Ed.* **2002**, *41*, 1290–1309. (b) S. Díez-González, S. P. Nolan, *Coord. Chem. Rev.*, **2007**, *251*, 874–883.
- 6 G. Schwarzenbach, *Helv. Chim. Acta* **1952**, *35*, 2344–2359.
- 7 A. A. Danopoulos, N. Tsoureas, J. A. Wright, M. E. Light, *Organometallics* **2004**, *23*, 166–168.
- 8 D. S. McGuinness, V. C. Gibson, J. W. Steed, *Organometallics*, **2004**, *23*, 6288–6292.
- 9 B. Liu, Q. Xia, W. Chen, *Angew. Chem. Int. Ed.* **2009**, *48*, 5513–5516.
- 10 O. Kaufhold, F.E. Hahn, T. Pape, A. Hepp, *J. Organometallic. Chem.* **2008**, *693*, 3435–3440.
- 11 B. Liu, Y. Zhang, D. Xu, W. Chen, *Chem. Commun.*, **2011**, *47*, 2883–2885.
- 12 Y. Zhang, B. Liu, H. Wu, W. Chen, *Chin Sci Bull.* **2012**, *57*, 2368–2376.
- 13 A. Francés-Monerris, K. Magra, M. Darari, C. Cebrián, M. Beley, E. Domenichini, S. Haacke, M. Pastore, X. Assfeld, P. C. Gros, A. Monari, *Inorg. Chem.* **2018**, *57*, 10431–10441.
- 14 A. Donner, B. Trepka, S. Theiss, F. Immler, J. Traber, S. Polarz, *Langmuir* **2019**, *35*, 16514–16520.
- 15 T. Duchanois, T. Etienne, C. Cebrián, L. Liu, A. Monari, M. Beley, X. Assfeld, S. Haacke, P. C. Gros, *Eur. J. Inorg. Chem.* **2015**, 2469–2477.
- 16 (a) P. Zimmer, P. Müller, L. Burkhardt, R. Schepper, A. Neuba, J. Steube, F. Dietrich, U. Flörke, S. Mangold, M. Gerhards, M. Bauer, *Eur. J. Inorg. Chem.* **2017**, 1504–1509. (b) P. Zimmer, L. Burkhardt, R. Schepper, K. Zheng, D. Gosztola, A. Neuba, U. Flörke, C. Wölper, R. Schoch, W. Gawelda, S. E. Canton, M. Bauer, *Eur. J. Inorg. Chem.* **2018**, 5203–5214.

- 17 Z. Tang, X.-Y. Chang, Q. Wan, J. Wang, C. Ma, K.-C. Law, Y. Liu, C.-M. Che, *Organometallics* **2020**, *39*, 2791–2802.
- 18 S. M. Rummelt, J. M. Darmon, R. P. Yu, P. Viereck, T. P. Pabst, Z. R. Turner, G. W. Margulieux, S. Gu, P. J. Chirik, *Organometallics* **2019**, *38*, 3159–3168.
- 19 F. Chen, N. Liu, B. Dai, *ACS Sustainable Chem. Eng.* **2017**, *5*, 9065–9075.
- 20 F. Chen, Q.-C. Zhang, D. Wei, Q. Bu, B. Dai, N. Liu, *J. Org. Chem.* **2019**, *84*, 11407–11416.
- 21 F. Chen, M. Li, J. Wang, B. Dai, N. Liu, *J. CO₂ Util.*, **2018**, *28*, 181–188.
- 22 A. Raba, M. Cokoja, S. Ewald, K. Riener, E. Herdtweck, A. Pöthig, W. A. Herrmann, F. E. Kühn, *Organometallics* **2012**, *31*, 2793–2800.
- 23 (a) A. Raba, M. Cokoja, W. A. Herrmann, F. E. Kühn, *Chem. Commun.*, **2014**, *50*, 11454–11457. (b) A. C. Lindhorst, M. Drees, W. Bonrath, J. Schütz, T. Netscher, F. E. Kühn, *J. Catal.*, **2017**, *352*, 599–605. (c) A. C. Lindhorst, J. Schütz, T. Netscher, W. Bonrath, F. E. Kühn, *Catal. Sci. Technol.*, **2017**, *7*, 1902–1911.
- 24 S. Haslinger, A. Raba, M. Cokoja, A. Pöthig and F. E. Kühn, *J. Catal.*, **2015**, *331*, 147–153.
- 25 Ö. Karaca, M. R. Anneser, J. W. Kück, A. C. Lindhorst, M. Cokoja, F. E. Kühn, *J. Catal.*, **2016**, *344*, 213–220.
- 26 D. T. Weiss, M. R. Anneser, S. Haslinger, A. Pöthig, M. Cokoja, J.-M. Basset, F. E. Kühn, *Organometallics* **2015**, *34*, 5155–5166
- 27 P. J. Fraser, W. R. Roper, F. G. A. Stone, *J. Chem. Soc., Dalton Trans.* **1974**, 760–764.
- 28 (a) S. K. Schneider, P. Roembke, G. R. Julius, C. Loschen, H. G. Raubenheimer, G. Frenking, W. A. Herrmann, *Eur. J. Inorg. Chem.* **2005**, 2973–2977. (b) S. K. Schneider, G. R. Julius, C. Loschen, H. G. Raubenheimer, G. Frenking, W. A. Herrmann, *Dalton Trans.* **2006**, 1226–1233. (c) O. Schuster, H. G. Raubenheimer, *Inorg. Chem.* **2006**, 7997–7999. (d) E. T. J. Strong, J. T. Price, N. D. Jones, *Dalton Trans.* **2009**, 9123–9125. (e) E. Stander, O. Schuster, G. Heydenrych, S. Cronje, E. Tosh, M. Albrecht, G. Frenking, H. G. Raubenheimer, *Organometallics*. **2010**, *29*, 5821–5833. (f) T. Yoshidomi, Y. Segawa, K. Itami, *Chem. Commun.* **2013**, *49*, 5648–5650. (g) T. Yoshidomi, T. Fukushima, K. Itami, Y. Segawa, *Chem. Lett.* **2017**, *46*, 587–590.
- 29 L. Canovese, F. Visentin, P. Uguagliati, F. D. Bianca, A. Fontana, B. Crociani, *J. Organomet. Chem.* **1996**, *525*, 43–48.
- 30 (a) M. Green, F. G. A. Stone, M. Underhill, *J. Chem. Soc., Dalton Trans.* **1975**, 939–943. (b) U. Kirchgassner, H. Piana, U. Schubert, *J. Am. Chem. Soc.* **1991**, *113*, 2228–2232. (c)

- J. Schubert, S. Mock, U. Schubert, *Chem. Ber.* **1993**, *126*, 657–664. (d) Schubert, U.; Seebald, S. *J. Organomet. Chem.* **1994**, *472*, C15–C17. (e) W. H. Meyer, M. Deetlefs, M. Pohlmann, R. Scholz, M. W. Esterhuysen, G. R. Julius, H. G. Raubenheimer, *Dalton Trans.* **2004**, 413–420.
- 31 (a) K. Isobe, E. Kai, Y. Nakamura, K. Nishimoto, T. Miwa, S. Kawaguchi, K. Kinoshita, K. Nakatsu, *J. Am. Chem. Soc.* **1980**, *102*, 2475–2476. (b) K. Isobe, Y. Nakamura, T. Miwa, S. Kawaguchi, *Bull. Chem. Soc. Jpn.* **1987**, *60*, 149–157. (c) B. Crociani, F. Di Bianca, A. Giovenco, A. Scrivanti, *J. Organomet. Chem.* **1983**, *251*, 393–411. (d) B. Crociani, F. Di Bianca, A. Giovenco, A. Scrivanti, *J. Organomet. Chem.* **1984**, *269*, 295–304. (e) B. Crociani, F. Di Bianca, A. Giovenco, A. J. *Organomet. Chem.* **1987**, *323*, 123–134. (f) B. Crociani, F. Di Bianca, A. Giovenco, A. Bertoni, R. Bertani, *J. Organomet. Chem.* **1989**, *361*, 255–267. (g) F. P. Fanizzi, G. J. Sunley, J. A. Wheeler, H. Adams, N. A. Bailey, P. M. Maitlis, *Organometallics* **1990**, *9*, 131–136. (h) B. Crociani, F. Di Bianca, F. Benetollo, G. Bombieri, *J. Chem. Res., Synop.* **1992**, 296–297. (i) L. Canovese, F. Visentin, P. Uguagliati, F. Di Bianca, A. Fontana, B. Crociani, *J. Organomet. Chem.* **1996**, *525*, 43–48. (j) H. Meguro, T.-A. Koizumi, T. Yamamoto, T. Kanbara, *J. Organomet. Chem.* **2008**, *693*, 1109–1116. (k) A. Poulain, A. Neels, M. Albrecht, *Eur. J. Inorg. Chem.* **2009**, 1871–1881. (l) T. Fukushima, R. Fukuda, K. Kobayashi, G. F. Caramori, G. Frenking, M. Ehara, K. Tanaka, *Chem. - Eur. J.* **2015**, *21*, 106–110.
- 32 H. G. Raubenheimer, J. G. Toerien, G. J. Kruger, R. Otte, W. van Zyl, P. Olivier, *J. Organomet. Chem.* **1994**, *466*, 291–295.
- 33 (a) M. Gomez, J. M. Kisenyi, G. J. Sunley, P. M. Maitlis, *J. Organomet. Chem.* **1985**, *296*, 197–207. (b) F. P. Fanizzi, G. J. Sunley, J. A. Wheeler, H. Adams, N. A. Bailey, P. M. Maitlis, *Organometallics* **1990**, *9*, 131–136.
- 34 (a) R. Cordone, W. D. Harman, H. Taube, *J. Am. Chem. Soc.* **1989**, *111*, 2896–2900. (b) G. W. V. Cave, A. J. Hallett, W. Errington, J. P. Rourke, *Angew. Chem., Int. Ed.* **1998**, *37*, 3270–3272. (c) M. Albrecht, H. Stoeckli-Evans, *Chem. Commun.* **2005**, 4705–4707. (d) A. S. Ionkin, W. J. Marshall, D. C. Roe, Y. Wang, *Dalton Trans.* **2006**, 2468–2478. (e) S. Gómez-Bujedo, M. Alcarazo, C. Pichon, E. Alvarez, R. Fernandez, J. M. Lassaletta, *Chem. Commun.* **2007**, 1180–1182. (f) J. A. Cabeza, I. Del Río, E. Pérez-Carreño, M. G. Sánchez-Vega, D. Vázquez-García, *Angew. Chem., Int. Ed.* **2009**, *48*, 555–558. (g) J. A. Cabeza, I. Del Río, E. Pérez-Carreño, M. G. Sánchez-Vega, D. Vázquez-García, *Organometallics* **2010**, *29*, 4464–4471. (h) K. Hata, Y. Segawa, K. Itami, *Chem. Commun.* **2012**, 6642–6644.
- 35 W. A. Wickramasinghe, P. H. Bird, N. Serpone, *J. Chem. Soc., Chem. Commun.* **1981**, 1284–1286.
- 36 (a) S. Dholakia, R. D. Gillard, F. L. Wimmer, *Inorg. Chim. Acta* **1983**, *69*, 179–181. (b) F. L. Wimmer, S. Wimmer, *Polyhedron* **1985**, *4*, 1665–1666. (c) P. Castan, F. Dahan, S.

- Wimmer, F. L. Wimmer, *J. Chem. Soc., Dalton Trans.* **1990**, 2971–2977. (d) P. Castan, B. Labiad, D. Villemin, F. L. Wimmer, S. Wimmer, *J. Organomet. Chem.* **1994**, *479*, 153–157. (e) S. Wimmer, F. L. Wimmer, *J. Chem. Soc., Dalton Trans.* **1994**, 879–884.
- 37 (a) T. Koizumi, T. Tomon, K. Tanaka, *Organometallics* **2003**, *22*, 970–975. (b) T. Koizumi, T. Tomon, K. Tanaka, *Bull. Chem. Soc. Jpn.* **2003**, *76*, 1969–1975. (c) T. Koizumi, T. Tomon, K. Tanaka, *J. Organomet. Chem.* **2005**, *690*, 1258–1264. (d) T. Koizumi, T. Tomon, K. Tanaka, *J. Organomet. Chem.* **2005**, *690*, 4272–4279.
- 38 (a) J. S. Owen, J. A. Labinger, J. E. Bercaw, *J. Am. Chem. Soc.* **2004**, *126*, 8247–8255. (b) N. A. Piro, J. S. Owen, J. E. Bercaw, *Polyhedron* **2004**, *23*, 2797–2804.
- 39 (a) E. Alvarez, S. Conejero, M. Paneque, A. Petronilho, M. L. Poveda, O. Serrano, E. Carmona, *J. Am. Chem. Soc.* **2006**, *128*, 13060–13061. (b) E. Alvarez, S. Conejero, P. Lara, J. A. Lopez, M. Paneque, A. Petronilho, M. L. Poveda, D. Del Rio, O. Serrano, E. Carmona, *J. Am. Chem. Soc.* **2007**, *129*, 14130–14131. (c) G. Song, Y. Zhang, Y. Su, W. Deng, K. Han, X. Li, *Organometallics* **2008**, *27*, 6193–6201. (d) S. Conejero, P. Lara, M. Paneque, A. Petronilho, M. L. Poveda, O. Serrano, F. Vattier, E. Álvarez, C. Maya, V. Salazar, *Angew. Chem., Int. Ed.* **2008**, *47*, 4380–4383. (e) M. A. Esteruelas, F. J. Fernández-Alvarez, M. Oliván, E. Oñate, *Organometallics* **2009**, *28*, 2276–2284. (f) M. Paneque, M. L. Poveda, F. Vattier, E. Alvarez, E. Carmona, *Chem. Commun.* **2009**, *45*, 5561–5563. (g) G. Song, Y. Su, R. A. Periana, R. H. Crabtree, K. Han, H. Zhang, X. Li, *Angew. Chem., Int. Ed.* **2010**, *49*, 912–917. (h) R. Lalrempuia, N. D. McDaniel, H. Müller-Bunz, S. Bernhard, M. Albrecht, *Angew. Chem., Int. Ed.* **2010**, *49*, 9765–9768. (i) S. Conejero, C. Maya, M. Paneque, A. Petronilho, M. L. Poveda, F. Vattier, E. Álvarez, E. Carmona, A. Laguna, O. Crespo, *Dalton Trans.* **2012**, *41*, 14126–14136. (j) S. Bajo, M. A. Esteruelas, A. M. López, E. Oñate, *Organometallics* **2012**, *31*, 8618–8626. (k) A. McSkimming, G. E. Ball, M. M. Bhadbhade, S. B. Colbran, *Inorg. Chem.* **2012**, *51*, 2191–2203. (l) C. Segarra, E. Mas-Marzá, M. Benítez, J. A. Mata, E. Peris, *Angew. Chem., Int. Ed.* **2012**, *51*, 10841–10845. (m) C. Segarra, E. Mas-Marzá, J. A. Mata, E. Peris, *Organometallics* **2012**, *31*, 5169–5176. (n) B. J. Coe, M. Helliwell, S. Sánchez, M. K. Peers, N. S. Scrutton, *Dalton Trans.*, **2015**, *44*, 15420–15423. (o) S. Semwal, J. Choudhury, *ACS Catal.* **2016**, *6*, 2424–2428. (p) C.-H. Tseng, M. A. Fox, J.-L. Liao, C.-H. Ku, Z.-T. Sie, C.-H. Chang, J.-Y. Wang, Z.-N. Chen, G.-H. Lee, Y. Chi, *J. Mater. Chem. C* **2017**, *5*, 1420–1435.
- 40 (a) R. J. Watts, J. S. Harrington, J. Van Houten, *J. Am. Chem. Soc.* **1977**, *99*, 2179–2187. (b) R. J. Watts, S. F. Bergeron, *J. Phys. Chem.* **1979**, *83*, 424–425. (c) J. L. Kahl, K. Hanck, K. DeArmond, *J. Inorg. Nucl. Chem.* **1979**, *41*, 495–502. (d) R. D. Gillard, R. J. Lancashire, P. A. Williams, *J. Chem. Soc., Dalton Trans.* **1979**, 190–192. (e) P. J. Spellane, R. J. Watts, *Inorg. Chem.* **1981**, *20*, 3561–3563.

- 41 (a) M. D. Ward, *J. Chem. Soc., Dalton Trans.* **1993**, 1321–1325. (b) E. C. Constable, M. W. Alexander, C. Thompson, J. Cherryman, T. Liddiment, *Inorg. Chim. Acta* **1995**, 235, 165–171.
- 42 Holubek, J. C. *Spectral data and physical constants in Alkaloids*; Academie: Prague, **1972**; Vol VII.
- 43 P. R. Cheeke, *Symposium on Pyrrolizidine (Senecio) Alkaloids: Toxicity, Metabolism and Poisonous Plant Control Measures : the proceedings of a symposium held at Oregon State University, February 23 and 24, 1979*; Nutrition Research Institute, Oregon State University: Corvallis, Oregon, **1979**.
- 44 G. Ysart, P. Miller, H. Crews, P. Robb, M. Baxter, C. D. L'Argy, S. Lofthouse, C. Sargent, N. Harrison, *Food Addit. Contam.* **1999**, 16, 391–403.
- 45 P. Gandeepan, T. Müller, D. Zell, G. Cera, S. Warratz, L. Ackermann, *Chem. Rev.* **2019**, 119, 2192–2452.
- 46 J. Kaplan, D.M. Ward, *Curr. Biol.* **2013**, 23, 642–646.
- 47 M. Darwish, M. Wills, *Catal. Sci. Technol.* **2012**, 2, 243–255.
- 48 A. Fürstner, *ACS Cent. Sci.* **2016**, 2, 778–789.
- 49 For reviews on asymmetric iron catalysis, see: (a) R. H. Morris, *Chem. Soc. Rev.* **2009**, 38, 2282–2291. (b) K. Gopalaiah, *Chem. Rev.* **2013**, 113, 3248–3296. (c) T. Ollevier, H. Keipour, *Top. Organomet. Chem.* **2015**, 50, 259–309. (d) H. Pellissier, *Coord. Chem. Rev.* **2019**, 386, 1–31. (e) A. Casnati, M. Lanzi, G. Cera, *Molecules* **2020**, 25, 3889–3917.
- 50 J. T. Groves, R. S. Myers, *J. Am. Chem. Soc.* **1983**, 105, 5791–5796.
- 51 M. Gautam, T. Yatabe, S. Tanaka, N. Satou, T. Takeshita, K. Yamaguchi, Y. Nakajima, *ChemistrySelect* **2020**, 5, 15–17.
- 52 (a) C. Duboc-Toia, S. Ménage, C. Lambeaux, M. Fontecave, *Tetrahedron Lett.* **1997**, 38, 3727–3730. (b) C. Duboc-Toia, S. Ménage, R. Y. N. Ho, L. Jr. Que, C. T. Lambeaux, M. Fontecave, *Inorg. Chem.* **1999**, 38, 1261–1268. (c) Y. Mekmouche, H. Hummel, R. Y. N. Ho, L. Jr. Que, V. Schünemann, F. Thomas, A. X. Trautwein, C. Lebrun, K. Gorgy, J.-C. Leprêtre, M.-N. Collomb, A. Deronzier, M. Fontecave, S. Ménage, *Chem. -Eur. J.* **2002**, 8, 1196–1204.
- 53 C. Marchi-Delapierre, A. Jorge-Robin, A. Thibon, S. Ménage, *Chem. Commun.* **2007**, 1166–1168.

- 54 Y. Nishikawa, H. Yamamoto, *J. Am. Chem. Soc.* **2011**, *133*, 8432–8435.
- 55 M. Costas, A. K. Tipton, K. Chen, D.-H. Jo, L. Jr. Que, *J. Am. Chem. Soc.* **2001**, *123*, 6722–6723.
- 56 K. Suzuki, P. D. Oldenburg, L. Jr. Que, *Angew. Chem., Int. Ed.* **2008**, *47*, 1887–1889.
- 57 X. C. Zang, Y. Liu, Z.-J. Xu, C.-W. Tse, X. Guan, J. Wei, J.-S. Huang, C.-M. Che, *Angew. Chem. Int. Ed.* **2016**, *55*, 10253–10257.
- 58 M. Wu, C.-X. Miao, S. Wang, X. Hu, C. Xia, F. E. Kühn, W. Sun, *Adv. Synth. Catal.* **2011**, *353*, 3014–3022.
- 59 O. Y. Lyakin, R. V. Ottenbacher, K. P. Bryliakov, E. P. Talsi, *ACS Catal.* **2012**, *2*, 1196–1202.
- 60 (a) A. M. Zima, O. Y. Lyakin, R. V. Ottenbacher, K. P. Bryliakov, E. P. Talsi, *ACS Catal.* **2016**, *6*, 5399–5404. (b) A. M. Zima, O. Y. Lyakin, R. V. Ottenbacher, K. P. Bryliakov, *ACS Catal.* **2017**, *7*, 60–69.
- 61 (a) O. Cusso, I. Garcia-Bosch, X. Ribas, J. Lloret-Fillol, M. Costas, *J. Am. Chem. Soc.* **2013**, *135*, 14871–14878. (b) O. Cusso, X. Ribas, J. Lloret-Fillol, M. Costas, *Angew. Chem., Int. Ed.* **2015**, *54*, 2729–2733.
- 62 O. Cusso, M. W. Giuliano, X. Ribas, S. J. Miller, M. Costas, *Chem. Sci.* **2017**, *8*, 3660–3667.
- 63 W. Wang, Q. Sun, D. Xu, C. Xia, W. Sun, *ChemCatChem.* **2017**, *9*, 420–424.
- 64 O. Cusso, M. Cianfanelli, X. Ribas, R. J. M. Klein, Gebbink, M. Costas, *J. Am. Chem. Soc.* **2016**, *138*, 2732–2738.
- 65 N. V. Tkachenko, O. Y. Lyakin, D. G. Samsonenko, E. P. Talsi, K. P. Bryliakov, *Catal. Commun.* **2018**, *104*, 112–117.
- 66 J. Wei, B. Cao, C.-W. Tse, X.-Y. Chang, C.-Y. Zhou, C.-M. Che, *Chem. Sci.* **2020**, *11*, 684–693.
- 67 (a) C. Bonaccorsi, M. Althaus, C. Becker, A. Togni, A. Mezzetti, *Pure. Appl. Chem.* **2006**, *78*, 391–396. (b) C. Bonaccorsi, A. Mezzetti, *Current Organic Chemistry*, **2006**, *10*, 225–240. (c) A. Mezzetti, *Dalton Trans.*, **2010**, *39*, 7851–7869.
- 68 A. Mikhailine, A. J. Lough, R. H. Morris, *J. Am. Chem. Soc.* **2009**, *131*, 1394–1395.
- 69 P. O. Lagaditis, A. J. Lough, R. H. Morris, *Inorg. Chem.* **2010**, *49*, 10057–10066.
- 70 A. A. Mikhailine, R. H. Morris, *Inorg. Chem.* **2010**, *49*, 11039–11044.
- 71 P. E. Sues, A. J. Lough, R. H. Morris, *Organometallics* **2011**, *30*, 4418–4431.
- 72 A. A. Mikhailine, M. I. Maishan, R. H. Morris, *Org. Lett.*, **2012**, *14*, 4638–4641.
- 73 8 W. Zuo, Y. Li, A. J. Lough, R. H. Morris, *Science* **2013**, *342*, 1080–1083.
- 74 9 W. Zuo, S. Tauer, D. E. Prokopchuk, R. H. Morris, *Organometallics* **2014**, *33*, 5791–5801.

- 75 (a) S. A. M. Smith, R. H. Morris, *Synthesis*, **2015**, *47*, 1775–1779. (b) W. Zuo, D. E. Prokopchuk, A. J. Lough, R. H. Morris, *ACS Catal.* **2016**, *6*, 301–314. (c) S. A. M. Smith, D. E. Prokopchuk, R.H. Morris, *Isr. J. Chem.* **2017**, *57*, 1204–1215.
- 76 K. Z. Demmans, O. W. K. Ko, R. H. Morris, *RSC Adv.* **2016**, *6*, 88580–88587.
- 77 (a) R. Bigler, E. Otth, A. Mezzetti, *Organometallics* **2014**, *33*, 4086–4099. (b) R. Bigler, A. Mezzetti, *Org. Lett.* **2014**, *16*, 6460–6463.
- 78 (a) R. Bigler, R. Huber, A. Mezzetti, *Angew. Chem. Int. Ed.* **2015**, *54*, 5171–5174. (b) R. Bigler, R. Huber, M. Stöckli, A. Mezzetti, *ACS Catal.* **2016**, *6*, 6455–6464.
- 79 R. Bigler, A. Mezzetti, *Org. Proc. Res. Dev.* **2016**, *20*, 253–261.
- 80 L. D. Luca, A. Mezzetti, *Angew. Chem. Int. Ed.* **2017**, *56*, 11949–11953.
- 81 A. Zirakzadeh, S.R.M.M. de Aguiar, M. Widhalm, K. Mereiter, *J. Organomet. Chem.* **2016**, *819*, 260–265.
- 82 A. Zirakzadeh, K. Kirchner, A. Roller, B. Stöger, M. Widhalm, R.H. Morris, *Organometallics* **2016**, *35*, 3781–3787.
- 83 (a) S.A.M. Smith, P.O. Lagaditis, A. Lüpke, A.J. Lough, R.H. Morris, *Chem. Eur. J.* **2017**, *23*, 7212–7216. (b) J.F. Sonnenberg, K.Y. Wan, P.E. Sues, R.H. Morris, *ACS Catal.* **2017**, *7*, 316–326.
- 84 P. J. Walsh, M. C. Kozlowski, *Fundamentals of Asymmetric Catalysis*; University Science Books: Sausalito, CA, **2009**.
- 85 L. Zhang, E. Meggers, *Chem. - Asian J.* **2017**, *12*, 2335–2342.
- 86 L. Zhang, E. Meggers, *Acc. Chem. Res.* **2017**, *50*, 320–330.
- 87 (a) H. Huo, C. Fu, K. Harms, E. Meggers, *J. Am. Chem. Soc.* **2014**, *136*, 2990–2993. (b) H. Huo, X. Shen, C. Wang, L. Zhang, P. Röse, L.-A. Chen, K. Harms, M. Marsch, G. Hilt, E. Meggers, *Nature* **2014**, *515*, 100–103. (c) G.-Q. Xu, H. Liang, J. Fang, Z.-L. Jia, J.-Q. Chen, P.-F. Xu, *Chem. - Asian J.* **2016**, *11*, 3355–3358.
- 88 (a) C. Wang, L.-A. Chen, H. Huo, X. Shen, K. Harms,; L. Gong, E. Meggers, *Chem. Sci.* **2015**, *6*, 1094–1100. (b) J. Ma, X. Shen, K. Harms, E. Meggers, *Dalton Trans* **2016**, *45*, 8320–8323. (c) S.-W. Li, J. Gong, Q. Kang, *Org. Lett.* **2017**, *19*, 1350–1353. (d) S. Qurban, Y. Du, J. Gong, S.-X. Lin, Q. Kang, *Chem. Commun.* **2019**, *55*, 249–252. (e) Y. Grell, Y. Hong, X. Huang, T. Mochizuki, X. Xie, K. Harms, E. Meggers, *organometallics*, **2019**, *38*,

- 3948–3954. (f) P. Steinlandt, W. Zuo, K. Harms, E. Meggers, *Chem - Eur J.* **2019**, *25*, 15333–15340.
- 89 M. Carmona, R. Rodríguez, V. Passarelli, F. J. Lahoz, P. García-Orduña, D. Carmona, *J. Am. Chem. Soc.* **2018**, *140*, 912–915.
- 90 J. Hartung, R. H. Grubbs, *J. Am. Chem. Soc.* **2013**, *135*, 10183–10185.
- 91 Y. Zheng, Y. Tan, K. Harms, M. Marsch, R. Riedel, L. Zhang, E. Meggers, *J. Am. Chem. Soc.* **2017**, *139*, 4322–4325.
- 92 For review on asymmetric photocatalysis with chiral-at-metal complexes, see: X. Huang, E. Meggers, *Acc. Chem. Res.* **2019**, *52*, 833–847.
- 93 X. Huang, Q. Zhang, J. Lin, K. Harms, E. Meggers, *Nat. Catal.* **2019**, *2*, 34–40.
- 94 (a) J. Qin, Z. Zhou, T. Cui, M. Hemming, E. Meggers, *Chem. Sci.* **2019**, *10*, 3202–3207. (b) Z. Zhou, S. Chen, J. Qin, X. Nie, X. Zheng, K. Harms, R. Riedel, K. N. Houk, E. Meggers, *Angew. Chem. Int. Ed.* **2019**, *58*, 1088–1093. (c) Y. Tan, S. Chen, Z. Zhou, Y. Hong, S. Ivlev, K. N. Houk, E. Meggers, *Angew. Chem. Int. Ed.* **2020**, 21706–21710. (d) Y. Tan, F. Han, M. Hemming, J. Wang, K. Harms, E. Meggers, *Org. Lett.* **2020**, 6653–6656.
- 95 R. Gleiter, R. Hoffmann, *J. Am. Chem. Soc.* **1968**, *90*, 5457–5460.
- 96 Note that this refers to reactive chiral-at-metal complexes in which the metal is directly involved in catalysis as opposed to chiral metal complexes in which catalysis is mediated entirely through the ligand sphere (metal-templated catalysis).
- 97 P. Chirik, R. Morris, *Acc. Chem. Res.* **2015**, *48*, 2495.

Chapter 2: Synthesis and Characterization of Chiral-at-Ruthenium Complexes with Pyridylidene Ligands

2.1 Catalyst Design

Pyridylidenes, as one type of NHCs, have attracted less attention because of the much higher electron density and relatively lower stability.¹ These characteristics along with limited synthesis strategies for the metalation of much less acidic C-H bonds lead to less exploration of their metal complexes, compared to five-membered 2-imidazolylidenes.² Despite these aspects, chemists are interested in the design and the use of such kind of ligands due to their unique features, generally stronger σ -donating and better π -accepting, which lead to the potentially high activity of corresponding complexes.³⁻⁵ Ruthenium complexes have been known due to their versatile catalytic properties and are less costly than other platinum-group metals. These characteristics make them a class of promising catalysts. Recently, Meggers has proved that a new class of chiral-at-ruthenium complexes can serve as highly efficient catalysts for various enantioselective transformations.⁶ The highly catalytic activities of these robust ruthenium complexes might be attributed to the strong σ -donating and weak π -accepting characters of the chelating pyridyl imidazolylidene ligands. Given the unique characters of pyridylidenes and the advantageous nature of ruthenium, we here introduce a new class of chiral-at-ruthenium complexes where ruthenium is cyclometalated by two pyridine-pyridinium N-heterocyclic carbenes ligands, resulting in chelating pyridyl pyridylidene ligands (Figure 13). We consider that the pyridylidene ligands with a pyridyl-donor can coordinate tightly with ruthenium and create a more stable complex.

Chapter 2: Synthesis and Characterization of A New Family of Octahedral Chiral-at-Ruthenium Complexes with Pyridylidene Ligands

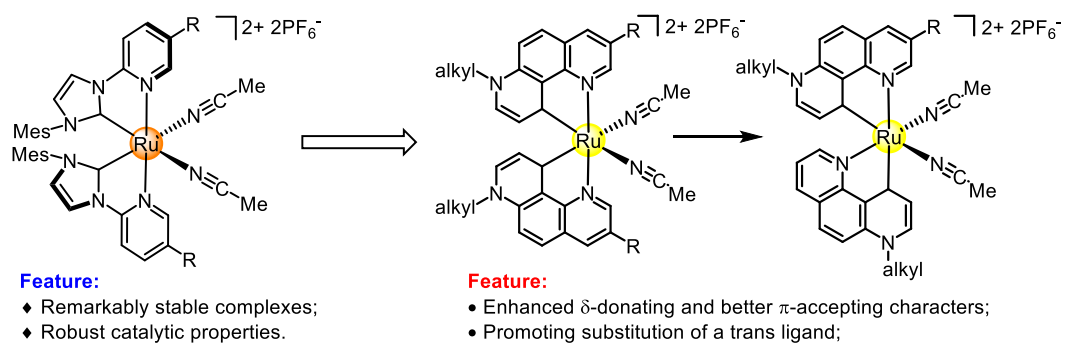


Figure 13. Design of new chiral-at-ruthenium catalysts.

Before exploratory research, the advances made in the complexes containing N-donors-pyridylidenes have been exemplified. Pyridylidenes functionalized with pyridine moieties have been recognized as a class of useful ligands for transition metals,¹ including Pt, Ir, Pd, Ru, Ni. The early example of this type was reported by Watts et al.,⁷ involving the synthesis of an abnormal pyridylidene iridium complex. However, the clear molecular structure was defined by Serpone.⁸ After that, Wimmer and co-workers successively reported several palladium and platinum dichloride complexes based on *N'*-methyl-2,2'-bipyridinium and *N'*-methyl-2,4'-bipyridinium salts, resulting in the abnormal pyridylidene ligands.⁹ In 1995, Constable and Thompson presented the first example of an octahedral ruthenium complex bearing an abnormal terpyridinium-derived pyridylidene.¹⁰ Following this work, Tanaka and co-workers reported the synthesis and characterization of several terpyridinium-derived N,N,C- and N,C,N-chelating ruthenium complexes,¹¹ including the first reported remote-type pyridylidene complex.^{11a} These authors demonstrated that the remote-type pyridylidenes exhibited a higher carbene character in comparison to abnormal analogues by ¹³C NMR analysis and CV study. Interestingly, the selective activation of the intramolecular C-H bonds is more favored at para- than ortho-position, owing to the electronic preference of para-position metalation and the steric crowd of the ortho-position metalation. This same regioselectivity of the C-H metalation was also found in the work of Coe, who presented a series of bis(*r*NHC)iridium complexes with the same bidentate pyridyl pyridylidene ligand.¹² Bercaw and co-workers introduced a new type of bidentate ligands, where the N-donors were substituted on pyridyl ring, to achieve the high regioselectivity of ortho-position metalation products.¹³ Another strategy to improve the regioselectivity was reported by Li and colleagues, which involved the use of pyridylidene

ligands with blocking groups for the synthesis of the iridium(III) complexes that only contained normal or remote pyridylidene, respectively.¹⁴ It worth pointing that Choudhury gave an example of (benzimidazole-2-yl)-pyridylidene iridium complex, which can be understood as another type of C,N-chelating complexes.¹⁵ Although there has been increased use of pyridylidenes in organometallic chemistry, the asymmetric complexes with pyridylidene ligands have not yet been realized.¹

2.2 Synthesis and Characterization of Racemic Ruthenium Complexes

2.2.1 Ruthenium Complex with 3'-Methyl 2,3'-Bipyridinium Ligand

Our initial work was carried out by using a 3'-methyl 2,3'-bipyridinium ligand that was easily prepared by methylation of commercially available 2,3'-bipyridine with iodomethane. Previous study reported by Coe group showed that the direct reaction between 3'-methylated 2,3'-bipyridinium salt (L^{Py-1}) and $IrCl_3$ in mixed solvents of 2-methoxyethanol and water yielded a cyclometalated chloride-bridged iridium complex $[Ir^{III}(C^{\wedge}N)_2(Cl)_2]^{4+}$.¹² Accordingly, L^{Py-1} was allowed to react with 0.5 equivalent of $RuCl_3$ hydrate in a mixed solvent (2-ethoxyethanol/water, volume ratio is 3:1) at 120 °C, followed by treatment with $AgPF_6$ to obtain a brownish yellow solid (Figure 14a).

1H NMR spectrum of this solid in the CD_3CN showed the complete disappearance of the N-Me resonance (δ 4.39) of ligand and the formation of a new strong single peak resonated at δ 3.09 which might be attributed to chelating pyridylidene ligand (Figure 15a). Attempts to isolate this major isomer by column chromatography on silica gel with CH_2Cl_2 and MeCN as the eluent were not successful, however, and gave unidentified mixtures with difficulty of isolation. The 1H NMR spectrum of this mixture showed that the signals resonated at δ 4.43 and 3.38 in the N- CH_3 region became strong in comparison to the initial single peak at δ 3.09, indicating the initial major isomer was unstable during the column chromatography (Figure 15b).

Fortunately, we were able to separate a few crystals from this mixture. Single crystals suitable for X-ray were obtained by diffusion of Et_2O in MeCN solution at room temperature

Chapter 2: Synthesis and Characterization of A New Family of Octahedral Chiral-at-Ruthenium Complexes with Pyridylidene Ligands

for 1 day. Only one isomer could be determined, which was appointed as *rac*-**Ru1**. As displayed in Figure 16, the central Ru atom had approximate octahedral coordination, one chelating pyridylidene ring was trans to the pyridine ring of the second 2,3'-bipyridinium ligand and the two *cis*-acetonitrile ligands lied *trans* to the remained pyridine ring and pyridylidene ring, respectively, resulting in a non- C_2 -symmetric (C -*Trans*-N) scaffold. To our surprise, the metalation of pyridinium occurred mainly at the shielded para-position^{19c}, which was distinctive from that of the $\{[\text{Ir}^{\text{III}}(\text{C}^{\wedge}\text{N})_2(\text{N}^{\wedge}\text{N})]^{3+}\}^{12}$ and $\{[\text{Ru}^{\text{II}}(\text{C}^{\wedge}\text{N})(\text{N}^{\wedge}\text{N})_2]^{2+}\}^{11c}$ complexes reported by Coe and Tanaka, respectively. The structure of *rac*-**Ru1** was then characterized by ¹H NMR analysis, a set of non- C_2 -symmetric signals containing twelve aromatic proton resonances, and two inequivalent N-CH₃ resonances at δ 4.43 and 3.38 in a 1:1 ratio was expected (Figure 15c), which indeed had been observed for *rac*-**Ru1**. However, it was hard to identify the major product since there might exist several isomers (Figure 14b).

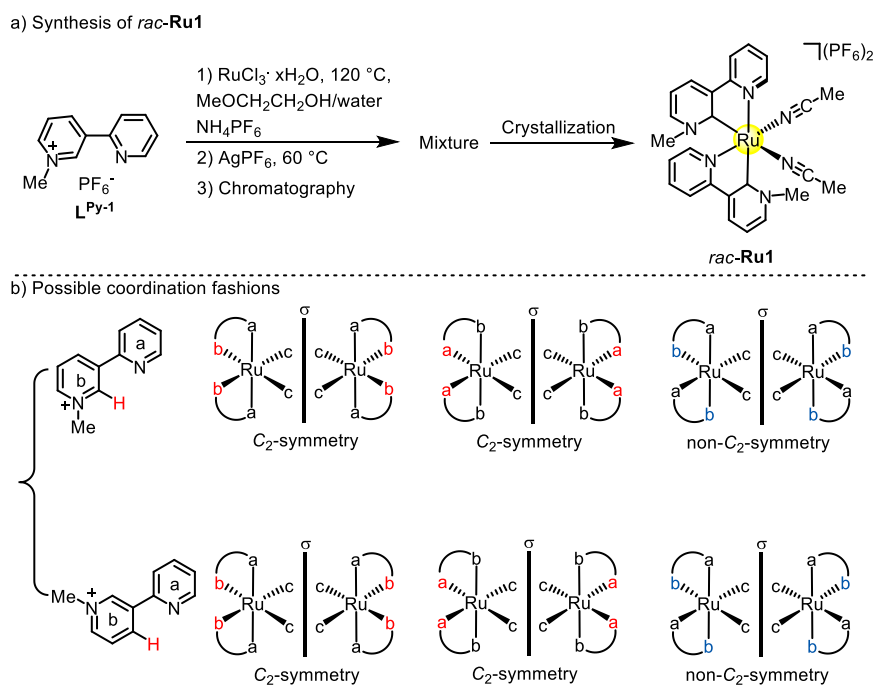


Figure 14. Ruthenium complex with 3'-methyl 2,3'-bipyridinium ligands.

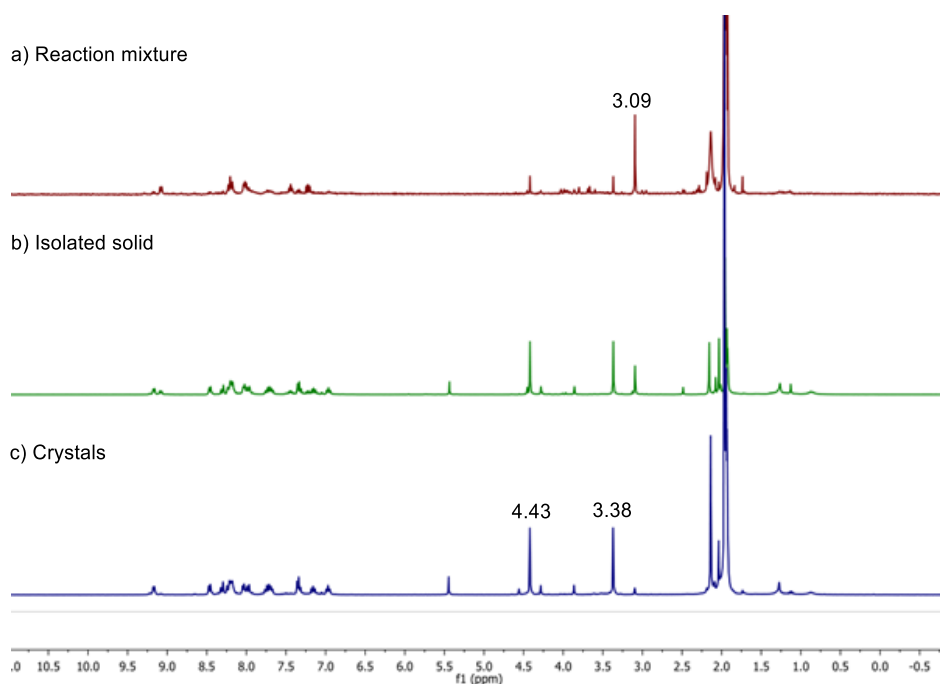


Figure 15. ¹H NMR (300 MHz, CD₃CN) spectra: (a) Reaction mixture; (b) Isolated solid; (c) Crystals.

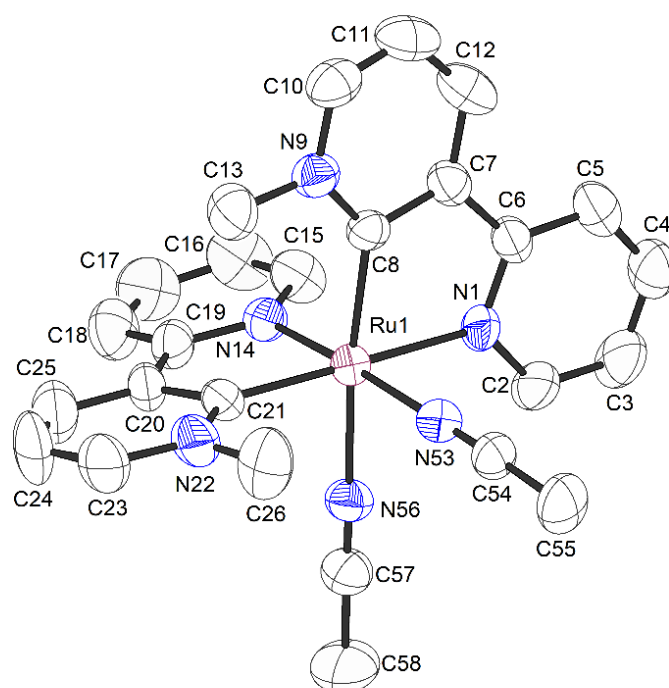


Figure 16. Crystal structure of *rac*-**Ru1**. ORTEP drawing with 50% probability thermal ellipsoids. The hexafluorophosphate counteranion and all hydrogens are omitted for clarity.

To the best of our knowledge, *rac*-**Ru1** was the first case of an octahedral cyclometalated

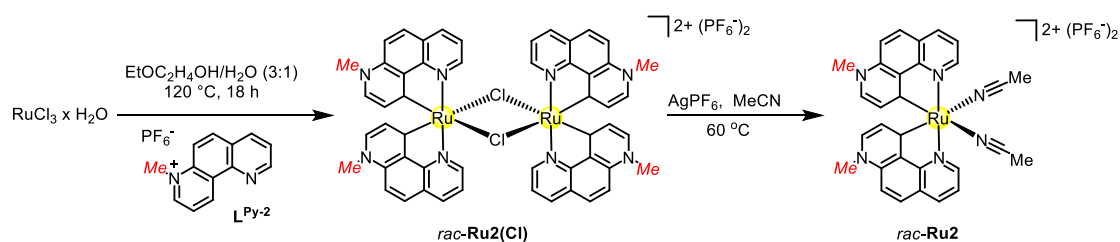
ruthenium complex, containing two nonsymmetric bidentate and two monodentate ligands coordinated to a central metal in a non- C_2 -symmetric fashion, which was apparently different from previous chiral-at-metal catalysts developed in our group. We could imagine that a larger structural diversity might lead to more diverse chiral catalysts for a broader variety of asymmetric transformations. For example, one could assume non- C_2 -symmetric diastereomers, expecting that the relative metal-centered stereochemistry affects the overall reactivity of such chiral-at-metal catalysts.

Although challenges remained with respect to synthesis, purification as well as the stability problem for the 2,3'-bipyridinium system, we believed that a suitable ligand could not only elevate the selectivity of C-H activation but also provide the chelation-stabilized complex. We therefore chose the heterocycle 7-methyl-1,7-phenanthroline hexafluorophosphate, named **L^{Py-2}**, as our ligand of choice, in which we reasoned that metalation could be activated only at the C_{10} -H bond. Moreover, the highly conjugational phenanthroline ligand coordinated around the metal center might also stabilize the complex.

2.2.2 Ruthenium Complex with 7-Methyl 1,7-Phenanthroline Ligand

The racemic ruthenium complex was prepared by the same procedure for the preparation of *rac*-**Ru1**. The reaction of $RuCl_3$ hydrate with **L^{Py-2}** in 2-ethoxyethanol and water (3:1) at 120 °C under an atmosphere of nitrogen provided the racemic chloride-bridged dimer *rac*-**Ru2(Cl)**, which was used without further purification and analysis. Two bridged chlorides of *rac*-**Ru2(Cl)** were removed upon treatment with $AgPF_6$ in acetonitrile at 60 °C to give the related bis-acetonitrile remote NHC ruthenium complex *rac*-**Ru2** in 85% yield (Scheme 38). The *rac*-**Ru2** was stable enough to purify by column chromatography on silica gel with CH_2Cl_2 and MeCN as an eluent. Ligand coordination to the Ru center resulted in the loss of the acidic pyridinium proton signal and in a marked upfield shift of the N-Me proton signal from δ 4.65 in **L^{Py-2}** to δ 4.02 in *rac*-**Ru2**, which were observed by 1H NMR analysis. Unfortunately, we could not observe coordinated carbon resonance signals in the ^{13}C NMR spectrum of complex, which generally appeared within a range of δ 180 to 200^{14,16,17}. However, unlike major isomer in that of *rac*-**Ru1**, only a set of C_2 -symmetric resonance signals was detected in the reaction mixture of *rac*-**Ru2**, indicating the higher C-H metalation selectivity of such a ruthenium

complex bearing the 1,7-phenanthroline ligand compared to that of the 2,3'-bipyridinium ligand. The *rac*-**Ru2** was further characterized by single-crystal X-ray diffraction. Figure 17 depicted the ORTEP of *rac*-**Ru2**, showing octahedral arrangement around the Ru metal center. Two *cis*-acetonitrile ligands lied *trans* to the cyclometalated C atoms of each chelating pyridylidene moieties and the N atoms of individual pyridine moieties were located at the mutual opposite disposition, which was good agreement with those structures developed in our group.



Scheme 38. Synthesis of *rac*-**Ru2**.

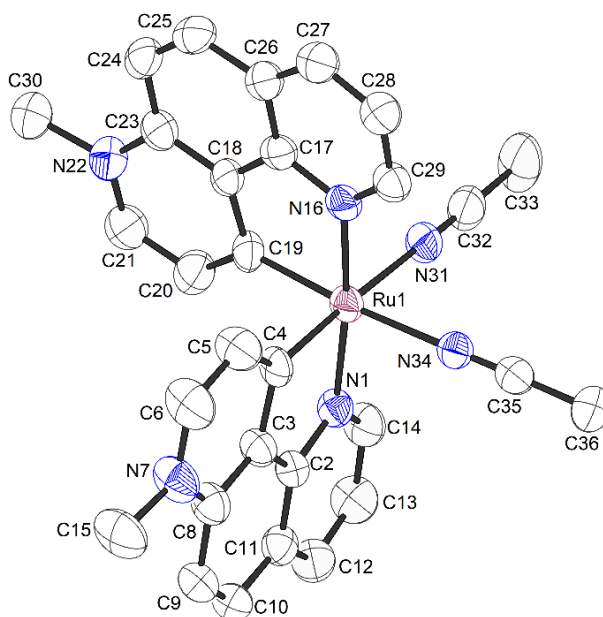


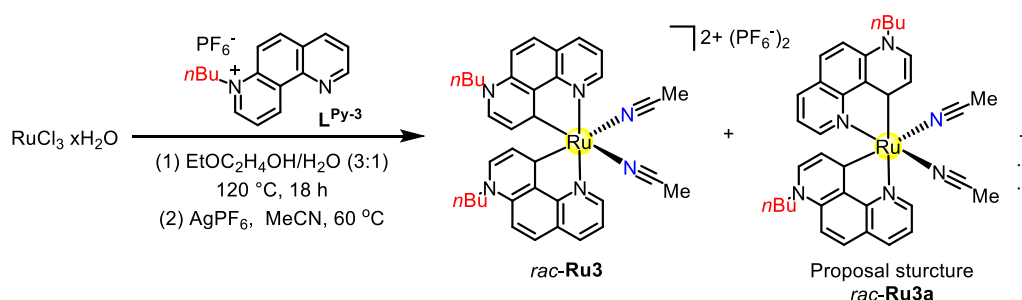
Figure 17. Crystal structure of *rac*-**Ru2**. ORTEP drawing with 50% probability thermal ellipsoids. The hexafluorophosphate counteranion and all hydrogens are omitted for clarity.

The racemic complex *rac*-**Ru2** showed good solubility in MeCN and MeOH, however, poor solubility in other organic solvents, such as DCM, DCE, THF and toluene, which might lead to limited catalytic applications. To improve the solubility of this class of complex, the

ligand was modified with a long-chain *n*-butyl substituent on the N7 position, resulting in 7-*n*Bu-1,7-phenanthrolium hexafluorophosphate (**L^{Py-3}**), which was first employed as carbene precursor owing to the simple synthesis. On the other hand, we also introduced C3-substituted ligands that might be able to not only improve the solubility of the complex but also provide the steric hindrance for the asymmetric induction in further catalysis.

2.2.3 Ruthenium Complex with Modified 1,7-Phenanthrolium Ligands

The complex *rac*-**Ru3** was prepared similarly to that of *rac*-**Ru2** by using **L^{Py-3}** instead of **L^{Py-2}** (Scheme 39). However, the ¹H NMR spectrum of the crude product was very complicated, this may due to the high reactivity of stronger electron-donor **L^{Py-3}** in the course of C-H activation in comparison to **L^{Py-2}** (Figure 18). The crude product was carefully purified by column chromatography on silica gel using DCM and MeCN as eluent to obtain three fractions that were next determined by ¹H NMR analysis. Only one set of *C*₂-symmetric resonance signals were detected in the first fraction, which was assigned as *rac*-**Ru3** (Figure 18a). ¹H NMR of the second fraction showed two sets of resonance signals corresponding to the methylene protons of the *n*Bu group (Figure 18b). The well-resolved triplet resonated at δ 4.41 belonged to *rac*-**Ru3**. Another two triplets resonated at 4.79 and 4.55 in a 1:1 ratio that were proposed as the non-*C*₂-symmetric species, *rac*-**Ru3a**, in which the molecular structure was similar to *rac*-**Ru1** (see Figure 16). The third fraction in the ¹H NMR spectrum was complicated and could not be securely assigned because of more than two possible isomers (Figure 18c).



Scheme 39. Synthesis of *rac*-**Ru3**.

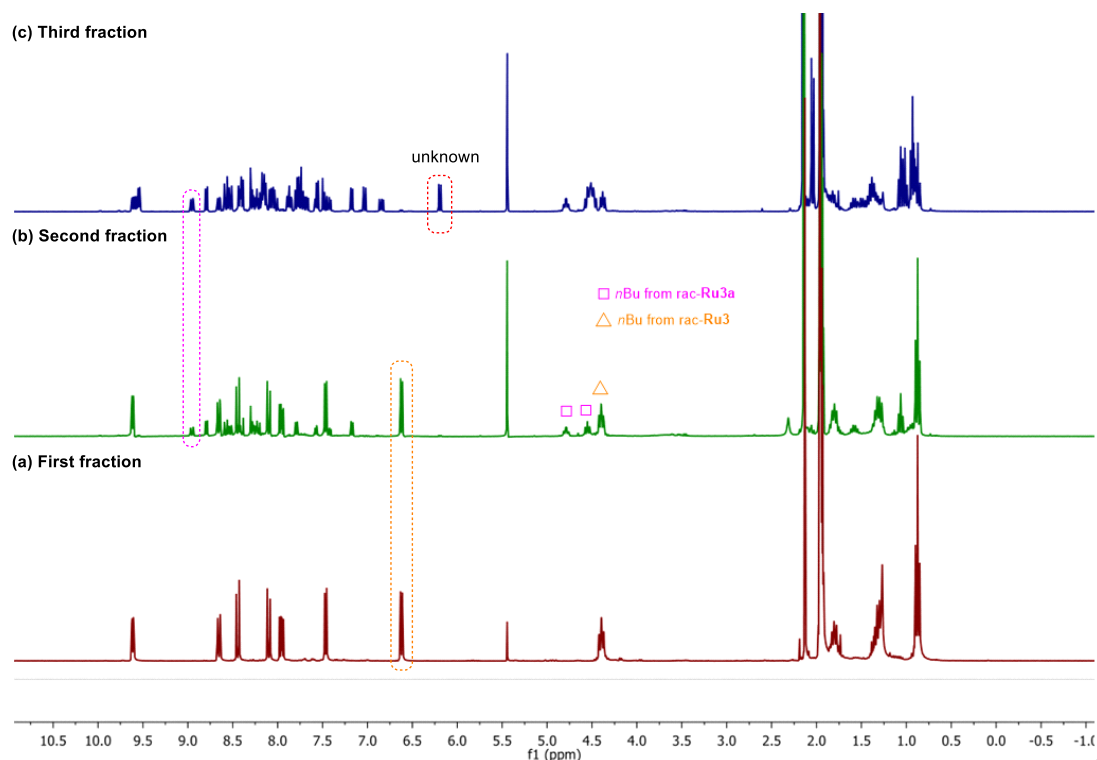


Figure 18. ^1H NMR (300 MHz, CD_3CN) spectra. (a) First fraction. (b) Second fraction. (c) Third fraction.

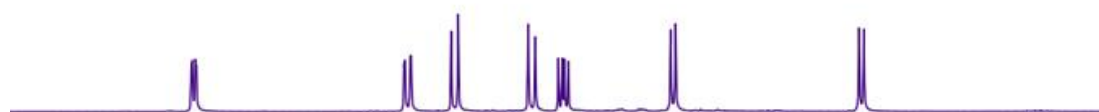
In order to improve the yield of isolated *rac*-**Ru3**, several reaction conditions were carried out using different temperatures and solvents. The detailed conditions and results are shown in Table 1 and Figure 19, respectively. Lower reaction temperature (100 degrees, Figure 19d) led to poor selectivity in comparison to the initial condition by ^1H NMR analysis. Besides, the reaction was only slightly changed by increasing the temperature to 140 degrees (Figure 19b). Further increasing the temperature to 200 degrees and reaction in ethylene glycol could not produce the desired complex. Single crystals of *rac*-**Ru3** suitable for X-ray diffraction were grown at room temperature by slow diffusion of diethyl ether into its acetonitrile solution. As shown in Figure 20, the central Ru atom is also hexa-coordinated by two 1,7-phenanthroline ligands and two acetonitrile ligands, displaying octahedral geometry. Two acetonitrile ligands and two cyclometalated C atoms are *cis*-orientated, two N atoms are arranged in a *trans* pattern. *Rac*-**Ru3** showed good solubility in either polar solvents (MeCN and MeOH) or less polar solvents (DCM, THF and chlorobenzene).

Chapter 2: Synthesis and Characterization of A New Family of Octahedral Chiral-at-Ruthenium Complexes with Pyridylidene Ligands

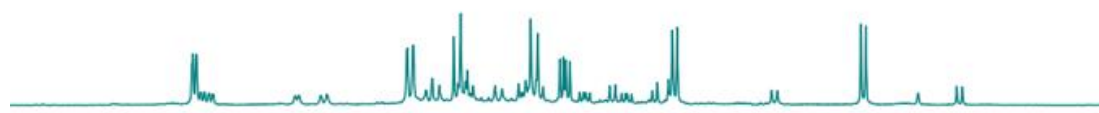
Table 1. Reaction optimization

Entry	Conditions	Results
1	2-ethoxyethanol and water, 120°C	20% yield
2	2-ethoxyethanol and water, 100°C	No purification
3	2-ethoxyethanol and water, 140°C	No purification
4	HOCH ₂ CH ₂ OH, 200 °C	Messy NMR spectra

(a) Pure complex



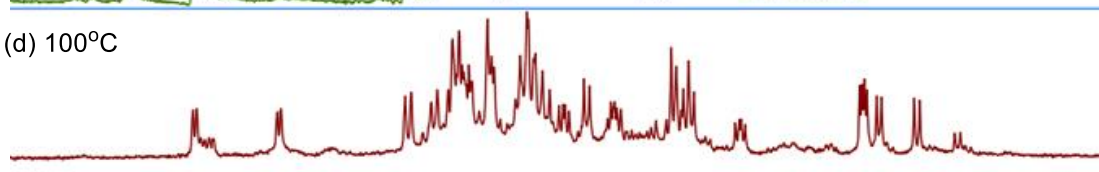
(b) 140°C



(c) 120°C



(d) 100°C



0.4 10.2 10.0 9.8 9.6 9.4 9.2 9.0 8.8 8.6 8.4 8.2 8.0 7.8 7.6 7.4 7.2 7.0 6.8 6.6 6.4 6.2 6.0 5.8 5.6
f1 (ppm)

Figure 19. ¹H NMR (300 MHz, CD₃CN) spectra of reactions: (a) pure *rac*-**Ru3**. (b) At the 130 °C. (c) At the 120 °C. (d) At the 100 °C.

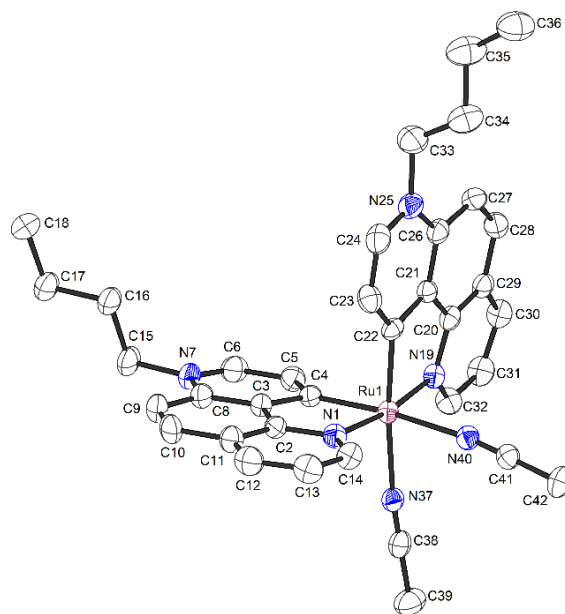
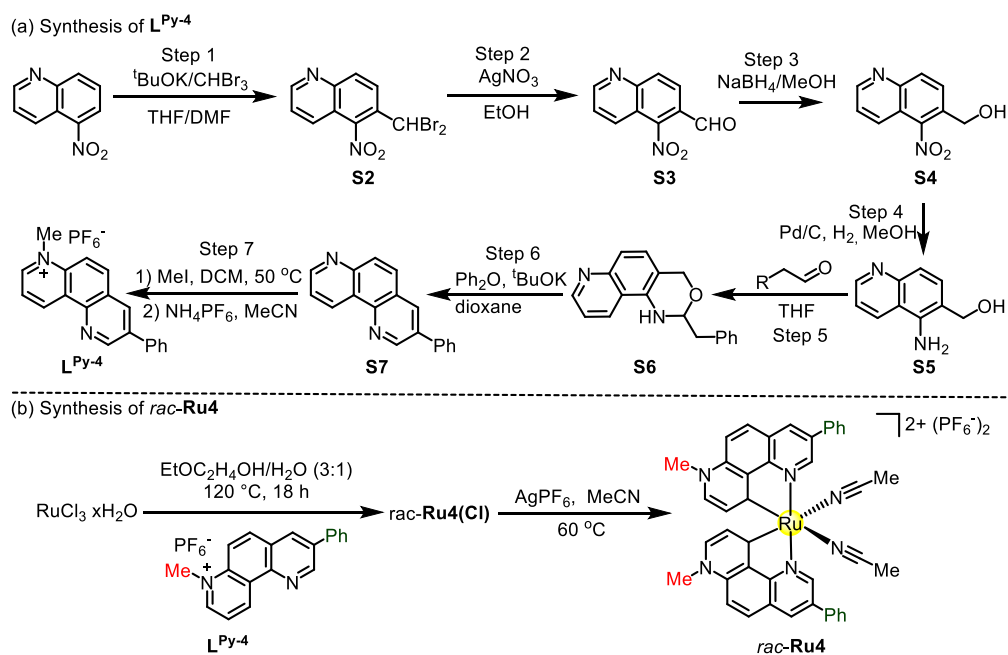


Figure 20. Crystal structure of *rac*-**Ru3**. ORTEP drawing with 50% probability thermal ellipsoids. The hexafluorophosphate counteranion and all hydrogens are omitted for clarity.

Due to the poor metalation of the stronger electron-donor N7-substituted ligand, we therefore mainly focused on the C3-substituted ligands. 7-Methyl-3-phenyl-1,7-phenanthroline hexafluorophosphate, **L^{Py-4}** as a standard C3-substituted ligand, was synthesized starting from 5-nitroquinoline in 7 steps (Scheme 40a),¹⁸ which was then employed as carbene precursor to produce the related racemic complex, *rac*-**Ru4**, as a dark red solid in 51% yield (Scheme 40b). Single crystals suitable for X-ray diffraction analysis were formed by slow diffusion of diethyl ether to its MeCN solution at room temperature for 1 day, which identified complex *rac*-**Ru4** as a C_2 -symmetric structure (Figure 21). Molecular unit in the crystal composed of a Ru center bound to two bidentate chelating pyridylidene ligands, and two acetonitrile ligands as well as two hexafluorophosphate counterion. Each one substituted benzene rings formed the dihedral angle of *ca.* 29.5° and 30.1° with their parent 1,7-phenanthroline rings, respectively, possibly the result of a steric hindrance. Moreover, the conjugation of the substituted benzene ring with the phenanthroline ring makes it possible to tune the electronic properties of the ruthenium complex through modification of chelating pyridylidene ligands around the metal center.

Chapter 2: Synthesis and Characterization of A New Family of Octahedral Chiral-at-Ruthenium Complexes with Pyridylidene Ligands



Scheme 40. Synthesis of ruthenium complex with 7-methyl-3-phenyl-1,7-phenanthrolium ligands.

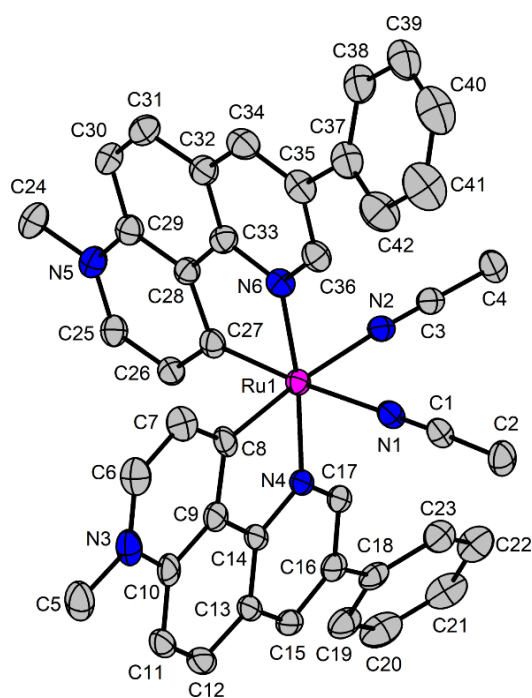
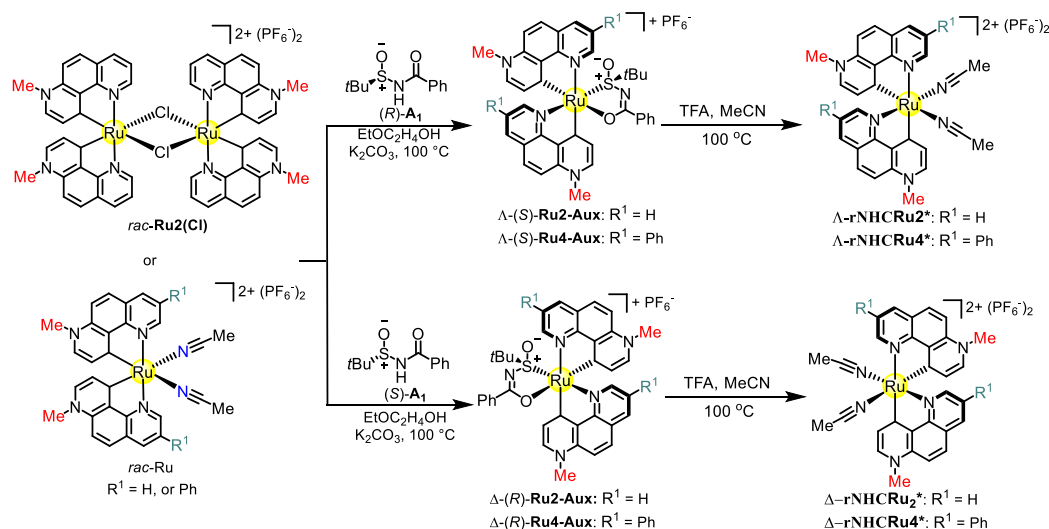


Figure 21. Crystal structure of **rac-Ru4**. Displacement ellipsoids are shown at 50 % probability level at 100 K. The hexafluorophosphate counteranion, the acetonitrile solvent molecule and all hydrogens are not shown.

2.3. Synthesis and Characterization of Non-Racemic Ruthenium Complexes



Scheme 41. Synthesis of non-racemic ruthenium complexes.

2.3.1 Synthesis and Characterization of Λ/Δ -rNHCRu2*

Several chiral ligands were used as candidates to synthesize the non-racemic complexes, while *N*-benzoyl-*tert*butanesulfinamide (**A1**)¹⁹ was finally chosen as the auxiliary of choice. The non-racemic chiral-at-ruthenium complexes were synthesized following the established procedure developed in our group (Scheme 41).²⁰ The racemic mixture was next reacted with (*R*)-**A1** in the presence of K_2CO_3 to provide the ruthenium auxiliary complex Λ -(*S*)-**Ru2-Aux** as a single diastereoisomer in 46% yield, regrettably, another single diastereoisomer Δ -(*S*)-**Ru2-Aux** could not be obtained due to instability on the silica gel column. Accordingly, Δ -(*R*)-**Ru2-Aux** was obtained in 41% yield using the same procedure by replacement of (*R*)- to (*S*)-**A1**. The further discovery showed that the ruthenium auxiliary complexes could be directly obtained by the employment of the chloride-bridged ruthenium complexes with related (*R*)- or (*S*)-**A1**.

Λ -(*S*)-**Ru2-Aux** and Δ -(*R*)-**Ru2-Aux** were fully characterized by 1H , ^{13}C , ^{19}F NMR spectrum and HRMS analysis as well as IR analysis. A non- C_2 -symmetric 1H NMR spectrum was displayed, which was expected due to the nonsymmetric bidentate auxiliary compound. The molecular structure of Λ -(*S*)-**Ru2-Aux**, acquired from slow diffusion of *n*-hexane to its dichloromethane solution, was next determined by X-ray diffraction. However, interestingly, in

the course of the formation of the *N*-sulfinylcarboximidate complexes, an unexpected but important isomerization of the chelating pyridylidene ligands occurred. As illustrated in Figure 22, Λ -(*S*)-**Ru2-Aux** was configured octahedral arrangement with two chelating pyridylidene ligands and *N*-benzoyl-*tert*-butanesulfinamide ligand around the metal center that was responsible for the overall chirality through a helical arrangement in the coordination sphere. One N atom of the first 1,7-phenanthroline ligand was shifted to a new position trans to the S atom of *N*-benzoyl-*tert*-butanesulfinamide ligand, whereas the N atom of the second 1,7-phenanthroline ligand resides trans to cyclometalated C atom of the first 1,7-phenanthroline ligand. This distinct structural feature demonstrated that one 1,7-phenanthroline ligand underwent a 180° rotation around the metal center during the reaction. The same rearrangement behavior had been found in bis-cyclometalated Ru complexes [Ru(CO)₂(BQ)₂] and [Ru(CO)₂(DBQ)₂] reported by Chou and co-workers.²¹ The Ru-N bond length of the first 1,7-phenanthroline ligand (Ru-N16 = 2.133 Å) was shorter than that of the other Ru-N bond (Ru-N1 = 2.155 Å) of the second ligand, on the contrary, much longer than those of the mutually *trans*-oriented Ru-N bonds of its parent complex *rac*-**Ru2** (2.059-2.066 Å), which manifested that trans competition between the strong δ donor pyridylidene ligand and sulfinamide ligand should be responsible for the isomerization of the complex. The flack parameter was refined to 0.001(3) which provided evidence for the absolute structure. The circular dichroism (CD) spectra of two single diastereoisomers Λ -(*S*)-**Ru2-Aux** and Δ -(*R*)-**Ru2-Aux** were measured (Figure 23), illustrating that both of them were enantiomerically enriched complexes.

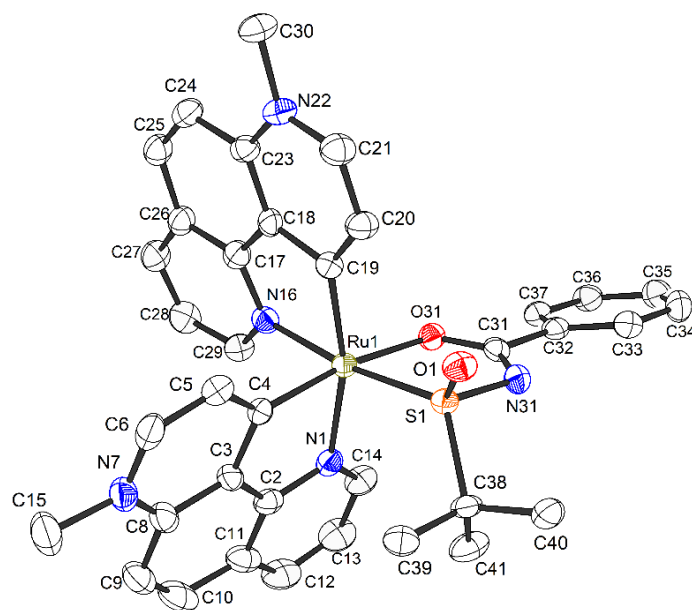


Figure 22. Crystal structure of Λ -(S)-Ru2-Aux. ORTEP drawing with 50% probability thermal ellipsoids. The hexafluorophosphate counteranion and all hydrogens are omitted for clarity.

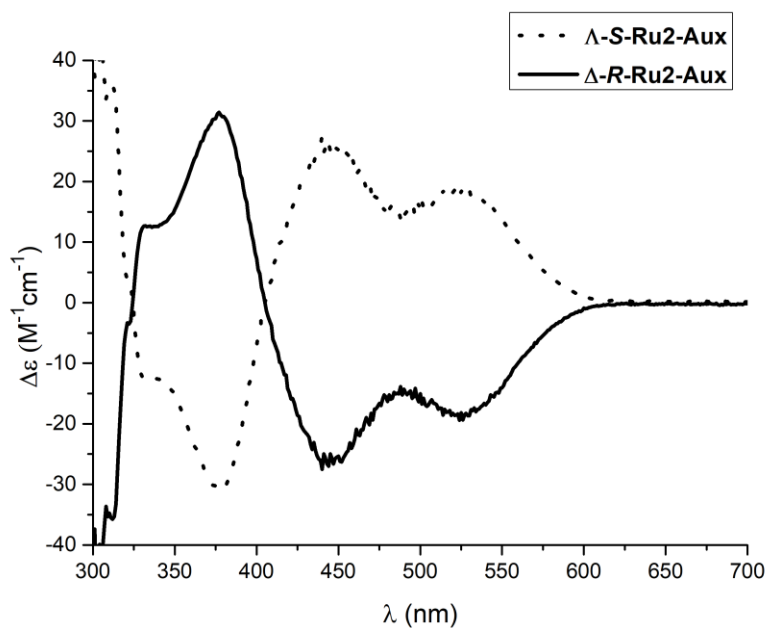


Figure 23. CD spectrum of complexes Λ -(S)-/ Δ -(R)-Ru2-Aux in CH₃CN (1.0 mM).

Finally, non-racemic complexes Λ -rNHCRu2* and Δ -rNHC-Ru2* were afforded in 83% and 81% yield via the treatment of auxiliary complexes with the acid TFA at 100 °C in acetonitrile, respectively. ¹H and ¹³C NMR spectrum showed one set of non-C₂-symmetric

resonance signals, indicating that two 1,7-phenanthroline ligands remained bound, in the *C-trans-N* fashion, to the Ru metal center. X-ray diffraction analysis of the Λ -**rNHCRu2***, as depicted in Figure 24, confirmed its structure but also enabled to determine its absolute configuration. The absolute structure of the complex was determined by the flack parameter that was refined to 0.001(3). CD spectra are shown in Figure 25 and moreover confirmed the optical activity and mirror-imaged structures of the complexes Λ -**rNHCRu2*** and Δ -**rNHCRu2***.

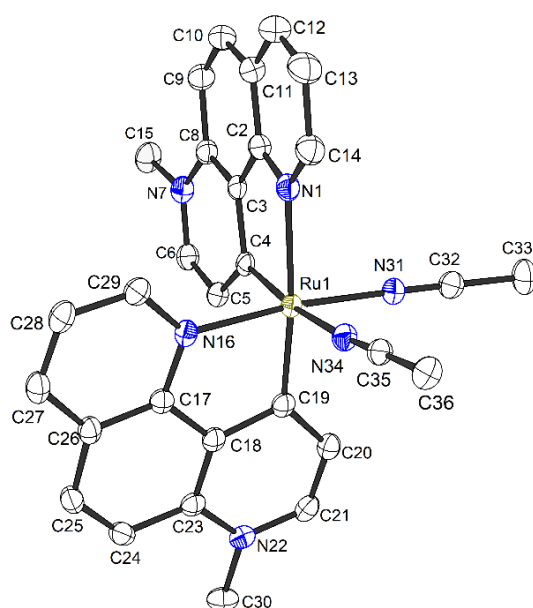


Figure 24. Crystal structure of Λ -**rNHCRu2***. ORTEP drawing with 50% probability thermal ellipsoids. The hexafluorophosphate counteranion and all hydrogens are omitted for clarity.

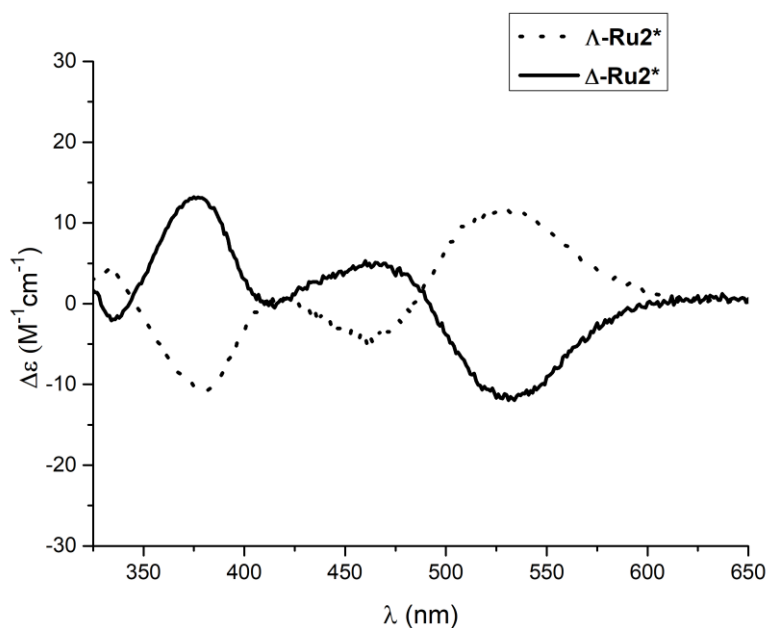


Figure 25. CD spectrum of complexes Λ -/ Δ -**rNHCRu2*** in CH_3CN (1.0 mM).

2.3.2 Synthesis and Characterization of Λ -/ Δ -**rNHCRu4***

Accordingly, the single stereoisomers Λ -(*S*)-**Ru4-Aux** or Δ -(*R*)-**Ru4-Aux** could be prepared starting from racemic complex *rac*-**Ru4** with (*R*)- or (*S*)-**A1** in the presence of K_2CO_3 in 44% and 44% yield, respectively. The CD spectra shown in Figure 26 confirmed the Λ -(*S*)-**Ru4-Aux** or Δ -(*R*)-**Ru4-Aux** to be the enantiomerically enriched complexes. Treatment with the TFA and reaction with acetonitrile afforded the complexes Λ -**rNHCRu4*** and Δ -**rNHCRu4*** in 85% and 85% yield, respectively. Λ -**rNHCRu4*** also had a non- C_2 -symmetric NMR spectrum distinctly similar to that observed for the Λ -**rNHCRu2***, demonstrating the same geometrical structure as Λ -**rNHCRu2***. The CD spectra, affording optical properties of the Λ -**rNHCRu4*** and Δ -**rNHCRu4*** complexes, showed expected mirror-image spectra for both enantiomers (Figure 27).

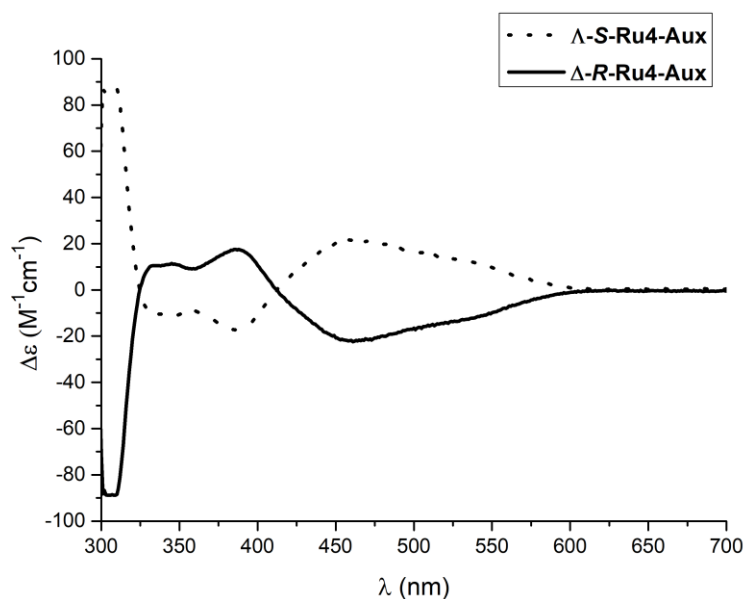


Figure 26. CD spectrum of complexes Λ -(S)-/ Δ -(R)-Ru4-Aux in CH₃CN (1.0 mM).

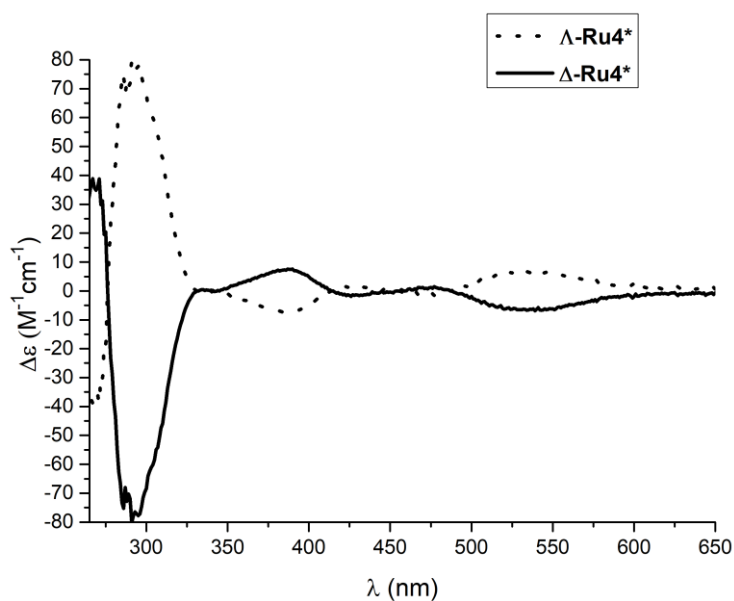


Figure 27. CD spectrum of complexes Λ -/ Δ -rNHCRu4* in CH₃CN (1.0 mM).

2.4 Stability of Enantiomerically Enriched Ruthenium Complexes

¹H NMR was used to characterize the stability of enantiomerically enriched ruthenium complexes. A solution of Λ -rNHCRu2* or Λ -rNHCRu4* in CD₃CN was monitored by ¹H NMR spectroscopy at room temperature under an atmosphere of air after 0.5 h, 8 h, 16h and 24 h, respectively. The NMR signals of Λ -rNHCRu2* and Λ -rNHCRu4*, shown in Figure 28

and Figure 29, respectively, did not change after 24 hours, indicating the highly constitutionally stability of Λ -rNHCRu2* and Λ -rNHCRu4*.

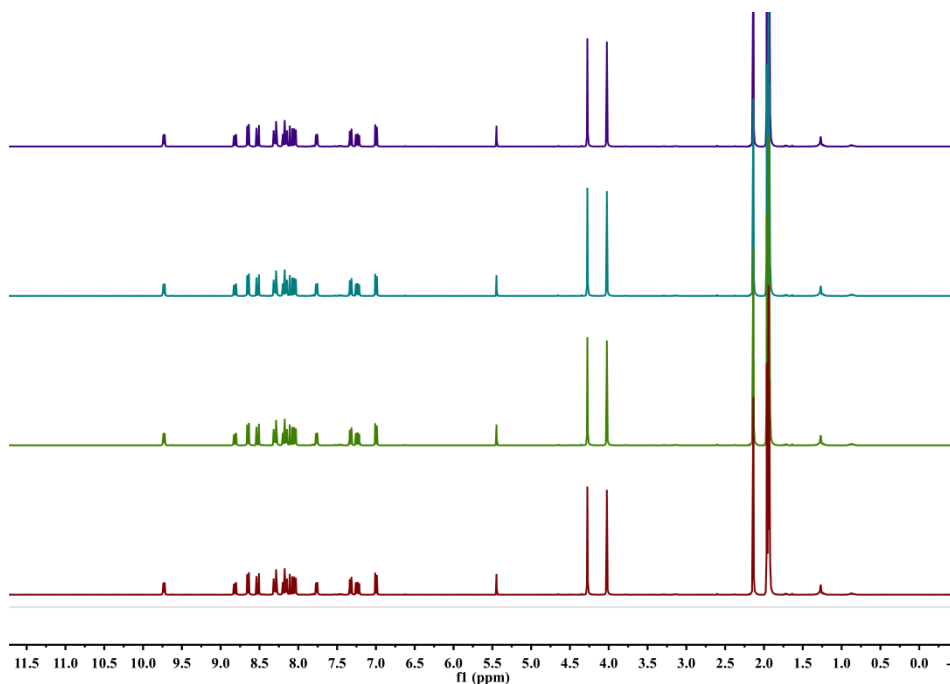


Figure 28. ^1H NMR (300 MHz) spectra of Λ -rNHCRu2* recorded in CD_3CN .

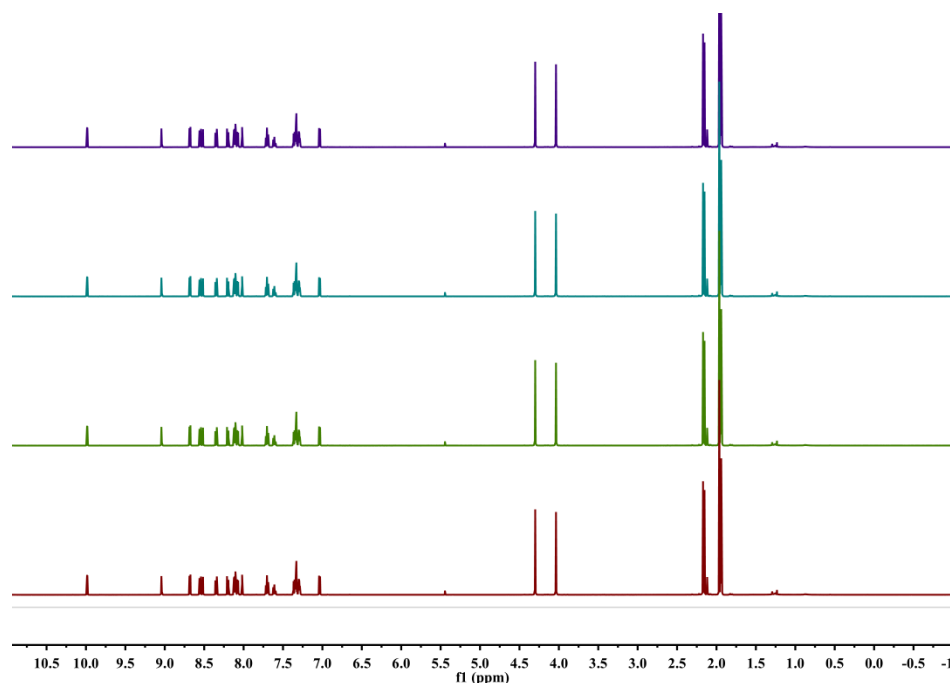


Figure 29. ^1H NMR (300 MHz) spectra of Λ -rNHCRu4* recorded in CD_3CN .

2.5 *Trans*-Influence of Octahedral Pyridylidene Ruthenium Complexes

To understand the donor properties of pyridylidenes in such class of octahedral ruthenium complexes, we next investigated their structural *trans*-effect by analysis of the Ru–N_{Ace} bond lengths (Ru–N bonds to coordinated MeCN ligands) in comparison to the analogous octahedral ruthenium complex [(L^{imi}H)₂Ru(NMe₃)₂](PF₆)₂ developed in our group.⁶

2.5.1 *Trans*-Effect of Pyridylidene versus 2-Imidazolylidene and Pyridine Ligands

The related structures of ruthenium complexes and collected Ru–N_{Ace} bond lengths are shown in Figure 30 and Table 2, respectively. For C₂-symmetric pyridylidene ruthenium complexes, *rac*-**Ru2**, the Ru–N_{Ace} bonds range between 2.128 and 2.134 Å, and as the consequence, are remarkably longer compared to those observed in [(L^{imi}H)₂Ru(NMe₃)₂](PF₆)₂ (2.098 Å) (Figure 30a). Apparently, the *trans*-effect through metal–C sigma (σ) bond was more pronounced in this pyridylidene complex. These results were consistent with previously reported remote pyridylidene palladium complexes and their imidazolylidenes analogues.⁴ The *trans*-effect of pyridylidene ligands was further disclosed by bond length comparison in non-C₂-symmetric ruthenium complexes (Figure 30b). For chiral-at-ruthenium complex Λ-**rNHCRu2***, the Ru–N_{Ace} (2.150 Å) of the first acetonitrile ligand was significantly longer than the respective Ru–N_{Ace} (2.022 Å) of the second acetonitrile ligand, exhibiting a large labialization effect attributed to its *trans* strong metal–C sigma bond versus that of the *trans* acetonitrile ligand exerted to the pyridyl unit of phenanthroline ligand. The same *trans*-influence was also found in *rac*-**Ru1**, pyridyl ring was weaker σ-donor than pyridylidene unit, and hence, the *trans*-influence of pyridine results in a significantly shorter Ru–N_{Ace} bond (2.051 Å vs 2.126 Å).

Table 2. The Ru–N_{Ace} bonds to the acetonitrile ligands

Complexes	Ru–N _{Ace} bond lengths (Å)	References
[(L ^{imi} H) ₂ Ru(NMe ₃) ₂](PF ₆) ₂	2.098, 2.098	[6]
<i>Rac</i> - Ru2	2.128, 2.134	This work
<i>Rac</i> - Ru1	2.126, 2.051	This work
rNHCRu2*	2.150, 2.022	This work

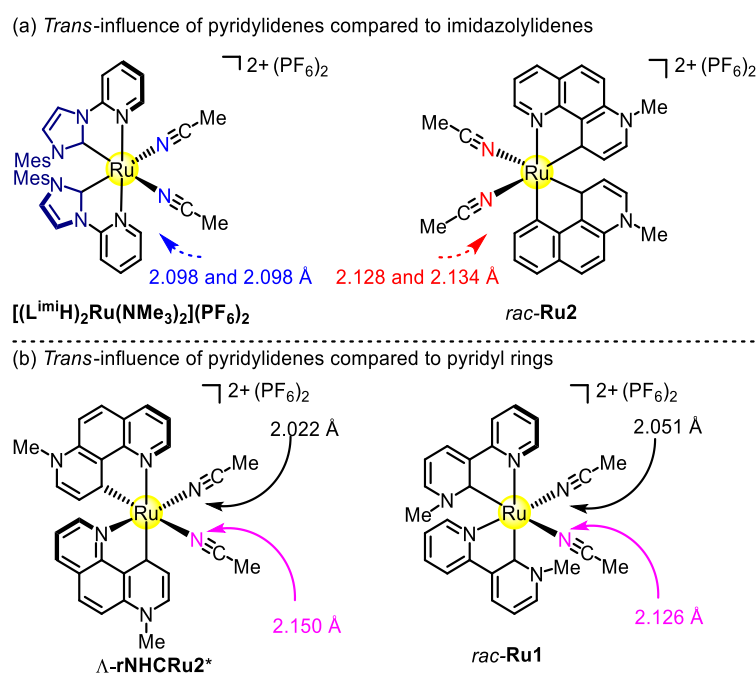


Figure 30. *Trans*-effect studied by bond length comparison of metal-acetonitrile. (a) *Trans*-effect of pyridylidenes versus imidazolylidene. (b) *Trans*-effect of pyridylidenes versus pyridyl ring.

2.5.2 *Trans*-Effect of Pyridylidene Ligands with Different Substituents

Furthermore, we were interested in the study of the *trans*-effect of pyridylidene ligands in these C_2 -symmetric ruthenium complexes (Figure 31). *Rac*-**Ru2-4** provided an interesting comparison toward the *trans*-influences of the pyridylidene based on different substituents on the C3 or N7 positions of 1,7-phenanthroline ligands. The Ru-N_{Acc} bond lengths in *rac*-**Ru3** were 2.140 and 2.141 Å, which were much longer than in *rac*-**Ru2** complex (2.128 and 2.134 Å) presented above. This comparison illustrated that the increased *trans*-influence was undoubtedly relevant to stronger electron-donor ability imposed by the *n*Bu substituted pyridylidene when compared to that of methyl-substituted analogue, and at the same time impacted the activity and selectivity of C-H activation. Besides, Ru-N_{Acc} bond lengths in *rac*-**Ru4** featuring the C3-H replaced by C3-Ph were comparable to in that of *rac*-**Ru2** yet shorter than that of *rac*-**Ru3** complex, indicating that the substituted benzene ring on C3-position did not change the δ donor ability, which supported our hypothesis and displays the feasibility of the ligand modification.

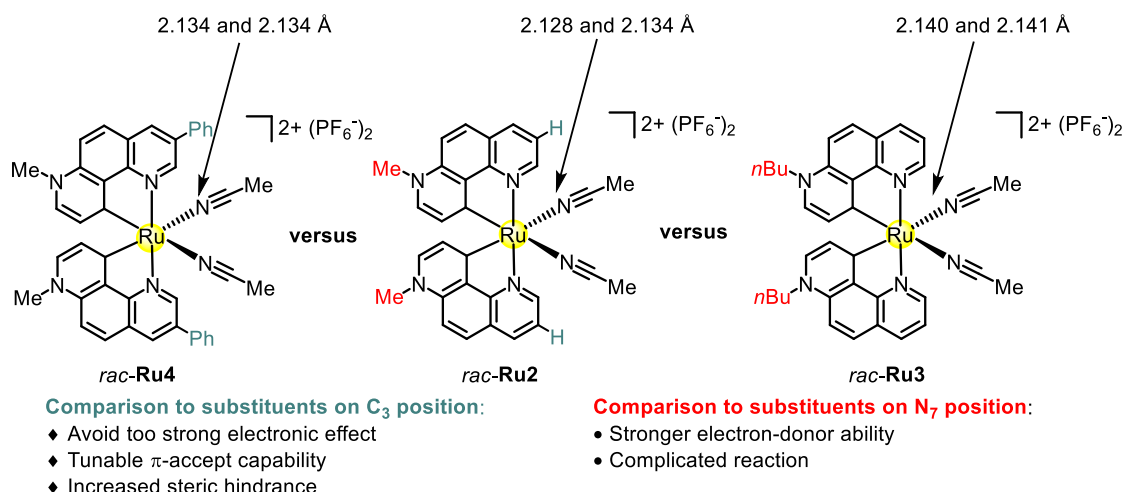


Figure 31. Comparison of *trans*-effect of pyridylidene ligands with different substituents.

2.6 Conclusion

In conclusion, we introduced the design and synthesis of a series of new octahedral racemic and chiral-at-ruthenium complexes bearing cyclometalated phenanthroline ligands, resulting in chelating pyridylidene ligands. Non-racemic complexes were synthesized using a chiral-auxiliary approach. These complexes are fully characterized by X-ray crystallography, NMR spectroscopy, and IR. Non-racemic complexes were further confirmed by CD spectroscopy. Changes in the ligand structure tremendously impacted the selectivity of C-H activation, stability and coordination mode of the complexes. In addition, the stability of enantiomerically enriched ruthenium complexes was also studied and showed significant stability in the acetonitrile. It was notable that the *trans*-effect of M-C(pyridylidene) in these complexes was much stronger than that of the complex $[(L^{imH})_2Ru(NMe_3)_2](PF_6)_2$, where $L^{imH} = 1$ -mesityl-3-(pyridin-2-yl)-1*H*-imidazol-2-ylidene, by bond length comparison of metal-acetonitriles. The *trans*-influence of pyridylidenes was further revealed in the non- C_2 -symmetric complex Λ -**rNHCRu2***, indicating a markedly larger *trans*-effect of pyridylidenes compared to pyridyl units. Moreover, the *trans*-influence was evaluated with racemic pyridylidene complexes that contained different substituents at the N7-position or C3-position of phenanthroline rings, respectively. The way of former provided enhanced *trans*-effect when replacing methyl with an *n*-butyl group. In contrast, the latter had a weak influence if switching H to phenyl moiety. Such stronger donating property may impact the potentially activity in transition metal catalysis. We thus believe that the results presented here may turn out to be of great importance in the design

of chiral ruthenium complexes and their catalytic application.

References

- 1 (a) Á. Vivancos, C. Segarra, M. Albrecht, *Chem. Rev.* **2018**, *118*, 9493–9586. (b) O. Schuster, L. Yang, H. G. Raubenheimer, M. Albrecht, *Chem. Rev.* **2009**, *109*, 3445–3478.
- 2 G. Song, Y. Zhang, Y. Su, W. Deng, K. Han, X. Li, *Organomet. Chem.* **2008**, *27*, 6193–6201.
- 3 R. Gleiter, R. Hoffmann, *J. Am. Chem. Soc.* **1968**, *90*, 5457–5460.
- 4 S. K. Schneider, P. Roembke, G. R. Julius, C. Loschen, H. G. Raubenheimer, G. Frenking, W. A. Herrmann, *Eur. J. Inorg. Chem.* **2005**, 2973–2977.
- 5 R. Lalrempuia, N. D. McDaniel, H. Müller-Bunz, S. Bernhard, M. Albrecht, *Angew. Chem., Int. Ed.* **2010**, *49*, 9765–9768.
- 6 (a) Y. Zheng, Y. Tan, K. Harms, M. Marsch, R. Riedel, L. Zhang, E. Meggers, *J. Am. Chem. Soc.* **2017**, *139*, 4322–4325. (b) J. Qin, Z. Zhou, T. Cui, M. Hemming, E. Meggers, *Chem. Sci.* **2019**, *10*, 3202–3207. (c) Z. Zhou, S. Chen, J. Qin, X. Nie, X. Zheng, K. Harms, R. Riedel, K. N. Houk, E. Meggers, *Angew. Chem. Int. Ed.* **2019**, *58*, 1088–1093. (d) Y. Tan, S. Chen, Z. Zhou, Y. Hong, S. Ivlev, K. N. Houk, E. Meggers, *Angew. Chem. Int. Ed.* **2020**, *59*, 21706–21710. (e) Y. Tan, F. Han, M. Hemming, J. Wang, K. Harms, E. Meggers, *Org. Lett.* **2020**, *22*, 6653–6656.
- 7 (a) R. J. Watts, J. S. Harrington, J. Van Houten, *J. Am. Chem. Soc.* **1977**, *99*, 2179–2187. (b) R. J. Watts, S. F. Bergeron, *J. Phys. Chem.* **1979**, *83*, 424–425. (c) J. L. Kahl, K. Hanck, K. DeArmond, *J. Inorg. Nucl. Chem.* **1979**, *41*, 495–502. (d) R. D. Gillard, R. J. Lancashire, P. A. Williams, *J. Chem. Soc., Dalton Trans.* **1979**, 190–192. (e) P. J. Spellane, R. J. Watts, *Inorg. Chem.* **1981**, *20*, 3561–3563.
- 8 W. A. Wickramasinghe, P. H. Bird, N. Serpone, *J. Chem. Soc., Chem. Commun.* **1981**, 1284–1286.
- 9 (a) S. Dholakia, R. D. Gillard, F. L. Wimmer, *Inorg. Chim. Acta* **1983**, *69*, 179–181. (b) F. L. Wimmer, S. Wimmer, *Polyhedron* **1985**, *4*, 1665–1666. (c) P. Castan, F. Dahan, S. Wimmer, F. L. Wimmer, *J. Chem. Soc., Dalton Trans.* **1990**, 2971–2977. (d) P. Castan, B. Labiad, D. Villemin, F. L. Wimmer, S. Wimmer, *J. Organomet. Chem.* **1994**, *479*, 153–157. (e) S. Wimmer, F. L. Wimmer, *J. Chem. Soc., Dalton Trans.* **1994**, 879–884.

Chapter 2: Synthesis and Characterization of A New Family of Octahedral Chiral-at-Ruthenium Complexes with Pyridylidene Ligands

- 10 (a) M. D. Ward, *J. Chem. Soc., Dalton Trans.* **1993**, 1321–1325. (b) E. C. Constable, M. W. Alexander, C. Thompson, J. Cherryman, T. Liddiment, *Inorg. Chim. Acta* **1995**, 235, 165–171.
- 11 (a) T. Koizumi, T. Tomon, K. Tanaka, *Organometallics* **2003**, 22, 970–975. (b) T. Koizumi, T. Tomon, K. Tanaka, *Bull. Chem. Soc. Jpn.* **2003**, 76, 1969–1975. (c) T. Koizumi, T. Tomon, K. Tanaka, *J. Organomet. Chem.* **2005**, 690, 1258–1264. (d) T. Koizumi, T. Tomon, K. Tanaka, *J. Organomet. Chem.* **2005**, 690, 4272–4279.
- 12 B. J. Coe, M. Helliwell, S. Sánchez, M. K. Peers, N. S. Scrutton, *Dalton Trans.*, **2015**, 44, 15420–15423.
- 13 (a) J. S. Owen, J. A. Labinger, J. E. Bercaw, *J. Am. Chem. Soc.* **2004**, 126, 8247–8255. (b) N. A. Piro, J. S. Owen, J. E. Bercaw, *Polyhedron* **2004**, 23, 2797–2804.
- 14 G. Song, Y. Zhang, Y. Su, W. Deng, K. Han, X. Li, *Organometallics* **2008**, 27, 6193–6201.
- 15 S. Semwal, J. Choudhury, *ACS Catal.* **2016**, 6, 2424–2428.
- 16 E. Stander, O. Schuster, G. Heydenrych, S. Cronje, E. Tosh, M. Albrecht, G. Frenking, H. G. Raubenheimer, *Organometallics*. **2010**, 29, 5821–5833
- 17 T. Fukushima, R. Fukuda, K. Kobayashi, G. F. Caramori, G. Frenking, M. Ehara, K. Tanaka, *Chem. - Eur. J.* **2015**, 21, 106–110.
- 18 (a) H. V. Mierde, P. V. D. Voort, F. Verpoort, *Tetrahedron Lett.* **2009**, 50, 201–203. (b) G. D. Couch, P. J. Burke, R. J. Knox, C. J. Moody, *Tetrahedron* **2008**, 64, 2816–2823.
- 19 Z. Lin, M. A. Celik, C. Fu, K. Harms, G. Frenking, E. Meggers, *Chem. - Eur. J.* **2011**, 17, 12602–12605.
- 20 L. Gong, M. Wenzel, E. Meggers, *Acc. Chem. Res.* **2013**, 46, 2635–2644.
E. Y. Li, Y.-M. Cheng, C.-C. Hsu, P.-T. Chou, G.-H. Lee, *Inorg. Chem.* **2006**, 45, 8041–8051.

Chapter 3

3.1 Chiral-at-Iron Catalysts: Expanding the Chemical Space for Asymmetric Earth-Abundant Metal Catalysis

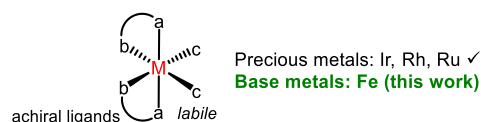
3.1.1 Catalyst Design

One of the major area in organometallic chemistry and homogeneous catalysis of the last decades has emerged from the use of chiral transition metal catalysts that contain carefully tailored chiral organic ligands.^{1,2} Meggers and others have recently demonstrated that efficiently asymmetric transition metal catalysis does not rely on chiral ligands, in which the chiral transition metal catalysts are composed solely of achiral ligands.³ In this approach, the required chirality was the consequence of asymmetric coordination of the achiral ligands around the central metal, thereby implementing metal-centered chirality. However, the efforts to develop such chiral-at-metal complexes have mainly focused on precious metals based on iridium,⁴ rhodium,^{5,6} and ruthenium^{7,8}, but the design of reactive chiral-at-metal catalysts based on earth-abundant metals, which had economical (cheap) and environmental (less toxic and benign) benefits, was elusive (Figure 32a).⁹ This could be pinpointed to the much higher lability of coordinative bonds of 3d as compared to 4d and 5d transition metals, and it was an unresolved challenge to combine a configurationally inert metal stereocenter with a reactive metal center in a single transition metal catalyst. The design strategy was especially appealing for its combination of sustainability (base metals)¹⁰ and simplicity (achiral ligands). More importantly, it was expected that without the requirement for chiral structural motifs in the ligand sphere untapped opportunities emerge for the design of earth-abundant metal complexes with new electronic properties and structural architectures that were expected to provide distinct catalytic properties for applications in academia and industry.

2-Imidazolyliidenes, as a class of electron-rich carbon-centered neutral donors, have been demonstrated to be the popular ligands in iron chemistry.¹¹ Among these, impressive progress has been made in the synthesis and organometallic chemistry of iron complexes, bearing the N-(2-pyridyl)-based 2-imidazolyliidenes. Such ligands are capable of inducing the more stable octahedral iron complexes by the chelating effect, including the bidentate N-(2-pyridyl)-substituted,¹²⁻¹⁵ tridentate pincer CNC-¹⁶⁻²¹ or CNN-²² chelating, and tetradentate NCCN-,²³⁻²⁵ NCNN-,²⁵⁻²⁸ or CNNC-²⁵ chelating 2-imidazolylidene complexes. Herein we reported a chiral transition metal catalyst scaffold that was assembled exclusively

from achiral N-(2-pyridyl)-substituted imidazolylidene bidentate ligands and monodentate acetonitrile ligands around the metal iron, the most abundant transition metal on earth (~ 4.7 wt%)²⁹ (Figure 32b). This work demonstrated the feasibility of designing chiral-at-metal catalysts from earth-abundant metals and provided a blueprint for a whole new class of earth-abundant metal asymmetric catalysts.

(a) Design from precious metals to earth-abundant metals



Challenge for 3d metals: Configurationally stable and reactive metal!

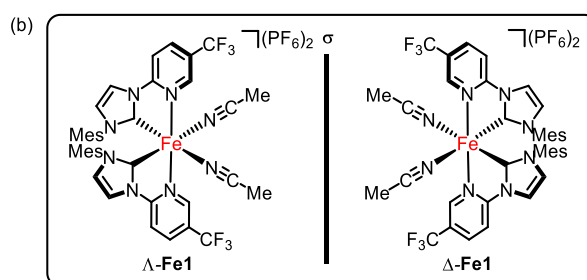


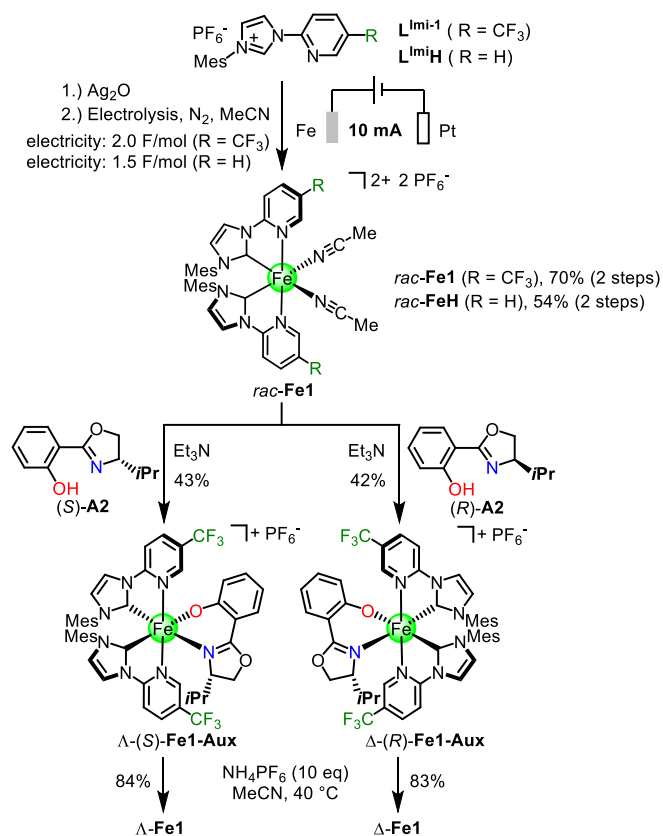
Figure 32. Chiral transition metal catalysis. (a) Combining configurational stability of a metal center with some labile ligands. (b) Chiral-at-iron catalyst developed in this study.

3.1.2 Synthesis of Chiral-at-Iron Catalyst

The chiral-at-iron catalyst design went back to related racemic complexes first reported by Hahn.¹² Two N-(2-pyridyl)-substituted N-heterocyclic carbene bidentate ligands provide a helical arrangement with metal-centered Λ (left-handed helix) or Δ configuration (right-handed helix). These two *cis*-coordinated bidentate ligands are complemented by two labile acetonitrile ligands and two hexafluorophosphate counterions. However, the disadvantage of the synthetic method described by Hahn involved handling unstable carbenes, which were generated from the deprotonation of imidazolium salts by a strong base, in combination with air and moisture sensitive iron precursor. Recently, Chen group described a convenient electrochemical procedure for the preparation of metal complex, which occurred through in situ generated unstable free carbene intermediate and the metal ion in the reactions, respectively.¹³ For example, the imidazolium salt or corresponding silver-NHC complex received an electron releasing free NHC and H_2 or Ag on the cathode, and the formed free NHC was able to react with Fe^{II} species, which was simultaneously oxidized from an elemental iron anode, to provide the related iron-NHC complexes. The racemic version of the complex *rac*-**FeH** was synthesized from elemental iron following a procedure by Chen by converting the pyridine-based imidazolium salt

Chapter 3

L^{ImiH} into its silver-carbene complex followed by electrolysis in MeCN using an iron plate as a sacrificial anode to provide *rac*- FeH in a yield of 54% over two steps (Scheme 42). It was worth noting that excess of electricity ($> 1.5 \text{ F/mol}$) was required to completely consume the ligand in combination with a constant current of 10 mA. However, *rac*- FeH showed slight decomposition in CD_2Cl_2 at room temperature under an atmosphere of air after 24 hours by ^1H NMR analysis (Figure 33, see high light part). A CF_3 group at the 5-position of the pyridyl group was next introduced to provide steric hindrance for an increased asymmetric induction and to remove electron density for higher configurational and air stability. According to the same procedure, starting from imidazolium salt, 2-(3-mesityl-1*H*-imidazol-1-yl)-5-(trifluoromethyl)pyridine hexafluorophosphate salt ($L^{\text{Imi-1}}$), to provide *rac*- Fe1 as an orange solid in a yield of 70% over two steps (Scheme 42). The NMR signal of Fe1 did not change in CD_2Cl_2 at room temperature under an atmosphere of air after 24 hours, indicating that the stability of Fe1 is higher compared to FeH (Figure 34).



Scheme 42. Synthesis of octahedral chiral-at-iron complexes.

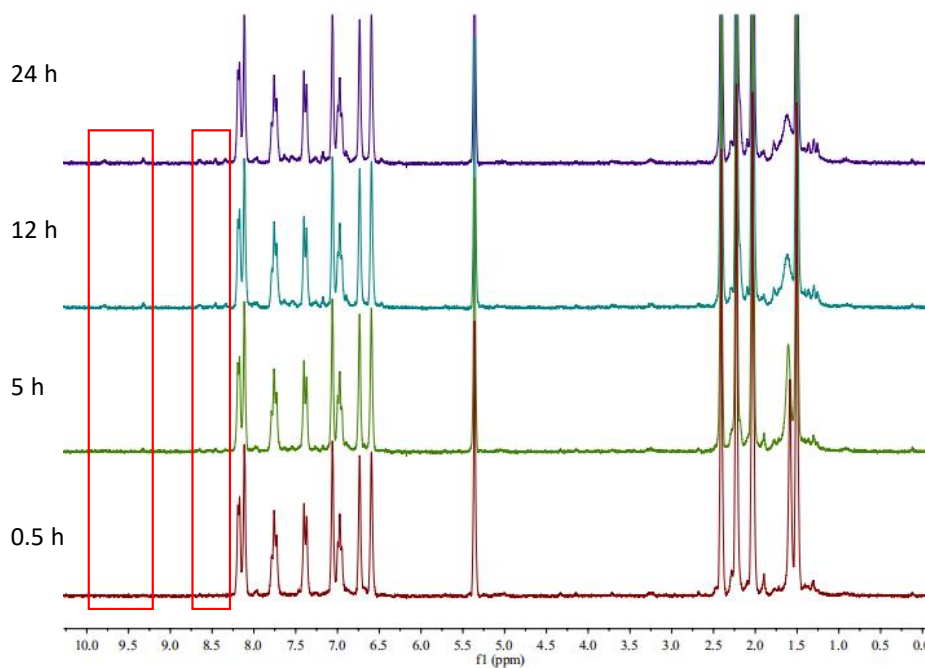


Figure 33. ^1H NMR (300 MHz) spectra of *rac*-**FeH** recorded in CD_2Cl_2 .

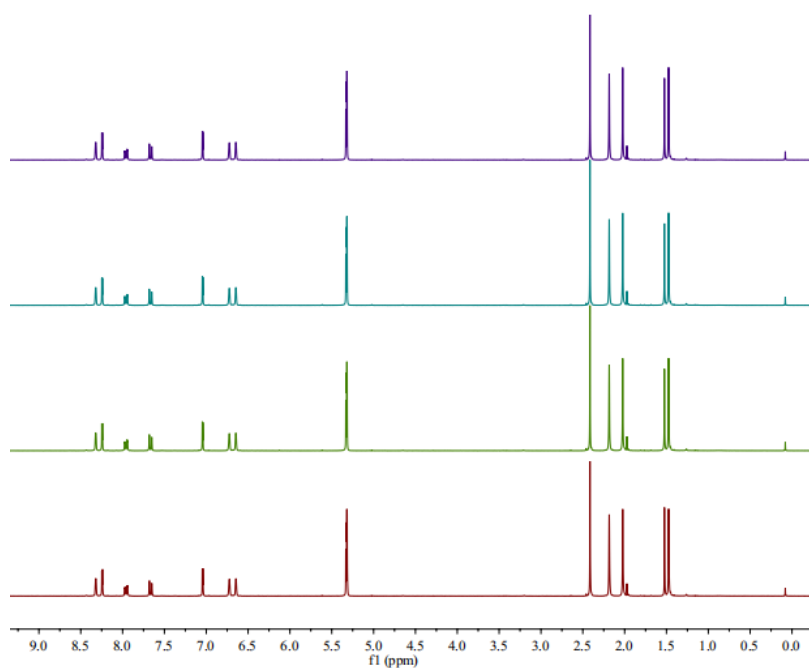


Figure 34. ^1H NMR (300 MHz) spectra of **Fe1** recorded in CD_2Cl_2 .

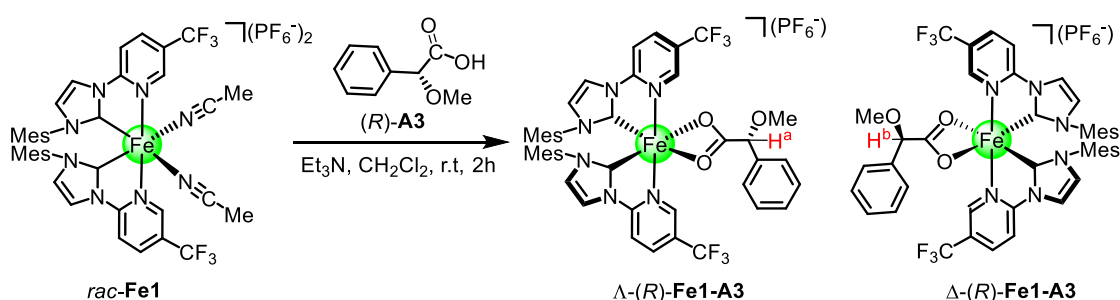
After some exploration, the chiral ligand, (*S*)- or (*R*)-2-(4-isopropyl-4,5-dihydrooxazol-2-yl)phenol (**A2**, >99% ee), was chosen as the best auxiliary of choice for the synthesis of non-racemic **Fe1** complexes (Scheme 42). Reaction of the racemic mixture with the chiral auxiliaries (*S*)-**A2** or (*R*)-**A2** in the presence of Et_3N provided the complexes Λ -(*S*)-**Fe1-Aux** or Δ -(*R*)-**Fe1-Aux** as single enantiomers and single diastereomers in 43% and 42% yield, respectively. Finally, treatment of the individual

complexes with NH_4PF_6 in MeCN at 40 °C afforded the individual enantiomers Λ - and Δ -**Fe1** as the analytically pure orange solids in 84% and 83% yields, respectively. These enantiopure catalysts Λ - and Δ -**Fe1** could be further purified via recrystallization by slow diffusion of Et_2O to its $\text{CH}_3\text{CN}/\text{THF}$ solution (volume ratio 1:1).

3.1.3 Characterization of the Iron Catalysts

(1) Enantiomeric excess of iron complexes

The enantiomeric purity of these diamagnetic low-spin complexes was determined by ^1H NMR analysis after coordination to a chiral ligand (*R*)- α -methoxyphenylacetic acid (Scheme 43).



Scheme 43. Reaction of *rac*-**Fe1** with (*R*)- α -methoxyphenylacetic acid in CH_2Cl_2 .

Method: Coordination to the enantiomerically pure chiral ligand (*R*)- α -methoxyphenylacetic acid (*R*)-**A3** was used to determine enantiomeric ratios of Λ - and Δ -**Fe1**. Λ -**Fe1** leads to Λ -(*R*)-**Fe1-A3** and Δ -**Fe1** to Δ -(*R*)-**Fe1-A3**. These two diastereomers can be distinguished by ^1H NMR (Figure 35).

Procedure: A mixture of *rac*-**Fe1**, Λ -**Fe1**, or Δ -**Fe1** (3.5 mg, 0.003 mmol), chiral ligand (*R*)- α -methoxyphenylacetic acid (99% ee, 0.1 mL, 0.03 M in CH_2Cl_2 , 1.0 eq) and triethylamine (10 eq) in CH_2Cl_2 (0.4 mL, containing 0.1% MeCN) was stirred at room temperature for 1 hour. The resulting mixture was concentrated to dryness, the residue re-dissolved in CD_2Cl_2 , and analyzed by ^1H NMR.

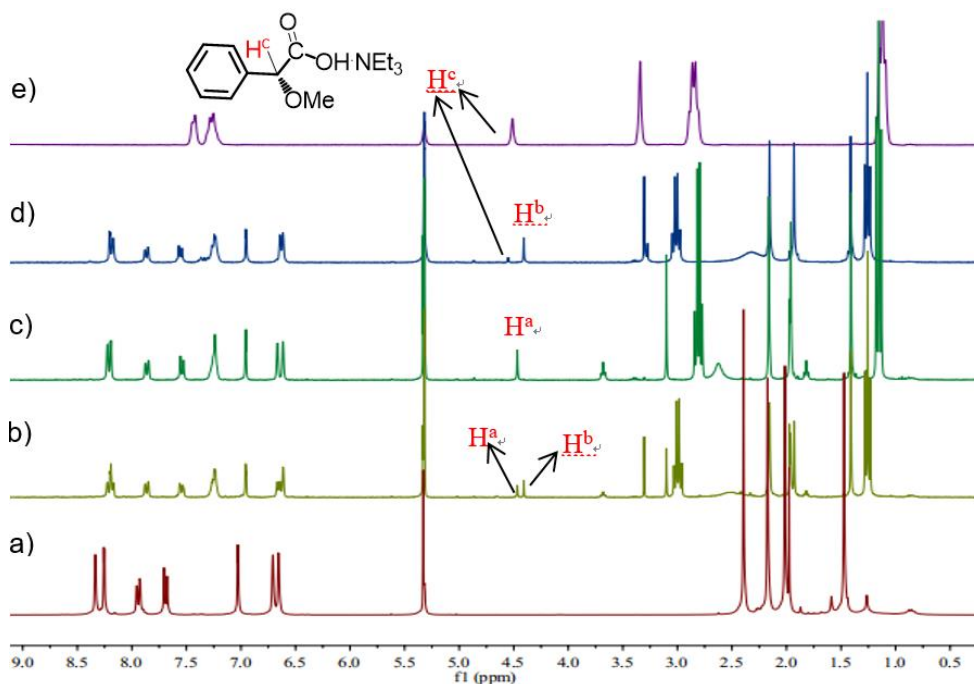


Figure 35. ^1H NMR (300 MHz, CD_2Cl_2) spectra. (a) Complex rac-Fe1 . (b) Reaction of rac-Fe1 with chiral ligand in the presence of Et_3N . (c) Reaction of $\Lambda\text{-Fe1}$ with chiral ligand in the presence of Et_3N . (d) Reaction of $\Delta\text{-Fe1}$ with chiral ligand in the presence of Et_3N . (e) Chiral ligand in the presence of triethylamine.

Results: For the reactions starting from rac-Fe1 , ^1H NMR spectroscopy showed that two sets of new peaks formed with a ratio of 1:1 (Figure 35, b), which are assigned to be the signals of $\Lambda\text{-(R)-Fe1-A3}$ and $\Delta\text{-(R)-Fe1-A3}$. For the reactions starting from $\Lambda\text{-}$ or $\Delta\text{-Fe1}$, only one set of peaks was observed (Figure 35, c or d), which were used to calculate the enantiomeric ratios of $\Delta\text{-Fe1}$ and $\Lambda\text{-Fe1}$ complexes to be $\geq 99:1$ e.r.

(2) Single-crystal X-ray diffraction and circular dichroism spectroscopy studies of $\Delta\text{-Fe1}$

A crystal structure of $\Delta\text{-Fe1}$ is shown in Figure 36 and reveals the relative and absolute metal-centered configuration. The geometry of the hexacoordinate Fe^{II} centers is best described as near octahedral, where the two *cis*-coordinated NHC rings are *trans* to the bound acetonitrile ligands and the apical positions are occupied by two pyridine rings. Noteworthy is also the inter-ligand π -stacking interactions of the mesityl moieties with the pyridyl groups of the respective other bidentate ligands, and thus their dihedral of ca. 5.5° and 8.9° , respectively. CD-spectra shown in Figure 37 furthermore confirm the optical activity and mirror-imaged structures of the complexes $\Lambda\text{-}$ and $\Delta\text{-Fe1}$.

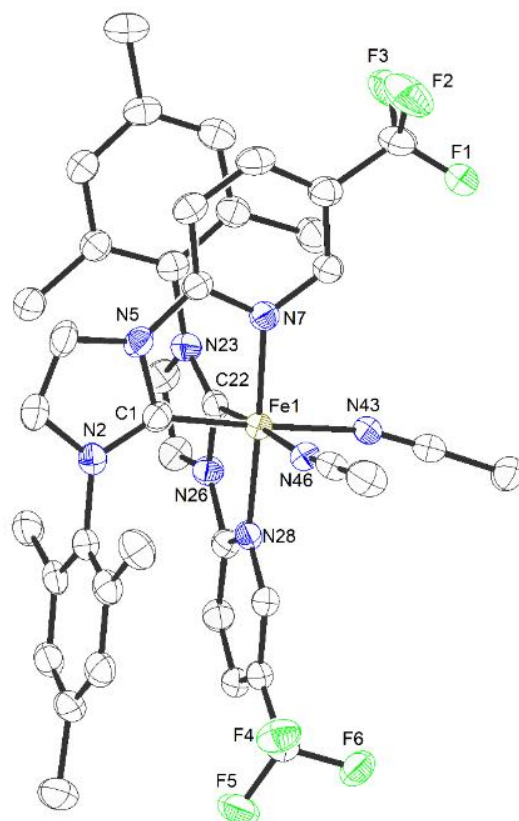


Figure 36. Single crystal X-ray structure of Δ -Fe1 (CCDC 1892226). ORTEP drawing with 50% probability thermal ellipsoids. Solvent and counterion are omitted for clarity.

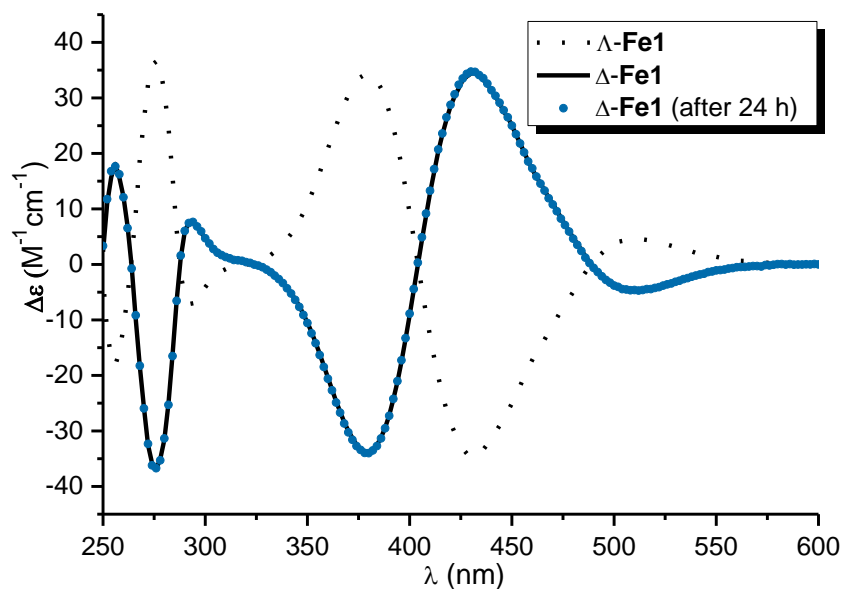


Figure 37. CD spectra of Δ -/ Δ -Fe1 (MeCN at 1.0 mM).

3.1.4 Stability Study of Iron Catalyst

Next, we evaluated the stability of the chiral-at-iron complex. Δ -Fe1 could also be handled in the

CD_2Cl_2 under air without any decomposition by ^1H NMR analysis. At room temperature in acetonitrile overnight, $\Delta\text{-Fe1}$ did not show any racemization as confirmed by CD-spectroscopy (Figure 37).

This configurational stability which was clearly distinguished from typical iron(II) complexes³⁰ with bidentate ligands could be rationalized with the electronic nature of the N-(2-pyridyl)-based imidazole-2-ylidene ligand. A strong σ -donating NHC moiety^{11,31} was combined with a σ -donating and significantly π -accepting pyridyl ligand, the latter of which was further increased by the electron withdrawing effect of the CF_3 group. It was established that kinetic and thermodynamic properties of transition metal complexes correlate, among other parameters, with the ligand field stabilization energy, which increased in octahedral complexes with strong σ -donating and π -accepting ligands.³² At the same time, the kinetic *trans*-effect of the σ -donating NHC ligand assured a high lability of the two acetonitrile ligands.³³ Thus, the *cis*-coordinated pyridyl imidazolylidene ligands with the two MeCN ligands in *trans*-orientation to the two NHC ligands provided a structural blueprint for combining configurational stability of the metal stereocenter with a high reactivity of the monodentate ligands. The same design principle had already resulted in configurationally very stable chiral-at-ruthenium catalysts (Figure 38)⁸ but it was unexpected to us that this could be even applied to the much more labile congener iron.

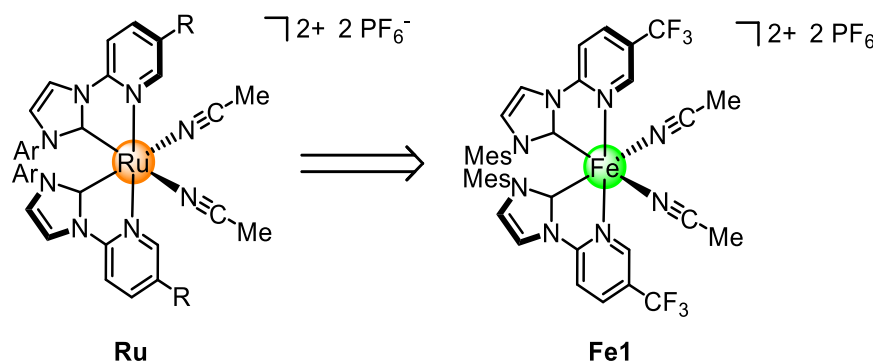


Figure 38. The structures of chiral-at-ruthenium and iron complexes.

3.1.5 Iron-Catalyzed Enantioselective Intramolecular Cannizzaro Reaction

The use of less toxic and high earth-abundance iron catalysts instead of precious metals catalysts in the development of more sustainable catalysts for homogeneous catalysis has gained considerable recent attention and has undergone explosive growth.^{12d,35} Iron-catalyzed reactions have made significant progress, whereas the homogeneous asymmetric iron catalysis is far behind.³⁶ The octahedral coordination geometry represents one of the most important coordination modes of chiral iron catalysts. These iron catalysts supported by carefully tailored chiral ligands, including types of chiral bipyridine,

N4-type, PNNP and PNP ligands, have been shown to exhibit remarkable catalytic activities in asymmetric transformations.³⁶ Although impressive developments in the design and the application of chiral catalysts over the past decade,³⁷ catalytic performance, new catalytic mechanisms, and the economic synthesis of the chiral-at-iron catalysts remain ample room for exploration.

Chiral transition metal-catalyzed intramolecular Cannizzaro reaction of α -keto aldehydes is one of the most straightforward strategies to access chiral α -hydroxyl carboxylic acid derivatives. The early asymmetric type of this reaction was reported by Nishinaga in 1992 and involved the use of cobalt metal source in combination with chiral 2,2'-diamino-1,1'-binaphthalene(DABN)-derived Schiff-base ligands.³⁴ Further work published by Moriken,³⁸ Ishihara,³⁹ and Tang,⁴⁰ respectively, and used chiral Cu(II) complexes based on oxazoline-type ligands as the catalysts. Moreover, Feng and co-worker presented the study on asymmetric Cannizzaro reaction by employed a chiral N,N'-dioxide-Fe(III) complex as the catalyst.⁴¹ It is worth noting that Tang's TOX ligand displayed excellent catalytic activity and enantioselectivity (up to 99% yield and 98% ee).⁴⁰

Inspired by these studies on enantioselective intramolecular Cannizzaro reactions of glyoxal monohydrates, we next investigated the catalytic properties of the new chiral-at-iron complex and found that **Fe1** can smoothly catalyze the conversion of phenylglyoxal monohydrate (**1**) to mandelate ester (**2**) (Table 3). Under optimized reaction conditions, 5 mol% Λ -**Fe1**, isopropanol as the alcohol of choice, and 4 Å molecular sieves induced the 1,2-hydride shift at room temperature to provide (*R*)-isopropyl mandelate (*R*)-**2a** with 99% NMR yield, 96% isolated yield and 87.5% ee (entry 1). As to be expected, Δ -**Fe1** afforded the mirror-imaged mandelate (*S*)-**2a** instead (entry 2). Lower catalyst loading resulted in a slightly decreased enantioselectivity (entry 3), whereas molecular sieves is crucial for the conversion (entry 4), and the reaction is very sensitive to the nature of the alcohol (entries 5-11).

Table 3. Enantioselective intramolecular Cannizzaro reaction catalyzed by Λ - or Δ -**Fe1**^a

Λ - or Δ -**Fe1** (cat.)
 standard conditions:
 CH₂Cl₂ (0.05 M), r.t.
 4 Å molecular sieves (MS)

entry	cat. (mol%)	R	cond. ^b	yield (%) ^c	ee (%) ^d
1	Λ - Fe1 (5.0)	<i>i</i> Pr	standard	99 (96) ^e	87.5 (<i>R</i>)
2	Δ - Fe1 (5.0)	<i>i</i> Pr	standard	99	87.0 (<i>S</i>)
3	Λ - Fe1 (3.0)	<i>i</i> Pr	standard	99	86 (<i>R</i>)
4	Λ - Fe1 (3.0)	<i>i</i> Pr	no 4Å MS	0	-
5	Δ - Fe1 (3.0)	<i>i</i> Pr	toluene	98	32 (<i>S</i>)
6	Δ - Fe1 (3.0)	<i>i</i> Pr	THF	80	20 (<i>S</i>)
7	Λ - Fe1 (3.0)	Et ₂ CH	standard	50	67 (<i>R</i>)
8	Λ - Fe1 (3.0)	<i>t</i> Bu	standard	11	n.d. ^f
9	Λ - Fe1 (3.0)	<i>n</i> Pr	standard	98	68 (<i>R</i>)
10	Λ - Fe1 (3.0)	Et	standard	98	54 (<i>R</i>)
11	Λ - Fe1 (3.0)	Me	standard	91	10 (<i>R</i>)

^aStandard conditions: **1** (0.05 mmol), ROH (0.5 mmol), 4 Å MS (25 mg powder), and **Fe** cat. (0.0015 or 0.0025 mmol) in CH₂Cl₂ (1.0 mL) stirred at r.t. for 16 h under nitrogen. ^bDeviations from standard conditions shown. ^cDetermined by ¹H NMR of the crude product using Cl₂CHCHCl₂ as internal standard. ^dEnantiomeric excess determined by HPLC analysis of purified products on a chiral stationary phase. ^eIsolated yield in brackets (0.2 mmol scale). ^fNot determined.

3.1.6 Iron-Catalyzed Asymmetric Intramolecular Nazarov Cyclization

Finally, we also investigated an asymmetric intramolecular Nazarov cyclization of **3** to **4**, which has been successfully achieved by using the related iridium-based chiral-at-metal catalysts in our group.⁴²⁻⁴⁴ Under optimized reaction conditions, Λ -**Fe1** (5 mol%) provided (1*R*,2*S*)-**4** in 89% yield, >20:1 d.r. and 83% ee (Table 4, entry 1). Yields and enantiomeric excess are strongly dependent on concentration (entry 2) and the solvent (entries 3-6). This work was developed by postdoctoral researcher Dr. Lucie Jarrige.

Table 4. Asymmetric Nazarov cyclization catalyzed by Λ -Fe1^a

entry	conditions ^b	concentration (M)	yield (%) ^c	d.r. ^d	ee (%) ^e
1	standard	0.2	89 ^f	>20:1	83
2	standard	0.05	89	>20:1	61
3	HFIP	0.2	81	>20:1	71
4	chloroform	0.2	28	>20:1	34
5	toluene	0.2	5	>20:1	n.d.
6	THF	0.2	0	-	-

^a Standard conditions: **3** (0.025 mmol), Λ -Fe1 catalyst (0.00125 mmol, 5 mol%) in CH₂Cl₂ (0.125 mL, 0.2 M) stirred at room temperature for 24 h under nitrogen.
^b Deviations from standard conditions are shown. ^c Isolated yields. ^d Diastereoselective ratio determined by ¹H NMR analysis of the crude product. ^e Enantiomeric excess determined by HPLC analysis of purified products on a chiral stationary phase.
^f Isolated yield from a 0.1 mmol scale reaction. n.d. = not determined.

Finally, time course experiments were performed with compound **3** (0.025 mmol) and Λ -Fe1 (0.00125 mmol, 5.0 mol %) in CH₂Cl₂ (0.125 mL, 0.2 M) at room temperature under an atmosphere of nitrogen. Three reactions were performed and terminated at the indicated times. Isolated yields and enantiomeric excess were provided in Table 5. The ee was not affected by the conversion, which revealed configurational stability of the iron complex throughout the catalysis.

Table 5. Time course experiments

entry	Time	yield (%) ^a	d.r.d	ee (%) ^b
1	1 h	46	>20:1	81
2	12 h	62	>20:1	83
3	24 h	90	>20:1	83

^a Isolated yield. ^b Determined by chiral HPLC analysis.

3.1.7 Conclusion

In conclusion, we here introduced the first example of an asymmetric iron catalyst that is exclusively composed of achiral ligands with the overall chirality being the result of a stereogenic iron center, implemented and retained by two surprisingly stable bidentate N-(2-pyridyl)-substituted N-heterocyclic carbene ligands. The chiral-at-iron complex combines sustainability (iron as the metal) and

simplicity (easily accessible achiral ligands). Without the requirement for chirality in the ligand sphere, new avenues emerge for the design of chiral earth-abundant metal complexes for asymmetric catalysis.

3.2 Chiral-at-Iron Catalyst for Highly Enantioselective and Diastereoselective Hetero-Diels-Alder Reaction

3.2.1 Catalysts Design

As mentioned above, chiral-at-iron catalyst **Fe1** has been proved to be an active Lewis acid catalyst for asymmetric intramolecular Cannizzaro and Nazarov reactions (Figure 39c, top). However, the limitations of this chiral Lewis acid in catalysis was the performance of only moderate enantioselectivity. Since the steric factor generally plays a crucial role in highly enantioselective catalysis, the second-generation iron complexes were therefore designed and synthesized, in which the chelating pyridyl imidazolylidene ligands were modified either by modifying the substituents at the pyridyl ring or by modulating the aryl groups (Figure 39a). We achieved this by increasing the steric bulk of the substituent at the NHC moieties from a previous 2,4,6-trimethylphenyl (Mes, **Fe1**) to a 2,6-diisopropylphenyl (Dipp, **Fe5**) moiety (Figure 39b). The use of Dipp moieties, which directly reach into the active site, results in a more restricted coordination environment and affects the asymmetric induction. We demonstrate in this work that the Λ -enantiomer of **Fe5** catalyzes Oxa-Diels-Alder^{45,46} reactions with high diastereoselectivity and up to 98% enantiomeric excess (ee) (Figure 39d, bottom). Considering that modification considerably vary the enantioselectivity and catalytic activity of the coordinated iron center toward the different asymmetric transformation, one can envision that this class of chiral catalysts will have a broad range of applications.

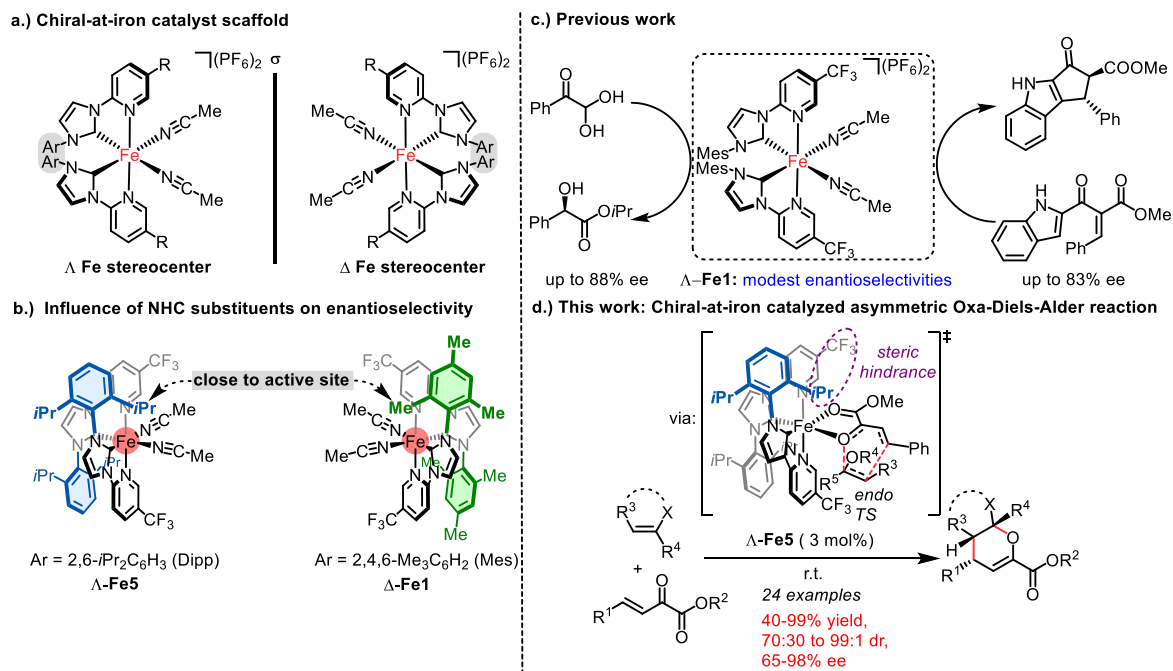
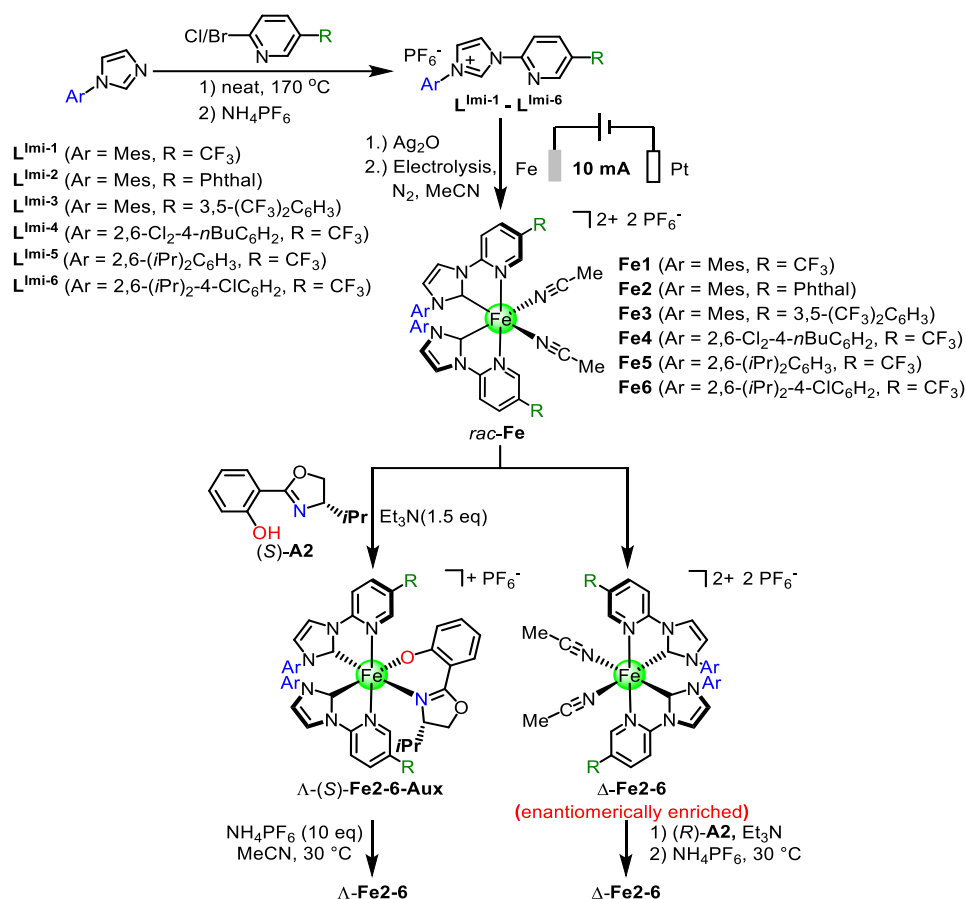


Figure 39. Chiral-at-iron complexes for asymmetric catalysis. X = alkoxy or azide.

3.2.2 Synthesis and Characterization of New Iron Complexes

(1) Synthesis of iron complexes

The new imidazolium salt ligands were synthesized following the previous synthetic procedure for **L^{Imi-1}** with slight modification, starting from *N*-substituted imidazole and 5-substituted 2-bromopyridine or 2-chloropyridine. The electrolysis strategy was tolerant to different substituted imidazolium salts, giving the analytically pure iron complexes **Fe2-6** as orange solids after passing consumption of 2.0-2.8 F/mol of electricity. All the iron complexes dissolved well in polar solvents, such as acetonitrile and methanol, and showed good solubility in DCM and THF. The synthesis of non-racemic iron complexes **Fe2-6** was a similar procedure as that of **Fe1**. A mixture of racemic complex and (*S*)-configured chiral auxiliary [(*S*)-**A2**, 1.0 eq.] was stirred in the presence of triethylamine (1.5 eq.) at room temperature overnight to provide the single diastereomer Λ -(*S*)-**Fe-Aux** complex in a moderate to high yield, and at the same time the unreacted Δ -**Fe** enantiomer was recovered and treated with (*R*)-**A2** and triethylamine in the same manner to produce the other single diastereomer Δ -(*R*)-**Fe-Aux** complex. The auxiliary was easily removed by treatment of single diastereomer Λ -(*S*)-**Fe-Aux** or Δ -(*R*)-**Fe-Aux** with NH₄PF₆ in acetonitrile at 30 °C for 18 hours to obtain the enantiopure complex Λ -**Fe2-6** or Δ -**Fe2-6**, respectively (Scheme 44). All of the enantiopure iron complexes were configurationally and constitutionally stable in the solid state for several weeks without requiring any protection from an atmosphere of air.



Scheme 44. Synthesis of chiral-at-iron complexes via the slightly modified procedure.

(2) Enantiomeric excess of non-racemic iron complexes

Enantiomeric ratios of these chiral-at-iron complexes were determined according to a method and procedure noticed above with subtle change. Compared to the previous procedure, reducing the equivalent of triethylamine from 10.0 to 1.2 was required to avoid overlapping ¹H NMR signals between the ethyl groups of triethylamine and the methoxyl moiety of (*R*)-**A3**. The results of the representative **Fe5** complexes are illustrated in Figure 40. Only one set of signals was detected by discrimination of the characteristic peaks OMe^a and OMe^b for the reaction starting from Λ-**Fe5** or Δ-**Fe5**, respectively, confirming that both Λ-**Fe5** and Δ-**Fe5** were synthesized as enantiomerically pure complexes (≥ 99:1 e.r.).

Note: The conclusion was made based on the following measurement conditions. The sample of **Fe5** for the experiment was about 2.5 mg and dissolved in 0.5 mL CD₂Cl₂. ¹H NMR measurement was performed on a Bruker AV 300 MHz spectrometer, the spectrum obtained with 256 scans (measurement time of 13 min).

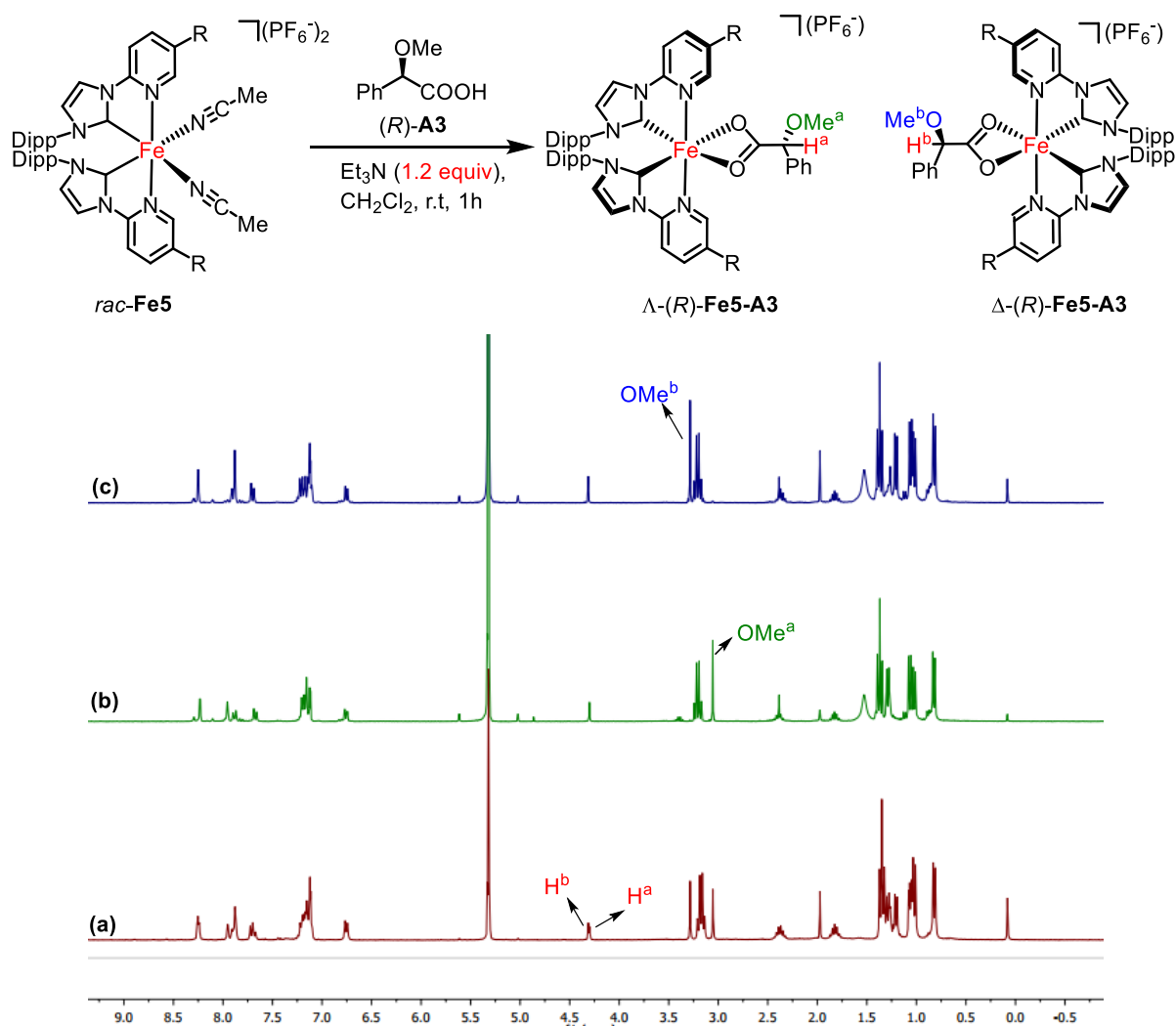


Figure 40. ¹H NMR (300 MHz, CD₂Cl₂) spectra of representative **Fe5** complexes. (a) Reaction of *rac*-**Fe5** with chiral ligand in the presence of Et₃N. (b) Reaction of Λ -**Fe5** with chiral ligand in the presence of Et₃N. (c) Reaction of Δ -**Fe5** with chiral ligand in the presence of Et₃N.

(3) Molecular structure of iron complexes

Single crystals of racemic complexes **Fe2**, **Fe5** and **Fe6** were obtained by slow diffusion of diethyl ether to its acetonitrile solutions. X-ray diffraction analysis showed that the cationic structure of complexes **Fe2**, **Fe5** and **Fe6** were analogous to **Fe1**, consisting of one iron metal center, two chelating pyridyl imidazolylidene ligands and two acetonitrile ligands, respectively. In the molecular structure of **Fe2** (Figure 41), the two mesityl rings from the respective pyridyl imidazolylidene ligands are approximately co-planar with the pyridine groups of intimate NHCs ligands with a dihedral angle of *ca.* 8.9° and 12.1°, respectively, resulting in a π - π interaction. In addition, two bulky electron-withdrawing phthalimide groups are adjusted to a dihedral angle of *ca.* 33.9° and 33.3° with their parent pyridine rings, offering potential steric hindrance in catalysis.

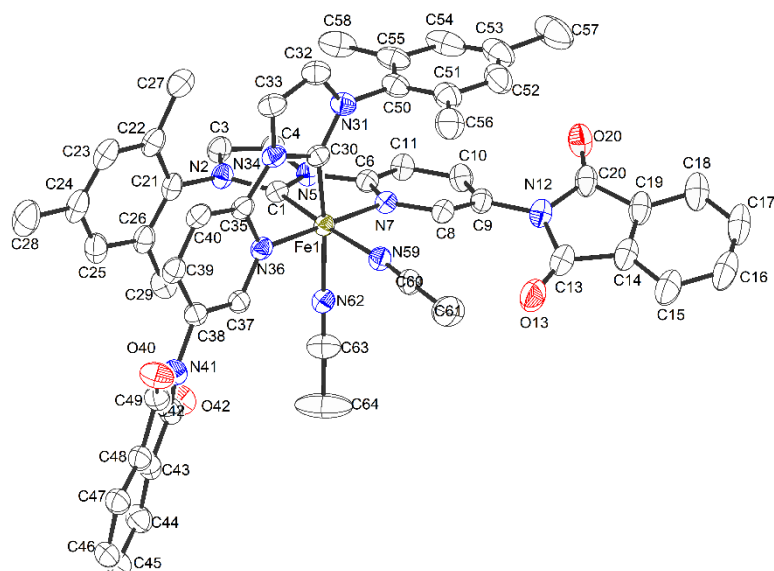


Figure 41. Crystal structure of racemic **Fe2**. ORTEP drawing with 50% probability thermal ellipsoids. The $[\text{PF}_6]^-$ anions, solvent molecules and all hydrogens are not shown.

Figure 42 shows a crystal structure of the racemic **Fe5** complex. The Dipp substituents of the individual NHC ligands stack against the pyridyl moieties of the neighboring bidentate ligand, in which one isopropyl group of each Dipp moiety reaches towards the catalytic site composed of the two labile acetonitrile ligands, imposing a sterically crowded environment, being crucial for stereoselective catalysis. It is surprising that such bulky Dipp substituted imidazolium ligands can be successfully assembled around the small first-row 3d metal iron, in which the radius of the hexa-coordinated low spin Fe^{II} is 0.61 \AA ^{47a} and is obviously smaller related to the same group 4d Ru^{II} (about 0.73 \AA)^{47b}. The overcrowded chelate environment enforced each Dipp substituent away from the intimate pyridyl ring, leading to dihedral angles of *ca.* 10.4° and 13.9° , which are obviously larger than those of **Fe2** (*ca.* 8.9° and 12.1°) and **Fe1** (*ca.* 5.5° and 8.9°) complexes.

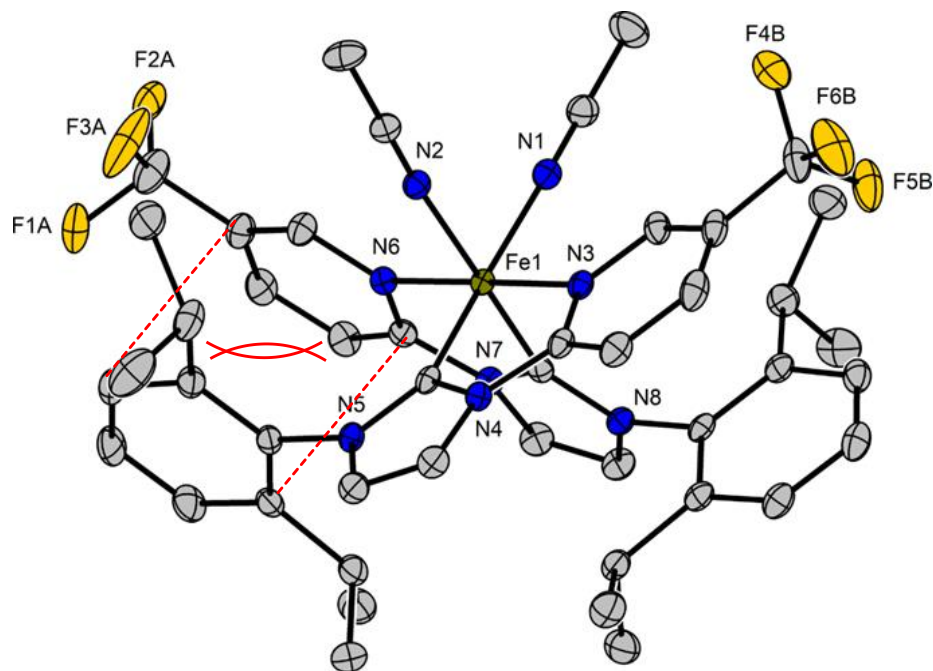


Figure 42. X-ray crystal structure of racemic **Fe5**. Only one enantiomer is shown. Only one disordered species of the CF_3 groups is shown. The hexafluorophosphate anions, the acetonitrile solvent molecule and the hydrogen atoms are omitted. Displacement ellipsoids are shown at 50 % probability level at 100 K.

3.2.3 Iron-Catalyzed Asymmetric Oxa-Diels-Alder Cycloadditions

(1) Reaction background

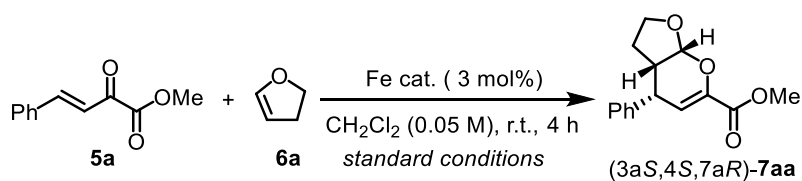
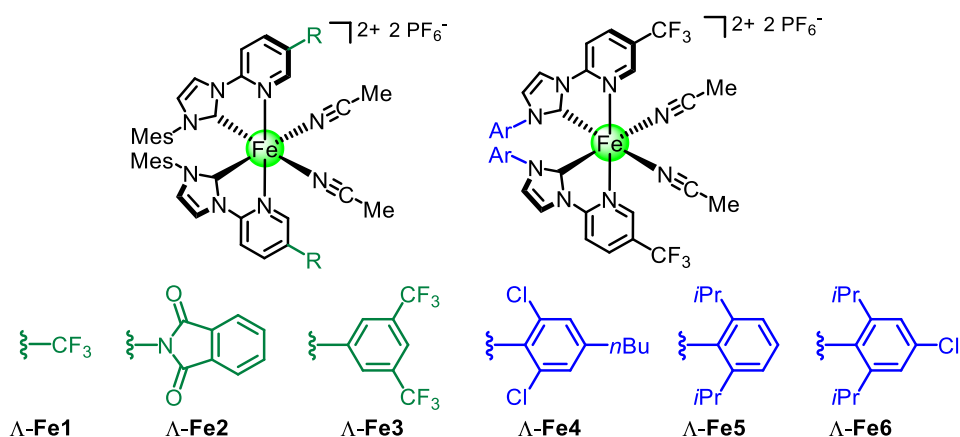
Before conducting this investigation, we reviewed the reaction background. Jørgensen et al.⁴⁸ and Evans et al.⁴⁹ independently set the gold standard for asymmetric inverse electron demand hetero-Diels-Alder reactions between β,γ -unsaturated α -ketoester and electron-rich dienophiles using readily available copper(II)-bis(oxazoline) catalysts, leading to valuable substituted 3,4-dihydro-2*H*-pyrans. Jørgensen and Evans established the preference of an endo transition state. DFT calculations by Houk and coworkers confirmed the preference for the endo diastereoselectivity due to secondary orbital interactions between the oxadiene and a lone pair of the heteroatom at the dienophile (see transition state in Figure 39c).⁵⁰ Xu recently demonstrated that copper(II)-bis(oxazoline) catalysts can also be applied to the reaction of β,γ -unsaturated α -ketoester with vinyl azides.⁵¹ Feng and coworkers introduced chiral N,N'-dioxide/erbium(III) catalyst erbium(III)-N,N'-dioxide catalysts for the asymmetric reaction of β,γ -unsaturated α -ketoester with enolether,⁵² while X.-W. Wang, Xia, and Z. Wang recently reported a copper(II)-bis(oxalamide) catalyst for this transformation.⁵³ However, to the best of our knowledge, our work marks the first example of iron-catalyzed asymmetric hetero-Diels-Alder cycloadditions between

β,γ -unsaturated α -ketoester and enoether, including one example with vinylazide as the dienophile.

(2) Initial experiments and optimization

We began our investigation by examining the role of the substituents on the para position of pyridyl rings, which showed a significant increase of constitutional stability by the introduction of an electron-withdrawing CF_3 group (**Fe1** versus **FeH**). Since this substituent is in close proximity to the site of catalysis, we aimed at increasing the asymmetric induction by replacing the CF_3 groups with bulkier electron-withdrawing substituents. However, the application of these new iron catalysts with various substituents, including phthalimides (Λ -**Fe2**) and 3,5-bis(trifluoromethyl)phenyl moieties (Λ -**Fe3**), for the reaction of the inverse electron demand hetero-Diels-Alder reaction^{45,46} of the β,γ -unsaturated α -ketoester **5a**, serving as a heterodiene, with the dienophile 2,3-dihydrofuran (**6a**), provided the corresponding bicyclic compound **7aa** with a decreased stereoselectivity. With 3 mol% of Λ -**Fe1**, (3*aS*,4*S*,7*aR*)-**7aa** was obtained in 50% yield with a dr of 98:2 and 91% ee (Table 6, entry 1), Whereas Λ -**Fe2** and Λ -**Fe3** exhibited a slightly decreased diastereoselectivity and only 88% ee (entries 2 and 3). We then evaluated the structural features of the substituents on another wing nitrogen atom. We reasoned that these substituents possessed inter-ligand π - π -stacking with the pyridyl moiety of the second pyridyl imidazol-2-ylidene ligand and therefore are in close proximity to the catalytic site providing potentially a high level of stereoselectivity. When we introduced the 2,6-dichloro-4-*n*-butyl group (Λ -**Fe4**), both catalytic activity and stereocontrol (98:2 dr and 91% ee) were identical to our previous catalyst Λ -**Fe1** (entry 4). Most gratifying results were gained after exchanging the mesityl group with a bulkier Dipp group (Λ -**Fe5**). Using 3 mol% of Λ -**Fe5**, an almost full conversion was observed after 4 hours at room temperature and (3*aS*,4*S*,7*aR*)-**7aa** was isolated in 98% yield with 97% ee and 99:1 dr (entry 5). The higher enantioselectivity of catalyst Λ -**Fe5** over Λ -**Fe1** could be attributed to a more sterically crowded active site of the bulkier Dipp group in close proximity to the iron metal center. Encouraged by the enhanced catalytic activity and enantioselectivity obtained for Λ -**Fe5**, iron complex Λ -**Fe6** bearing the bulkiest 4-chloro-2,6-diisopropylphenyl groups was used to screen the reaction, however could not provide the improved result (98% yield, 97% ee, 99:1 dr) (entry 6). We next tested some reaction parameters. Reducing the reaction temperature from room temperature to 5 °C did not produce improvement of the stereoselectivity but markedly reduced the catalytic activity (entry 9). Executing the reaction under air instead of under nitrogen reduced somewhat the catalytic activity (93% conversion after 4 hours) and enantioselectivity (94% ee, $\Delta = -3\%$ ee) (entry 10). More problematic is the presence

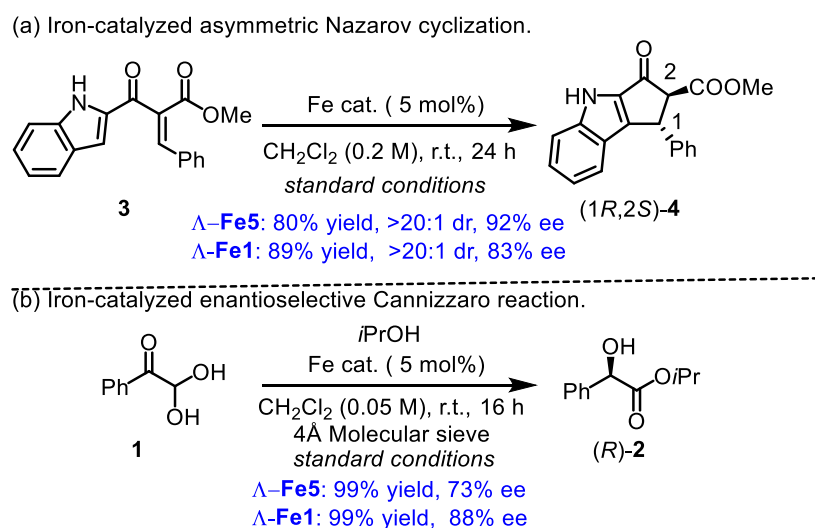
of water: the addition of 0.1% water reduced the enantioselectivity to 82% ee ($\Delta = -15\%$ ee) (entry 11). The combination of air atmosphere and 0.1% water is most deleterious. While catalytic activity and diastereoselectivity remained satisfactory, the enantioselectivity dropped to just 63% ee ($\Delta = -34\%$ ee), which we rationalized with a racemization of the catalyst during the reaction (see below) (entry 12). Interestingly, when we added just one equivalent of MeCN, the enantioselectivity recovered but the overall catalytic activity suffered, most likely due to a competition between ketoester substrate and MeCN for binding to the iron catalyst. To verify the influence of different solvents, the experiment using distilled THF as solvent was first carried out, (3*aS*,4*S*,7*aR*)-**7aa** was isolated without any erosion of activity and diastereoselectivity, however, with a tremendous decrease of the enantioselectivity of 11% ee ($\Delta = -86\%$ ee). Replacement of THF by MeOH could not supply any enantioselectivity, at the same time retarded the catalyst activation (25% conversion), which possibly occurred via a coordinated contest between the MeOH and substrate, as well as the presence of one MeO \cdots H \cdots O=C hydrogen bond interaction.

Table 6. Initial experiments and optimization^a

entry	catalyst	conditions ^a	conversion (%) ^b	dr ^c	ee (%) ^d
1	Λ -Fe1	standard	50	98:2	91
2	Λ -Fe2	standard	60	93:7	88
3	Λ -Fe3	standard	64	94:6	88
4	Λ -Fe4	standard	77	98:2	91
5	Λ -Fe5	standard	99 (98) ^e	99:1	97
6	Λ -Fe6	Standard	99	99:1	97
7	Λ -Fe5	2 mol% Λ -Fe5	99	99:1	96
8	Λ -Fe5	1 mol% Λ -Fe5	89 ^f	99:1	95.5
9	Λ -Fe5	5 °C instead of r.t.	32	99:1	97
10	Λ -Fe5	under air	93	99:1	94
11	Λ -Fe5	added H ₂ O (0.1%)	99	99:1	82
12	Λ -Fe5	air, H ₂ O (0.1%)	97	99:1	63
13	Λ -Fe5	air, H ₂ O (0.1%), MeCN ^g	19 (92) ^h	99:1	97 (86) ^h
14	Λ -Fe5	THF instead of DCM	99	99:1	11
15	Λ -Fe5	MeOH instead of DCM	25	99:1	0

^a Standard condition: **5a** (0.1 mmol), **6a** (0.15 mmol), catalyst (0.003 mmol, 3 mol%) in distilled CH₂Cl₂ (2.0 mL) stirred at r.t. for 4 h under N₂. Deviations from these standard conditions are shown. ^b Determined by ¹H NMR of crude products using Cl₂CHCHCl₂ as internal standard. ^c Diastereomeric ratios determined by ¹H NMR. ^d Determined with the purified products by HPLC on chiral stationary phase. ^e Isolated yield. ^f Reaction time of 8 h. ^g 1 equivalent of MeCN added. ^h Results in brackets are for extended reaction time of 24 h.

To further understand the steric influence of these catalysts in catalysis, we evaluated the catalytic activity and stereoselectivity of sterically hindered **Fe5** catalyst in the intramolecular Cannizzaro reaction and Nazarov cyclization reactions in comparison to **Fe1**. This same steric effect was also found in asymmetric Nazarov cyclization, 92% ee was reached for Λ -**Fe5** with a yield of 85% and a dr of >20:1 (Δ = 9% ee vs Λ -**Fe1**) (Scheme 45a). However, the bulkier Dipp substituent was not favorable for the enantioselective intramolecular Cannizzaro reaction, resulting in lower enantioselectivity of 73% ee in the presence of 5 mol% Λ -**Fe5** (Δ = -15% ee vs Λ -**Fe1**) (Scheme 45b).



Scheme 45. Asymmetric Nazarov cyclization and enantioselective Cannizzaro reaction catalyzed by **Fe5** versus **Fe1**.

(3) Substrate scope study

Having an improved chiral-at-iron catalyst in hand, we next performed a substrate scope. We initiated our work by evaluating reaction of modified methyl (*E*)-2-oxo-4-phenyl-3-butenate with the dienophile 2,3-dihydrofuran (**6a**) under the optimized condition (3mol% Λ -**Fe5**, room temperature). As presented in Figure 43, the proposed system allowed the formation of bicyclic products with high yields and excellent stereoselectivity for all selected examples. Replacing the methyl ester of **5a** with an ethyl ester provided the desired product **7ba** in 96% yield with 96% ee as a single diastereomer (99:1 dr). The obtained results for β,γ -unsaturated α -ketoester substrates bearing groups placed in the phenyl moiety (**7ca–7ha**) suggested that steric hindrance and electronic perturbations were not significant for yields and stereoselectivity (96-99% yield, 98:1-99:1 dr, 96-98% ee). Besides, the catalytic system was tolerant for enantioselective Oxa-Diels-Alder reaction of a naphthyl, an indole, and a furan substituted substrates, affording the corresponding products with high yields and excellent stereoselectivities (**7ia-7ka**, 92-99%

yield, 95:5-99:1 dr, 96-98% ee). Likewise, bicyclic products with alkenyl, cyclohexenyl, and a variety of different alkynyl groups in 4-position are also accessible with very high yields and high stereoselectivity (products **7la-7sa**, 80-98% yield, 95:5 – 98:2 dr, 90-97% ee). A crystal structure of **7sa** confirmed the preference for the *endo* stereochemistry. We also tested other dienophiles. Accordingly, the reaction of 3,4-dihydro-2*H*-pyran (**6b**) with ketoester **5a** afforded the bicyclic product **7ab** in 83% yield with 94:6 dr and 96% ee by using two equivalents of the dienophile. The reaction of ketoester **5a** with 5 equivalents of the dienophile ethyl vinyl ether (**6c**) afforded the Oxa-Diels-Alder product **7ac** in 95% yield with 88:12 dr and 91% ee. 1,1-Disubstituted enol ether 2-methoxypropene (**6d**) gave dihydropyrene product **7ad** with slightly lower enantioselectivity and diastereoselectivity (88% ee, 70:30 dr) but higher yield (98%) in comparison with **6c**. 1-Methoxyvinylbenzene is not a suitable dienophile and provided the dihydropyrene **7ae** in only 40% yield and with 83% dr and 65% ee after an elongated reaction time of 24 hours. 1-Azidoethenylbenzene can also be used as the dienophile and the reaction with ketoester **5a** afforded the azidopyrene product **7af** with 95:5 dr and 95% ee, albeit only a modest yield of 42% was observed.

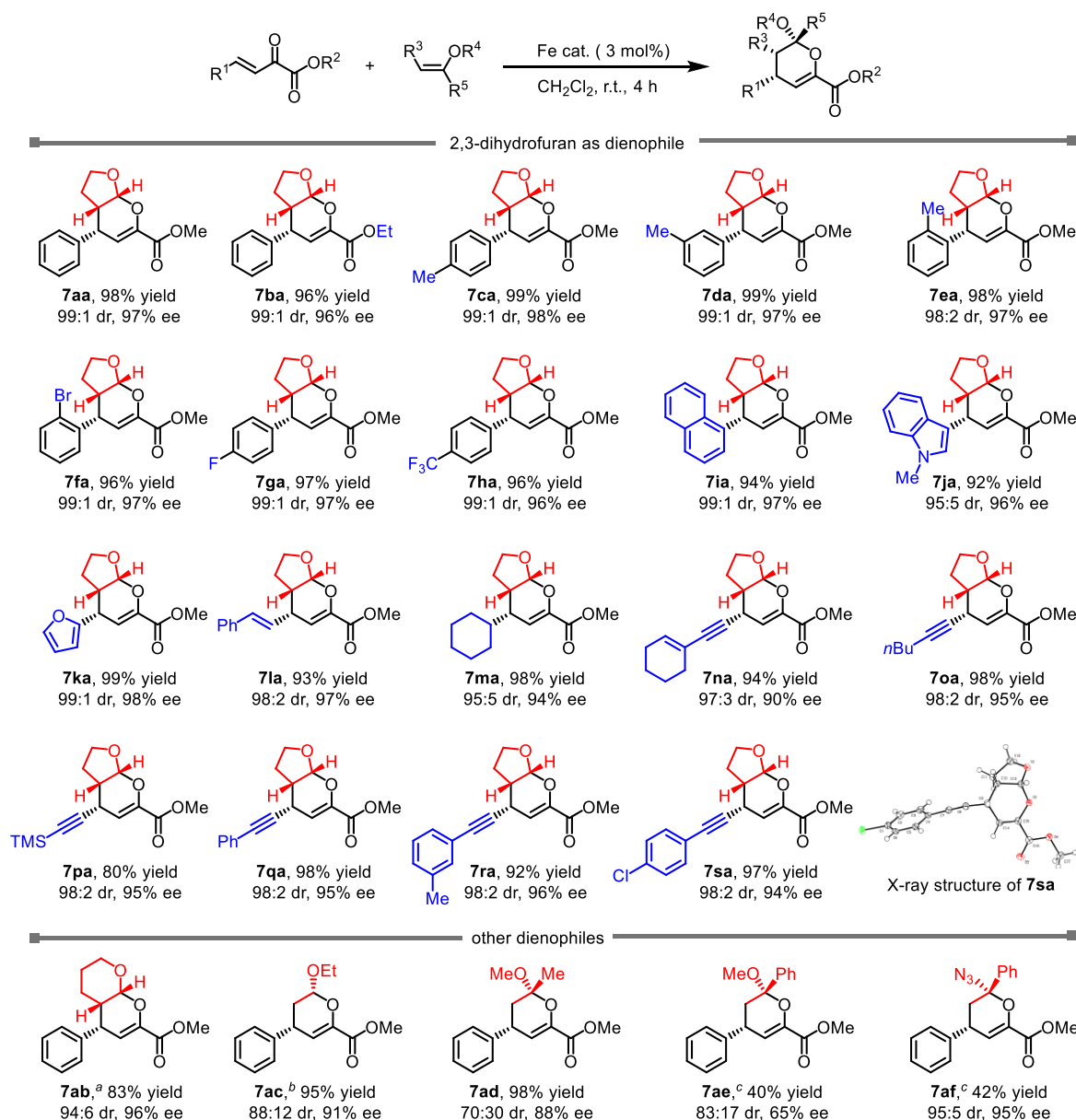


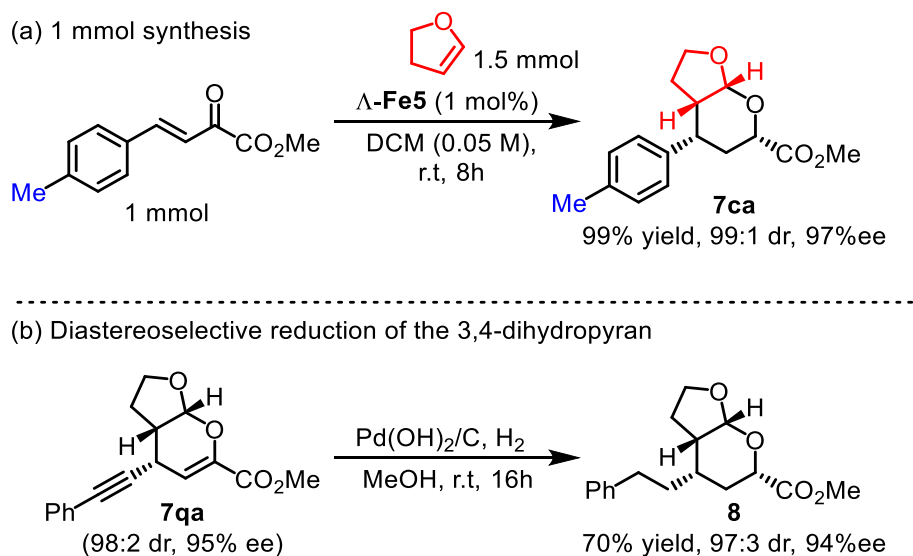
Figure 43. Substrate scope. Reaction conditions: ketoester (0.10 mmol), dienophile (0.15 mmol) and Λ -**Fe5** (0.003 mmol, 3.0 mol%) in distilled CH_2Cl_2 (2.0 mL) stirred at r.t. for 4 h under N_2 . ^aPerformed with 2 equivalents of dienophile (0.20 mmol). ^bPerformed with 5 equivalents of dienophile (0.5 mmol). ^cReaction time increased to 24 h and scale doubled (0.2 mmol ketoester).

(4) Scale of synthesis and synthetic transformation

It is worth pointing out that this approach not only exhibited outstanding functional group tolerance but also could be easily scaled without any loss in performance: using just 1 mol% of Λ -**Fe5**, ketoester **5a** at a scale of 1 mmol reacted with 2,3-dihydrofuran to furnish bicyclic 3,4-dihydro-2H-pyran **7ca** in 99% yield with 99:1 dr and 97% ee (Scheme 46a).

Considering the great importance of chiral tetrahydropyrans, we then investigated a reaction of the

obtained chiral 3,4-dihydropyran **7qa** (98:2 dr, 95% ee) with an alkynyl functional group, affording a highly diastereoselective reduction product **8** (70%, 97:3 dr, 94% ee) as a colorless oil (Scheme 46b).



Scheme 46. (a) 1 mmol scale synthesis. (b) Diastereoselective reduction of the 3,4-dihydropyran.

3.2.4. Racemization Study

Since configurational stability is a key requirement of chiral-at-metal complexes featuring exclusively achiral ligands in asymmetric catalysis, we implemented the racemization studies of **Fe5** and the initial **Fe1** (Figure 44). We began the investigation with the best candidate of catalysts, Δ -**Fe5** (>99:1 er), which was subjected to different conditions and afterward coordinated to (*R*)-**A3** (99% ee). Racemization causes the formation of a diastereomeric mixture of Δ -(*R*)-**Fe5-A3** and Δ -(*S*)-**Fe5-A3**, which can then be analyzed by $^1\text{H-NMR}$, allowing a calculation of the degree of racemization. Note, for all results presented in Figure 44, the α -ketoester **5a** was added because it provided high reproducibility of the racemization experiments. This was not the case in the absence of the α -ketoester. For example, first batch of enantiopure Δ -**Fe5** was inert in dry DCM under a nitrogen atmosphere after 4 hours, while the second batch racemized (Δ : Δ = 83:17) under the same condition. One of the differences between these two batches of Δ -**Fe5** was the small amount of remained free acetonitrile (0.1-0.2 equivalent for first batch and < 0.1 equivalent for second batch, determined by $^1\text{H-NMR}$ analysis), indicating that the free acetonitrile most likely prevented the racemization. However, it was difficult to handle the remained free acetonitrile to keep the same quality for each batch of catalyst without erosion of their enantiopurity, and hence the racemization study of Δ -**Fe5** without α -ketoester displayed the low reproducibility. Furthermore, when we used the dry DCE instead of DCM as solvent, racemization for second batch

catalyst was almost completely inhibited ($\Lambda:\Delta = 99:1$), which was certainly difficult to understand for this similar solvent alternative. In addition to the factor of free acetonitrile, there might remain other influences. Anyways, since at the beginning of the catalysis, α -ketoester is always present in the solution in a large-excess, these conditions are representative for the catalysis solutions.

Accordingly, dissolving Λ -**Fe5** and α -ketoester **5a** in a ratio of 1:5 in dry CH_2Cl_2 (1 mL) for 4 hours under nitrogen atmosphere demonstrated configurational inertness of Λ -**Fe5** under these conditions ($\Lambda:\Delta = 99:1$). However, the same conditions but under an atmosphere of air resulted in a significant racemization ($\Lambda:\Delta = 81:19$). The presence of 0.1% water (volume ratio) under an inert atmosphere resulted in $\Lambda:\Delta = 60:40$, while the combination of 0.1% water and air atmosphere led to a complete racemization. When we added just 0.1% MeCN (volume ratio) to the conditions in the presence of 0.1% water under air atmosphere, racemization was almost completely suppressed ($\Lambda:\Delta = 99:1$), which confirmed that **Fe5** is configurationally robust in the presence of MeCN. In non-coordinating solvents such as CH_2Cl_2 water and air must be omitted which is consistent with results shown in Table 6 (entries 9-11). We also screened the influence of the configuration stability on various solvents, such as THF and MeOH, leading to a diastereomeric excess of 4% ($\Lambda:\Delta = 52:48$) and a complete racemization, respectively, in line with the results described in Table 6 (entries 13-14).

To further gain insight into the racemization of this class of chiral-at-iron complexes, we then examined the racemization of Λ -**Fe1** in the presence of ketoester **5a**. Λ -**Fe1** is configurationally stable in dry DCM under inert atmosphere ($\Lambda:\Delta = 99:1$). However, when employing under the same conditions but with an atmosphere of air, a moderate diastereomeric excess of 54% ($\Lambda:\Delta = 77:23$) was observed. Under an atmosphere of nitrogen and in the presence of 0.1% water a significant racemization occurred ($\Lambda:\Delta = 70:30$). Like Λ -**Fe5**, a further deterioration of diastereomeric excess in Λ -**Fe1** occurred under the combined reaction conditions of 0.1% water and air atmosphere ($\Lambda:\Delta = 55:45$). However, this racemization was totally inhibited by the addition of only 0.1% MeCN. To be expected, the employment of dry THF or MeOH instead of dry DCM afforded serious racemization ($\Lambda:\Delta = 56:44$ or $\Lambda:\Delta = 50:40$, respectively).

From these experiments it becomes apparent that air and polar solvents (except for acetonitrile) affect the configurational stability of such chiral-at-iron complexes and thus must influence the enantioselectivity throughout the catalytic reactions. However, it is worth alluding that α -ketoesters **5a** may not be an innocent substrate and might play a role in stabilizing the configuration of the catalyst by

bidentate coordination in the resting state during catalysis.

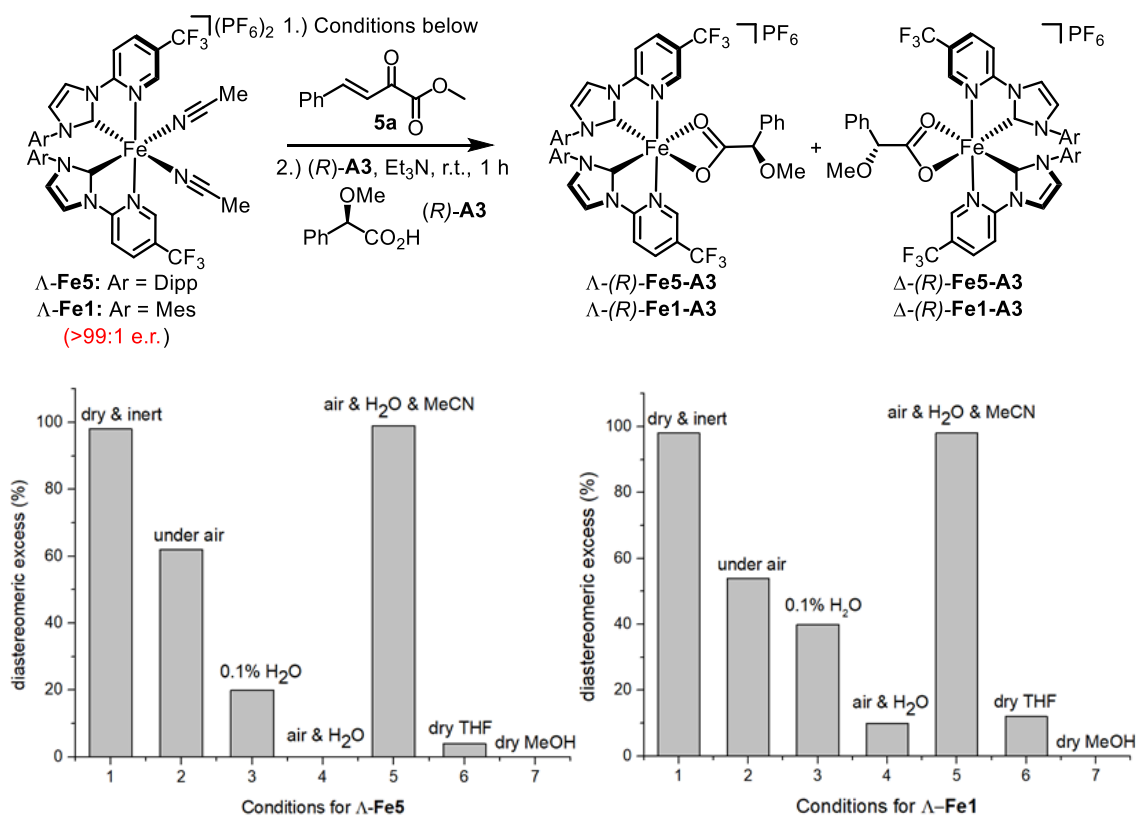


Figure 44. Racemization study. Conditions: All reactions were performed with Λ -Fe5 (1.8 mg, 1.5 μ mol) or Λ -Fe1 (1.6 mg, 1.5 μ mol) (>99:1 e.r., 1.0 eq.) and ketoester **5a** (1.4 mg, 7.5 μ mol, 5.0 eq.) in dry CH₂Cl₂ (1 mL) for 4 hours. After a certain incubation time under conditions described below, (*R*)-A3 solution (150 μ L, 0.01 M, 1.0 eq.) was added by syringe, followed by triethylamine solution (180 μ L, 0.01 M, 1.2 eq.). The resulting mixture was concentrated to dryness before stirred for 1 hour and analyzed in CD₂Cl₂ by ¹H NMR spectroscopy. Different reaction conditions for the initial incubation: (1) Under nitrogen atmosphere. (2) Under air atmosphere instead. (3) Under nitrogen atmosphere and addition of 0.1% H₂O. (4) Under air atmosphere and addition of 0.1% H₂O. (5) Under air atmosphere, addition of 0.1% H₂O, and addition of 0.1% MeCN. (6) In dry THF instead. (7) In dry MeOH instead.

Note: 0.1% H₂O or MeCN means that the dry CH₂Cl₂ was used in this work contained 0.1% H₂O or MeCN. H₂O or MeCN (20 μ L) were dissolved in dry CH₂Cl₂ (20 mL), the resulting mixture was sonicated for 10 minutes.

3.2.5 Conclusion

We here demonstrated for the first time that chiral-at-iron complexes, in which all coordinated ligands are achiral and the overall chirality is exclusively due to a stereogenic iron center, are capable of catalyzing asymmetric transformations with very high enantioselectivities. By introducing bulky 2,6-diisopropylphenyl substituents at the imidazolylidene ligands, the steric hindrance at the catalytic site

was increased, thus providing a markedly improved asymmetric induction. The new chiral-at-iron catalyst was applied to the hetero-Diels-Alder reaction between β,γ -unsaturated α -ketoester and enol ethers provide 3,4-dihydro-2*H*-pyrans in high yields with excellent diastereoselectivities (up to 99:1 dr) and excellent enantioselectivities (up to 99:1 er). Other electron rich dienophiles are also suitable as demonstrated for a reaction with a vinyl azide. Chiral 3,4-dihydro-2*H*-pyrans and their corresponding tetrahydropyrans are frequent motifs in natural products and other bioactive molecules.⁵⁴

References

- 1 P. J. Walsh, M. C. Kozlowski, *Fundamentals of Asymmetric Catalysis*; University Science Books: Sausalito, CA, **2009**.
- 2 L. Zhang, E. Meggers, *Chem. - Asian J.* **2017**, *12*, 2335–2342.
- 3 L. Zhang, E. Meggers, *Acc. Chem. Res.* **2017**, *50*, 320–330.
- 4 (a) H. Huo, C. Fu, K. Harms, E. Meggers, *J. Am. Chem. Soc.* **2014**, *136*, 2990–2993. (b) H. Huo, X. Shen, C. Wang, L. Zhang, P. Röse, L.-A. Chen, K. Harms, M. Marsch, G. Hilt, E. Meggers, *Nature* **2014**, *515*, 100–103. (c) G.-Q. Xu, H. Liang, J. Fang, Z.-L. Jia, J.-Q. Chen, P.-F. Xu, *Chem. - Asian J.* **2016**, *11*, 3355–3358.
- 5 (a) C. Wang, L.-A. Chen, H. Huo, X. Shen, K. Harms,; L. Gong, E. Meggers, *Chem. Sci.* **2015**, *6*, 1094–1100. (b) J. Ma, X. Shen, K. Harms, E. Meggers, *Dalton Trans* **2016**, *45*, 8320–8323. (c) S.-W. Li, J. Gong, Q. Kang, *Org. Lett.* **2017**, *19*, 1350–1353. (d) S. Qurban, Y. Du, J. Gong, S.-X. Lin, Q. Kang, *Chem. Commun.* **2019**, *55*, 249–252. (e) Y. Grell, Y. Hong, X. Huang, T. Mochizuki, X. Xie, K. Harms, E. Meggers, *organometallics*, **2019**, *38*, 3948–3954. (f) P. Steinlandt, W. Zuo, K. Harms, E. Meggers, *Chem - Eur J.* **2019**, *25*, 15333–15340.
- 6 M. Carmona, R. Rodríguez, V. Passarelli, F. J. Lahoz, P. García-Orduña, D. Carmona, *J. Am. Chem. Soc.* **2018**, *140*, 912–915.
- 7 J. Hartung, R. H. Grubbs, *J. Am. Chem. Soc.* **2013**, *135*, 10183–10185.
- 8 (a) Y. Zheng, Y. Tan, K. Harms, M. Marsch, R. Riedel, L. Zhang, E. Meggers, *J. Am. Chem. Soc.* **2017**, *139*, 4322–4325. (b) J. Qin, Z. Zhou, T. Cui, M. Hemming, E. Meggers, *Chem. Sci.* **2019**, *10*, 3202–3207. (c) Z. Zhou, S. Chen, J. Qin, X. Nie, X. Zheng, K. Harms, R. Riedel, K. N. Houk, E. Meggers, *Angew. Chem. Int. Ed.* **2019**, *58*, 1088–1093. (d) Y. Tan, S. Chen, Z. Zhou, Y. Hong, S. Ivlev, K. N. Houk, E. Meggers, *Angew. Chem. Int. Ed.* **2020**, *59*, 21706–21710. (e) Y. Tan, F. Han, M. Hemming, J. Wang, K. Harms, E. Meggers, *Org. Lett.* **2020**, *22*, 6653–6656.
- 9 Note that this refers to reactive chiral-at-metal complexes in which the metal is directly involved

in catalysis as opposed to chiral metal complexes in which catalysis is mediated entirely through the ligand sphere (metal-templated catalysis).

- 10 P. Chirik, R. Morris, *Acc. Chem. Res.* **2015**, *48*, 2495.
- 11 For reviews on iron complexes with 2-Imidazolylidenes. (a) In *N-Heterocyclic Carbenes: From Laboratory Curiosities to Efficient Synthetic Tools*; Diez-Gonzalez, S., Ed.; Catalysis Series; The Royal Society of Chemistry: Cambridge, UK, **2011**. (b) K. Riener, S. Haslinger, A. Raba, M. P. Högerl, M. Cokoja, W. A. Herrmann, F. E. Kühn, *Chem. Rev.*, **2014**, *114*, 5215–5272. (c) C. Johnson, M. Albrecht, *Coord. Chem. Rev.*, **2017**, *352*, 1–14. (d) Q. Liang, D. Song, *Chem. Soc. Rev.*, **2020**, *49*, 1209–1232.
- 12 O. Kaufhold, F.E. Hahn, T. Pape, A. Hepp, *J. Organometallic Chem.* **2008**, *693*, 3435–3440.
- 13 B. Liu, Y. Zhang, D. Xu, W. Chen, *Chem. Commun.*, **2011**, *47*, 2883–2885.
- 14 Y. Zhang, B. Liu, H. Wu, W. Chen, *Chin Sci Bull.* **2012**, *57*, 2368–2376.
- 15 A. Francés-Monerris, K. Magra, M. Darari, C. Cebrián, M. Beley, E. Domenichini, S. Haacke, M. Pastore, X. Assfeld, P. C. Gros, A. Monari, *Inorg. Chem.* **2018**, *57*, 10431–10441.
- 16 A. A. Danopoulos, N. Tsoureas, J. A. Wright, M. E. Light, *Organometallics* **2004**, *23*, 166–168.
- 17 D. S. McGuinness, V. C. Gibson, J. W. Steed, *Organometallics*, **2004**, *23*, 6288–6292.
- 18 A. Donner, B. Trepka, S. Theiss, F. Immler, J. Traber, S. Polarz, *Langmuir* **2019**, *35*, 16514–16520.
- 19 T. Duchanois, T. Etienne, C. Cebrián, L. Liu, A. Monari, M. Beley, X. Assfeld, S. Haacke, P. C. Gros, *Eur. J. Inorg. Chem.* **2015**, 2469–2477.
- 20 (a) P. Zimmer, P. Müller, L. Burkhardt, R. Schepper, A. Neuba, J. Steube, F. Dietrich, U. Flörke, S. Mangold, M. Gerhards, M. Bauer, *Eur. J. Inorg. Chem.* **2017**, 1504–1509. (b) P. Zimmer, L. Burkhardt, R. Schepper, K. Zheng, D. Gosztola, A. Neuba, U. Flörke, C. Wölper, R. Schoch, W. Gawelda, S. E. Canton, M. Bauer, *Eur. J. Inorg. Chem.* **2018**, 5203–5214.
- 21 S. M. Rummelt, J. M. Darmon, R. P. Yu, P. Viereck, T. P. Pabst, Z. R. Turner, G. W. Margulieux, S. Gu, P. J. Chirik, *Organometallics* **2019**, *38*, 3159–3168.
- 22 (a) F. Chen, N. Liu, B. Dai, *ACS Sustainable Chem. Eng.* **2017**, *5*, 9065–9075. (b) F. Chen, M. Li, J. Wang, B. Dai, N. Liu, *J. CO2 Util.*, **2018**, *28*, 181–188. (c) F. Chen, Q.-C. Zhang, D. Wei, Q. Bu, B. Dai, N. Liu, *J. Org. Chem.* **2019**, *84*, 11407–11416.
- 23 B. Liu, Q. Xia, W. Chen, *Angew. Chem. Int. Ed.* **2009**, *48*, 5513–5516.

- 24 A. Raba, M. Cokoja, S. Ewald, K. Riener, E. Herdtweck, A. Pöthig, W. A. Herrmann, F. E. Kühn, *Organometallics* **2012**, *31*, 2793–2800.
- 25 D. T. Weiss, M. R. Anneser, S. Haslinger, A. Pöthig, M. Cokoja, J.-M. Basset, F. E. Kühn, *Organometallics* **2015**, *34*, 5155–5166.
- 26 (a) A. Raba, M. Cokoja, W. A. Herrmann, F. E. Kühn, *Chem. Commun.*, **2014**, *50*, 11454–11457. (b) A. C. Lindhorst, M. Drees, W. Bonrath, J. Schütz, T. Netscher, F. E. Kühn, *J. Catal.*, **2017**, *352*, 599–605. (c) A. C. Lindhorst, J. Schütz, T. Netscher, W. Bonrath, F. E. Kühn, *Catal. Sci. Technol.*, **2017**, *7*, 1902–1911.
- 27 S. Haslinger, A. Raba, M. Cokoja, A. Pöthig and F. E. Kühn, *J. Catal.*, **2015**, *331*, 147–153.
- 28 Ö. Karaca, M. R. Anneser, J. W. Kück, A. C. Lindhorst, M. Cokoja, F. E. Kühn, *J. Catal.*, **2016**, *344*, 213–220.
- 29 Halka, M.; Nordstrom, B. *Transition metals*; Facts On File: London, **2011**.
- 30 (a) F. M. Van Meter, H. M. Neumann, *J. Am. Chem. Soc.* **1976**, *98*, 1388–1394. (b) J. Lacour, J. J. Jodry, C. Ginglinger, S. Torche-Haldimann, *Angew. Chem. Int. Ed.* **1998**, *37*, 2379–2380.
- 31 S. Díez-González, S. P. Nolan, *Coord. Chem. Rev.*, **2007**, *251*, 874–883.
- 32 Crabtree, R. H. *The Organometallic Chemistry of Transition Metals*; John Wiley & Sons Inc.: Hoboken, New Jersey, **2014**.
- 33 Coe, B. J.; Glenwright, S. J. Trans-effects in octahedral transition metal complexes. *Coord. Chem. Rev.* **2000**, *203*, 5–80.
- 34 K. Maruyama, Y. Murakami, K. Yoda, T. Mashino, A. Nishinaga, *J. Chem. Soc., Chem. Commun.*, **1992**, 1617–1618.
- 35 For reviews on iron catalysis for organic synthesis, see: (a) C. Bolm, J. Legros, J. Le Paih, L. Zani, *Chem. Rev.* **2004**, *104*, 6217–6254. (b) S. Enthaler, K. Junge, M. Beller, *Angew. Chem. Int. Ed.* **2008**, *47*, 3317–3321. (c) I. Bauer, H.-J. Knölker, *Chem. Rev.* **2015**, *115*, 3170–3387. (d) A. Fürstner, *ACS Centr. Sci.* **2016**, *2*, 778–789. (e) G. Olivio, O. Cussó, M. Costas, *Chem. Asian J.* **2016**, *11*, 3148–3158 (f) R. Shang, L. Ilies, E. Nakamura, *Chem. Rev.* **2017**, *117*, 9086–9039. (g) A. Piontek, E. Bisz, M. Szostak, *Angew. Chem. Int. Ed.* **2018**, *57*, 11116–11128. (g) M. Guo, T. Corona, K. Ray, W. Nam, *ACS Centr. Sci.* **2019**, *5*, 13–28. (h) Batista, V. F.; D. C. G. A. Pinto, A. M. S. Silva, *ACS Catal.* **2020**, *10*, 10096–10116. (i) C. Damiano, P. Sonzini, E. Gallo, *Chem. Soc. Rev.* **2020**, *49*,

- 4867–4905. (j) Y. Liu, T. You, H.-X. Wang, Z. Tang, C.-Y. Zhou, C.-M. Che, *Chem. Soc. Rev.* **2020**, *49*, 5310–5358.
- 36 J. T. Groves, R. S. Myers, *J. Am. Chem. Soc.* **1983**, *105*, 5791–5796.
- 37 For reviews on asymmetric iron catalysis, see: (a) R. H. Morris, *Chem. Soc. Rev.* **2009**, *38*, 2282–2291. (b) K. Gopalaiah, *Chem. Rev.* **2013**, *113*, 3248–3296. (c) T. Ollevier, H. Keipour, *Top. Organomet. Chem.* **2015**, *50*, 259–309. (d) H. Pellissier, *Coord. Chem. Rev.* **2019**, *386*, 1–31. (e) A. Casnati, M. Lanzi, G. Cera, *Molecules* **2020**, *25*, 3889–3917.
- 38 A. E. Russell, S. P. Miller, J. P. Morken, *J. Org. Chem.*, **2000**, *65*, 8381–8383.
- 39 K. Ishihara, T. Yano, M. Fushimi, *J. Fluorine Chem.*, **2008**, *129*, 994–997.
- 40 P. Wang, W.-J. Tao, X.-L. Sun, S. Liao, Y. Tang, *J. Am. Chem. Soc.*, **2013**, *135*, 16849–16852.
- 41 W. Wu, X. Liu, Y. Zhang, J. Ji, T. Huang, L. Lin, X. Feng, *Chem. Commun.* **2015**, *51*, 11646–11649.
- 42 For recent reviews on catalytic asymmetric Nazarov cyclizations, see: (a) S. P. Simeonov, J. P. M. Nunes, K. Guerra, V. B. Kurteva, C. A. M. Afonso, *Chem. Rev.* **2016**, *116*, 5744–5893. (b) M. G. Vinogradov, O. V. Turova, S. G. Zlotin, *Org. Biomol. Chem.* **2017**, *15*, 8245–8269.
- 43 For an Fe(II)/Pybox-catalyzed asymmetric Nazarov cyclization, see: M. Kawatsura, K. Kajita, S. Hayase, T. Itoh, *Synlett* **2010**, 1243–1246.
- 44 S. Raja, M. Nakajima, M. Rueping, *Angew. Chem. Int. Ed.* **2015**, *54*, 2762–2765.
- 45 X. Jiang, R. Wang, *Chem. Rev.* **2013**, *113*, 5515–5546.
- 46 G. Desimoni, G. Faita, P. Quadrelli, *Chem. Rev.* **2018**, *118*, 2080–2248.
- 47 (a) R. D. Shannon, *Acta. Crystallogr. A* **1976**, *32*, 751–767. (b) M. Valigi, D. Gazzoli, *Z. Phys. Chem (NF)*. **1981**, *125*, 89–97.
- 48 (a) J. Thorhauge, M. Johannsen, K. A. Jørgensen, *Angew. Chem. Int. Ed.* **1998**, *37*, 2404–2406. (b) H. Audrain, J. Thorhauge, R. G. Hazell, K. A. Jørgensen, *J. Org. Chem.* **2000**, *65*, 4487–4497.
- 49 (a) D. A. Evans, E. J. Olhava, J. S. Johnson, J. M. Janey, *Angew. Chem. Int. Ed.* **1998**, *37*, 3372–3375. (b) D. A. Evans, J. S. Johnson, E. J. Olhava, *J. Am. Chem. Soc.* **2000**, *122*, 1635–1649.
- 50 J. Liu, S. Niwayama, Y. You, K. N. Houk, *J. Org. Chem.* **1998**, *63*, 1064–1618.
- 51 N. Thirupathi, F. Wei, C.-H. Tung, Z. Xu, *Nat. Commun.* **2019**, *10*, 3158–3165.
- 52 Y. Zhu, M. Xie, S. Dong, X. Zhao, L. Lin, X. Liu, X. Feng, *Chem. Eur. J.* **2011**, *17*, 8202–8208.
- 53 J.-B. Chen, M. Xu, J.-Q. Zhang, B.-B. Sun, J.-M. Hu, J.-Q. Yu, X.-W. Wang, Y. Xia, Z. Wang, *ACS Catal.* **2020**, *10*, 3556–3563.

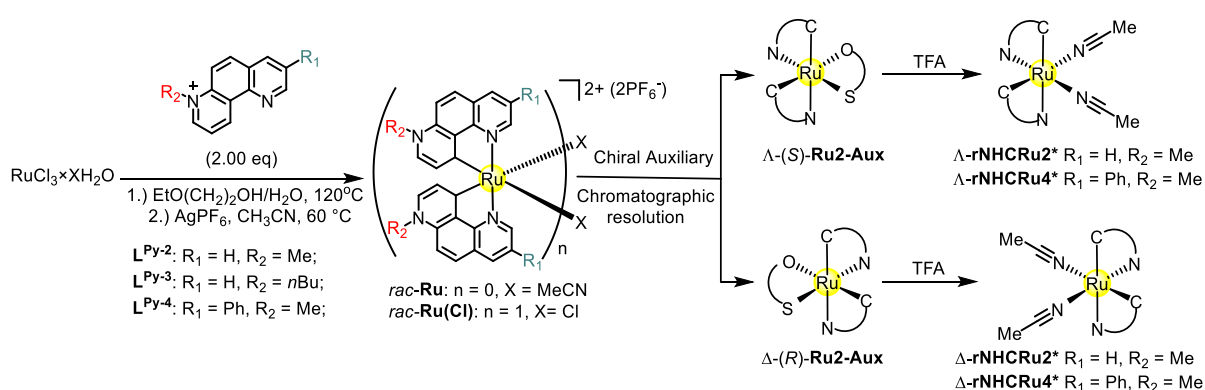
- 54 For selective bioactive dihydropyrans and tetrahydropyrans, see: (a) K. L. Jackson, J. A. Henderson, A. J. Phillips, *Chem. Rev.* **2009**, *109*, 3044–3079. (b) I. Paterson, S. M. Dalby, *Nat. Prod. Rep.*, **2009**, *26*, 865–873. (c) K. Trisuwan, V. Rukachaisirikul, Y. Sukpondma, S. Phongpaichit, S. Preedanon, J. Sakayaroj, *Chem. Pharm. Bull.* **2009**, *57*, 1100–1102. (d) A. K. Ghosh, B. D. Chapsal, Chapter 13: Design of the anti-HIV protease inhibitor darunavir. *Introduction to Biological and Small Molecule Drug Research and Development*. **2013**, 355. (e) R. Jacques, R. Pal, N. A. Parker, C. E. Sear, P. W. Smith, A. Ribaucourt, D. M. Hodgson, *Org. Biomol. Chem.* **2016**, *14*, 5875–5893. (f) B. Pande, *ChemistrySelect*, **2019**, 9143–9164. (g) W. A. Donaldson, *Beilstein J. Org. Chem.* **2020**, *16*, 1991–2006. (h) B. Roy, N. Rout, P. Kuila, *J Heterocyclic Chem.* **2020**, 1–4. (i) N. Ogawa, S. Mamada, T. Hama, H. Koshino, S. Takahashi, *J. Nat. Prod.* **2020**, *83*, 2537–2541. (j) K. Sakurai, K. Sakamoto, M. Sasaki, H. Fuwa, *Chem Asian J.* **2020**, *15*, 3494–3502. (k) J. N. Manda, B. B. Butler, Jr, A. Aponick, *J. Org. Chem.* **2020**, *85*, 13694–13709.

Chapter 4: Summary and Outlook

4.1 Summary

(1) Synthesis and Characterization of A New Family of Octahedral Chiral-at-Ruthenium Complexes with Pyridylidene Ligands

We here introduced a new kind of racemic and non-racemic octahedral ruthenium complexes where the metal center is coordinated with two 7-alkyl-1,7-phenanthroline, giving chelating pyridylidene remote N-heterocyclic carbene ligands. The octahedral coordination sphere incorporates two acetonitriles and the dicationic complex is complemented by two hexafluorophosphate counterions. The racemic complexes were synthesized in a C_2 -symmetric geometry. The resolution of racemic complexes with a chiral sulfonamide auxiliary, followed by treating with TFA, resulted in an isomerization of the coordination sphere and provided non-racemic, non- C_2 -symmetric chiral ruthenium complexes. Single crystal X-ray analysis showed that one of the bidentate ligands underwent an 180° rotation around the Ru center (Scheme 47). These chiral-at-ruthenium complexes were enantiomeric enriched and stable.



Scheme 47. Synthesis of racemic and non-racemic octahedral ruthenium complexes.

It is notable that the *trans*-effect of the pyridylidenes in these complexes is much stronger than that of the reference complex $[(L^{imi}H)_2Ru(NMe_3)_2](PF_6)_2$ by bond length comparison of metal-coordinated acetonitrile (Figure 45a). The *trans*-effect of pyridylidenes was further revealed in the non- C_2 -symmetric complex $\Delta-rNHCRu_2^*$, indicating a markedly larger *trans*-influence of pyridylidenes compared to pyridyl units (Figure 45b). Furthermore, the *trans*-influence was evaluated with racemic pyridylidene complexes that contained different substituents at the N7-position or C3-position of the phenanthroline heterocycle. The way of former provided enhanced *trans*-effect when replacing methyl with a *n*-butyl group (Figure 45c). In contrast, the latter had a weak influence if switching H to phenyl

moiety. These complexes represent a new family of high electron-donor chiral-at-ruthenium complexes that exhibit a unique coordination behavior, providing a new vision for the ligand design of related Ru catalysts.

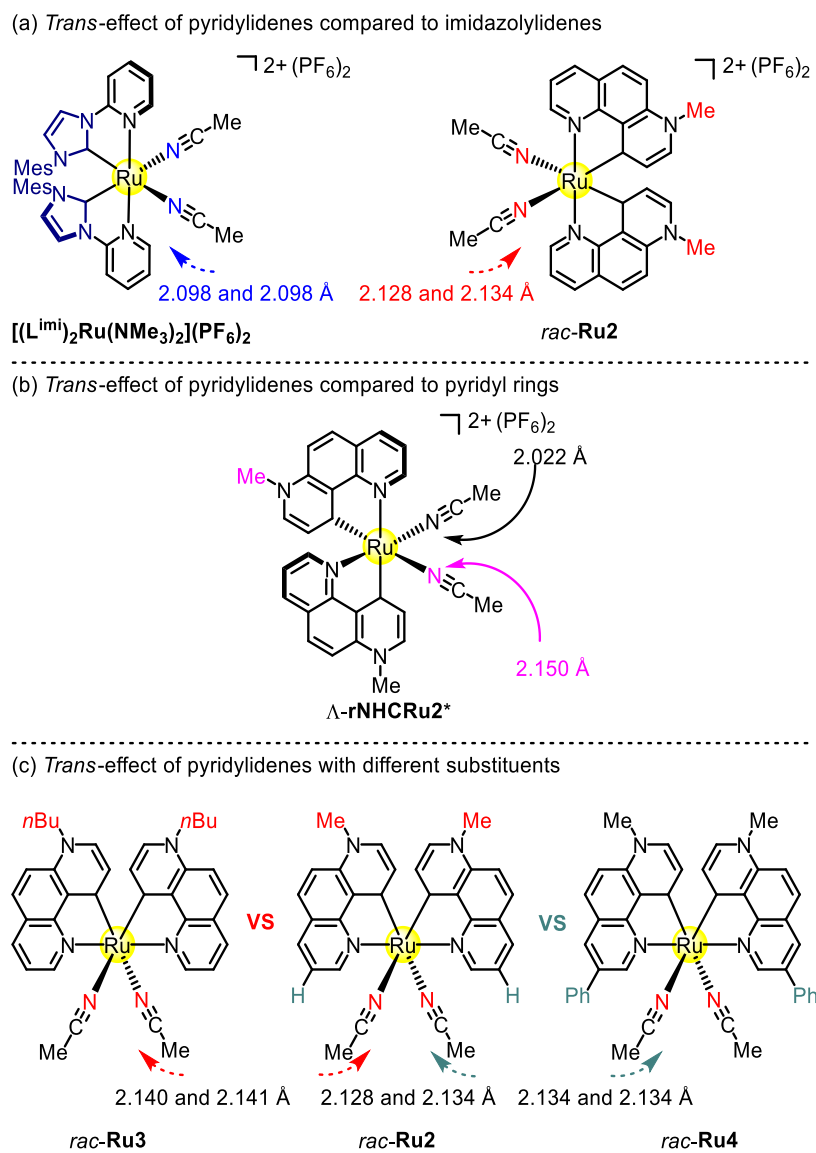
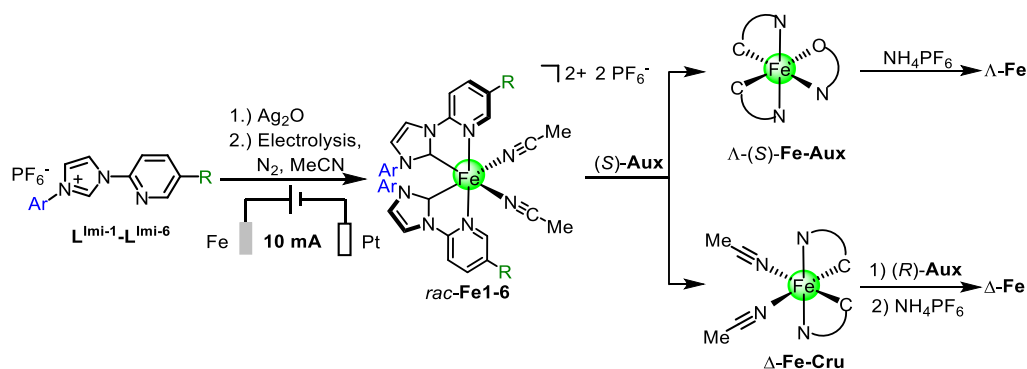


Figure 45. *Trans*-effect by bond length comparison of metal-acetonitrile.

(2) Chiral-at-Iron Catalyst: Expanding the Chemical Space for Asymmetric Earth-Abundant Metal Catalysis

The first example of chiral-at-iron catalyst **Fe1** has been developed that contains exclusively achiral ligands with the overall chirality being the result of a stereogenic iron center. Specifically, iron(II) was *cis*-coordinated to two N-(2-(5-trifluoromethylpyridyl)-substituted imidazolylidene) ligands in a bidentate fashion in addition to two monodentate acetonitriles, and the dicationic complex was complemented by two hexafluorophosphate ions. The racemic iron complex was synthesized through an electrolysis strategy to avoid the use of sensitive iron precursors. The enantiomers Λ and Δ -**Fe1** were generated through a chiral-auxiliary-mediated method with an enantiopurity of up to >99:1 e.r. (Scheme 48). It was demonstrated that the developed enantiopure chiral-at-iron catalyst was efficient for an enantioselective Cannizzaro reaction (96% yield, 89% ee) and an asymmetric Nazarov cyclization (89% yield, >20:1 d.r., 83% ee) (Figure 46).



Scheme 48. Synthesis of octahedral chiral-at-iron complexes.

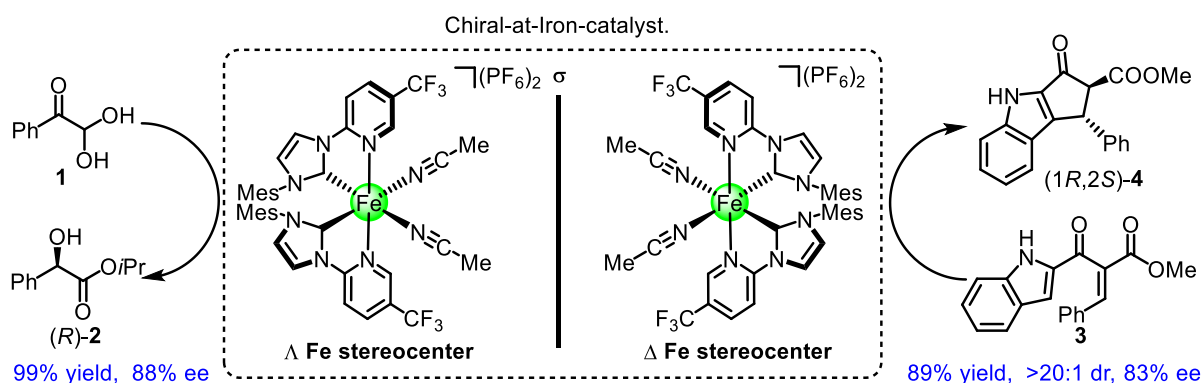


Figure 46. Iron-catalyzed asymmetric Nazarov cyclization and enantioselective Cannizzaro reaction.

(3) Chiral-at-Iron Catalyst for Highly Enantioselective and Diastereoselective Hetero-Diels-Alder Reaction

We demonstrated for the first time that chiral-at-iron complexes, in which the overall chirality originates exclusively from a stereogenic iron center with all coordinating ligands being achiral, can be served as highly efficient catalysts for asymmetric catalysis. The introduction of bulky Dipp moieties at imidazolylidenes is essential to obtain high stereoselectivity. Applying of optimal catalyst **Fe5**, the Oxa-Diels-Alder cycloadditions of β,γ -unsaturated α -ketoesters with electron-rich dienophiles allowed for the synthesis of 3,4-dihydro-2*H*-pyrans in 40-99% yields with moderate to excellent enantioselectivities (65-98% ee) and excellent diastereoselectivities (up to 99:1 d.r.) (Figure 47).

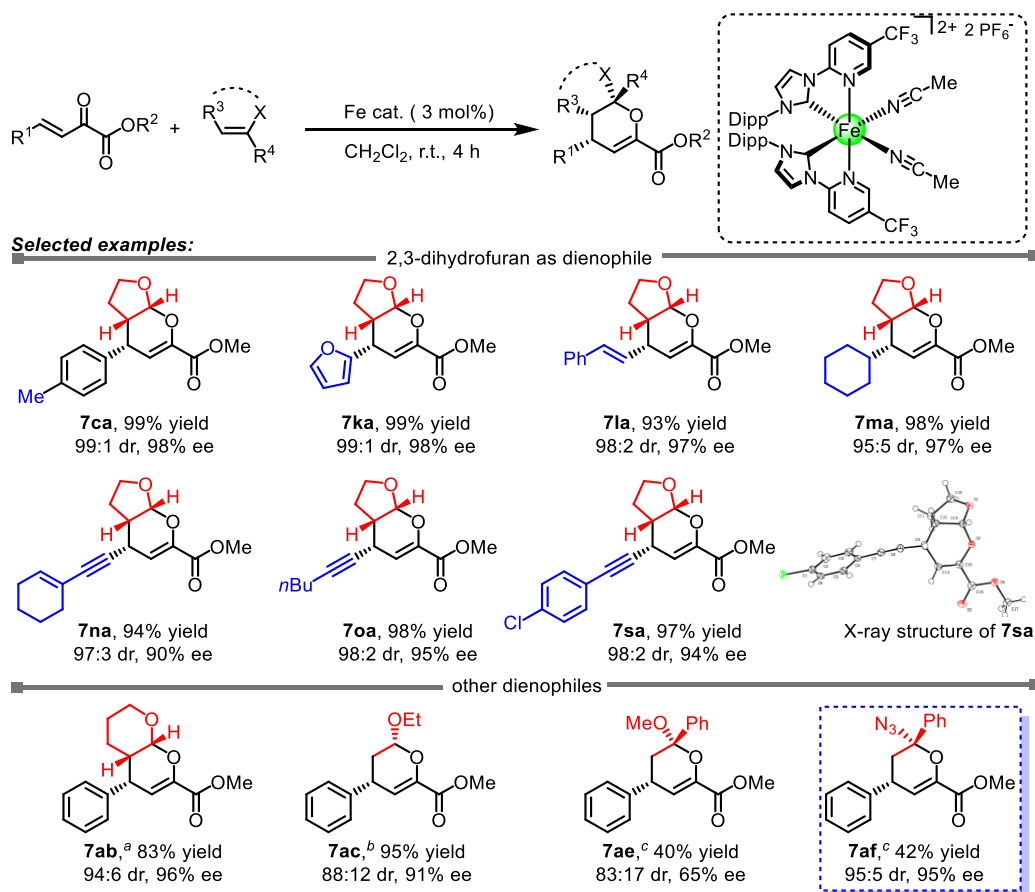


Figure 47. Selected examples of asymmetric Oxa-Diels-Alder cycloadditions.

4.2 Outlook

This thesis mainly focused on the investigation of new octahedral chiral-at-metal complexes with exclusively achiral ligands and their applications in asymmetric catalysis. Firstly, a new series of chiral-at-ruthenium complexes containing pyridylidene ligands were synthesized and exhibited stronger donating property. However, adjusting the properties of Ru-NHCs complexes via modification of 1,7-phenanthroline ligands is limited because of the difficulty of the introduction of substituents. Secondly, a new family of chiral-at-metal complexes based on the earth-abundant transition metal iron was introduced and demonstrated as a highly efficient Lewis acid catalyst for several asymmetric transformations. The design strategy was especially appealing for its combination of sustainability (cheap or base metals) and simplicity (achiral ligands). Such a system still has two drawbacks: (a) Racemization because of a limited configurational stability, and (b) limited catalytic properties. Therefore, our further research interest might be to explore new chiral-at-metal complexes that combine cheap metals (Ru, Fe or other 3d metals) and more promising ligands, which at the same time display significant configuration stability and catalytic activity.

(1) Explore new chiral-at-metal (ruthenium, iron or other 3d metals) complexes: Recently, the studies of pyridylidene amide (PYA) complexes has been emerging because of their unique structures and attractive properties.¹⁻¹⁰ The easily modifiable nature of PYA ligands and their electronically flexible behavior imparts unique properties. For example, the chelating PYA ligand can change the coordination mode on the metal center from neutral to mesoionic resonance for discriminative binding of the neutral or charged ligands. Owing to this electronic property, PYA ligands can stabilize multiple oxidation states on a metal center and their use has aroused striking results to different transition metals like Ru and Fe complexes in many types of reactions. Given this fact, it is promising to apply our strategies for the synthesis of chiral-at-metal complexes based on pyridylidene amide ligands.

(2) Explore C(sp³)-H activation reactions catalyzed by octahedral chiral-at-metal complexes: Asymmetric C-H activation is one of the most attractive and promising areas of organic catalysis nowadays.¹¹ Previous work developed in our group showed a broad catalytic application in asymmetric nitrene insertion reaction using chiral-at-Ru catalysts. However, it is

remarkable that asymmetric nitrene insertion reaction by chiral iron complexes is restricted. As mentioned above, the N-coordination and donor flexibility make PYA ligands particularly attractive for hard and earth-abundant first row transition metals, offering the opportunity to stabilize catalytic intermediates of different oxidation states. Since our newly developed chiral NHCs iron catalysts are somehow limited in other asymmetric transformation, it is time to explore other chiral-at-iron complexes which may provide more promising catalytic properties.

References

- 1 (a) M. E. Doster, S. A. Johnson, *Angew. Chem. Int. Ed.* **2009**, *48*, 2185–2187. (b) Q. Shi, R. J. Thatcher, J. Slattery, P. S. Sauri, A. C. Whitwood, P. C. McGowan, R. E. Douthwaite, *Chem. Eur. J.* **2009**, *15*, 11346–11360. (c) P. D. W. Boyd, L. J. Wright, M. N. Zafar, *Inorg. Chem.* **2011**, *50*, 10522–10524.
- 2 V. Leigh, D. J. Carleton, J. Olguin, H. Mueller-Bunz, L. J. Wright, M. Albrecht, *Inorg. Chem.* **2014**, *53*, 8054–8060
- 3 M. Navarro, C. A. Smith, M. Albrecht, *Inorg. Chem.* **2017**, *56*, 11688–11701.
- 4 P. Melle, Y. Manoharan, M. Albrecht, *Inorg. Chem.* **2018**, *57*, 11761–11774.
- 5 M. Navarro, V. Rosar, T. Montini, B. Milani, M. Albrecht, *Organometallics* **2018**, *37*, 3619–3630.
- 6 M. Navarro, M. Li, S. Bernhard, M. Albrecht, *Chem. Eur. J.* **2018**, *24*, 6386–6398.
- 7 P. Melle, M. Albrecht, *Chimia* **2019**, *73*, 299–303.
- 8 K. Salzmann, C. Segarra, M. Albrecht, *Angew. Chem. Int. Ed.* **2020**, *59*, 8932–8936.
- 9 M. Navarro, C. Segarra, T. Pfister, M. Albrecht, *Organometallics* **2020**, *39*, 2383–2391.
- 10 P. Melle, J. Thiede, D. A. Hey, M. Albrecht, *Chem. Eur. J.* **2020**, *26*, 13226–13234.
- 11 For select reviews on enantioselective C-H functionalization, see: (a) B. Ye, N. Cramer, *Acc. Chem. Res.* **2015**, *48*, 1308–1318. (b) Y.-M. Cui, Y. Lin, L.-W. Xu, *Coord. Chem. Rev.* **2017**, *330*, 37–52. (c) C. G. Newton, S.-G. Wang, C. C. Oliveira, N. Cramer, *Chem. Rev.* **2017**, *117*, 8908–8976. (d) T. G. Saint-Denis, R.-Y. Zhu, G. Chen, Q.-F. Wu, J.-Q. Yu, *Science* **2018**, *359*, 759–771. (e) Ł. Woźniak, N. Cramer, *Trends Chem.* **2019**, *1*, 471–484. (f) J. Diesel, N. Cramer, *ACS Catal.* **2019**, *9*, 9164–9177.

Chapter 5: Experimental Part

5.1 Materials and Methods

All reactions were carried out under an atmosphere of nitrogen with magnetic stirring unless indicated otherwise. The catalytic reactions were performed in Schlenk tube.

Solvents and Reagents

The oxygen free and water free solvents were distilled from calcium hydride (CHCl_3 , CH_2Cl_2 and CH_3CN), magnesium turnings/iodine (MeOH) or sodium/benzophenone (Et_2O , THF and toluene) under nitrogen. HPLC grade solvents, such as MeOH, EtOH, *i*PrOH, CH_2Cl_2 , $\text{Cl}(\text{CH}_2)_2\text{Cl}$ and THF are used directly for the catalytic reaction. All reagents were purchased from Acros, Alfa aesar, Sigma Aldrich, TCI, ChemPur and Fluorochem and used without further purification.

Chromatographic Methods

The course of the reactions and the column chromatographic elution were monitored by thin layer chromatography (TLC) [Macherey-Nagel (ALUGRAM®Xtra Sil G/UV254)]. Flash column chromatography was performed with silica gel 60 M from Macherey-Nagel (irregular shaped, 230-400 mesh, pH 6.8, pore volume: $0.81 \text{ mL} \times \text{g}^{-1}$, mean pore size: 66 \AA , specific surface: $492 \text{ m}^2 \times \text{g}^{-1}$, particle size distribution: 0.5% < 25 \mu m and 1.7% > 71 \mu m , water content: 1.6%).

Nuclear Magnetic Resonance Spectroscopy (NMR)

^1H NMR, proton decoupled ^{13}C NMR, and proton coupled ^{19}F NMR spectra were recorded on Bruker Avance 300 system (^1H NMR: 300 MHz, ^{13}C NMR: 75 MHz, ^{19}F NMR: 282 MHz) spectrometers and Bruker Avance 250 system (^1H NMR: 250 MHz, ^{19}F NMR: 235 MHz) spectrometers at ambient temperature. Chemical shifts are given in ppm on the δ scale, and were determined after calibration to the residual signals of the solvents, which were used as an internal standard. NMR standards were used are as follows: ^1H NMR spectroscopy: $\delta = 7.26 \text{ ppm}$ (CDCl_3), $\delta = 5.32 \text{ ppm}$ (CD_2Cl_2), $\delta = 1.94 \text{ ppm}$ (CD_3CN), $\delta = 4.78, 3.31 \text{ ppm}$ (CD_3OD), $\delta = 2.50 \text{ ppm}$ ($(\text{CD}_3)_2\text{SO}$); ^{13}C NMR spectroscopy: $\delta = 77.16 \text{ ppm}$ (CDCl_3), $\delta = 54.0 \text{ ppm}$ (CD_2Cl_2), $\delta = 118.26, 1.32 \text{ ppm}$ (CD_3CN), $\delta = 49.0 \text{ ppm}$ (CD_3OD), $\delta = 39.52 \text{ ppm}$ ($(\text{CD}_3)_2\text{SO}$). ^{19}F NMR spectroscopy: $\delta = 0 \text{ ppm}$ (CFCl_3). The characteristic signals were specified from the low field to high field with the chemical shifts (δ in ppm). ^1H NMR spectra peak multiplicities indicated as singlet (s), doublet (d), doublet of doublet (dd), doublet of doublet of doublet (ddd), doublet of doublet of doublet of doublet (dddd), triplet (t), doublet of triplet (dt), triplet of triplet (tt), quartet (q), multiplet (m). The coupling constant J indicated in hertz (Hz).

NMR yields were determined using 1,1,2,2-tetrachloroethane as internal standard.

High-Performance Liquid Chromatography (HPLC)

Chiral HPLC was performed with an Agilent 1200 Series or Agilent 1260 Series HPLC System. All the HPLC conditions were detailed in the individual procedures. The type of the columns, mobile phase and the flow rate were specified in the individual procedures.

Infrared Spectroscopy (IR)

IR measurements were recorded on a Bruker Alpha-PFT-IR spectrometer. The absorption bands were indicated a wave numbers ν (cm^{-1}). All substances were measured as films or solids.

Mass Spectrometry (MS)

High-resolution mass spectra were recorded on a Bruker En Apex Ultra 7.0 TFT-MS instrument using ESI or APCI or FD technique. Ionic masses are given in units of m/z for the isotopes with the highest natural abundance.

Circular Dichroism Spectroscopy (CD)

CD spectra were recorded on a JASCO J-810 CD spectropolarimeter. The parameters we used as follows: from 700 nm to 200 nm; data pitch (1.0 nm); band with (1.0 nm); response (1 second); sensitivity (standard); scanning speed (50 nm/min); accumulation (3 times). The concentration of the compounds for the measurements was 1.0 mM. The formula for converting θ to ϵ is shown as below.

$$\Delta\epsilon = \frac{\theta[m \text{ deg}]}{32980 \times c(\text{mol} / L) \times L(\text{cm})}$$

c = concentration of the sample; L = thickness of the measurement vessel

Crystal Structure Analysis

Crystal X-ray measurements and the crystal structure analysis were carried out by Dr. Klaus Harms and Dr. Sergei Ivlev (Chemistry Department, Philipps University of Marburg). X-ray data were collected with an STOE STADIVARI diffractometer equipped with with CuK radiation, a graded multilayer mirror monochromator ($\lambda = 1.54178 \text{ \AA}$) and a DECTRIS PILATUS 300K detector using an oil-coated shock-cooled crystal at 100(2) K. Absorption effects were corrected semi-empirical using multiscanned reflexions (STOE LANA, absorption correction by scaling of reflection intensities.). Cell constants were refined using 34108 of observed reflections of the data collection. The structure was solved by direct methods by using the program XT V2014/1 (Bruker AXS Inc., 2014) and refined by full matrix least squares procedures on F^2 using SHELXL-2018/1 (Sheldrick, 2018). The non-hydrogen atoms have been refined anisotropically, carbon bonded hydrogen atoms were included at calculated positions and refined using the 'riding model' with isotropic temperature factors at 1.2 times (for CH_3 groups 1.5 times) that of the preceding carbon atom. The

Flack parameter is a factor used to estimate the absolute configuration of the compounds. CH₃ groups were allowed to rotate about the bond to their next atom to fit the electron density. Severe disorder was refined for PF₆ anions and solvent. Nitrogen or oxygen bonded hydrogen atoms were located and allowed to refine isotropically.

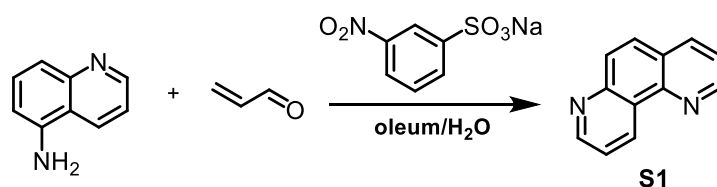
Optical Rotation Polarimeter

Optical rotations were measured on a Krüss P8000-T or Perkin-Elmer 241 polarimeter with $[\alpha]_D^{25}$ values reported in degrees with concentrations reported in g/100 mL.

5.2 Synthesis and Characterization of Chiral-at-Ruthenium Complexes with Pyridylidene Ligands

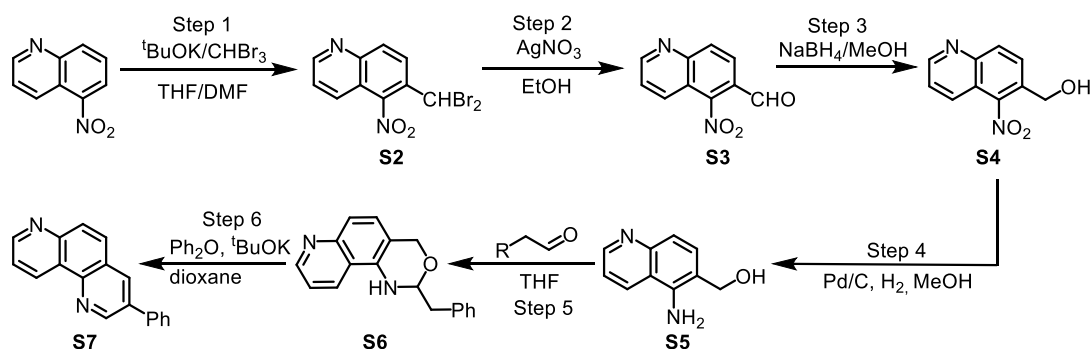
5.2.1 Synthesis of Ligands

(1) Synthesis of 1,7-phenanthroline



Compound S1 can be synthesized following a published procedure with slight modifications¹, although it is commercially available. To a mixture of sodium 3-nitrobenzenesulfonate (0.72 g, 3.2 mmol) in oleum (3 mL) and water (4 mL) was added quinolin-5-amine (0.77 g, 5.35 mmol). The mixture was stirred and heated to 105 °C. Acrolein (0.75 g, 10.7 mmol) was added dropwise over 5 min. The resulting mixture was stirred at 105 °C for 16 hours. The mixture was then poured into ice (12 g) and the pH value was adjusted to 11 with 1 N aqueous sodium hydroxide solution. The mixture was extracted with EtOAc (3 × 60 mL) and the combined organic layers were dried over anhydrous sodium sulfate and concentrated under reduced pressure. The residue was purified by column chromatography eluting with *n*-hexane/ethyl acetate (5:1 to 2:1) to afford 1,7-phenanthroline as a light yellow solid (0.39 g, 2.14 mmol, 40% yield). All the spectroscopic data of **S1** are in agreement with reported result.

(2) Synthesis of substituted 1,7-phenanthroline



The 3-substituted 1,7-phenanthroline ligands were synthesized following a published procedure with some modifications.²

Step 1: To a well-stirred solution of potassium *tert*-butoxide (4.40 g, 39 mmol), in a mixture of dry THF (5 mL) and dry DMF (3 mL) cooled to around -73 °C, a solution of 5-nitroquinoline (1.60 g, 9 mmol) and bromoform (2.53 g, 10 mmol) in dry DMF (4 mL) was added dropwise, being careful that the temperature did not exceed -68 °C. The mixture was allowed to stir for 1 minute and then acidified with acetic acid (5 mL). After allowing the mixture to return to room temperature it was poured into water (300 mL) and the aqueous solution was extracted with dichloromethane (3 × 250 mL). The combined organic extracts were washed with water (3 × 350 mL), dried (Na₂SO₄), and concentrated in vacuo to provide brown residue. This residue was purified by column chromatography eluting with *n*-hexane/ethyl acetate (3:1) to give the desired compound **S2** as a yellow solid (2.57 g, 7.47 mmol, 83% yield).

¹H NMR (300 MHz, CDCl₃) δ 9.06 (dd, *J* = 4.2, 0.6 Hz, 1H), 8.39 (d, *J* = 9.3 Hz, 1H), 8.34 (d, *J* = 9.0 Hz, 1H), 8.17 (ddd, *J* = 8.7, 1.5, 0.6 Hz, 1H), 7.63 (dd, *J* = 8.7, 4.2 Hz, 1H), 6.90 (s, 1H).

¹³C NMR (75 MHz, CDCl₃) δ 153.0, 148.1, 134.4, 131.7, 131.4, 129.8, 124.2, 119.3, 32.3.

All other data were consistent with previously reported data.

Step 2: To a solution of 6-(dibromomethyl)-5-nitroquinoline **S2** (2.42 g, 7 mmol) in ethanol (150 mL) was added a solution of silver nitrate (2.50 g, 14.7 mmol) in hot (60 °C) distilled water (16 mL), and the reaction mixture was heated under reflux for 2 hours. After cooling, concentrated hydrochloric acid was added (16 mL) and solvent was removed in vacuo. The residue was treated with saturated sodium hydrogen carbonate solution, extracted with dichloromethane (3 × 150 mL) and the organic phases were washed with water (100 mL). The combined organic phases were dried (Na₂SO₄) and concentrated to dry. Purification by column chromatography eluting with *n*-hexane/ethyl acetate (5:1 to 2:1) to give the desired compound as a yellow solid give the target compound **S3** as a yellow solid (1.10 g, 5.46 mmol, 78% yield).

¹H NMR (300 MHz, CDCl₃) δ 10.23 (d, *J* = 0.6, 1H), 9.15 (dd, *J* = 4.2, 1.8 Hz, 1H), 8.42 (d, *J* = 8.7 Hz, 1H), 8.33 (ddd, *J* = 8.7, 1.5, 0.9 Hz, 1H), 8.25 (d, *J* = 8.7, 1H), 7.69 (dd, *J* = 8.7, 4.2 Hz, 1H).

¹³C NMR (75 MHz, CDCl₃) δ 186.4, 154.3, 150.3, 136.6, 134.0, 131.7, 126.7, 124.4, 120.0.

All other data were consistent with previously reported data.

Step 3: To a solution of 5-nitroquinoline-6-carbaldehyde **S3** (500 mg, 2.48 mmol) in methanol (40 mL) was added sodium borohydride (0.15 g, 3.95 mmol) portionwise. The reaction was stirred at room temperature until completely consumption of starting material. The reaction mixture was quenched with water and the solvent removed in vacuo. The residue was partitioned between ethyl acetate (100 mL) and water (50 mL), the layers were separated, the organic layer was dried with Na₂SO₄ and concentrated in vacuo to give a pale yellow solid **S4** (500 mg, 2.45 mmol, 99% yield). This crude product was taken for the next step without any further purification.

¹H NMR (300 MHz, CDCl₃) δ 8.98 (d, *J* = 4.2, 1.5 Hz, 1H), 8.32 (d, *J* = 9.0 Hz, 1H), 8.25 (d, *J* = 8.7 Hz, 1H), 7.97 (d, *J* = 8.7 Hz, 1H), 7.59 (dd, *J* = 8.7, 4.2 Hz, 1H), 4.92 (d, *J* = 3.9 Hz, 2H).

^{13}C NMR (75 MHz, CDCl_3) δ 151.8, 147.3, 133.5, 132.6, 130.9, 129.1, 123.6, 120.4, 61.3.

HRMS (ESI, m/z) calcd for $\text{C}_{18}\text{H}_{12}\text{N}_2$ $[\text{M}+\text{H}]^+$: 205.0608, found: 205.0609.

Step 4: To a solution of **S4** (500 mg, 2.45 mmol) in MeOH (50 mL) was added Pd/C (50 mg) under N_2 atmosphere, the resulting solution was degassed and filled in H_2 three times (using H_2 balloon) and then stirred at room temperature for 2 hours. Reaction mixture was filtered with a thin layer of celite and washed with MeOH (3×10 mL), the solvent was removed and concentrated in vacuo to give the desired compound **S5** as a yellow solid (345 mg, 1.96 mmol, 80% yield). This crude product was taken for the next step without any further purification.

^1H NMR (300 MHz, $(\text{CD}_3)_2\text{SO}$) δ 8.75 (dd, $J = 4.2, 1.5$ Hz, 1H), 8.60 (d, $J = 8.4$ Hz, 1H), 7.51 (d, $J = 8.4$ Hz, 1H), 7.36 (dd, $J = 8.4, 4.2$ Hz, 1H), 7.21 (d, $J = 8.4$, 1H), 5.76 (br, 2H), 5.14 (t, $J = 4.2$, 1H), 4.59 (d, $J = 4.2$, 1H), 3.17 (d, $J = 4.2$, 1H).

^{13}C NMR (75 MHz, $(\text{CD}_3)_2\text{SO}$) δ 149.4, 148.1, 141.9, 130.6, 130.3, 118.8, 118.7, 117.5, 115.7, 61.0.

HRMS (ESI, m/z) calcd for $\text{C}_{18}\text{H}_{12}\text{N}_2$ $[\text{M}+\text{H}]^+$: 175.0866, found: 175.0866.

Step 5: A mixture of (5-aminoquinolin-6-yl)methanol **S5** (345 mg, 1.96 mmol) and phenylacetaldehyde (235 mg, 1.96 mmol) in THF (10 mL) were heated to 80 °C and stirred for 15 hours under N_2 atmosphere. The reaction mixture was partitioned between ethyl acetate (100 mL) and water (50 mL), the layers were separated and organic layer was dried with Na_2SO_4 and concentrated in vacuo to give a yellow residue. This residue was purified by column chromatography eluting with *n*-hexane/ethyl acetate (5:1 to 2:1) to give the desired compound **S6** as a yellow solid (400 mg, 1.45 mmol, 74% yield).

^1H NMR (300 MHz, CDCl_3) δ 8.83 (d, $J = 3.0$ Hz, 1H), 8.09 (d, $J = 8.7$ Hz, 1H), 7.60 (d, $J = 8.7$ Hz, 1H), 7.37-7.26 (m, 5H), 7.23 (s, 2H), 5.06 (d, $J = 15.0$ Hz, 1H), 4.94 (d, $J = 15.3$ Hz, 1H), 4.86 (dd, $J = 12.6, 2.7$ Hz, 1H), 4.10-4.03 (m, 1H), 3.26-3.12 (m, 2H).

^{13}C NMR (75 MHz, CDCl_3) δ 150.0, 148.1, 136.3, 136.1, 129.8, 129.0, 128.9, 127.2, 126.9, 122.0, 120.8, 120.4, 119.2, 84.5, 67.6, 41.3.

HRMS (ESI, m/z) calcd for $\text{C}_{18}\text{H}_{12}\text{N}_2$ $[\text{M}+\text{H}]^+$: 277.1335, found: 277.1340.

Step 6: A mixture of **S6** (380 mg, 1.38 mmol), benzophenone (551 mg, 3.03 mmol) and potassium tert-butoxide (370 mg, 3.30 mmol) in anhydrous dioxane (6 mL) were stirred at 80 °C for 18 hours under N_2 atmosphere. The reaction mixture was partitioned between ethyl acetate (100 mL) and water (50 mL), the layers were separated and organic layer was dried with Na_2SO_4 and concentrated in vacuo to give a yellow residue. The desired compound was purified by column chromatography eluting with *n*-hexane/ethyl acetate (5:1 to 3:1) to give the desired compound **S7** as a white solid (320 mg, 1.25 mmol, 91% yield).

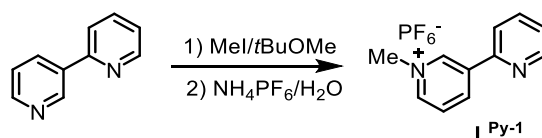
^1H NMR (300 MHz, CDCl_3) δ 9.57 (dd, $J = 8.1, 1.2$ Hz, 1H), 9.29 (d, $J = 2.4$ Hz, 1H), 9.06 (dd, $J = 4.2, 1.5$ Hz, 1H), 8.39 (d, $J = 2.1$, 1H), 8.12 (d, $J = 9.0$, 1H), 8.01 (d, $J = 9.3$, 1H), 7.77 (d, $J = 8.4$, 2H), 7.67 (dd, $J = 8.4, 4.5$, 1H), 7.56 (t, $J = 7.2$, 2H), 7.47 (t, $J = 7.2$, 1H).

^{13}C NMR (75 MHz, CDCl_3) δ 151.4, 149.7, 148.8, 145.0, 137.8, 135.5, 133.5, 132.8, 129.7, 129.4, 129.3,

128.5, 127.6, 127.1, 126.2, 122.2.

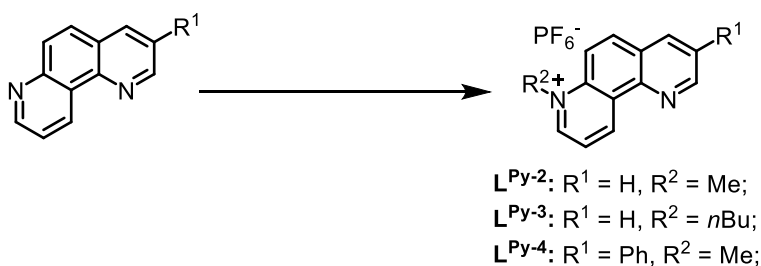
HRMS (ESI, m/z) calcd for $C_{18}H_{12}N_2 [M+H]^+$: 257.1073, found: 257.1078.

3) Synthesis of pyridinium salts



L^{Py-1} was prepared according to the literature procedure.³ Methyl iodide (2 mL, 32.1 mmol) was added to a solution of 2,3'-bipyridyl (500 mg, 3.20 mmol) in tert-butyl methyl ether (20 mL), and the mixture heated at reflux for 36 hours. After cooling to room temperature, the solid was filtered off, washed with tert-butyl methyl ether then n-pentane and dried to give 1-methyl-3-(2'-pyridyl)pyridinium iodide as an off-white powder. The collected powder was dissolved in a minimum of water and filtered, giving a pale yellow solution to which NH_4PF_6 was added. The precipitate was filtered off, washed extensively with cold water and dried to afford a near quantitative yield.

All the spectroscopic data of L^{Py-1} are in agreement with reported result.³



L^{Py-2} was prepared according to the literature procedure with some modification.³ To a solution of 1,7-phenanthroline (**S1**, 100 mg, 0.56 mmol) in acetone (3 mL) was added MeI (1.0 mL). The reaction was stirred at room temperature until completely consumption of starting material. The reaction mixture was filtered and washed with methyl *tert*-butyl ether three times to obtain a light yellow solid. The collected solid was dissolved in a minimum of water. A light yellow solid was precipitated when saturated NH_4PF_6 aqueous solution was added. This precipitate was filtered and washed with cold water and dried under vacuo to afford a near quantitative yield.

1H NMR (300 MHz, CD_3CN) δ 10.32 (d, $J = 8.4$ Hz, 1H), 9.26 (dd, $J = 4.2, 1.8$ Hz, 1H), 9.12 (dd, $J = 6.0$ Hz, 1H), 8.64 (d, $J = 2.4$ Hz, 1H), 8.61 (br, 1H), 8.33 (d, $J = 9.6$ Hz, 1H), 8.22 (dd, $J = 8.4, 6.0$ Hz, 1H) 7.93 (dd, $J = 8.4, 4.2$ Hz, 1H), 4.65 (s, 3H).

^{13}C NMR (75 MHz, CD_3CN) δ 153.7, 149.7, 144.6, 143.9, 138.3, 138.0, 130.6, 127.5, 126.2, 124.1, 117.4, 47.2.

^{19}F NMR (235 MHz, CD_3CN) δ -72.92 (d, $J = 705.2$ Hz, 6F).

HRMS (ESI, m/z) calcd for $C_{13}H_{11}N_2 [M-PF_6]^+$: 195.0917, found: 195.0918.

L^{Py-3} was prepared according to the literature procedure with some modification.⁴ A dried 10 mL Schlenk tube

was charged with 1,7-phenanthroline (150 mg, 0.83 mmol). Then, the acetonitrile (4 mL) was added via syringe followed by 1-iodobutane (153 mg, 0.83 mmol), the resulting mixture was stirred at 120 °C for 24 hours. The solvent was then removed under reduced pressure. The residue obtained was washed with diethyl ether to give a light yellow solid, which was used without further purification. The collected solid was dissolved in water (10 mL). A light yellow solid was precipitated when saturated NH_4PF_6 aqueous solution was added. This precipitate was filtered and washed with cold water and dried under vacuo to afford to give pale yellow solid (253 mg, 0.66 mmol, 80% yield). $\text{L}^{\text{Py-3}}$ can be further purified via precipitation by slowly addition of its CH_2Cl_2 solution to *n*-Hexane.

^1H NMR (300 MHz, CD_3CN) δ 10.30 (d, $J = 8.4$ Hz, 1H), 9.22 (dd, $J = 4.2, 1.8$ Hz, 1H), 9.15 (dd, $J = 6.0, 1.5$ Hz, 1H), 8.62-8.57 (m, 2H), 8.36 (d, $J = 9.6$ Hz, 1H), 8.22 (dd, $J = 8.4, 6.0$ Hz, 1H), 7.91 (ddd, $J = 8.1, 4.5, 1.5$ Hz, 1H), 5.02 (t, $J = 7.6$ Hz, 2H), 2.13-2.03 (m, 2H), 1.58-1.46 (m, 2H), 1.01 (t, $J = 7.4$ Hz, 3H).

^{13}C NMR (75 MHz, CD_3CN) δ 153.6, 148.9, 144.9, 143.8, 141.5, 138.2, 138.0, 131.3, 127.4, 126.3, 124.3, 117.4, 59.6, 32.8, 20.4, 13.8.

^{19}F NMR (235 MHz, CD_3CN) δ -72.82 (d, $J = 705.9$ Hz, 6F).

HRMS (ESI, m/z) calcd for $\text{C}_{13}\text{H}_{11}\text{N}_2$ $[\text{M-PF}_6]^+$: 237.1386, found: 237.1389.

Synthesis of $\text{L}^{\text{Py-4}}$: To a solution of 3-phenyl-1,7-phenanthroline **S7** (300 mg, 1.17 mmol) in DCM (15 mL) was added MeI (1.5 mL). The reaction was stirred at 50 °C for 4 hours. After cooling to room temperature, the reaction mixture was concentrated to obtain a yellow solid. To a suspension solution of above solid in MeCN was added excess solid NH_4PF_6 , the resulting mixture was then stirred at room temperature for 2 hours. After reaction, the solvent was removed under vacuo to give residue, this residue was redissolved in CH_2Cl_2 and resulting mixture was filtered. The filtrate was evaporated to dryness and purified by column chromatograph on silica gel ($\text{CH}_2\text{Cl}_2/\text{MeOH} = 100:1$ to $50:1$) to give desired $\text{L}^{\text{Py-4}}$ as a pale yellow solid (263 mg, 0.63 mmol, 54% yield).

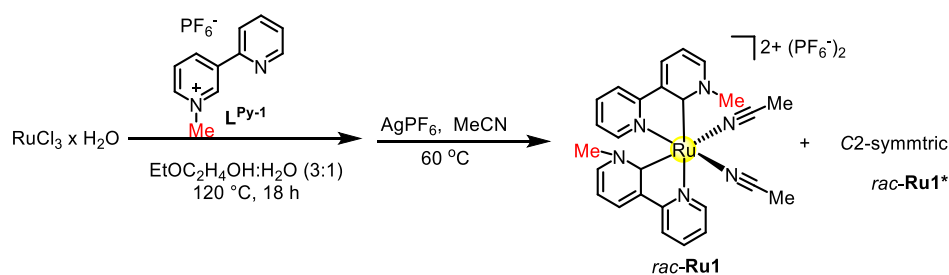
^1H NMR (300 MHz, CD_3CN) δ 10.31 (d, $J = 8.4$ Hz, 1H), 9.55 (d, $J = 2.1$ Hz, 1H), 9.12 (d, $J = 5.7$ Hz, 1H), 8.82 (d, $J = 2.4$ Hz, 1H), 8.67 (d, $J = 9.6$ Hz, 1H), 8.36 (dd, $J = 9.6, 0.9$ Hz, 1H), 8.22 (dd, $J = 8.4, 6.0$ Hz, 1H) 7.94-7.90 (m, 2H), 7.66-7.52 (m, 3H), 4.66 (s, 3H).

^{13}C NMR (75 MHz, CD_3CN) δ 152.5, 149.6, 143.6, 143.5, 142.0, 138.3, 138.0, 137.3, 135.2, 130.5, 130.2, 128.6, 127.4, 124.2, 47.2.

^{19}F NMR (235 MHz, CD_3CN) δ -72.91 (d, $J = 705.2$ Hz, 6F).

HRMS (ESI, m/z) calcd for $\text{C}_{19}\text{H}_{15}\text{N}_2$ $[\text{M-PF}_6]^+$: 271.1230, found: 271.1227.

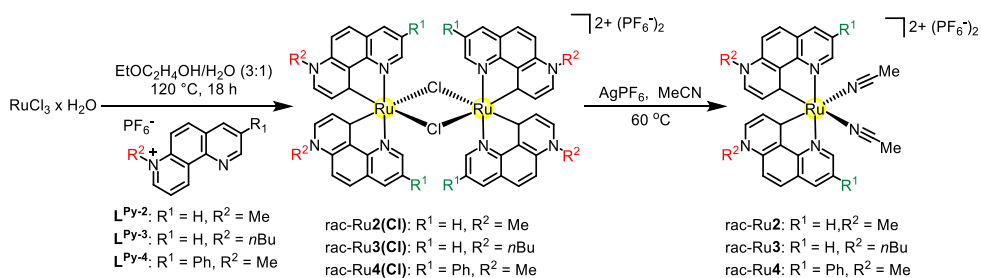
5.2.2 Synthesis of Racemic Ruthenium Complexes



Rac-Ru1: A dried 10 mL Schlenk tube was charged with $\text{L}^{\text{Py}-1}$ (64 mg, 0.20 mmol) and $\text{RuCl}_3 \cdot x\text{H}_2\text{O}$ (24 mg, 0.10 mmol). Then 2-ethoxyethanol and water (3:1, 4.0 mL) were added via syringe and resulting mixture was degassed and heated at 120 °C for 18 hours under an atmosphere of nitrogen. After cooling to room temperature, the reaction mixture was treated with saturated NH_4PF_6 aqueous solution (1-2 mL), a yellow precipitate formed which was separated by filtration, washed with cold water and dried to obtain red-orange solid. A mixture of collected red-orange solid and AgPF_6 (59 mg, 0.233 mmol) in MeCN (5 mL) was stirred at 60 °C for 2 hours. After cooling to room temperature, the mixture was filtered. The filtrate was collected, evaporated to dryness and purified by column chromatograph on silica gel ($\text{CH}_2\text{Cl}_2/\text{CH}_3\text{CN} = 10:1$ to 5:1) to give a mixture which were assigned as **rac-Ru1** and **rac-Ru1*** (red-orange solid, 45 mg, 0.055 mmol, 55% overall yield), respectively. The crystal of **rac-Ru1** suitable for measurement was obtained by slow diffusion of diethyl ether to a mixture solution of **rac-Ru1** and **rac-Ru1*** in acetonitrile.

^1H NMR (300 MHz, CD_3CN) for **rac-Ru1**: δ 9.17 (d, $J = 5.4$ Hz, 1H), 8.47 (d, $J = 6.3$ Hz, 1H), 8.23 (d, $J = 8.7$ Hz, 1H), 8.21-8.18 (m, 2H), 8.04 (d, $J = 6.3$ Hz, 1H), 7.98 (d, $J = 8.4$ Hz, 1H), 7.77-7.67 (m, 2H), 7.34 (dd, $J = 7.5, 6.0$ Hz, 2H), 7.16 (dd, $J = 7.8, 6.3$ Hz, 1H), 6.97 (ddd, $J = 7.2, 6.3, 0.9$ Hz, 1H), 4.42 (s, 3H), 3.37 (s, 3H).

^1H NMR (300 MHz, CD_3CN) for **rac-Ru1***: δ 9.09 (d, $J = 5.7$ Hz, 2H), 8.20 (t, $J = 7.8$ Hz, 4H), 8.04-8.00 (m, 4H), 7.45 (ddd, $J = 7.2, 6.0, 1.2$ Hz, 2H), 6.62 (dd, $J = 7.8, 6.6$ Hz, 2H), 4.03 (s, 6H).



Rac-Ru2: A dried 10 mL Schlenk tube was charged with $\text{L}^{\text{Py}-2}$ (102 mg, 0.30 mmol) and $\text{RuCl}_3 \cdot x\text{H}_2\text{O}$ (34 mg, 0.15 mmol). Then 2-ethoxyethanol and water (3:1, 4 mL) were added via syringe and resulting mixture was degassed and heated at 120 °C for 18 hours under an atmosphere of nitrogen. After cooling to room temperature, the resulting precipitate was collected by filtration before saturated NH_4PF_6 aqueous solution (1-2 mL) was added, washed with cold water and dried to obtain related chloride bridged ruthenium complexes as a black-purple solid (**rac-Ru2(Cl)**), which was used without further purification. To this black-purple solid in CH_3CN (10 mL) was added AgPF_6 (76 mg, 0.30 mmol) in one portion, and then stirred at 60 °C overnight. After cooling to room temperature, the reaction mixture was filtered diatomite to remove insoluble materials. The filtrate was concentrated to dryness and purified by column chromatograph on silica gel ($\text{CH}_2\text{Cl}_2/\text{CH}_3\text{CN} = 15:1$ to

5:1) to give pure product *rac*-**Ru2** (110 mg, 0.128 mmol, 85% yield for two steps) as a dark red solid.

^1H NMR (300 MHz, CD_3CN) δ 9.63 (dd, $J = 5.1, 1.2$ Hz, 2H), 8.67 (d, $J = 8.4, 1.2$ Hz, 2H), 8.47 (d, $J = 9.3$ Hz, 2H), 8.07 (d, $J = 9.3, 2\text{H}$), 7.96 (dd, $J = 8.4, 5.4$ Hz, 2H), 7.44 (d, $J = 6.6$ Hz, 2H), 6.62 (d, $J = 6.3$ Hz, 2H), 4.02 (s, 6H).

^{13}C NMR (75 MHz, CD_3CN) δ 156.0, 155.8, 142.3, 138.0, 135.9, 135.0, 133.6, 130.7, 127.3, 125.5, 119.5, 43.3.

^{19}F NMR (235 MHz, CD_3CN) δ -72.79 (d, $J = 705.5$ Hz, 6F).

Rac-**Ru3**: A dried 10 mL Schlenk tube was charged with $\text{L}^{\text{Py-3}}$ (76 mg, 0.20 mmol) and $\text{RuCl}_3 \cdot x\text{H}_2\text{O}$ (24 mg, 0.10 mmol). Then 2-ethoxyethanol and water (3:1, 2.8 mL) were added via syringe and resulting mixture was degassed and heated at 120 °C for 18 hours under an atmosphere of nitrogen. After cooling to room temperature, the resulting precipitate was collected by filtration before saturated NH_4PF_6 aqueous solution (1-2 mL) was added, washed with cold water and dried to obtain related chloride bridged ruthenium complexes as a purple solid (*rac*-**Ru3(Cl)**), which was used without further purification. To this black-purple solid in CH_3CN (3 mL) was added AgPF_6 (25 mg, 0.10 mmol) in one portion, and then stirred at 60 °C overnight. After cooling to room temperature, the reaction mixture was filtered diatomite to remove insoluble materials. The filtrate was concentrated to dryness and purified by column chromatograph on silica gel ($\text{CH}_2\text{Cl}_2/\text{CH}_3\text{CN} = 50:1$ to 20:1) to give pure product *rac*-**Ru3** (20 mg, 0.02 mmol, 20% yield for two steps) as a dark red solid. The crystal suitable for measurement is obtained by slow diffusion of diethyl ether to its acetonitrile solution.

^1H NMR (300 MHz, CD_3CN) δ 9.61 (dd, $J = 5.1, 1.2$ Hz, 2H), 8.66 (dd, $J = 8.1, 1.2$ Hz, 2H), 8.45 (d, $J = 9.3$ Hz, 2H), 8.10 (d, $J = 9.3, 2\text{H}$), 7.96 (dd, $J = 8.1, 5.1$ Hz, 2H), 7.47 (d, $J = 6.3$ Hz, 2H), 6.62 (d, $J = 6.3$ Hz, 2H), 4.47-4.32 (m, 4H), 1.86-1.75 (m, 4H), 1.38-1.25 (m, 4H), 0.88 (t, $J = 7.4$ Hz, 6H).

^{13}C NMR (75 MHz, CD_3CN) δ 156.0, 137.1, 135.9, 134.2, 133.7, 127.2, 125.5, 119.5, 55.7, 32.5, 20.3, 13.7.

^{19}F NMR (235 MHz, CD_3CN) δ -72.81 (d, $J = 705.7$ Hz, 6F).

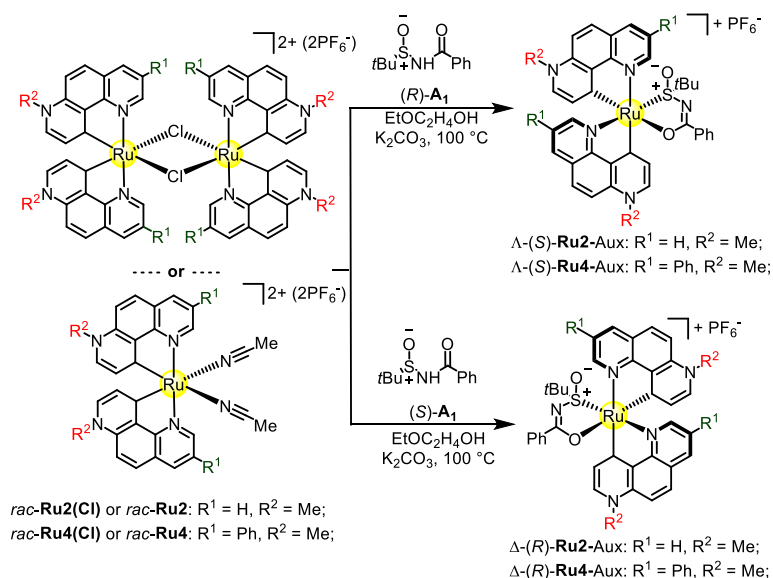
Rac-**Ru4**: A dried 10 mL Schlenk tube was charged with $\text{L}^{\text{Py-4}}$ (125 mg, 0.30 mmol) and $\text{RuCl}_3 \cdot x\text{H}_2\text{O}$ (34 mg, 0.15 mmol). Then 2-ethoxyethanol and water (3:1, 2.8 mL) were added via syringe and resulting mixture was degassed and heated at 120 °C for 18 hours under an atmosphere of nitrogen. After cooling to room temperature, the resulting precipitate was collected by filtration before saturated NH_4PF_6 aqueous solution (1-2 mL) was added, washed with cold water and dried to obtain related chloride bridged ruthenium complexes as a black-purple solid (*rac*-**Ru4(Cl)**), which was used without further purification. To this black-purple solid in CH_3CN (5 mL) was added AgPF_6 (76 mg, 0.30 mmol) in one portion, and then stirred at 60 °C overnight. After cooling to room temperature, the reaction mixture was filtered diatomite to remove insoluble materials. The filtrate was concentrated to dryness and purified by column chromatograph on silica gel ($\text{CH}_2\text{Cl}_2/\text{CH}_3\text{CN} = 25:1$ to 15:1) to give pure product *rac*-**Ru4** (78 mg, 0.077 mmol, 51% yield for two steps) as a dark red solid.

^1H NMR (300 MHz, CD_3CN) δ 9.82 (d, $J = 1.8$ Hz, 2H), 8.89 (d, $J = 1.8$ Hz, 2H), 8.51 (d, $J = 9.0$ Hz, 2H), 8.11 (d, $J = 9.3, 2\text{H}$), 8.05-8.01 (m, 4H), 7.69 (tt, $J = 7.4, 1.5$ Hz, 4H), 7.63-7.57 (m, 2H), 7.46 (d, $J = 6.3$ Hz, 2H), 6.77 (d, $J = 6.3$ Hz, 2H), 4.04 (s, 6H).

^{13}C NMR (75 MHz, CD_3CN) δ 154.6, 154.4, 142.2, 138.6, 137.9, 137.5, 135.0, 133.7, 133.4, 131.0, 130.8, 130.1, 128.8, 128.2, 120.0, 43.3.

^{19}F NMR (235 MHz, CD_3CN) δ -72.58 (d, J = 706.2 Hz, 6F).

5.2.3 Synthesis of Non-Racemic Ruthenium Complexes



$\Delta\text{-(S)-Ru-Aux}$ and $\Delta\text{-(R)-Ru-Aux}$ were synthesized according to our reported method with some modification.⁵ Typical procedure is shown below.

A mixture of rac-Ru (1.5 eq.) or rac-Ru(Cl) (1.0 eq.), N -(tert-butylsulfinyl)benzamide (R)-**A1** or (S)-**A1** (3.0 eq) and K_2CO_3 (1.5 eq) in 2-ethoxyethanol was stirred at 100 °C overnight. After cooling to room temperature, the resulting mixture was treated with saturated NH_4PF_6 and extracted with CH_2Cl_2 , combined CH_2Cl_2 layers were dried with Na_2SO_4 , evaporated to dryness to obtain and the residue was subjected to a flash silica gel chromatography ($\text{CH}_2\text{Cl}_2/\text{MeCN}$) to give a single diastereomer, which was assigned as $\Delta\text{-(S)-Ru-Aux}$ or $\Delta\text{-(R)-Ru-Aux}$, respectively.

$\Delta\text{-(S)-Ru2-Aux}$ and $\Delta\text{-(R)-Ru2-Aux}$

According to typical procedure, starting from rac-Ru2(Cl) (79 mg, 0.059 mmol), chiral auxiliary (R)-**A1** or (S)-**A1** (40 mg, 0.18 mmol), K_2CO_3 (12 mg, 0.088 mmol) in 2-ethoxyethanol (1.5 mL), $\Delta\text{-(S)-Ru2-Aux}$ (46 mg, 46% yield) or $\Delta\text{-(R)-Ru2-Aux}$ (41 mg, 41% yield) was obtained as a dark red solid, respectively. Purification condition: $\text{CH}_2\text{Cl}_2/\text{MeOH} = 50:1$. The crystal suitable for measurement is obtained by slow diffusion of n -hexane to a $\text{CH}_2\text{Cl}_2/\text{THF}$ solution of $\Delta\text{-(S)-Ru2-Aux}$ complexes.

^1H NMR (500 MHz, CD_3CN) δ 10.15 (d, J = 6.9 Hz, 1H), 9.23 (dd, J = 5.0, 1.4 Hz, 1H), 8.78 (dd, J = 8.2, 1.4 Hz, 1H), 8.48 (d, J = 9.3 Hz, 1H), 8.28 (dd, J = 8.1, 1.3 Hz, 1H), 8.14 (d, J = 9.3 Hz, 1H), 8.10-8.04 (m, 4H), 8.00 (d, J = 9.2 Hz, 1H), 7.95 (d, J = 6.9 Hz, 1H), 7.44-7.39 (m, 3H), 7.36-7.29 (m, 4H), 4.12 (s, 3H), 3.97 (s, 3H), 0.46 (s, 9H).

^{13}C NMR (126 MHz, CD_3CN) δ 177.2, 153.6, 153.1, 152.0, 151.8, 142.3, 142.2, 138.1, 137.3, 136.2, 136.0, 135.6, 135.6, 135.3, 135.0, 133.3, 132.1, 131.7, 130.2, 128.9, 127.3, 126.2, 125.7, 123.8, 119.9, 119.8, 68.3,

55.3, 43.1, 42.9, 23.8.

^{19}F NMR (282 MHz, CD_3CN) δ -72.92 (d, J = 846.3 Hz, 6F).

IR (film): ν (cm^{-1}) 1612, 1531, 1504, 1455, 1330, 1173, 830, 779, 718, 669, 586, 556, 491, 428, 398.

HRMS (ESI, m/z) calcd. for $\text{C}_{37}\text{H}_{34}\text{Ru}_1\text{N}_5\text{O}_2\text{S}_1$ $[\text{M-PF}_6]^+$: 714.1480, found: 714.1483.

Λ -(*S*)-**Ru2-Aux**: CD (CH_3CN): λ , nm ($\Delta\epsilon$, $\text{M}^{-1}\text{cm}^{-1}$) 524 (+19), 478 (+15), 440 (+27), 377 (-31), 302 (+45).

Δ -(*R*)-**Ru2-Aux**: CD (CH_3CN): λ , nm ($\Delta\epsilon$, $\text{M}^{-1}\text{cm}^{-1}$) 524 (-19), 478 (-15), 440 (-27), 377 (+31), 302 (-45).

Λ -(*S*)-**Ru4-Aux** and Δ -(*R*)-**Ru4-Aux**

According to typical procedure, starting from *rac*-**Ru4** (60 mg, 0.059 mmol), chiral auxiliary (*R*)-**A1** or (*S*)-**A1** (20 mg, 0.089 mmol), K_2CO_3 (8 mg, 0.059 mmol) in 2-ethoxyethanol (1.5 mL), Λ -(*S*)-**Ru4-Aux** (26 mg, 44% yield) or Δ -(*R*)-**Ru4-Aux** (25 mg, 42% yield) was obtained as a red-yellow solid, respectively. Purification condition: $\text{CH}_2\text{Cl}_2/\text{MeOH}$ = 100:1 to 50:1.

^1H NMR (500 MHz, CD_3CN) δ 10.11 (d, J = 6.9 Hz, 1H), 9.50 (d, J = 2.0 Hz, 1H), 9.00 (d, J = 2.0 Hz, 1H), 8.49 (d, J = 9.3 Hz, 1H), 8.43 (d, J = 1.9 Hz, 1H), 8.22-8.12 (m, 3H), 8.09 (d, J = 9.3 Hz, 1H), 7.99 (dd, J = 13.3, 8.1 Hz, 2H), 7.73-7.64 (m, 2H), 7.56 (d, J = 1.9 Hz, 1H), 7.48 (ddd, J = 22.7, 10.4, 5.4 Hz, 5H), 7.34 (dddd, J = 11.8, 8.9, 6.1, 4.7 Hz, 6H), 7.19-7.07 (m, 2H), 4.13 (s, 3H), 3.97 (s, 3H), 0.56 (s, 9H).

^{13}C NMR (126 MHz, CD_3CN) δ 177.6, 151.8, 151.5, 150.7, 150.3, 142.2, 141.8, 138.1, 137.1, 136.8, 136.2, 136.1, 136.0, 135.7, 135.6, 135.6, 135.3, 135.3, 134.3, 133.4, 132.1, 131.9, 130.5, 130.3, 130.2, 130.1, 129.7, 129.0, 128.2, 127.6, 127.2, 125.9, 120.7, 120.4, 68.0, 55.3, 43.1, 42.9, 28.4, 23.7.

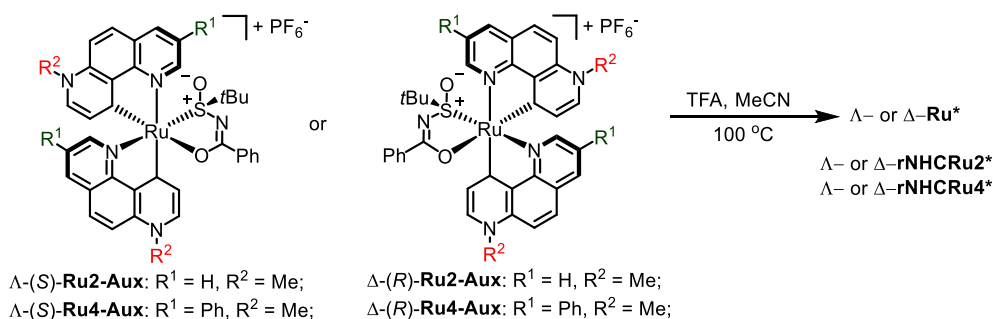
^{19}F NMR (282 MHz, CD_3CN) δ -72.27 (d, J = 705.0 Hz, 6F).

IR (film): ν (cm^{-1}) 1612, 1531, 1504, 1455, 1330, 1173, 830, 779, 718, 669, 586, 556, 491, 428, 398.

HRMS (ESI, m/z) calcd. for $\text{C}_{49}\text{H}_{42}\text{N}_5\text{O}_2\text{Ru}_1\text{S}_1$ $[\text{M-PF}_6]^+$: 866.2110, found: 866.2117

Λ -(*S*)-**Ru4-Aux**: CD (CH_3CN): λ , nm ($\Delta\epsilon$, $\text{M}^{-1}\text{cm}^{-1}$) 549 (+10), 501 (+17), 461 (+22), 386 (-17), 358 (-9), 345 (-11), 306 (+87).

Δ -(*R*)-**Ru4-Aux**: CD (CH_3CN): λ , nm ($\Delta\epsilon$, $\text{M}^{-1}\text{cm}^{-1}$) 549 (-10), 501 (-17), 461 (-22), 377 (+18), 358 (+9), 345 (+11), 306 (-87).



Λ -**rNHCRu*** and Δ -**rNHCRu*** were synthesized according to our reported method with some modification.⁵

Preparation of Λ -**rNHCRu***: To a solution of Λ -(*S*)-**Ru2-Aux** (40 mg, 0.042 mmol) in MeCN (1.5 mL) was added TFA (48 mg, 0.42 mmol). The resulting mixture was stirred at 100 °C for 4 hours. After cooling to room temperature, NH_4PF_6 was added and reaction mixture was stirred for 30 minutes. Then solvent was removed

to give red residue, this residue was then purified by column chromatography on silica gel ($\text{CH}_2\text{Cl}_2/\text{MeCN} = 50:1$ to $10:1$) to give the enantiopure complexes $\Lambda\text{-rNHCRu2}^*$ (30 mg, 0.035 mmol, 83% yield).

Accordingly, starting from $\Delta\text{-}(R)\text{-Ru2-Aux}$ (40 mg, 0.042 mmol), $\Delta\text{-rNHCRu2}^*$ was obtained by the same procedure in 81% yield.

The crystal suitable for measurement is obtained by slow diffusion of diethyl ether to its acetonitrile solution.

^1H NMR (300 MHz, CD_3CN) δ 9.74 (dd, $J = 4.8, 1.2$ Hz, 1H), 8.82 (dd, $J = 8.1, 1.2$ Hz, 1H), 8.65 (d, $J = 6.6$ Hz, 1H), 8.52 (d, $J = 9.3$ Hz, 1H), 8.30 (d, $J = 9.6$ Hz, 1H), 8.29 (dd, $J = 8.1, 0.9$ Hz, 1H), 8.19 (d, $J = 7.2$ Hz, 1H), 8.17 (dd, $J = 8.4, 3.3$ Hz, 1H), 8.10 (d, $J = 9.3$ Hz, 1H), 8.04 (d, $J = 6.6$ Hz, 1H), 7.76 (dd, $J = 5.4, 0.9$ Hz, 1H), 7.33 (d, $J = 6.3$ Hz, 1H), 7.24 (dd, $J = 8.1, 5.1$ Hz, 1H), 7.00 (d, $J = 6.3$ Hz, 1H), 4.28 (s, 3H), 4.02 (s, 3H).

^{13}C NMR (75 MHz, CD_3CN) δ 155.3, 155.2, 153.4, 151.8, 142.4, 142.2, 137.8, 137.7, 136.4, 136.1, 135.9, 134.6, 133.9, 133.5, 132.9, 132.4, 128.4, 127.3, 126.5, 125.8, 125.2, 124.3, 119.9, 119.5, 43.4, 43.1.

^{19}F NMR (235 MHz, CD_3CN) δ -72.88 (d, $J = 705.5$ Hz, 6F).

$\Lambda\text{-rNHCRu2}^*$: CD (CH_3CN): λ , nm ($\Delta\epsilon$, $\text{M}^{-1}\text{cm}^{-1}$) 530 (+12), 464 (-5), 429 (-1), 378 (-11), 336 (+4).

$\Delta\text{-rNHCRu2}^*$: CD (CH_3CN): λ , nm ($\Delta\epsilon$, $\text{M}^{-1}\text{cm}^{-1}$) 531 (-12), 465 (+5), 429 (+2), 377 (+13), 334 (-2).

Preparation of $\Lambda\text{-rNHCRu4}^*$: To a solution of $\Lambda\text{-}(S)\text{-Ru4-Aux}$ (20 mg, 0.020 mmol) in MeCN (1.0 mL) was added TFA (23 mg, 0.20 mmol). The resulting mixture was stirred at 80 °C for 4 hours. After cooling to room temperature, NH_4PF_6 was added and reaction mixture was stirred for 30 minutes. Then solvent was removed to give red residue, this residue was then purified by column chromatography on silica gel ($\text{CH}_2\text{Cl}_2/\text{MeCN} = 50:1$ to $10:1$) to give the enantiopure complexes $\Lambda\text{-rNHCRu4}^*$ (18 mg, 0.178 mmol, 88 % yield).

Accordingly, starting from $\Delta\text{-}(R)\text{-Ru4-Aux}$ (20 mg, 0.02 mmol), $\Delta\text{-Ru4}^*$ was obtained by the same procedure in 85% yield.

^1H NMR (300 MHz, CD_3CN) δ 9.98 (d, $J = 1.8$ Hz, 1H), 9.03 (d, $J = 2.1$ Hz, 1H), 8.67 (d, $J = 6.3$ Hz, 1H), 8.55 (d, $J = 9.3$ Hz, 1H), 8.51 (d, $J = 1.8$ Hz, 1H), 8.35 (d, $J = 9.3$ Hz, 1H), 8.20 (d, $J = 9.0$ Hz, 1H), 8.12-8.09 (m, 3H), 8.06 (d, $J = 6.6$ Hz, 1H), 8.01 (d, $J = 2.1$ Hz, 1H), 7.70 (t, $J = 7.5$ Hz, 2H), 7.63-7.58 (m, 1H), 7.36-7.27 (m, 6H), 7.04 (d, $J = 6.6$ Hz, 1H), 4.30 (s, 3H), 4.03 (s, 3H).

^{13}C NMR (126 MHz, CD_3CN) δ 155.4, 155.3, 153.4, 151.7, 142.8, 142.2, 137.8, 137.7, 136.3, 136.1, 135.8, 134.8, 134.5, 133.9, 132.9, 132.3, 127.3, 126.6, 126.4, 125.7, 125.2, 124.3, 119.9, 119.5, 43.4, 43.1, 4.2.

^{19}F NMR (235 MHz, CD_3CN) δ -72.90 (d, $J = 705.5$ Hz, 6F).

$\Lambda\text{-rNHCRu4}$: CD (CH_3CN): λ , nm ($\Delta\epsilon$, $\text{M}^{-1}\text{cm}^{-1}$) 539 (+7), 473 (-0.7), 426 (+2), 387 (-8), 291 (+80), 267 (-39).

$\Delta\text{-rNHCRu4}$: CD (CH_3CN): λ , nm ($\Delta\epsilon$, $\text{M}^{-1}\text{cm}^{-1}$) 561 (-7), 552 (+0.7), 426 (-2), 387 (+8), 291 (-80), 267 (+39).

5.2.4 Single Crystal X-Ray Diffraction Studies

(1) Single crystal X-ray analysis of *rac*-Ru1

Data was collected with an STOE STADIVARI diffractometer equipped with with CuK α radiation, a graded multilayer mirror monochromator ($\lambda = 1.54178 \text{ \AA}$) and a DECTRIS PILATUS 300K detector using an oil-coated shock-cooled crystal at 230(2) K. Data was integrated as a two domain twin. Cell constants were refined using 25021 of observed reflections of the data collection. A combined data set (“hklf 5” format) was used for the following steps. Absorption effects were corrected semi-empirical using multiscanned reflexions (STOE LANA, absorption correction by scaling of reflection intensities). The structure was solved by direct methods by using the program XT V2014/1 (Bruker AXS Inc., 2014) and refined by full matrix least squares procedures on F^2 using SHELXL-2018/1 (Sheldrick, 2018). The non-hydrogen atoms have been refined anisotropically, carbon bonded hydrogen atoms were included at calculated positions and refined using the ‘riding model’ with isotropic temperature factors at 1.2 times (for CH₃ groups 1.5 times) that of the preceding carbon atom. CH₃ groups were allowed to rotate about the bond to their next atom to fit the electron density. SQUEEZE routine had to be applied to remove spurious electron density corresponding to 182 electrons (ca. 6 ether molecules).

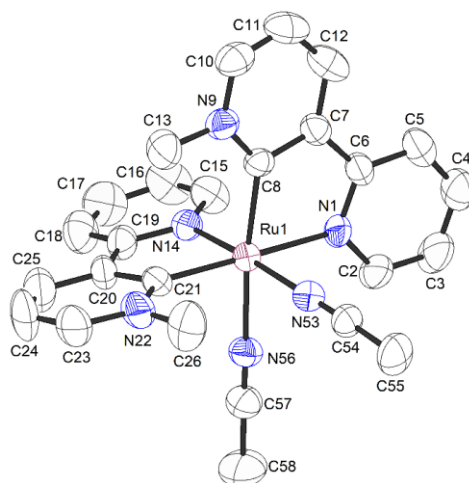


Figure 48. Crystal structure of *rac*-Ru1. ORTEP drawing with 50% probability thermal ellipsoids. The hexafluorophosphate counteranion and all hydrogens are omitted for clarity.

Selected bond lengths [\AA] and angles [deg]: Ru-C21 2.022(6), Ru-C8 2.033(6), Ru-N53 2.051(5), Ru-N14 2.063(5), Ru-N56 2.126(5), Ru-N1 2.151(5), C21-Ru-C8 102.9(2), C21-Ru-N53 101.7(2), C8-Ru-N53 93.8(2), C21-Ru-N14 79.8(2), C8-Ru-N14 91.1(2), N53-Ru-N14 174.5(2), C21-Ru-N56 85.9(2), C8-Ru-N56 170.6(2), N53-Ru-N56 87.5(2), N14-Ru-N56 87.3(2), C21-Ru-N1 174.4(2), C8-Ru-N1 79.1(2), N53-Ru-N1 83.4(2), N14-Ru-N1 95.0(2), N56-Ru-N1 91.8(2).

Table 7. Crystal data and structure refinement for *rac-Ru1*

Identification code	rbpyRu1_230K_5_sq	
Habitus, colour	nugget, orange	
Crystal size	0.24 x 0.19 x 0.16 mm ³	
Crystal system	Monoclinic	
Space group	P2 ₁ /c	Z = 4
Unit cell dimensions	a = 33.4019(6) Å	α = 90°.
	b = 16.5265(3) Å	β = 93.757(2)°.
	c = 13.7937(3) Å	γ = 90°.
Volume	7598.0(3) Å ³	
Cell determination	25021 peaks with Theta 4.4 to 72.3°.	
Empirical formula	C ₅₆ H ₆₂ F ₂₄ N ₁₂ OP ₄ Ru ₂	
Moiety formula	2(C ₂₆ H ₂₆ N ₆ Ru), 2(F ₆ P), C ₄ H ₁₀ O	
Formula weight	1701.19	
Density (calculated)	1.487 Mg/m ³	
Absorption coefficient	4.945 mm ⁻¹	
F(000)	3416	
Diffractometer type	STOE STADIVARI	
Wavelength	1.54178 Å	
Temperature	230(2) K	
Theta range for data collection	2.984 to 72.278°.	
Index ranges	-41 ≤ h ≤ 41, -20 ≤ k ≤ 20, -16 ≤ l ≤ 16	
Reflections collected	24486	
Independent reflections	24486 [R(int) = 0.0665]	
Completeness to theta = 67.679°	99.9 %	
Observed reflections	14569 [I > 2σ(I)]	
Reflections used for refinement	24486	
Max. and min. transmission	0.363 and 0.110	
Largest diff. peak and hole	1.833 and -0.870 e.Å ⁻³	
Refinement	Full-matrix least-squares on F ²	
Treatment of hydrogen atoms	Calculated positions, constr. ref.	
Data / restraints / parameters	24486 / 0 / 904	
Goodness-of-fit on F ²	0.897	
R index (all data)	wR2 = 0.1591	
R index conventional [I > 2σ(I)]	R1 = 0.0573	

(2) Single crystal X-ray analysis of *rac*-Ru2

Data was collected with an STOE STADIVARI diffractometer equipped with with CuK α radiation, a graded multilayer mirror monochromator ($\lambda = 1.54186 \text{ \AA}$) and a DECTRIS PILATUS 300K detector using an oil-coated shock-cooled crystal at 100(2) K. Absorption effects were corrected semi-empirical using multiscanned reflexions (X-Area LANA 1.68.2.0 (STOE, 2016)). Cell constants were refined using 46428 of observed reflections of the data collection. The structure was solved by direct methods by using the program XT V2014/1 (Bruker AXS Inc., 2014) and refined by full matrix least squares procedures on F^2 using SHELXL-2018/1 (Sheldrick, 2018). The non-hydrogen atoms have been refined anisotropically, carbon bonded hydrogen atoms were included at calculated positions and refined using the ‘riding model’ with isotropic temperature factors at 1.2 times (for CH₃ groups 1.5 times) that of the preceding carbon atom. CH₃ groups were allowed to rotate about the bond to their next atom to fit the electron density. PLATON/SQUEEZE^[7] routine had to be applied to remove spurious electron density corresponding to 52 electrons (disordered CH₃CN and/or Et₂O).

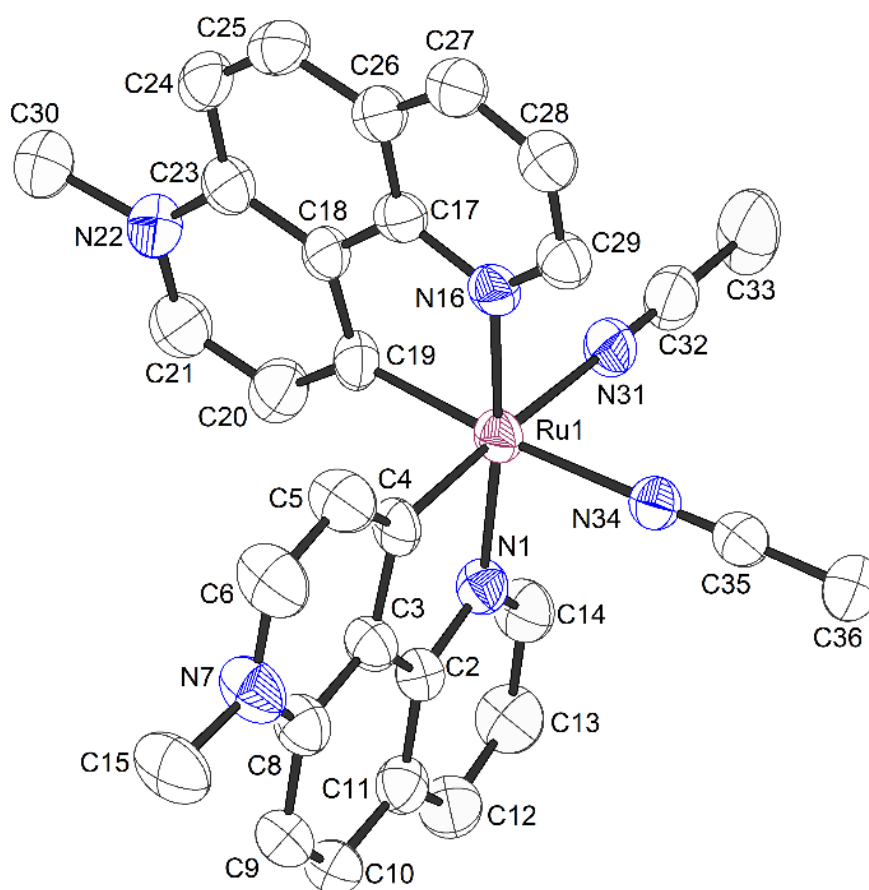


Figure 49. Crystal structure of *rac*-Ru2. ORTEP drawing with 50% probability thermal ellipsoids. The hexafluorophosphate counteranion and all hydrogens are omitted for clarity.

Selected bond lengths [\AA] and angles [deg]: Ru-C4 1.972(3), Ru-C19 1.991(3), Ru-N16 2.059(3), Ru-N1 2.066(3), Ru-N31 2.128(3), Ru-N34 2.134(3), C4-Ru-C19 88.32(13), C4-Ru-N16 93.53(12), C19-Ru-N16 81.01(13), C4-Ru-N1 80.48(12), C19-Ru-N1 95.12(13), N16-Ru-N1 173.01(10), C4-Ru-N31 176.47(12), C19-Ru-N31 92.68(12), N16-Ru-N31 89.97(10), N1-Ru-N31 96.05(11), C4-Ru-N34 93.73(12), C19-Ru-N34 175.22(12), N16-Ru-N34 94.54(10), N1-Ru-N34 89.48(10), N31-Ru-N34 85.53(10).

Table 8. Crystal data and structure refinement for *rac*-Ru2

Identification code	rNHCRu2_sq	
Habitus, colour	plate, red	
Crystal size	0.18 x 0.10 x 0.07 mm ³	
Crystal system	Monoclinic	
Space group	P2/c	Z = 4
Unit cell dimensions	a = 13.6186(4) Å	α = 90°.
	b = 13.0969(4) Å	β = 97.059(2)°.
	c = 19.9906(5) Å	γ = 90°.
Volume	3538.53(17) Å ³	
Cell determination	46428 peaks with Theta 4.1 to 75.7°.	
Empirical formula	C ₃₀ H ₂₆ F ₁₂ N ₆ P ₂ Ru	
Moiety formula	C ₃₀ H ₂₆ N ₆ Ru, 2(F ₆ P)	
Formula weight	861.58	
Density (calculated)	1.617 Mg/m ³	
Absorption coefficient	5.312 mm ⁻¹	
F(000)	1720	
Diffractometer type	STOE STADIVARI	
Wavelength	1.54186 Å	
Temperature	100(2) K	
Theta range for data collection	4.045 to 67.498°.	
Index ranges	-16 ≤ h ≤ 12, -15 ≤ k ≤ 14, -23 ≤ l ≤ 23	
Reflections collected	32747	
Independent reflections	6369 [R(int) = 0.0572]	
Completeness to theta = 67.498°	99.6 %	
Observed reflections	4561 [I > 2σ(I)]	
Reflections used for refinement	6369	
Max. and min. transmission	0.3558 and 0.0817	
Largest diff. peak and hole	0.636 and -0.343 e.Å ⁻³	
Refinement	Full-matrix least-squares on F ²	
Treatment of hydrogen atoms	Calculated positions, constr. ref.	
Data / restraints / parameters	6369 / 505 / 531	
Goodness-of-fit on F ²	0.923	
R index (all data)	wR2 = 0.0921	
R index conventional [I > 2σ(I)]	R1 = 0.0362	

(3) Single crystal X-ray analysis of *rac*-Ru3

Data was collected with an STOE STADIVARI diffractometer equipped with with CuK α radiation, a graded multilayer mirror monochromator ($\lambda = 1.54178 \text{ \AA}$) and a DECTRIS PILATUS 300K detector using an oil-coated shock-cooled crystal at 100(2) K. Absorption effects were corrected semi-empirical using multiscanned reflexions (STOE LANA, absorption correction by scaling of reflection intensities.). Cell constants were refined using 34108 of observed reflections of the data collection. The structure was solved by direct methods by using the program XT V2014/1 (Bruker AXS Inc., 2014) and refined by full matrix least squares procedures on F^2 using SHELXL-2018/1 (Sheldrick, 2018). The non-hydrogen atoms have been refined anisotropically, carbon bonded hydrogen atoms were included at calculated positions and refined using the ‘riding model’ with isotropic temperature factors at 1.2 times (for CH₃ groups 1.5 times) that of the preceding carbon atom. CH₃ groups were allowed to rotate about the bond to their next atom to fit the electron density. SQUEEZE routine had to be applied to remove spurious electron density corresponding to 104 electrons in the unit cell (ca. 4 ether molecules).

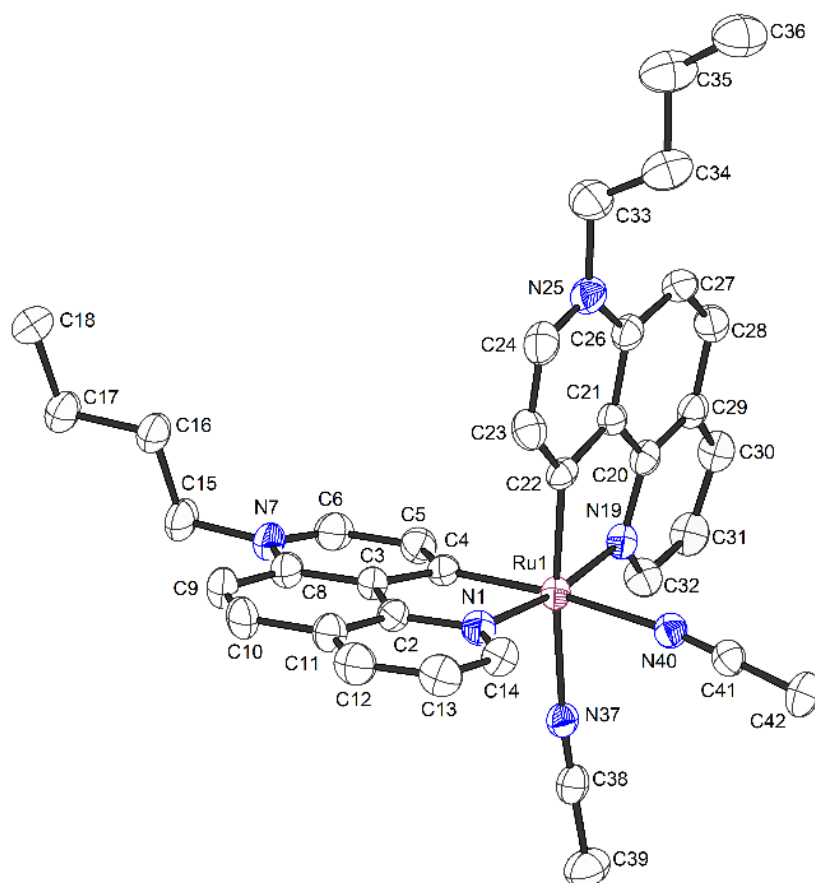


Figure 50. Crystal structure of *rac*-Ru3. ORTEP drawing with 50% probability thermal ellipsoids. The hexafluorophosphate counteranion and all hydrogens are omitted for clarity.

Selected bond lengths [\AA] and angles [deg]: Ru-C4 1.972(4), Ru-C22 1.984(3), Ru-N1 2.070(3), Ru-N19 2.077(3), Ru-N37 2.140(3), Ru-N40 2.141(3), C4-Ru-C22 90.23(14), C4-Ru-N1 81.26(14), C22-Ru-N1 91.98(13), C4-Ru-N19 93.09(13), C22-Ru-N19 81.23(13), N1-Ru-N19 171.19(12), C4-Ru-N37 93.47(13), C22-Ru-N37 173.14(13), N1-Ru-N37 94.29(11), N19-Ru-N37 92.79(11), C4-Ru-N40 173.48(13), C22-Ru-N40 93.86(13), N1-Ru-N40 93.51(12), N19-Ru-N40 92.55(11), N37-Ru-N40 82.99(11).

Table 9. Crystal data and structure refinement for *rac*-Ru3

Identification code	rNHCRu3_sq	
Habitus, colour	prism, red	
Crystal size	0.220 x 0.050 x 0.030 mm ³	
Crystal system	Monoclinic	
Space group	P2 ₁ /c	Z = 4
Unit cell dimensions	a = 13.3649(2) Å	α = 90°.
	b = 30.4566(4) Å	β = 114.5510(10)°.
	c = 11.8500(2) Å	γ = 90°.
Volume	4387.45(12) Å ³	
Cell determination	34108 peaks with Theta 2.9 to 75.9°.	
Empirical formula	C _{37.20} H _{39.80} F ₁₂ N _{6.60} P ₂ Ru	
Moiety formula	C ₃₆ H ₃₈ N ₆ Ru, 2(F ₆ P), 0.6(C ₂ H ₃ N)	
Formula weight	970.36	
Density (calculated)	1.469 Mg/m ³	
Absorption coefficient	4.353 mm ⁻¹	
F(000)	1965	
Diffractometer type	STOE STADIVARI	
Wavelength	1.54178 Å	
Temperature	100(2) K	
Theta range for data collection	3.636 to 69.992°.	
Index ranges	-16<=h<=16, -36<=k<=16, -14<=l<=14	
Reflections collected	49378	
Independent reflections	8310 [R(int) = 0.0698]	
Completeness to theta = 67.679°	99.8 %	
Observed reflections	6264[I > 2σ(I)]	
Reflections used for refinement	8310	
Absorption correction	Semi-empirical from equivalents	
Max. and min. transmission	0.5479 and 0.1174	
Largest diff. peak and hole	0.952 and -0.757 e.Å ⁻³	
Refinement	Full-matrix least-squares on F ²	
Treatment of hydrogen atoms	Calculated positions, constr. ref.	
Data / restraints / parameters	8310 / 0 / 547	
Goodness-of-fit on F ²	1.010	
R index (all data)	wR2 = 0.1213	
R index conventional [I>2sigma(I)]	R1 = 0.0435	

(4) Single crystal X-ray analysis of *rac*-Ru4

A suitable crystal of $C_{42}H_{34}N_6Ru(PF_6)_2 \cdot C_2H_3N$ was selected under inert oil and mounted using a MiTeGen loop. Intensity data of the crystal were recorded with a D8 Quest diffractometer (Bruker AXS). The instrument was operated with Mo-K α radiation ($\lambda = 0.71073 \text{ \AA}$, microfocus source) and equipped with a PHOTON 100 detector. Evaluation, integration and reduction of the diffraction data was carried out using the Bruker APEX 3 software suite. Multi-scan and numerical absorption corrections were applied using the SADABS program. The structure was solved using dual-space methods (SHELXT-2014/5) and refined against F^2 (SHELXL-2018/3 using ShelXle interface). All non-hydrogen atoms were refined with anisotropic displacement parameters. The hydrogen atoms were refined using the “riding model” approach with isotropic displacement parameters 1.2 times (1.5 times for terminal methyl groups) of that of the preceding carbon atom. One $[PF_6]^-$ anion exhibit rotational disorder and was refined accordingly using the DSR plugin implemented in ShelXle.

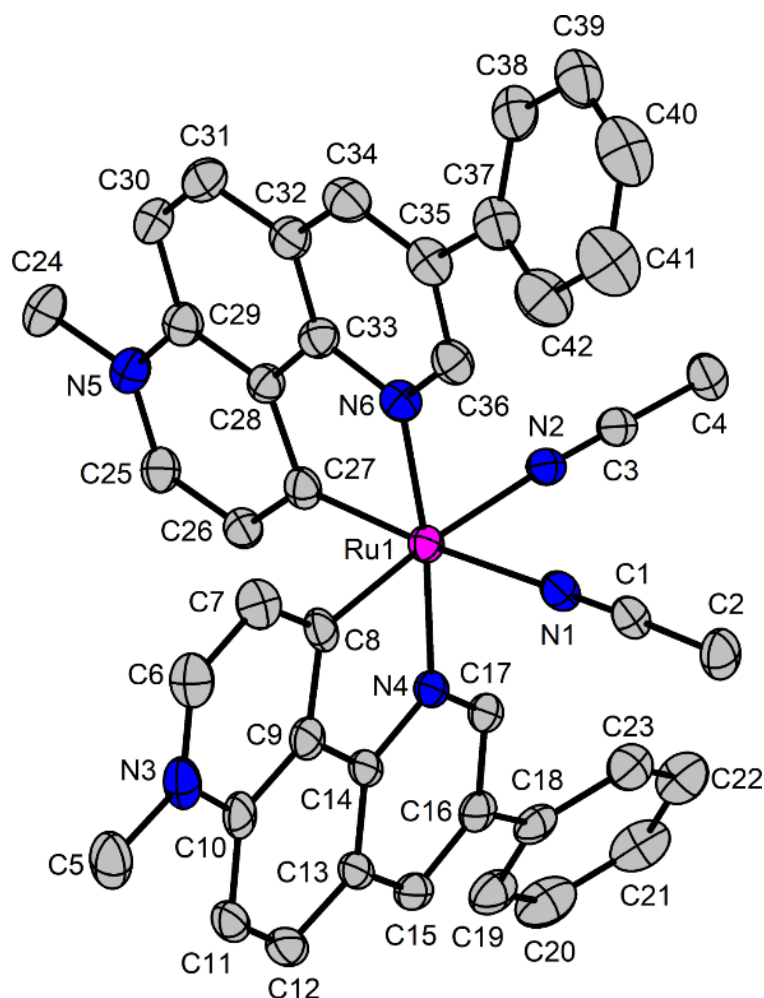


Figure 51. Crystal structure of *rac*-Ru4. Displacement ellipsoids are shown at 50 % probability level at 100 K. The hexafluorophosphate counteranion, the acetonitrile solvent molecule and all hydrogens are not shown. Selected bond lengths [\AA] and angles [deg]: Ru-C27 1.981(3), Ru-C8 2.004(3), Ru-N4 2.072(3), Ru-N6 2.076(3), Ru-N1 2.134(3), Ru-N2 2.134(3), C27-Ru-C8 88.76(12), C27-Ru-N4 93.38(11), C8-Ru-N4 80.76(12), C27-Ru-N6 81.41(12), C8-Ru-N6 94.56(12), N4-Ru-N6 173.10(10), C27-Ru-N1 175.11(12), C8-Ru-N1 92.76(11), N4-Ru-N1 91.45(10), N6-Ru-N1 93.84(10), C27-Ru-N2 94.48(11), C8-Ru-N2 174.63(12), N4-Ru-N2 94.76(10), N6-Ru-N2 90.16(10), N1-Ru-N2 84.36(10).

Table 10. Selected crystallographic data and details of the structure determination for *rac*-Ru4

Identification code	<i>rac</i> Ru4
Empirical formula	C ₄₄ H ₃₇ F ₁₂ N ₇ P ₂ Ru
Molar mass / g·mol ⁻¹	1054.81
Space group (No.)	<i>P</i> 2 ₁ / <i>n</i> (14)
<i>a</i> / Å	9.1326(8)
<i>b</i> / Å	32.252(3)
<i>c</i> / Å	14.7036(14)
β / °	94.894(3)
<i>V</i> / Å ³	4315.0(7)
<i>Z</i>	4
$\rho_{calc.}$ / g·cm ⁻³	1.624
μ / mm ⁻¹	0.532
Color	red
Crystal habitus	plate
Crystal size / mm ³	0.422 x 0.146 x 0.044
<i>T</i> / K	100
λ / Å	0.71073 (Mo-K α)
θ range / °	2.326 to 28.346
Range of Miller indices	-12 ≤ <i>h</i> ≤ 12 -43 ≤ <i>k</i> ≤ 42 -19 ≤ <i>l</i> ≤ 19
Absorption correction	multi-scan and numerical
<i>T</i> _{min} , <i>T</i> _{max}	0.7610, 1.0000
<i>R</i> _{int} , <i>R</i> _{σ}	0.0787, 0.0527
Completeness of the data set	1.000
No. of measured reflections	79493
No. of independent reflections	10740
No. of parameters	664
No. of restrains	448
<i>S</i> (all data)	1.056
<i>R</i> (<i>F</i>) (<i>I</i> ≥ 2 σ (<i>I</i>), all data)	0.0507, 0.0822
<i>wR</i> (<i>F</i> ²) (<i>I</i> ≥ 2 σ (<i>I</i>), all data)	0.0982, 0.1110
Extinction coefficient	not refined
$\Delta\rho_{max}$, $\Delta\rho_{min}$ / e·Å ⁻³	0.815, -1.059

(5) Single crystal X-ray analysis of Λ -(S)-Ru2-Aux

Data was collected with an STOE STADIVARI diffractometer equipped with with $\text{CuK}\alpha$ radiation, a graded multilayer mirror monochromator ($\lambda = 1.54186 \text{ \AA}$) and a DECTRIS PILATUS 300K detector using an oil-coated shock-cooled crystal at 100(2) K. Absorption effects were corrected semi-empirical using multiscanned reflexions (STOE LANA, absorption correction by scaling of reflection intensities.). Cell constants were refined using 121299 of observed reflections of the data collection. The structure was solved by direct methods by using the program XT V2014/1 (Bruker AXS Inc., 2014) and refined by full matrix least squares procedures on F^2 using SHELXL-2018/3 (Sheldrick, 2018). The non-hydrogen atoms have been refined anisotropically, carbon bonded hydrogen atoms were included at calculated positions and refined using the ‘riding model’ with isotropic temperature factors at 1.2 times (for CH_3 groups 1.5 times) that of the preceding carbon atom. CH_3 groups were allowed to rotate about the bond to their next atom to fit the electron density. Nitrogen or oxygen bonded hydrogen atoms were located and allowed to refine isotropically. The Flack parameter refined to -0.025(3). The absolute structure of the crystal was determined.

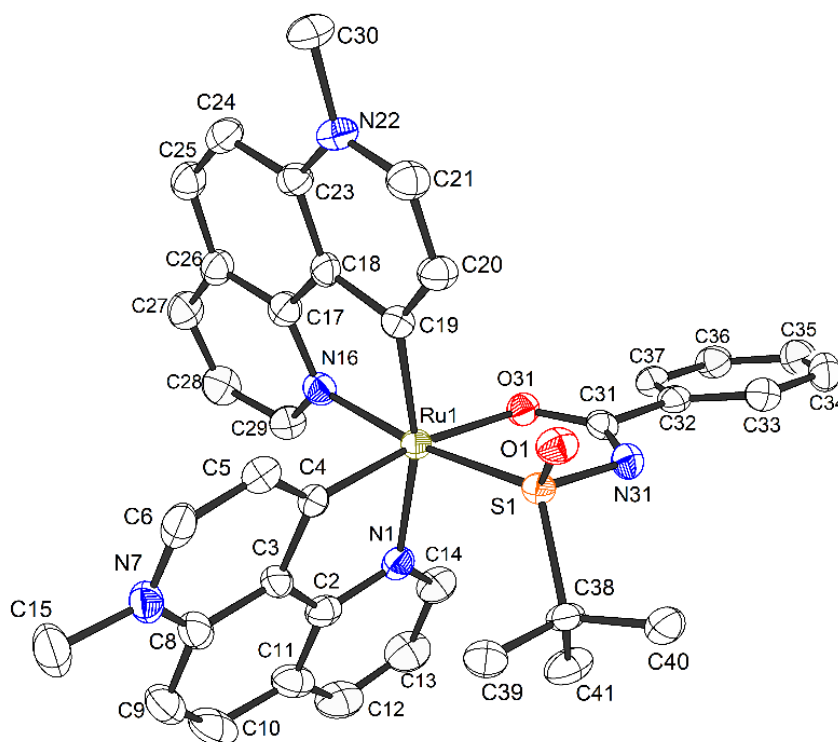


Figure 52. Crystal structure of Λ -(S)-Ru2-Aux. ORTEP drawing with 50% probability thermal ellipsoids. The hexafluorophosphate counteranion and all hydrogens are omitted for clarity.

Selected bond lengths [\AA] and angles [deg]: Ru1-C4 1.975(4), Ru1-C19 1.987(4), Ru1-N16 2.133(3), Ru1-O31 2.139(3), Ru1-N1 2.155(3), Ru1-S1 2.2526(9), C4-Ru1-C19 91.13(15), C4-Ru1-N16 88.19(13), C19-Ru1-N16 80.63(14), C4-Ru1-O31 169.82(13), C19-Ru1-O31 99.06(12), N16-Ru1-O31 93.65(11), C4-Ru1-N1 80.78(14), C19-Ru1-N1 164.32(14), N16-Ru1-N1 85.68(12), O31-Ru1-N1 89.37(11), C4-Ru1-S1 99.17(11), C19-Ru1-S1 95.05(11), N16-Ru1-S1 171.58(9), O31-Ru1-S1 79.82(7), N1-Ru1-S1 99.47(9).

Table 11. Crystal data and structure refinement for Λ -(S)-Ru2-Aux

Identification code	Ru2aux	
Habitus, colour	nugget, red	
Crystal size	0.15 x 0.15 x 0.06 mm ³	
Crystal system	Tetragonal	
Space group	P4 ₃ 2 ₁ 2	Z = 8
Unit cell dimensions	a = 13.4873(1) Å	$\alpha = 90^\circ$.
	b = 13.4873(1) Å	$\beta = 90^\circ$.
	c = 42.0533(3) Å	$\gamma = 90^\circ$.
Volume	7649.80(13) Å ³	
Cell determination	121299 peaks with Theta 3.4 to 76.2°.	
Empirical formula	C ₃₈ H ₃₆ Cl ₂ F ₆ N ₅ O ₂ P Ru S	
Moiety formula	C ₃₇ H ₃₄ N ₅ O ₂ Ru S, F ₆ P, C H ₂ Cl ₂	
Formula weight	943.72	
Density (calculated)	1.639 Mg/m ³	
Absorption coefficient	6.142 mm ⁻¹	
F(000)	3824	
Diffractometer type	STOE STADIVARI	
Wavelength	1.54186 Å	
Temperature	100(2) K	
Theta range for data collection	3.441 to 75.939°.	
Index ranges	-7<=h<=16, -16<=k<=16, -52<=l<=52	
Reflections collected	119089	
Independent reflections	7924 [R(int) = 0.0549]	
Completeness to theta = 67.686°	100.0 %	
Observed reflections	7340[I > 2 σ (I)]	
Reflections used for refinement	7924	
Max. and min. transmission	0.4100 and 0.1056	
Flack parameter (absolute struct.)	-0.025(3)	
Largest diff. peak and hole	0.555 and -0.510 e.Å ⁻³	
Refinement	Full-matrix least-squares on F ²	
Data / restraints / parameters	7924 / 0 / 510	
Goodness-of-fit on F ²	1.054	
R index (all data)	wR ₂ = 0.0717	
R index conventional [I>2sigma(I)]	R ₁ = 0.0280	

(6) Single crystal X-ray analysis of Λ -Ru2*

Data was collected with an STOE STADIVARI diffractometer equipped with with CuK α radiation, a graded multilayer mirror monochromator ($\lambda = 1.54186 \text{ \AA}$) and DECTRIS PILATUS 300K detector using an oil-coated shock-cooled crystal at 100(2) K. Absorption effects were corrected semi-empirical using multiscanned reflexions (STOE LANA, absorption correction by scaling of reflection intensities). Cell constants were refined using 41901 of observed reflections of the data collection. The structure was solved by direct methods by using the program XT V2014/1 (Bruker AXS Inc., 2014) and refined by full matrix least squares procedures on F^2 using SHELXL-2018/3 (Sheldrick, 2018). The non-hydrogen atoms have been refined anisotropically, carbon bonded hydrogen atoms were included at calculated positions and refined using the ‘riding model’ with isotropic temperature factors at 1.2 times (for CH₃ groups 1.5 times) that of the preceding carbon atom. CH₃ groups were allowed to rotate about the bond to their next atom to fit the electron density. Nitrogen or oxygen bonded hydrogen atoms were located and allowed to refine isotropically. The Flack parameter refined to 0.001(3). The absolute structure of the crystal was determined.

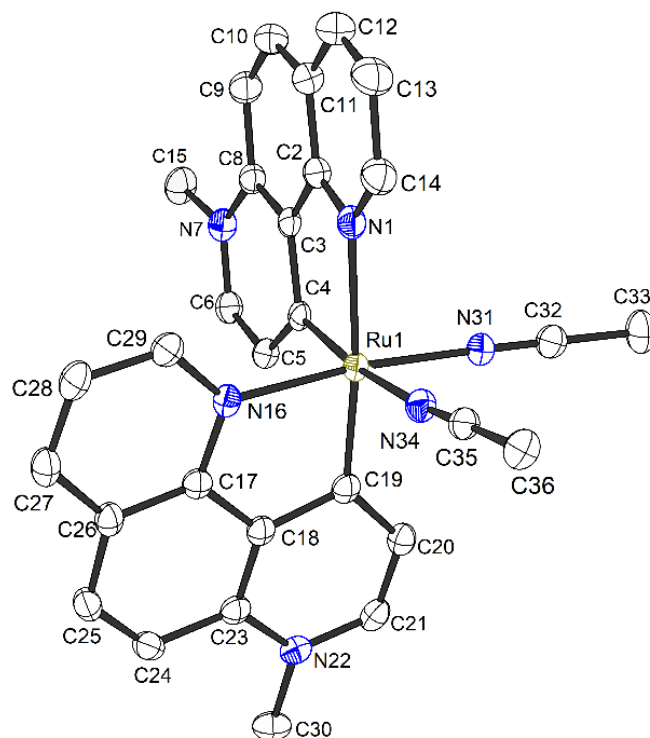


Figure 53. Crystal structure of Λ -rNHCru2*. ORTEP drawing with 50% probability thermal ellipsoids. The hexafluorophosphate counteranion and all hydrogens are omitted for clarity.

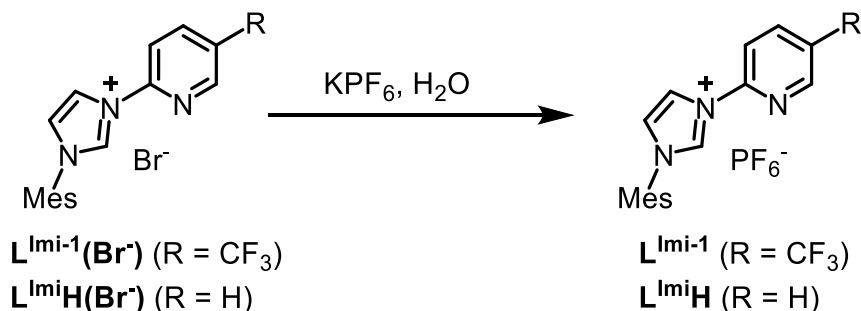
Selected bond lengths [\AA] and angles [deg]: Ru1-C19 1.977(3), Ru1-C4 1.984(3), Ru1-N31 2.022(3), Ru1-N16 2.067(2), Ru1-N34 2.150(3), Ru1-N1 2.188(2), C19-Ru1-C4 92.28(11), C19-Ru1-N31 93.57(11), C4-Ru1-N31 94.31(11), C19-Ru1-N16 81.08(11), C4-Ru1-N16 89.10(10), N31-Ru1-N16 173.78(10), C19-Ru1-N34 96.77(10), C4-Ru1-N34 170.83(10), N31-Ru1-N34 86.63(10), N16-Ru1-N34 90.83(10), C19-Ru1-N1 171.78(11), C4-Ru1-N1 80.01(10), N31-Ru1-N1 89.86(10), N16-Ru1-N1 95.86(10), N34-Ru1-N1 90.88(9).

Table 12. Crystal data and structure refinement for Λ -rNHCRu2*

Identification code	Ru2pure	
Habitus, colour	prism, red	
Crystal size	0.19 x 0.16 x 0.10 mm ³	
Crystal system	Monoclinic	
Space group	P2 ₁	Z = 2
Unit cell dimensions	a = 8.4324(1) Å	$\alpha = 90^\circ$.
	b = 9.6046(1) Å	$\beta = 99.680(1)^\circ$.
	c = 21.8222(3) Å	$\gamma = 90^\circ$.
Volume	1742.21(4) Å ³	
Cell determination	41901 peaks with Theta 4.1 to 76.3°.	
Empirical formula	C ₃₂ H ₂₉ F ₁₂ N ₇ P ₂ Ru	
Moiety formula	C ₃₀ H ₂₆ N ₆ Ru, 2(F6 P), C ₂ H ₃ N	
Formula weight	902.63	
Density (calculated)	1.721 Mg/m ³	
Absorption coefficient	5.435 mm ⁻¹	
F(000)	904	
Diffractometer type	STOE STADIVARI	
Wavelength	1.54186 Å	
Temperature	100(2) K	
Theta range for data collection	4.110 to 75.610°.	
Index ranges	-10 ≤ h ≤ 4, -11 ≤ k ≤ 12, -27 ≤ l ≤ 27	
Reflections collected	28521	
Independent reflections	6963 [R(int) = 0.0191]	
Completeness to theta = 67.686°	99.1 %	
Observed reflections	6845 [I > 2σ(I)]	
Reflections used for refinement	6963	
Max. and min. transmission	0.4566 and 0.0608	
Flack parameter (absolute struct.)	0.001(3)	
Largest diff. peak and hole	0.600 and -0.319 e.Å ⁻³	
Refinement	Full-matrix least-squares on F ²	
Data / restraints / parameters	6963 / 310 / 547	
Goodness-of-fit on F ²	1.021	
R index (all data)	wR2 = 0.0491	
R index conventional [I > 2σ(I)]	R1 = 0.0191	

5.3 Chiral-at-Iron Catalyst: Expanding the Chemical Space for Asymmetric Earth-Abundant Metal Catalysis

5.3.1 Synthesis of Imidazolium Ligands



$\text{L}^{\text{Imi-1}}(\text{Br}^-)$ was prepared according to a reported literature procedure.⁶ L^{ImiH} was prepared according to a reported literature procedure with slight modifications.⁷ $\text{L}^{\text{Imi-1}}$ was synthesized by addition of a solution of KPF_6 (770 mg, 4.19 mmol) in water (25 mL) to a clear solution of $\text{L}^{\text{Imi-1}}(\text{Br}^-)$ (1.73 g, 4.19 mmol) in water (150 mL). The mixture was stirred for 10 minutes, and the precipitate was collected by filtration and dried under reduced pressure to obtain desired product as a white solid (1.40 g, 70% yield).

¹H NMR (300 MHz, CD₂Cl₂) δ 9.37 (t, J = 1.6 Hz, 1H), 8.89 (s, 1H), 8.51 (t, J = 1.8 Hz, 1H), 8.39 (dd, J = 8.7, 2.1 Hz, 1H), 8.20 (d, J = 8.4 Hz, 1H), 7.53 (t, J = 1.8 Hz, 1H), 7.14 (s, 2H), 2.40 (s, 3H), 2.14 (s, 6H).

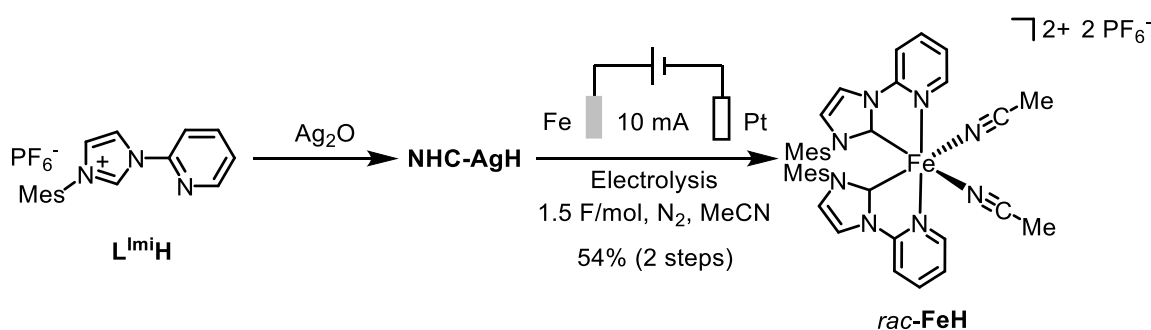
¹³C NMR (75 MHz, CD₂Cl₂) δ 148.6, 147.4 (q, J = 4.0 Hz), 142.9, 139.1 (q, J = 3.2 Hz), 134.8, 134.7, 130.9, 130.6, 129.2 (q, J = 34.0 Hz), 126.2, 123.3 (q, J = 271.0 Hz), 121.2, 115.2, 21.5, 17.7.

¹⁹F NMR (282 MHz, CD₂Cl₂) δ -62.96, -72.96 (d, J = 846.0 Hz, 6F).

IR (film): ν (cm⁻¹) 3162, 1605, 1542, 1489, 1458, 1408, 1329, 1243, 1174, 1138, 1071, 1020, 821, 760, 712, 668, 582, 554, 468, 427.

HRMS (ESI, m/z) calcd for C₁₈H₁₇N₃F₃ [M-PF₆]⁺: 332.1375, found: 332.1370.

5.3.2 Synthesis of Iron Complex *Rac*-FeH



The racemic complex *rac*-**FeH** was prepared according to a reported literature⁸ procedure with slight modifications as follows: A mixture of L^{ImiH} (204.5 mg, 0.5 mmol) and Ag_2O (72 mg, 0.5 mmol) was stirred in CH₃CN (5 mL) in the dark at 50 °C overnight. The solution was filtered by diatomite to remove insoluble materials, then the filtrate was evaporated to dryness to provide the crude NHC-based silver carbene complex (**NHC-AgH**) as a light brown solid. This crude product was taken to the next step without any further purification.

^1H NMR (300 MHz, CD_3CN) δ 8.35 (dq, $J = 4.8, 0.9$ Hz, 1H), 8.00 (d, $J = 1.8$ Hz, 1H), 7.92 (dt, $J = 7.8, 1.8$ Hz, 1H), 7.81 (d, $J = 8.2$ Hz, 1H), 7.47 (m, 1H), 7.33 (d, $J = 1.9$ Hz, 1H), 7.04 (s, 2H), 2.39 (s, 3H), 1.90 (s, 6H).



The electrochemical reaction was performed by using an IKA ElectroSyn 2.0.⁹ In a 15 mL ElectroSyn vial with a magnetic stirring bar, an iron plate (1×3.0 cm²) was used as the anode and a platinum plate (1×3.0 cm²) was used as the cathode. A solution of **NHC-AgH** (0.5 mmol) in anhydrous CH_3CN (7.5 mL) was electrolyzed under a constant current of 10 mA. After passing through 1.5 F/mol of electricity under nitrogen atmosphere in the dark, the solution was evaporated to dryness and purified by column chromatography on silica gel ($\text{CH}_2\text{Cl}_2/\text{CH}_3\text{CN} = 25:1$) to provide *rac*-**FeH** (130 mg, 0.136 mmol, 54% yield over two steps) as a orange solid.

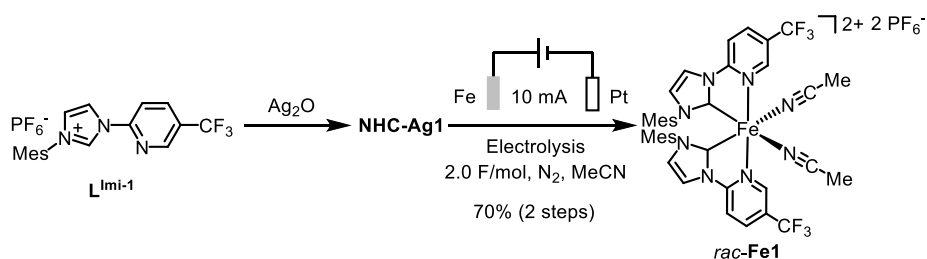
^1H NMR (300 MHz, CD_3CN) δ 8.14 (d, $J = 5.8$ Hz, 2H), 8.06 (d, $J = 2.1$ Hz, 2H), 7.72 (t, $J = 9.3$ Hz, 2H), 7.34 (d, $J = 9.3$ Hz, 2H), 7.02 (d, $J = 2.1$ Hz, 2H), 6.93 (t, $J = 7.0$ Hz, 2H), 6.70 (s, 2H), 6.55 (s, 2H), 2.37 (s, 6H), 2.19 (s, 6H), 1.99 (s, 6H), 1.46 (s, 6H).

^{13}C NMR (75 MHz, CD_3CN) δ 200.2, 155.3, 154.3, 140.4, 139.4, 136.2, 134.6, 134.5, 130.4, 128.9, 122.8, 119.4, 111.4, 20.8, 17.6, 17.3.

^{19}F NMR (282 MHz, CD_3CN) δ -72.88 (d, $J = 846.0$ Hz).

All the spectroscopic data of *rac*-**FeH** were in agreement with published data.¹⁰

5.3.3 Synthesis of Iron Complex *Rac*-Fe1



According to the same procedure used as for the preparation of NHC-AgH, 244mg of ligand L^{Imi-1} (0.8 mmol) provided NHC-Ag1 as a white solid.

¹H NMR (300 MHz, CD₂Cl₂) δ 8.70 (s, 1H), 8.26 (d, *J* = 9.6 Hz, 1H), 8.05 (s, 1H), 7.99 (d, *J* = 9.6 Hz, 1H), 7.27 (s, 1H), 7.03 (s, 2H), 2.37 (s, 3H), 2.26 (s, 3H), 2.00 (s, 6H).

¹⁹F NMR (282 MHz, CD₂Cl₂) δ -62.59, -72.87 (d, *J* = 851.5 Hz, 6F).

According to the same procedure used as for the preparation of *rac*-FeH, electrolysis of NHC-Ag1 (0.8 mmol) with a consumption of 2.0 F/mol electricity, provided *rac*-Fe1 (310 mg, 0.28 mmol, 70% yield over two steps) as a orange solid.

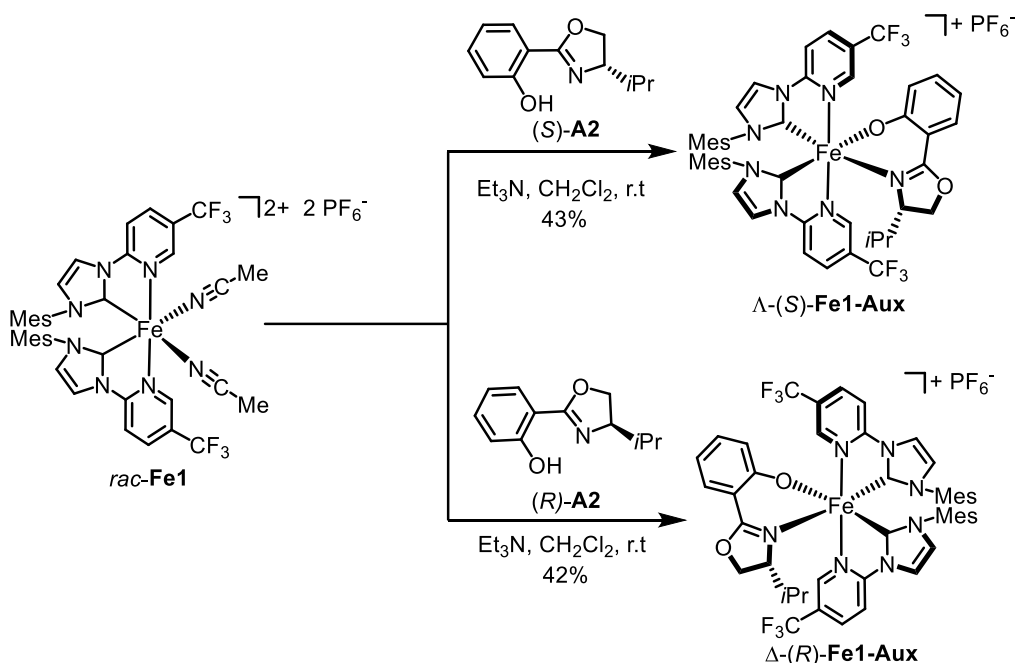
¹H NMR (300 MHz, CD₂Cl₂) δ 8.34 (s, 2H), 8.26 (d, *J* = 2.1 Hz, 2H), 7.94 (dd, *J* = 8.7, 1.4 Hz, 2H), 7.69 (d, *J* = 8.7 Hz, 2H), 7.03 (d, *J* = 2.1 Hz, 2H), 6.71 (s, 2H), 6.66 (s, 2H), 2.40 (s, 6H), 2.18 (s, 6H), 2.02 (s, 6H), 1.47 (s, 6H).

¹³C NMR (75 MHz, CD₂Cl₂) δ 199.1, 157.3, 150.2 (q, *J* = 3.9 Hz), 141.0, 137.2 (q, *J* = 2.7 Hz), 135.0, 134.1, 133.6, 132.4, 130.4, 129.2, 125.3 (q, *J* = 34.4 Hz), 122.7 (q, *J* = 270.8 Hz), 120.1, 119.5, 112.2, 20.9, 17.4, 17.3, 4.6.

¹⁹F NMR (282 MHz, CD₂Cl₂) δ -62.86, -72.88 (d, *J* = 846.0 Hz, 6F).

IR (film): ν (cm⁻¹) 3146, 2219, 1621, 1508, 1426, 1327, 1304, 1260, 1174, 1138, 1076, 1039, 930, 826, 734, 708, 626, 584, 554, 506, 468, 433.

5.3.4 Synthesis of Non-Racemic Iron Complexes



Δ-(S)-Fe1-Aux and Δ-(R)-Fe1-Aux: A mixture of *rac*-Fe1 (250 mg, 0.23 mmol), chiral auxiliary (S)- or (R)-2-(4-isopropyl-4,5-dihydrooxazol-2-yl)phenol (A2) (56.4 mg, 0.28 mmol), and triethylamine (84.0 mg, 1.83 mmol) in CH₂Cl₂ (4.0 mL) was stirred at room temperature for 18 hours. The reaction mixture was concentrated to dryness. The residue was subjected to flash silica gel chromatography (CH₂Cl₂/CH₃CN = 200:1) to obtain a single diastereomer, which was assigned as single diastereoisomer Δ-(S)-Fe1-Aux (deep purple

solid, 105 mg, 0.098 mmol, 43%) or Δ -(*R*)-**Fe1-Aux** (deep purple solid, 102 mg, 0.096 mmol, 42%), respectively.

^1H NMR (300 MHz, CD_2Cl_2) δ 8.69 (s, 1H), 8.30 (d, $J = 2.3$ Hz, 1H), 8.10 (d, $J = 2.2$ Hz, 1H), 7.86 (s, 1H), 7.81 (dd, $J = 8.7, 1.8$ Hz, 1H), 7.65 (dd, $J = 8.6, 1.8$ Hz, 1H), 7.57 (d, $J = 8.6$ Hz, 1H), 7.43 (d, $J = 8.6$ Hz, 1H), 7.32 (dd, $J = 8.0, 1.8$ Hz, 1H), 7.06 (d, $J = 2.2$ Hz, 1H), 6.93 (d, $J = 2.2$ Hz, 1H), 6.92-6.84 (m, 1H), 6.72 (s, 1H), 6.67 (s, 2H), 6.45 (d, $J = 9.4$ Hz, 2H), 6.19 (t, $J = 7.4$ Hz, 1H), 4.38 (dd, $J = 9.5, 2.8$ Hz, 1H), 4.20 (t, $J = 9.0$ Hz, 1H), 3.74 (dt, $J = 7.5, 2.8$ Hz, 1H), 2.26 (s, 3H), 2.19 (s, 3H), 2.13 (s, 3H), 2.11 (s, 3H), 1.55 (s, 3H), 1.28 (s, 3H), 0.52 (d, $J = 7.0$ Hz, 3H), 0.52 (d, $J = 6.8$ Hz, 3H), $-0.22 - -0.32$ (m, 1H).

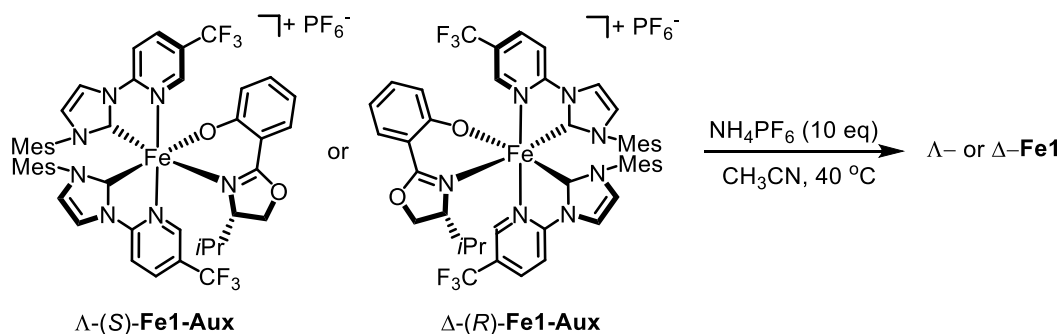
^{13}C NMR (125 MHz, CD_2Cl_2) δ 209.4, 207.0, 173.6, 167.2, 158.6, 158.3, 150.9 (q, $J = 4.7$ Hz), 150.8 (q, $J = 4.7$ Hz), 140.2, 140.1, 137.1, 134.9, 134.5, 134.3, 134.2 (m, 134.3-134.2, 2CJ), 134.16, 134.11, 133.8, 130.4, 130.1, 130.06, 139.8, 129.5, 129.1, 128.3, 123.9, 123.6 (q, $J = 33.8$ Hz), 123.1 (q, $J = 270.5$ Hz), 122.7 (q, $J = 33.9$ Hz), 122.4 (q, $J = 270.5$ Hz), 121.1, 118.4, 115.1, 113.2, 110.9, 110.4, 109.8, 74.8, 67.2, 30.5, 20.9, 20.8, 19.2, 18.4, 17.9, 17.8, 17.2, 13.8.

^{19}F NMR (282 MHz, CD_2Cl_2) δ $-62.8, -63.4, -72.75$ (d, $J = 851.6$ Hz, 6F).

IR (film): ν (cm^{-1}) 3142, 2923, 2179, 2113, 1923, 1726, 1610, 1538, 1501, 1474, 1421, 1383, 1321, 1253, 1169, 1133, 1070, 1034, 955, 926, 829, 756, 705, 626, 581, 555, 504, 467, 433.

Λ -(*S*)-**Fe2**: CD (CH_3CN): λ , nm ($\Delta\epsilon, \text{M}^{-1}\text{cm}^{-1}$) 550 (-14), 490 ($+0.4$), 426 ($+24$), 378 ($+9$), 348 ($+30$), 308 (-4), 290 ($+10$), 272 (-10).

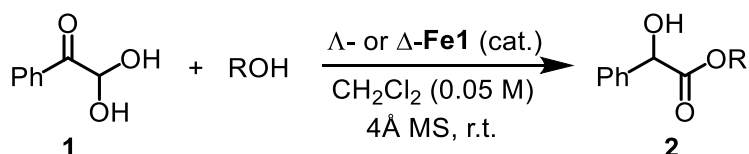
Δ -(*R*)-**Fe2**: CD (CH_3CN): λ , nm ($\Delta\epsilon, \text{M}^{-1}\text{cm}^{-1}$) 552 ($+14$), 488 (-0.4), 424 (-24), 378 (-9), 348 (-30), 308 ($+4$), 290 (-10), 270 ($+10$).



To a solution of Λ -(*S*)-**Fe1-Aux** (90 mg, 0.084 mmol) or Δ -(*R*)-**Fe1-Aux** (90 mg, 0.084 mmol) in CH_3CN (5 mL) was added NH_4PF_6 (137 mg). The resulting mixture was stirred at 40 °C for 5 hours. The reaction mixture was evaporated to dryness, redissolved in CH_2Cl_2 , filtered through a thin pad of diatomite, the red-yellow filtrate was concentrated, and then subjected to column chromatography on silica gel ($\text{CH}_2\text{Cl}_2/\text{CH}_3\text{CN} = 50:1$ to 25:1) to give the enantiopure catalyst Λ -**Fe1** (76 mg, 0.070 mmol, 84% yield) or Δ -**Fe1** (75 mg, 0.070 mmol, 83% yield), respectively. These enantiopure catalysts Λ - and Δ -**Fe1** can be further purified via recrystallization by slow diffusion of Et_2O to a $\text{CH}_3\text{CN}/\text{THF}$ solution (volume ratio 1:1) of the iron complexes. CD (CH_3CN) for Λ -**Fe1**: λ , nm ($\Delta\epsilon, \text{M}^{-1}\text{cm}^{-1}$) 510 ($+5$), 430 (-34), 380 ($+34$), 292 (-7), 276 ($+36$), 256 (-18). CD (CH_3CN) for Δ -**Fe1**: λ , nm ($\Delta\epsilon, \text{M}^{-1}\text{cm}^{-1}$) 510 (-5), 430 ($+35$), 378 (-34), 292 ($+8$), 276 (-36), 256 ($+18$).

All other spectroscopic data of enantiopure iron catalysts were in agreement with the racemic catalysts.

5.3.5 Iron-Catalyzed Enantioselective Intramolecular Cannizzaro Reaction



General catalysis procedure: A dried 10 mL Schlenk tube was charged with the catalyst Δ - or Λ -**Fe1** (3.0–5.0 mol%), phenylglyoxale monohydrate **1** (7.6 mg, 0.05 mmol, 1.0 eq) and 4Å MS (25 mg). The tube was purged with nitrogen, CH_2Cl_2 (1.0 mL) was added via syringe, and followed by the corresponding alcohol (10 eq). The vial was sealed and the reaction mixture was stirred at room temperature for 16 hours under nitrogen atmosphere. Then, the solvent was removed and the residue was submitted to determine the yield by ^1H NMR using $\text{Cl}_2\text{CHCHCl}_2$ as internal standard. After ^1H NMR, the mixture was purified by preparative TLC (*n*-hexane/EtOAc = 3:1) to obtain pure mandelate ester **2**. Racemic samples were obtained by using the racemic catalyst *rac*-**Fe1**. The products (*R*)- and (*S*)-**2** were obtained using Λ - and Δ -**Fe1** as catalysts, respectively.

For a 0.2 mmol scale reaction, the resulting mixture was purified by flash chromatography on silica gel (*n*-hexane/EtOAc = 10:1) to afford the **2a** (R = *i*Pr) as a white solid. (37mg, 0.191 mmol, 96%, Table 3, entry 1). The (*R*)-configuration of the product **2a** was assigned by comparison with published optical rotation and chiral HPLC retention time data.⁶ Optical rotation: $[\alpha]_{\text{D}}^{22} = -88.8^\circ$ (*c* 1.0, CH_2Cl_2 , 87.5% ee). Lit.¹¹: $[\alpha]_{\text{D}}^{11} = +90.77$ (*c* = 0.206, CH_2Cl_2 , 81% ee for *S*-configuration). Enantiomeric excess of 88% ee was determined by HPLC on a chiral stationary phase: Daicel Chiralcel OD-H column, UV detection at 210 nm, mobile phase *n*-hexane/isopropanol = 90:10, flow rate 1.0 mL/min, column temperature 25 °C, t_{r} (minor) = 5.56 min, t_{r} (major) = 10.16 min.

^1H NMR (300 MHz, CDCl_3) δ 7.44–7.28 (m, 5H), 5.12 (d, *J* = 5.1 Hz, 1H), 5.09–5.00 (m, 1H), 3.51 (d, *J* = 5.7 Hz, 1H), 1.28 (d, *J* = 6.3 Hz, 3H), 1.11 (t, *J* = 6.3 Hz, 1H).

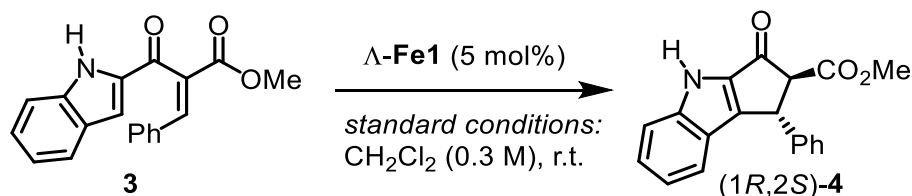
^{13}C NMR (75 MHz, CDCl_3) δ 173.4, 138.7, 128.6, 128.4, 126.6, 73.0, 70.3, 21.8, 21.5.

HRMS (ESI, *m/z*) calcd for $\text{C}_{11}\text{H}_{14}\text{O}_3$ [$\text{M} + \text{Na}$]⁺: 217.0841, found: 217.0835.

All other products were assigned accordingly.

5.3.6 Iron-Catalyzed Asymmetric Nazarov Cyclization

Indole-functionalized α -unsaturated β -ketoester **3** was synthesized according to literature procedures and data were already described.¹²



General procedure for the asymmetric Nazarov cyclization catalyzed by Λ -Fe1: A vial (1.5 mL) was charged with indole-functionalized α -unsaturated β -ketoester **3** (30.5 mg, 0.1 mmol, 20:1 *E/Z*-mixture), Λ -Fe1 (5.4 mg, 0.005 mmol, 5 mol%), and CH_2Cl_2 (0.2 M). The vial was then tightly capped with a rubber-sealed screw cap and kept at room temperature for 24 hours. After completion (monitored by TLC), the solvent was removed under reduced pressure and the crude product was directly purified by flash chromatography on silica gel employing mixtures of *n*-hexane and ethyl acetate (8:2) as eluents to afford the desired Nazarov cyclization product **4** as a white solid (27.1 mg, 89%).

Enantiomeric excess of 83% ee was determined by HPLC on a chiral stationary phase: Daicel Chiralpak AD-H, mobile phase hexane/EtOH = 90/10, flow rate = 0.6 mL/min, column temperature 25 °C, UV detection 254 nm, major isomer: t_{R} = 22.4 min, minor isomer: t_{R} = 32.9 min. The spectral data for **4** matched with previously reported data.¹²

^1H NMR (300 MHz, CDCl_3) δ 9.30 (br s, 1H), 7.52 (d, J = 8.1 Hz, 1H), 7.41 (t, J = 7.5 Hz, 1H), 7.36–7.28 (m, 4H), 7.26–7.23 (m, 2H), 7.09 (t, J = 7.8 Hz, 1H), 5.08 (d, J = 2.9 Hz, 1H), 3.93 (d, J = 2.9 Hz, 1H), 3.86 (s, 3H).

^{13}C NMR (75 MHz, CDCl_3) δ 186.8, 169.6, 148.0, 144.5, 140.8, 137.2, 129.1 (2C), 128.2, 127.6, 127.5 (2C), 123.0, 122.4, 121.4, 113.8, 67.9, 53.0, 44.2.

5.3.7 Single Crystal X-Ray Diffraction Study

Single-crystal X-ray analysis of Δ -Fe1.

Data was collected with STOE STADIVARI area detector diffractometer equipped with with $\text{CuK}\alpha$ radiation, a graded multilayer mirror monochromator ($\lambda = 1.54186 \text{ \AA}$) and a DECTRIS PILATUS 300K detector using an oil-coated shock-cooled crystal at 100(2) K. Absorption effects were corrected semi-empirical using multiscanned reflexions (STOE LANA, absorption correction by scaling of reflection intensities). Cell constants were refined using 36237 of observed reflections of the data collection. The structure was solved by direct methods by using the program XT V2014/1 (Bruker AXS Inc., 2014) and refined by full matrix least squares procedures on F^2 using SHELXL-2018/1 (Sheldrick, 2018). The non-hydrogen atoms have been refined anisotropically, carbon bonded hydrogen atoms were included at calculated positions and refined using the ‘riding model’ with isotropic temperature factors at 1.2 times (for CH_3 groups 1.5 times) that of the preceding carbon atom. CH_3 groups were allowed to rotate about the bond to their next atom to fit the electron density. Nitrogen or oxygen bonded hydrogen atoms were located and allowed to refine isotropically. The absolute configuration could be determined. The Flack parameter refined to -0.009(2).

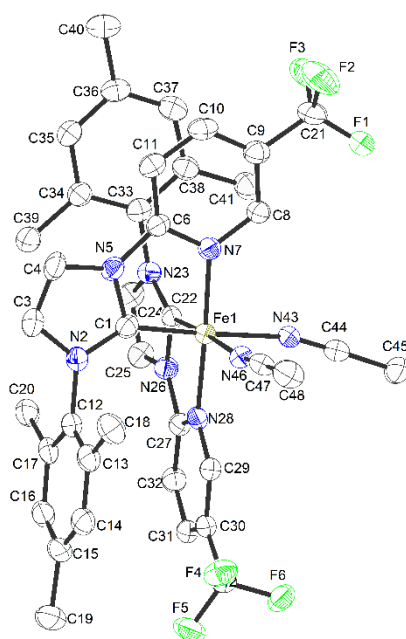


Figure 54. Crystal structure of Δ -Fe1. ORTEP drawing with 50% probability thermal ellipsoids. The hexafluorophosphate counteranion, solvent and all hydrogens are omitted for clarity.

Selected bond lengths [\AA] and angles [$^\circ$]: Fe-N7 1.965(3), Fe-N28 1.980(3), Fe-N43 1.989(3), Fe-N46 1.969(3), Fe-C1 1.897(4), Fe-C22 1.912(4), N7-Fe1-N28 177.03(13), N7-Fe1-N43 95.55(13), N7-Fe1-N46 88.34(13), N28-Fe1-N43 85.76(12), N46-Fe1-N28 94.41(13), N46-Fe1-N43 86.55(13), C1-Fe1-N7 81.07(14), C22-Fe1-N7 96.17(14), C1-Fe1-C22 90.16(15), C1-Fe1-N46 91.56(14), C1-Fe1-N28 97.70(14), C1-Fe1-N43 176.18(15), C22-Fe1-N46 175.38(15), C22-Fe1-N28 81.11(14), C22-Fe1-N43 91.98(14).

Table 13. Crystal data and structure refinement for Δ -Fe1

Identification code	FePyCF ₃
Habitus, colour	needle, orange
Crystal size	0.35 x 0.09 x 0.04 mm ³

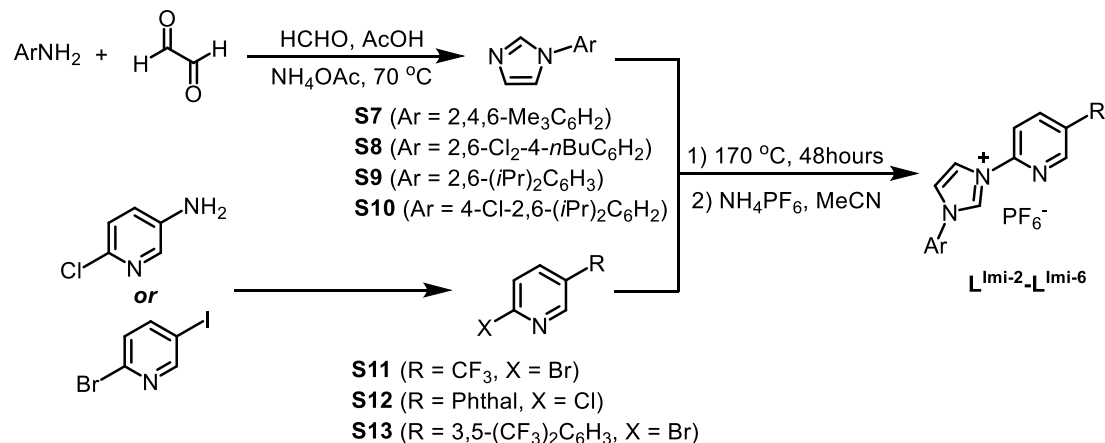
Chapter 5. Experimental Part

Crystal system	Orthorhombic	
Space group	P2 ₁ 2 ₁ 2 ₁	Z = 4
Unit cell dimensions	a = 12.8763(1) Å	α = 90°.
	b = 15.3531(2) Å	β = 90°.
	c = 24.2529(4) Å	γ = 90°.
Volume	4794.58(11) Å ³	
Cell determination	36237 peaks with Theta 3.4 to 76.4°.	
Empirical formula	C _{43.50} H _{44.75} F ₁₈ FeN _{8.25} O _{0.75} P ₂	
Moiety formula	C ₄₀ H ₃₈ F ₆ FeN ₈ ,2(F ₆ P),0.75(C ₄ H ₈ O),0.25(C ₂ H ₃ N)	
Formula weight	1154.91	
Density (calculated)	1.600 Mg/m ³	
Absorption coefficient	4.198 mm ⁻¹	
F(000)	2350	
Diffractometer type	Bruker D8 QUEST area detector	
Wavelength	1.54186 Å	
Temperature	100(2) K	
Theta range for data collection	3.407 to 75.796°.	
Index ranges	-16 ≤ h ≤ 15, -14 ≤ k ≤ 19, -27 ≤ l ≤ 30	
Reflections collected	50701	
Independent reflections	9872 [R(int) = 0.0504]	
Completeness to theta = 67.686°	99.9 %	
Observed reflections	8379 [I > 2σ(I)]	
Reflections used for refinement	9872	
Extinction coefficient	X = 0.00020(4)	
Absorption correction	Semi-empirical from equivalents	
Max. and min. transmission	0.5714 and 0.0895	
Flack parameter (absolute struct.)	-0.009(2)	
Largest diff. peak and hole	0.323 and -0.380 e.Å ⁻³	
Solution	intrinsic phases	
Refinement	Full-matrix least-squares on F ²	
Treatment of hydrogen atoms	Calculated positions, constr. ref.	
Programs used	XT V2014/1 (Bruker AXS Inc., 2014)	
Data / restraints / parameters	9872 / 313 / 731	
Goodness-of-fit on F ²	0.960	
R index (all data)	wR2 = 0.0913	
R index conventional [I > 2σ(I)]	R1 = 0.0381	

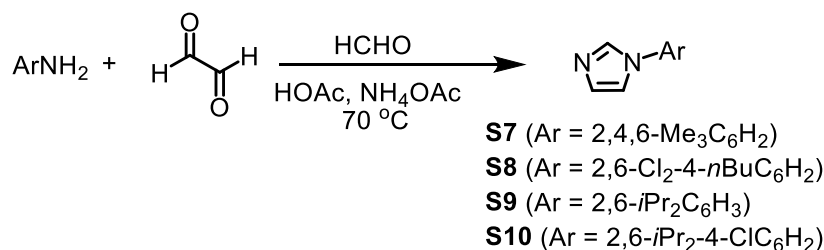
5.4 Chiral-at-Iron Catalyst for Highly Enantioselective and Diastereoselective Hetero-Diels-Alder Reaction

5.4.1 Synthesis of Imidazolium Ligands

Imidazolium ligands were synthesized according to the following route.

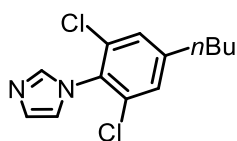


(1) Synthesis of N-substituted imidazoles



General procedure for imidazolium ligands preparation: **S7-S10** were prepared according to a reported literature procedure with slight modifications.¹³ A solution of substituted aniline (10 mmol, 1.0 eq.) and ammonium acetate (770 mg, 10 mmol) in water (1 mL) and glacial acetic acid (5 mL) was added after which the reaction mixture was stirred at 70 °C for 24 hours. After cooling to room temperature, the resulting brown solution was added very slowly to a stirred solution of 7.4 g NaHCO₃ in 100 mL water and extracted with EtOAc (30 mL × 3). Combined organic layers were then washed with water, brine, dried with Na₂SO₄, and concentrated to give a brown residue. This followed by addition of solid NH₄PF₆ (1.2 eq.) and stirred for 1 hour. The solvent was then removed to obtain brown residue, this residue was purified by chromatography on silica gel eluted with *n*-hexane/EtOAc (10:1 to 3:1) to obtain desired products **S8-S10**. The compounds **S7**^{13a} and **S9**^{13b} are reported. The data of new compound **S8** and **S10** are shown below:

1-(4-Butyl-2,6-dichlorophenyl)-1*H*-imidazole (**S8**)



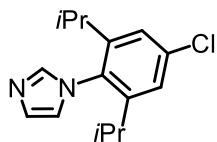
Light yellow oil, 1.67 g (6.2 mmol, 62% yield).

^1H NMR (300 MHz, CDCl_3) δ 7.52 (s, 1H), 7.27 (s, 2H), 7.24 (s, 1H), 6.98 (t, $J = 1.2$ Hz, 1H), 2.64 (t, $J = 7.8$ Hz, 2H), 1.68-1.58 (m, 2H), 1.45-1.32 (m, 2H), 0.96 (t, $J = 7.2$ Hz, 1H).

^{13}C NMR (75 MHz, CDCl_3) δ 146.6, 137.8, 133.5, 130.8, 129.6, 128.8, 120.3, 35.1, 33.1, 22.3, 13.9.

HRMS (ESI, m/z) calcd for $\text{C}_{18}\text{H}_{17}\text{N}_3\text{F}_3$ $[\text{M}+\text{H}]^+$: 269.0607, found: 269.0610.

1-(4-Chloro-2,6-diisopropylphenyl)-1H-imidazole (S10)



White solid, 1.31g (5.0 mmol, 50% yield).

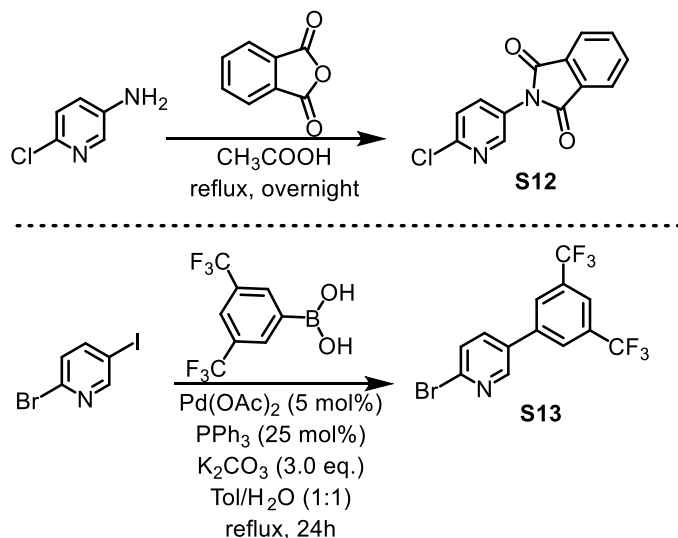
^1H NMR (300 MHz, CDCl_3) δ 7.42 (s, 1H), 7.23 (s, 1H), 7.20 (s, 2H), 6.89 (t, $J = 1.0$ Hz, 1H), 2.44-2.30 (m, 2H), 1.11 (d, $J = 6.9$ Hz, 12H).

^{13}C NMR (75 MHz, CDCl_3) δ 148.7, 138.5, 136.0, 131.5, 129.8, 124.3, 121.6, 28.4, 24.34, 24.27.

HRMS (ESI, m/z) calcd for $\text{C}_{18}\text{H}_{17}\text{N}_3\text{F}_3$ $[\text{M}+\text{H}]^+$: 263.1310, found: 263.1311.

(2) Synthesis of pyridine intermediates

2-Bromo-5-(trifluoromethyl)pyridine **S11** is commercially available, the compounds **S12**¹⁴ and **S13**¹⁵ were prepared following related literature procedures.



2-(6-Chloropyridin-3-yl)isoindoline-1,3-dione (S12) was prepared according to a reported literature procedure with slight modifications.¹⁴ 6-Chloropyridin-3-amine (865 mg, 5.00 mmol) and phthalic anhydride (740 mg, 5.00 mmol) in acetic acid (15 mL) were stirred at 120 °C for 10 hours. Once at room temperature, water was added and the precipitate was recovered by filtration. After drying under vacuum, the desired product was obtained as an off-white foam (1.02 g, 3.94 mmol, 79% yield).

^1H NMR (300 MHz, CDCl_3) δ 8.60 (d, $J = 2.7$ Hz, 1H), 7.99-7.95 (m, 2H), 7.86-7.82 (m, 3H), 7.48 (d, $J = 8.4$ Hz, 1H).

^{13}C NMR (75 MHz, CDCl_3) δ 166.6, 150.2, 147.0, 136.1, 135.1, 131.6, 128.0, 124.6, 124.3.

HRMS (ESI, m/z) calcd for $\text{C}_{18}\text{H}_{17}\text{N}_3\text{F}_3$ $[\text{M}-\text{PF}_6]^+$: 259.0271, found: 259.0271.

5-(3,5-Bis(trifluoromethyl)phenyl)-2-bromopyridine (S13) was prepared according to a reported literature procedure with some modifications.¹⁵ A mixture of 2-bromo-5-iodopyridine (849 mg, 3.00 mmol) and (3,5-bis(trifluoromethyl)phenyl)boronic acid (774 mg, 3.00 mmol), Pd(OAc)₂ (33.7 mg, 0.15 mmol), PPh₃ (197 mg, 0.75 mmol) and K₂CO₃ (1.24 g, 9.00 mmol) in toluene (12 mL) and water (12 mL) was heated to 125 °C and stirred overnight under nitrogen. After cooling to room temperature, the reaction mixture was filtered by celite, and the filtrate was extracted with EtOAc (20 mL × 3). The combined organic phase was washed with brine, dried with MgSO₄, and concentrated. Chromatography over silica eluting with n-hexane/EtOAc (150:1 to 100:1) afforded the title compound as an off-white solid (758 mg, 2.05 mmol, 68% yield).

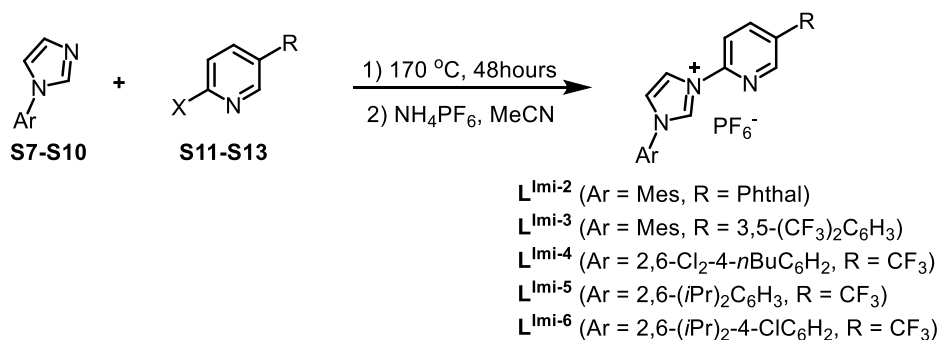
¹H NMR (300 MHz, CDCl₃) δ 8.62 (d, *J* = 2.7 Hz, 1H), 7.97 (s, 1H), 7.95 (s, 1H), 7.78 (dd, *J* = 8.4, 2.7 Hz, 1H), 7.64 (d, *J* = 8.1 Hz, 1H).

¹³C NMR (75 MHz, CDCl₃) δ 148.6, 143.0, 139.0, 137.1, 133.4, 133.0 (q, *J* = 33.4 Hz), 128.7, 127.3 (q, *J* = 2.7 Hz), 123.2 (q, *J* = 271.2 Hz), 122.4 (m, 122.3-122.5).

¹⁹F NMR (235 MHz, CDCl₃) δ -62.92.

HRMS (ESI, *m/z*) calcd for C₁₈H₁₇N₃F₃ [M-PF₆]⁺: 369.9661, found: 369.9661.

(3) Synthesis of imidazolium ligands



General procedure for imidazolium ligands preparation: L^{Imi-2}-L^{Imi-6} were prepared according to the same procedure as L^{Imi-1} with slight modifications.⁶ A dried 10 mL Schlenk tube was charged with substituted imidazole (2-5 mmol, 1.05 eq.) and substituted 2-bromo- or 2-chloropyridine (2-5 mmol, 1.0 eq.), the flask was sealed and stirred at 170 °C for 48 hours. After cooling to room temperature, the resulting mixture was dissolved in acetonitrile (20 mL), followed by the addition of solid NH₄PF₆ (391-978 mg, 2.4-6 mmol, 1.2 eq.), and stirred for 1 h. The solvent was then removed under reduced pressure to obtain a brown residue, this residue was re-dissolved in dichloromethane and filtered. The resulting filtrate was dried under reduced pressure and purified by chromatography on silica gel eluted with CH₂Cl₂/CH₃CN to obtain ligand L^{Imi-2}-L^{Imi-6} as a white or light yellow solid.

L^{Imi-2}: According to the general procedure, 1-mesityl-1*H*-imidazole **S7** (600 mg, 3.22 mmol) and 2-(6-chloropyridin-3-yl) isoindoline-1,3-dione **S12** (800 mg, 3.09 mmol) were used to provide the L^{Imi-2} as a white solid (1.20 g, 70% yield). Purification condition: CH₂Cl₂/CH₃CN = 25:1.

¹H NMR (300 MHz, CD₃CN) δ 9.48 (t, *J* = 1.5 Hz, 1H), 8.78 (d, *J* = 2.4 Hz, 1H), 8.41 (t, *J* = 1.8 Hz, 1H), 8.31 (dd, *J* = 8.7, 2.4 Hz, 1H), 8.03 (d, *J* = 8.7 Hz, 1H), 8.00-7.96 (m, 2H), 7.94-7.90 (m, 2H), 7.69 (t, *J* = 1.8 Hz,

1H), 7.16 (s, 2H), 2.38 (s, 3H), 2.14 (s, 6H).

¹³C NMR (75 MHz, CD₃CN) δ 167.7, 147.7, 145.9, 142.7, 138.8, 136.2, 136.1, 135.8, 132.6, 131.9, 131.6, 130.6, 126.2, 124.8, 121.5, 115.9, 21.2, 17.6.

¹⁹F NMR (235 MHz, CD₃CN) δ -72.62 (d, *J* = 706.2 Hz, 6F).

IR (film): ν (cm⁻¹) 3154, 1740, 1715, 1598, 1547, 1488, 1412, 1373, 1331, 1308, 1241, 1094, 1078, 878, 821, 748, 716, 668, 555, 529, 408.

HRMS (ESI, *m/z*) calcd for C₁₈H₁₇N₃F₃ [M-PF₆]⁺: 409.1659, found: 409.1651.

L^{Imi-3}: According to the general procedure, 1-mesityl-1*H*-imidazole **S7** (372 mg, 2.0 mmol) and 5-(3,5-bis(trifluoromethyl)phenyl)-2-bromopyridine **S13** (740 mg, 2.0 mmol) were used to provide the **L^{Imi-3}** as a white solid (599 mg, 49%). Purification condition: CH₂Cl₂/CH₃CN = 50:1.

¹H NMR (300 MHz, CD₂Cl₂) δ 9.54 (t, *J* = 1.5 Hz, 1H), 8.87 (d, *J* = 1.8 Hz, 1H), 8.55 (t, *J* = 1.8 Hz, 1H), 8.37 (dd, *J* = 8.4, 2.4 Hz, 1H), 8.26 (dd, *J* = 8.4, 0.3 Hz, 1H), 8.14 (s, 2H), 8.03 (s, 1H), 7.54 (s, 1H), 7.14 (s, 2H), 2.40 (s, 3H), 2.17 (s, 6H).

¹³C NMR (75 MHz, CD₂Cl₂) δ 148.3, 146.5, 142.8, 139.9, 138.6, 136.8, 134.8, 134.6, 133.2 (q, *J* = 33.4 Hz), 131.0, 130.6, 128.2 (q, *J* = 4.3 Hz), 125.9, 123.8 (q, *J* = 271.0 Hz), 123.4 (m, 123.5-123.3), 121.1, 115.4, 21.5, 17.8.

¹⁹F NMR (235 MHz, CD₂Cl₂) δ -63.24, -72.52 (d, *J* = 710.2 Hz, 6F).

IR (film): ν (cm⁻¹) 3162, 1594, 1539, 1494, 1463, 1379, 1330, 1275, 1245, 1187, 1130, 1109, 1098, 1063, 901, 827, 752, 705, 681, 669, 635, 567, 475, 418.

HRMS (ESI, *m/z*) calcd for C₁₈H₁₇N₃F₃ [M-PF₆]⁺: 476.1556, found: 476.1552.

L^{Imi-4}: According to the general procedure, 1-(4-butyl-2,6-dichlorophenyl)-1*H*-imidazole **S8** (538 mg, 2.0 mmol) and 2-bromo-5-(trifluoromethyl)pyridine **S11** (452 mg, 2.0 mmol) were used to provide the **L^{Imi-4}** as a light yellow solid (893 mg, 80% yield). Purification condition: CH₂Cl₂/CH₃CN = 50:1.

¹H NMR (300 MHz, CD₂Cl₂) δ 9.55 (t, *J* = 1.6 Hz, 1H), 8.91 (q, *J* = 0.6 Hz, 1H), 8.54 (t, *J* = 1.8 Hz, 1H), 8.41 (dd, *J* = 8.4, 1.5 Hz, 1H), 8.18 (d, *J* = 8.7 Hz, 1H), 7.66 (t, *J* = 1.6 Hz, 1H), 7.48 (s, 2H), 2.74 (t, *J* = 1.8 Hz, 2H), 1.72-1.62 (m, 2H), 1.47-1.35 (m, 2H), 0.97 (t, *J* = 1.5 Hz, 3H).

¹³C NMR (75 MHz, CD₂Cl₂) δ 151.1, 148.4, 147.5 (q, *J* = 4.0 Hz), 139.3 (q, *J* = 2.9 Hz), 135.9, 132.6, 130.1, 129.5 (q, *J* = 31.5 Hz), 127.5, 126.4, 126.2 (q, *J* = 271.0 Hz), 121.0, 115.2, 35.7, 33.2, 22.7, 14.1.

¹⁹F NMR (235 MHz, CD₂Cl₂) δ -62.78, -72.47 (d, *J* = 710.4 Hz, 6F).

IR (film): ν (cm⁻¹) 3164, 2932, 1604, 1547, 1491, 1408, 1326, 1262, 1215, 1172, 1139, 1089, 1071, 1054, 1018, 934, 880, 840, 822, 648, 556, 434.

HRMS (ESI, *m/z*) calcd for C₁₈H₁₇N₃F₃ [M-PF₆]⁺: 414.0746, found: 414.0742.

L^{Imi-5}: According to the general procedure, 1-(2,6-diisopropylphenyl)-1*H*-imidazole **S9** (1.14 g, 5.0 mmol) and 2-bromo-5-(trifluoromethyl)pyridine **S11** (1.13 g, 5.0 mmol) were used to provide the **L^{Imi-5}** as a white solid (2.15 g, 83% yield). Purification condition: CH₂Cl₂/CH₃CN = 50:1.

¹H NMR (300 MHz, CD₂Cl₂) δ 9.40 (t, *J* = 1.6 Hz, 1H), 8.89 (q, *J* = 0.6 Hz, 1H), 8.54 (t, *J* = 1.8 Hz, 1H), 8.41 (dd, *J* = 8.6, 2.1 Hz, 1H), 8.21 (d, *J* = 8.6 Hz, 1H), 7.66 (t, *J* = 7.8 Hz, 1H), 7.58 (t, *J* = 2.1 Hz, 1H), 7.44 (s, 1H), 7.42 (s, 1H), 2.45-2.36 (m, 2H), 1.23 (t, *J* = 6.3 Hz, 12H).

^{13}C NMR (75 MHz, CD_2Cl_2) δ 148.0, 146.8 (q, $J = 4.0$ Hz), 145.2, 138.7 (q, $J = 3.2$ Hz), 134.2, 132.6, 129.7, 128.7 (q, $J = 34.0$ Hz), 126.7, 125.0, 122.7 (q, $J = 271.0$ Hz), 120.6, 114.7, 28.8, 24.0, 23.7.

^{19}F NMR (235 MHz, CD_2Cl_2) δ -62.75, -72.45 (d, $J = 710.2$ Hz, 6F).

IR (film): ν (cm^{-1}) 3140, 2973, 1608, 1541, 1494, 1463, 1413, 1331, 1219, 1172, 1129, 1100, 1061, 1019, 954, 840, 823, 756, 669, 556, 437.

HRMS (ESI, m/z) calcd for $\text{C}_{18}\text{H}_{17}\text{N}_3\text{F}_3$ $[\text{M}-\text{PF}_6]^+$: 374.1839, found: 374.1833.

L^{Imi-6}: According to the general procedure, 1-(4-chloro-2,6-diisopropylphenyl)-1*H*-imidazole **S10** (1.31 g, 5.0 mmol) and 2-bromo-5-(trifluoromethyl)pyridine **S11** (1.13 g, 5.0 mmol) were used to provide the **L^{Imi-6}** as a white solid (2.48 g, 90% yield). Purification condition: $\text{CH}_2\text{Cl}_2/\text{CH}_3\text{CN} = 50:1$.

^1H NMR (300 MHz, CD_2Cl_2) δ 9.41 (t, $J = 1.8$ Hz, 1H), 8.90 (q, $J = 0.6$ Hz, 1H), 8.54 (t, $J = 1.8$ Hz, 1H), 8.40 (dd, $J = 8.7, 2.4$ Hz, 1H), 8.19 (d, $J = 8.7$ Hz, 1H), 7.56 (t, $J = 1.8$ Hz, 1H), 7.40 (s, 2H), 2.47-2.33 (m, 2H), 1.22 (t, $J = 6.6$ Hz, 12H).

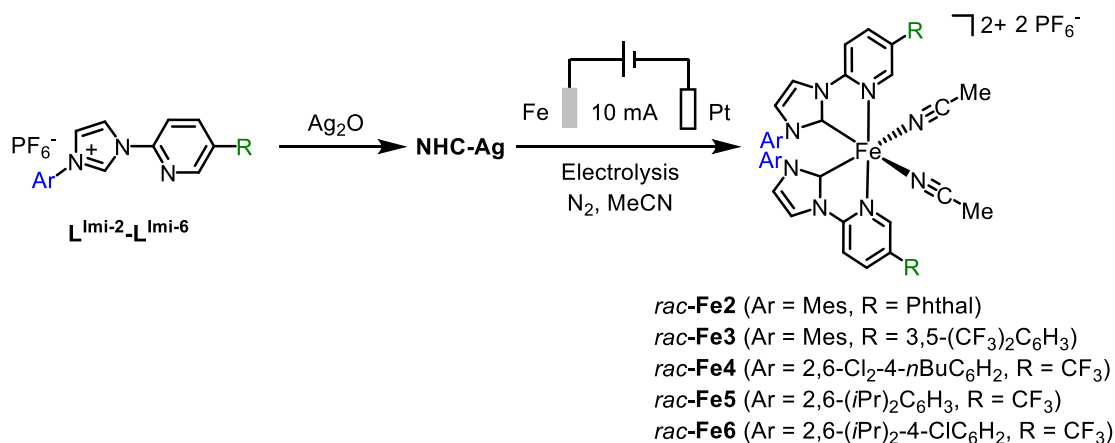
^{13}C NMR (75 MHz, CD_2Cl_2) δ 147.9, 147.3, 146.8 (q, $J = 4.0$ Hz), 138.8, 138.6 (q, $J = 3.4$ Hz), 134.4, 128.8 (q, $J = 34.0$ Hz), 128.2, 126.6, 125.4, 122.6 (q, $J = 271.2$ Hz), 120.9, 114.8, 29.0, 23.9, 23.4.

^{19}F NMR (235 MHz, CD_2Cl_2) δ -62.76, -72.35 (d, $J = 710.7$ Hz, 6F).

IR (film): ν (cm^{-1}) 3136, 2975, 1605, 1580, 1542, 1493, 1467, 1413, 1333, 1319, 1257, 1220, 1173, 1136, 1078, 1016, 953, 908, 836, 813, 748, 674, 630, 556, 500, 460, 436.

HRMS (ESI, m/z) calcd for $\text{C}_{18}\text{H}_{17}\text{N}_3\text{F}_3$ $[\text{M}-\text{PF}_6]^+$: 408.1449, found: 408.1443.

5.4.2 Synthesis of Racemic Iron Complexes



General procedure for racemic iron complexes preparation: The racemic complexes **Fe2-6** were synthesized according to the same procedure as for the preparation of **Fe1**^{8,9}:

Step 1: A mixture of ligand (0.8 mmol) and Ag_2O (0.8 mmol) were stirred in CH_3CN (8 mL) in the dark at 50 °C for 4 hours. The solution was diluted with dichloromethane and filtered by diatomite to remove insoluble materials, then the filtrate was evaporated to dryness to provide the crude NHC-based silver carbene complex (**NHC-Ag**) as a white or light yellow solid. These crude **NHC-Ag** complexes were taken to the next step without any further purification.

Step 2: The electrochemical reaction was performed by using an IKA ElectraSyn 2.0. In a 15 mL ElectraSyn

vial with a magnetic stirring bar, an iron plate ($1 \times 3.0 \text{ cm}^2$) was used as the anode and a platinum plate ($1 \times 3.0 \text{ cm}^2$) was used as the cathode. A solution of **NHC-Ag** in anhydrous CH_3CN (10.0 mL) was electrolyzed under a constant current of 10 mA. After passing through 2.0-2.8 F/mol of electricity under nitrogen atmosphere in the dark, the solution was evaporated to dryness and purified by column chromatography on silica gel ($\text{CH}_2\text{Cl}_2/\text{CH}_3\text{CN}$) to provide *rac*-**Fe2-6** as orange solids.

Rac-**Fe2** was synthesized according to the general procedure starting from **L^{Imi-2}** (443 mg, 0.8 mmol) and Ag_2O (116 mg, 0.8 mmol) after passing through 2.8 F/mol of electricity and obtain as a red-yellow solid (224 mg, 45% yield over two step). Purification condition: $\text{CH}_2\text{Cl}_2/\text{CH}_3\text{CN} = 25:1$ to $10:1$. Characteristic data of *rac*-**Fe2** are shown below:

^1H NMR (300 MHz, CD_3CN) δ 8.64 (d, $J = 2.1$ Hz, 2H), 8.23 (d, 2.1 Hz, 2H), 8.12 (dd, $J = 9.0, 2.4$ Hz, 2H), 8.06-8.00 (m, 4H), 7.98-7.92 (m, 4H), 7.53 (d, $J = 9.0$ Hz, 2H), 7.22 (d, $J = 2.4$ Hz, 2H), 6.67 (s, 2H), 6.62 (s, 2H), 2.12 (s, 6H), 2.02 (s, 6H), 1.56 (s, 6H).

^{13}C NMR (75 MHz, CD_3CN) δ 199.7, 167.6, 153.9, 149.8, 140.7, 136.5, 136.3, 135.7, 134.4, 132.6, 131.8, 130.6, 129.9, 129.1, 128.5, 124.8, 120.0, 111.5, 21.0, 17.8, 17.7.

^{19}F NMR (235 MHz, CD_3CN) δ -67.54 (d, $J = 705.7$ Hz, 12F).

IR (film): ν (cm^{-1}) 1784, 1749, 1717, 1611, 1501, 1381, 1363, 1328, 1300, 1257, 1227, 1151, 1098, 957, 932, 834, 716, 660, 555, 485.

Rac-**Fe3** was synthesized according to the general procedure starting from **L^{Imi-3}** (497 mg, 0.8 mmol) and Ag_2O (116 mg, 0.8 mmol) after passing through 2.0 F/mol of electricity and obtain as a red-yellow solid (261 mg, 52% yield over two step). Purification condition: $\text{CH}_2\text{Cl}_2/\text{CH}_3\text{CN} = 50:1$ to $20:1$. Characteristic data of *rac*-**Fe3** are shown below:

^1H NMR (300 MHz, CD_3CN) δ 8.43 (d, $J = 2.1$ Hz, 2H), 8.36 (d, $J = 2.1$ Hz, 2H), 8.23 (dd, $J = 8.7, 2.1$ Hz, 2H), 8.18 (s, 6H), 7.71 (d, $J = 8.7$ Hz, 2H), 7.21 (d, $J = 2.1$ Hz, 2H), 6.66 (s, 2H), 6.49 (s, 2H), 2.03 (s, 6H), 1.98 (s, 6H), 1.54 (s, 6H).

^{13}C NMR (150 MHz, CD_3CN) δ 199.9, 155.8, 151.9, 140.5, 138.7, 138.4, 136.0, 135.2, 134.9, 133.2 (q, $J = 33.2$ Hz), 132.3, 132.2, 130.8, 129.6, 129.5, 128.4 (q, $J = 2.8$ Hz), 124.6 (q, $J = 270.4$ Hz), 123.6 (m, 123.6-123.5), 120.2, 112.3, 20.9, 17.8, 17.5.

^{19}F NMR (235 MHz, CD_3CN) δ -63.22, -72.50 (d, $J = 706.4$ Hz, 6F).

IR (film): ν (cm^{-1}) 1721, 1610, 1507, 1468, 1424, 1371, 1336, 1302, 1278, 1181, 1130, 1063, 956, 932, 897, 837, 740, 704, 682, 622, 590, 556, 494, 452, 416.

Rac-**Fe4** was synthesized according to the general procedure starting from **L^{Imi-4}** (447 mg, 0.8 mmol) and Ag_2O (116 mg, 0.8 mmol) after passing through 2.0 F/mol of electricity and obtain as a red-yellow solid (417 mg, 85% yield over two step). Purification condition: $\text{CH}_2\text{Cl}_2/\text{CH}_3\text{CN} = 50:1$ to $25:1$. Characteristic data of *rac*-**Fe4** are shown below:

^1H NMR (300 MHz, CD_2Cl_2) δ 8.49 (s, 2H), 8.27 (d, $J = 2.4$ Hz, 2H), 8.00 (dd, $J = 8.7, 1.8$ Hz, 2H), 7.07 (s,

2H), 7.04 (m, 4H), 2.55-2.49 (m, 4H), 2.41 (s, 6H, NCMe), 1.59-1.49 (m, 4H), 1.43-1.31 (m, 4H), 0.96 (t, $J = 7.2$ Hz, 6H).

^{13}C NMR (75 MHz, CD_2Cl_2) δ 202.0, 157.5, 150.3 (q, $J = 4.5$ Hz), 149.3, 137.9 (q, $J = 2.8$ Hz), 133.4, 132.9, 132.1, 130.7, 129.9, 129.7, 129.0, 125.4 (q, $J = 34.4$ Hz), 122.6 (q, $J = 271.0$ Hz), 120.4, 112.5, 35.1, 32.8, 22.8, 14.0, 4.6.

^{19}F NMR (235 MHz, CD_2Cl_2) δ -62.70, -72.52 (d, $J = 713.2$ Hz, 6F).

IR (film): ν (cm^{-1}) 2959, 1622, 1592, 1557, 1508, 1489, 1427, 1406, 1326, 1305, 1266, 1210, 1174, 1137, 1077, 1040, 951, 825, 758, 737, 701, 665, 626, 556, 513, 421.

Rac-Fe5 was synthesized according to the general procedure starting from **L^{Imi-5}** (415 mg, 0.8 mmol) and Ag_2O (116 mg, 0.8 mmol) after passing through 2.5 F/mol of electricity and obtain as a red-yellow solid (262 mg, 56% yield over two step). Purification condition: $\text{CH}_2\text{Cl}_2/\text{CH}_3\text{CN} = 50:1$ to $25:1$. Characteristic data of **rac-Fe5** are shown below:

^1H NMR (300 MHz, CD_2Cl_2) δ 8.39 (d, $J = 2.1$ Hz, 2H), 8.16 (d, $J = 0.6$ Hz, 2H), 8.05 (dd, $J = 8.7, 1.8$ Hz, 2H), 7.84 (d, $J = 8.7$ Hz, 2H), 7.44 (d, $J = 2.1$ Hz, 2H), 7.21 (d, $J = 4.8$ Hz, 4H), 6.88-6.82 (m, 2H), 2.54-2.45 (m, 2H), 1.93-1.87 (m, 2H), 1.38 (d, $J = 6.6$ Hz, 6H), 1.07 (dd, $J = 6.6, 2.4$ Hz, 12H), 0.88 (d, $J = 6.6$ Hz, 6H).

^{13}C NMR (75 MHz, CD_3CN) δ 200.6, 157.8, 151.7 (q, $J = 4.3$ Hz), 146.6, 144.4, 138.5 (q, $J = 3.1$ Hz), 134.8, 132.7, 132.0, 125.8, 124.8 (q, $J = 34.3$ Hz), 124.7, 123.3 (q, $J = 270.0$ Hz), 120.1, 112.6, 29.7, 28.9, 27.1, 26.0, 22.6, 22.3.

^{19}F NMR (235 MHz, CD_3CN) δ -62.22, -72.86 (d, $J = 705.5$ Hz, 6F).

IR (film): ν (cm^{-1}) 2969, 1621, 1510, 1464, 1426, 1387, 1325, 1303, 1262, 1175, 1136, 1074, 1039, 947, 835, 762, 739, 711, 622, 556, 507, 463.

Rac-Fe6 was synthesized according to the general procedure starting from **L^{Imi-6}** (442 mg, 0.8 mmol) and Ag_2O (116 mg, 0.8 mmol) after passing through 2.5 F/mol of electricity and obtain as a red-yellow solid (315 mg, 63% yield over two step). Purification condition: $\text{CH}_2\text{Cl}_2/\text{CH}_3\text{CN} = 50:1$ to $25:1$. Characteristic data of **rac-Fe6** are shown below:

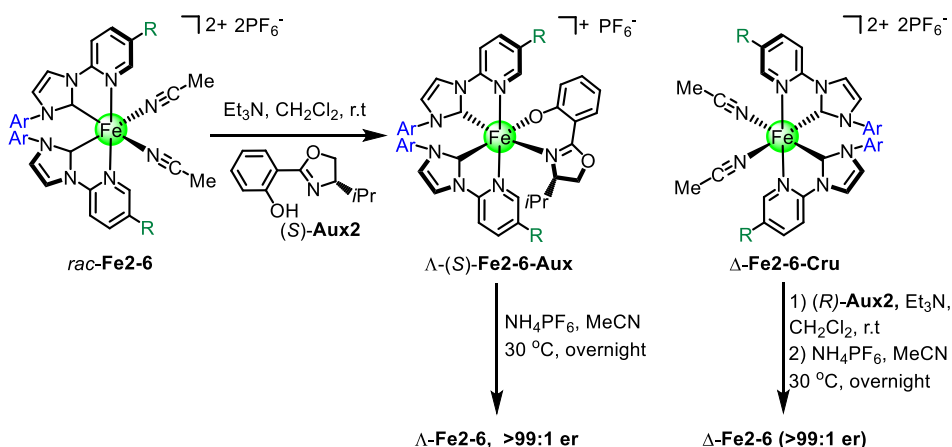
^1H NMR (300 MHz, CD_3CN) δ 8.41 (d, $J = 2.1$ Hz, 2H), 8.24 (d, $J = 0.6$ Hz, 2H), 8.18 (dd, $J = 8.7, 1.8$ Hz, 2H), 7.90 (d, $J = 8.7$ Hz, 2H), 7.45 (d, $J = 2.4$ Hz, 2H), 7.21 (d, $J = 2.1$ Hz, 2H), 6.85 (d, $J = 2.1$ Hz, 2H), 2.54-2.45 (m, 2H), 1.87-1.81 (m, 2H), 1.36 (d, $J = 6.9$ Hz, 6H), 1.06 (t, $J = 7.2$ Hz, 12H), 0.89 (d, $J = 6.6$ Hz, 6H).

^{13}C NMR (75 MHz, CD_3CN) δ 201.1, 157.9, 151.9 (q, $J = 4.3$ Hz), 149.1, 146.9, 138.2 (q, $J = 3.2$ Hz), 137.4, 133.6, 133.0, 131.9, 126.1, 125.1 (q, $J = 34.3$ Hz), 125.0, 123.3 (q, $J = 270.6$ Hz), 113.0, 30.0, 29.3, 26.8, 25.8, 22.5, 22.0.

^{19}F NMR (235 MHz, CD_3CN) δ -62.29, -72.68 (d, $J = 705.9$ Hz, 6F).

IR (film): ν (cm^{-1}) 2973, 1621, 1578, 1509, 1466, 1426, 1388, 1324, 1303, 1255, 1223, 1175, 1140, 1073, 947, 826, 738, 713, 636, 556, 518, 465.

5.4.3 Synthesis of Non-Racemic Iron Complexes

**General procedure for non-racemic iron complexes preparation:**

Step 1: A mixture of racemic iron complex *rac-Fe2-6* (1.0 eq.), chiral auxiliary (*S*)-**A2** (1.0 eq.), and triethylamine (1.5 eq.) in CH_2Cl_2 ($c = 0.04 \text{ M}$) was stirred at room temperature for 18 h. The reaction mixture was concentrated to dryness. The residue was subjected to flash silica gel chromatography ($\text{CH}_2\text{Cl}_2/\text{CH}_3\text{CN} = 100:1$ or $25:1$) to obtain a single diastereomer, which was assigned as the diastereomer $\Delta\text{-(S)-Fe-Aux}$ (deep purple solid, contained a small amount of free auxiliary), followed by using $\text{CH}_2\text{Cl}_2/\text{CH}_3\text{CN} = 25:1$ or $10:1$ as eluent to afford the enantiomerically enriched complex $\Delta\text{-Fe-Cru}$ as a red-yellow solid (enantiopurity: $>90\%$). The other diastereomer complex $\Delta\text{-(R)-Fe}$ was provided by the same procedure as described above, but starting from $\Delta\text{-Fe-Cru}$ (1.0 eq.), chiral auxiliary (*R*)-**A2** (1.1 eq.) and triethylamine (1.5 eq.).

 $\Delta\text{-(S)-Fe2-Aux}$ and $\Delta\text{-(R)-Fe2-Aux}$:

According to the general procedure, starting from *rac-Fe2* (270 mg, 0.217 mmol), chiral auxiliary (*S*)-**A2** (33 mg, 0.161 mmol), and triethylamine (24.6 mg, 0.241 mmol) to afford a single diastereomer $\Delta\text{-(S)-Fe2-Aux}$ (95 mg, 0.0781 mmol, 36% yield) and $\Delta\text{-Fe2-Cru}$ (110 mg, 0.0883 mmol, 41% yield). Purification condition: $\text{CH}_2\text{Cl}_2/\text{CH}_3\text{CN} = 25:1$ to $10:1$

According to the general procedure, starting from $\Delta\text{-Fe2-Cru}$ (100 mg, 0.0804 mmol) and chiral auxiliary (*R*)-**A2** (18 mg, 0.0884 mmol), the single diastereomer $\Delta\text{-(R)-Fe2-Aux}$ was obtained in 75% yield (73.6 mg, 0.0603 mmol).

$^1\text{H NMR}$ (300 MHz, CD_2Cl_2) δ 8.56 (s, 1H), 8.32 (s, 1H), 8.20 (d, $J = 9.0 \text{ Hz}$, 1H), 8.12 (d, $J = 2.1 \text{ Hz}$, 1H), 8.01-7.81 (m, 10H), 7.46 (d, $J = 7.8 \text{ Hz}$, 1H), 7.33 (d, $J = 9.0 \text{ Hz}$, 1H), 7.25 (d, $J = 9.0 \text{ Hz}$, 1H), 7.00 (d, $J = 2.1 \text{ Hz}$, 1H), 6.93 (dd, $J = 6.9, 2.1 \text{ Hz}$, 1H), 6.73 (s, 1H), 6.56 (s, 1H), 6.53 (s, 1H), 6.49 (d, $J = 8.1 \text{ Hz}$, 1H), 6.42 (s, 1H), 6.03 (br, s, 1H), 4.53 (t, $J = 9.0 \text{ Hz}$, 1H), 4.36 (dd, $J = 9.0, 3.0 \text{ Hz}$, 1H), 4.18 (br, s, 1H), 2.27 (s, 3H), 2.21 (s, 3H), 2.17 (s, 3H), 1.96 (s, 3H), 1.63 (s, 3H), 1.31 (s, 3H), 0.58 (d, $J = 6.6 \text{ Hz}$, 3H), 0.22-0.11 (m, 1H), 0.06 (d, $J = 6.3 \text{ Hz}$, 1H).

$^{13}\text{C NMR}$ (75 MHz, CD_2Cl_2) δ 166.9, 166.6, 155.1, 154.2, 153.2, 148.8, 147.6, 147.5, 140.1, 139.7, 139.6,

137.7, 137.6, 135.9, 135.5, 135.2, 135.0, 134.4, 133.9, 133.0, 131.8, 131.5, 131.4, 130.4, 129.7, 129.5, 129.3, 128.5, 128.4, 126.6, 124.6, 124.5, 117.6, 117.5, 117.4, 109.4, 109.3, 109.1, 109.0, 73.7, 66.5, 21.2, 20.9, 19.4, 18.9, 18.1, 17.5, 14.0.

^{19}F NMR (235 MHz, CD_2Cl_2) δ -72.95 (d, $J = 709.7$ Hz, 6F).

IR (film): ν (cm^{-1}) 2961, 1610, 1583, 1538, 1504, 1468, 1420, 1383, 1326, 1310, 1297, 1285, 1230, 1170, 1132, 1067, 951, 928, 825, 755, 712, 661, 624, 532, 503, 435.

Λ -(*S*)-**Fe2-Aux**: CD (CH_3CN): λ , nm ($\Delta\epsilon$, $\text{M}^{-1}\text{cm}^{-1}$) 561 (-18), 552 (-19), 488 (-0.4), 475 (-2), 425 (+30), 378 (+9), 349 (+36), 308 (-8), 289 (+11), 269 (-16).

Δ -(*R*)-**Fe2-Aux**: CD (CH_3CN): λ , nm ($\Delta\epsilon$, $\text{M}^{-1}\text{cm}^{-1}$) 561 (+18), 552 (+19), 488 (+0.4), 475 (+2), 425 (-30), 378 (-9), 349 (-36), 308 (+8), 289 (-11), 269 (+16).

Λ -(*S*)-**Fe3-Aux** and Δ -(*R*)-**Fe3-Aux**:

According to the general procedure, starting from *rac*-**Fe3** (220 mg, 0.160 mmol), chiral auxiliary (*S*)-**A2** (32.8 mg, 0.160 mmol), and triethylamine (24.3 mg, 0.240 mmol) to afford a single diastereomer Λ -(*S*)-**Fe3-Aux** (100 mg, 0.0738 mmol, 46% yield) and Δ -**Fe3-Cru** (87 mg, 0.0633 mmol, 40%). Purification condition: $\text{CH}_2\text{Cl}_2/\text{CH}_3\text{CN} = 100:1$ to 25:1

According to the general procedure, starting from Δ -**Fe3-Cru** (87 mg, 0.0633 mmol), chiral auxiliary (*R*)-**A2** (14 mg, 0.0696 mmol), the single diastereomer Δ -(*R*)-**Fe3-Aux** was obtained in 89% yield (76.4 mg, 0.0563 mmol).

^1H NMR (300 MHz, CD_2Cl_2) δ 8.63 (s, 1H), 8.38 (s, 1H), 8.22 (s, 1H), 8.02 (s, 1H), 7.99-7.93 (m, 3H), 7.90 (s, 2H), 7.77 (s, 2H), 7.74 (dd, $J = 8.7$, 1.8 Hz, 1H), 7.70-7.67 (m, 1H), 7.56 (dd, $J = 8.4$, 2.4 Hz, 1H), 7.46 (d, $J = 8.1$ Hz, 1H), 7.06 (s, 1H), 6.98 (d, $J = 1.2$ Hz, 1H), 6.94 (d, $J = 7.5$ Hz, 1H), 6.68 (s, 1H), 6.62 (d, $J = 8.4$ Hz, 2H), 6.48 (s, 1H), 6.42 (s, 1H), 6.17 (t, $J = 7.4$ Hz, 1H), 4.44 (t, $J = 9.3$ Hz, 1H), 4.15 (d, $J = 8.2$ Hz, 1H), 3.95 (d, $J = 5.7$ Hz, 1H), 2.38 (s, 3H), 2.05 (s, 6H), 1.95 (s, 3H), 1.65 (s, 3H), 1.39 (s, 3H), 0.60 (d, $J = 6.3$ Hz, 3H), 0.21-0.10 (m, 1H), 0.03 (d, $J = 6.3$ Hz, 3H).

^{13}C NMR (75 MHz, CD_2Cl_2) δ 173.6, 167.0, 156.8, 156.5, 151.9, 151.3, 139.7, 139.6, 138.6, 138.4, 136.9, 135.5, 135.3 (2C), 134.9, 134.32, 134.27, 134.1, 133.3 (q, $J = 33.4$ Hz, 2CJ), 133.1 (q, $J = 33.4$ Hz, 2CJ), 130.6, 130.3, 129.9, 129.3, 129.2, 128.9, 128.1, 126.9 (q, $J = 2.7$ Hz, 4CJ), 124.4, 123.8 (q, $J = 271.1$ Hz, 4CJ), 122.7 (m, 122.8-122.6, 2CJ), 122.0, 118.5, 118.3, 118.2, 111.2, 111.0, 110.8, 110.4, 75.3, 67.0, 30.6, 20.9, 20.8, 19.2, 18.5, 18.1, 17.8, 17.2, 13.9.

^{19}F NMR (235 MHz, CD_2Cl_2) δ -63.25, -63.26, -72.30 (d, $J = 710.2$ Hz, 6F).

Λ -(*S*)-**Fe3-Aux**: CD (CH_3CN): λ , nm ($\Delta\epsilon$, $\text{M}^{-1}\text{cm}^{-1}$) 569 (-16), 434 (+19), 385 (+5), 352 (+25), 314 (+3), 306 (+4).

Δ -(*R*)-**Fe3-Aux**: CD (CH_3CN): λ , nm ($\Delta\epsilon$, $\text{M}^{-1}\text{cm}^{-1}$) 569 (+16), 434 (-19), 383 (-5), 351 (-25), 314 (-3), 306 (-4).

Λ -(*S*)-**Fe4-Aux** and Δ -(*R*)-**Fe4-Aux**:

According to the general procedure, starting from *rac*-**Fe4** (200 mg, 0.159 mmol), chiral auxiliary (*S*)-**A2** (33 mg, 0.159 mmol), and triethylamine (24.6 mg, 0.241 mmol) to afford a single diastereomer Λ -(*S*)-**Fe4-Aux** (86.3 mg, 0.0700 mmol, 44% yield) and Δ -**Fe4-Cru** (90 mg, 0.0716 mmol, 45% yield). Purification condition: CH₂Cl₂/CH₃CN = 100:1 to 25:1

According to the general procedure, starting from Δ -**Fe4-Cru** (90 mg, 0.0716 mmol), chiral auxiliary (*R*)-**A2** (16 mg, 0.0788 mmol), the single diastereomer Δ -(*R*)-**Fe4-Aux** was obtained in 85% (75 mg, 0.0608 mmol).

¹H NMR (300 MHz, CD₂Cl₂) δ 8.86 (s, 1H), 8.32 (d, *J* = 2.4 Hz, 2H), 8.14 (s, 1H), 7.95 (s, 1H), 7.83 (d, *J* = 8.7 Hz, 1H), 7.73 (dd, *J* = 7.8, 3.0 Hz, 1H), 7.69 (dd, *J* = 8.7, 0.6 Hz, 1H), 7.61 (d, *J* = 8.4 Hz, 1H), 7.32 (dd, *J* = 8.1, 1.5 Hz, 1H), 7.10-7.01 (m, 4H), 6.92 (d, *J* = 2.1 Hz, 1H), 6.90 (ddd, *J* = 9.0, 6.9, 2.1 Hz, 1H), 6.84 (s, 1H), 6.52 (d, *J* = 8.4 Hz, 1H), 6.18 (ddd, *J* = 7.8, 6.9, 0.9 Hz, 1H), 4.37 (dd, *J* = 9.0, 2.7 Hz, 1H), 4.24 (t, *J* = 9.0 Hz, 1H), 4.12 (d, *J* = 9.0 Hz, 1H), 2.60-2.42 (m, 4H), 1.62-1.45 (m, 4H), 1.43-1.28 (m, 4H), 0.97 (t, *J* = 7.4 Hz, 3H), 0.53 (t, *J* = 7.4 Hz, 3H), 0.03 (d, *J* = 6.6 Hz, 3H), -0.11 - -0.20 (m, 1H).

¹³C NMR (75 MHz, CD₂Cl₂) δ 212.2, 210.1, 173.6, 167.3, 159.1, 158.6, 150.9 (m, 151.0-150.8, 2C), 148.6, 148.3, 134.9, 134.8 (m, 134.8-134.6, 2C), 134.1, 132.8, 132.7, 129.7, 129.6, 129.5, 129.4, 128.8, 128.1, 124.4, 123.6 (q, *J* = 34.0 Hz), 123.1 (q, *J* = 270.8 Hz), 122.9 (q, *J* = 34.0 Hz), 122.8 (q, *J* = 270.6 Hz), 118.9, 118.7, 113.0, 111.0, 110.5, 110.2, 110.1, 74.5, 67.5, 35.1, 35.0, 32.9, 32.8, 30.7, 22.9, 22.8, 19.2, 14.1, 14.0, 13.7.

¹⁹F NMR (235 MHz, CD₂Cl₂) δ -62.70, -63.08, -72.29 (d, *J* = 710.4 Hz, 6F).

IR (film): ν (cm⁻¹) 2922, 1611, 1584, 1538, 1504, 1485, 1467, 1421, 1326, 1312, 1298, 1259, 1234, 1170, 1028, 917, 842, 827, 755, 694, 660, 556, 512, 463, 423.

Λ -(*S*)-**Fe4-Aux**: CD (CH₃CN): λ , nm ($\Delta\epsilon$, M⁻¹cm⁻¹) 598 (-25), 496 (-2), 475 (-3), 421 (+50), 375 (+17), 347 (+52), 309 (-8), 286 (+28), 266 (-45).

Δ -(*R*)-**Fe4-Aux**: CD (CH₃CN): λ , nm ($\Delta\epsilon$, M⁻¹cm⁻¹) 597 (+24), 494 (+2), 475 (+4), 421 (+48), 376 (-17), 347 (-50), 308 (+9), 284 (-28), 265 (+44).

Λ -(*S*)-**Fe5-Aux** and Δ -(*R*)-**Fe5-Aux**:

According to the general procedure, starting from *rac*-**Fe5** (260 mg, 0.222 mmol), chiral auxiliary (*S*)-**A2** (45 mg, 0.222 mmol), and triethylamine (33.6 mg, 0.333 mmol) to afford a single diastereomer Λ -(*S*)-**Fe5-Aux** (116.3 mg, 0.101 mmol, 46% yield) and Δ -**Fe5-Cru** (114 mg, 0.097 mmol, 44% yield). Purification condition: CH₂Cl₂/CH₃CN = 100:1 to 25:1

According to the general procedure, starting from Δ -**Fe5-Cru** (46 mg, 0.0392 mmol), chiral auxiliary (*R*)-**A2** (8.8 mg, 0.0431 mmol), the single diastereomer Δ -(*R*)-**Fe5-Aux** was obtained in 85% yield (38 mg, 0.0330 mmol).

¹H NMR (300 MHz, CD₂Cl₂) δ 8.55 (s, 1H), 8.39 (d, *J* = 2.1 Hz, 1H), 8.15 (s, 1H), 7.85 (dd, *J* = 8.7, 1.8 Hz, 1H), 7.77 (d, *J* = 8.4 Hz, 1H), 7.72 (s, 1H), 7.64 (dd, *J* = 8.4, 1.5 Hz, 1H), 7.56 (d, *J* = 8.7 Hz, 1H), 7.24-7.12 (m, 7H), 6.89-6.81 (m, 2H), 6.70 (t, *J* = 1.5 Hz, 1H), 6.36 (d, *J* = 8.4 Hz, 1H), 6.15 (td, *J* = 7.5, 0.9 Hz, 1H), 4.29-4.27 (m, 2H), 3.71-3.66 (m, 1H), 3.02-2.91 (m, 1H), 2.80-2.67 (m, 1H), 2.13-2.02 (m, 1H), 1.92-1.78 (m, 1H), 1.41 (d, *J* = 6.6 Hz, 3H), 1.36 (d, *J* = 6.9 Hz, 3H), 1.20-1.14 (m, 9H), 0.93 (d, *J* = 6.6 Hz, 3H), 0.85 (d, *J*

= 6.9 Hz, 3H), 0.76 (d, $J = 7.2$ Hz, 3H), 0.52 (d, $J = 6.9$ Hz, 3H), -0.04 (d, $J = 6.6$ Hz, 3H), -0.20 - -0.28 (m, 1H).

^{13}C NMR (75 MHz, CD_2Cl_2) δ 209.4, 207.1, 173.9, 167.0, 158.5, 158.3, 151.6 (m, 151.6-151.5, 2C), 147.1, 145.5, 144.9, 143.6, 135.4 (q, $J = 3.2$ Hz), 135.2 (q, $J = 3.6$ Hz), 135.0, 134.7, 134.2, 131.2, 131.1, 131.0, 130.3, 129.5, 126.0, 125.4, 123.9, 123.7, 123.12 (q, $J = 34.6$ Hz), 123.09 (q, $J = 34.0$ Hz), 122.9 (q, $J = 271.0$ Hz), 122.7 (q, $J = 270.8$ Hz), 117.9, 117.8, 113.5, 111.8, 110.4, 110.2, 110.1, 75.0, 67.3, 30.4, 29.7, 29.5, 29.1, 28.5, 27.5, 27.3, 26.2, 26.0, 23.5, 22.8, 22.4, 22.1, 19.1, 13.6.

^{19}F NMR (235 MHz, CD_2Cl_2) δ -61.82 , -62.42 , -72.80 (d, $J = 709.7$ Hz, 6F).

IR (film): ν (cm^{-1}) 2963, 1611, 1583, 1540, 1507, 1445, 1421, 1398, 1326, 1286, 1262, 1134, 1088, 1068, 944, 841, 803, 710, 662, 620, 522, 464, 408.

Δ -(*S*)-**Fe5-Aux**: CD (CH_3CN): λ , nm ($\Delta\epsilon$, $\text{M}^{-1}\text{cm}^{-1}$) 592 (-27), 489 ($+9$), 480 ($+8$), 432 ($+31$), 391 ($+10$), 351 ($+47$), 310 (-6), 291 ($+6$), 278 (-11).

Δ -(*R*)-**Fe5-Aux**: CD (CH_3CN): λ , nm ($\Delta\epsilon$, $\text{M}^{-1}\text{cm}^{-1}$) 592 ($+27$), 490 (-9), 480 (-8), 432 (-31), 391 (-10), 351 (-47), 310 ($+6$), 291 (-6), 278 ($+11$).

Δ -(*S*)-**Fe6-Aux** and Δ -(*R*)-**Fe6-Aux**:

According to the general procedure, starting from *rac*-**Fe6** (375 mg, 0.300 mmol), chiral auxiliary (*S*)-**A2** (62 mg, 0.300 mmol), and triethylamine (45.6 mg, 0.450 mmol) to afford a single diastereomer Δ -(*S*)-**Fe6-Aux** (169 mg, 0.138 mmol, 46% yield) and Δ -**Fe6-Cru** (175 mg, 0.140 mmol, 47% yield). Purification condition: $\text{CH}_2\text{Cl}_2/\text{CH}_3\text{CN} = 100:1$ to $25:1$

According to the general procedure, starting from Δ -**Fe6-Cru** (100 mg, 0.0804 mmol), chiral auxiliary (*R*)-**A2** (18.1 mg, 0.0885 mmol), the single diastereomer Δ -(*R*)-**Fe6-Aux** was obtained in 91% yield (89 mg, 0.0732 mmol).

^1H NMR (300 MHz, CD_2Cl_2) δ 8.60 (br, s, 1H), 8.47 (t, $J = 3.0$ Hz, 1H), 8.25 (br, s, 1H), 8.00 (d, $J = 8.4$, 1H), 7.87 (dd, $J = 8.4$, 3.6 Hz, 1H), 7.77 (d, $J = 7.5$ Hz, 1H), 7.76 (br, s, 1H), 7.67 (d, $J = 7.8$ Hz, 1H), 7.25 (dd, $J = 7.8$, 1.6 Hz, 1H), 7.21 (d, $J = 0.9$ Hz, 1H), 6.88 (ddd, $J = 8.4$, 6.6, 1.8 Hz, 1H), 6.80 (d, $J = 2.1$ Hz, 1H), 6.68 (d, $J = 1.8$ Hz, 1H), 6.36 (d, $J = 8.7$ Hz, 2H), 6.18 (ddd, $J = 7.8$, 7.2, 0.6 Hz, 1H), 4.35-4.25 (m, 2H), 3.68-3.63 (m, 1H), 3.03-2.92 (m, 1H), 2.78-2.67 (m, 1H), 2.05-1.93 (m, 1H), 1.84-1.75 (m, 1H), 1.40 (d, $J = 6.6$ Hz, 3H), 1.35 (d, $J = 6.9$ Hz, 3H), 1.20 (d, $J = 6.9$ Hz, 3H), 1.16 (d, $J = 6.9$ Hz, 3H), 1.14 (d, $J = 6.3$ Hz, 3H), 0.93 (d, $J = 6.9$ Hz, 3H), 0.86 (d, $J = 6.9$ Hz, 3H), 0.77 (d, $J = 6.9$ Hz, 3H), 0.53 (d, $J = 6.9$ Hz, 3H), -0.02 (d, $J = 6.9$ Hz, 3H), -0.17 - -0.29 (m, 1H).

^{13}C NMR (75 MHz, CD_2Cl_2) δ 209.9, 207.4, 173.7, 167.2, 158.5, 158.3, 151.7 (m, 151.8-151.6, 2C), 149.4, 147.6, 147.2, 145.8, 137.1, 136.8, 135.0 (m, 151.8-151.6, 2C), 134.4, 133.6, 133.3, 130.9, 130.1, 129.6, 126.2, 125.7, 124.3, 124.1, 123.7, 123.3 (q, $J = 34.1$ Hz, 2C), 122.9, (q, $J = 270.8$ Hz), 122.6 (q, $J = 271.2$ Hz), 118.5, 118.3, 113.7, 111.7, 110.8, 110.5, 75.0, 67.4, 30.4, 29.9, 29.7, 29.2, 28.8, 27.2, 27.1, 26.0, 25.7, 23.3, 22.6, 22.3, 21.9, 19.1, 13.6.

^{19}F NMR (235 MHz, CD_2Cl_2) δ -61.96 , -62.62 , -72.20 (d, $J = 709.7$ Hz, 6F).

IR (film): ν (cm⁻¹) 2968, 1610, 1581, 1540, 1506, 1445, 1421, 1386, 1309, 1262, 1234, 1220, 1172, 1137, 1070, 943, 826, 757, 735, 711, 556, 463.

Λ -(*S*)-**Fe6-Aux**: CD (CH₃CN): λ , nm ($\Delta\epsilon$, M⁻¹cm⁻¹) 581 (-13), 492 (+4), 479 (+3), 434 (+15), 390 (+5), 352 (+22), 309 (-4), 289 (+6), 272 (-21).

Δ -(*R*)-**Fe6-Aux**: CD (CH₃CN): λ , nm ($\Delta\epsilon$, M⁻¹cm⁻¹) 581 (+13), 492 (-4), 479 (-3), 434 (-15), 390 (-5), 352 (-22), 309 (+4), 287 (-6), 269 (+21).

Note: Λ -(*S*)-**Fe1-Aux** and Δ -(*R*)-**Fe1-Aux** can also be synthesized by this method.

According to the general procedure, starting from a mixture of *rac*-**Fe1** (250 mg, 0.23 mmol), chiral auxiliary (*S*)-**A2** (56.4 mg, 0.28 mmol), and triethylamine (34.9 mg, 0.345 mmol) to afford a single diastereomer Λ -(*S*)-**Fe1-Aux** (105 mg, 0.098 mmol, 43% yield) and Δ -**Fe1-Cru** (137 mg, 0.126 mmol, 45% yield). Purification condition: CH₂Cl₂/CH₃CN = 50:1 to 25:1.

According to the general procedure, starting from Δ -**Fe1-Cru** (100 mg, 0.092 mmol), chiral auxiliary (*R*)-**A2** (18 mg, 0.101 mmol), the single diastereomer Δ -(*R*)-**Fe1-Aux** was obtained in 92% yield (90 mg, 0.084 mmol).

Step 2: To a solution of single diastereomers Λ -(*S*)-**Fe-Aux** or Δ -(*R*)-**Fe-Aux** in CH₃CN ($c = 0.02$ M) was added solid NH₄PF₆ (10 eq.), the resulting mixture was then stirred at 30 °C under nitrogen atmosphere for 18 hours. The reaction mixture was evaporated to dryness, redissolved in CH₂Cl₂/CH₃CN (100:1), filtered through a thin pad of diatomite, the red-yellow filtrate was concentrated, and then subjected to column chromatography on silica gel (CH₂Cl₂/CH₃CN = 25:1 or 15:1) to give the related enantiopure catalyst Λ -**Fe2-6** or Δ -**Fe2-6**, respectively.

Λ -**Fe2** and Δ -**Fe2**:

According to general procedure, starting from Λ -(*S*)-**Fe2-Aux** (80 mg, 0.0655 mmol) or Δ -(*R*)-**Fe2-Aux** (74 mg, 0.0603 mmol) to afford enantiopure catalyst Λ -**Fe2** (64.1 mg, 0.0515 mmol) in 79% yield and enantiopure catalyst Δ -**Fe2** (60 mg, 0.0482 mmol) in 80% yield, respectively. Purification condition: CH₂Cl₂/CH₃CN = 25:1 or 10:1

Λ -**Fe2**: CD (CH₃CN): λ , nm ($\Delta\epsilon$, M⁻¹cm⁻¹) 502 (+2), 424 (-28), 374 (+29), 298 (-15), 262 (+38).

Δ -**Fe2**: CD (CH₃CN): λ , nm ($\Delta\epsilon$, M⁻¹cm⁻¹) 502 (-2), 424 (+28), 374 (-29), 298 (+15), 262 (-38).

Λ -**Fe3** and Δ -**Fe3**:

According to general procedure, starting from Λ -(*S*)-**Fe3-Aux** (100 mg, 0.0738 mmol) or Δ -(*R*)-**Fe3-Aux** (76.4 mg, 0.0563 mmol) to afford enantiopure catalyst Λ -**Fe3** (93 mg, 0.0686 mmol) in 93% yield and enantiopure catalyst Δ -**Fe3** (73 mg, 0.0529 mmol) in 94% yield, respectively. Purification condition: CH₂Cl₂/CH₃CN = 50:1 to 20:1

Λ -**Fe3**: CD (CH₃CN): λ , nm ($\Delta\epsilon$, M⁻¹cm⁻¹) 502 (+1), 437 (-36), 384 (+40), 309 (-10), 286 (+35).

Δ -**Fe3**: CD (CH₃CN): λ , nm ($\Delta\epsilon$, M⁻¹cm⁻¹) 502 (-1), 437 (+36), 384 (-40), 309 (+10), 286 (-35).

Λ -Fe4 and Δ -Fe4:

According to general procedure, starting from Λ -(*S*)-**Fe4-Aux** (86.3 mg, 0.0700 mmol) or Δ -(*R*)-**Fe4-Aux** (75 mg, 0.0608 mmol) to afford enantiopure catalyst Λ -**Fe4** (62 mg, 0.159 mmol) in 70% yield and enantiopure catalyst Δ -**Fe4** (54 mg, 0.0432 mmol) in 71%, respectively. Purification condition: CH₂Cl₂/CH₃CN = 50:1 to 20:1

Λ -**Fe4**: CD (CH₃CN): λ , nm ($\Delta\epsilon$, M⁻¹cm⁻¹) 510 (+4), 431 (-28), 378 (+30), 315 (-1), 274 (+23), 256 (-39).

Δ -**Fe4**: CD (CH₃CN): λ , nm ($\Delta\epsilon$, M⁻¹cm⁻¹) 510 (-4), 431 (+28), 378 (-30), 315 (+1), 274 (-23), 256 (+39).

 Λ -Fe5 and Δ -Fe5:

According to general procedure, starting from Λ -(*S*)-**Fe5-Aux** (116.3 mg, 0.101 mmol) and Δ -(*R*)-**Fe5-Aux** (38 mg, 0.033 mmol) to afford enantiopure catalyst Λ -**Fe5** (109 mg, 0.093 mmol) in 92% yield and enantiopure catalyst Δ -**Fe5** (35 mg, 0.0299 mmol) in 90% yield, respectively. Purification condition: CH₂Cl₂/CH₃CN = 50:1 to 20:1

Λ -**Fe5**: CD (CH₃CN): λ , nm ($\Delta\epsilon$, M⁻¹cm⁻¹) 524 (+5), 442 (-52), 386 (+59), 320 (-8), 307 (-6), 294 (-13), 278 (+63), 260 (-69).

Δ -**Fe5**: CD (CH₃CN): λ , nm ($\Delta\epsilon$, M⁻¹cm⁻¹) 524 (-4), 441 (+51), 386 (-59), 319 (+9), 308 (+8), 295 (+13), 278 (-63), 261(+70).

 Λ -Fe6 and Δ -Fe6:

According to general procedure, starting from Λ -(*S*)-**Fe6-Aux** (169 mg, 0.138 mmol) or Δ -(*R*)-**Fe6-Aux** (89 mg, 0.0732 mmol) to afford enantiopure catalyst Λ -**Fe6** (163 mg, 0.131 mmol) in 95% yield and enantiopure catalyst Δ -**Fe6** (83 mg, 0.0668 mmol) in 91% yield, respectively. Purification condition: CH₂Cl₂/CH₃CN = 50:1 to 20:1

Λ -**Fe6**: CD (CH₃CN): λ , nm ($\Delta\epsilon$, M⁻¹cm⁻¹) 527 (+4), 442 (-44), 387 (+54), 323 (-6), 284 (+38).

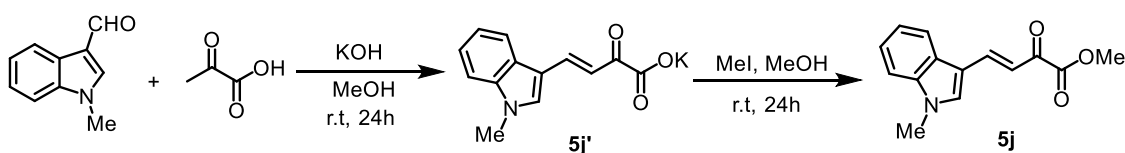
Δ -**Fe6**: CD (CH₃CN): λ , nm ($\Delta\epsilon$, M⁻¹cm⁻¹) 527 (-4), 441 (+44), 387 (-54), 322 (+5), 283 (-40).

All other spectroscopic data of enantiopure iron catalysts were in agreement with the racemic catalysts.

5.4.4 Synthesis of Substrates

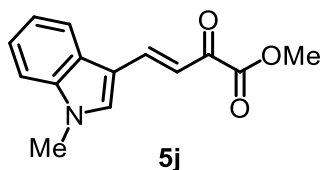
β,γ -Unsaturated α -ketoesters **5a-i**, and **5k-m** were prepared by well-established methods.¹⁶ Dienophiles **6a-d** are commercially available, **6e**¹⁷ and **6f**¹⁸ used in this work are reported, which were prepared according to related literature procedures.

(1) Synthesis of β,γ -unsaturated α -ketoester 5j



β,γ -Unsaturated α -ketoester **5j** was synthesized according to a reported procedure¹⁶ with some modification. To a solution of 1-methyl-1*H*-indole-3-carbaldehyde (477 mg, 3.0 mmol) and pyruvic acid (264 mg, 3.0 mmol) in MeOH (1 mL) at 0 °C was added a solution of potassium hydroxide (252 mg, 4.5 mmol) in MeOH (3 mL). The reaction was stirred at 40 °C for 1 hour followed by r.t for 24 hours. The solvent was removed under reduced pressure and the residue was diluted with water (20 mL) then extracted with EtOAc (20 \times 5 mL). The aqueous layer was acidified by HCl (1M) and extracted with EtOAc until the water was colorless. Combined organic layers were washed with brine, dried with MgSO₄, filtered and concentrated in vacuo to give the crude potassium salt which was used as an intermediate and without further purification.

To a solution of potassium salt in anhydrous MeOH was added MeI (426 mg, 3mmol) at 0 °C, the resulting mixture was then stirred at room temperature overnight. The reaction mixture was concentrated, and then subjected to column chromatography on silica gel (*n*-hexane /EtOAc = 3:1) to afford the (*E*)-methyl 4-(1-methyl-1*H*-indol-3-yl)-2-oxobut-3-enoate as a yellow oil. This yellow oil can be further purified via recrystallization in the mixed solvent of *n*-hexane/CH₂Cl₂ to obtain the pure compound as a yellow solid (110 mg, 15% yield).



¹H NMR (300 MHz, CDCl₃) δ 8.14 (d, *J* = 15.9 Hz, 1H), 8.02-7.97 (m, 1H), 7.53 (s, 1H), 7.38 (d, *J* = 15.9 Hz, 1H), 7.38-7.30 (m, 3H), 3.94 (s, 3H), 3.86 (s, 3H).

¹³C NMR (75 MHz, CDCl₃) δ 182.0, 163.7, 142.5, 138.6, 136.4, 126.2, 123.8, 122.4, 121.2, 115.3, 113.3, 110.4, 52.9, 33.6.

IR (film): ν (cm⁻¹) 3085, 2949, 1730, 1667, 1581, 1560, 1523, 1465, 1440, 1426, 1389, 1373, 1346, 1314, 1243, 1185, 1160, 1129, 1092, 1071, 976, 879, 850, 787, 738, 651, 493, 424.

HRMS (ESI, *m/z*) calcd for C₁₁H₁₄O₃ [M + H]⁺: 244.0974, found: 244.0968.

(2) Synthesis of β,γ -unsaturated α -ketoesters **5n-5s**

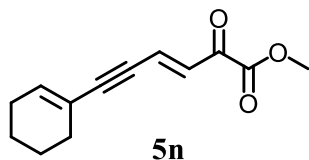
5n-5s were synthesized according to a reported procedure with slight modification.¹⁹

Step 1: A solution of methyl bromopyruvate (4.5 g, 25 mmol) in anhydrous THF (10 mL) was added dropwise over 3 hours to a stirred and cooled (0 °C) solution of triphenylphosphine (6.6 g, 25 mmol) in anhydrous THF (75 mL). The reaction warmed to room temperature and then stirred for an additional 36 hours. The supernatant was filtered and washed with anhydrous ether (200 mL). The resulting dried solid was dissolved in methanol (10 mL) and the solution cooled to 0 °C. The pH was adjusted to 10 by a gradual addition of iced aqueous sodium carbonate (1 N). The solution was diluted to 200 mL with ice water and stirred for 1 hour at 0 °C, after

which the precipitate was collected and washed with cold water and dried under vacuum to give the phosphorus ylide as a yellow solid which was pure enough for the next step.

All the spectroscopic data of phosphorus ylide were in agreement with published data.¹⁹

Step 2: To a solution of phosphorus ylide (1 eq.) and 10 mol % of benzoic acid in CH₂Cl₂ (*c* = 0.5 M) was added aldehyde (2.5-5.0 eq.). The solution was stirred at 40 °C for 24 hours. The solvent was then removed under reduced pressure. Desired products were obtained after chromatography on silica gel with *n*-hexane/EtOAc as eluent.



(E)-Methyl 6-(cyclohex-1-en-1-yl)-2-oxohex-3-en-5-ynoate (5n)

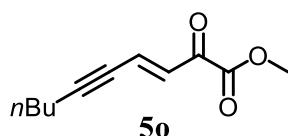
According to the general procedure, starting from phosphorus ylide (543 mg, 1.5 mmol) and 3-(cyclohex-1-en-1-yl) propionaldehyde²⁰ (670 mg, 5.0 mmol) to give the **5n** as a yellow oil (121 mg, 37% yield). Purification condition: *n*-hexane/EtOAc = 150:1

¹H NMR (300 MHz, CDCl₃) δ 7.10 (d, *J* = 15.9 Hz, 1H), 7.04 (d, *J* = 15.9 Hz, 1H), 6.33 (m, 1H), 3.90 (s, 3H), 2.22-2.12 (m, 4H), 1.71-1.61 (m, 4H).

¹³C NMR (75 MHz, CDCl₃) δ 181.6, 162.2, 140.2, 130.8, 130.1, 120.7, 106.4, 85.9, 53.2, 28.8, 26.3, 22.2, 21.4.

IR (film): ν (cm⁻¹) 3018, 2951, 2927, 2859, 2172, 1734, 1686, 1571, 1447, 1436, 1336, 1283, 1255, 1220, 1137, 1084, 1046, 980, 955, 918, 870, 840, 797, 777, 728, 579, 502, 458.

HRMS (ESI, *m/z*) calcd for C₁₁H₁₄O₃ [M + Na]⁺: 241.0836, found: 241.0835.



(E)-Methyl 2-oxodec-3-en-5-ynoate (5o)

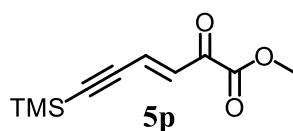
According to the general procedure, starting from phosphorus ylide (543 mg, 1.5 mmol) and hept-2-ynal²¹ (550 mg, 5.0 mmol) to give the **5o** as a yellow oil (102 mg, 35% yield). Purification condition: *n*-hexane/EtOAc = 200:1

¹H NMR (300 MHz, CDCl₃) δ 7.02 (d, *J* = 16.2 Hz, 1H), 6.94 (dt, *J* = 15.9, 2.0 Hz, 1H), 3.89 (s, 3H), 2.43 (td, *J* = 6.9, 1.8 Hz, 2H), 1.61-1.52 (m, 2H), 1.49-1.37 (m, 2H), 0.93 (t, *J* = 7.2 Hz, 3H).

¹³C NMR (75 MHz, CDCl₃) δ 181.8, 162.2, 131.5, 130.8, 106.8, 79.4, 53.2, 30.4, 22.1, 19.9, 13.7.

IR (film): ν (cm⁻¹) 2958, 2934, 2873, 2206, 1733, 1693, 1672, 1588, 1456, 1437, 1380, 1299, 1248, 1195, 1143, 1073, 961, 893, 867, 801, 779, 748, 728, 696, 635.

HRMS (ESI, *m/z*) calcd for C₁₁H₁₄O₃ [M + Na]⁺: 217.0835, found: 217.0835.



(E)-Methyl 2-oxo-6-(trimethylsilyl)hex-3-en-5-ynoate (5p)

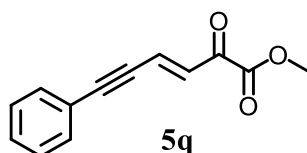
According to the general procedure, starting from phosphorus ylide (543 mg, 1.5 mmol) and 3-(trimethylsilyl) propionaldehyde²¹ (945 mg, 7.5 mmol) to give the **5p** as a yellow oil (101 mg, 32% yield). Purification condition: *n*-hexane/EtOAc = 200:1 to 150:1

¹H NMR (300 MHz, CDCl₃) δ 7.13 (d, *J* = 16.2 Hz, 1H), 6.91 (dt, *J* = 16.2 Hz, 1H), 3.90 (s, 3H), 0.23 (s, 9H).

¹³C NMR (75 MHz, CDCl₃) δ 181.6, 161.9, 132.9, 129.0, 110.7, 102.1, 79.4, 53.3, -0.4.

IR (film): ν (cm⁻¹) 2958, 2901, 1735, 1696, 1676, 1586, 1438, 1329, 1298, 1247, 1195, 1145, 1107, 1084, 1046, 961, 840, 760, 702, 639, 546, 439.

HRMS (ESI, *m/z*) calcd for C₁₁H₁₄O₃ [M + Na]⁺: 233.0611, found: 233.0604.



(E)-Methyl 2-oxo-6-phenylhex-3-en-5-ynoate (5q)

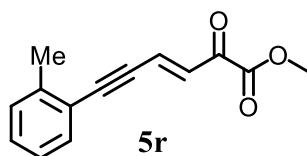
According to the general procedure, starting from phosphorus ylide (362 mg, 1.0 mmol) and 3-phenylpropionaldehyde²⁰ (325 mg, 2.5 mmol) to give the **5q** as a yellow solid (120 mg, 56% yield). Purification condition: *n*-hexane/EtOAc = 150:1

¹H NMR (300 MHz, CDCl₃) δ 7.53-7.50 (m, 2H), 7.42-7.34 (m, 3H), 7.19 (t, *J* = 16.2 Hz, 2H), 3.94 (s, 3H).

¹³C NMR (75 MHz, CDCl₃) δ 181.4, 162.0, 132.4, 131.8, 130.1, 129.3, 128.7, 122.0, 103.4, 87.7, 53.3.

IR (film): ν (cm⁻¹) 3066, 2192, 1725, 1684, 1599, 1579, 1489, 1451, 1437, 1341, 1276, 1237, 1146, 1083, 1031, 1013, 994, 976, 950, 917, 886, 783, 751, 686, 570, 524, 486, 459, 413.

HRMS (ESI, *m/z*) calcd for C₁₁H₁₄O₃ [M + Na]⁺: 237.0527, found: 237.0522.



(E)-Methyl 2-oxo-6-(o-tolyl)hex-3-en-5-ynoate (5r)

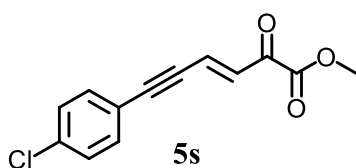
According to the general procedure, starting from phosphorus ylide (362 mg, 1.0 mmol) and 3-(*m*-tolyl) propionaldehyde²⁰ (360 mg, 2.5 mmol) to give the **5r** as a yellow solid (100 mg, 44% yield). Purification condition: *n*-hexane/EtOAc = 200:1 to 150:1

¹H NMR (300 MHz, CDCl₃) δ 7.34-7.21 (m, 4H), 7.18 (s, 2H), 3.92 (s, 3H), 2.36 (s, 3H).

¹³C NMR (75 MHz, CDCl₃) δ 181.5, 162.1, 138.5, 133.0, 131.6, 131.1, 129.6, 129.5, 128.6, 121.8, 103.9, 87.5, 53.3, 21.3.

IR (film): ν (cm⁻¹) 2954, 2183, 1731, 1682, 1602, 1583, 1482, 1444, 1277, 1242, 1192, 1246, 1086, 1036, 997, 956, 894, 684, 850, 774, 680, 565, 501, 439, 414.

HRMS (ESI, m/z) calcd for C₁₁H₁₄O₃ [M + Na]⁺: 251.0681, found: 251.0679.



(*E*)-Methyl 6-(4-chlorophenyl)-2-oxohex-3-en-5-ynoate (**5s**)

According to the general procedure, starting from phosphorus ylide (362 mg, 1.0 mmol) and 3-(4-chlorophenyl) propionaldehyde²⁰ (410 mg, 2.5 mmol) to give the **5s** as a yellow solid (146 mg, 59% yield). Purification condition: *n*-hexane/EtOAc = 100:1

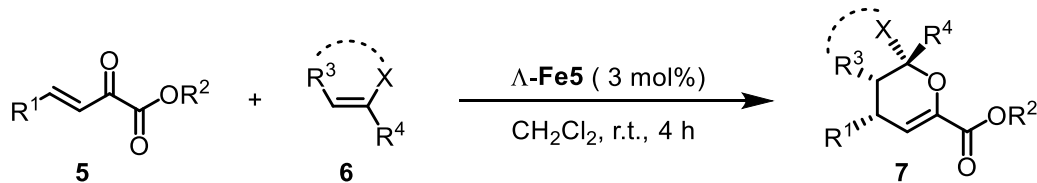
¹H NMR (300 MHz, CDCl₃) δ 7.44 (dt, J = 8.4, 1.8 Hz, 2H), 7.35 (dt, J = 8.4, 1.8 Hz, 2H), 7.21 (d, J = 15.9 Hz, 1H), 7.14 (d, J = 15.9 Hz, 1H), 3.92 (s, 3H).

¹³C NMR (75 MHz, CDCl₃) δ 181.3, 162.0, 136.4, 133.6, 132.0, 129.2, 128.8, 120.4, 101.8, 88.5, 53.3.

IR (film): ν (cm⁻¹) 2952, 2188, 1728, 1680, 1596, 1572, 1487, 1457, 1444, 1396, 1343, 1285, 1273, 1236, 1176, 1086, 1014, 957, 870, 823, 811, 790, 782, 740, 580, 526, 502, 450.

HRMS (ESI, m/z) calcd for C₁₁H₁₄O₃ [M + Na]⁺: 271.0133, found: 271.0133.

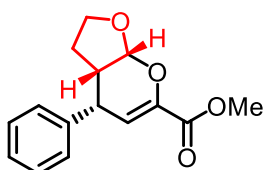
5.4.5 Typical Procedure for Iron-catalyzed Asymmetric Oxa-Diels-Alder Reaction



A dried 10 mL Schlenk tube was charged with β,γ -unsaturated α -ketoester (0.1 mmol) and Λ -**Fe5** (3.5 mg, 0.003 mmol), and the flask was purged with nitrogen. Then, CH₂Cl₂ (2.0 mL, 0.01 M) was added via syringe followed by enoether or vinyl azide (0.15 mmol) and the flask was sealed and stirred at room temperature for 4 hours. The solvent was removed under reduced pressure and the crude residue was subjected to ¹H NMR analysis to determine the d.r. value except otherwise noted. The crude product was purified by flash chromatography on silica gel eluted with *n*-hexane/EtOAc to afford the desired bicyclic product.

5.4.6 Experimental and Characterization Data of the Products

Methyl 4-phenyl-3,3a,4,7a-tetrahydro-2H-furo[2,3-*b*]pyran-6-carboxylate (**7aa**)

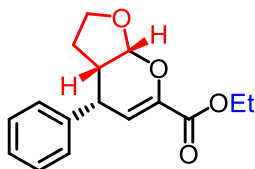


Compound **7aa** was prepared according to the typical procedure from β,γ -unsaturated α -ketoester **5a** (19.0 mg, 0.1 mmol) and enolether **6a** (10.5 mg, 0.15 mmol) as starting material. Purification on a column of silica gel with a mixture of *n*-hexane/EtOAc (5:1) as eluent gave the desired product **7aa** as a colorless oil (25.5 mg, 98% yield, 99:1 d.r., 97% ee). The d.r. value was determined through ^1H NMR of crude materials. Enantiomeric excess was established by HPLC analysis using a Chiralpak IG column. HPLC conditions: UV-absorption = 254 nm, *n*-hexane/isopropanol = 90:10, flow rate = 1.0 mL/min, column temperature = 25 °C, $t_r(\text{major})$ = 20.5 min, $t_r(\text{minor})$ = 24.8 min. $[\alpha]_{\text{D}}^{22} = -65.8$ ($c = 1.0$, CH_2Cl_2), lit.^{22a} $[\alpha]_{\text{D}} = -65.7$ ($c = 0.5$, Et_2O). The analytical data for **7aa** matched with previously reported data.²²

^1H NMR (300 MHz, CDCl_3) δ 7.37-7.20 (m, 5H), 6.21 (dd, $J = 2.7, 1.5$ Hz, 1H), 5.65 (d, $J = 3.6$ Hz, 1H), 4.22-4.15 (m, 2H), 3.90-3.82 (m, 1H), 3.84 (s, 3H), 2.71-2.61 (m, 1H), 1.72 (tt, $J = 12.3, 9.7$ Hz, 1H), 1.35 (dddd, $J = 12.3, 7.2, 7.2, 2.1$ Hz, 1H).

^{13}C NMR (75 MHz, CDCl_3) δ 163.1, 142.7, 141.1, 128.8, 127.7, 127.2, 110.2, 101.5, 68.6, 52.5, 44.1, 38.3, 24.7.

Ethyl 4-phenyl-3,3a,4,7a-tetrahydro-2H-furo[2,3-*b*]pyran-6-carboxylate (**7ba**)



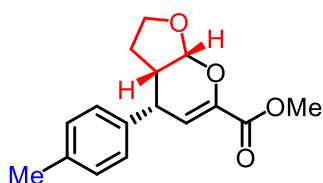
Compound **7ba** was prepared according to the typical procedure from β,γ -unsaturated α -ketoester **5b** (20.4 mg, 0.1 mmol) and enolether **6a** (10.5 mg, 0.15 mmol) as starting material. Purification on a column of silica gel with a mixture of *n*-hexane/EtOAc (5:1) as eluent gave the desired product **7ba** as a colorless oil (26.3 mg, 96% yield, 99:1 d.r., 96% ee). The d.r. value was determined through ^1H NMR of crude materials. Enantiomeric excess was established by HPLC analysis using a Chiralpak IG column. HPLC conditions: UV-absorption = 254 nm, *n*-hexane/isopropanol = 90:10, flow rate = 1.0 mL/min, column temperature = 25 °C, $t_r(\text{major})$ = 19.9 min, $t_r(\text{minor})$ = 24.0 min. $[\alpha]_{\text{D}}^{22} = -57.6$ ($c = 1.0$, CH_2Cl_2), lit.^{22a} $[\alpha]_{\text{D}} = -70.9$ ($c = 0.5$, CH_2Cl_2). The analytical data for **7ba** matched with previously reported data.²²

^1H NMR (300 MHz, CDCl_3) δ 7.37-7.27 (m, 3H), 7.24-7.21 (m, 2H), 6.18 (dd, $J = 2.7, 1.5$ Hz, 1H), 5.64 (d, $J = 3.6$ Hz, 1H), 4.30 (q, $J = 7.2$ Hz, 2H), 4.21-4.15 (m, 2H), 3.90-3.81 (m, 1H), 2.70-2.60 (m, 1H), 1.73 (tt, $J = 12.3, 9.6$ Hz, 1H), 1.40-1.30 (m, 1H), 1.34 (t, $J = 7.2$ Hz, 3H).

^{13}C NMR (75 MHz, CDCl_3) δ 162.2, 142.9, 141.3, 128.8, 127.7, 127.2, 109.9, 101.4, 68.6, 61.5, 44.1, 38.3, 24.7, 14.4.

HRMS (ESI, m/z) calcd for $\text{C}_{11}\text{H}_{14}\text{O}_3$ $[\text{M} + \text{Na}]^+$: 297.1097, found: 297.1198.

Methyl 4-(*p*-tolyl)-3,3a,4,7a-tetrahydro-2H-furo[2,3-*b*]pyran-6-carboxylate (**7ca**)



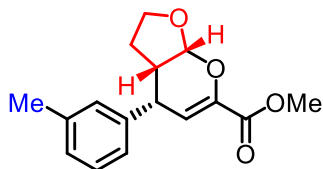
Compound **7ca** was prepared according to the typical procedure from β,γ -unsaturated α -ketoester **5c** (20.4 mg, 0.1 mmol) and enolether **6a** (10.5 mg, 0.15 mmol) as starting material. Purification on a column of silica gel with a mixture of *n*-hexane/EtOAc (5:1) as eluent gave the desired product **7ca** as a white solid (27.0 mg, 99% yield, 99:1 d.r., 98% ee). The d.r. value was determined through ^1H NMR of crude materials. Enantiomeric excess was established by HPLC analysis using a Chiralpak IG column. HPLC conditions: UV-absorption = 254 nm, *n*-hexane/isopropanol = 90:10, flow rate = 1.0 mL/min, column temperature = 25 °C, $t_r(\text{major})$ = 20.0 min, $t_r(\text{minor})$ = 23.1 min. $[\alpha]_{\text{D}}^{22} = -58.0$ ($c = 1.0$, CH_2Cl_2), lit.^{22a} $[\alpha]_{\text{D}} = -64.1$ ($c = 0.5$, CH_2Cl_2). The analytical data for **7ca** matched with previously reported data.²²

^1H NMR (300 MHz, CDCl_3) δ 7.14 (d, $J = 8.1$ Hz, 2H), 7.10 (d, $J = 8.1$ Hz, 2H), 6.19 (dd, $J = 2.4, 1.2$ Hz, 1H), 5.63 (d, $J = 3.6$ Hz, 1H), 4.21–4.10 (m, 2H), 3.90–3.81 (m, 1H), 3.84 (s, 3H), 2.69–2.58 (m, 1H), 2.34 (s, 3H), 1.71 (tt, $J = 12.3, 9.6$ Hz, 1H), 1.36 (dddd, $J = 12.3, 7.5, 7.5, 2.1$ Hz, 1H).

^{13}C NMR (75 MHz, CDCl_3) δ 163.1, 142.5, 138.1, 136.8, 129.5, 127.6, 110.6, 101.5, 68.6, 52.5, 44.2, 37.9, 24.7, 21.2.

HRMS (ESI, m/z) calcd for $\text{C}_{11}\text{H}_{14}\text{O}_3$ $[\text{M} + \text{Na}]^+$: 297.1197, found: 297.1199.

Methyl 4-(*m*-tolyl)-3,3a,4,7a-tetrahydro-2*H*-furo[2,3-*b*]pyran-6-carboxylate (**7da**)



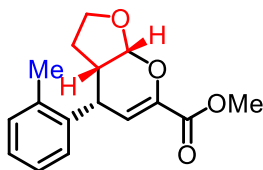
Compound **7da** was prepared according to the typical procedure from β,γ -unsaturated α -ketoester **5d** (20.4 mg, 0.1 mmol) and enolether **6a** (10.5 mg, 0.15 mmol) as starting material. Purification on a column of silica gel with a mixture of *n*-hexane/EtOAc (5:1) as eluent gave the desired product **7da** as a colorless oil (27.1 mg, 99% yield, 99:1 d.r., 97% ee). The d.r. value was determined through ^1H NMR of crude materials. Enantiomeric excess was established by HPLC analysis using a Chiralpak IG column. HPLC conditions: UV-absorption = 254 nm, *n*-hexane/isopropanol = 90:10, flow rate = 1.0 mL/min, column temperature = 25 °C, $t_r(\text{major})$ = 17.4 min, $t_r(\text{minor})$ = 22.1 min. $[\alpha]_{\text{D}}^{22} = -59.2$ ($c = 1.0$, CH_2Cl_2). lit.^{22b} $[\alpha]_{\text{D}} = -52.7$ ($c = 0.35$, CH_2Cl_2). The analytical data for **7da** matched with previously reported data.^{22b}

^1H NMR (300 MHz, CDCl_3) δ 7.22 (dt, $J = 6.9, 1.8$ Hz, 1H), 7.08 (d, $J = 7.5$ Hz, 1H), 7.02 (s, 1H), 7.01 (d, $J = 6.9$ Hz, 1H), 6.20 (dd, $J = 2.4, 1.2$ Hz, 1H), 5.64 (d, $J = 3.6$ Hz, 1H), 4.18 (ddd, 10.2, 8.1, 2.1 Hz, 1H), 4.12 (dd, 6.6, 2.7 Hz, 1H), 3.90–3.82 (m, 1H), 3.84 (s, 3H), 2.70–2.59 (m, 1H), 2.35 (s, 3H), 1.72 (tt, $J = 12.3, 9.6$ Hz, 1H), 1.36 (dddd, $J = 12.3, 7.5, 7.5, 2.1$ Hz, 1H).

^{13}C NMR (75 MHz, CDCl_3) δ 163.1, 142.6, 141.1, 138.5, 128.7, 128.4, 127.9, 124.8, 110.4, 101.5, 68.6, 52.5, 44.1, 38.2, 24.7, 21.6.

HRMS (ESI, m/z) calcd for $C_{11}H_{14}O_3$ $[M + Na]^+$: 297.1197, found: 297.1198.

Methyl 4-(*o*-tolyl)-3,3a,4,7a-tetrahydro-2*H*-furo[2,3-*b*]pyran-6-carboxylate (7ea)



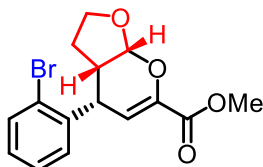
Compound **7ea** was prepared according to the typical procedure from β,γ -unsaturated α -ketoester **5e** (20.4 mg, 0.1 mmol) and enolether **6a** (10.5 mg, 0.15 mmol) as starting material. Purification on a column of silica gel with a mixture of *n*-hexane/EtOAc (5:1) as eluent gave the desired product **7ea** as a colorless oil (26.9 mg, 98% yield, 98:2 d.r., 97% ee). The d.r. value was determined through 1H NMR of crude materials. Enantiomeric excess was established by HPLC analysis using a Chiralpak IG column. HPLC conditions: UV-absorption = 254 nm, *n*-hexane/isopropanol = 90:10, flow rate = 1.0 mL/min, column temperature = 25 °C, t_r (major) = 17.5 min, t_r (minor) = 22.5 min. $[\alpha]_D^{22} = -83.2$ ($c = 1.0$, CH_2Cl_2).

1H NMR (300 MHz, $CDCl_3$) δ 7.18-7.12 (m, 4H), 6.17 (dd, $J = 2.7, 1.2$ Hz, 1H), 5.62 (d, $J = 3.6$ Hz, 1H), 4.34 (dd, 6.6, 2.7 Hz, 1H), 4.18 (ddd, 9.9, 8.1, 1.8 Hz, 1H), 3.90–3.81 (m, 1H), 3.84 (s, 3H), 2.75-2.64 (m, 1H), 2.38 (s, 3H), 1.74 (tt, $J = 12.3, 9.6$ Hz, 1H), 1.27 (dddd, $J = 12.3, 7.5, 7.5, 2.1$ Hz, 1H).

^{13}C NMR (75 MHz, $CDCl_3$) δ 163.1, 142.6, 139.3, 135.5, 130.6, 127.7, 127.2, 126.3, 111.7, 101.4, 68.6, 52.5, 44.1, 34.9, 24.9, 19.3.

HRMS (ESI, m/z) calcd for $C_{11}H_{14}O_3$ $[M + Na]^+$: 297.1197, found: 297.1199.

Methyl 4-(2-bromophenyl)-3,3a,4,7a-tetrahydro-2*H*-furo[2,3-*b*]pyran-6-carboxylate (7fa)



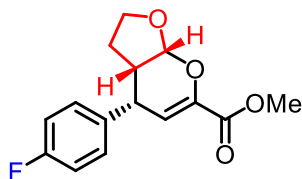
Compound **7fa** was prepared according to the typical procedure from β,γ -unsaturated α -ketoester **5f** (26.8 mg, 0.1 mmol) and enolether **6a** (10.5 mg, 0.15 mmol) as starting material. Purification on a column of silica gel with a mixture of *n*-hexane/EtOAc (5:1) as eluent gave the desired product **7fa** as a colorless oil (32.5 mg, 96% yield, 99:1 d.r., 97% ee). The d.r. value was determined through 1H NMR of crude materials. Enantiomeric excess was established by HPLC analysis using a Chiralpak IG column. HPLC conditions: UV-absorption = 254 nm, *n*-hexane/isopropanol = 90:10, flow rate = 1.0 mL/min, column temperature = 25 °C, t_r (major) = 17.0 min, t_r (minor) = 23.2 min. $[\alpha]_D^{22} = -104.8$ ($c = 1.0$, CH_2Cl_2).

1H NMR (300 MHz, $CDCl_3$) δ 7.57 (dd, $J = 7.8, 0.9$ Hz, 1H), 7.28 (td, $J = 7.8, 1.2$ Hz, 1H), 7.21 (dd, $J = 7.8, 1.8$ Hz, 1H), 7.14 (td, $J = 7.8, 1.8$ Hz, 1H), 6.11 (dd, $J = 2.7, 0.9$ Hz, 1H), 5.63 (d, $J = 3.6$ Hz, 1H), 4.54 (dd, 6.9, 2.7 Hz, 1H), 4.18 (ddd, 9.9, 8.1, 1.8 Hz, 1H), 3.92–3.86 (m, 1H), 3.84 (s, 3H), 3.00-2.90 (m, 1H), 1.65 (tt, $J = 12.3, 9.9$ Hz, 1H), 1.26 (dddd, $J = 12.3, 7.5, 7.5, 2.1$ Hz, 1H).

^{13}C NMR (75 MHz, $CDCl_3$) δ 163.0, 143.0, 140.3, 133.1, 129.3, 128.9, 127.8, 124.3, 110.2, 101.4, 68.6, 52.5, 40.1, 38.1, 24.7.

HRMS (ESI, m/z) calcd for $C_{11}H_{14}O_3$ $[M + Na]^+$: 361.0046, found: 361.0047.

Methyl 4-(4-fluorophenyl)-3,3a,4,7a-tetrahydro-2H-furo[2,3-*b*]pyran-6-carboxylate (7ga)



Compound **7ga** was prepared according to the typical procedure from β,γ -unsaturated α -ketoester **5g** (20.8 mg, 0.1 mmol) and enolether **6a** (10.5 mg, 0.15 mmol) as starting material. Purification on a column of silica gel with a mixture of *n*-hexane/EtOAc (5:1) as eluent gave the desired product **7ga** as a white solid (27.0 mg, 97% yield, 99:1 d.r., 97% ee). The d.r. value was determined through 1H NMR of crude materials. Enantiomeric excess was established by HPLC analysis using a Chiralpak IG column. HPLC conditions: UV-absorption = 254 nm, *n*-hexane/isopropanol = 90:10, flow rate = 1.0 mL/min, column temperature = 25 °C, t_r (major) = 21.6 min, t_r (minor) = 24.6 min. $[\alpha]_D^{22} = -65.8$ ($c = 1.0$, CH_2Cl_2). Lit.^{22b} $[\alpha]_D^{25} = -59.3$ ($c = 0.45$, CH_2Cl_2). The analytical data for **7ga** matched with previously reported data.²²

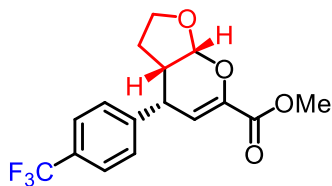
1H NMR (300 MHz, $CDCl_3$) δ 7.22-7.15 (m, 2H), 7.06-7.00 (m, 2H), 6.14 (dd, $J = 2.4, 1.2$ Hz, 1H), 5.64 (d, $J = 3.6$ Hz, 1H), 4.22-4.13 (m, 2H), 3.91-3.85 (m, 1H), 3.84 (s, 3H), 2.68-2.58 (m, 1H), 1.69 (tt, $J = 12.3, 9.6$ Hz, 1H), 1.35 (dddd, $J = 12.3, 7.2, 7.2, 2.1$ Hz, 1H).

^{13}C NMR (75 MHz, $CDCl_3$) δ 163.5 (d, $J = 244.2$ Hz), 163.0, 142.8, 136.9 (d, $J = 3.2$ Hz), 129.2 (d, $J = 8.0$ Hz), 115.7 (d, $J = 21.2$ Hz), 109.8, 101.4, 68.6, 52.5, 44.1, 37.6, 24.7.

^{19}F NMR (235 MHz, CD_2Cl_2) δ -115.55.

HRMS (ESI, m/z) calcd for $C_{11}H_{14}O_3$ $[M + Na]^+$: 301.0847, found: 301.0846.

Methyl 4-(4-(trifluoromethyl)phenyl)-3,3a,4,7a-tetrahydro-2H-furo[2,3-*b*]pyran-6-carboxylate (7ha)



Compound **7ha** was prepared according to the typical procedure from β,γ -unsaturated α -ketoester **5h** (25.8 mg, 0.1 mmol) and enolether **6a** (10.5 mg, 0.15 mmol) as starting material. Purification on a column of silica gel with a mixture of *n*-hexane/EtOAc (5:1) as eluent gave the desired product **7ha** as a white solid (31.5 mg, 96% yield, 99:1 d.r., 96% ee). The d.r. value was determined through 1H NMR of crude materials. Enantiomeric excess was established by HPLC analysis using a Chiralpak OD-H column. HPLC conditions: UV-absorption = 254 nm, *n*-hexane/isopropanol = 90:10, flow rate = 1.0 mL/min, column temperature = 25 °C, t_r (minor) = 17.2 min, t_r (major) = 19.1 min. $[\alpha]_D^{22} = -50.0$ ($c = 1.0$, CH_2Cl_2). Lit.^{22b} $[\alpha]_D^{25} = -42.6$ ($c = 0.25$, CH_2Cl_2). The analytical data for **7ha** matched with previously reported data.^{22b}

1H NMR (300 MHz, $CDCl_3$) δ 7.61 (d, $J = 8.1$ Hz, 2H), 7.35 (d, $J = 8.1$ Hz, 2H), 6.16 (dd, $J = 2.7, 1.2$ Hz, 1H), 5.66 (d, $J = 3.6$ Hz, 1H), 4.24 (dd, $J = 6.6, 2.4$ Hz, 1H), 4.23-4.16 (m, 1H), 3.92-3.86 (m, 1H), 3.85 (s, 3H),

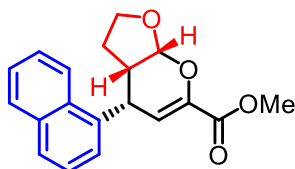
2.72-2.62 (m, 1H), 1.70 (tt, $J = 12.3, 9.6$ Hz, 1H), 1.34 (dddd, $J = 12.3, 7.2, 7.2, 2.1$ Hz, 1H).

^{13}C NMR (75 MHz, CDCl_3) δ 162.9, 145.3 (q, $J = 1.4$ Hz), 143.1, 129.9, 129.6 (q, $J = 32.4$ Hz), 128.1, 125.8 (q, $J = 3.8$ Hz), 124.3 (q, $J = 270.2$ Hz), 108.8, 101.4, 68.6, 52.6, 43.7, 38.2, 24.6.

^{19}F NMR (235 MHz, CD_2Cl_2) δ -62.50.

HRMS (ESI, m/z) calcd for $\text{C}_{11}\text{H}_{14}\text{O}_3$ $[\text{M} + \text{Na}]^+$: 351.0815, found: 351.0815.

Methyl 4-(naphthalen-1-yl)-3,3a,4,7a-tetrahydro-2H-furo[2,3-*b*]pyran-6-carboxylate (**7ia**)



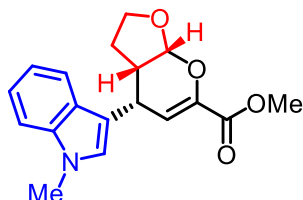
Compound **7ia** was prepared according to the typical procedure from β,γ -unsaturated α -ketoester **5i** (24.0 mg, 0.1 mmol) and enolether **6a** (10.5 mg, 0.15 mmol) as starting material. Purification on a column of silica gel with a mixture of *n*-hexane/EtOAc (5:1) as eluent gave the desired product **7ia** as a white solid (29.1 mg, 94% yield, 99:1 d.r., 97% ee). The d.r. value was determined through ^1H NMR of crude materials. Enantiomeric excess was established by HPLC analysis using a Chiralpak IG column. HPLC conditions: UV-absorption = 254 nm, *n*-hexane/isopropanol = 90:10, flow rate = 1.0 mL/min, column temperature = 25 °C, $t_r(\text{major}) = 22.0$ min, $t_r(\text{minor}) = 28.4$ min. $[\alpha]_D^{22} = -169.6$ ($c = 1.0$, CH_2Cl_2), lit.^{22a} $[\alpha]_D = -11.0$ ($c = 0.57$, CH_2Cl_2). The analytical data for **7ia** matched with previously reported data.²²

^1H NMR (300 MHz, CDCl_3) δ 8.05 (d, $J = 8.4$ Hz, 1H), 7.91 (dd, $J = 7.5, 1.8$ Hz, 1H), 7.80 (d, $J = 8.1$ Hz, 1H), 7.61-7.50 (m, 2H), 7.45 (t, $J = 7.6$ Hz, 1H), 7.36 (dd, $J = 6.9, 0.6$ Hz, 1H), 6.32 (dd, $J = 2.6, 1.0$ Hz, 1H), 5.74 (d, $J = 3.3$ Hz, 1H), 4.95 (dd, $J = 6.9, 2.7$ Hz, 1H), 4.15 (ddd, $J = 10.2, 8.1, 2.1$ Hz, 1H), 3.88 (s, 3H), 3.78 (ddd, $J = 9.9, 8.4, 6.9$ Hz, 1H), 2.99-2.89 (m, 1H), 1.69 (tt, $J = 12.3, 9.9$ Hz, 1H), 1.07 (dddd, $J = 12.3, 7.2, 7.2, 2.1$ Hz, 1H).

^{13}C NMR (75 MHz, CDCl_3) δ 163.1, 142.9, 137.0, 134.0, 131.2, 129.4, 128.0, 126.7, 126.0, 125.6, 125.0, 122.5, 111.4, 101.4, 68.5, 52.6, 42.2, 34.2, 24.9.

HRMS (ESI, m/z) calcd for $\text{C}_{11}\text{H}_{14}\text{O}_3$ $[\text{M} + \text{Na}]^+$: 333.1097, found: 333.1099.

Methyl 4-(1-methyl-1H-indol-3-yl)-3,3a,4,7a-tetrahydro-2H-furo[2,3-*b*]pyran-6-carboxylate (**7ja**)



Compound **7ja** was prepared according to the typical procedure from β,γ -unsaturated α -ketoester **5j** (24.3 mg, 0.1 mmol) and enolether **6a** (10.5 mg, 0.15 mmol) as starting material. Purification on a column of silica gel with a mixture of *n*-hexane/EtOAc (3:1) as eluent gave the desired product **7ja** as a colorless oil (28.8 mg, 92% yield, >20:1 d.r., 96% ee). The d.r. value was determined through ^1H NMR of crude materials. Enantiomeric excess was established by HPLC analysis using a Chiralpak IG column. HPLC conditions: UV-absorption =

254 nm, *n*-hexane/isopropanol = 90:10, flow rate = 1.0 mL/min, column temperature = 25 °C, $t_r(\text{major}) = 17.8$ min, $t_r(\text{minor}) = 25.6$ min. $[\alpha]_D^{22} = -95.4$ ($c = 1.0$, CH_2Cl_2).

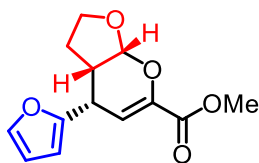
^1H NMR (300 MHz, CDCl_3) δ 7.61 (d, $J = 8.1$ Hz, 1H), 7.30 (d, $J = 8.1$ Hz, 1H), 7.29-7.23 (m, 1H), 6.90 (s, 1H), 7.13 (ddd, $J = 7.8, 6.6, 1.2$ Hz, 1H), 6.26 (dd, $J = 2.7, 0.9$ Hz, 1H), 5.69 (d, $J = 3.6$ Hz, 1H), 4.45 (dd, $J = 6.6, 2.7$ Hz, 1H), 4.15 (ddd, $J = 10.5, 8.4, 2.1$ Hz, 1H), 3.88-3.75 (m, 1H), 3.85 (s, 3H), 3.77 (s, 3H), 2.96-2.86 (m, 1H), 1.71 (tt, $J = 12.3, 9.6$ Hz, 1H), 1.43 (dddd, $J = 12.3, 7.5, 7.5, 2.1$ Hz, 1H).

^{13}C NMR (75 MHz, CDCl_3) δ 163.3, 142.1, 137.3, 127.0, 122.1, 119.3, 118.8, 114.6, 111.3, 109.6, 101.4, 68.5, 52.5, 43.2, 32.9, 30.1, 25.3.

IR (film): ν (cm^{-1}) 2950, 1726, 1250, 1736, 1372, 1316, 1289, 1241, 1205, 1154, 1126, 1074, 1045, 833, 735, 700, 427.

HRMS (ESI, m/z) calcd for $\text{C}_{11}\text{H}_{14}\text{O}_3$ $[\text{M} + \text{Na}]^+$: 336.1206, found: 336.1215.

Methyl 4-(furan-2-yl)-3,3a,4,7a-tetrahydro-2H-furo[2,3-*b*]pyran-6-carboxylate (7ka)



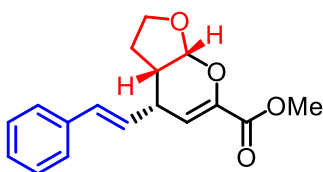
Compound **7ka** was prepared according to the typical procedure from β,γ -unsaturated α -ketoester **5k** (18.0 mg, 0.1 mmol) and enolether **6a** (10.5 mg, 0.15 mmol) as starting material. Purification on a column of silica gel with a mixture of *n*-hexane/EtOAc (5:1) as eluent gave the desired product **7ka** as a colorless oil (24.8 mg, 99% yield, 99:1 d.r., 98% ee). The d.r. value was determined through ^1H NMR of crude materials. Enantiomeric excess was established by HPLC analysis using a Chiralpak IG column. HPLC conditions: UV-absorption = 254 nm, *n*-hexane/isopropanol = 90:10, flow rate = 1.0 mL/min, column temperature = 25 °C, $t_r(\text{major}) = 19.0$ min, $t_r(\text{minor}) = 24.6$ min. $[\alpha]_D^{22} = -64.6$ ($c = 1.0$, CH_2Cl_2).

^1H NMR (300 MHz, CDCl_3) δ 7.35 (d, $J = 1.5$ Hz, 1H), 6.32 (dd, $J = 3.0, 1.8$ Hz, 1H), 6.13 (d, $J = 3.3$ Hz, 1H), 6.11 (dd, $J = 2.7, 1.2$ Hz, 1H), 5.63 (d, $J = 3.6$ Hz, 1H), 4.95 (dd, $J = 6.9, 2.7$ Hz, 1H), 4.18 (ddd, $J = 11.7, 6.0, 3.0$ Hz, 2H), 3.97-3.89 (m, 1H), 3.82 (s, 3H), 2.87-2.76 (m, 1H), 1.78-1.57 (m, 2H).

^{13}C NMR (75 MHz, CDCl_3) δ 162.9, 154.3, 142.6, 141.9, 110.4, 107.2, 105.9, 101.2, 68.6, 52.5, 41.8, 32.6, 24.7.

HRMS (ESI, m/z) calcd for $\text{C}_{11}\text{H}_{14}\text{O}_3$ $[\text{M} + \text{Na}]^+$: 273.0733, found: 273.0735.

Methyl 4-cinnamyl-3,3a,4,7a-tetrahydro-2H-furo[2,3-*b*]pyran-6-carboxylate (7la)



Compound **7la** was prepared according to the typical procedure from β,γ -unsaturated α -ketoester **5l** (21.6 mg, 0.1 mmol) and enolether **6a** (10.5 mg, 0.15 mmol) as starting material. Purification on a column of silica gel with a mixture of *n*-hexane/EtOAc (5:1) as eluent gave the desired product **7la** as a colorless oil (28.0 mg, 93%

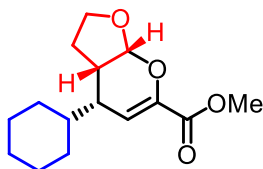
yield, 98:2 d.r., 97% ee). The d.r. value was determined through ^1H NMR of crude materials. Enantiomeric excess was established by HPLC analysis using a Chiralpak IG column. HPLC conditions: UV-absorption = 254 nm, *n*-hexane/isopropanol = 90:10, flow rate = 1.0 mL/min, column temperature = 25 °C, $t_r(\text{major})$ = 24.7 min, $t_r(\text{minor})$ = 28.7 min. $[\alpha]_D^{22} = +10.6$ ($c = 1.0$, CH_2Cl_2), lit.^{22a} $[\alpha]_{365}^{25} = 117.24$, ($c = 0.52$, in CH_2Cl_2). The analytical data for **7la** matched with previously reported data.²²

^1H NMR (300 MHz, CDCl_3) δ 7.38-7.24 (m, 1H), 6.54 (d, $J = 15.9$ Hz, 1H), 6.13 (dd, $J = 15.9, 1.5$ Hz, 1H), 6.03 (dd, $J = 2.7, 1.2$ Hz, 1H), 5.58 (d, $J = 3.6$ Hz, 1H), 4.23 (dd, $J = 9.6, 8.4, 2.4$ Hz, 1H), 4.02-3.93 (m, 1H), 3.82 (s, 3H), 3.66 (ddd, $J = 9.0, 6.9, 2.1$ Hz, 1H), 2.63-2.52 (m, 1H), 1.43 (dddd, $J = 12.3, 7.8, 2.4$ Hz, 1H), 1.80 (tt, $J = 12.3, 9.6$ Hz, 1H).

^{13}C NMR (75 MHz, CDCl_3) δ 163.1, 141.8, 136.9, 131.7, 128.8, 128.7, 127.8, 126.4, 110.0, 101.3, 68.7, 52.5, 42.6, 36.0, 24.5.

HRMS (ESI, m/z) calcd for $\text{C}_{11}\text{H}_{14}\text{O}_3$ $[\text{M} + \text{Na}]^+$: 309.1097, found: 309.1099.

Methyl 4-cyclohexyl-3,3a,4,7a-tetrahydro-2H-furo[2,3-*b*]pyran-6-carboxylate (**7ma**)



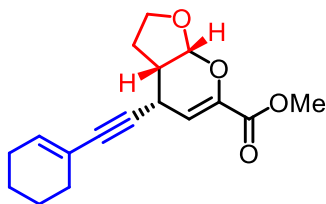
Compound **7ma** was prepared according to the typical procedure from β,γ -unsaturated α -ketoester **5m** (19.6 mg, 0.1 mmol) and enolether **6a** (10.5 mg, 0.15 mmol) as starting material. Purification on a column of silica gel with a mixture of *n*-hexane/EtOAc (5:1) as eluent gave the desired product **7ma** as a colorless oil (26.1 mg, 98% yield, >20:1 d.r., 94% ee). The d.r. value was determined through ^1H NMR of crude materials. Enantiomeric excess was established by HPLC analysis using a Chiralpak IG column. HPLC conditions: UV-absorption = 254 nm, *n*-hexane/isopropanol = 90:10, flow rate = 1.0 mL/min, column temperature = 25 °C, $t_r(\text{major})$ = 17.5 min, $t_r(\text{minor})$ = 19.2 min. $[\alpha]_D^{22} = -30.6$ ($c = 1.0$, CH_2Cl_2).

^1H NMR (300 MHz, CDCl_3) δ 6.05 (dd, $J = 2.1, 1.5$ Hz, 1H), 5.52 (d, $J = 3.9$ Hz, 1H), 4.17 (ddd, $J = 9.6, 8.4, 2.4$ Hz, 1H), 3.98-3.90 (m, 1H), 3.77 (s, 3H), 2.53-2.36 (m, 2H), 2.06-1.85 (m, 3H), 1.80-1.72 (m, 3H), 1.70-1.62 (m, 1H), 1.31-1.14 (m, 4H), 1.04-0.92 (m, 2H).

^{13}C NMR (75 MHz, CDCl_3) δ 163.3, 141.4, 110.1, 102.1, 68.5, 52.3, 40.6, 39.2, 38.1, 31.1, 31.0, 26.5, 26.2, 26.1, 23.5.

HRMS (ESI, m/z) calcd for $\text{C}_{11}\text{H}_{14}\text{O}_3$ $[\text{M} + \text{Na}]^+$: 289.1410, found: 289.1409.

Methyl 4-(cyclohex-1-en-1-ylethynyl)-3,3a,4,7a-tetrahydro-2H-furo[2,3-*b*]pyran-6-carboxylate (**7na**)



Compound **7na** was prepared according to the typical procedure from β,γ -unsaturated α -ketoester **5n** (21.8 mg,

0.1 mmol) and enolether **6a** (10.5 mg, 0.15 mmol) as starting material. Purification on a column of silica gel with a mixture of *n*-hexane/EtOAc (5:1) as eluent gave the desired product **7na** as a light yellow oil (27.0 mg, 94% yield, 97:3 d.r., 90% ee). The d.r. value was determined through ¹H NMR of crude materials. Enantiomeric excess was established by HPLC analysis using a Chiralpak IA column. HPLC conditions: UV-absorption = 254 nm, *n*-hexane/isopropanol = 98:2, flow rate = 0.8 mL/min, column temperature = 25 °C, *t*_r(major) = 19.0 min, *t*_r(minor) = 21.9 min. [α]_D²² = + 28.6 (*c* = 1.0, CH₂Cl₂).

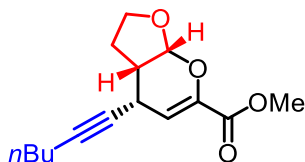
¹H NMR (300 MHz, CDCl₃) δ 6.08-6.03 (m, 1H), 5.95 (dd, *J* = 2.7, 1.2 Hz, 1H), 5.48 (d, *J* = 3.6 Hz, 1H), 4.22 (ddd, *J* = 9.6, 8.4, 2.4 Hz, 1H), 4.02-3.94 (m, 1H), 3.87 (dd, *J* = 6.3, 2.7 Hz, 1H), 3.80 (s, 3H), 2.71-2.60 (m, 1H), 2.22-2.04 (m, 5H), 1.92 (tt, *J* = 12.3, 9.6 Hz, 1H), 1.67-1.53 (m, 1H).

¹³C NMR (75 MHz, CDCl₃) δ 162.9, 141.1, 135.0, 120.5, 108.6, 100.6, 84.5, 84.0, 68.5, 52.5, 41.6, 29.5, 26.1, 25.7, 22.4, 21.6.

IR (film): ν (cm⁻¹) 2934, 1730, 1652, 1436, 1371, 1303, 1239, 1131, 1075, 1047, 1201, 980, 917, 766, 734.

HRMS (ESI, *m/z*) calcd for C₁₁H₁₄O₃ [M + Na]⁺: 311.1254, found: 311.1252.

Methyl 4-(hex-1-yn-1-yl)-3,3a,4,7a-tetrahydro-2H-furo[2,3-*b*]pyran-6-carboxylate (**7oa**)



Compound **7oa** was prepared according to the typical procedure from β,γ -unsaturated α -ketoester **5o** (19.4 mg, 0.1 mmol) and enolether **6a** (10.5 mg, 0.15 mmol) as starting material. Purification on a column of silica gel with a mixture of *n*-hexane/EtOAc (5:1) as eluent gave the desired product **7oa** as a light yellow oil (25.8 mg, 98% yield, 98:2 d.r., 95% ee). The d.r. value was determined through ¹H NMR of crude materials. Enantiomeric excess was established by HPLC analysis using a Chiralpak IA column. HPLC conditions: UV-absorption = 254 nm, *n*-hexane/isopropanol = 98:2, flow rate = 0.8 mL/min, column temperature = 25 °C, *t*_r(major) = 18.1 min, *t*_r(minor) = 21.3 min. [α]_D²² = - 36.0 (*c* = 1.0, CH₂Cl₂).

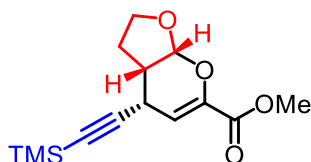
¹H NMR (300 MHz, CDCl₃) δ 5.92 (dd, *J* = 2.7, 1.2 Hz, 1H), 5.46 (d, *J* = 3.9 Hz, 1H), 4.21 (ddd, *J* = 9.6, 8.4, 2.7 Hz, 1H), 4.02-3.94 (m, 1H), 3.80 (s, 3H), 3.75-3.70 (m, 1H), 2.67-2.57 (m, 1H), 2.19-2.09 (m, 3H), 1.89 (tt, *J* = 12.3, 9.6 Hz, 1H), 1.52-1.33 (m, 4H), 0.91 (t, *J* = 7.0 Hz, 3H).

¹³C NMR (75 MHz, CDCl₃) δ 162.9, 141.0, 109.2, 100.6, 82.3, 77.9, 68.5, 52.5, 41.8, 31.0, 25.7, 25.6, 22.0, 18.4, 13.7.

IR (film): ν (cm⁻¹) 2956, 2934, 1732, 1652, 1438, 1372, 1252, 1130, 1085, 1047, 981, 922, 875, 840, 767, 736.

HRMS (ESI, *m/z*) calcd for C₁₁H₁₄O₃ [M + Na]⁺: 287.1254, found: 287.1253.

Methyl 4-((trimethylsilyl)ethynyl)-3,3a,4,7a-tetrahydro-2H-furo[2,3-*b*]pyran-6-carboxylate (**7pa**)



Compound **7pa** was prepared according to the typical procedure from β,γ -unsaturated α -ketoester **5p** (21.0 mg, 0.1 mmol) and enolether **6a** (10.5 mg, 0.15 mmol) as starting material. Purification on a column of silica gel with a mixture of *n*-hexane/EtOAc (5:1) as eluent gave the desired product **7pa** as a light yellow oil (22.4 mg, 80% yield, 98:2 d.r., 95% ee). The d.r. value was determined through ^1H NMR of crude materials. Enantiomeric excess was established by HPLC analysis using a Chiralpak IA column. HPLC conditions: UV-absorption = 254 nm, *n*-hexane/isopropanol = 98:2, flow rate = 0.8 mL/min, column temperature = 25 °C, $t_r(\text{major})$ = 11.9 min, $t_r(\text{minor})$ = 13.7 min. $[\alpha]_D^{22} = -6.0$ ($c = 1.0$, CH_2Cl_2).

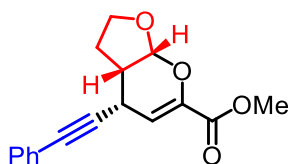
^1H NMR (300 MHz, CDCl_3) δ 5.94 (dd, $J = 2.4, 0.3$ Hz, 1H), 5.46 (d, $J = 3.9$ Hz, 1H), 4.23 (ddd, $J = 9.6, 8.4, 2.4$ Hz, 1H), 4.00-3.95 (m, 1H), 3.81 (s, 3H), 3.78 (dd, $J = 6.3, 2.7$ Hz, 1H), 2.70-2.60 (m, 1H), 2.22-2.12 (m, 1H), 1.92 (tt, $J = 12.3, 9.6$ Hz, 1H), 0.16 (s, 9H).

^{13}C NMR (75 MHz, CDCl_3) δ 162.8, 141.3, 107.9, 103.9, 100.4, 86.7, 68.5, 52.5, 41.2, 26.5, 25.6, 0.1.

IR (film): ν (cm^{-1}) 2957, 2900, 2175, 1745, 1652, 1508, 1438, 1380, 1304, 1249, 1202, 1133, 1064, 1024, 994, 927, 840, 761, 701, 646, 618.

HRMS (ESI, m/z) calcd for $\text{C}_{11}\text{H}_{14}\text{O}_3$ $[\text{M} + \text{Na}]^+$: 303.1023, found: 303.1024.

Methyl 4-(phenylethynyl)-3,3a,4,7a-tetrahydro-2H-furo[2,3-*b*]pyran-6-carboxylate (**7qa**)



Compound **7qa** was prepared according to the typical procedure from β,γ -unsaturated α -ketoester **7q** (21.4 mg, 0.1 mmol) and enolether **6a** (10.5 mg, 0.15 mmol) as starting material. Purification on a column of silica gel with a mixture of *n*-hexane/EtOAc (5:1) as eluent gave the desired product **7qa** as a light yellow oil (27.9 mg, 98% yield, 98:2 d.r., 95% ee). The d.r. value was determined through ^1H NMR of crude materials. Enantiomeric excess was established by HPLC analysis using a Chiralpak OD-H column. HPLC conditions: UV-absorption = 254 nm, *n*-hexane/isopropanol = 90:10, flow rate = 1.0 mL/min, column temperature = 25 °C, $t_r(\text{minor})$ = 18.6 min, $t_r(\text{major})$ = 20.3 min. $[\alpha]_D^{22} = +60.0$ ($c = 0.5$, CH_2Cl_2).

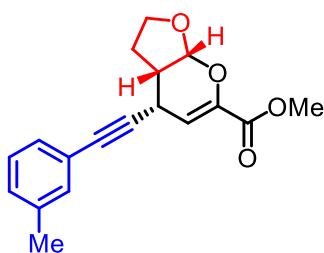
^1H NMR (300 MHz, CDCl_3) δ 7.42-7.39 (m, 2H), 7.32-7.28 (m, 3H), 6.03 (dd, $J = 2.7, 0.9$ Hz, 1H), 5.53 (d, $J = 3.9$ Hz, 1H), 4.25 (ddd, $J = 9.6, 8.4, 2.7$ Hz, 1H), 4.06-3.98 (m, 2H), 3.82 (s, 3H), 2.80-2.70 (m, 1H), 2.26 (dddd, $J = 12.3, 7.5, 7.5, 2.7$ Hz, 1H), 2.00 (tt, $J = 12.3, 9.6$ Hz, 1H).

^{13}C NMR (75 MHz, CDCl_3) δ 162.8, 141.4, 131.8, 128.5, 128.4, 123.0, 108.0, 100.6, 87.4, 82.2, 68.5, 52.5, 41.5, 26.2, 25.7.

IR (film): ν (cm^{-1}) 2192, 1725, 1684, 1579, 1437, 1276, 1237, 1083, 1031, 976, 950, 866, 783, 751, 685, 524, 459, 413.

HRMS (ESI, m/z) calcd for $\text{C}_{11}\text{H}_{14}\text{O}_3$ $[\text{M} + \text{Na}]^+$: 307.0941, found: 307.0940.

Methyl 4-(*m*-tolylethynyl)-3,3a,4,7a-tetrahydro-2H-furo[2,3-*b*]pyran-6-carboxylate (**7ra**)



Compound **7ra** was prepared according to the typical procedure from β,γ -unsaturated α -ketoester **5r** (22.8 mg, 0.1 mmol) and enolether **6a** (10.5 mg, 0.15 mmol) as starting material. Purification on a column of silica gel with a mixture of *n*-hexane/EtOAc (5:1) as eluent gave the desired product **7ra** as a light yellow colorless oil (27.3 mg, 92% yield, 98:2 d.r., 96% ee). The d.r. value was determined through ^1H NMR of crude materials. Enantiomeric excess was established by HPLC analysis using a Chiralpak IG column. HPLC conditions: UV-absorption = 254 nm, *n*-hexane/isopropanol = 90:10, flow rate = 1.0 mL/min, column temperature = 25 °C, $t_r(\text{major}) = 16.9$ min, $t_r(\text{minor}) = 20.9$ min. $[\alpha]_D^{22} = +32.2$ ($c = 1.0$, CH_2Cl_2).

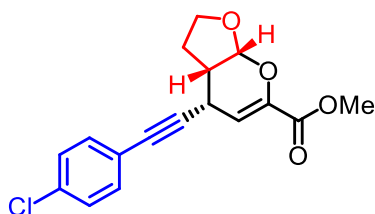
^1H NMR (300 MHz, CDCl_3) δ 7.23-7.18 (m, 3H), 7.16-7.09 (m, 1H), 6.03 (dd, $J = 2.4, 0.9$ Hz, 1H), 5.53 (d, $J = 3.9$ Hz, 1H), 4.25 (ddd, $J = 9.6, 8.4, 2.4$ Hz, 1H), 4.06-3.97 (m, 2H), 3.82 (s, 3H), 2.80-2.70 (m, 1H), 2.32 (s, 3H), 2.26 (dddd, $J = 12.3, 7.5, 7.5, 2.7$ Hz, 1H), 2.00 (tt, $J = 12.3, 9.6$ Hz, 1H).

^{13}C NMR (75 MHz, CDCl_3) δ 162.8, 141.4, 138.2, 132.4, 129.3, 128.8, 128.4, 122.8, 108.1, 100.6, 87.0, 82.3, 68.5, 52.5, 41.5, 26.2, 25.7, 21.3.

IR (film): ν (cm^{-1}) 2952, 1730, 1651, 1437, 1371, 1344, 1238, 1128, 1052, 921, 891, 839, 785, 765, 692.

HRMS (ESI, m/z) calcd for $\text{C}_{11}\text{H}_{14}\text{O}_3$ $[\text{M} + \text{Na}]^+$: 321.1097, found: 321.1097.

Methyl 4-((4-chlorophenyl)ethynyl)-3,3a,4,7a-tetrahydro-2H-furo[2,3-*b*]pyran-6-carboxylate (**7sa**)



Compound **7sa** was prepared according to the typical procedure from β,γ -unsaturated α -ketoester **5s** (24.8 mg, 0.1 mmol) and enolether **6a** (10.5 mg, 0.15 mmol) as starting material. Purification on a column of silica gel with a mixture of *n*-hexane/EtOAc (5:1) as eluent gave the desired product **7sa** as a light yellow solid (31.0 mg, 97% yield, 98:2 d.r., 94% ee). The d.r. value was determined through ^1H NMR of crude materials. Enantiomeric excess was established by HPLC analysis using a Chiralpak IG column. HPLC conditions: UV-absorption = 254 nm, *n*-hexane/isopropanol = 90:10, flow rate = 1.0 mL/min, column temperature = 25 °C, $t_r(\text{major}) = 19.1$ min, $t_r(\text{minor}) = 25.7$ min. $[\alpha]_D^{22} = +55.5$ ($c = 0.68$, CH_2Cl_2).

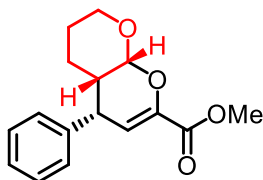
^1H NMR (300 MHz, CDCl_3) δ 7.33 (dd, $J = 6.6, 2.1$ Hz, 2H), 7.28 (dd, $J = 6.6, 2.1$ Hz, 2H), 6.01 (dd, $J = 2.4, 0.9$ Hz, 1H), 5.53 (d, $J = 3.6$ Hz, 1H), 4.25 (ddd, $J = 9.6, 8.4, 2.4$ Hz, 1H), 4.06-3.97 (m, 2H), 3.82 (s, 3H), 2.79-2.69 (m, 1H), 2.32 (s, 3H), 2.24 (dddd, $J = 12.3, 7.5, 2.4$ Hz, 1H), 1.99 (tt, $J = 12.3, 9.6$ Hz, 1H).

^{13}C NMR (75 MHz, CDCl_3) δ 162.8, 141.5, 134.5, 133.0, 128.8, 121.5, 107.4, 100.5, 88.5, 81.1, 68.5, 52.6, 41.4, 26.2, 25.7.

IR (film): ν (cm⁻¹) 2952, 1730, 1651, 1589, 1489, 1437, 1397, 1371, 1344, 1315, 1206, 1128, 1089, 1076, 1050, 920, 827, 767, 751, 737, 524, 470.

HRMS (ESI, m/z) calcd for C₁₁H₁₄O₃ [M + Na]⁺: 249.0313, found: 249.0318.

Methyl 5-phenyl-3,4,4a,8a-tetrahydro-2H,5H-pyrano[2,3-*b*]pyran-7-carboxylate (**7ab**)



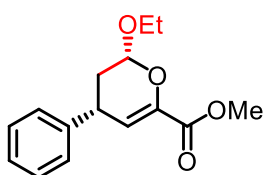
Compound **7ab** was prepared according to the typical procedure from β,γ -unsaturated α -ketoester **5a** (19.0 mg, 0.1 mmol) and enolether **6b** (16.8 mg, 0.2 mmol) as starting material. Purification on a column of silica gel with a mixture of *n*-hexane/EtOAc (5:1) as eluent gave the desired product **7ab** as a colorless oil (22.8 mg, 83% yield, 94:6 d.r., 96% ee). The d.r. value was determined through ¹H NMR of crude materials. Enantiomeric excess was established by HPLC analysis using a Chiralpak IG column. HPLC conditions: UV-absorption = 254 nm, *n*-hexane/isopropanol = 90:10, flow rate = 1.0 mL/min, column temperature = 25 °C, t_r (major) = 13.6 min, t_r (minor) = 19.1 min. $[\alpha]_D^{22} = +7.0$ ($c = 1.0$, CH₂Cl₂), lit.^{22a} $[\alpha]_{405} = +57.25$ ($c = 0.54$, in CH₂Cl₂, 94% ee). The analytical data for **7ab** matched with previously reported data.²²

¹H NMR (300 MHz, CDCl₃) δ 7.36-7.26 (m, 3H), 7.17-7.14 (m, 2H), 6.15 (s, 1H), 5.52 (s, 1H), 4.04 (dd, $J = 6.0, 2.4$ Hz, 1H), 4.04 (dd, $J = 11.4, 4.5$ Hz, 1H), 3.85 (s, 3H), 3.74-3.70 (m, 1H), 2.17-2.11 (m, 1H), 1.62-1.52 (m, 2H), 1.40-1.26 (m, 1H), 0.96-0.83 (m, 1H).

¹³C NMR (75 MHz, CDCl₃) δ 163.0, 143.3, 139.8, 128.6, 129.2, 127.0, 111.5, 98.2, 61.6, 52.4, 42.2, 37.8, 24.9, 19.2.

HRMS (ESI, m/z) calcd for C₁₁H₁₄O₃ [M + Na]⁺: 297.1097, found: 297.1098.

Methyl 2-ethoxy-4-phenyl-3,4-dihydro-2H-pyran-6-carboxylate (**7ac**)



Compound **7ac** was prepared according to the typical procedure from β,γ -unsaturated α -ketoester **5a** (19.0 mg, 0.1 mmol) and enolether **6c** (36 mg, 0.5 mmol) as starting material. Purification on a column of silica gel with a mixture of *n*-hexane/EtOAc (50:1 to 25:1) as eluent gave the desired product **7ac** as a colorless oil (24.9 mg, 95% yield, 88:12 d.r., 91% ee). The d.r. value was determined through ¹H NMR of crude materials. Enantiomeric excess was established by HPLC analysis using a Chiralpak IG column. HPLC conditions: UV-absorption = 254 nm, *n*-hexane/isopropanol = 95:5, flow rate = 1.0 mL/min, column temperature = 25 °C, t_r (major) = 8.7 min, t_r (minor) = 10.6 min. $[\alpha]_D^{22} = +14.0$ ($c = 1.0$, CH₂Cl₂), lit.^{22a} $[\alpha]_D = +3.52$ ($c = 0.31$, in CH₂Cl₂, 99% ee). The analytical data for **7ac** matched with previously reported data.^{22a}

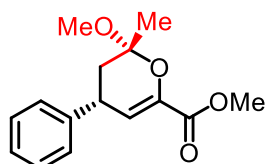
¹H NMR (300 MHz, CDCl₃) δ 7.34-7.28 (m, 2H), 7.26-7.19 (m, 3H), 6.16 (dd, $J = 9.0, 0.9$ Hz, 1H) 5.16 (dd, $J = 7.8, 2.1$ Hz, 1H), 4.03 (ddt, $J = 9.3, 7.2, 7.2$ Hz, 1H), 3.72 (ddd, $J = 9.6, 6.0, 3.0$ Hz, 1H), 3.64 (ddt, $J =$

9.6, 7.2, 7.2 Hz, 1H), 2.31 (dddd, $J = 13.5, 7.8, 1.8, 0.9$ Hz, 1H), 1.97 (ddd, $J = 13.5, 9.3, 7.8$ Hz, 1H), 1.23 (t, $J = 7.0$ Hz, 3H).

^{13}C NMR (75 MHz, CDCl_3) δ 163.3, 143.0, 142.5, 128.7, 127.7, 127.0, 114.6, 100.1, 64.8, 52.3, 37.9, 16.2, 15.2.

HRMS (ESI, m/z) calcd for $\text{C}_{11}\text{H}_{14}\text{O}_3$ $[\text{M} + \text{Na}]^+$: 285.1097, found: 285.1098.

Methyl 2-methoxy-2-methyl-4-phenyl-3,4-dihydro-2H-pyran-6-carboxylate (**7ad**)



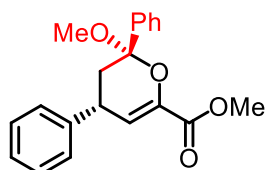
Compound **7ad** was prepared according to the typical procedure from β,γ -unsaturated α -ketoester **5a** (19.0 mg, 0.1 mmol) and enolether **6d** (10.8 mg, 0.15 mmol) as starting material. Purification on a column of silica gel with a mixture of *n*-hexane/EtOAc (50:1 to 25:1) as eluent gave the desired product **7ad** as a colorless oil (25.7 mg, 98% yield, 70:30 d.r., 88% ee). The d.r. value was determined through ^1H NMR of crude materials. Enantiomeric excess was established by HPLC analysis using a Chiralpak IG column. HPLC conditions: UV-absorption = 254 nm, *n*-hexane/isopropanol = 95:5, flow rate = 0.8 mL/min, column temperature = 25 °C, $t_r(\text{major}) = 10.6$ min, $t_r(\text{minor}) = 11.7$ min. $[\alpha]_{\text{D}}^{22} = +59.8$ ($c = 0.85$, CH_2Cl_2), lit.^{22a} $[\alpha]_{\text{D}} = +27.5$ ($c = 0.16$, CH_2Cl_2 , 99% ee). The analytical data for **7ad** matched with previously reported data.^{22a}

^1H NMR (300 MHz, CDCl_3) δ 7.35-7.29 (m, 2H), 7.25-7.20 (m, 3H), 6.24 (d, $J = 3.3$ Hz, 1H), 3.83 (s, 3H), 3.63 (td, $J = 7.2, 3.3$ Hz, 1H), 3.31 (s, 3H), 2.10 (d, $J = 7.2$ Hz, 2H).

^{13}C NMR (75 MHz, CDCl_3) δ 163.5, 143.4, 142.6, 128.6, 127.9, 126.8, 113.8, 101.4, 52.4, 49.3, 39.1, 37.4, 22.3.

HRMS (ESI, m/z) calcd for $\text{C}_{11}\text{H}_{14}\text{O}_3$ $[\text{M} + \text{Na}]^+$: 285.1097, found: 285.1102.

Methyl 2-methoxy-2,4-diphenyl-3,4-dihydro-2H-pyran-6-carboxylate (**7ae**)



Compound **7ae** was prepared according to the typical procedure from β,γ -unsaturated α -ketoester **5a** (38.0 mg, 0.2 mmol) and enolether **6e** (40.2 mg, 0.3 mmol) as starting material. Purification on a column of silica gel with a mixture of *n*-hexane/EtOAc (50:1 to 25:1) as eluent gave the desired product **7ae** as a colorless oil (26.0 mg, 40% yield, 83:17 d.r., 65% ee). The d.r. value was determined through ^1H NMR of crude materials. Enantiomeric excess was established by HPLC analysis using a Chiralpak IG column. HPLC conditions: UV-absorption = 254 nm, *n*-hexane/isopropanol = 95:5, flow rate = 0.8 mL/min, column temperature = 25 °C, $t_r(\text{minor}) = 10.0$ min, $t_r(\text{major}) = 10.5$ min. $[\alpha]_{\text{D}}^{22} = +27.1$ ($c = 0.5$, CH_2Cl_2). The analytical data for **7ae** matched with previously reported data.¹³

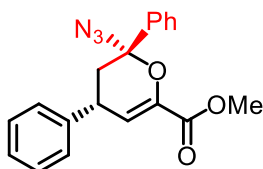
^1H NMR (300 MHz, CDCl_3) δ 7.48-7.36 (m, 5H), 7.34-7.28 (m, 2H), 7.26-7.19 (m, 3H), 6.26 (d, $J = 3.3$ Hz,

1H), 3.88 (s, 3H), 3.30 (td, $J = 7.5, 3.3$ Hz, 1H), 3.13 (s, 3H), 2.48 (dd, $J = 12.9, 6.9$ Hz, 1H), 2.32 (dd, $J = 13.5, 7.8$ Hz, 1H).

^{13}C NMR (75 MHz, CDCl_3) δ 163.3, 143.1, 142.5, 139.4, 128.7, 128.6, 127.9, 126.9, 126.4, 115.2, 103.0, 52.4, 50.4, 41.4, 37.1.

HRMS (ESI, m/z) calcd for $\text{C}_{11}\text{H}_{14}\text{O}_3$ $[\text{M} + \text{Na}]^+$: 347.1254, found: 347.1266.

Methyl 2-azido-2,4-diphenyl-3,4-dihydro-2H-pyran-6-carboxylate (**7af**)



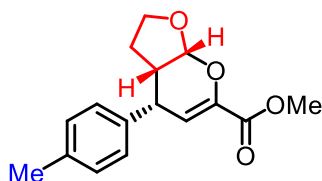
Compound **7af** was prepared according to the typical procedure from β,γ -unsaturated α -ketoester **5a** (38.0 mg, 0.2 mmol) and **6f** (43.5 mg, 0.30 mmol) as starting material. Purification on a column of silica gel with a mixture of *n*-hexane/EtOAc (50:1 to 25:1) as eluent gave the desired product **7af** as a colorless oil (28.1 mg, 42% yield, >20:1 d.r., 95% ee). The d.r. value was determined through ^1H NMR of crude materials. Enantiomeric excess was established by HPLC analysis using a Chiralpak OD-H column. HPLC conditions: UV-absorption = 254 nm, *n*-hexane/isopropanol = 99:1, flow rate = 1.0 mL/min, column temperature = 25 °C, $t_r(\text{major}) = 12.1$ min, $t_r(\text{minor}) = 15.2$ min. $[\alpha]_{\text{D}}^{22} = +17.1$ ($c = 0.5$, CHCl_3), lit.¹⁸ $[\alpha]_{\text{D}}^{18} = +11.5$ ($c = 0.51$, CHCl_3 , >99% ee). The analytical data for **7af** matched with previously reported data.¹⁸

^1H NMR (300 MHz, CDCl_3) δ 7.55-7.42 (m, 5H), 7.37-7.28 (m, 3H), 7.23-7.18 (m, 2H), 6.21 (dd, $J = 3.6, 1.5$ Hz, 1H), 3.90 (s, 3H), 3.29 (ddd, $J = 11.4, 7.8, 3.6$ Hz, 1H), 2.67 (ddd, $J = 16.8, 7.8, 1.5$ Hz, 1H), 2.23 (dd, $J = 16.5, 12.0$ Hz, 1H).

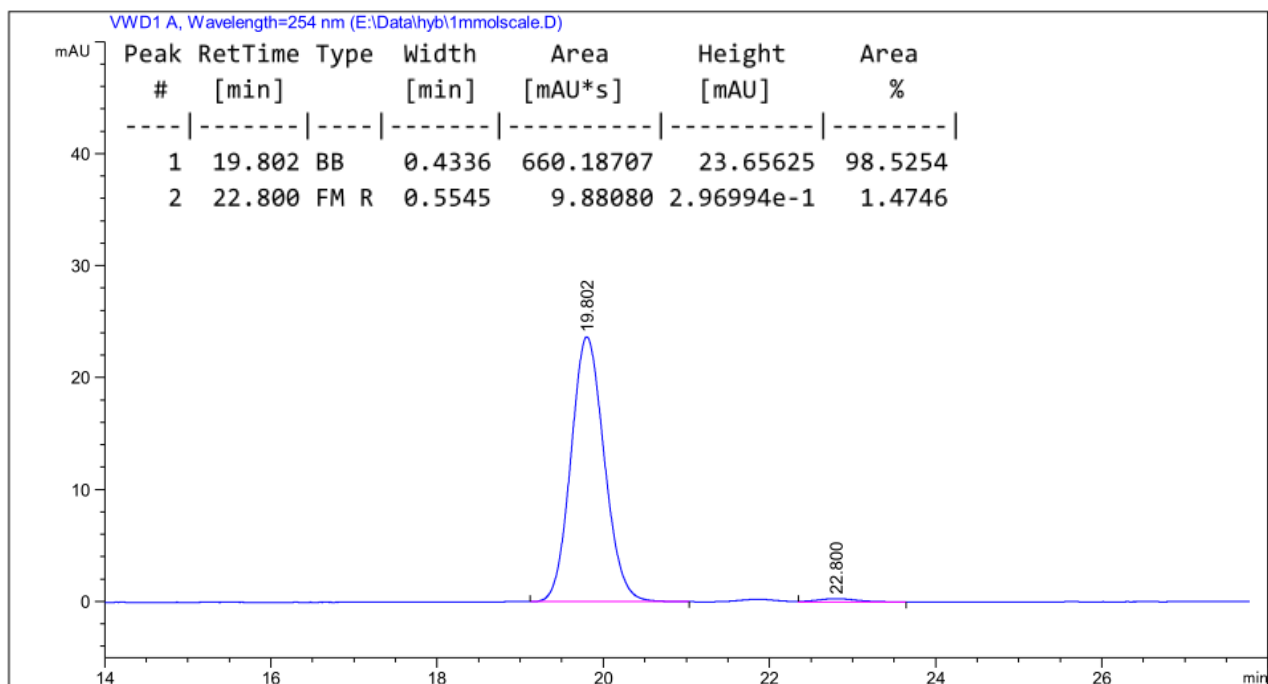
^{13}C NMR (75 MHz, CDCl_3) δ 162.6, 142.8, 141.9, 138.3, 129.4, 129.2, 129.0, 128.9, 127.7, 127.3, 125.4, 115.2, 94.5, 52.6, 39.9, 36.8.

HRMS (ESI, m/z) calcd for $\text{C}_{11}\text{H}_{14}\text{O}_3$ $[\text{M} + \text{Na}]^+$: 358.1162, found: 358.1169.

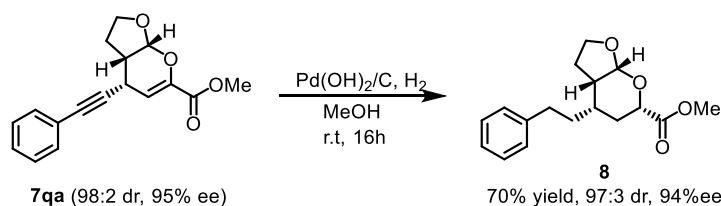
Synthesis on 1 mmol Scale:



1 mmol scale synthesis was performed according to the typical procedure from β,γ -unsaturated α -ketoester **5c** (204 mg, 1.0 mmol), **6a** (105 mg, 1.5 mmol) and $\Lambda\text{-Fe5}$ (11.7 mg, 0.01 mmol, 1 mol%) as starting material and reaction time of 8 hours. Purification on a column of silica gel with a mixture of *n*-hexane/EtOAc (20:1 to 5:1) as eluent gave the desired product **7ca** as a white solid (272 mg, 99% yield, 99:1 d.r., 97% ee). The d.r. value was determined through ^1H NMR of crude materials. Enantiomeric excess was established by HPLC analysis using a Chiralpak IG column.



Synthetic Transformation



To a solution of methyl 4-(phenylethynyl)-3,3a,4,7a-tetrahydro-2H-furo[2,3-*b*]pyran-6-carboxylate (**7qa**, 28.4 mg, 0.1 mmol) in methanol was added Pd(OH)₂/C (10 mg). The resulting mixture was bubbled with hydrogen for 10 min and stirred at room temperature for 16 hours. The reaction mixture was filtered by diatomite to remove insoluble materials, then the filtrate was concentrated and subjected to flash silica gel chromatography (*n*-hexane/EtOAc = 5:1 to 3:1) to give the methyl 4-phenethylhexahydro-2H-furo[2,3-*b*]pyran-6-carboxylate **8** as a colorless oil (20.3 mg, 70% yield, 97:3 d.r., 94% ee). The d.r. value was determined by ¹H NMR analysis of crude materials. Enantiomeric excess was established by HPLC analysis using a Chiralpak IG column. HPLC conditions: UV-absorption = 210 nm, *n*-hexane/isopropanol = 85:15, flow rate = 1.0 mL/min, column temperature = 25 °C, *t*_r(major) = 19.9 min, *t*_r(minor) = 21.5 min. [α]_D²² = +56.9 (*c* = 1.0, CH₂Cl₂).

¹H NMR (600 MHz, CDCl₃) δ 7.31-7.28 (m, 2H), 7.22-7.17 (m, 3H), 5.05 (d, *J* = 3.0 Hz, 1H), 4.27 (ddd, *J* = 9.0, 8.4, 2.4 Hz, 1H), 3.99 (dd, *J* = 12.0, 2.4 Hz, 1H), 3.94 (dt, *J* = 9.0, 7.8 Hz, 1H), 3.78 (s, 3H), 2.71-2.65 (m, 2H), 2.24-2.20 (m, 1H), 2.11-2.05 (m, 1H), 1.96-1.86 (m, 2H), 1.78-1.73 (m, 1H), 1.70-1.63 (m, 2H), 1.46 (q, *J* = 12.6 Hz, 1H).

¹³C NMR (75 MHz, CDCl₃) δ 171.1, 141.8, 128.6, 128.4, 126.2, 102.3, 73.3, 68.8, 52.4, 43.0, 36.2, 34.1, 33.0, 29.3, 21.7.

IR (film): ν (cm⁻¹) 2896, 2857, 1755, 1736, 1602, 1496, 1454, 1438, 1391, 1372, 1266, 1201, 1167, 1124, 1112, 1087, 1049, 1022, 988, 934, 919, 894, 750, 700, 569, 505, 467, 450, 417.

HRMS (ESI, m/z) calcd for $C_{11}H_{14}O_3$ $[M + Na]^+$: 313.1410, found: 313.1410.

5.4.7 Assignment of Absolute and Relative Configurations

The absolute configuration of **7sa** was established by the single crystal X-ray diffraction (see 5.4.9, Figure 70). The analytical data of the reported compounds **7aa-7da**, **7ga-7ia**, **7la** and **7ba-7fa** were consistent with the assigned structures. The absolute and relative configurations of the compounds **7ea**, **7fa**, **7ja**, **7ka** and **7ma-7ra** were assigned accordingly. The relative configuration of compound **8** was studied by NMR spectroscopy as shown below.

Relative configuration of **8** at C6 studied by NMR spectroscopy:

Experimental: Sample for NMR measurements was about 20 mg of the substance dissolved in 0.6 mL of $CDCl_3$. Experiments were performed on a Bruker AVII 600 MHz spectrometer equipped with a 5 mm TBI probe with z-gradient. NOESY experiment was performed with a mixing time of 2.5 s. Furthermore, ^{13}C , DQF-COSY, 1H - ^{13}C HSQC and 1H - ^{13}C HMBC spectra were recorded for an unambiguous signal assignment. Spectra were processed with Bruker program package Topspin 4.0.8.

Results and Discussion: Strong NOE contacts were observed between those diastereotopic germinal protons at positions 2, 3 and 5. Furthermore, medium NOE contacts were detected between protons attached to positions 3a - 4, 3a - 7a, 4 - 5^{proS}, 4 - 6, 4 - 7a, 6 - 5^{proS} and 6 - 7a. With the predefined configurations at positions 3a, 4 and 7a, the observed pattern of NOE interactions among H-3a, H-4, H-5, H-6 and H-7a confirmed a configuration 6S, as shown in Figure 55. The key NOE contacts which lead to the determined stereo structure are presented in Table 14.

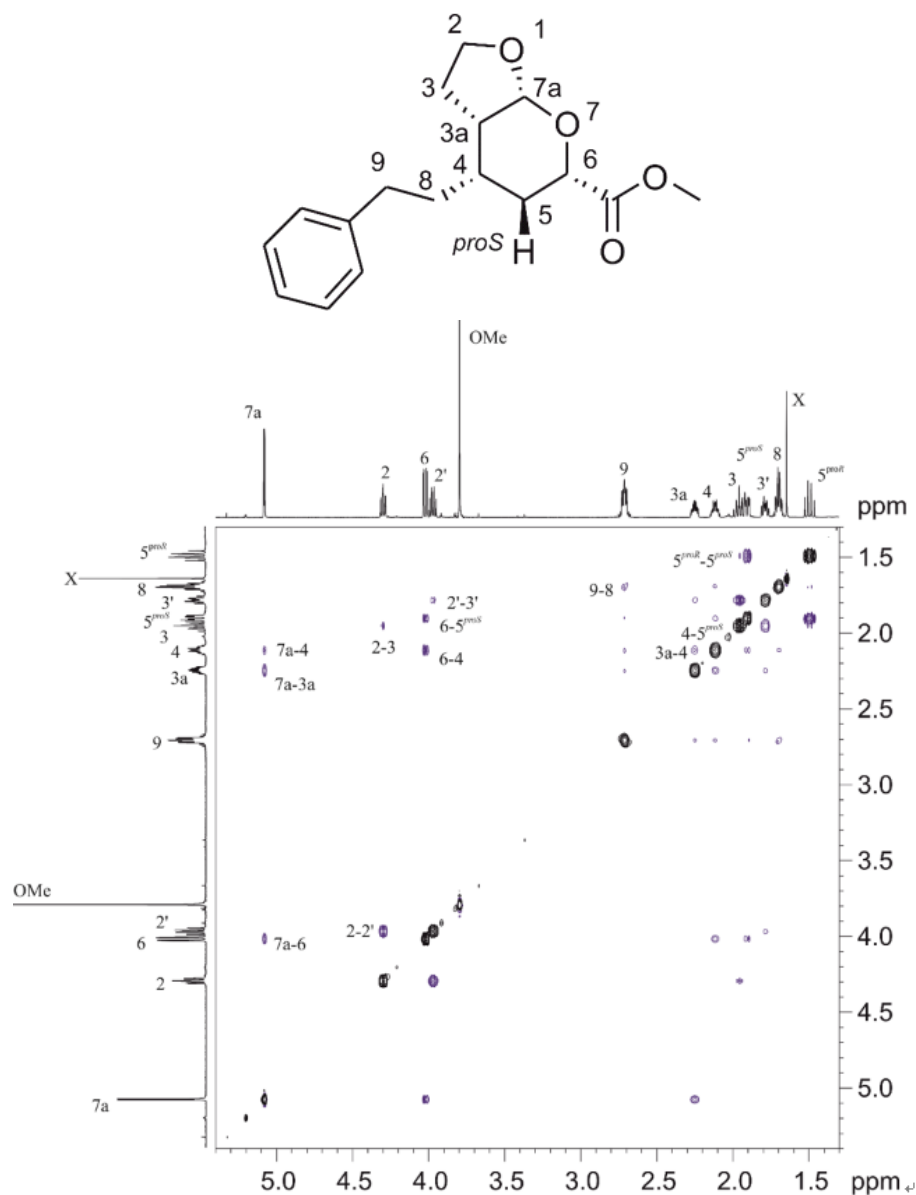


Figure 55. NOESY spectrum of **8** in CDCl_3 at 300 K, mixing time 2.5 s. Those configurations 3a*S*, 4*S* and 7a*R* were predefined, while 6*S* was determined by NMR.

Table 14. Key NOESY Cross Peaks of H85 in CDCl_3

No.	Positions	Strength	No.	Positions	Strength
1	2 – 2'	strong	6	4 – 6	medium
2	3 – 3'	strong	7	4 – 5 ^{pro<i>S</i>}	medium
3	5 ^{pro<i>R</i>} – 5 ^{pro<i>S</i>}	strong	8	4 – 7a	medium
4	3a – 4	medium	9	6 – 5 ^{pro<i>S</i>}	medium
5	3a – 7a	medium	10	6 – 7a	medium

5.4.8 CD Spectra of Chiral-at-Iron Complexes

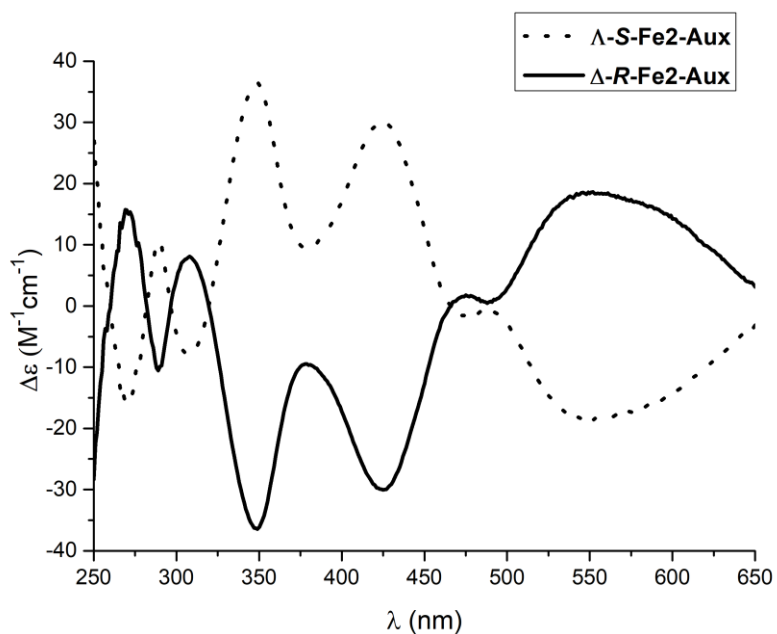


Figure 56. CD spectra of Λ -(S)/ Δ -(R)-Fe₂-Aux recorded in CH₃CN (1.0mM).

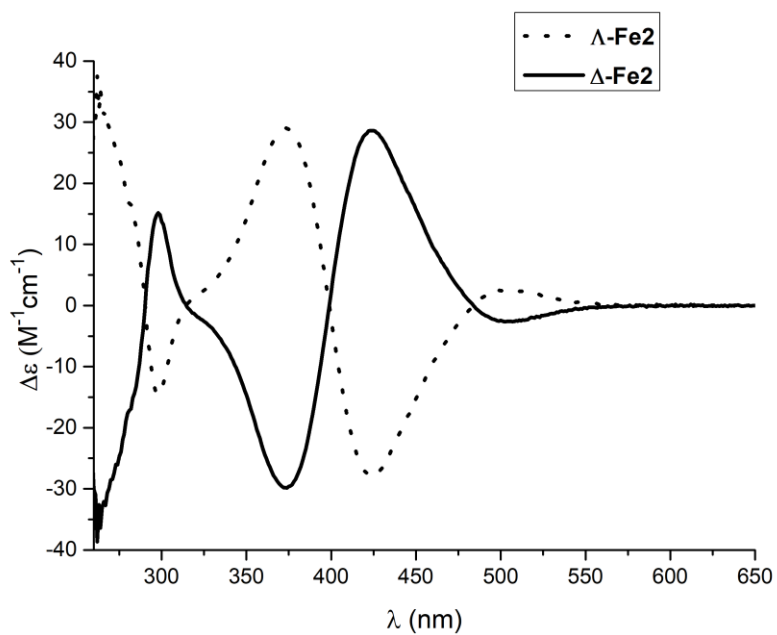


Figure 57. CD spectra of Λ / Δ -Fe₂ recorded in CH₃CN (1.0mM).

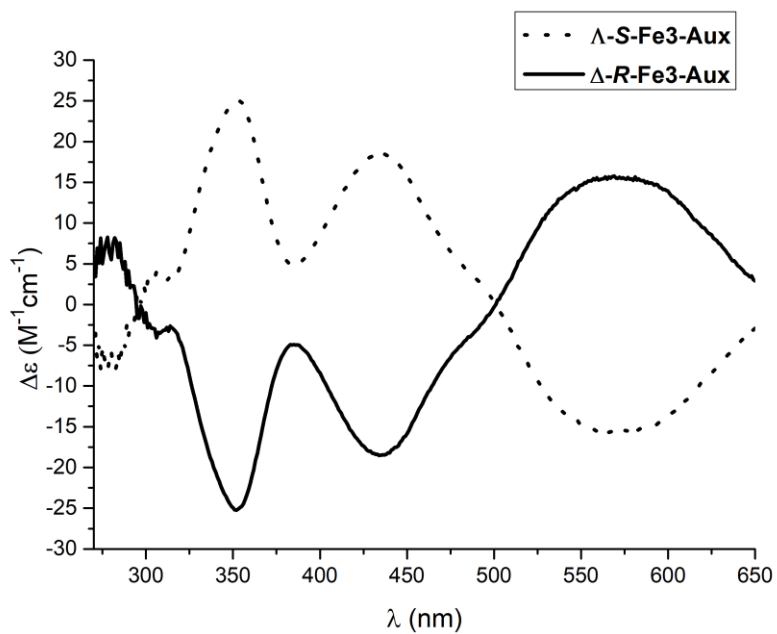


Figure 58. CD spectra of Λ -(S)/ Δ -(R)-Fe₃-Aux recorded in CH₃CN (1.0mM).

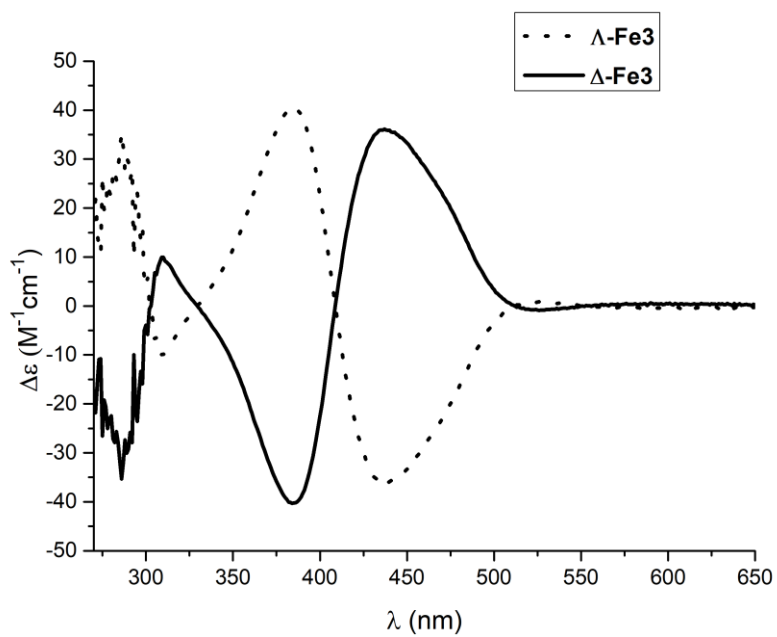


Figure 59. CD spectra of Λ / Δ -Fe₃ recorded in CH₃CN (1.0mM).

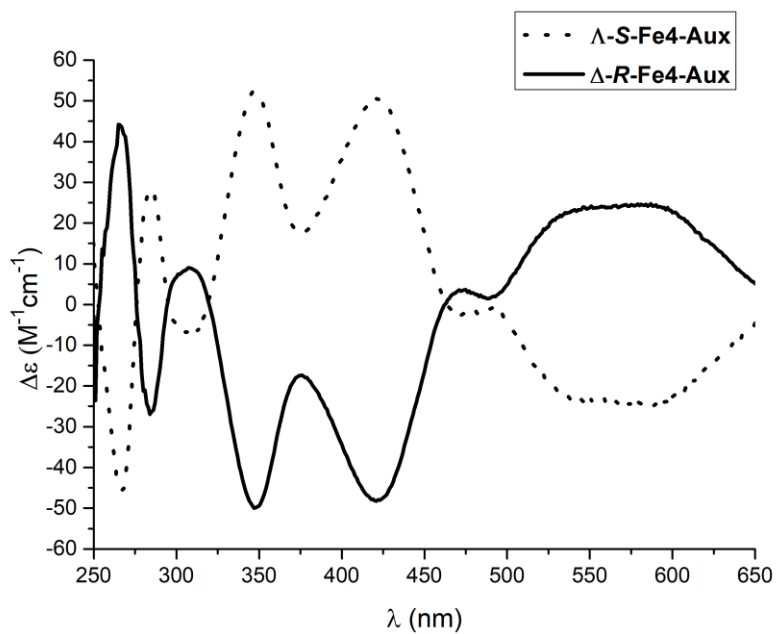


Figure 60. CD spectra of Λ -(S)/ Δ -(R)-Fe4-Aux recorded in CH₃CN (1.0mM).

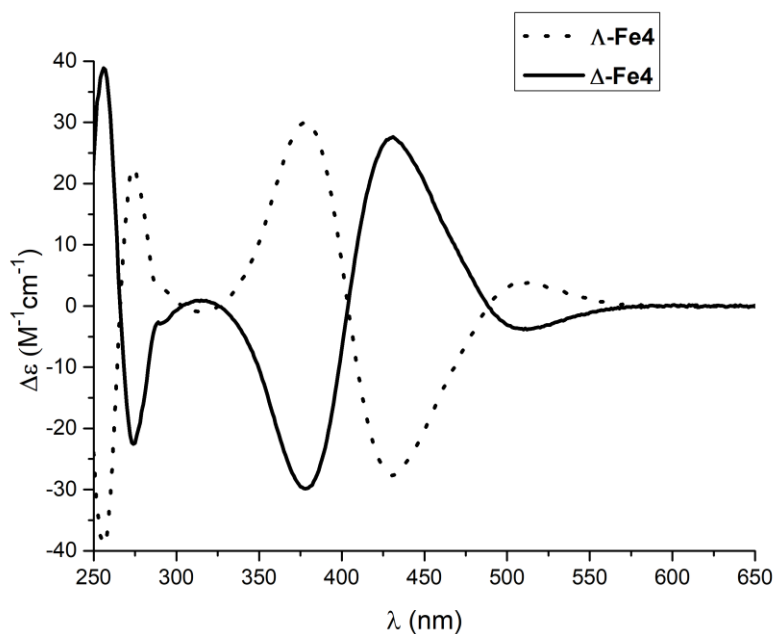


Figure 61. CD spectra of Λ / Δ -Fe4 recorded in CH₃CN (1.0mM).

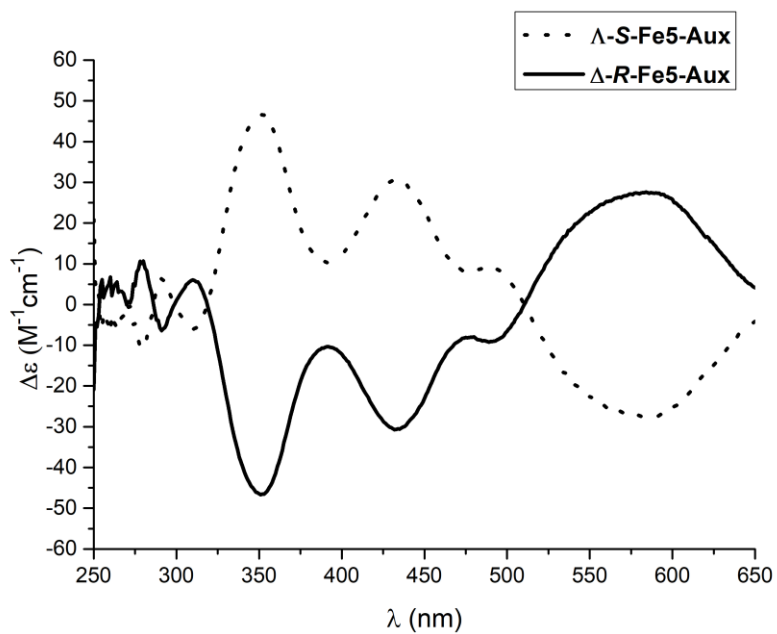


Figure 62. CD spectra of Λ -(S)/ Δ -(R)-Fe5-Aux recorded in CH_3CN (1.0mM).

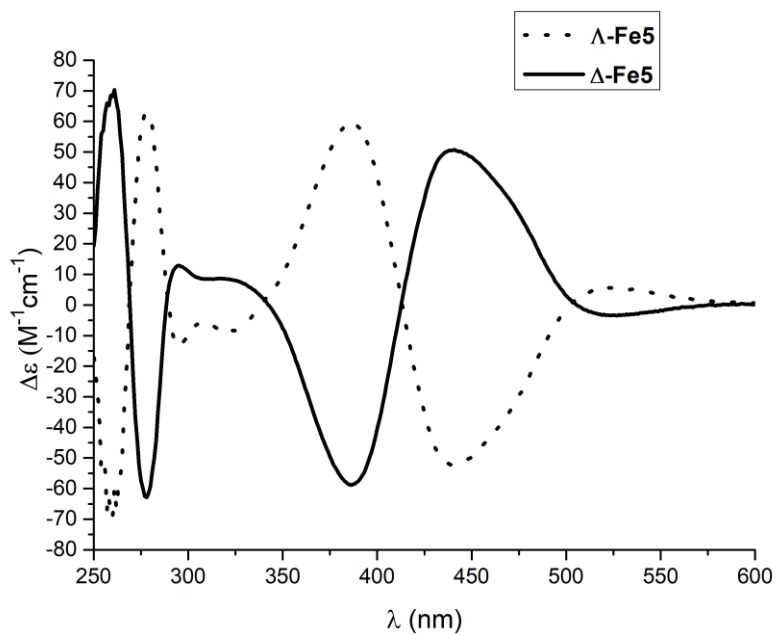


Figure 63. CD spectra of Λ / Δ -Fe5 recorded in CH_3CN (1.0mM).

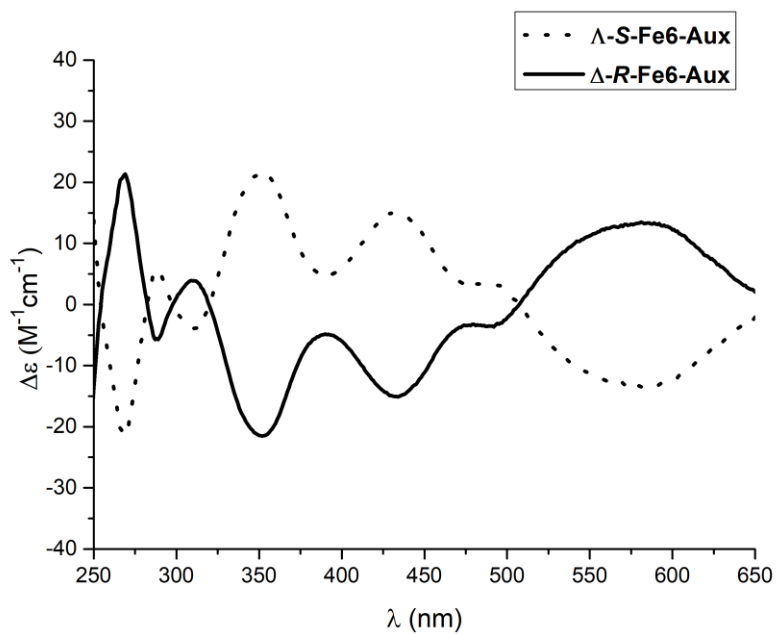


Figure 64. CD spectra of Λ -(S)/ Δ -(R)-Fe6-Aux recorded in CH_3CN (1.0mM).

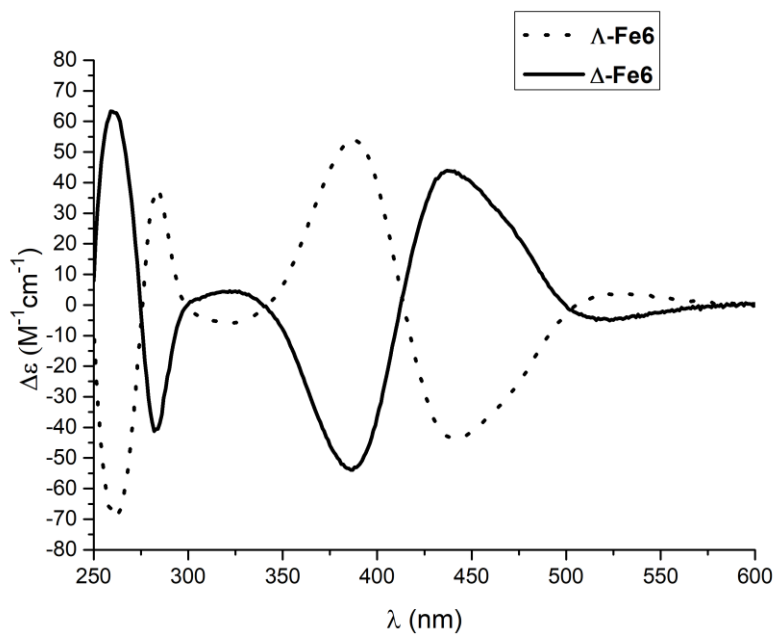


Figure 65. CD spectra of Λ / Δ -Fe6 recorded in CH_3CN (1.0mM).

5.4.9 Single Crystal X-Ray Diffraction

(1) Single crystal X-ray analysis of *rac*-Fe2

Single crystals of *rac*-Fe2 suitable for X-ray diffraction were obtained from slow diffusion of Et₂O to a solution of *rac*-Fe2 in CH₃CN at room temperature for 1 day in a NMR tube.

Data was collected with an STOE STADIVARI diffractometer equipped with CuK α radiation, a graded multilayer mirror monochromator ($\lambda = 1.54186 \text{ \AA}$) and a DECTRIS PILATUS 300K detector using an oil-coated shock-cooled crystal at 100(2) K. Absorption effects were corrected semi-empirical using multiscanned reflexions (STOE LANA, absorption correction by scaling of reflection intensities.). Cell constants were refined using 58115 of observed reflections of the data collection. The structure was solved by direct methods by using the program XT V2014/1 (Bruker AXS Inc., 2014) and refined by full matrix least squares procedures on F² using SHELXL-2018/3 (Sheldrick, 2018). The non-hydrogen atoms have been refined anisotropically, carbon bonded hydrogen atoms were included at calculated positions and refined using the 'riding model' with isotropic temperature factors at 1.2 times (for CH₃ groups 1.5 times) that of the preceding carbon atom. CH₃ groups were allowed to rotate about the bond to their next atom to fit the electron density. Severe disorder was refined for PF₆ anions and solvent.

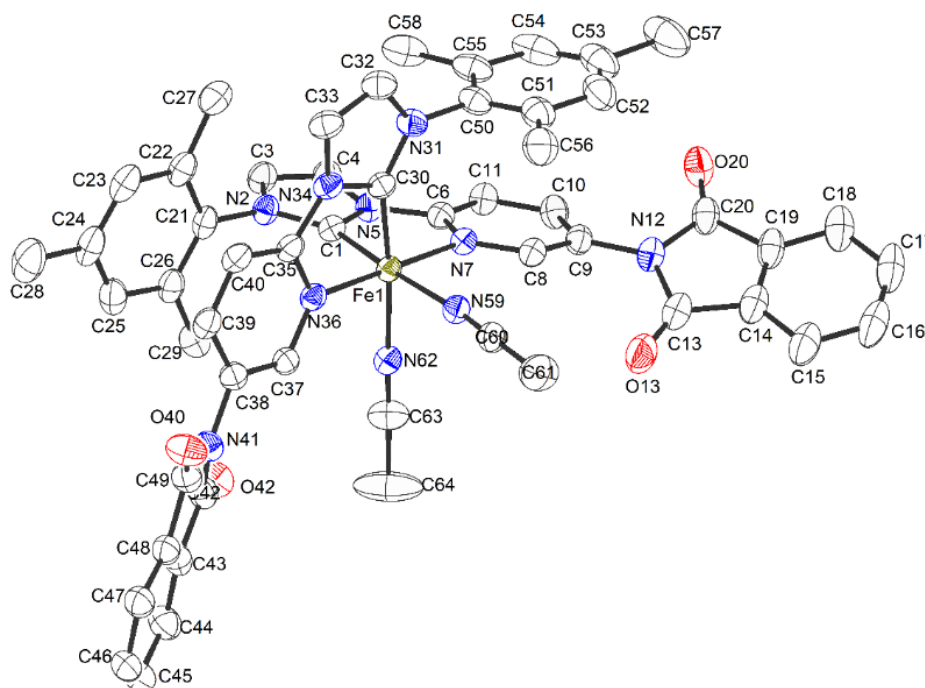


Figure 66. Crystal structure of *rac*-Fe2. ORTEP drawing with 50% probability thermal ellipsoids. The [PF₆]⁻ anions, solvent molecules and all hydrogens are not shown.

Selected bond lengths [Å] and angles [°]: Fe1-C30 1.911(2), Fe1-C1 1.927(2), Fe1-N62 1.9596(19), Fe1-N59 1.9677(19), Fe1-N36 1.9863(19), Fe1-N7 1.9986(19), C30-Fe1-C1 90.27(9), C30-Fe1-N62 171.97(9), C1-Fe1-N62 92.03(9), C30-Fe1-N59 92.00(9), C1-Fe1-N59 73.36(9), N62-Fe1-N59 86.57(8), C30-Fe1-N36 80.58(9), C1-Fe1-N36 97.96(8), N62-Fe1-N36 91.48(8), N59-Fe1-N36 88.57(8), C30-Fe1-N7 100.35(9), C1-Fe1-N7 80.92(8), N62-Fe1-N7 87.61(8), N59-Fe1-N7 92.52(8), N36-Fe1-N7 178.53(8).

Table 15. Crystal data and structure refinement for *rac*-Fe2

Identification code	<i>rac</i> Fe2
Habitus, colour	plate, yellow
Crystal size	0.22 x 0.22 x 0.06 mm ³
Crystal system	Orthorhombic
Space group	Pbca
Unit cell dimensions	a = 18.1016(2) Å b = 20.6527(2) Å c = 31.0270(4) Å
Volume	11599.3(2) Å ³
Cell determination	58115 peaks with Theta 2.8 to 76.4°.
Empirical formula	C _{57.12} H _{50.75} Cl _{0.25} F ₁₂ Fe N _{11.50} O ₄ P ₂
Moiety formula	C ₅₄ H ₄₆ FeN ₁₀ O ₄ , 2(F ₆ P), 0.125(CH ₂ Cl ₂), 1.5(C ₂ H ₃ N)
Formula weight	1316.99
Density (calculated)	1.508 Mg/m ³
Absorption coefficient	3.564 mm ⁻¹
F(000)	5394
Wavelength	1.54186 Å
Temperature	100(2) K
Theta range for data collection	3.546 to 76.297°.
Index ranges	-22 ≤ h ≤ 17, -25 ≤ k ≤ 17, -38 ≤ l ≤ 38
Reflections collected	75529
Independent reflections	11907 [R(int) = 0.0392]
Completeness to theta = 67.686°	99.6 %
Observed reflections	10298 [I > 2σ(I)]
Reflections used for refinement	11907
Absorption correction	Semi-empirical from equivalents ²⁴
Max. and min. transmission	0.6132 and 0.2808
Largest diff. peak and hole	0.527 and -0.410 e.Å ⁻³
Solution	intrinsic phases ²⁶
Refinement	Full-matrix least-squares on F ²⁷
Programs used	XT V2014/1 (Bruker AXS Inc., 2014) ²⁶
Data / restraints / parameters	11907 / 524 / 988
Goodness-of-fit on F ²	1.023
R index (all data)	wR2 = 0.1371
R index conventional [I > 2σ(I)]	R1 = 0.0507

(2) Single crystal X-ray analysis of *rac*-Fe5

Single crystals of *rac*-Fe5 suitable for X-ray diffraction were obtained from slow diffusion of Et₂O to its acetonitrile solution in a NMR tube at room temperature for 1 day.

A suitable crystal of Fe5 was selected under inert oil and mounted by using a MiTeGen loop. Intensity data of the crystal were recorded with a D8 Quest diffractometer (Bruker AXS). The instrument was operated with Mo-K α radiation ($\lambda = 0.71073 \text{ \AA}$, microfocus source) and equipped with a PHOTON 100 detector. Evaluation, integration and reduction of the diffraction data was carried out using the Bruker APEX 3 software suite.²⁸ Multi-scan and numerical absorption corrections were applied using the SADABS program.²⁹⁻³⁰ The structure was solved using dual-space methods (SHELXT-2014/5) and refined against F^2 (SHELXL-2018/3 using ShelXle interface).^{26-27,31} All non-hydrogen atoms were refined with anisotropic displacement parameters. The hydrogen atoms were refined using the “riding model” approach with isotropic displacement parameters 1.2 times (1.5 times for terminal methyl groups) of that of the preceding carbon atom. One [PF₆]⁻ anion and both CF₃ groups exhibit rotational disorder and were refined accordingly using the DSR plugin³² implemented in SHELXL.

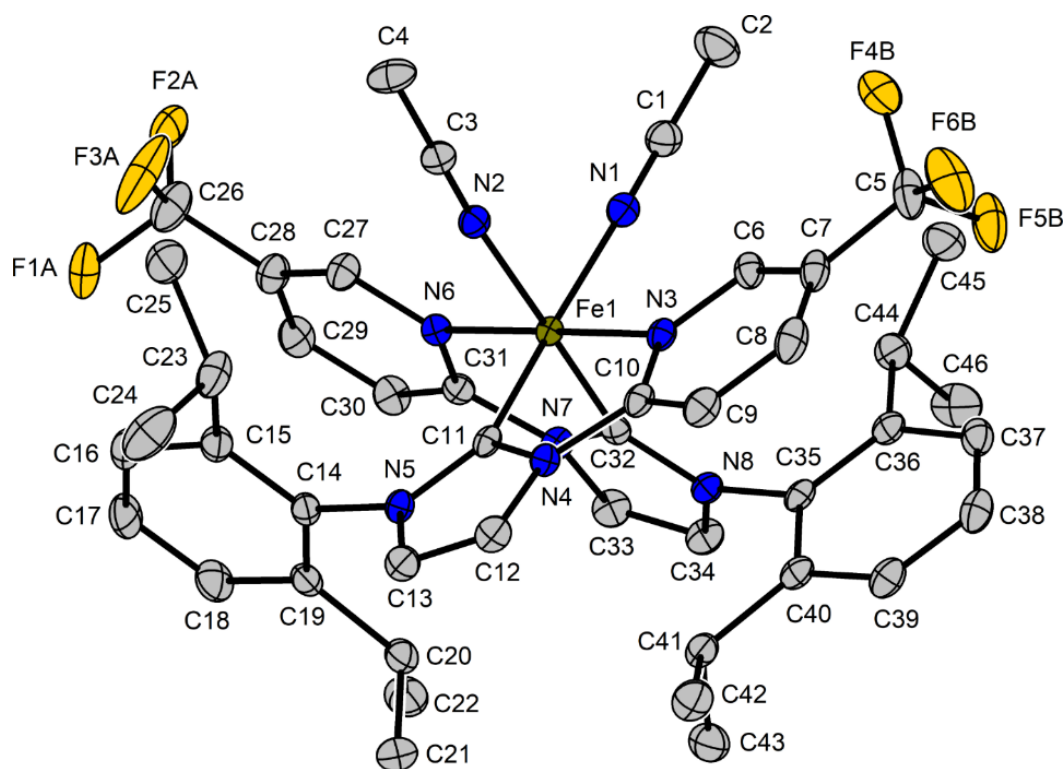


Figure 67. X-ray crystal structure of *rac*-Fe5. Only one enantiomer is shown. Only one disordered species of the CF₃ groups is shown. The hexafluorophosphate anions, the solvent molecule and the hydrogen atoms are omitted. Displacement ellipsoids are shown at 50 % probability level at 100 K.

Selected bond lengths [Å] and angles [deg]: Fe(1)-C(32) 1.9200(17), Fe(1)-C(11) 1.9259(17), Fe(1)-N(2) 1.9651(14), Fe(1)-N(1) 1.9721(15), Fe(1)-N(6) 1.9921(14), Fe(1)-N(3) 1.9951(14), C(32)-Fe(1)-C(11) 95.79(7), C(32)-Fe(1)-N(2) 173.12(7), C(11)-Fe(1)-N(2) 88.53(6), C(32)-Fe(1)-N(1) 89.16(6), C(11)-Fe(1)-N(1) 171.73(7), N(2)-Fe(1)-N(1) 87.19(6), C(32)-Fe(1)-N(6) 80.81(6), C(11)-Fe(1)-N(6) 98.25(6), N(2)-Fe(1)-N(6) 93.30(6), N(1)-Fe(1)-N(6) 89.06(6), C(32)-Fe(1)-N(3) 99.31(6), C(11)-Fe(1)-N(3) 80.76(7), N(2)-Fe(1)-N(3) 86.64(6), N(1)-Fe(1)-N(3) 91.93(6), N(6)-Fe(1)-N(3) 179.01(6).

Table 16. Crystal data and structure refinement for *rac*-Fe5

Identification code	Fe5
Empirical formula	C ₄₈ H ₅₃ F ₁₈ FeN ₉ P ₂
Molar mass / g·mol ⁻¹	1215.78
Space group (No.)	<i>P</i> 2 ₁ / <i>c</i> (14)
<i>a</i> / Å	11.5649(6)
<i>b</i> / Å	39.7488(19)
<i>c</i> / Å	12.3752(6)
β / °	107.1530(10)
<i>V</i> / Å ³	5435.7(5)
<i>Z</i>	4
$\rho_{calc.}$ / g·cm ⁻³	1.486
μ / mm ⁻¹	0.441
Color	orange
Crystal habitus	block
Crystal size / mm ³	0.391 x 0.188 x 0.121
<i>T</i> / K	100
λ / Å	0.71073 (Mo-K α)
θ range / °	1.913 to 28.356
Range of Miller indices	-15 ≤ <i>h</i> ≤ 15 -53 ≤ <i>k</i> ≤ 53 -16 ≤ <i>l</i> ≤ 16
<i>T</i> _{min} , <i>T</i> _{max}	0.8678, 0.9987
<i>R</i> _{int} , <i>R</i> _{σ}	0.0572, 0.0297
Completeness of the data set	1.000
No. of measured reflections	142338
No. of independent reflections	13584
No. of parameters	835
No. of restrains	802
<i>S</i> (all data)	1.078
<i>R</i> (<i>F</i>) (<i>I</i> ≥ 2σ(<i>I</i>), all data)	0.0427, 0.0602
<i>wR</i> (<i>F</i> ²) (<i>I</i> ≥ 2σ(<i>I</i>), all data)	0.0853, 0.0911
Extinction coefficient	0.00048(8)
$\Delta\rho_{max}$, $\Delta\rho_{min}$ / e·Å ⁻³	0.419, -0.395
CCDC	2064430

(3) Single crystal X-ray analysis of *rac*-Fe6

Single crystals of *rac*-Fe6 suitable for X-ray diffraction were obtained from slow diffusion of Et₂O to a solution of *rac*-Fe6 in CH₃CN at room temperature for 1 day in a NMR tube. A suitable crystal of *rac*-Fe6 was selected under inert oil and mounted by using a MiTeGen loop. Intensity data of the crystal were recorded with a D8 Quest diffractometer (Bruker AXS). The instrument was operated with Mo-K α radiation ($\lambda = 0.71073$ Å, microfocus source) and equipped with a PHOTON 100 detector. Evaluation, integration and reduction of the diffraction data was carried out using the Bruker APEX 3 software suite.²⁸ Multi-scan and numerical absorption corrections were applied using the SADABS program.²⁹⁻³⁰ The structure was solved using dual-space methods (SHELXT-2014/5) and refined against F^2 (SHELXL-2018/3 using ShelXle interface).^{26-27,31} All non-hydrogen atoms were refined with anisotropic displacement parameters. The hydrogen atoms were refined using the “riding model” approach with isotropic displacement parameters 1.2 times (for CH₃ groups 1.5 times) of that of the preceding carbon atom. The poorly resolved solvent molecules of diethylether and acetonitrile (with the exception of one non-disordered C₂H₃N molecule) were treated using the SQUEEZE algorithm implemented within the PLATON software.³³ Three out of the four [PF₆]⁻ anions showed signs of disorder (residual electron density on the Fourier difference map). One of them was refined using a suitable disorder model.

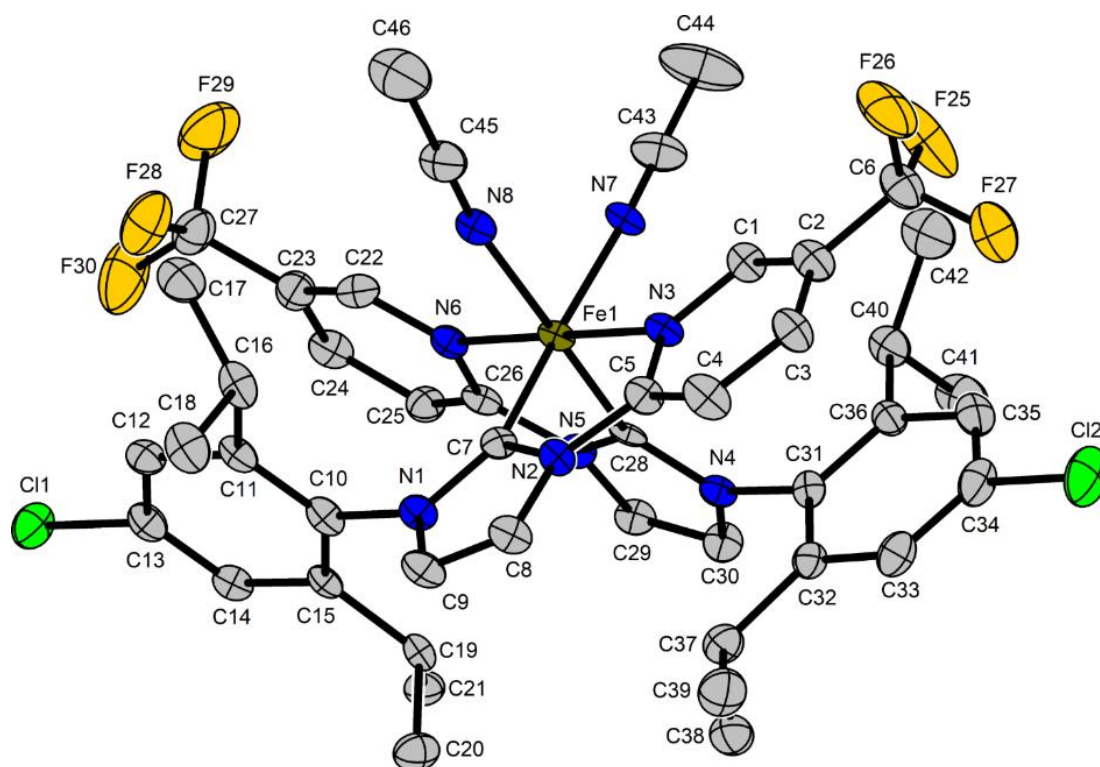


Figure 68. Crystal structure of *rac*-Fe6. ORTEP drawing with 50% probability thermal ellipsoids. The [PF₆]⁻ anions, solvent molecules and all hydrogens are not shown.

Selected bond lengths [Å] and angles [°]: Fe-C7 1.911(5), Fe-C28 1.912(6), Fe-N8 1.955(5), Fe-N7 1.975(5), Fe-N3 2.000(5), Fe-N6 2.006(5), C(7)-Fe(1)-C(28) 94.4(2), C(7)-Fe(1)-N(8) 90.0(2), C(28)-Fe(1)-N(8) 173.1(2), C(7)-Fe(1)-N(7) 173.5(2), C(28)-Fe(1)-N(7) 88.4(2), N(8)-Fe(1)-N(7) 87.7(2), C(7)-Fe(1)-N(3) 81.0(2), C(28)-Fe(1)-N(3) 98.4(2), N(8)-Fe(1)-N(3) 87.5(2), N(7)-Fe(1)-N(3) 92.82(19), C(7)-Fe(1)-N(6) 99.2(2), C(28)-Fe(1)-N(6) 81.3(2), N(8)-Fe(1)-N(6) 92.8(2), N(7)-Fe(1)-N(6) 87.07(19), N(3)-Fe(1)-N(6) 179.6(2).

Table 17. Crystal data and structure refinement for *rac*-Fe6

Identification code	yb4151s
Empirical formula	C ₄₇ H _{49.5} Cl ₂ F ₁₈ FeN _{8.5} P ₂
Molar mass / g·mol ⁻¹	1264.14
Space group (No.)	<i>P</i> 2 ₁ (4)
<i>a</i> / Å	11.7516(8)
<i>b</i> / Å	24.6067(18)
<i>c</i> / Å	21.2636(15)
β / °	91.702(2)
<i>V</i> / Å ³	6146.0(8)
<i>Z</i>	4
$\rho_{calc.}$ / g·cm ⁻³	1.366
μ / mm ⁻¹	0.477
Color	yellow
Crystal habitus	block
Crystal size / mm ³	0.490 x 0.193 x 0.102
<i>T</i> / K	100
λ / Å	0.71073 (Mo-K α)
θ range / °	2.124 to 26.488
Range of Miller indices	-14 ≤ <i>h</i> ≤ 14 -30 ≤ <i>k</i> ≤ 30 -26 ≤ <i>l</i> ≤ 26
Absorption correction	multi-scan and numerical
<i>T</i> _{min} , <i>T</i> _{max}	0.8380, 0.9818
<i>R</i> _{int} , <i>R</i> _{σ}	0.0535, 0.0474
Completeness of the data set	0.999
No. of measured reflections	130285
No. of independent reflections	25338
No. of parameters	1500
No. of restraints	443
<i>S</i> (all data)	1.022
<i>R</i> (<i>F</i>) (<i>I</i> ≥ 2σ(<i>I</i>), all data)	0.0558, 0.0699
<i>wR</i> (<i>F</i> ²) (<i>I</i> ≥ 2σ(<i>I</i>), all data)	0.1314, 0.1383
Extinction coefficient	not refined
Volume fraction of the 2 nd twin component	0.430(18)
$\Delta\rho_{max}$, $\Delta\rho_{min}$ / e·Å ⁻³	0.695, -0.437

(4) Single crystal X-ray analysis of **5s**

Single crystals of **5s** suitable for X-ray diffraction were obtained from its saturated solution in *n*-hexane at room temperature for several hours in a 1.5 mL vial.

A suitable crystal of **5s** was selected under inert oil and mounted by using a MiTeGen loop. Intensity data of the crystal were recorded with a STADIVARI diffractometer (Stoe & Cie). The diffractometer was operated with Cu-K α radiation ($\lambda = 1.54186 \text{ \AA}$, microfocus source) and equipped with a Dectris PILATUS 300K detector. Evaluation, integration and reduction of the diffraction data was carried out using the X-Area software suite.²⁸ Multi-scan and numerical absorption corrections were applied with the X-Red32 and LANA modules of the X-Area software suite.²⁹⁻³⁰ The structure was solved using dual-space methods (SHELXT-2014/5) and refined against F^2 (SHELXL-2018/3 using ShelXle interface).^{26-27,31} All non-hydrogen atoms were refined with anisotropic displacement parameters. The hydrogen atoms were refined using the “riding model” approach with isotropic displacement parameters 1.2 times (for CH₃ groups 1.5 times) of that of the preceding carbon atom. Crystal data and structure refinement for **5s** are listed in the Figure 69 and Table 18.

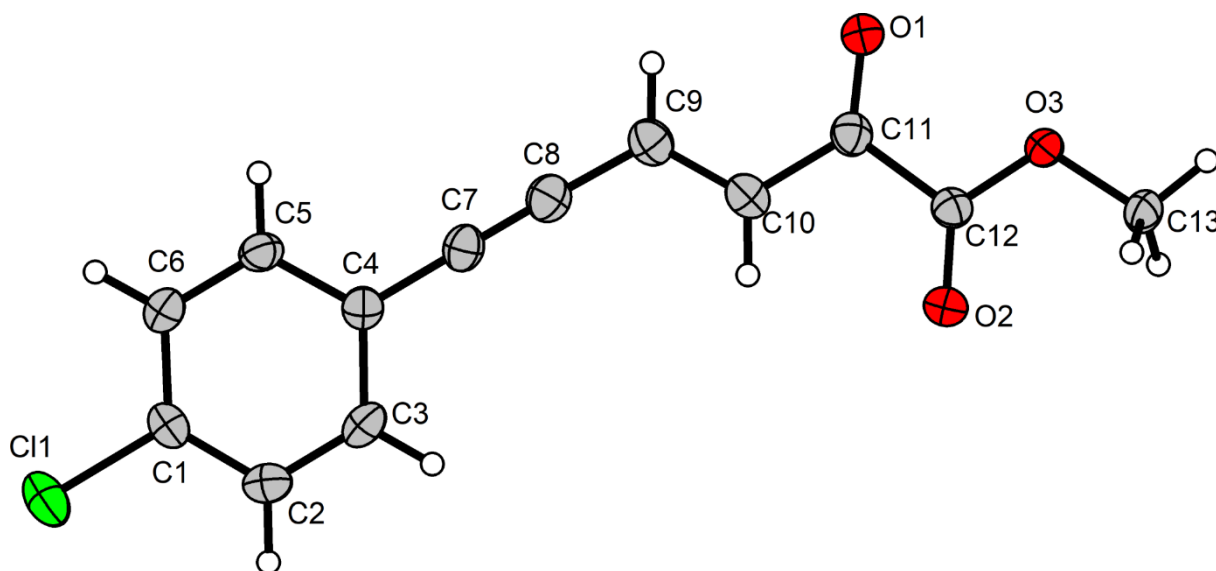


Figure 69. Crystal structure of **5s**. Displacement ellipsoids are shown at 50 % probability level at 100 K. Hydrogen atoms are shown with arbitrary radii.

Table 18. Selected crystallographic data and details of the structure determination for **5s**

Identification code	yb5078
Empirical formula	C ₁₃ H ₉ ClO ₃
Molar mass / g·mol ⁻¹	248.65
Space group (No.)	<i>P</i> 2 ₁ / <i>c</i> (14)
<i>a</i> / Å	3.79330(10)
<i>b</i> / Å	15.1450(3)
<i>c</i> / Å	20.0776(7)
β / °	93.624(3)
<i>V</i> / Å ³	1151.14(6)
<i>Z</i>	4
$\rho_{calc.}$ / g·cm ⁻³	1.435
μ / mm ⁻¹	2.893
Color	yellow
Crystal habitus	needle
Crystal size / mm ³	0.283 x 0.081 x 0.065
<i>T</i> / K	100
λ / Å	1.54186 (Cu-K α)
θ range / °	3.658 to 75.398
Range of Miller indices	-4 ≤ <i>h</i> ≤ 4 -12 ≤ <i>k</i> ≤ 19 -21 ≤ <i>l</i> ≤ 25
Absorption correction	multi-scan and numerical
<i>T</i> _{min} , <i>T</i> _{max}	0.2932, 0.7650
<i>R</i> _{int} , <i>R</i> _{σ}	0.0253, 0.0198
Completeness of the data set	0.999
No. of measured reflections	14616
No. of independent reflections	2374
No. of parameters	155
No. of restrains	0
<i>S</i> (all data)	1.087
<i>R</i> (<i>F</i>) (<i>I</i> ≥ 2σ(<i>I</i>), all data)	0.0399, 0.0482
<i>wR</i> (<i>F</i> ²) (<i>I</i> ≥ 2σ(<i>I</i>), all data)	0.1154, 0.1180
Extinction coefficient	not refined
$\Delta\rho_{max}$, $\Delta\rho_{min}$ / e·Å ⁻³	0.430, -0.294

(5) Single crystal X-ray analysis of product 7sa

Single crystals of product **7sa** suitable for X-ray diffraction were obtained from slow diffusion of n-hexane to its solution in CH₂Cl₂ at room temperature for 1 day in a 1.5 mL vial.

A suitable crystal of **7sa** was selected under inert oil and mounted by using a MiTeGen loop. Intensity data of the crystal were recorded with a STADIVARI diffractometer (Stoe & Cie). The diffractometer was operated with Cu-K α radiation ($\lambda = 1.54186 \text{ \AA}$, microfocus source) and equipped with a Dectris PILATUS 300K detector. Evaluation, integration and reduction of the diffraction data was carried out using the X-Area software suite.²⁸ Multi-scan and numerical absorption corrections were applied with the X-Red32 and LANA modules of the X-Area software suite.²⁹⁻³⁰ The structure was solved using dual-space methods (SHELXT-2014/5) and refined against F^2 (SHELXL-2018/3 using ShelXle interface).^{26-27,31} All non-hydrogen atoms were refined with anisotropic displacement parameters. The hydrogen atoms were refined using the “riding model” approach with isotropic displacement parameters 1.2 times (for CH₃ groups 1.5 times) of that of the preceding carbon atom. Crystal data and structure refinement for **7sa** are listed in the Figure 70 and Table 19.

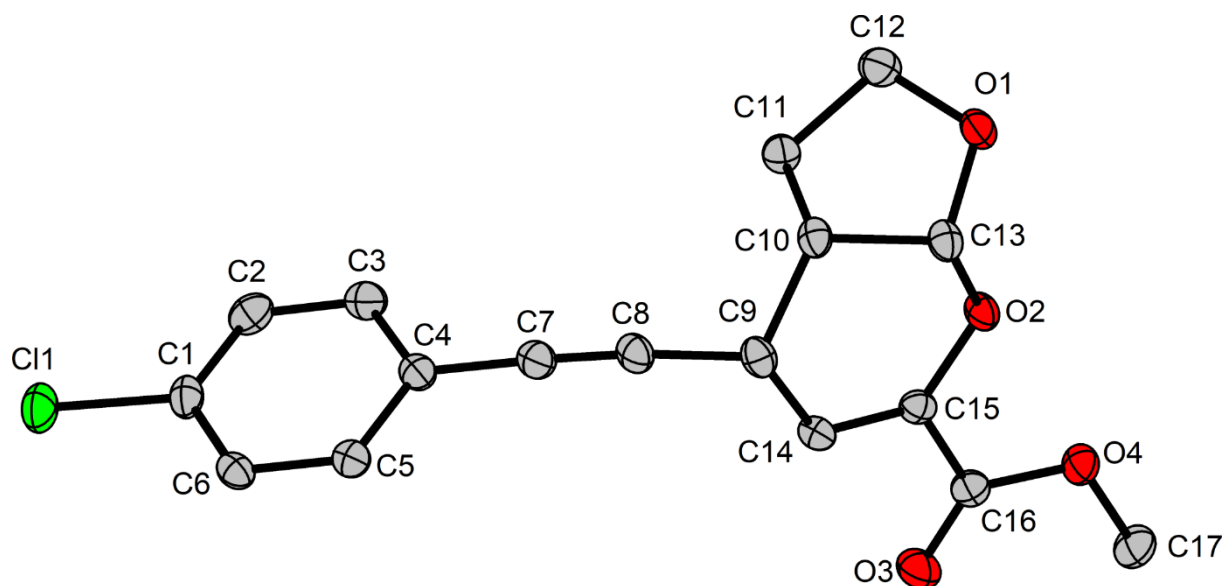


Figure 70. Crystal structure of **7sa**. Hydrogen atoms are not shown. Displacement ellipsoids are shown at 50 % probability level at 100 K.

Table 19. Selected crystallographic data and details of the structure determination for **7sa**

Identification code	yb5086
Empirical formula	C ₁₇ H ₁₅ ClO ₄
Molar mass / g·mol ⁻¹	318.74
Space group (No.)	<i>P</i> 2 ₁ 2 ₁ 2 ₁ (19)
<i>a</i> / Å	5.89230(10)
<i>b</i> / Å	12.3648(2)
<i>c</i> / Å	20.6450(4)
<i>V</i> / Å ³	1504.14(5)
<i>Z</i>	4
$\rho_{calc.}$ / g·cm ⁻³	1.408
μ / mm ⁻¹	2.392
Color	colorless
Crystal habitus	needle
Crystal size / mm ³	0.411 x 0.064 x 0.048
<i>T</i> / K	100
λ / Å	1.54186 (Cu-K α)
θ range / °	4.168 to 75.430
Range of Miller indices	$-7 \leq h \leq 7$ $-11 \leq k \leq 15$ $-25 \leq l \leq 18$
Absorption correction	multi-scan and numerical
<i>T</i> _{min} , <i>T</i> _{max}	0.2282, 0.8349
<i>R</i> _{int} , <i>R</i> _{σ}	0.0283, 0.0243
Completeness of the data set	0.994
No. of measured reflections	18238
No. of independent reflections	3060
No. of parameters	200
No. of restrains	0
<i>S</i> (all data)	1.021
<i>R</i> (<i>F</i>) (<i>I</i> ≥ 2σ(<i>I</i>), all data)	0.0258, 0.0281
<i>wR</i> (<i>F</i> ²) (<i>I</i> ≥ 2σ(<i>I</i>), all data)	0.0642, 0.0648
Flack parameter <i>x</i>	-0.008(6)
Extinction coefficient	not refined
$\Delta\rho_{max}$, $\Delta\rho_{min}$ / e·Å ⁻³	0.218, -0.169
CCDC	2064431

References

- 1 J. E. Campbell, M. C. Hewitt, P. Jones, L. Xie, *WO 2011-US38057*. **2011**.
- 2 (a) H. V. Mierde, P. V. D. Voort, F. Verpoort, *Tetrahedron Lett.* **2009**, *50*, 201–203. (b) G. D. Couch, P. J. Burke, R. J. Knox, C. J. Moody, *Tetrahedron* **2008**, *64*, 2816–2823.
- 3 B. J. Coe, M. Helliwell, S. Sánchez, M. K. Peers, N. S. Scrutton, *Dalton Transactions*, **2015**, *44*, 15420–15423.
- 4 G. Song, Y. Zhang, Y. Su, W. Deng, K. Han, X. Li, *Organometallics* **2008**, *27*, 6193–6201.
- 5 (a) Z. Lin, M. A. Celik, C. Fu, K. Harms, G. Frenking, E. Meggers, *Chem. - Eur. J.* **2011**, *17*, 12602–12605. (b) L. Gong, M. Wenzel, E. Meggers, *Acc. Chem. Res.* **2013**, *46*, 2635–2644.
- 6 Y. Zheng, Y. Tan, K. Harms, M. Marsch, R. Riedel, L. Zhang, E. Meggers, *J. Am. Chem. Soc.* **2017**, *139*, 4322–4325.
- 7 S. Gründemann, M. Albrecht, A. Kovacevic, J. W. Faller, R. H. Crabtree, *J. Chem. Soc., Dalton Trans.* **2002**, 2163–2167.
- 8 B. Liu, Y. Zhang, D. Xu, W. Chen, *Chem. Commun.* **2011**, *47*, 288–4325.
- 9 X. Huang, Q. Zhang, J. Lin, K. Harms, E. Meggers, *Nat. Catal.* **2019**, *2*, 34–40.
- 10 O. Kaufhold, F. E. Hahn, T. Pape, A. Hepp, *J. Organomet. Chem.* **2008**, *693*, 3435–3440.
- 11 W. Wu, X. Liu, Y. Zhang, J. Ji, T. Huang, L. Lin, X. Feng, *Chem. Commun.* **2015**, *51*, 11646–11649.
- 12 T. Mietke, T. Cruchter, V. A. Larionov, T. Faber, K. Harms, E. Meggers, *Adv. Synth. Catal.* **2018**, *360*, 2093–2100.
- 13 (a) Y. Zhao, S. R. Gilbertson, *Org. Lett.* **2014**, *16*, 1033–1035. (b) E. Alcalde, I. Dinarès, S. Dodríguez, C. G. Miguel, *Eur. J. Org. Chem.* **2005**, 1637–1643.
- 14 H. Kim, T. Kim, D. G Lee, S. W. Roh, C. Lee, *Chem. Commun.* **2014**, *50*, 9273–9276.
- 15 B. Sahoo, M. N. Hopkinson, F. Glorius, *Angew Chem, Int Ed*, **2015**, *54*, 15545–15549.
- 16 L. Gremaud, A. Alexakis, *Angew. Chem. Int. Ed*, **2012**, *51*, 794–797.
- 17 P. Gassman, S. Burns, K. Pfister, *J. Org. Chem*, **1993**, *58*, 1449–1457.
- 18 N. Thirupathi, F. Wei, C.-H. Tung, Z. Xu, *Nature. Commun*, **2019**, *10*, 3158–3165.
- 19 C. Allais, F. Liéby-Muller, J. Rodriguez, T. Constantieux, *Eur. J. Org. Chem*, **2013**, 4131–4145.
- 20 H.-C. Chiu, X. Y. See, I. A. Tonks, *ACS Catal.* **2019**, *9*, 216–223.
- 21 W.-H. Jung, S. Guyenne, C. Riesco-Fagundo, J. Mancuso, S. Nakamura, *Angew. Chem. Int. Ed*, **2008**, *47*, 1130–1133.
- 22 (a) Y. Zhu, M. Xie, S. Dong, X. Zhao, L. Lin, X. Liu, X. Feng, *Chem. Eur. J.*, **2011**, *17*, 8202–8208. (b) J.-B. Chen, M. Xu, J.-Q. Zhang, B.-B. Sun, J.-M. Hu, J.-Q. Yu, X.-W. Wang, Y. Xia, Z. Wang, *ACS Catal.* **2020**, *10*, 3556–3563.
- 23 A. Martel, S. Leconte, G. Dujardin, E. Brown, V. Maisonneuve, R. Retoux, *Eur. J. Org. Chem*, **2002**, 514–525.
- 24 *X-Area LANA*, STOE & Cie GmbH, Darmstadt, Germany, **2016**

- 25 S. Parsons, H. D. Flack, T. Wagner, *Acta Crystallogr., Sect. B: Struct. Sci., Cryst. Eng. Mater.* **2013**, *69*, 249–259.
- 26 G. M. Sheldrick, *Acta Crystallogr A Found Adv* **2015**, *71*, 3–8.
- 27 G. M. Sheldrick, *Acta crystallographica. Section C, Structural chemistry* **2015**, *71*, 3–8.
- 28 *APEX3*, Bruker AXS Inc., Madison, Wisconsin, USA, **2018**.
- 29 *SADABS*, Bruker AXS Inc., Madison, Wisconsin, USA, **2016**.
- 30 L. Krause, R. Herbst-Irmer, G. M. Sheldrick, D. Stalke, *J. Appl. Crystallogr.* **2015**, *48*, 3–10.
- 31 C. B. Hübschle, G. M. Sheldrick, B. Dittrich, *J. Appl. Crystallogr.* **2011**, *44*, 1281–1284.
- 32 D. Kratzert, I. Krossing, *J. Appl. Crystallogr.* **2018**, *51*, 928–934.
- 33 A. L. Spek, *PLATON-A Multipurpose Crystallographic Tool*, Utrecht University, Utrecht, The Netherlands, **2019**.

Chapter 6: Appendices

6.1 List of Abbreviations

^1H NMR	proton nuclear magnetic resonance spectroscopy
^{13}C NMR	carbon nuclear magnetic resonance spectroscopy
^{19}F NMR	fluorine nuclear magnetic resonance spectroscopy
δ	chemical shift
J	coupling constant
br	broad
s	singlet
d	doublet
t	triplet
q	quartet
m	multiplet
ppm	parts per million
AcOH	acetic acid
aq	aqueous
CD	circular dichroism
CH_2Cl_2 / DCM	dichloromethane
CD_2Cl_2	dideuteromethylenechloride
CHCl_3	chloroform
CDCl_3	deuteriochloroform
CH_3CN / MeCN	acetonitrile
conc	concentrated
DMF	dimethylformamide
DMSO	dimethyl sulfoxide
d.r.	diastereomeric ratio
ee	enantiomeric excesses
e.g.	exempli gratia (lat.: for example)
et al.	et alii (lat.: and others)
Fe	iron
ESI	electrospray ionization
EtOH	ethanol
Et_2O	diethyl ether
Et_3N	triethyl amine
EtOAc	ethyl acetate
EWG	electron withdrawing group
HAT	hydrogen atom transfer
h	hour(s)

HPLC	high performance liquid chromatography
HMDS	bis(trimethylsilyl)amide
HRMS	high resolution mass spectrometry
Hz	Hertz
IR spectra	infrared spectra
Ir	iridium
L	liter(s)
M	mol/liter
<i>m</i>	meta-
min	minute(s)
mL	milliliter(s)
mmol	millimole
MS	mass spectroscopy
N ₂	nitrogen
Nu	nucleophile
Ph	phenyl
Phen	Phenanthroline
PPh ₃	triphenylphosphine
ppm	parts per million
Py	pyridine
<i>rac</i>	racemate
Rh	rhodium
Ru	ruthenium
r.t.	room temperature
TFA	trifluoroacetic acid
THF	tetrahydrofuran
TLC	thin layer chromatography

6.2 List of Schemes

Scheme 1 Synthesis of bis(pyridyl-imidazol-2-ylidene)-iron complex via [FeCl ₂ (PPh ₃) ₂] and free NHC.....	3
Scheme 2 Synthesis of bis(pyridyl-imidazol-2-ylidene) iron complexes via electrolysis of iron element and silver-carbene complexes	4
Scheme 3 Iron-catalyzed Kumada cross-coupling reactions.....	4
Scheme 4 Synthesis of tris-(pyridyl-imidazol-2-ylidene) iron complex	4
Scheme 5 Synthesis of octahedral bis(arylimidazolylidene)pyridine iron complexes	5
Scheme 6 Synthesis of C ₂ -symmetric octahedral bis(carbene)pyridine iron complex	5
Scheme 7 Synthesis of bis(arylimidazolylidene)pyridine iron dialkyl complexes and their derivatives	7
Scheme 8 Synthesis of a family of CNN-pincer iron complexes.....	8
Scheme 9 CNN-pincer iron-catalyzed cycloaddition of CO ₂ to epoxides	8

Chapter 6. Appendices

Scheme 10 Synthesis of NCCN-iron complexes via Fe(HMDS) ₂ precursor and imidazolium salts	10
Scheme 11 Synthesis of NCCN-iron complex via imidazolium salt and iron powders	10
Scheme 12 NCCN-Fe-catalyzed oxidation of (a) arene. (b) cyclohexane.	11
Scheme 13 NCCN-Fe-catalyzed Wittig reaction	11
Scheme 14 Octahedral iron complexes based on tetradentate NHC ligands	12
Scheme 15 Synthesis of abnormal C,N-chelating pyridylidene palladium and platinum complexes	14
Scheme 16 Synthesis of remote or abnormal pyridylidene ruthenium complexes	15
Scheme 17 Highly selective synthesis of the normal and remote pyridylidene ruthenium complex	15
Scheme 18 Highly selective preparation of bis(<i>r</i> NHC)iridium complexes	16
Scheme 19 Synthesis of C ₂ -metallated pyridylidene complexes.....	16
Scheme 20 Highly selective synthesis of normal or remote pyridylidene iridium(III) complexes	17
Scheme 21 Synthesis of pyridylidene complexes via protonation of cyclometalated precursors	17
Scheme 22 Benzimidazole-pyridylidene iridium complexes for the hydrogenation of imine	18
Scheme 23 Chiral oxo-bridged dinuclear iron-catalyzed asymmetric catalysis.....	20
Scheme 24 Chiral N ₄ -Fe-catalyzed asymmetric <i>cis</i> -dihydroxylation.....	22
Scheme 25 Chiral N ₂ Py ₂ -Fe/organic acid-catalyzed asymmetric epoxidation of α,β -enones	23
Scheme 26 N ₂ Py ₂ -Fe/organic acid-catalyzed enantioselective epoxidation.....	24
Scheme 27 N ₂ Py ₂ -Fe/D-CPA-catalyzed enantioselective epoxidation	25
Scheme 28 C ₁ -symmetric iron catalyst/EHA-catalyzed enantioselective epoxidation of challenging cyclic α,β -enones	25
Scheme 29 N ₂ Py ₂ -Fe-catalyzed asymmetric coupling of 2-naphthols	26
Scheme 30 Iron-catalyzed alkylation reactions.....	27
Scheme 31 Synthesis and catalytic application of bis(imine)diphosphine iron complex.	28
Scheme 32 Chiral bis(imine)diphosphine-Fe-catalyzed ATH reactions.....	29
Scheme 33 Chiral bis(imine)diphosphine-Fe-catalyzed ATH reaction of imines	29
Scheme 34 Chiral amine(imine)diphosphine iron-catalyzed transformation. (a) ATH. (b)Hydrogenation. (c) ATH in aqueous biphasic media.	31
Scheme 35 Synthesis and catalytic application of bis(imine)diphosphine iron complexes.	32
Scheme 36 Iron-catalyzed asymmetric transfer hydrogenation of ketones or imines	33
Scheme 37 Iron-catalyzed enantioselective transfer hydrogenation of benzoin	34
Scheme 38 Synthesis of <i>rac</i> - Ru2	53
Scheme 39 Synthesis of <i>rac</i> - Ru3	54
Scheme 40 Synthesis of ruthenium complex with 7-methyl-3-phenyl-1,7-phenanthroline ligands	58
Scheme 41 Synthesis of non-racemic ruthenium complexes	59
Scheme 42 Synthesis of octahedral chiral-at-iron complexes.....	73
Scheme 43 Reaction of <i>rac</i> - Fe1 with (R)- α -methoxyphenylacetic acid in CH ₂ Cl ₂	75
Scheme 44 Synthesis of chiral-at-iron complexes via the slightly modified procedure	84
Scheme 45 Asymmetric Nazarov cyclization and enantioselective Cannizzaro reaction catalyzed by Fe5 versus	

Fe1	91
Scheme 46 (a) 1 mmol scale synthesis. (b) Diastereoselective reduction of the 3,4-dihydropyran.....	94
Scheme 48 Synthesis of racemic and non-racemic octahedral ruthenium complexes	102
Scheme 49 Synthesis of octahedral chiral-at-iron complexes.....	104

6.3 List of Figures

Figure 1 Amphiphilic bis(carbene)pyridine Fe(II) catalyst.	6
Figure 2 Iron-based photosensitizers	6
Figure 3 Proposal mechanism of iron-catalyzed cycloaddition of epoxides to CO ₂	9
Figure 4 First C,N-chelating abnormal pyridylidene complex	13
Figure 5 First terpyridinium-derived N,N,C-chelating ruthenium complex	14
Figure 6 Octahedral iron complex based on chiral 1,10-phenanthroline ligands	20
Figure 7 Proposed mechanism of bis(imine)diphosphine-Fe-catalyzed ATH reaction of ketones.	30
Figure 8 Chiral ferrocene-based bis(imine)diphosphine iron catalyst.....	34
Figure 9 PNP-based iron catalysts.....	35
Figure 10 Asymmetric transition metal catalyst. (a) Design from chiral ligands versus achiral ligands. (b) Metal-centered chirality exclusively	36
Figure 11 Aim 1: Design chiral-at-ruthenium complexes from 2-imidazolylidene versus pyridylidene ligands	37
Figure 12 Aim 2: Design and synthesis of chiral-at-iron catalyst	38
Figure 13 Design of new chiral-at-ruthenium catalysts.....	48
Figure 14 Ruthenium complex with 3'-methyl 2,3'-bipyridinium ligands.....	50
Figure 15 ¹ H NMR (300 MHz, CD ₃ CN) spectra: (a) Reaction mixture; (b) Isolated solid; (c) Crystals	51
Figure 16 Crystal structure of <i>rac</i> - Ru1 . ORTEP drawing with 50% probability thermal ellipsoids. The hexafluorophosphate counteranion and all hydrogens are omitted for clarity.....	51
Figure 17 Crystal structure of <i>rac</i> - Ru2 . ORTEP drawing with 50% probability thermal ellipsoids. The hexafluorophosphate counteranion and all hydrogens are omitted for clarity.....	53
Figure 18 ¹ H NMR (300 MHz, CD ₃ CN) spectra. (a) First fraction. (b) Second fraction. (c) Third fraction..	55
Figure 19 ¹ H NMR (300 MHz, CD ₃ CN) spectra of reactions: (a) pure <i>rac</i> - Ru3 . (b) At the 130 °C. (c) At the 120 °C. (d) At the 100 °C.....	56
Figure 20 Crystal structure of <i>rac</i> - Ru3 . ORTEP drawing with 50% probability thermal ellipsoids. The hexafluorophosphate counteranion and all hydrogens are omitted for clarity.....	57
Figure 21 Crystal structure of <i>rac</i> - Ru4 . Displacement ellipsoids are shown at 50 % probability level at 100 K. The hexafluorophosphate counteranion, the acetonitrile solvent molecule and all hydrogens are not shown	58
Figure 22 Crystal structure of Λ -(<i>S</i>)- Ru2-Aux . ORTEP drawing with 50% probability thermal ellipsoids. The hexafluorophosphate counteranion and all hydrogens are omitted for clarity.....	61
Figure 23 CD spectrum of complexes Λ -(<i>S</i>)/ Δ -(<i>R</i>)- Ru2-Aux in CH ₃ CN (1.0 mM).....	61
Figure 24 Crystal structure of Λ - rNHCRu2* . ORTEP drawing with 50% probability thermal ellipsoids. The	

hexafluorophosphate counteranion and all hydrogens are omitted for clarity.....	62
Figure 25 CD spectrum of complexes Λ -/ Δ - rNHCRu2* in CH ₃ CN (1.0 mM).....	63
Figure 26 CD spectrum of complexes Λ -(<i>S</i>)-/ Δ -(<i>R</i>)- Ru4-Aux in CH ₃ CN (1.0 mM).....	64
Figure 27 CD spectrum of complexes Λ -/ Δ - rNHCRu4* in CH ₃ CN (1.0 mM).....	64
Figure 28 ¹ H NMR (300 MHz) spectra of Λ - rNHCRu2* recorded in CD ₃ CN.....	65
Figure 29 ¹ H NMR (300 MHz) spectra of Λ - rNHCRu4* recorded in CD ₃ CN.....	65
Figure 30 <i>Trans</i> -effect studied by bond length comparison of metal-acetonitrile. (a) <i>Trans</i> -effect of pyridylidenes versus imidazolylidene. (b) <i>Trans</i> -effect of pyridylidenes versus pyridyl ring.	67
Figure 31 Comparison of <i>trans</i> -effect of pyridylidene ligands with different substituents.....	68
Figure 32 Chiral transition metal catalysis. (a) Combining configurational stability of a metal center with some labile ligands. (b) Chiral-at-iron catalyst developed in this study.....	72
Figure 33 ¹ H NMR (300 MHz) spectra of <i>rac</i> - FeH recorded in CD ₂ Cl ₂	74
Figure 34 ¹ H NMR (300 MHz) spectra of Fe1 recorded in CD ₂ Cl ₂	74
Figure 35 ¹ H NMR (300 MHz, CD ₂ Cl ₂) spectra. (a) Complex <i>rac</i> - Fe1 . (b) Reaction of <i>rac</i> - Fe1 with chiral ligand in the presence of Et ₃ N. (c) Reaction of Λ - Fe1 with chiral ligand in the presence of Et ₃ N. (d) Reaction of Δ - Fe1 with chiral ligand in the presence of Et ₃ N. (e) Chiral ligand in the presence of triethylamine.	76
Figure 36 Single crystal X-ray structure of Δ - Fe1 (CCDC 1892226). ORTEP drawing with 50% probability thermal ellipsoids. Solvent and counterion are omitted for clarity.....	77
Figure 37 CD spectra of Λ -/ Δ - Fe1 (MeCN at 1.0 mM).....	77
Figure 38 The structures of chiral-at-ruthenium and iron complexes.....	78
Figure 39 Chiral-at-iron complexes for asymmetric catalysis. X = alkoxy or azide.	83
Figure 40 ¹ H NMR (300 MHz, CD ₂ Cl ₂) spectra of representative Fe5 complexes. (a) Reaction of <i>rac</i> - Fe5 with chiral ligand in the presence of Et ₃ N. (b) Reaction of Λ - Fe5 with chiral ligand in the presence of Et ₃ N. (c) Reaction of Δ - Fe5 with chiral ligand in the presence of Et ₃ N.....	85
Figure 41 Crystal structure of racemic Fe2 . ORTEP drawing with 50% probability thermal ellipsoids. The [PF ₆] ⁻ anions, solvent molecules and all hydrogens are not shown.	86
Figure 42 X-ray crystal structure of racemic Fe5 . Only one enantiomer is shown. Only one disordered species of the CF ₃ groups is shown. The hexafluorophosphate anions, the acetonitrile solvent molecule and the hydrogen atoms are omitted. Displacement ellipsoids are shown at 50 % probability level at 100 K.	87
Figure 43 Substrate scope. Reaction conditions: ketoester (0.10 mmol), dienophile (0.15 mmol) and Λ - Fe5 (0.003 mmol, 3.0 mol%) in distilled CH ₂ Cl ₂ (2.0 mL) stirred at r.t. for 4 h under N ₂ . ^a Performed with 2 equivalents of dienophile (0.20 mmol). ^b Performed with 5 equivalents of dienophile (0.5 mmol). ^c Reaction time increased to 24 h and scale doubled (0.2 mmol ketoester).....	93
Figure 44 Racemization study. Conditions: All reactions were performed with Λ - Fe5 (2.0 mg, 1.71 μ mol) or Λ - Fe1 (1.9 mg, 1.71 μ mol) (>99:1 e.r., 1.0 eq) and ketoester 5a (1.6 mg, 8.55 μ mol, 5.0 eq) in dry CH ₂ Cl ₂ (1 mL) for 4 hours. After a certain incubation time under conditions described below, (<i>R</i>)- A3 solution (57 μ L, 0.03 M, 1.0 eq.) was added by syringe, followed by triethylamine solution (29 μ L, 0.07 M, 1.2 eq.). The resulting mixture was concentrated to dryness before stirred for 1 hour and analyzed in CD ₂ Cl ₂ by ¹ H NMR	

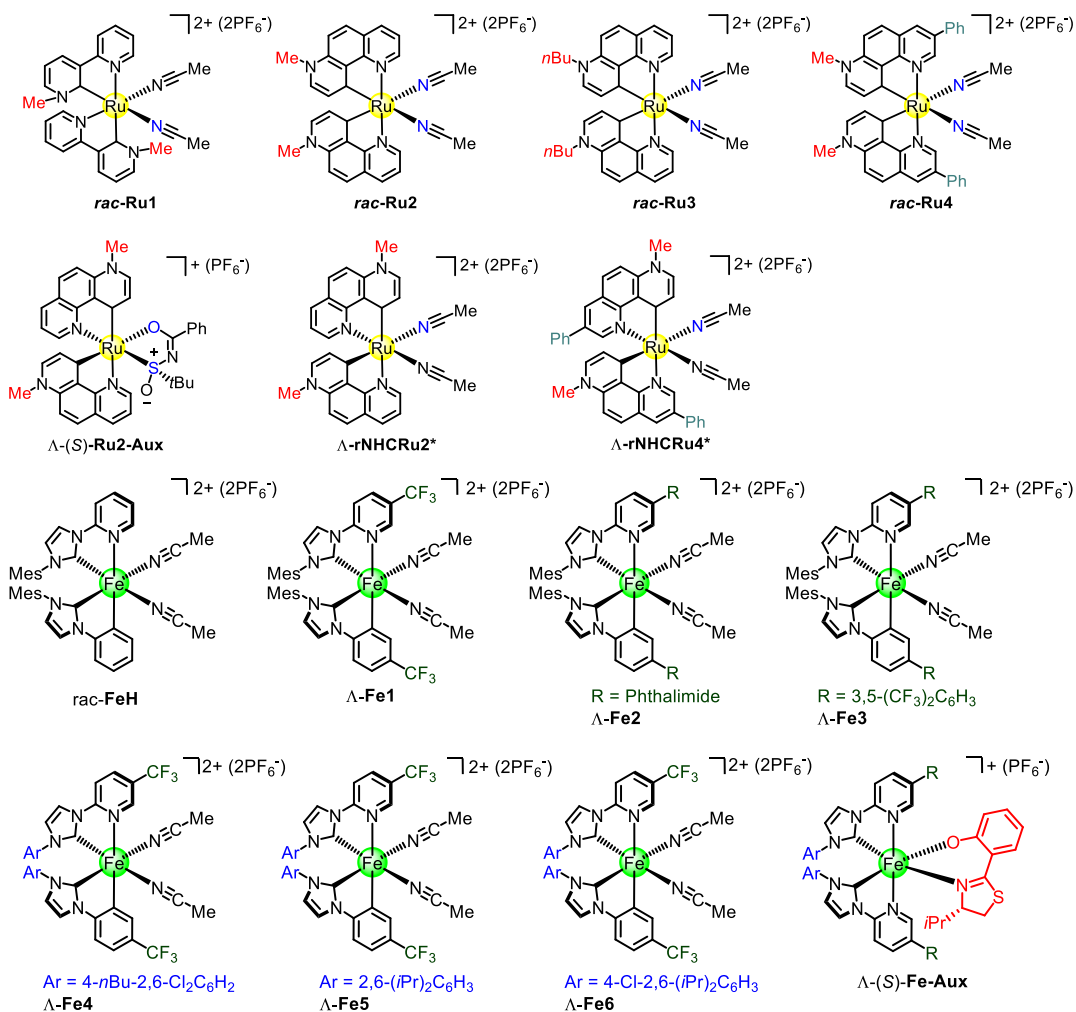
spectroscopy. Different reaction conditions for the initial incubation: (1) Under nitrogen atmosphere. (2) Under air atmosphere instead. (3) Under nitrogen atmosphere and addition of 0.1% H ₂ O. (4) Under air atmosphere and addition of 0.1% H ₂ O. (5) Under air atmosphere, addition of 0.1% H ₂ O, and addition of 0.1% MeCN. (6) In dry THF instead. (7) In dry MeOH instead	96
Figure 45 <i>Trans</i> -effect by bond length comparison of metal-acetonitrile	103
Figure 46 Iron-catalyzed asymmetric Nazarov cyclization and enantioselective Cannizzaro reaction	104
Figure 47 Selected examples of asymmetric Oxa-Diels-Alder cycloadditions	105
Figure 48 Crystal structure of <i>rac</i> - Ru1 . ORTEP drawing with 50% probability thermal ellipsoids. The hexafluorophosphate counteranion and all hydrogens are omitted for clarity.....	120
Figure 49 Crystal structure of <i>rac</i> - Ru2 . ORTEP drawing with 50% probability thermal ellipsoids. The hexafluorophosphate counteranion and all hydrogens are omitted for clarity.....	122
Figure 50 Crystal structure of <i>rac</i> - Ru3 . ORTEP drawing with 50% probability thermal ellipsoids. The hexafluorophosphate counteranion and all hydrogens are omitted for clarity.....	124
Figure 51 Crystal structure of <i>rac</i> - Ru4 . Displacement ellipsoids are shown at 50 % probability level at 100 K. The hexafluorophosphate counteranion, the acetonitrile solvent molecule and all hydrogens are not shown.	126
Figure 52 Crystal structure of Λ -(<i>S</i>)- Ru2-Aux . ORTEP drawing with 50% probability thermal ellipsoids. The hexafluorophosphate counteranion and all hydrogens are omitted for clarity.....	128
Figure 53 Crystal structure of Λ - rNHCRu2* . ORTEP drawing with 50% probability thermal ellipsoids. The hexafluorophosphate counteranion and all hydrogens are omitted for clarity.....	130
Figure 54 Crystal structure of Δ - Fe1 . ORTEP drawing with 50% probability thermal ellipsoids. The hexafluorophosphate counteranion, solvent and all hydrogens are omitted for clarity.	138
Figure 55 NOESY spectrum of 8 in CDCl ₃ at 300 K, mixing time 2.5 s. Those configurations 3a <i>S</i> , 4 <i>S</i> and 7a <i>R</i> were predefined, while 6 <i>S</i> was determined by NMR.	172
Figure 56 CD spectra of Λ -(<i>S</i>)/ Δ -(<i>R</i>)- Fe2-Aux recorded in CH ₃ CN (1.0mM).....	173
Figure 57 CD spectra of Λ / Δ - Fe2 recorded in CH ₃ CN (1.0mM)	173
Figure 58 CD spectra of Λ -(<i>S</i>)/ Δ -(<i>R</i>)- Fe3-Aux recorded in CH ₃ CN (1.0mM).....	174
Figure 59 CD spectra of Λ / Δ - Fe3 recorded in CH ₃ CN (1.0mM)	174
Figure 60 CD spectra of Λ -(<i>S</i>)/ Δ -(<i>R</i>)- Fe4-Aux recorded in CH ₃ CN (1.0mM).....	175
Figure 61 CD spectra of Λ / Δ - Fe4 recorded in CH ₃ CN (1.0mM)	175
Figure 62 CD spectra of Λ -(<i>S</i>)/ Δ -(<i>R</i>)- Fe5-Aux recorded in CH ₃ CN (1.0mM).....	176
Figure 63 CD spectra of Λ / Δ - Fe5 recorded in CH ₃ CN (1.0mM)	176
Figure 64 CD spectra of Λ -(<i>S</i>)/ Δ -(<i>R</i>)- Fe6-Aux recorded in CH ₃ CN (1.0mM).....	177
Figure 65 CD spectra of Λ / Δ - Fe6 recorded in CH ₃ CN (1.0mM)	177
Figure 66 Crystal structure of <i>rac</i> - Fe2 . ORTEP drawing with 50% probability thermal ellipsoids. The [PF ₆] ⁻ anions, solvent molecules and all hydrogens are not shown.	178
Figure 67 X-ray crystal structure of <i>rac</i> - Fe5 . Only one enantiomer is shown. Only one disordered species of the CF ₃ groups is shown. The hexafluorophosphate anions, the solvent molecule and the hydrogen atoms are	

omitted. Displacement ellipsoids are shown at 50 % probability level at 100 K.	180
Figure 68 Crystal structure of <i>rac</i> - Fe6 . ORTEP drawing with 50% probability thermal ellipsoids. The [PF ₆] ⁻ anions, solvent molecules and all hydrogens are not shown.	182
Figure 69 Crystal structure of 5s . Displacement ellipsoids are shown at 50 % probability level at 100 K. Hydrogen atoms are shown with arbitrary radii.	184
Figure 70 Crystal structure of 7sa . Hydrogen atoms are not shown. Displacement ellipsoids are shown at 50 % probability level at 100 K.	186

6.4 List of Tables

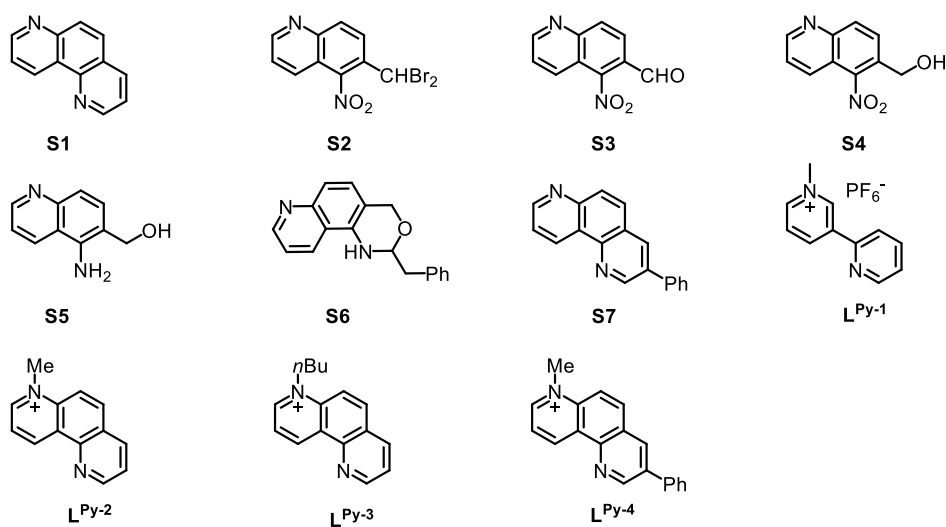
Table 1 Reaction optimization	56
Table 2 The Ru-N _{Acce} bonds to the acetonitrile ligands.....	66
Table 3 Enantioselective intramolecular Cannizzaro reaction catalyzed by Λ - or Δ - Fe1 ^a	80
Table 4 Asymmetric Nazarov cyclization catalyzed by Λ - Fe1 ^a	81
Table 5 Time course experiments.....	81
Table 6 Initial experiments and optimization ^a	90
Table 7 Crystal data and structure refinement for <i>rac</i> - Ru1	121
Table 8 Crystal data and structure refinement for <i>rac</i> - Ru2	123
Table 9 Crystal data and structure refinement for <i>rac</i> - Ru3	125
Table 10 Selected crystallographic data and details of the structure determination for <i>rac</i> - Ru4	127
Table 11 Crystal data and structure refinement for Λ -(<i>S</i>)- Ru2-Aux	129
Table 12 Crystal data and structure refinement for Λ -rNHCRu2*	131
Table 13 Crystal data and structure refinement for Δ - Fe1	138
Table 14 Key NOESY Cross Peaks of H85 in CDCl ₃	172
Table 15 Crystal data and structure refinement for <i>rac</i> - Fe2	179
Table 16 Crystal data and structure refinement for <i>rac</i> - Fe5	181
Table 17 Crystal data and structure refinement for <i>rac</i> - Fe6	183
Table 18 Selected crystallographic data and details of the structure determination for 5s	185
Table 19 Selected crystallographic data and details of the structure determination for 7sa	187

6.5 List of Octahedral Transition Metal Complexes

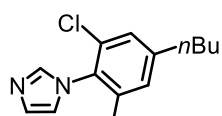


6.6 List of Organic Compounds

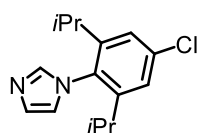
(1) Chapter 2 and its Experimental Part



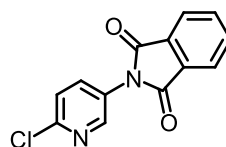
(2) Chapter 3 and its Experimental Part



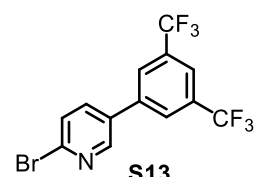
S8



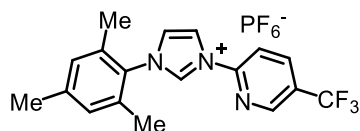
S10



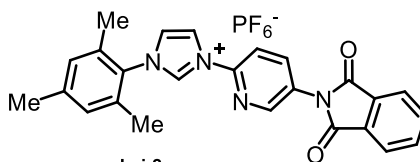
S12



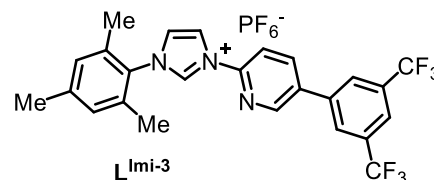
S13



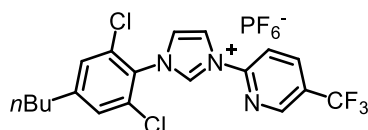
LImi-1



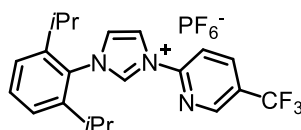
LImi-2



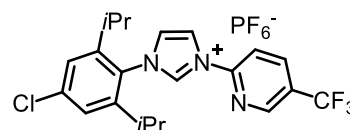
LImi-3



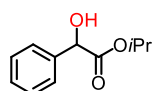
LImi-4



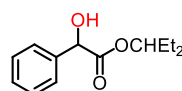
LImi-5



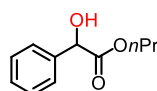
LImi-6



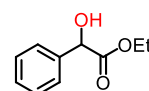
2a



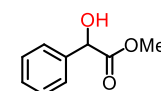
2b



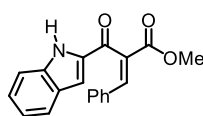
2c



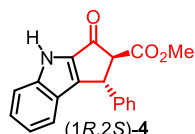
2d



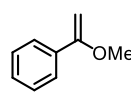
2e



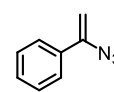
3



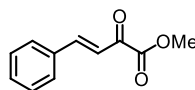
(1R,2S)-4



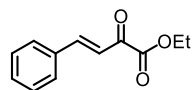
6e



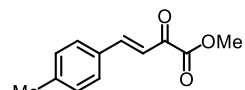
6f



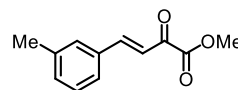
5a



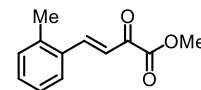
5b



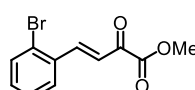
5c



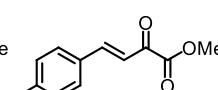
5d



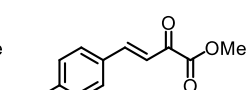
5e



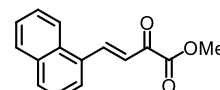
5f



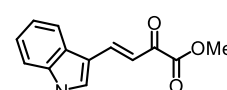
5g



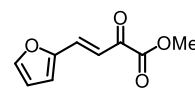
5h



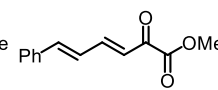
5i



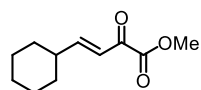
5j



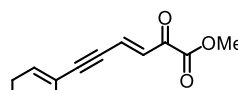
5k



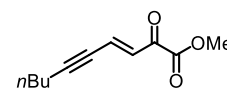
5l



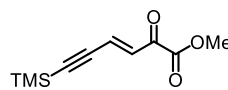
5m



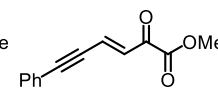
5n



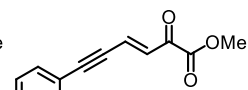
5o



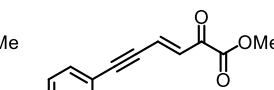
5p



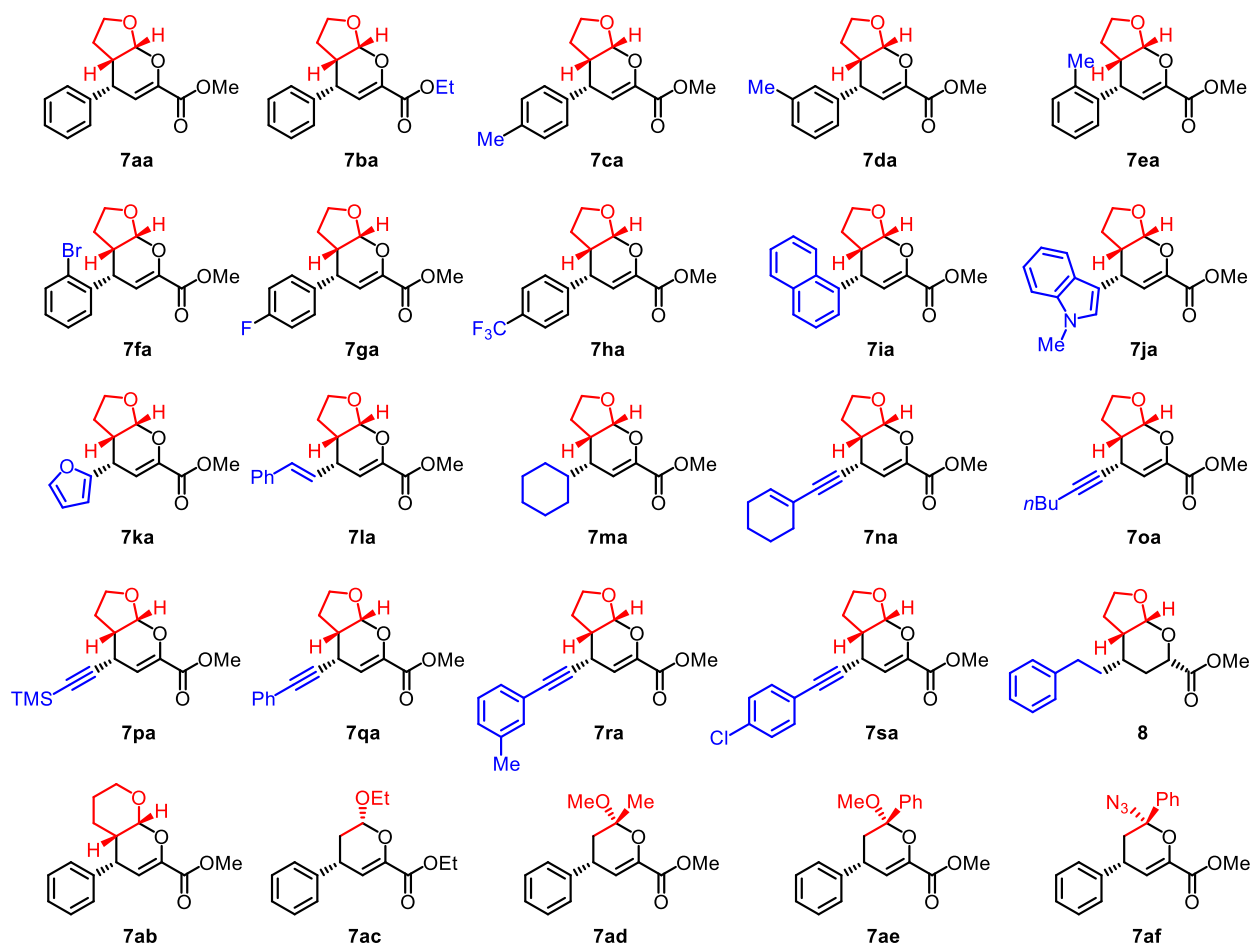
5q



5r,



5s



6.7 Enantiomeric Excess for Catalytic Reactions

Enantiomeric excess of the compounds **2a**, **4**, **7** and **8** were determined with a Daicel Chiralpak OD-H, AS-H, AD-H, IG or IA (250×4.6 mm) HPLC column on an Agilent 1260 Series HPLC System.

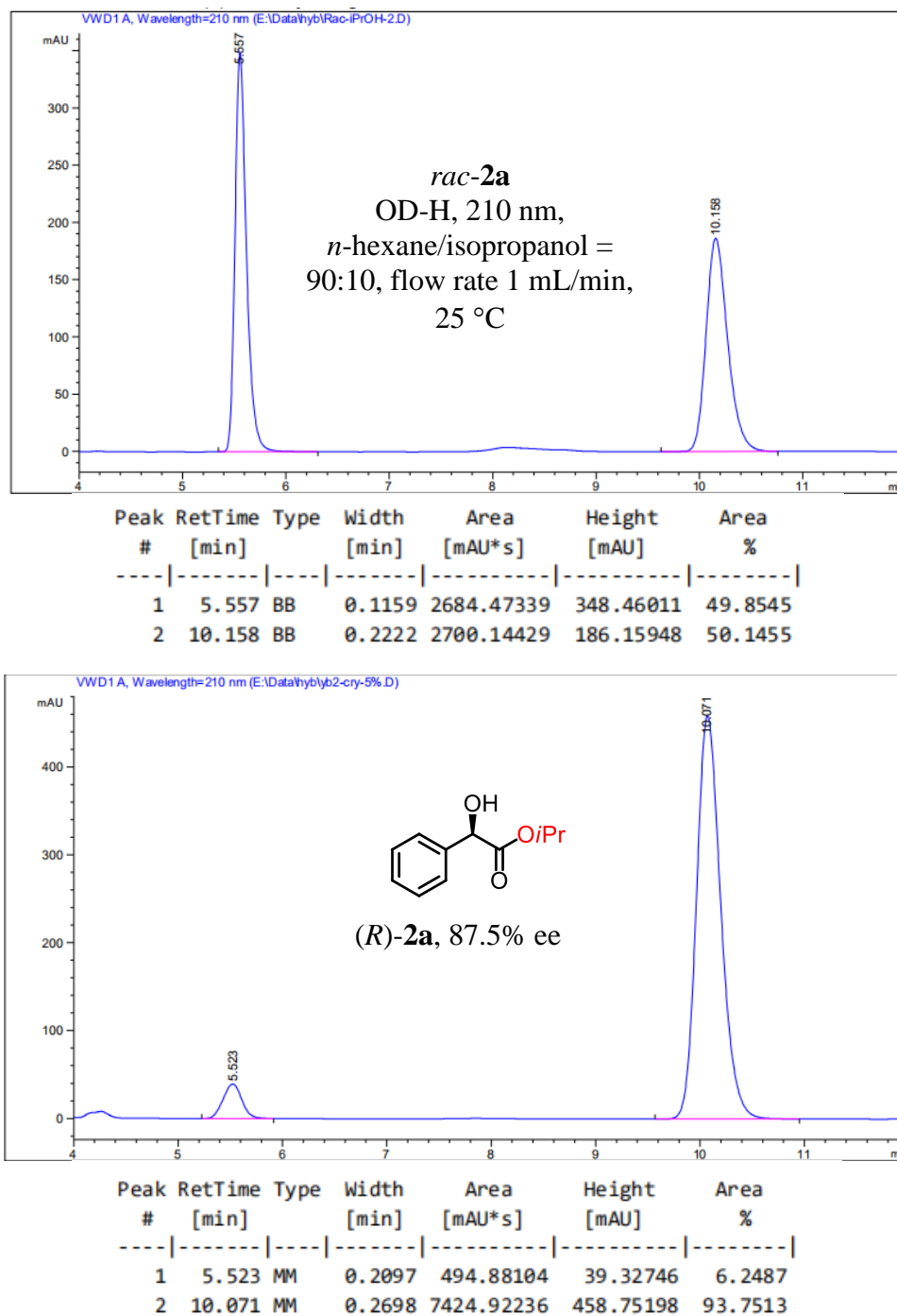
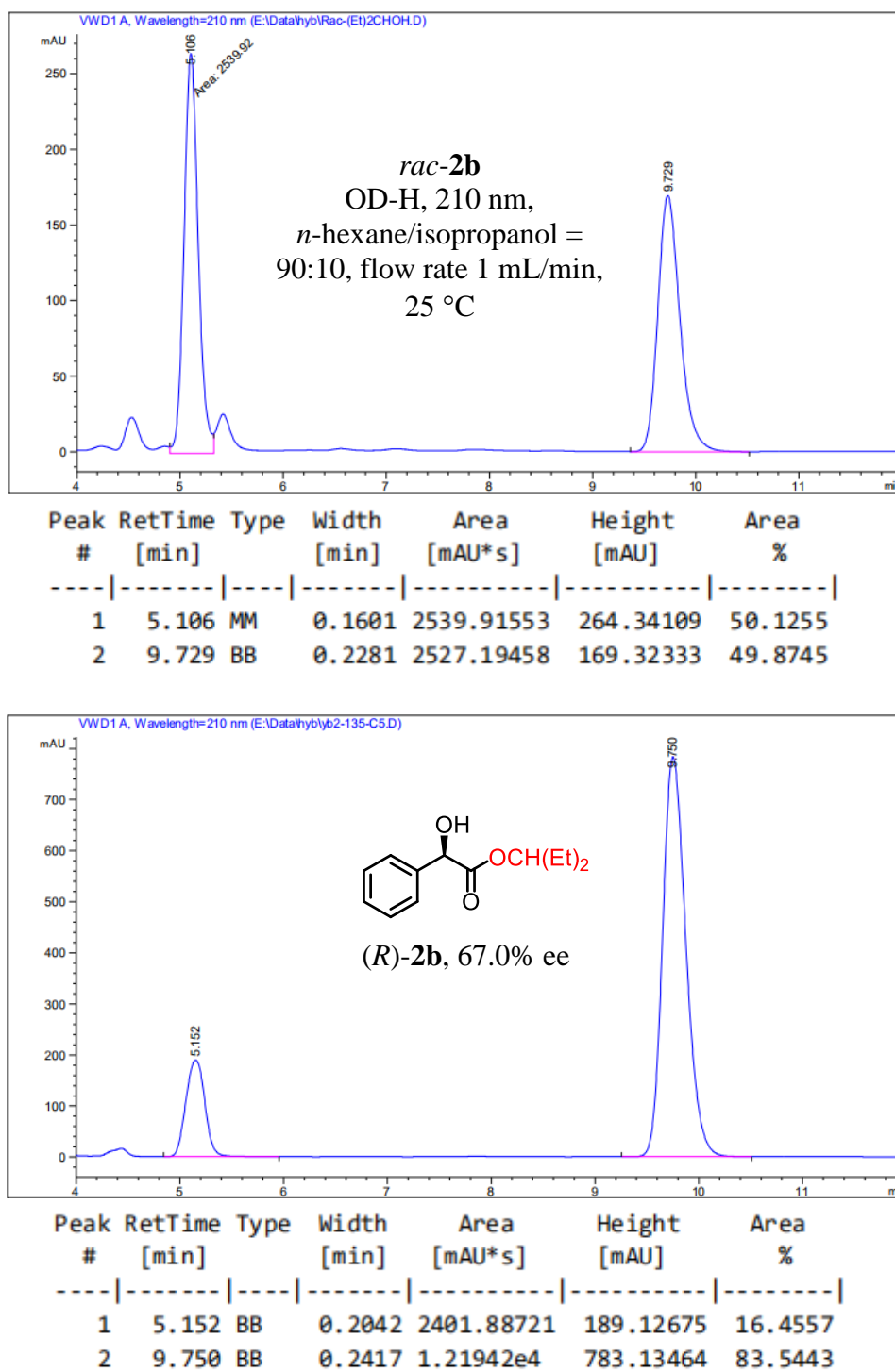
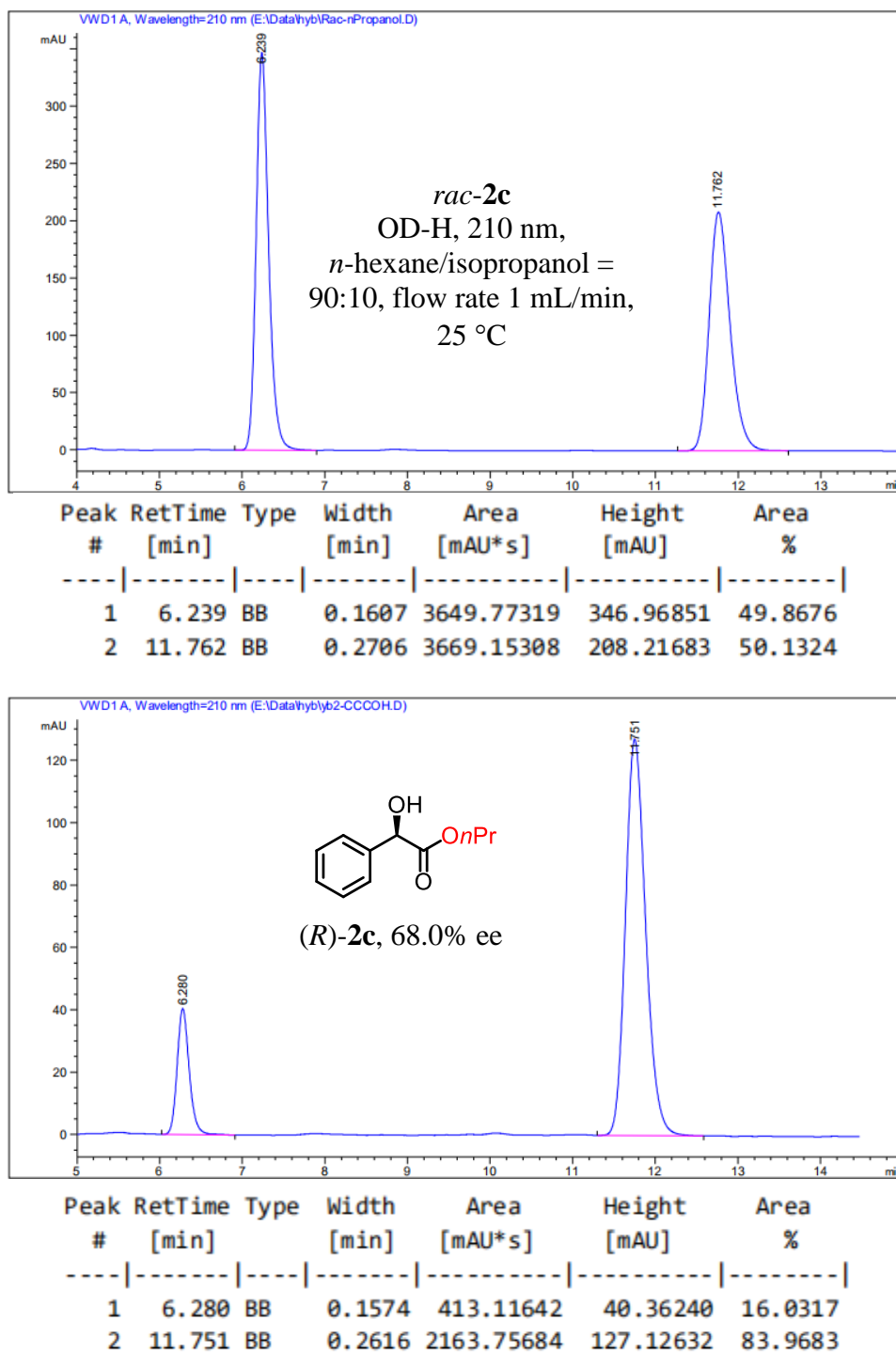
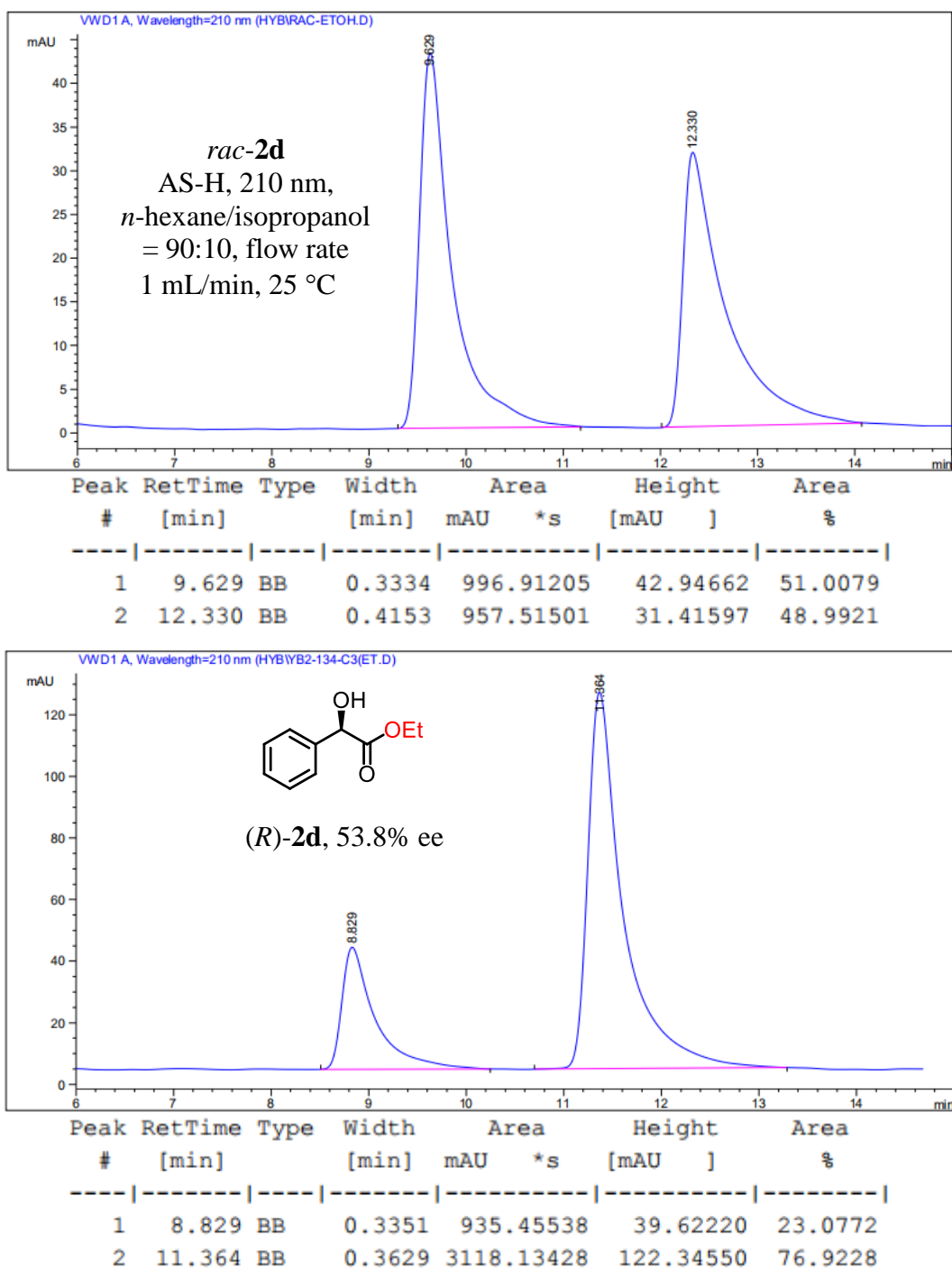
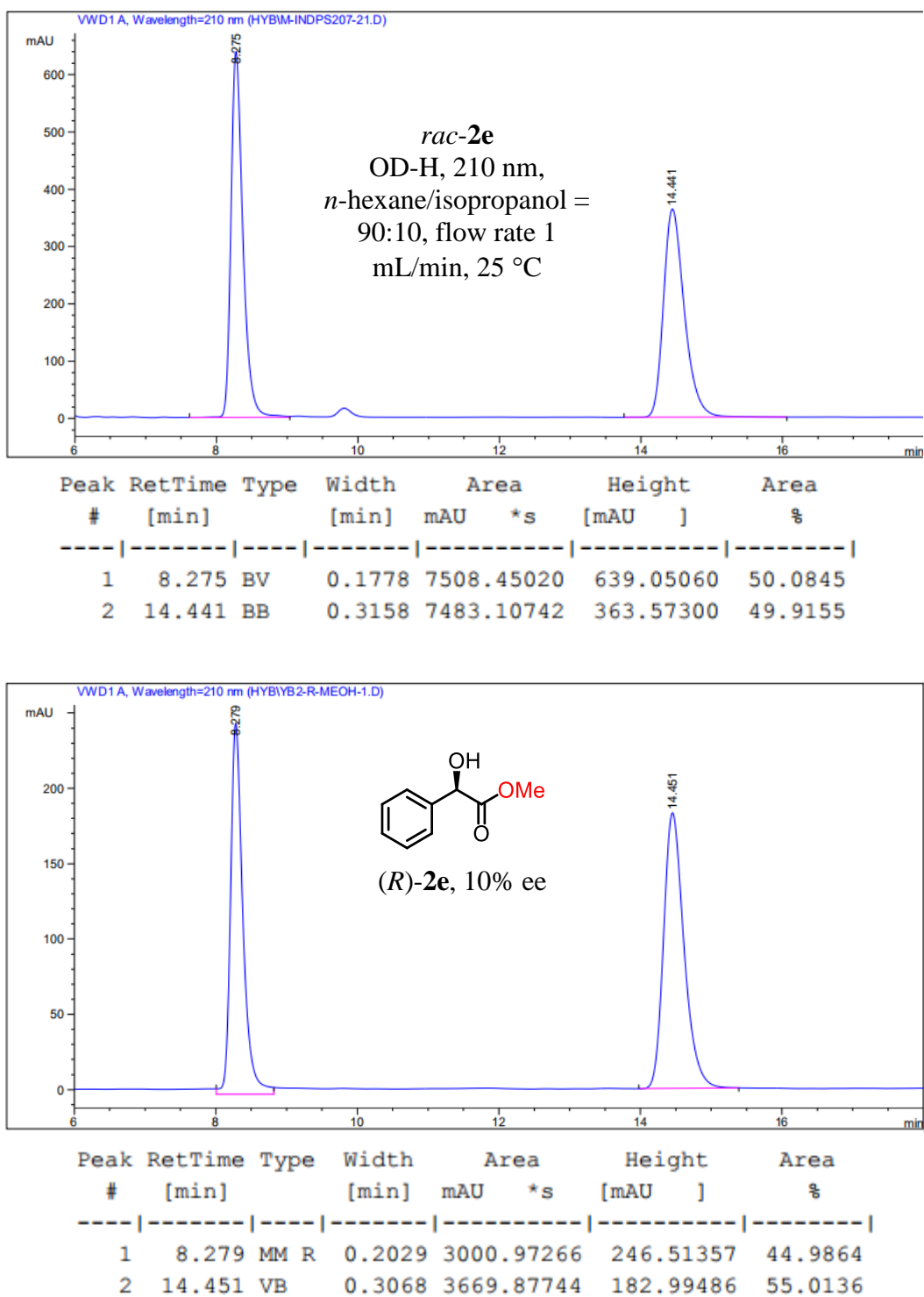


Figure 71. HPLC traces of *rac-2a* and *(R)-2a*.

Figure 72. HPLC traces of *rac-2b* and *(R)*-**2b**.

Figure 73. HPLC traces of *rac-2c* and *(R)-2c*.

Figure 74. HPLC traces of *rac*-**2d** and *(R)*-**2d**.

Figure 75. HPLC traces of *rac-2e* and *(R)*-**2e**.

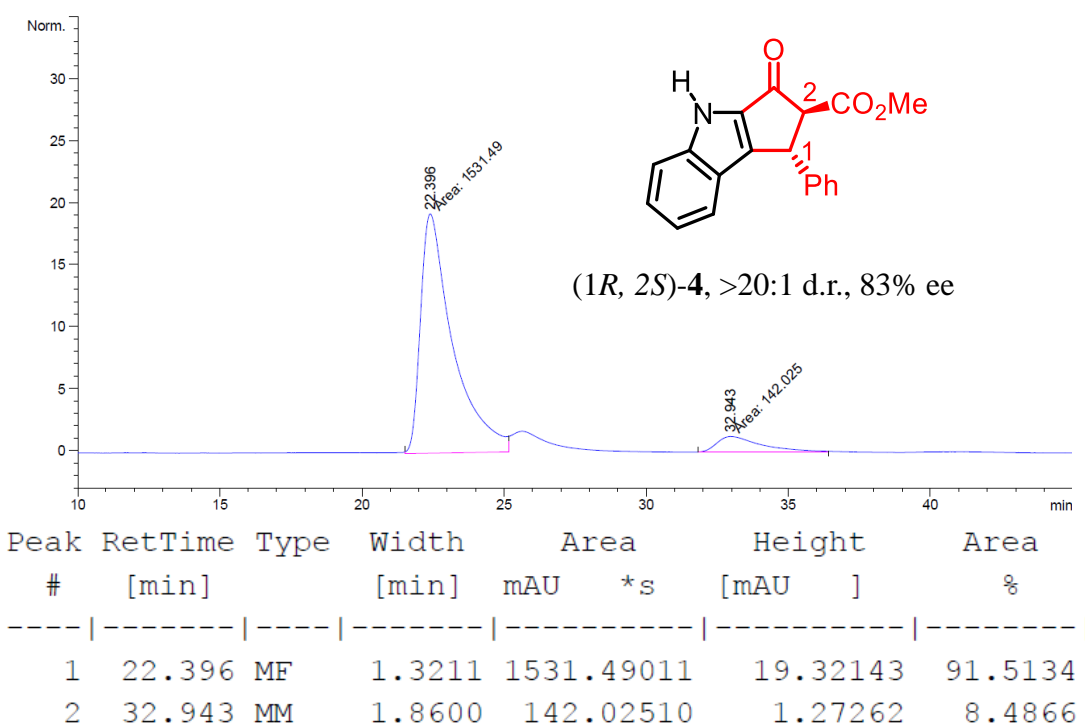
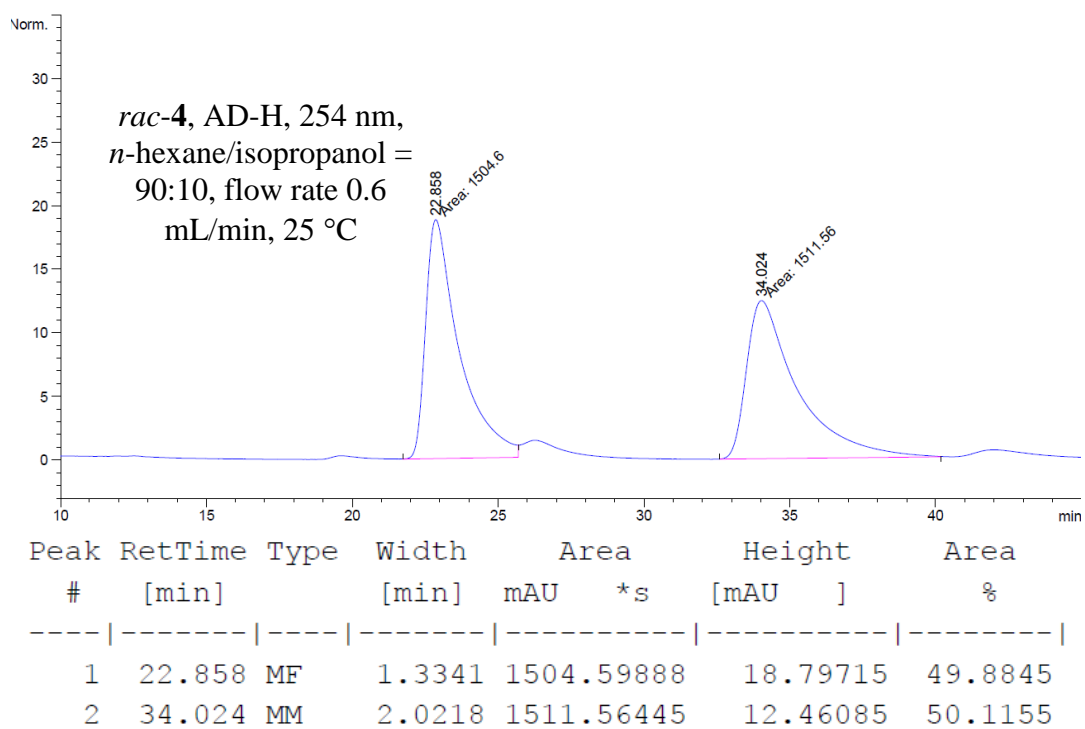
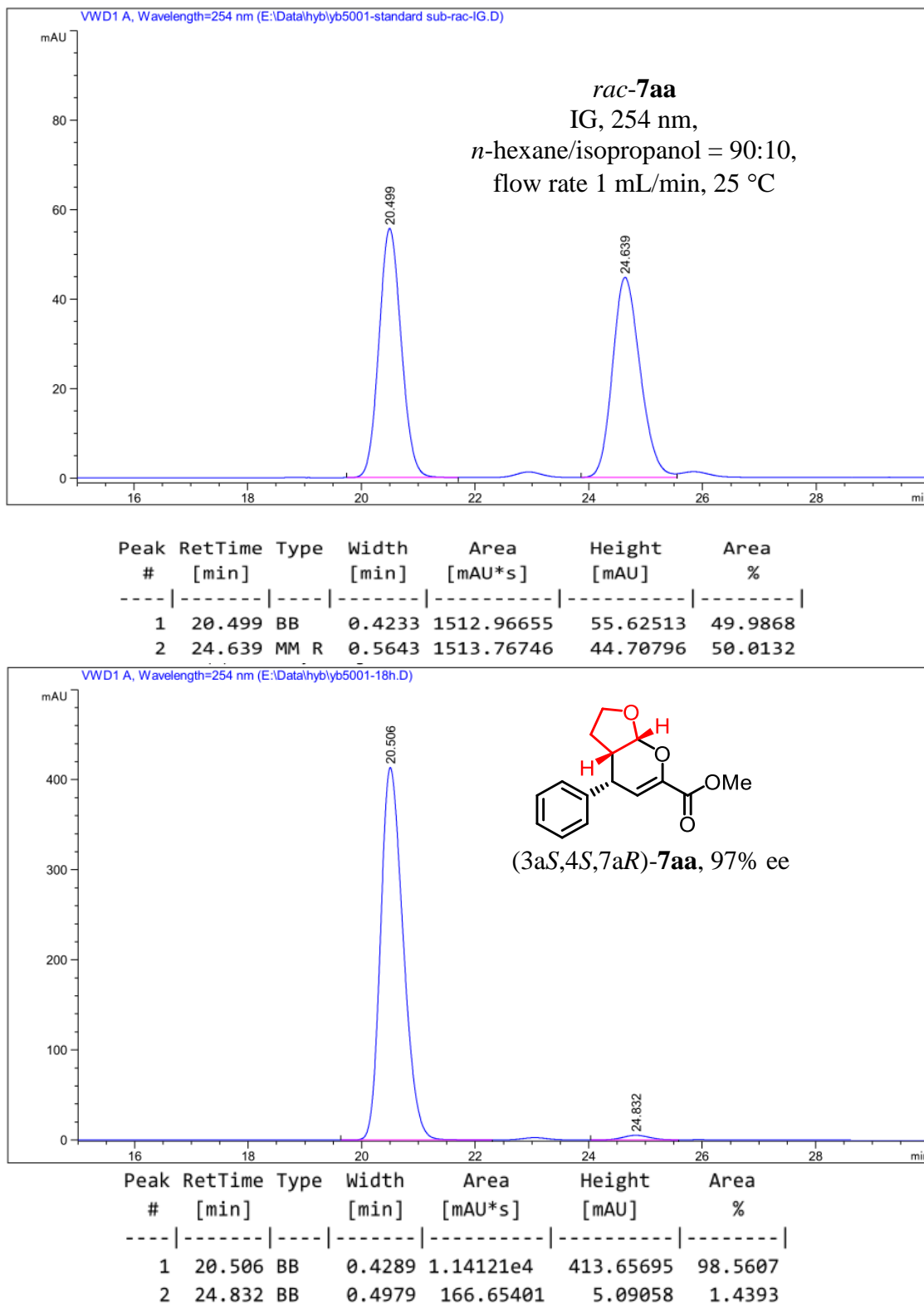


Figure 76. HPLC traces of *rac*-4 and (1*R*,2*S*)-4.

Figure 77. HPLC traces of *rac*-7aa and (3a*S*,4*S*,7a*R*)-7aa.

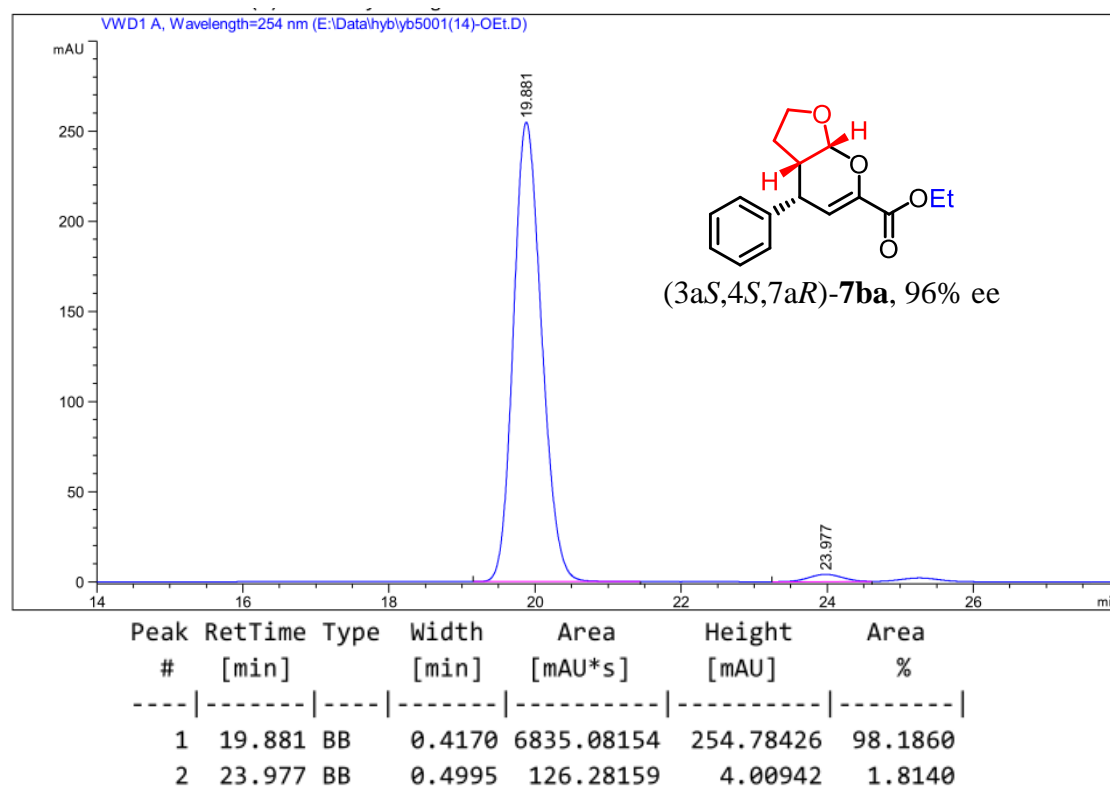
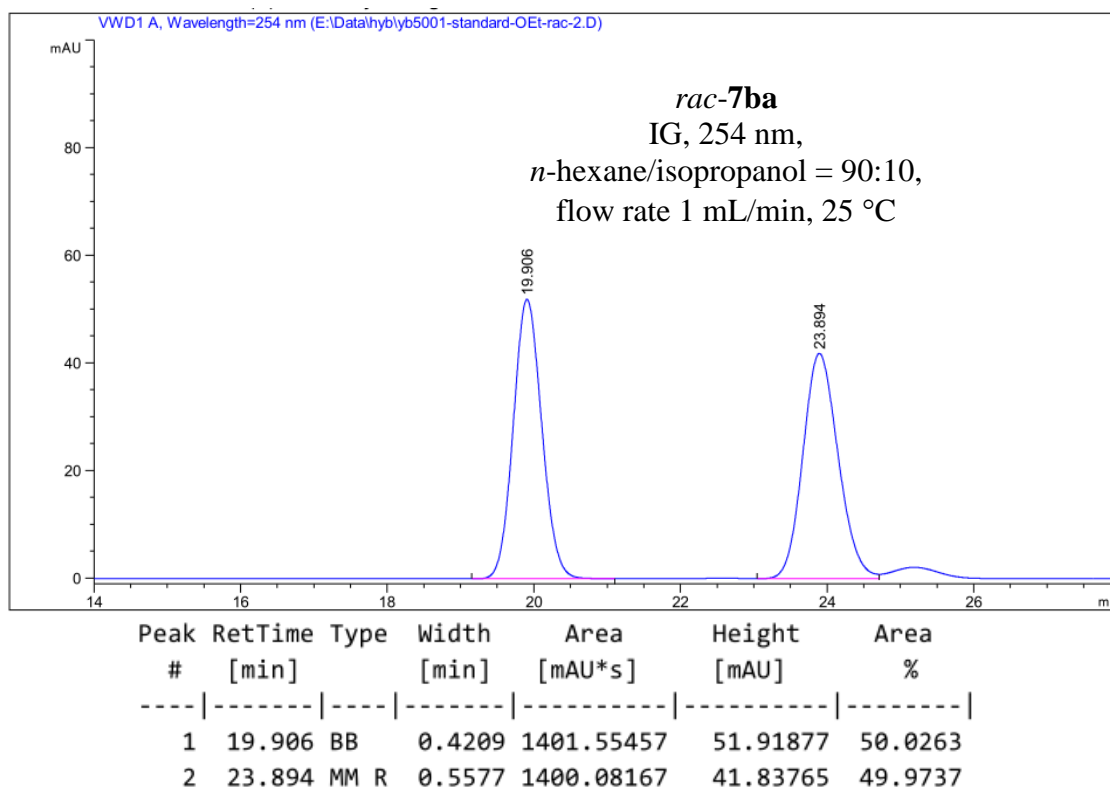


Figure 78. HPLC traces of *rac*-7ba and (3a*S*,4*S*,7a*R*)-7ba.

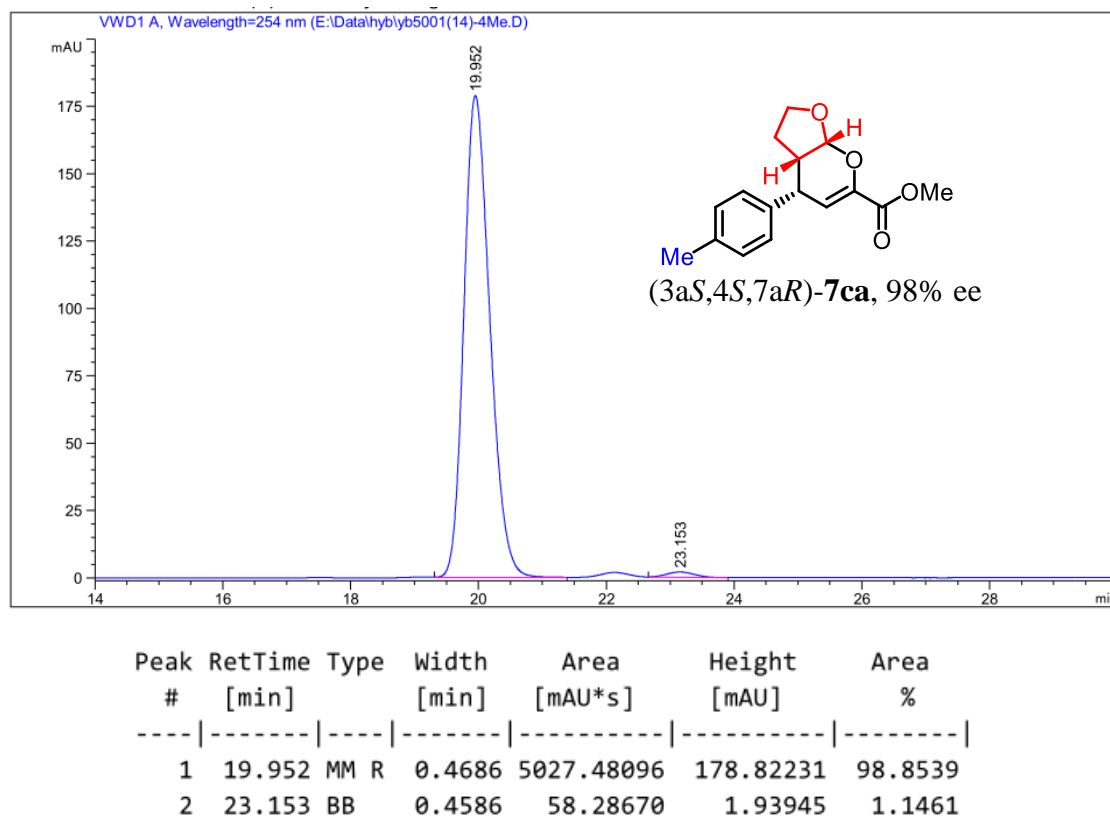
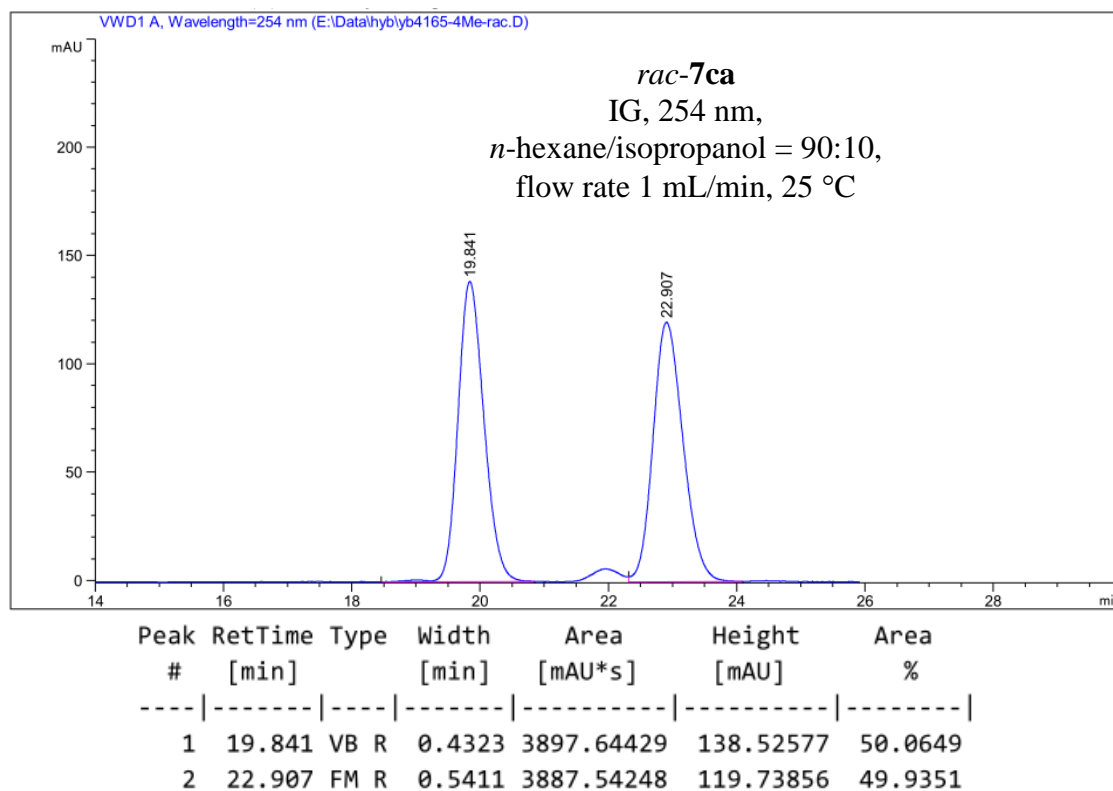
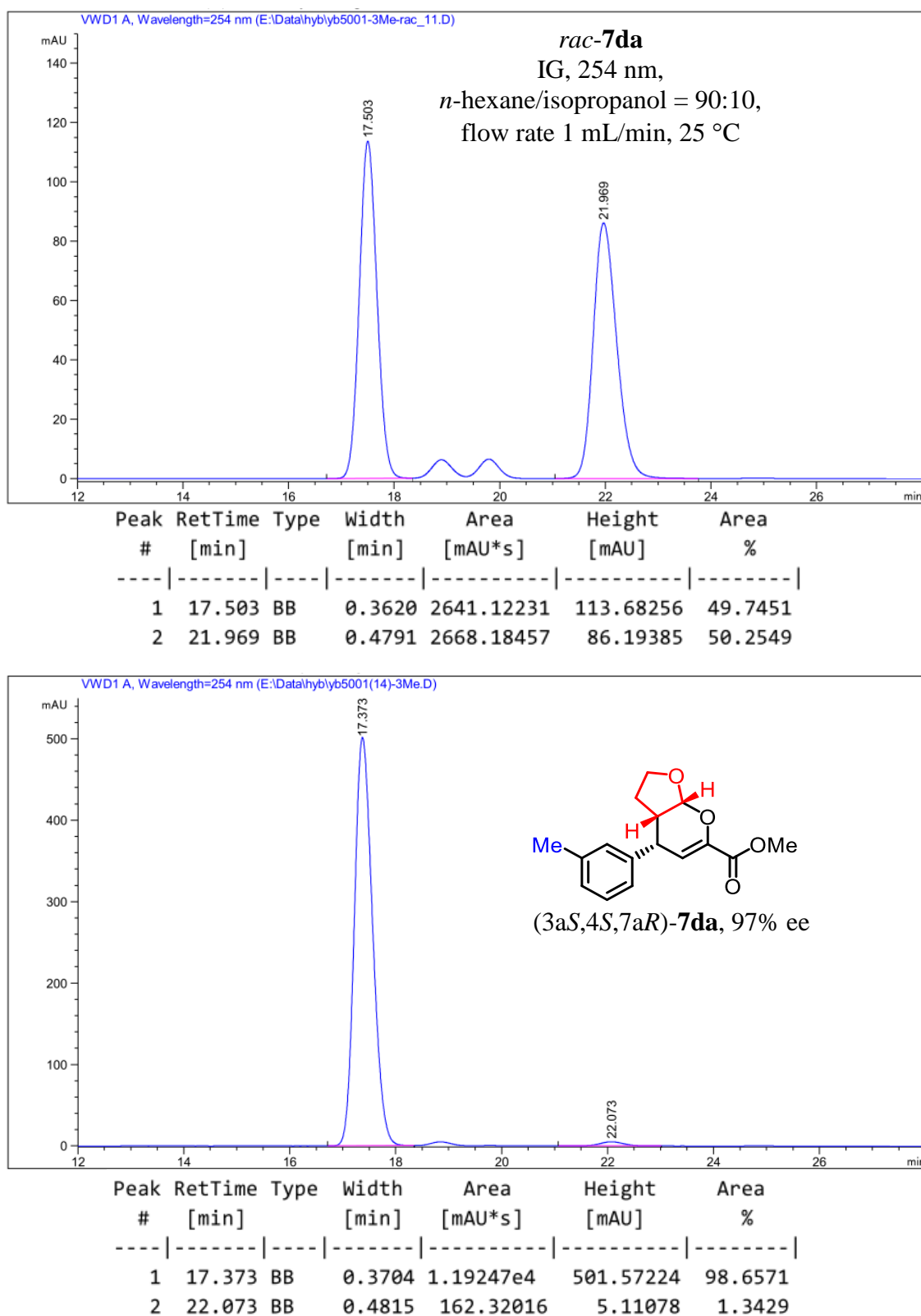
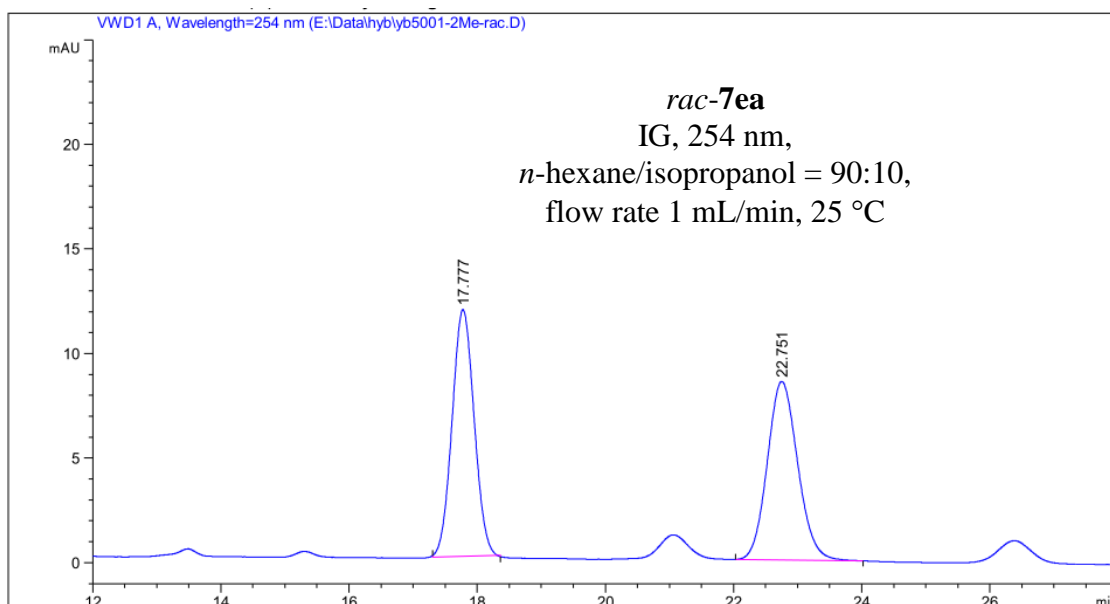
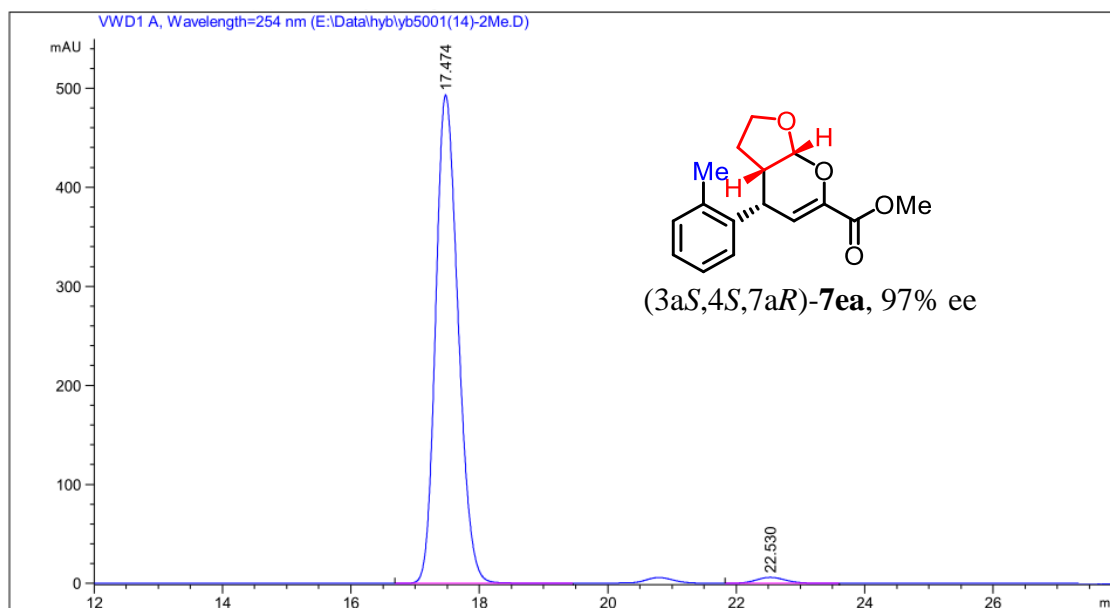


Figure 79. HPLC traces of *rac-7ca* and *(3aS,4S,7aR)-7ca*.

Figure 80. HPLC traces of *rac-7da* and (3*a**S*,4*S*,7*a**R*)-**7da**.



Peak #	RetTime [min]	Type	Width [min]	Area [mAU*s]	Height [mAU]	Area %
1	17.777	MM R	0.3984	282.18976	11.80505	50.0522
2	22.751	BB	0.5139	281.60117	8.53620	49.9478



Peak #	RetTime [min]	Type	Width [min]	Area [mAU*s]	Height [mAU]	Area %
1	17.474	BB	0.3778	1.19540e4	493.10492	98.3852
2	22.530	BB	0.4983	196.20491	6.08287	1.6148

Figure 81. HPLC traces of *rac-7ea* and (3*a**S*,4*S*,7*a**R*)-**7ea**.

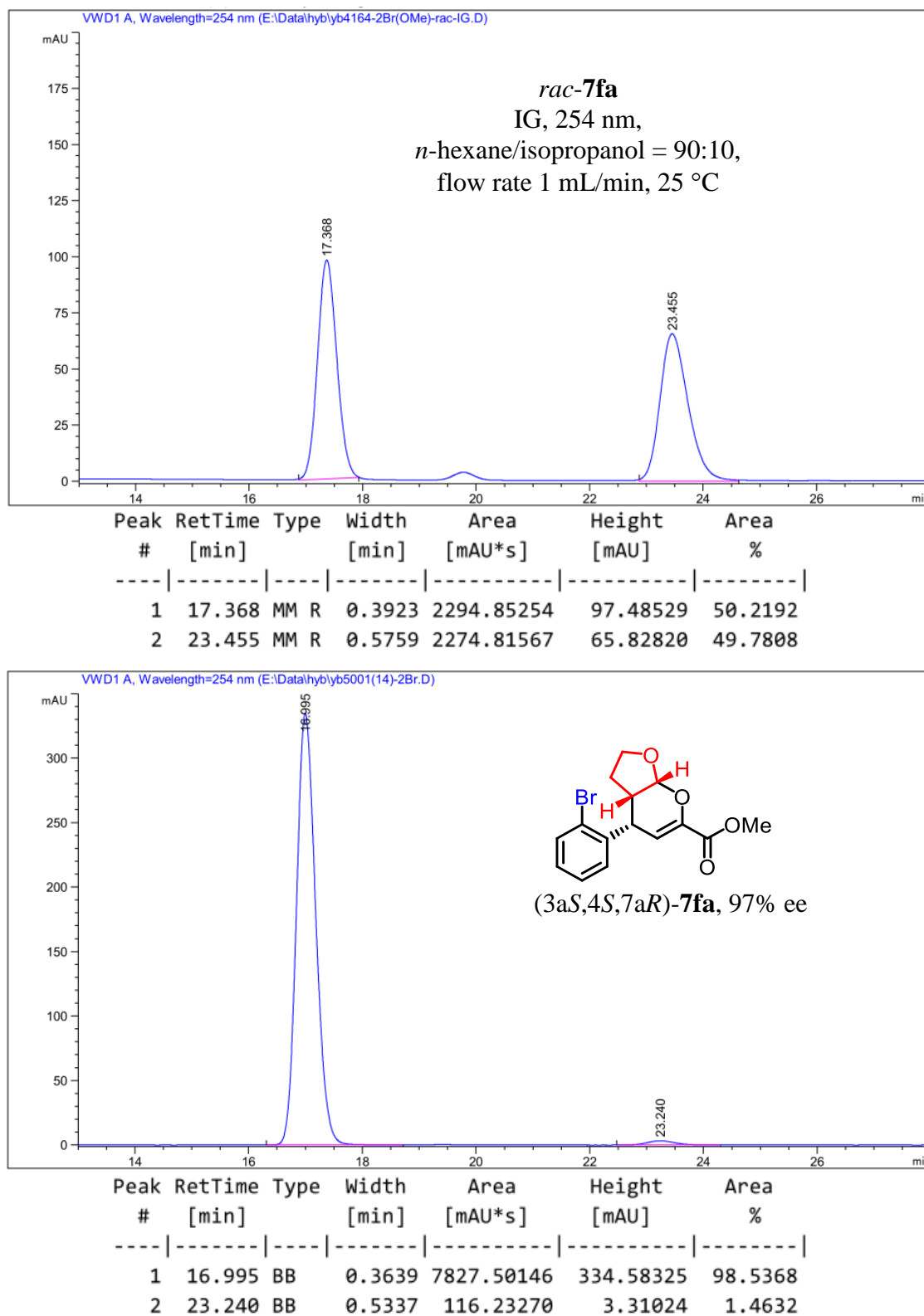


Figure 82. HPLC traces of *rac*-7fa and (3a*S*,4*S*,7a*R*)-7fa.

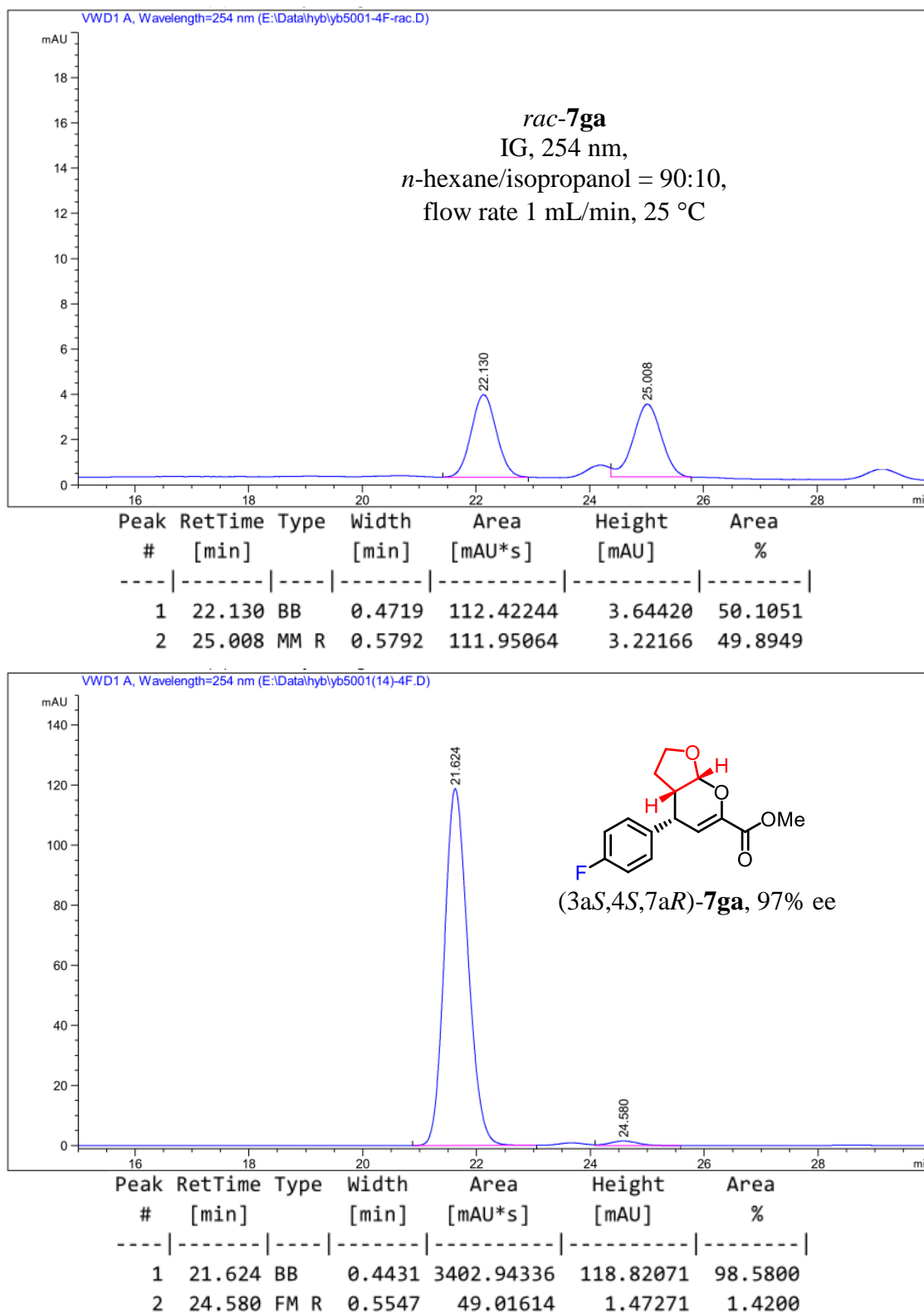
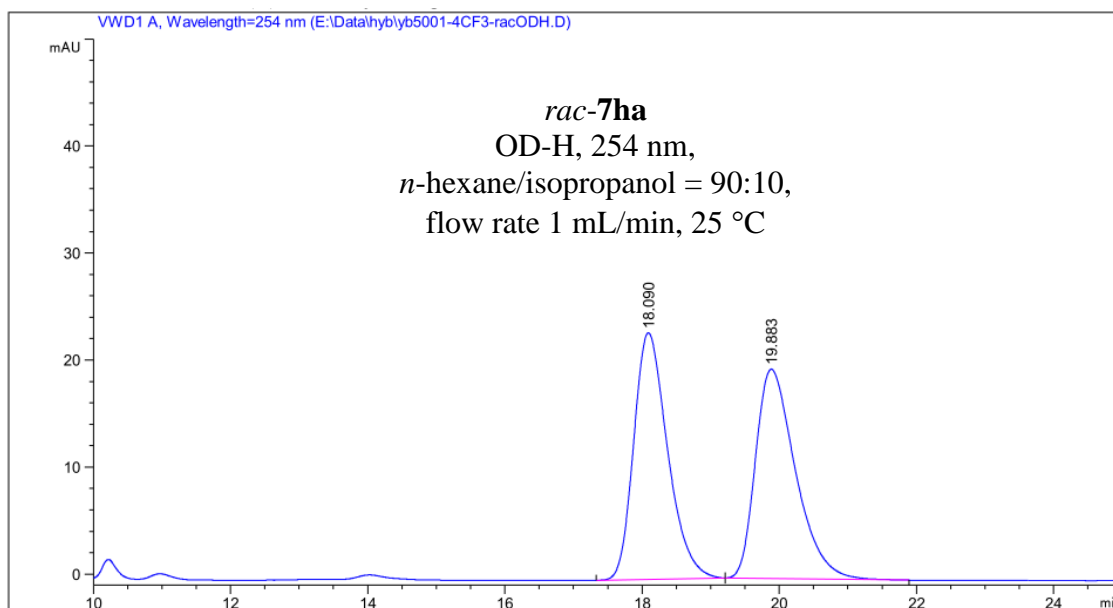
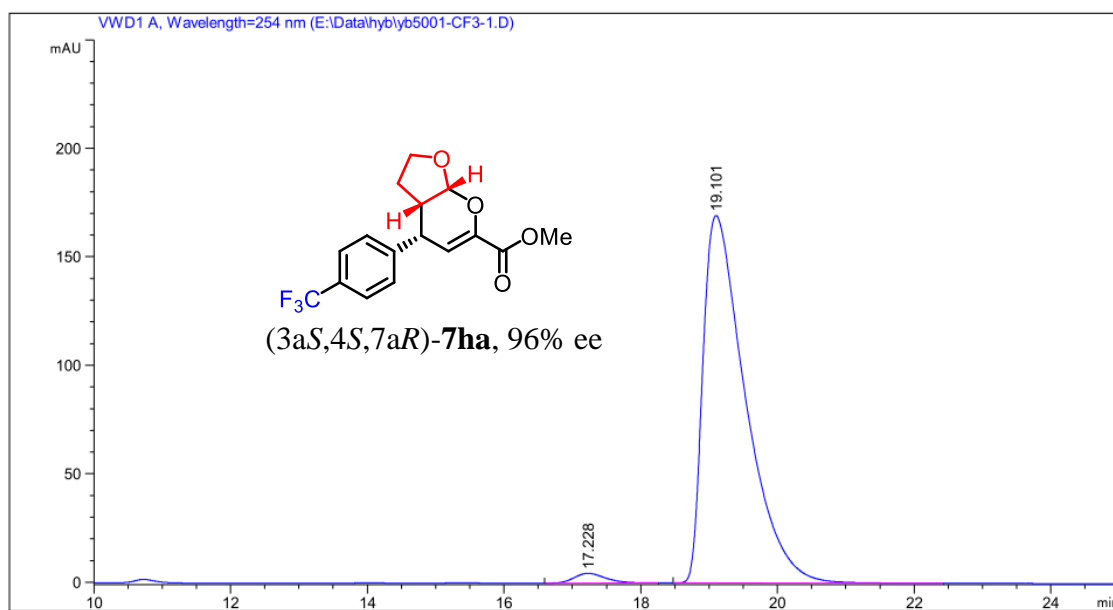


Figure 83. HPLC traces of *rac*-7ga and (3a*S*,4*S*,7a*R*)-7ga.

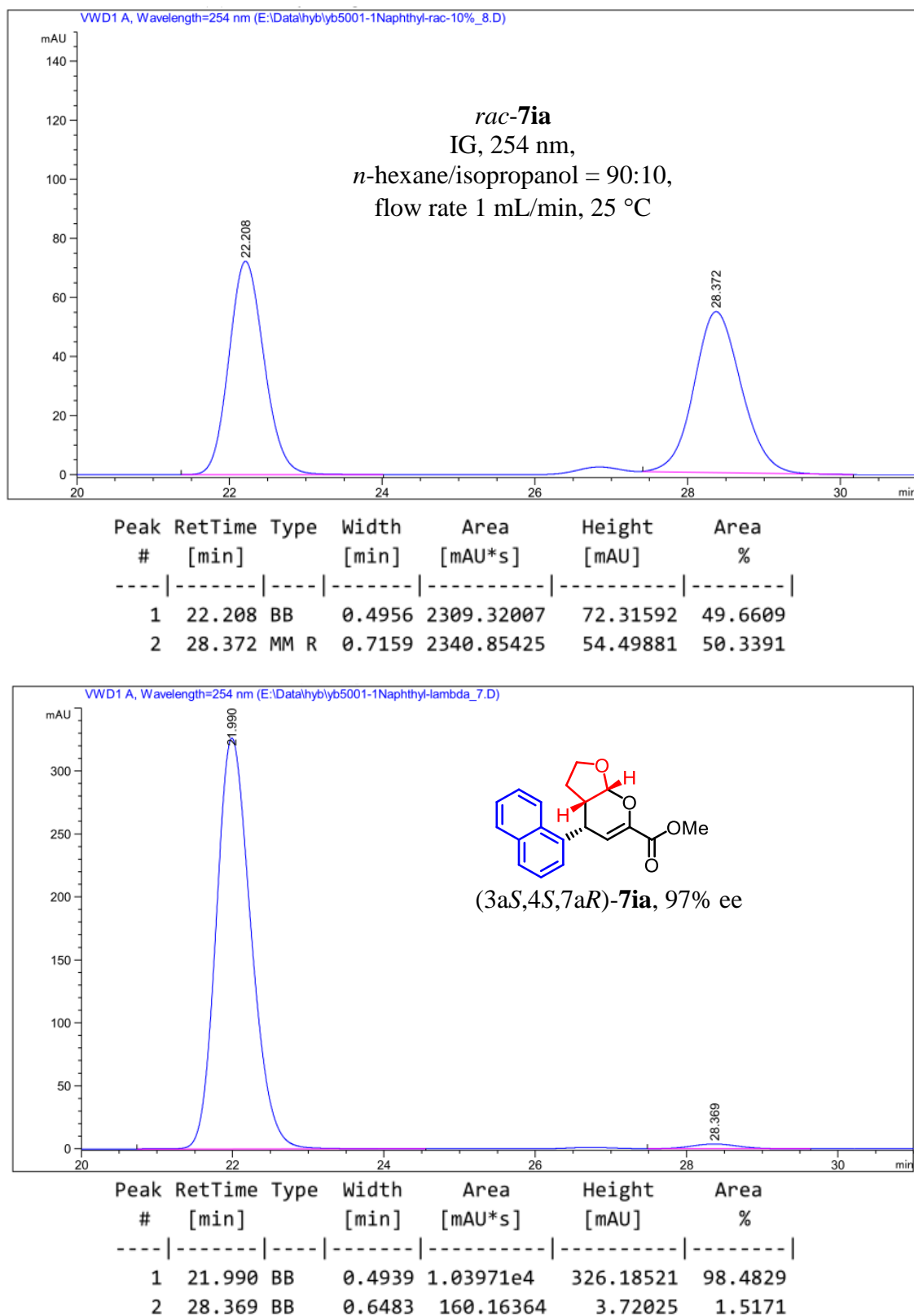


Peak #	RetTime [min]	Type	Width [min]	Area [mAU*s]	Height [mAU]	Area %
1	18.090	BB	0.5289	789.36633	23.03044	49.9472
2	19.883	BB	0.6227	791.03400	19.56499	50.0528



Peak #	RetTime [min]	Type	Width [min]	Area [mAU*s]	Height [mAU]	Area %
1	17.228	BB	0.4801	143.32990	4.49355	1.9228
2	19.101	BB	0.6456	7311.02783	169.37334	98.0772

Figure 84. HPLC traces of *rac-7ha* and (3*aS*,4*S*,7*aR*)-**7ha**.

Figure 85. HPLC traces of *rac-7ia* and (3*aS*,4*S*,7*aR*)-**7ia**.

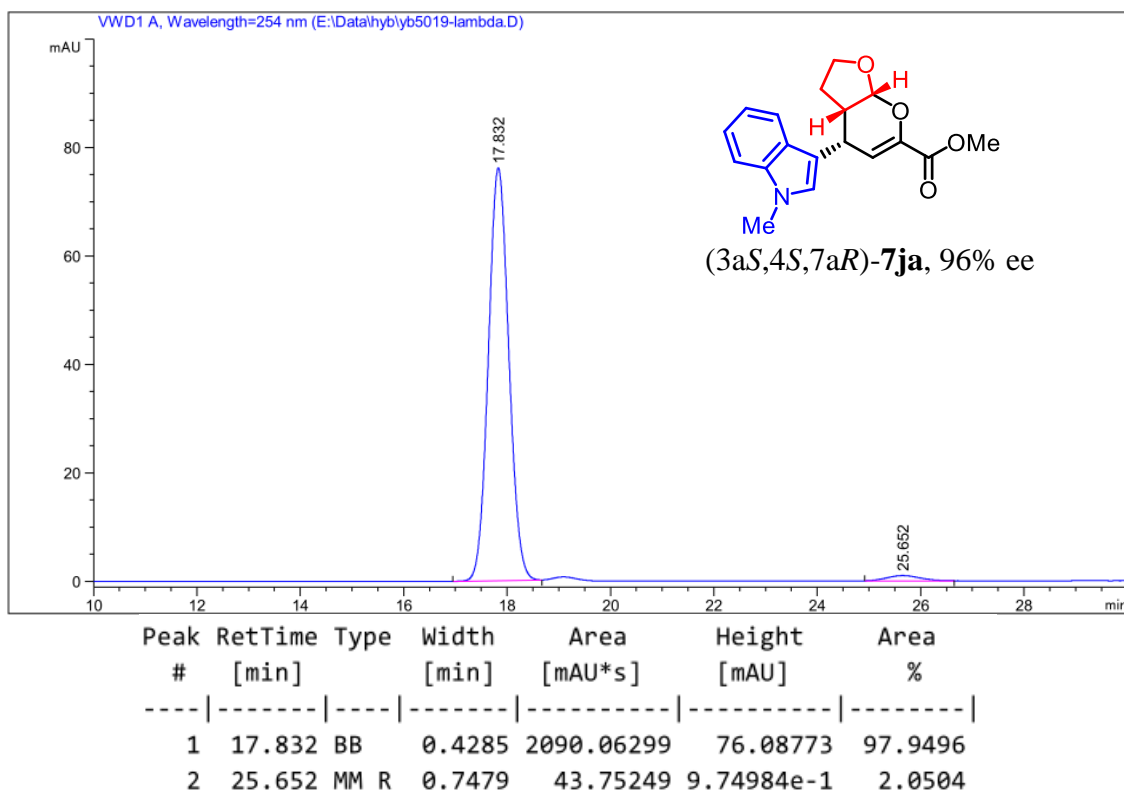
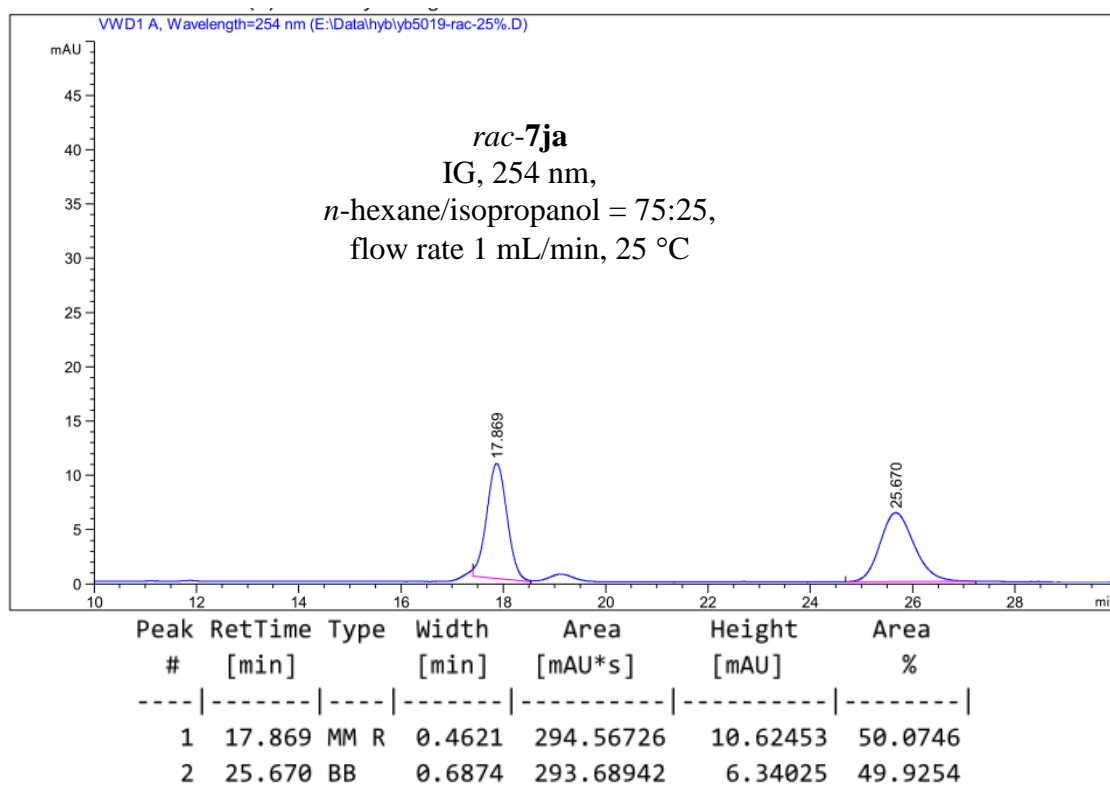


Figure 86. HPLC traces of *rac*-7ja and (3a*S*,4*S*,7a*R*)-7ja.

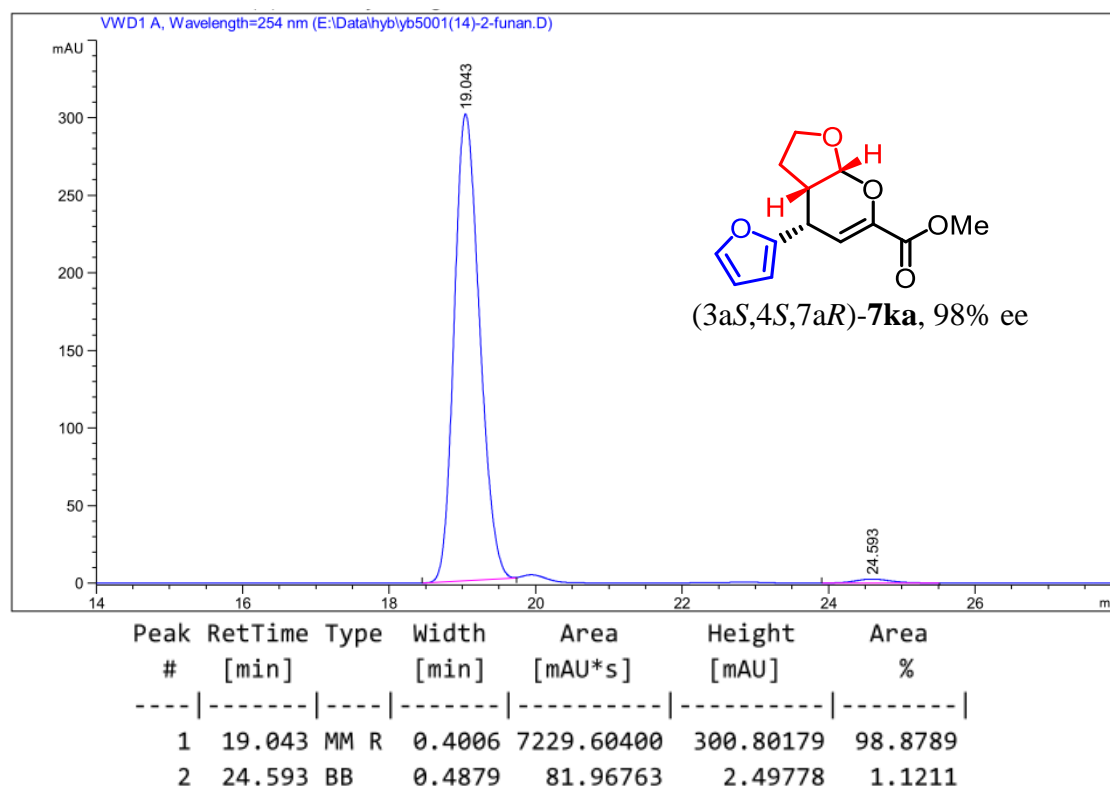
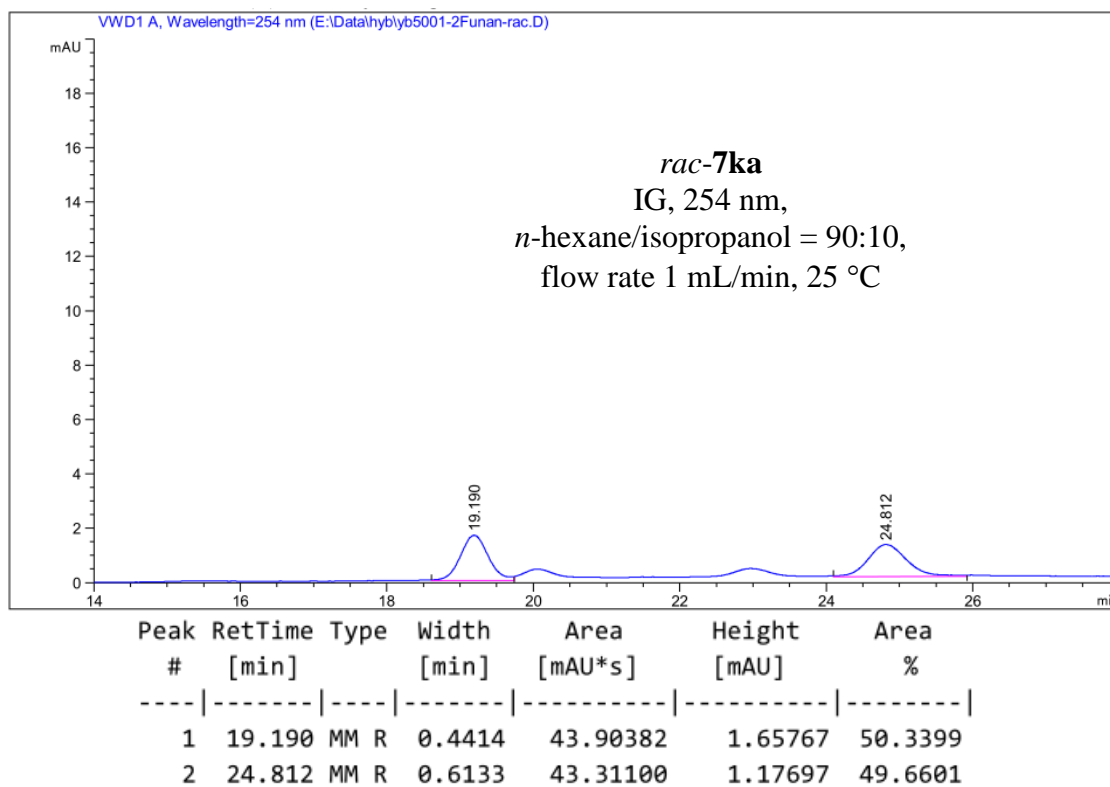


Figure 87. HPLC traces of *rac-7ka* and (3*aS*,4*S*,7*aR*)-7ka.

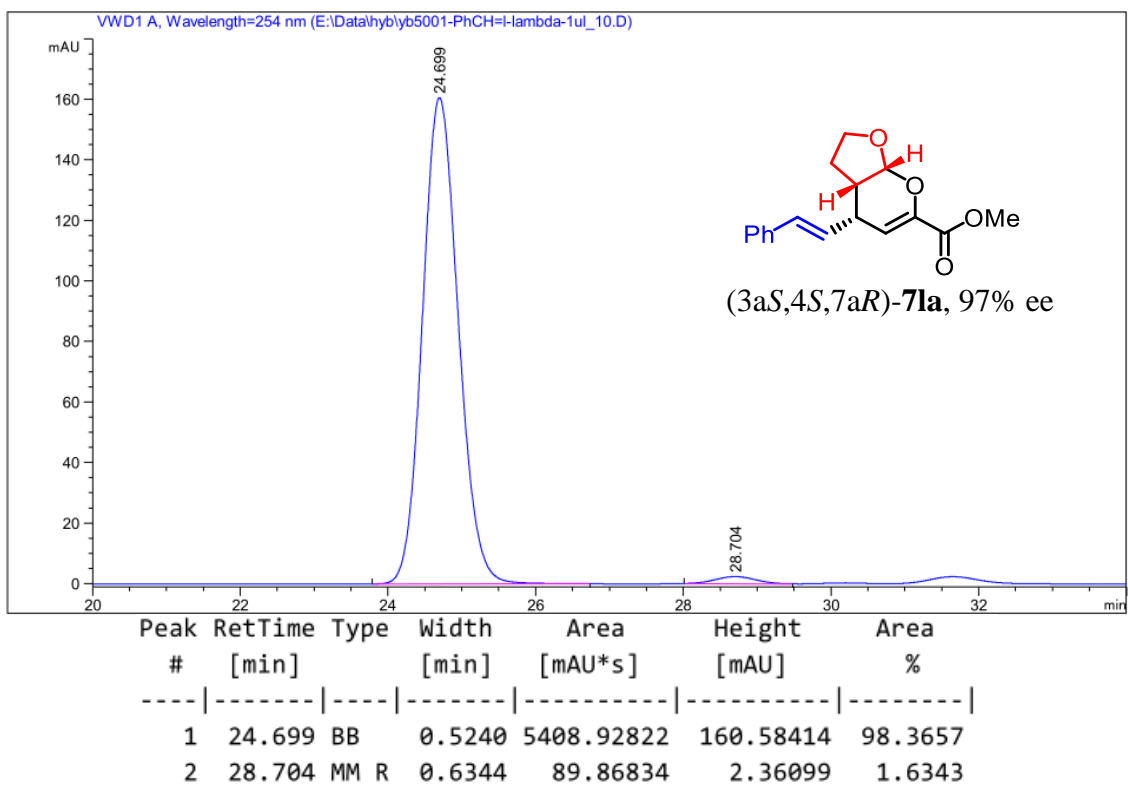
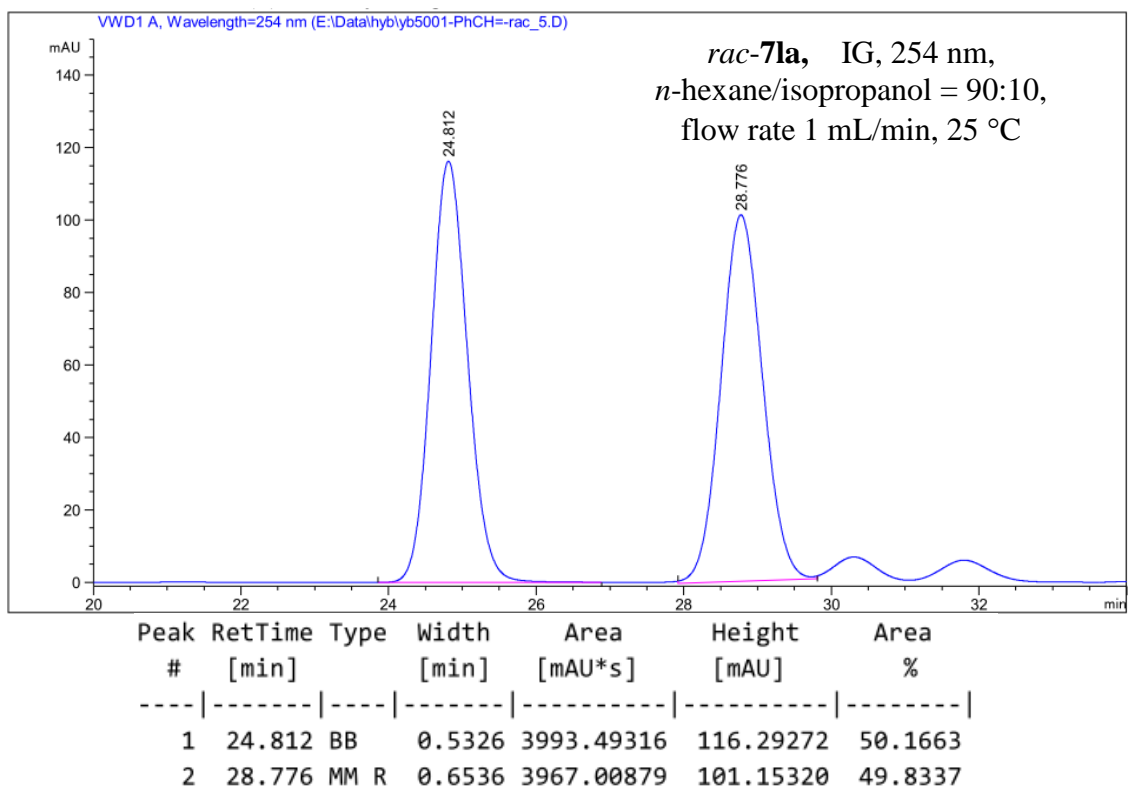


Figure 88. HPLC traces of *rac*-**7la** and (3*aS*,4*S*,7*aR*)-**7la**.

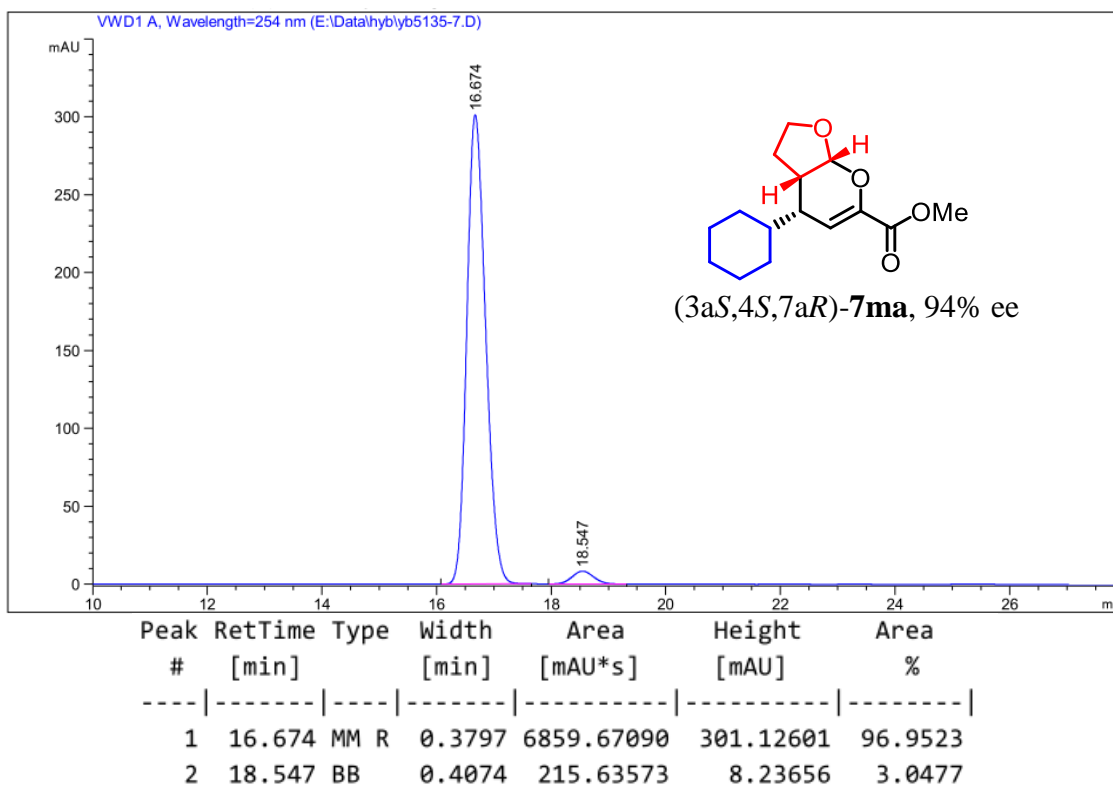
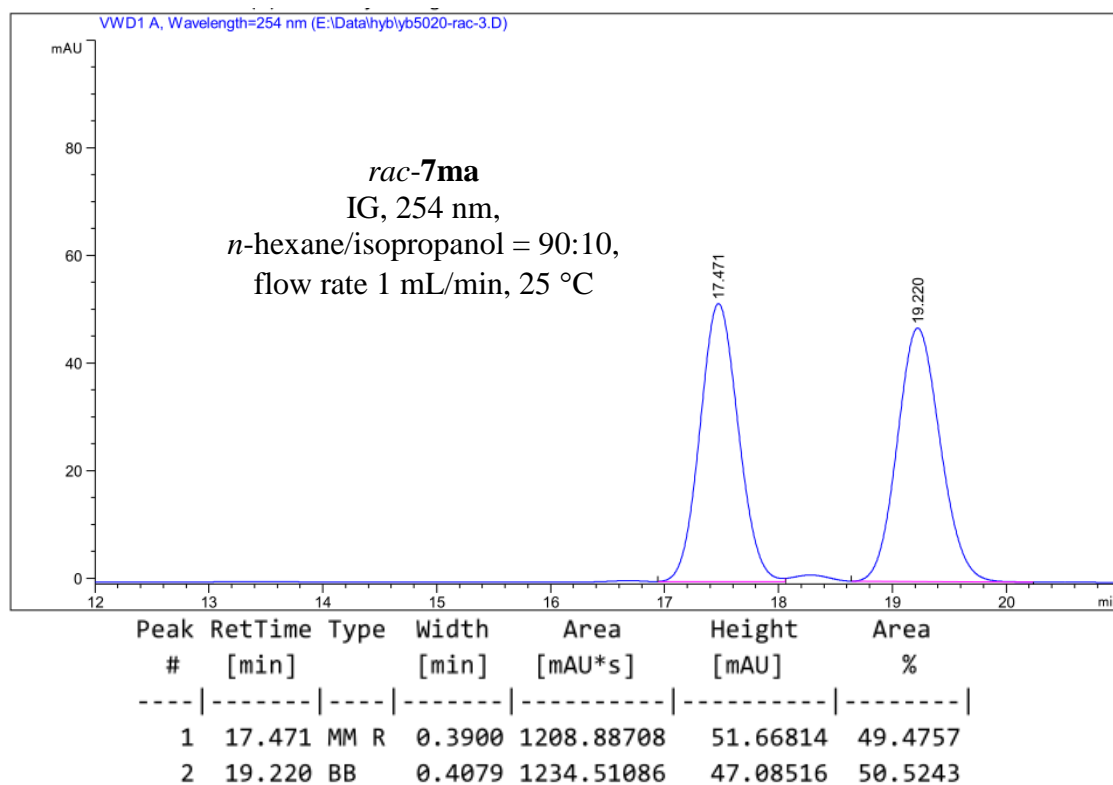


Figure 89. HPLC traces of *rac-7ma* and (3*a**S*,4*S*,7*a**R*)-**7ma**.

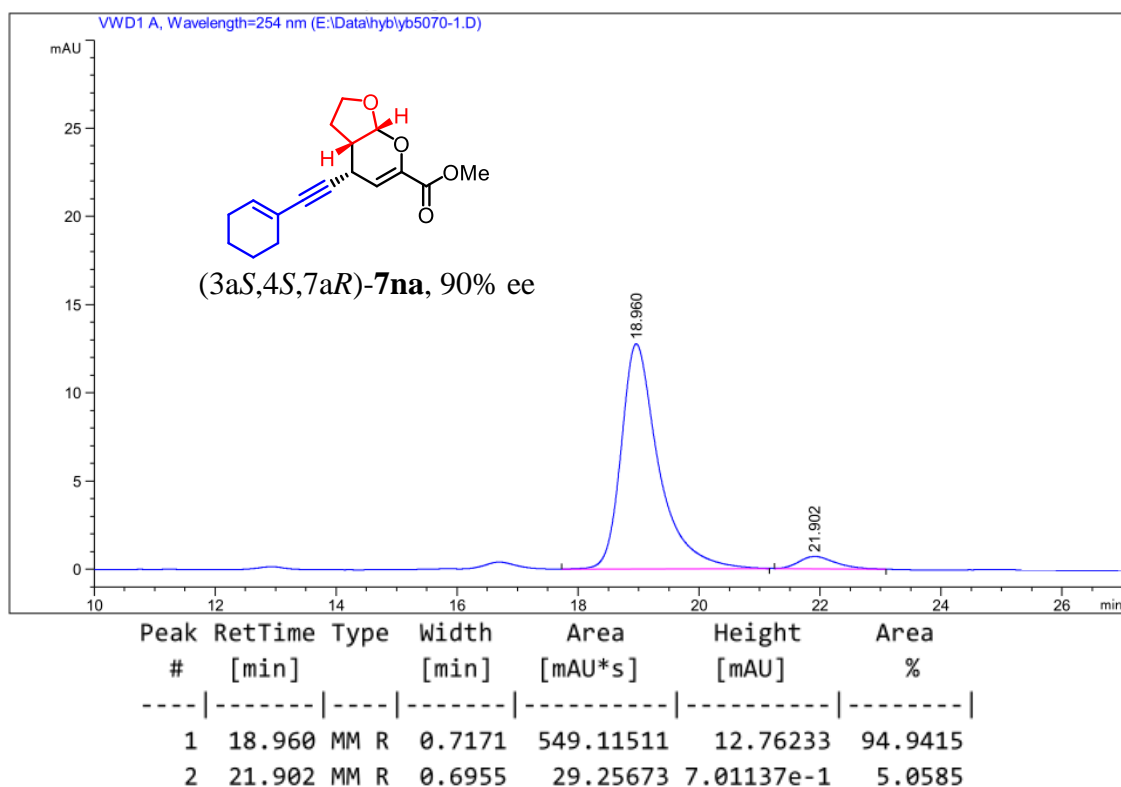
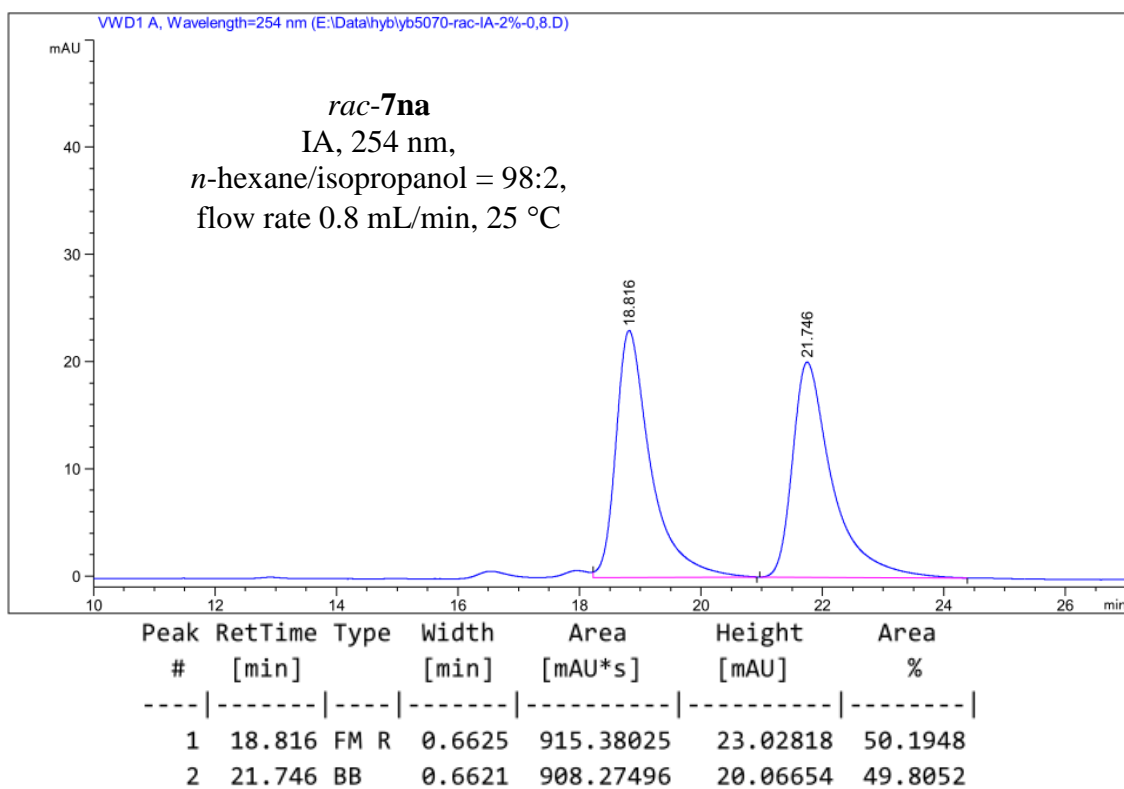


Figure 90. HPLC traces of *rac*-7na and (3a*S*,4*S*,7a*R*)-7na.

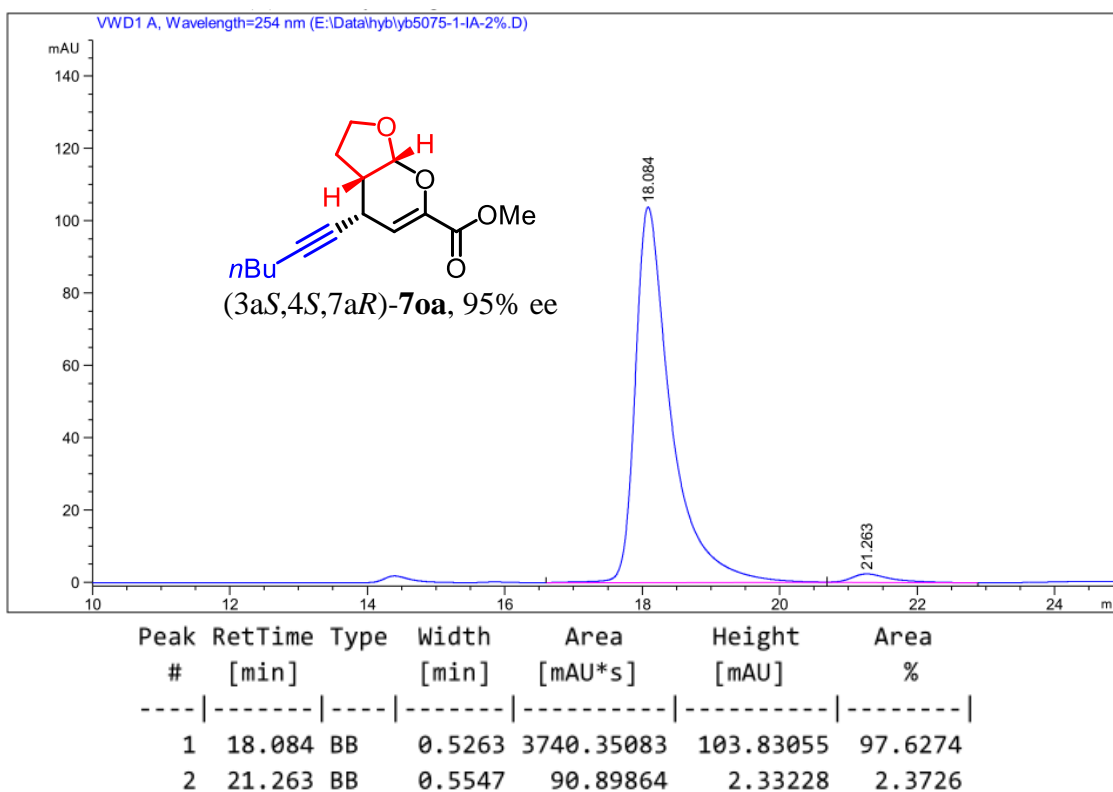
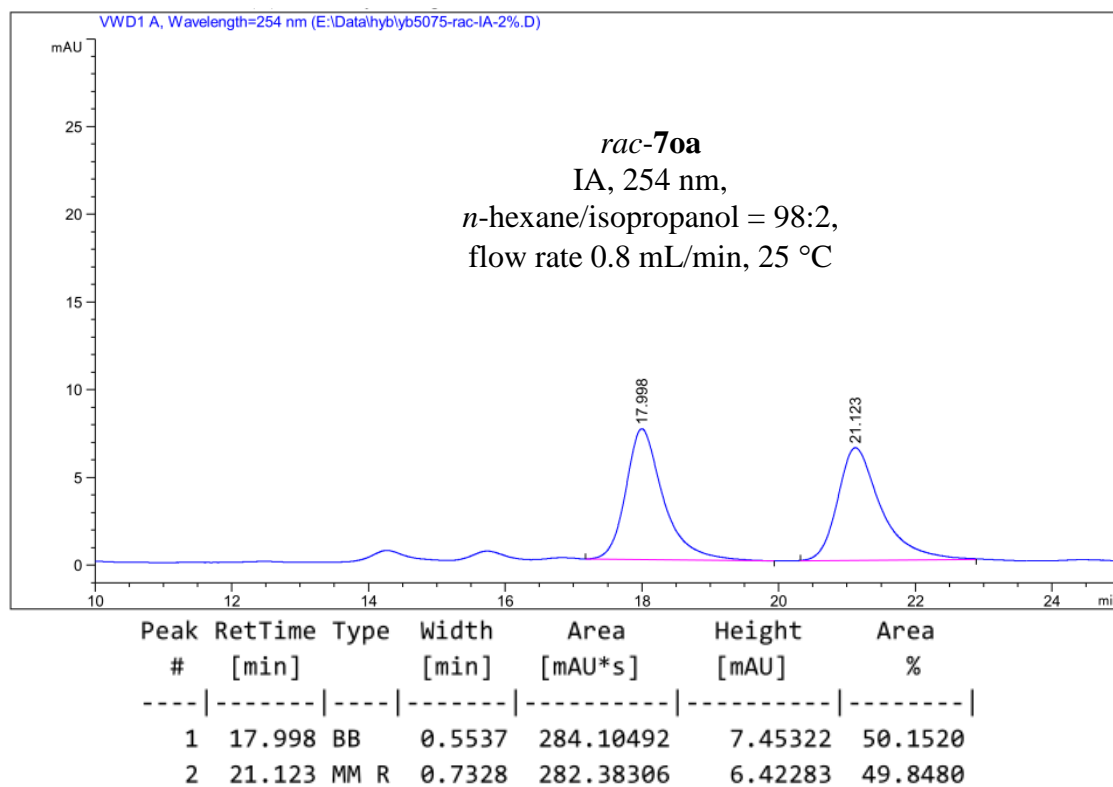


Figure 91. HPLC traces of *rac*-7oa and (3*a*S,4*S*,7*a*R)-7oa.

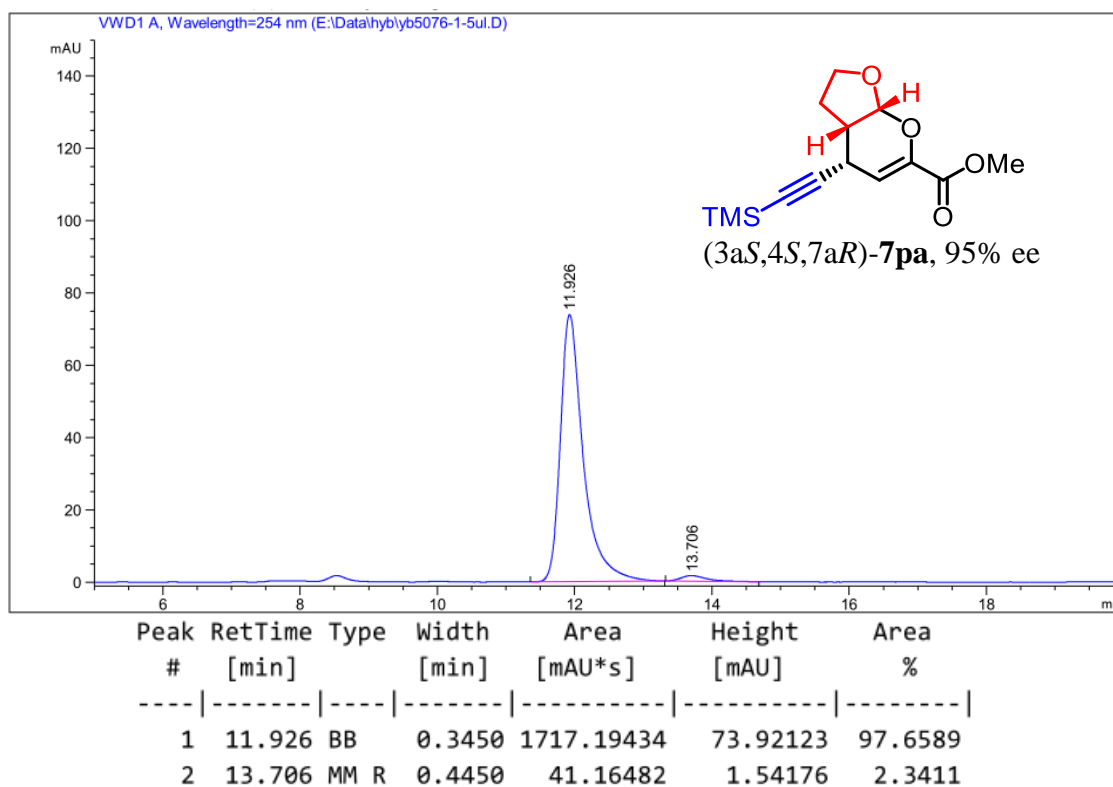
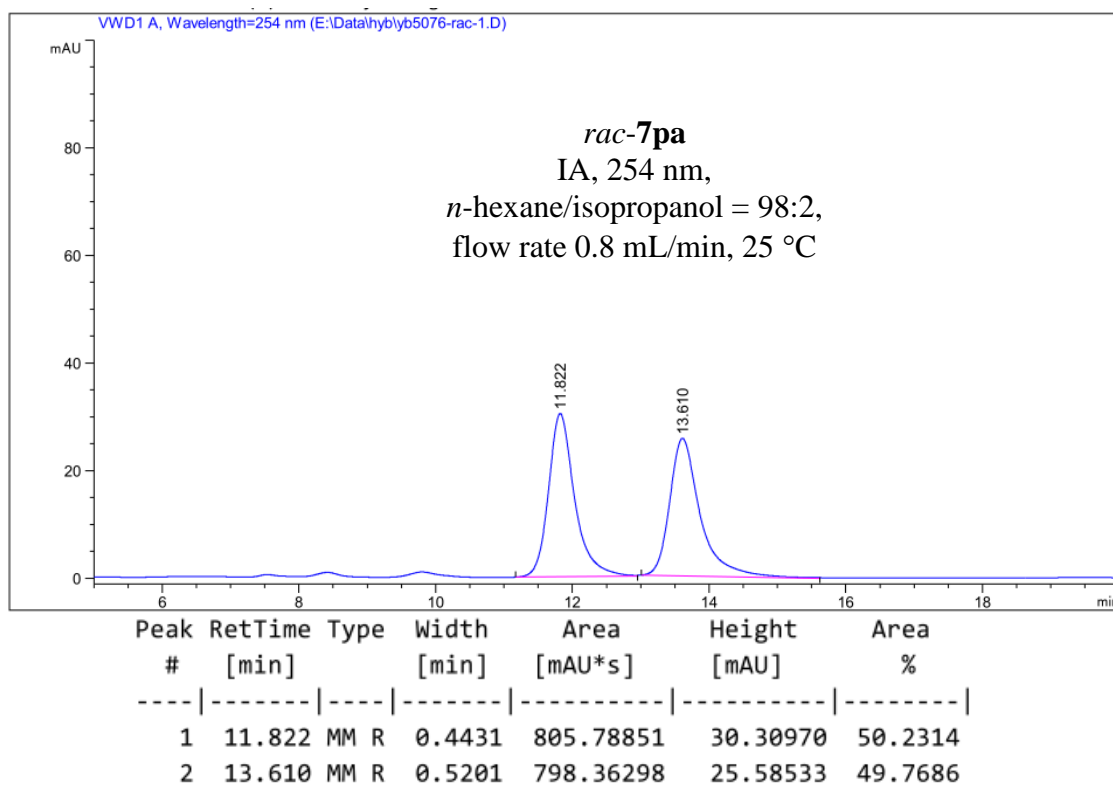


Figure 92. HPLC traces of *rac*-7pa and (3a*S*,4*S*,7a*R*)-7pa.

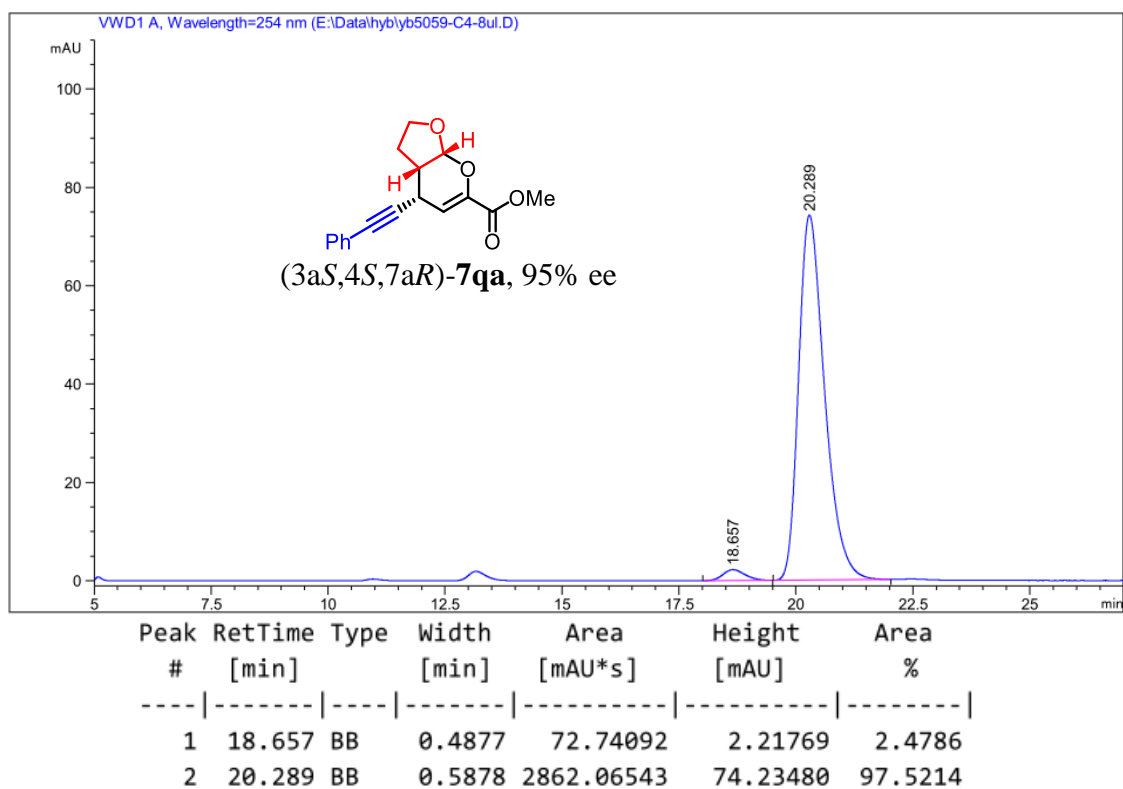
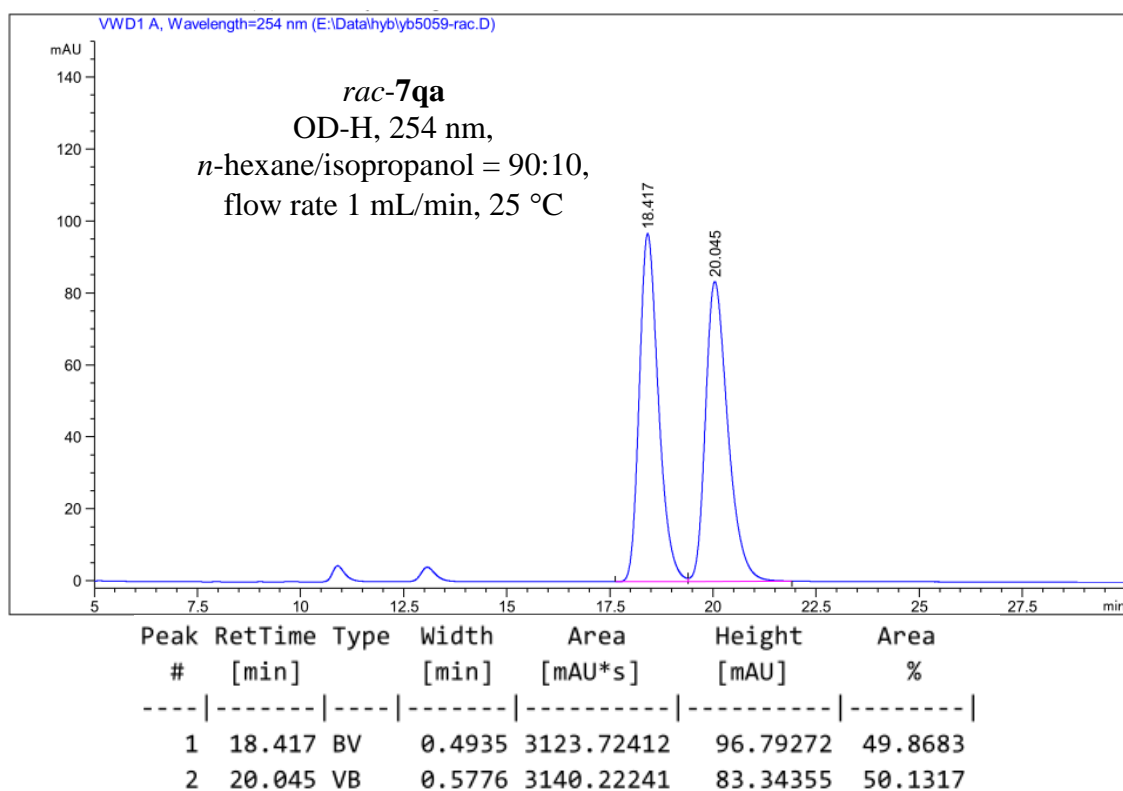
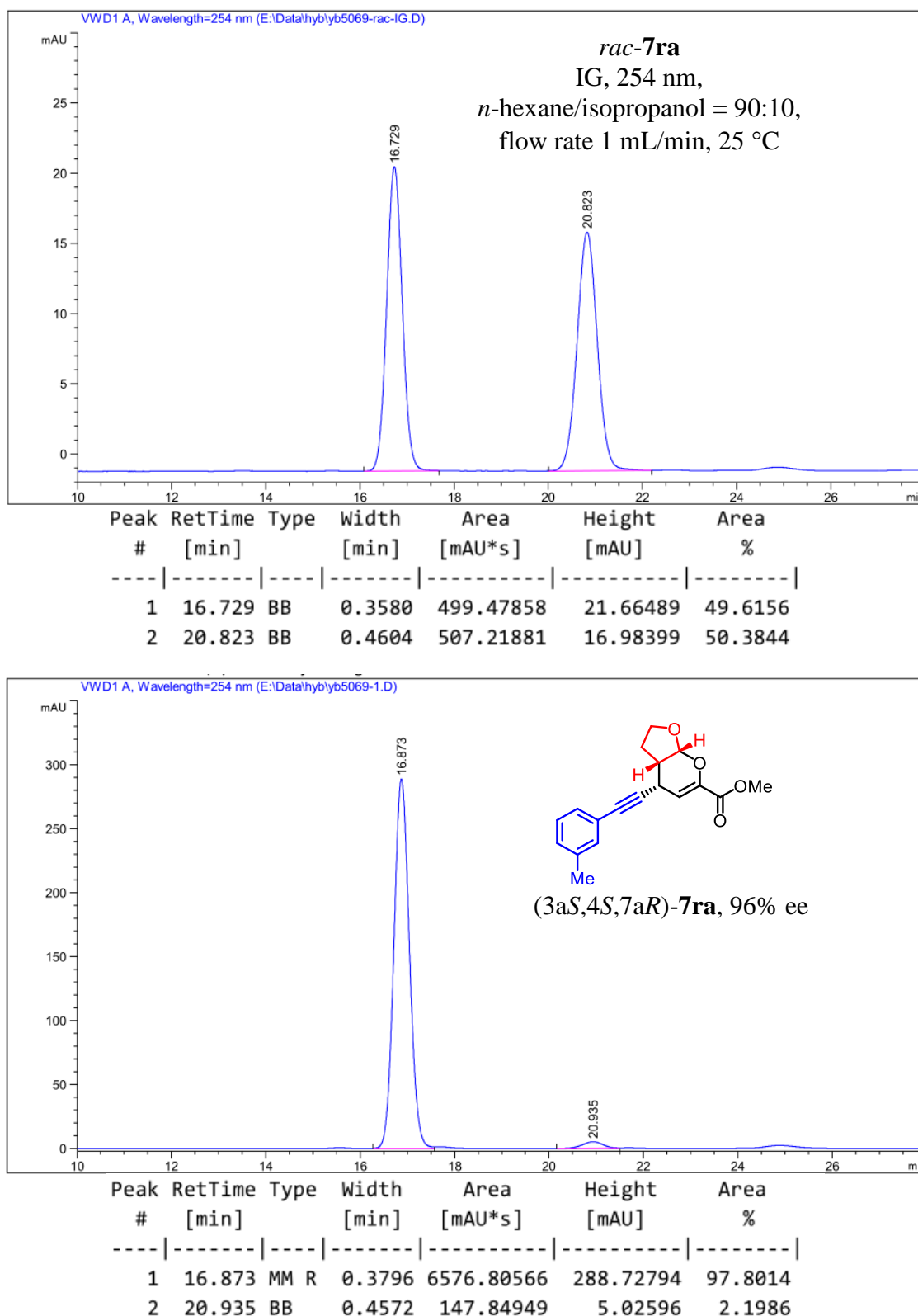


Figure 93. HPLC traces of *rac*-7qa and (3*a*S,4*S*,7*a*R)-7qa.

Figure 94. HPLC traces of *rac*-7ra and (3*aS*,4*S*,7*aR*)-7ra.

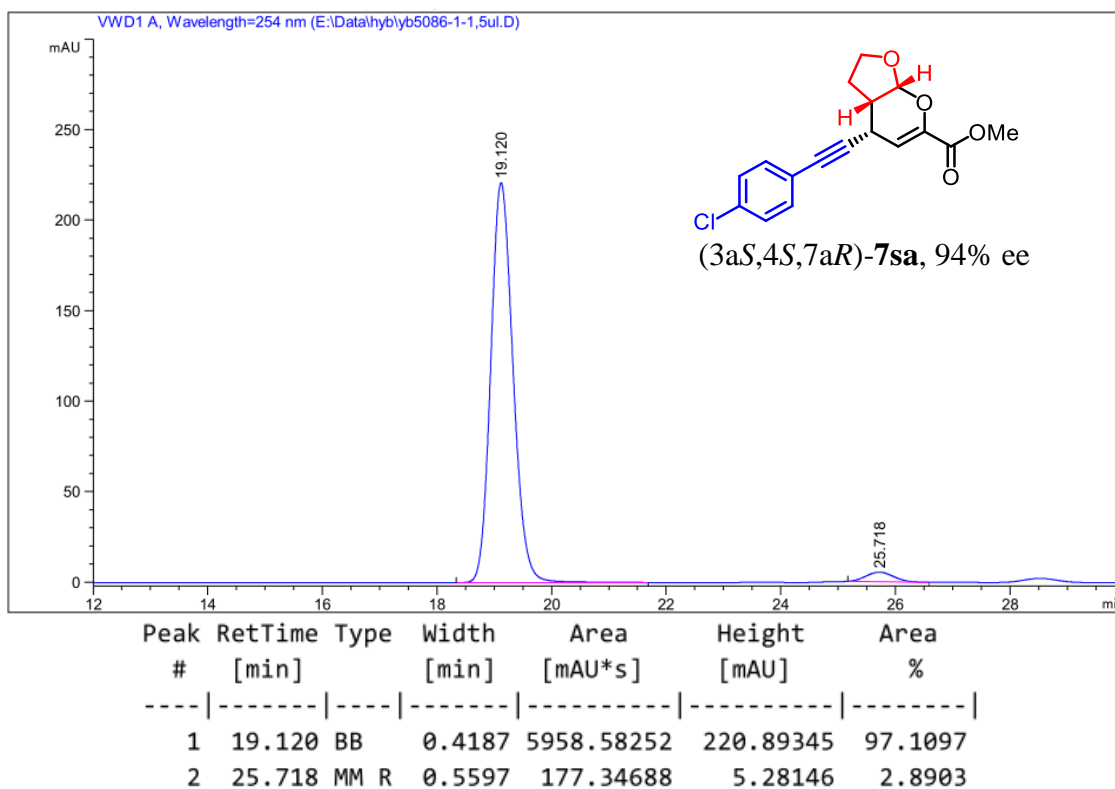
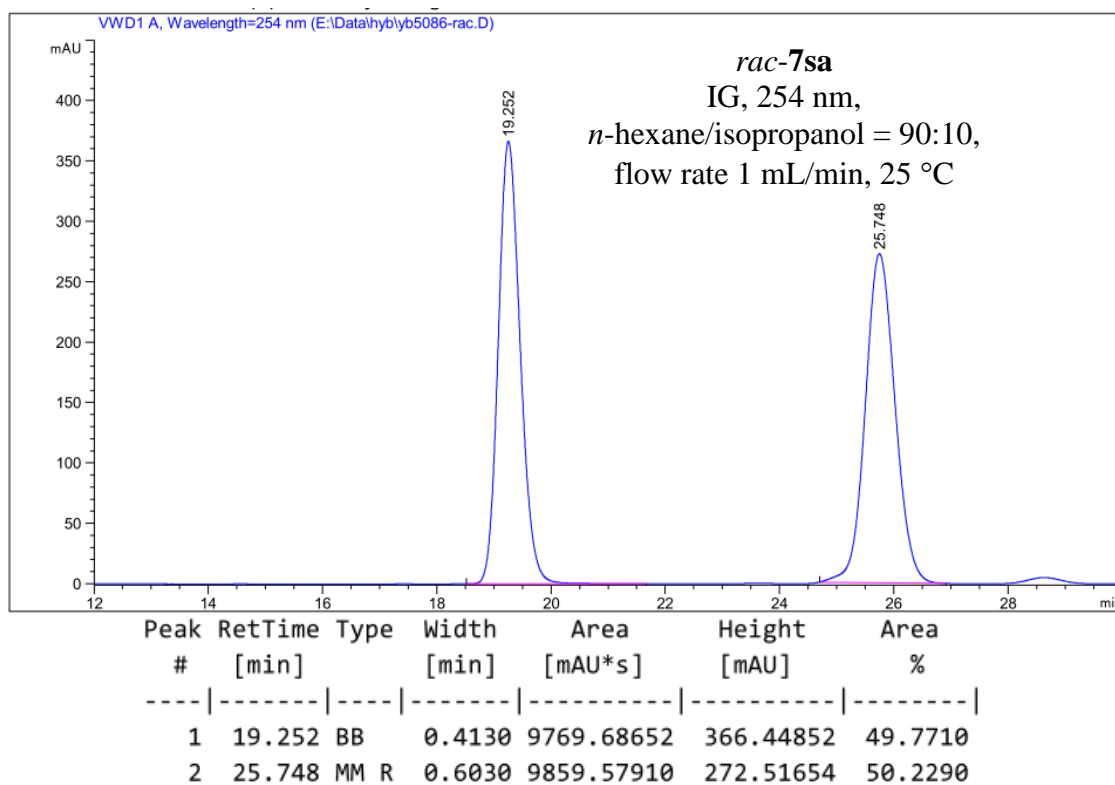


Figure 95. HPLC traces of *rac-7sa* and (3*a**S*,4*S*,7*a**R*)-**7sa**.

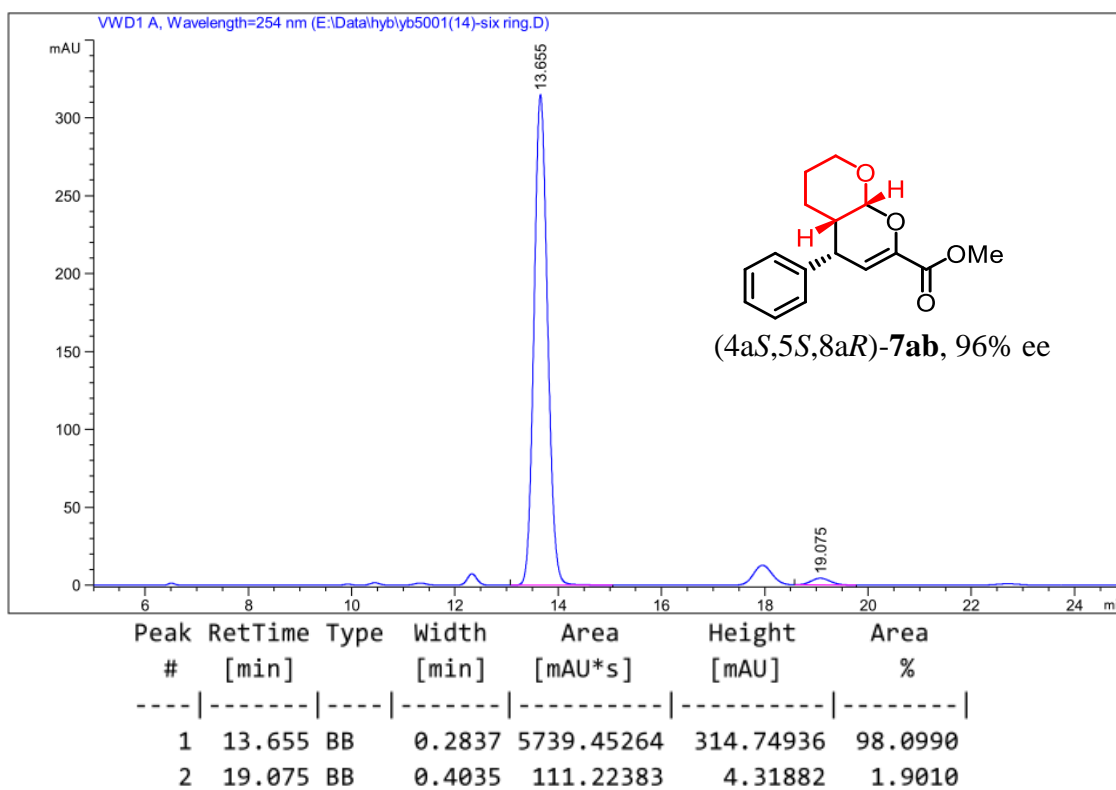
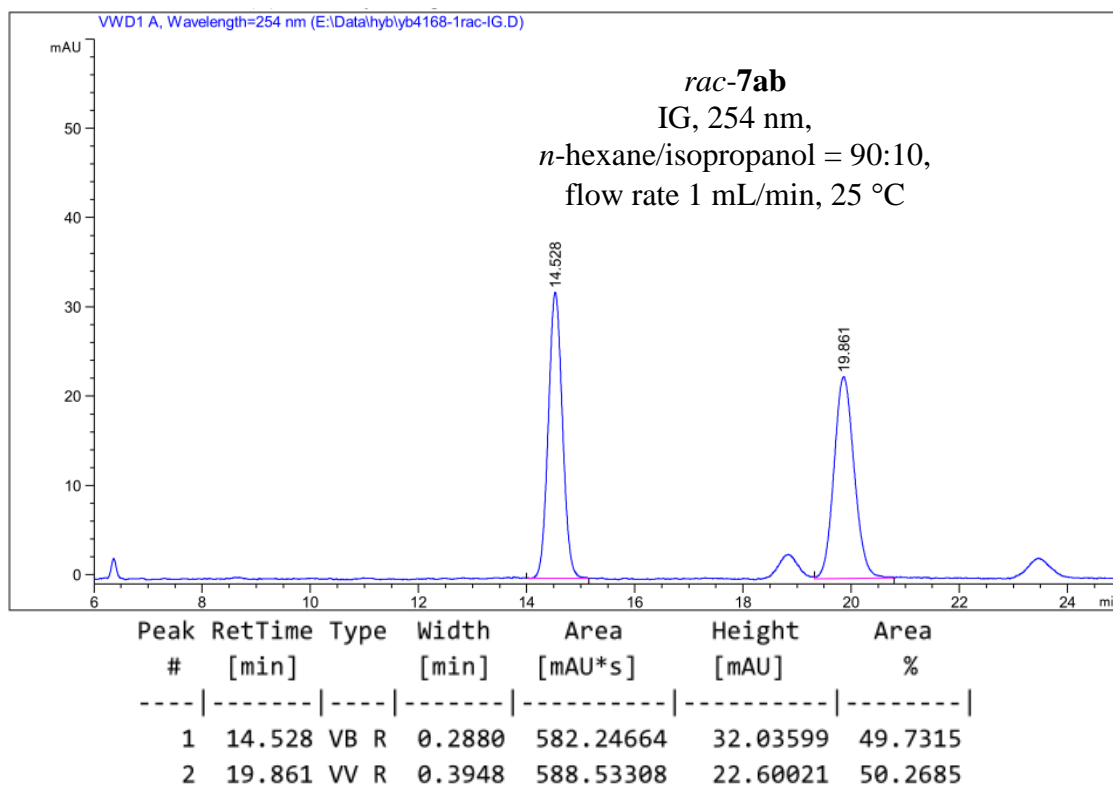


Figure 96. HPLC traces of *rac*-7ab and (4*aS*,5*S*,8*aR*)-7ab.

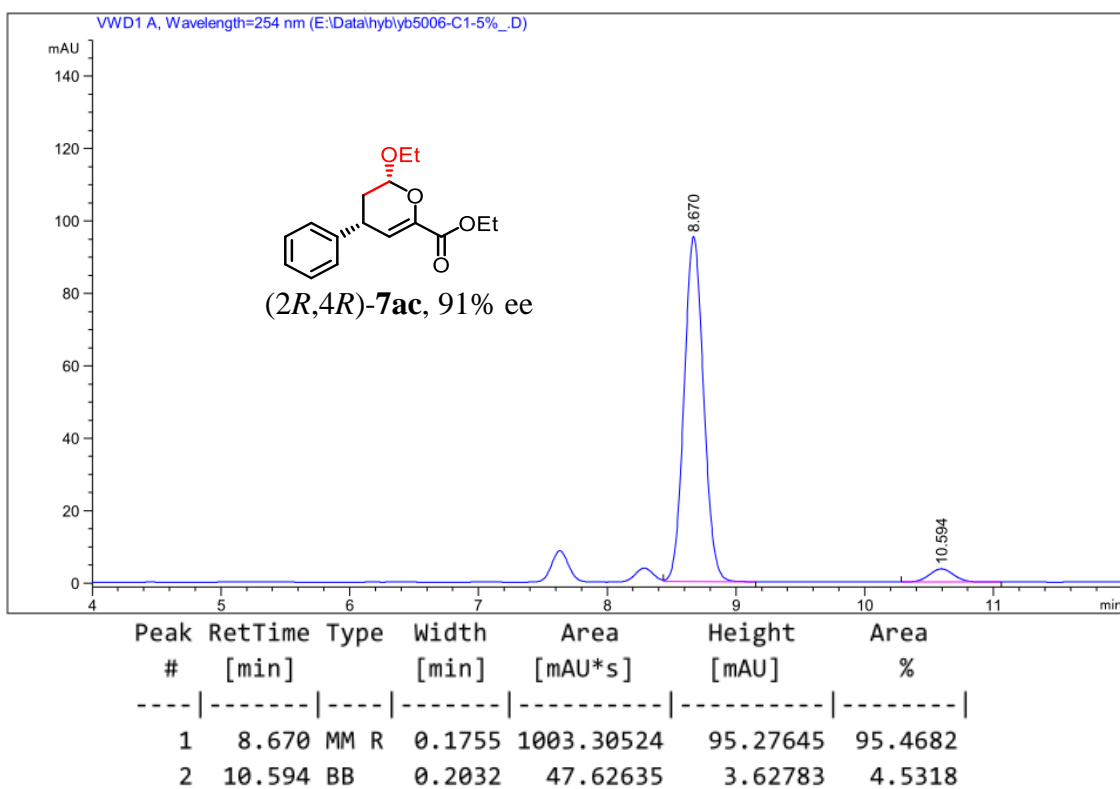
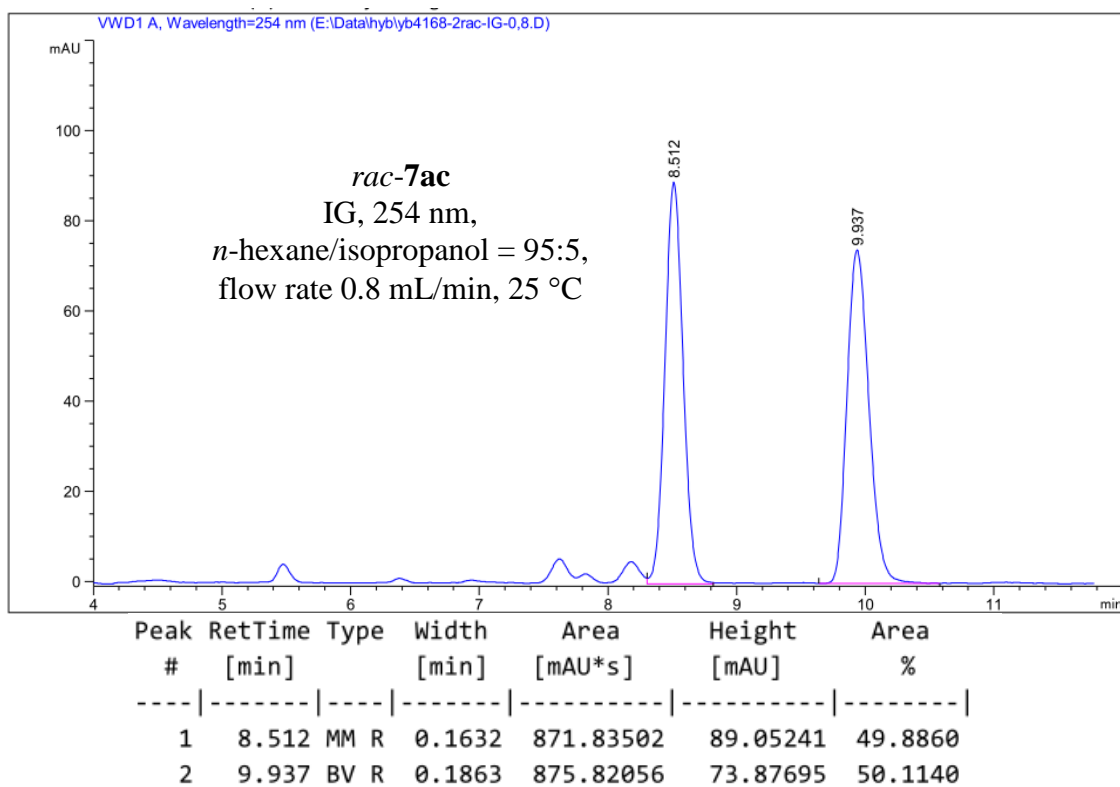
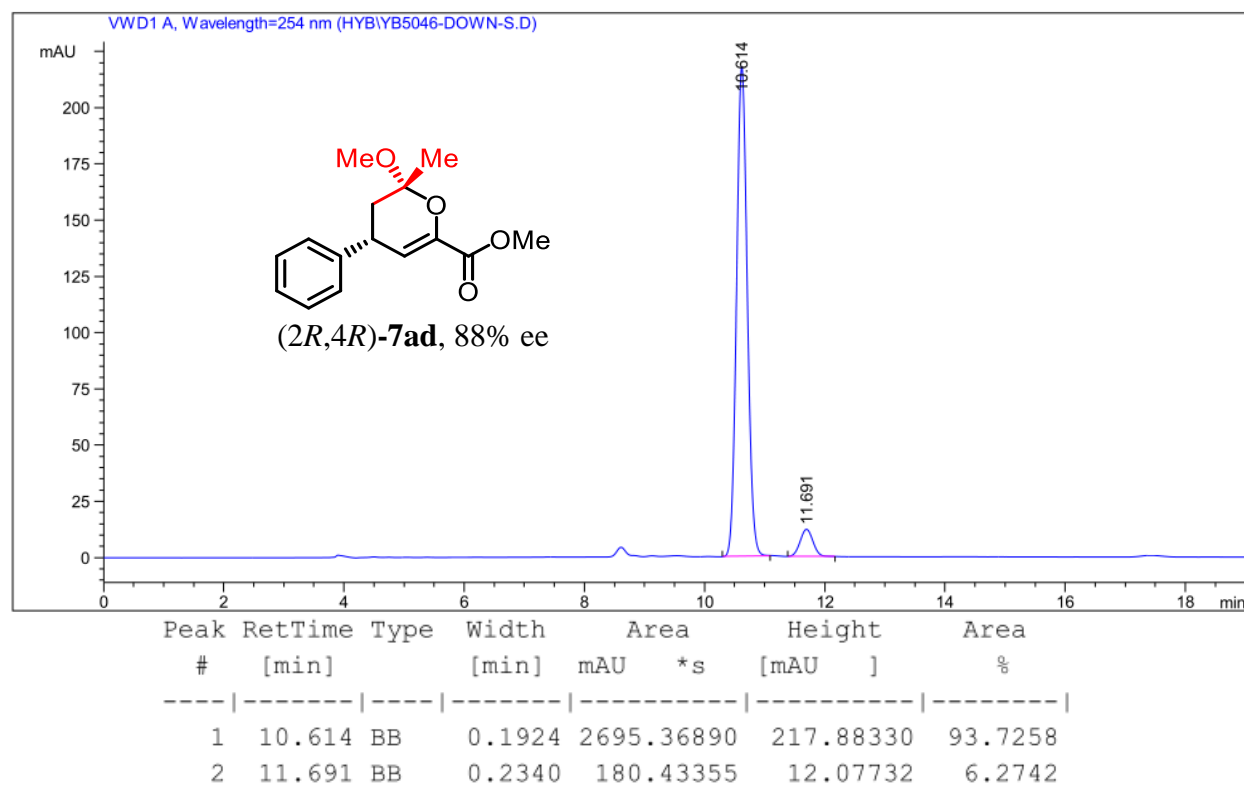
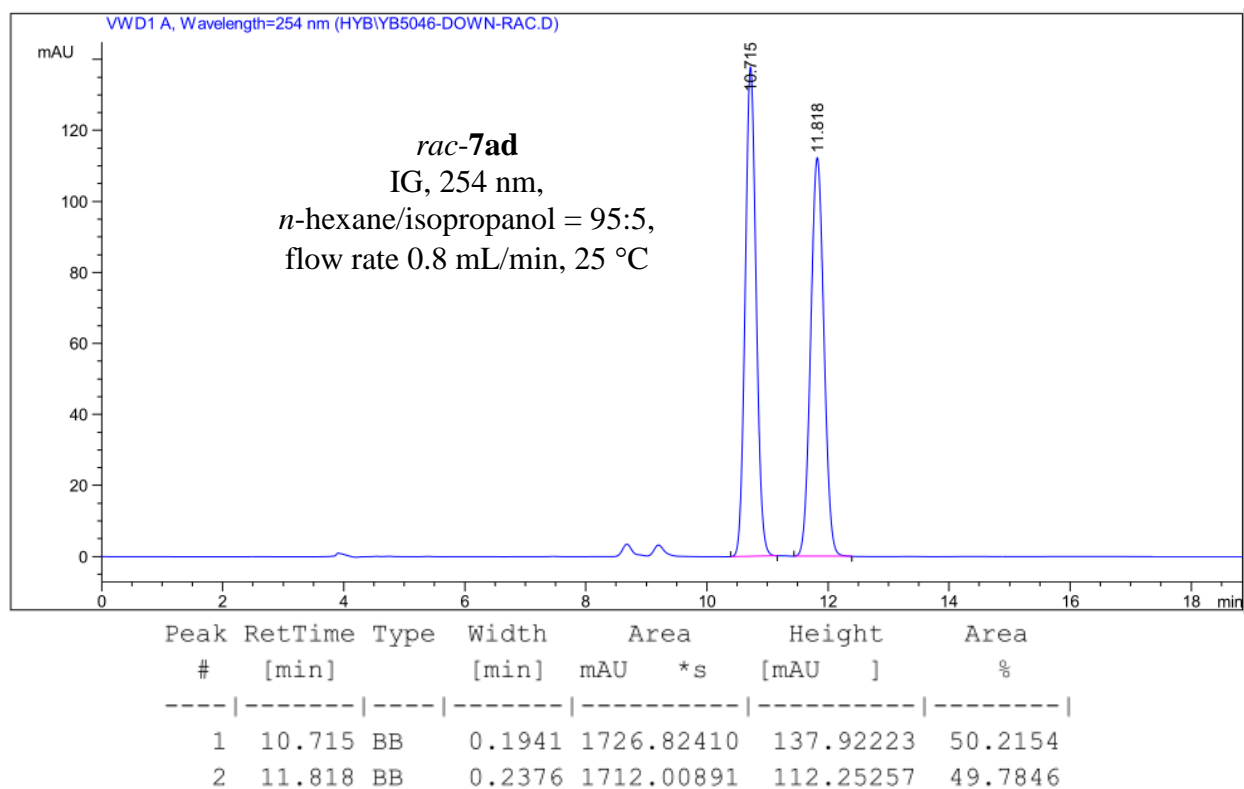


Figure 97. HPLC traces of *rac-7ac* and (2*R*,4*R*)-**7ac**.

Figure 98. HPLC traces of *rac*-7ad and *(2R,4R)*-7ad.

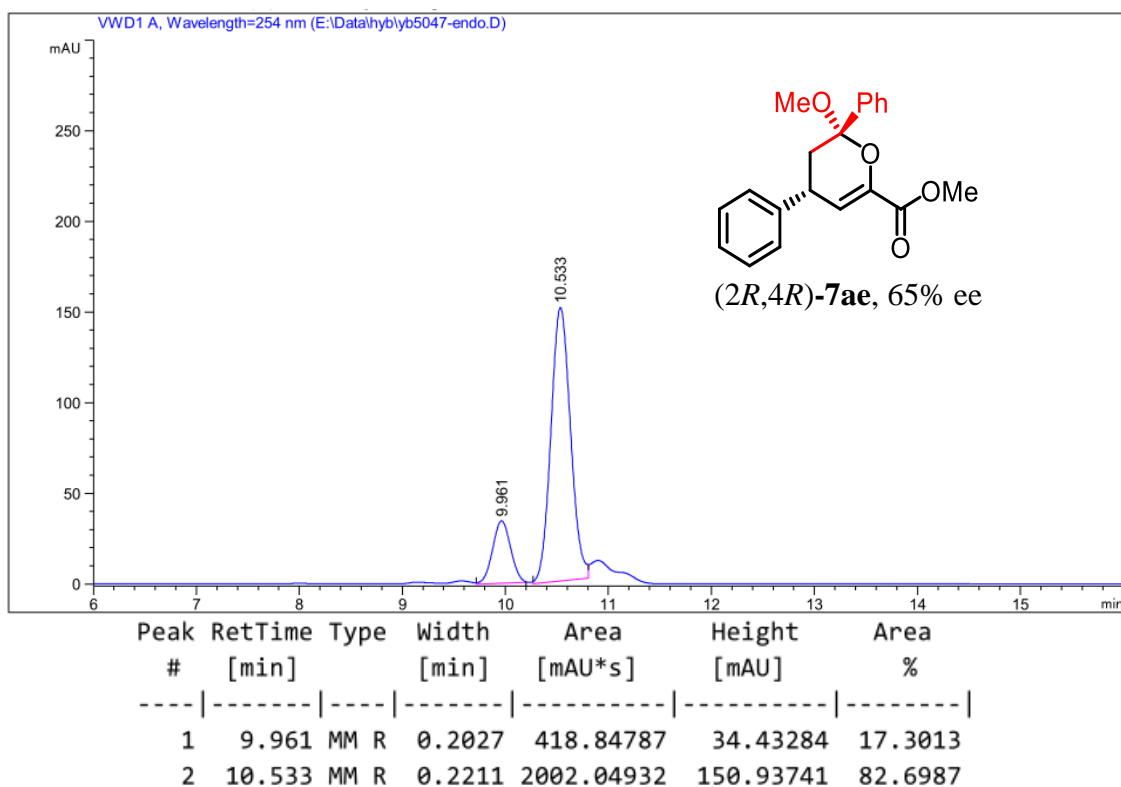
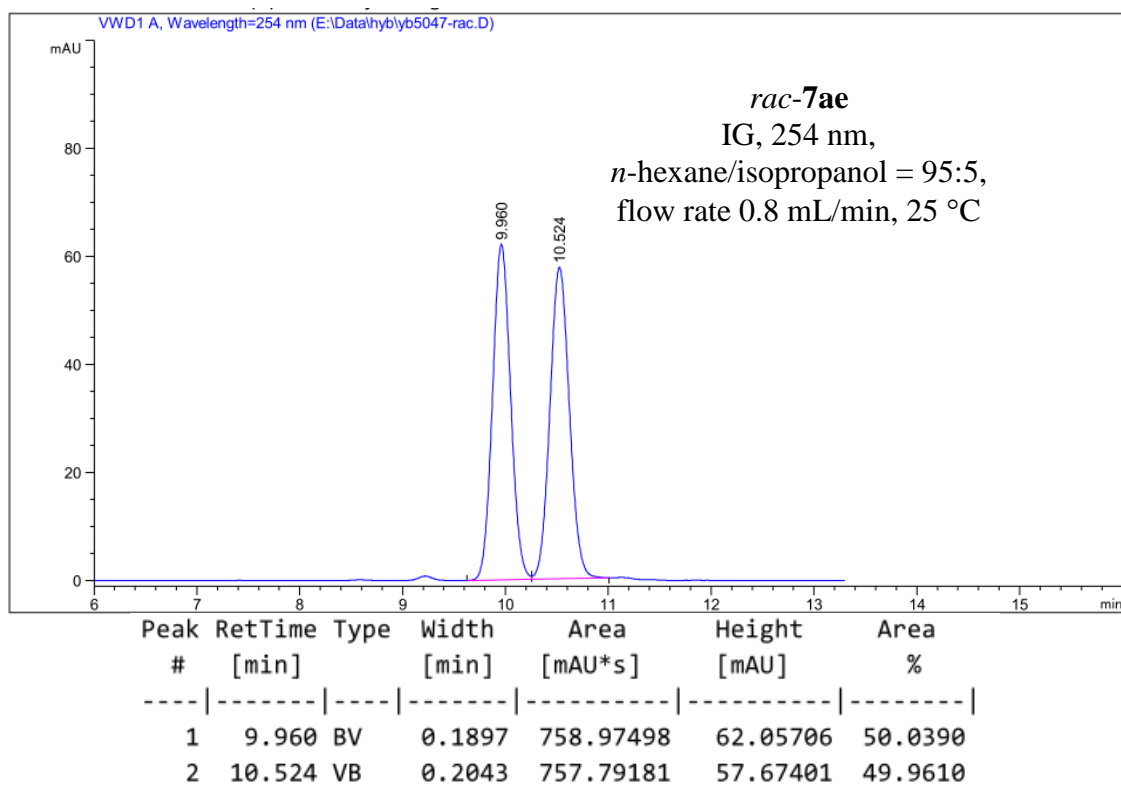


Figure 99. HPLC traces of *rac-7ae* and *(2R,4R)-7ae*.

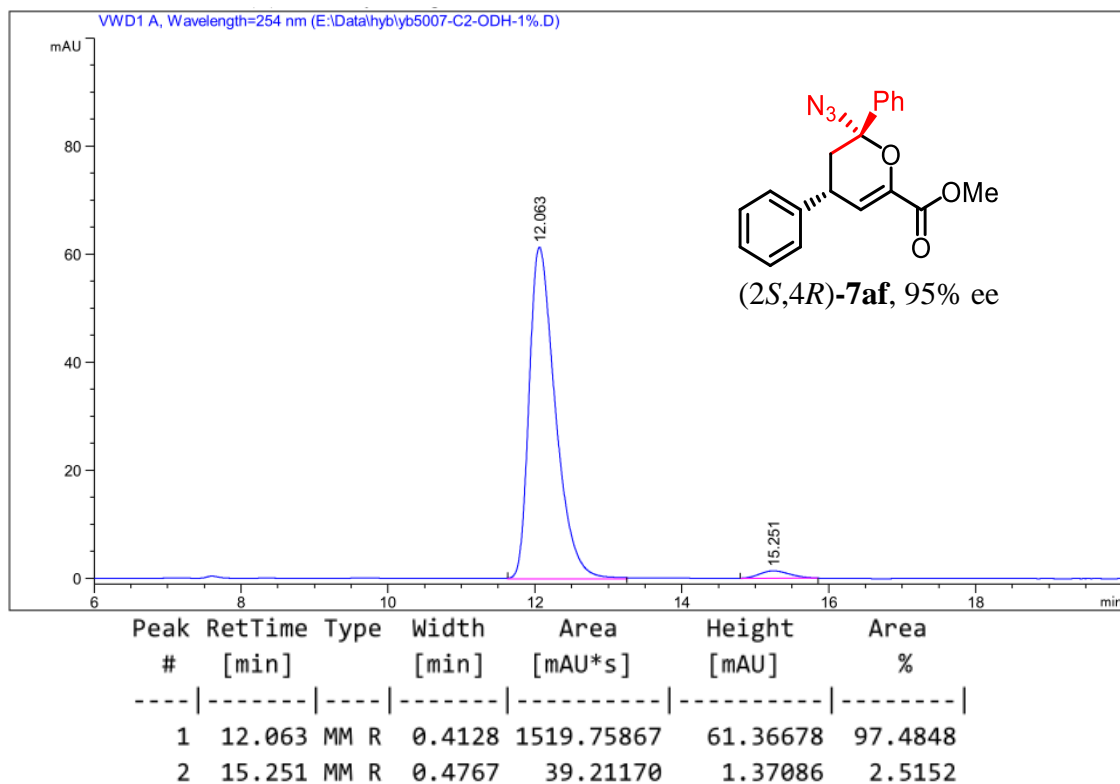
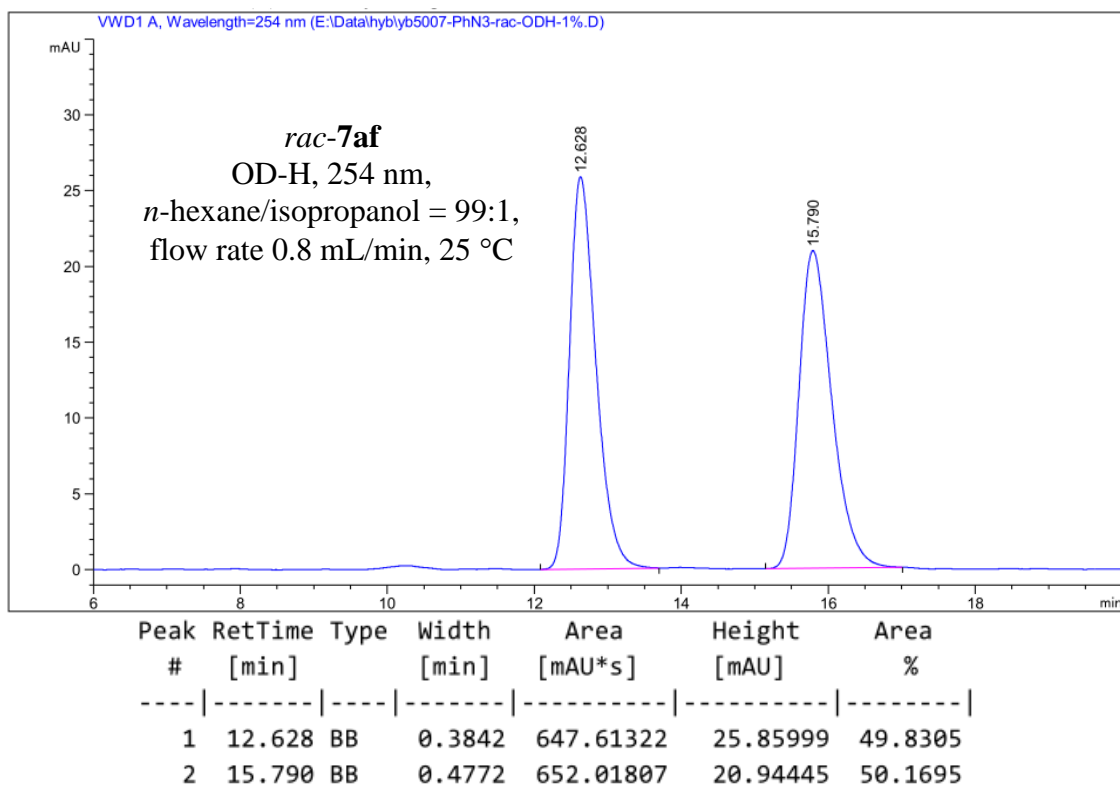
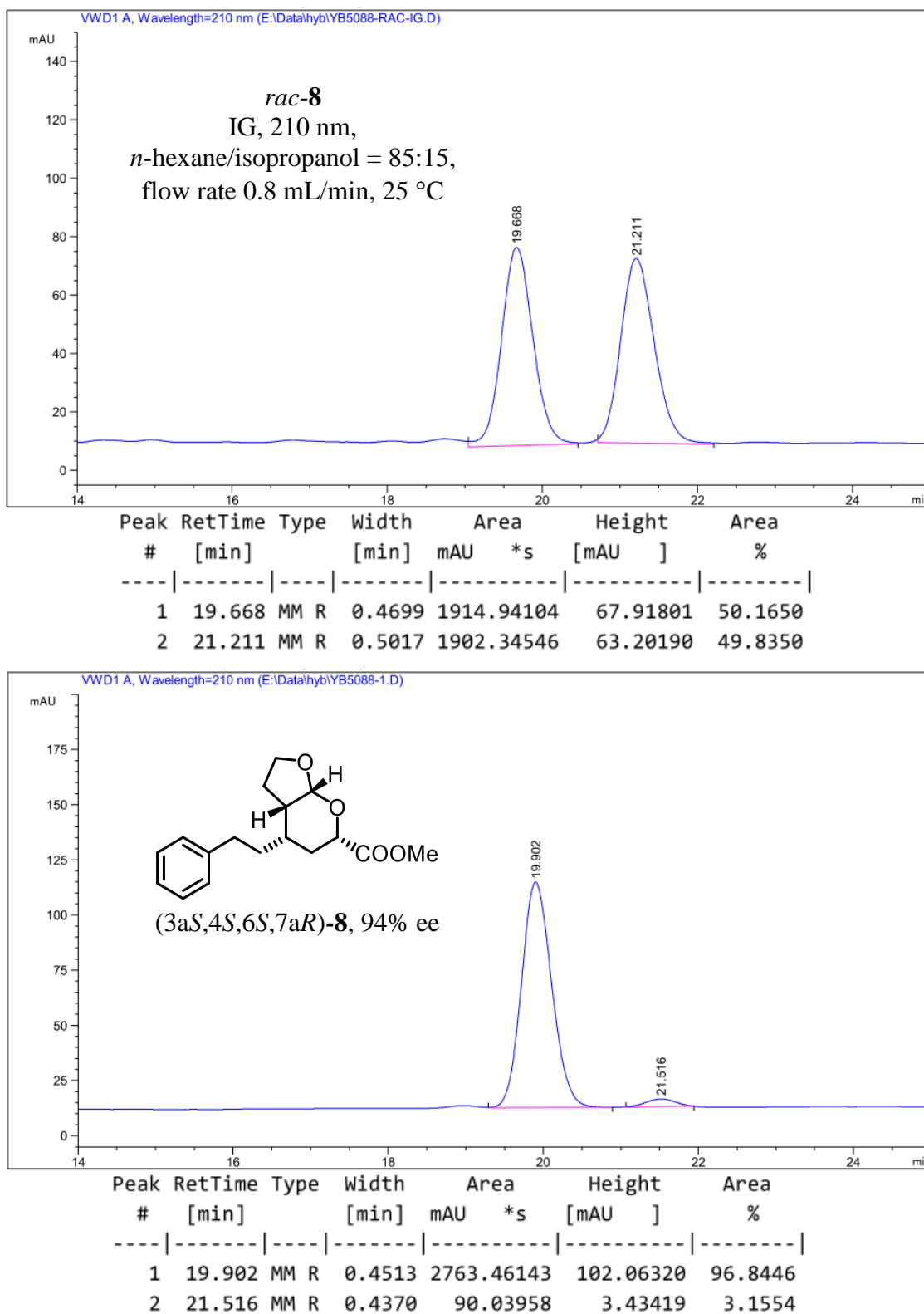
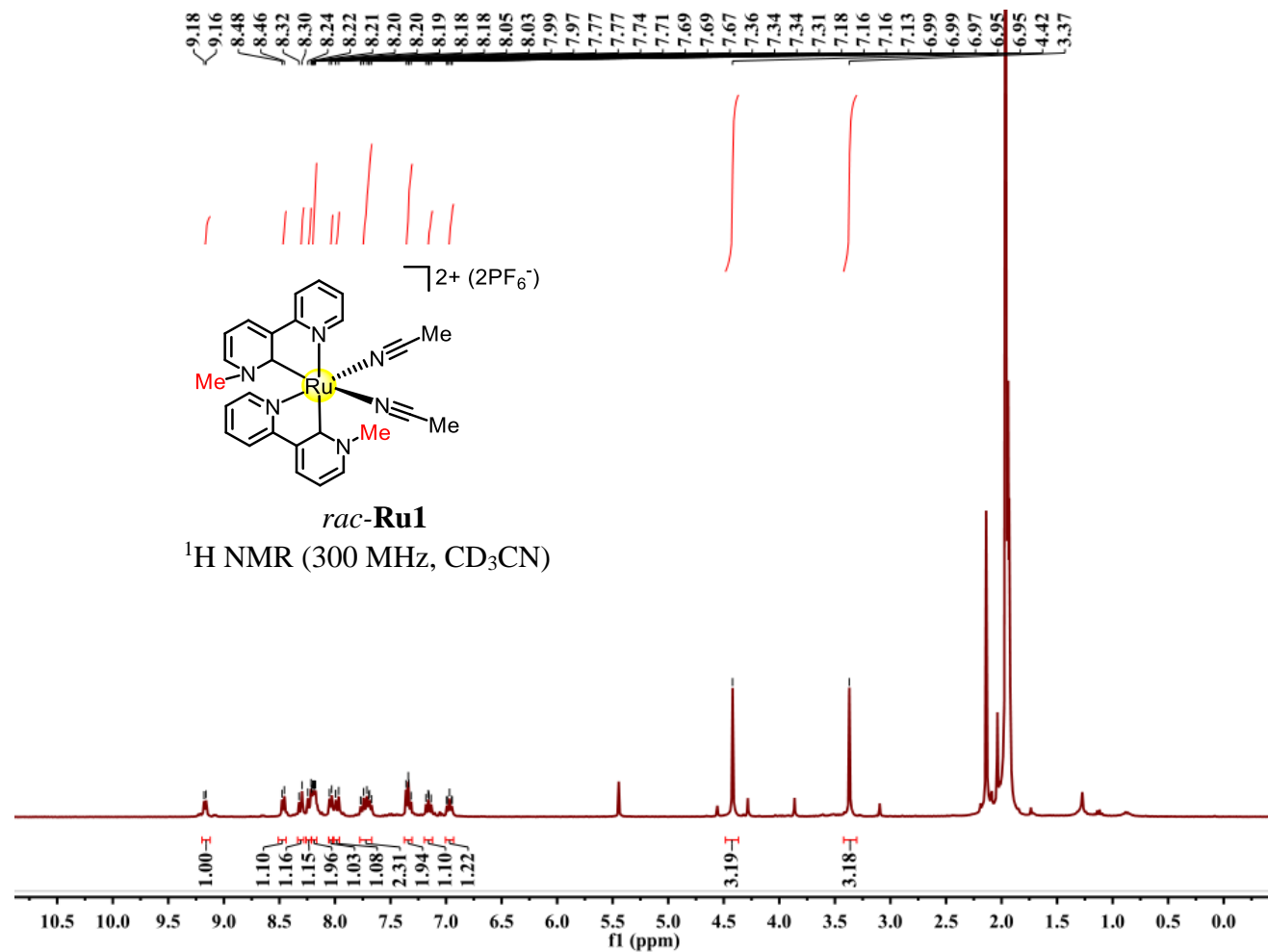
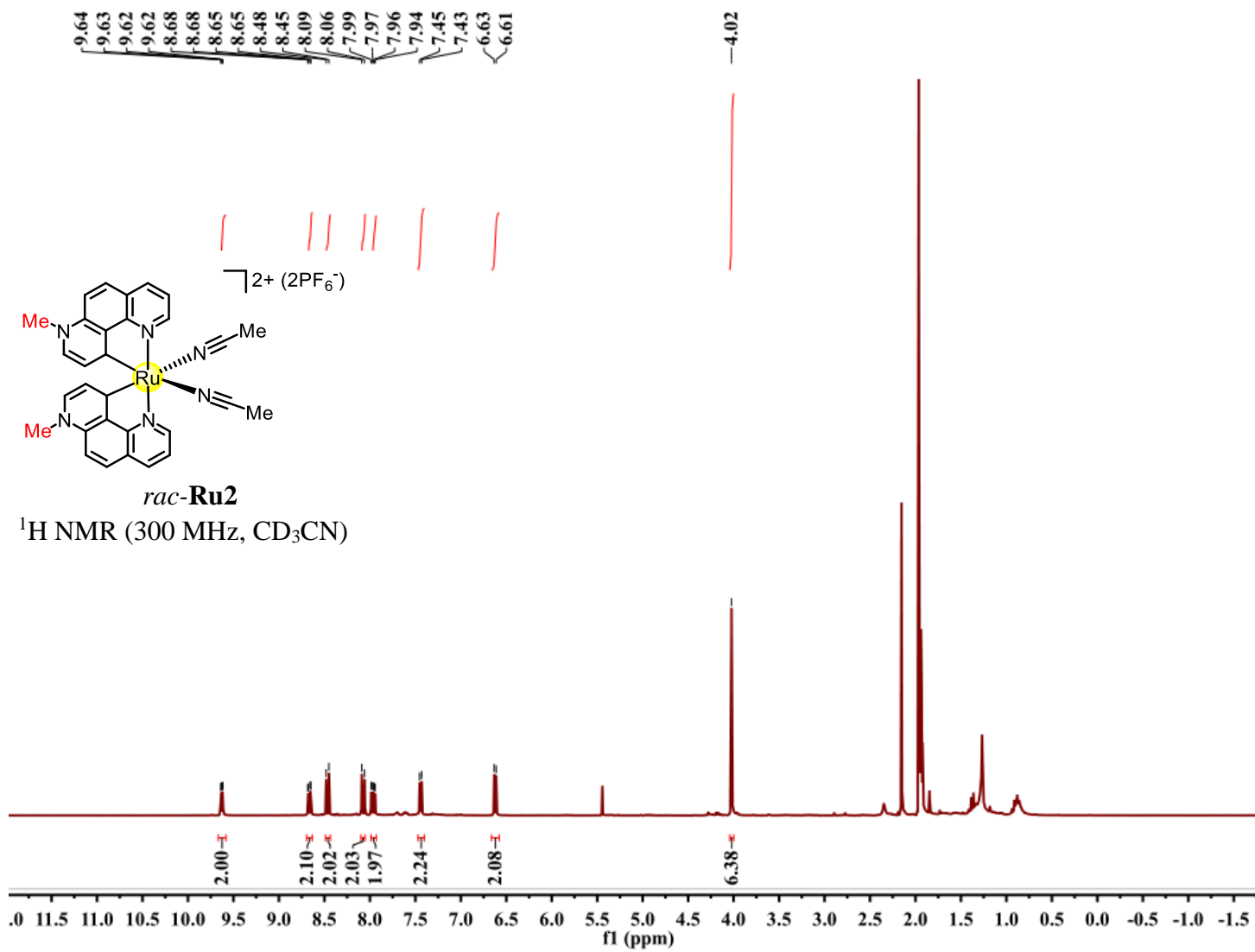


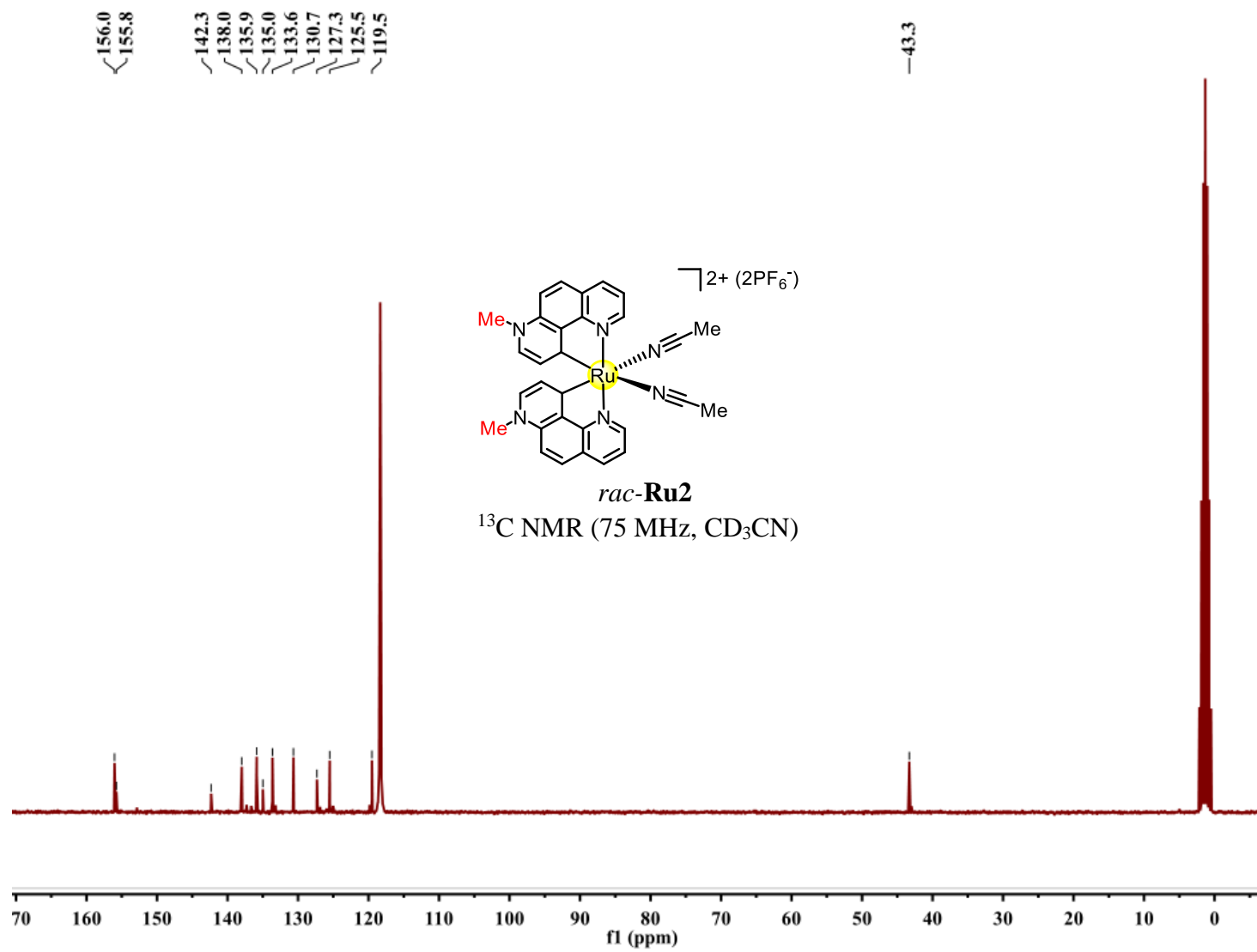
Figure 100. HPLC traces of *rac-7af* and (*2S,4R*)-**7af**.

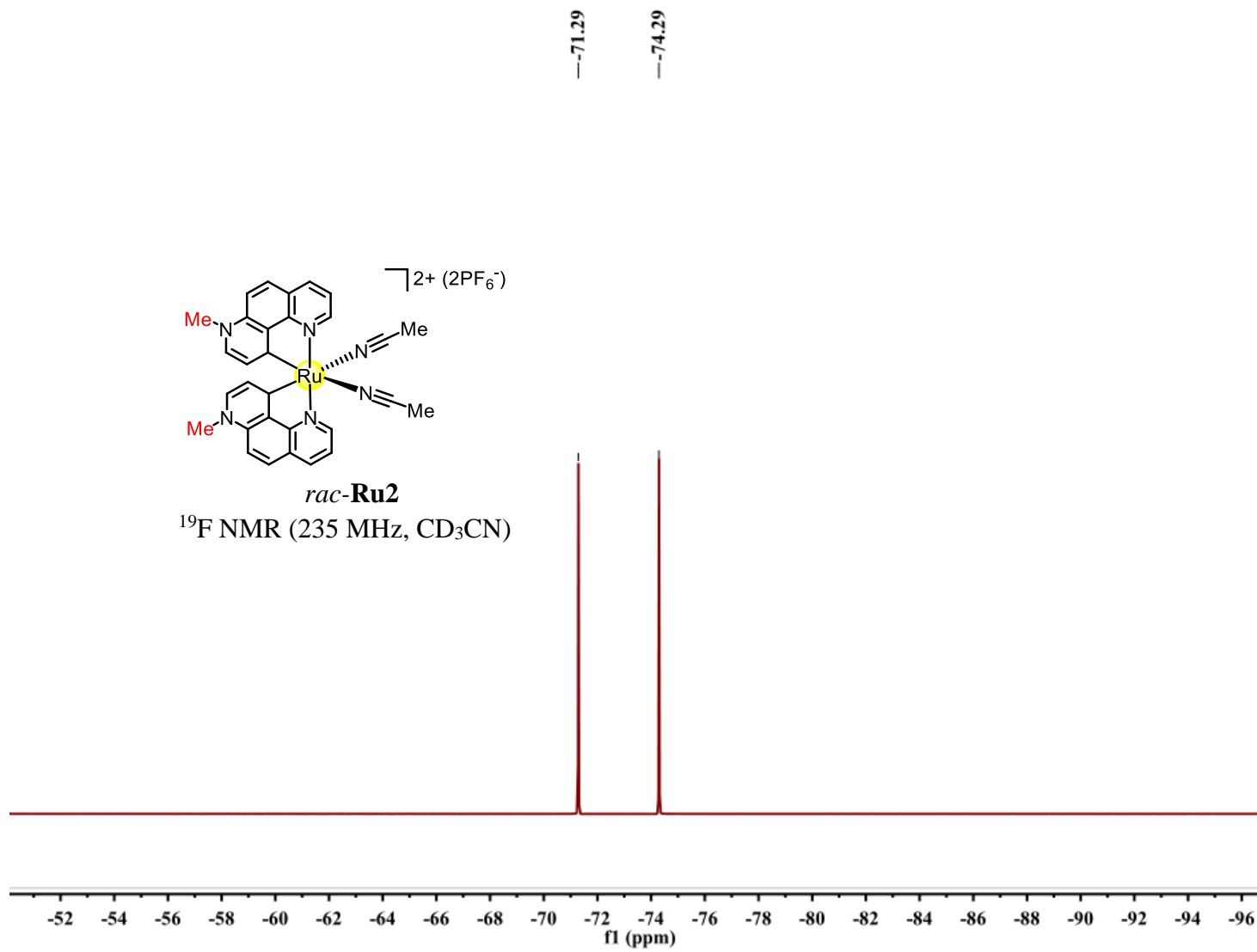
Figure 101. HPLC traces of *rac*-**8** and (3*aS*,4*S*,6*S*,7*aR*)-**8**.

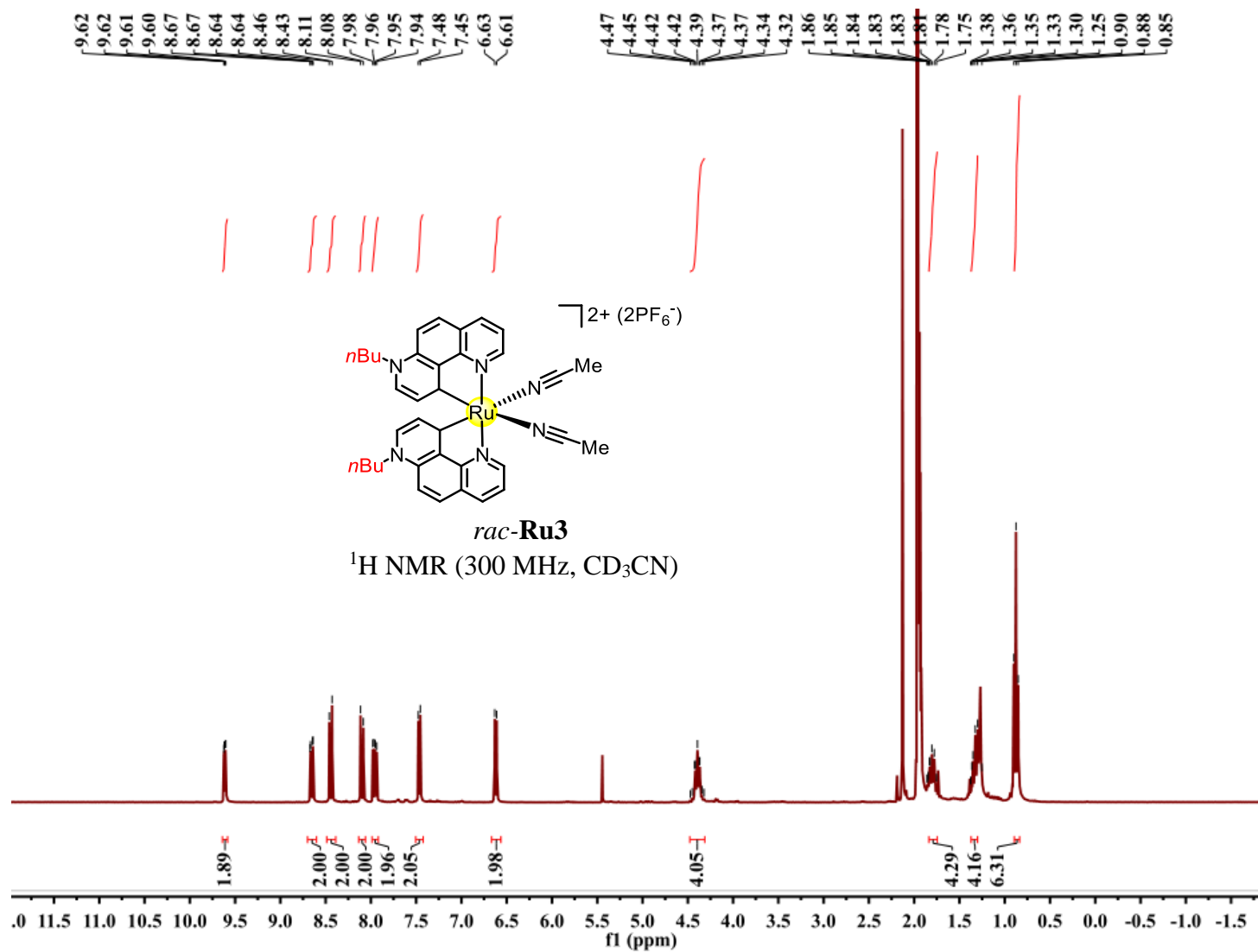
6.8 List of NMR Spectra of New Metal Complexes

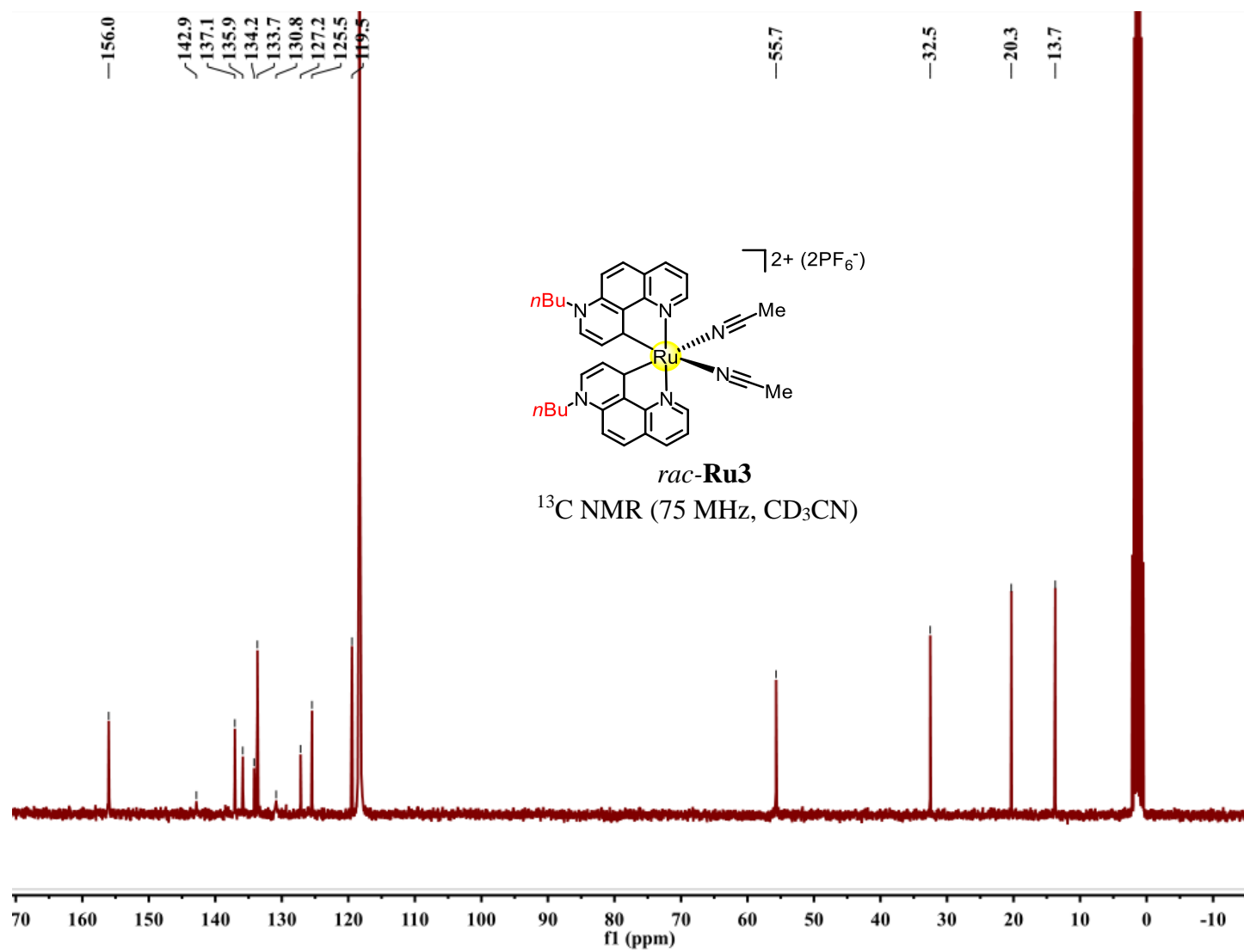


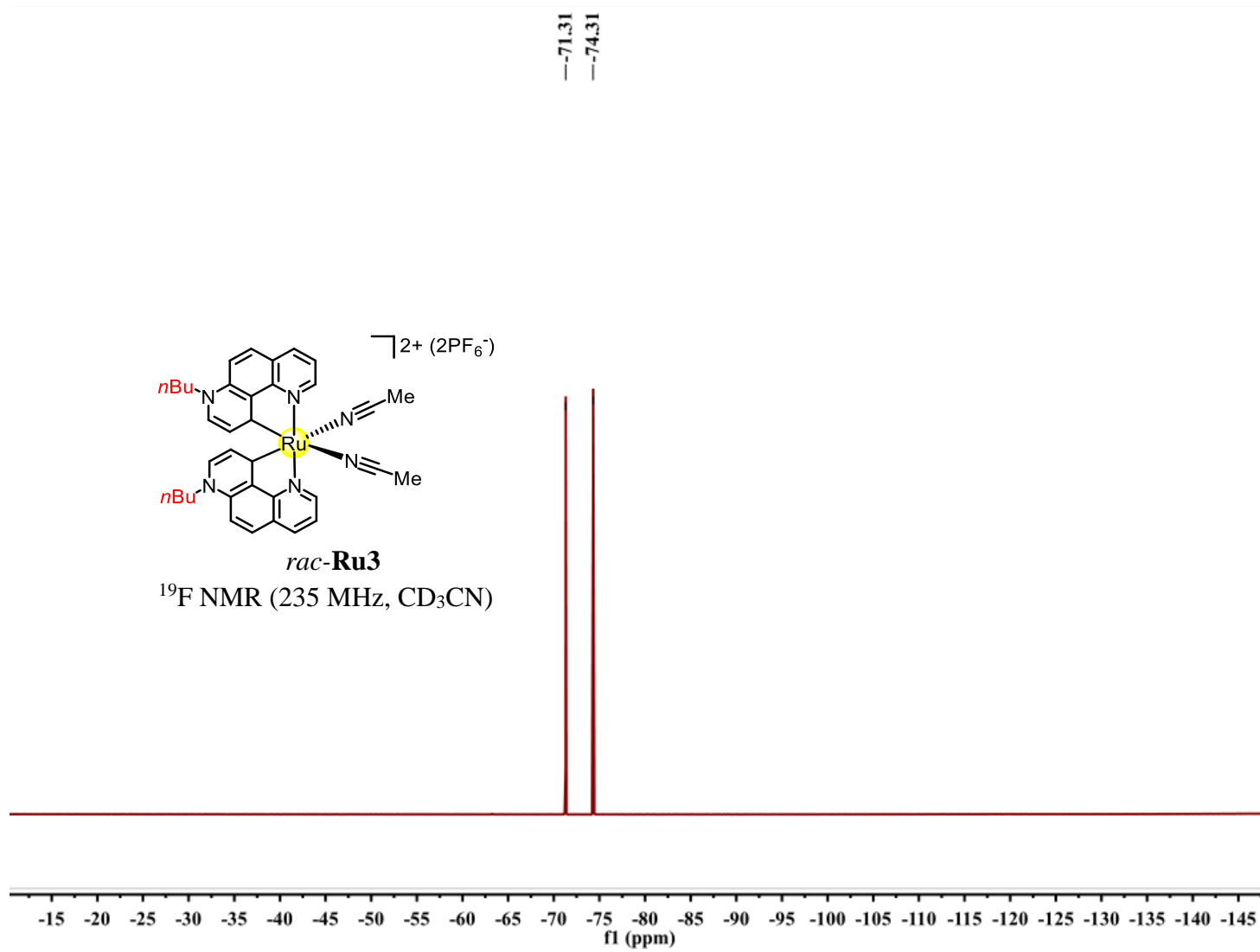


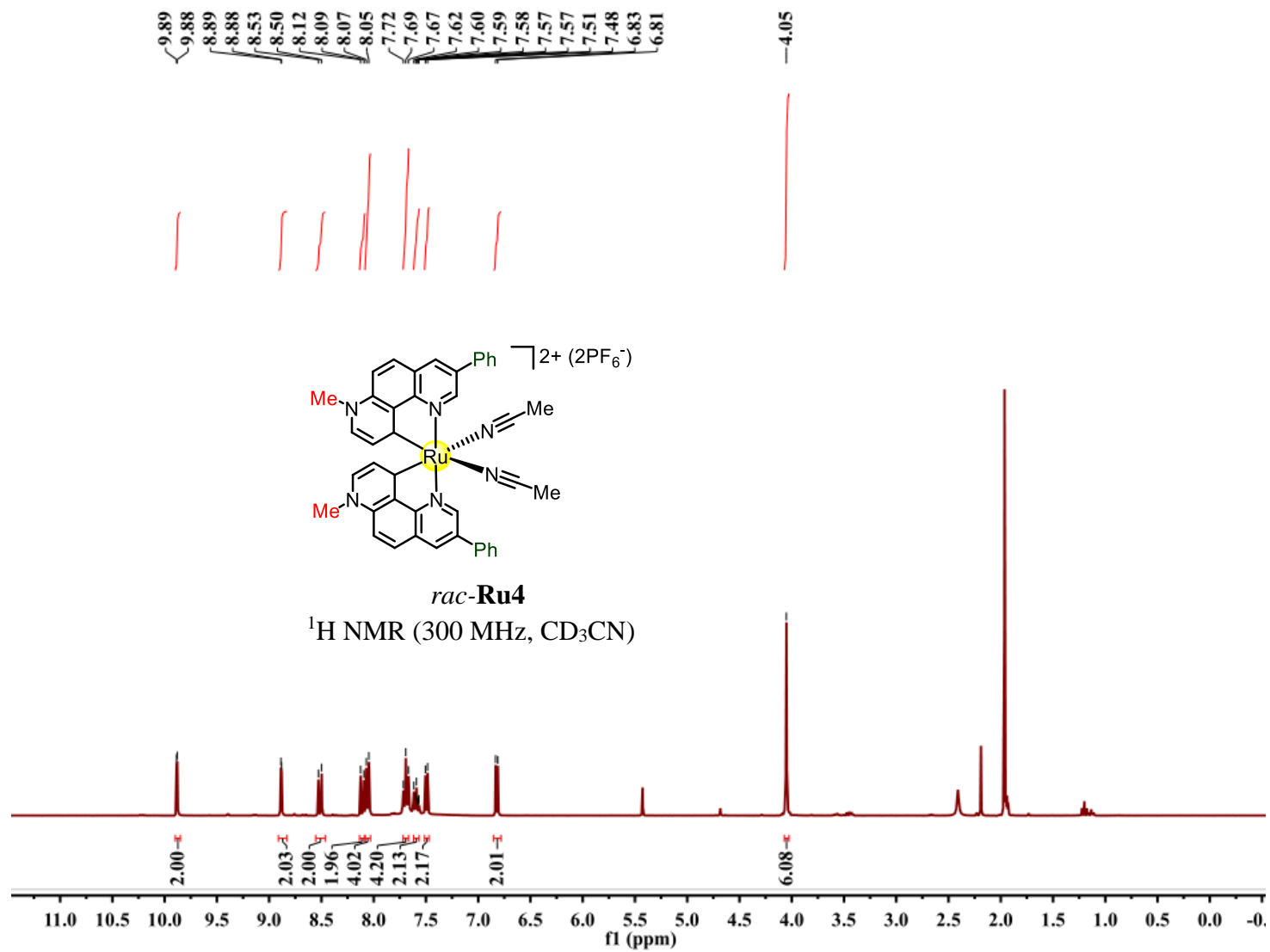


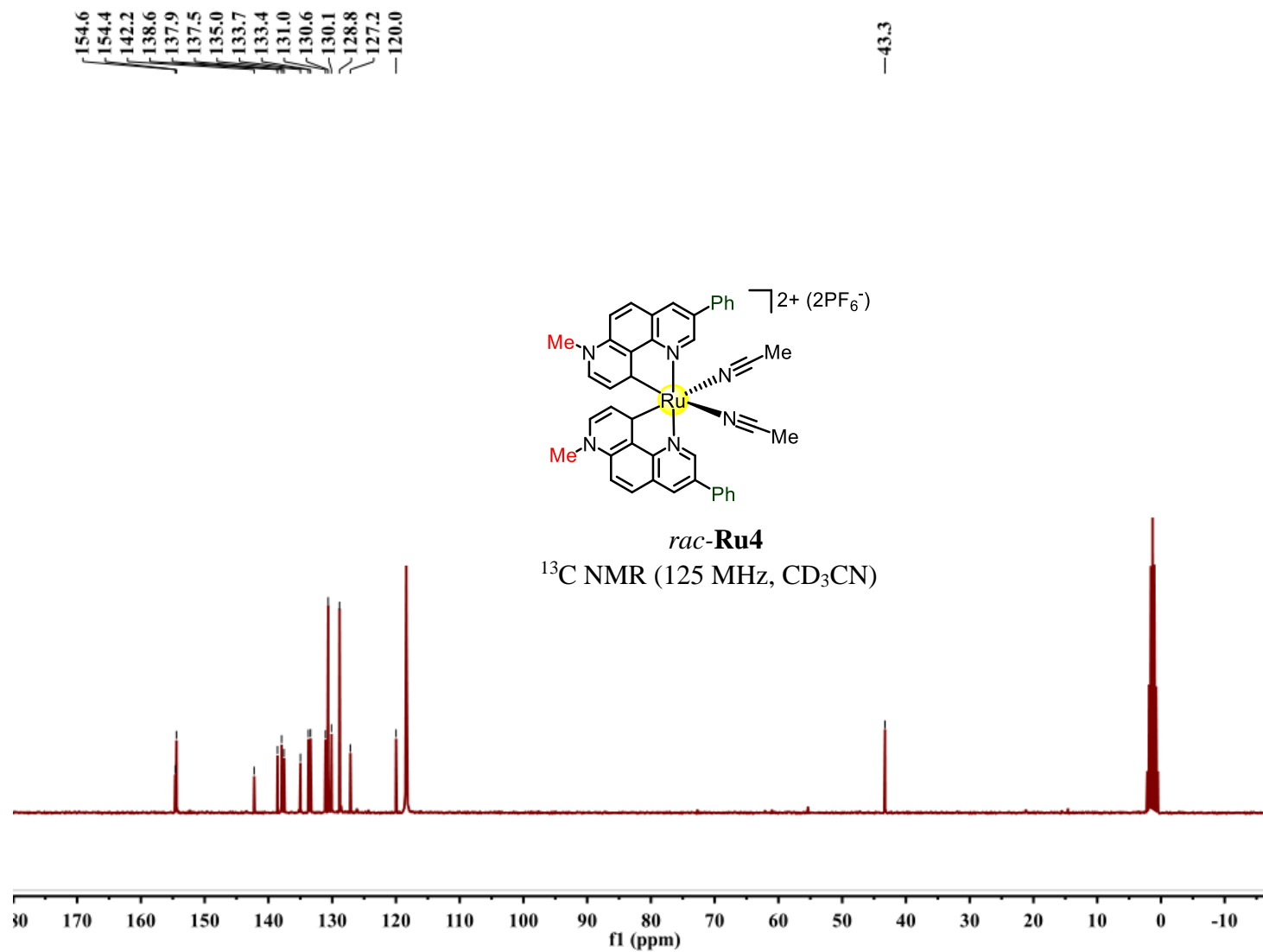


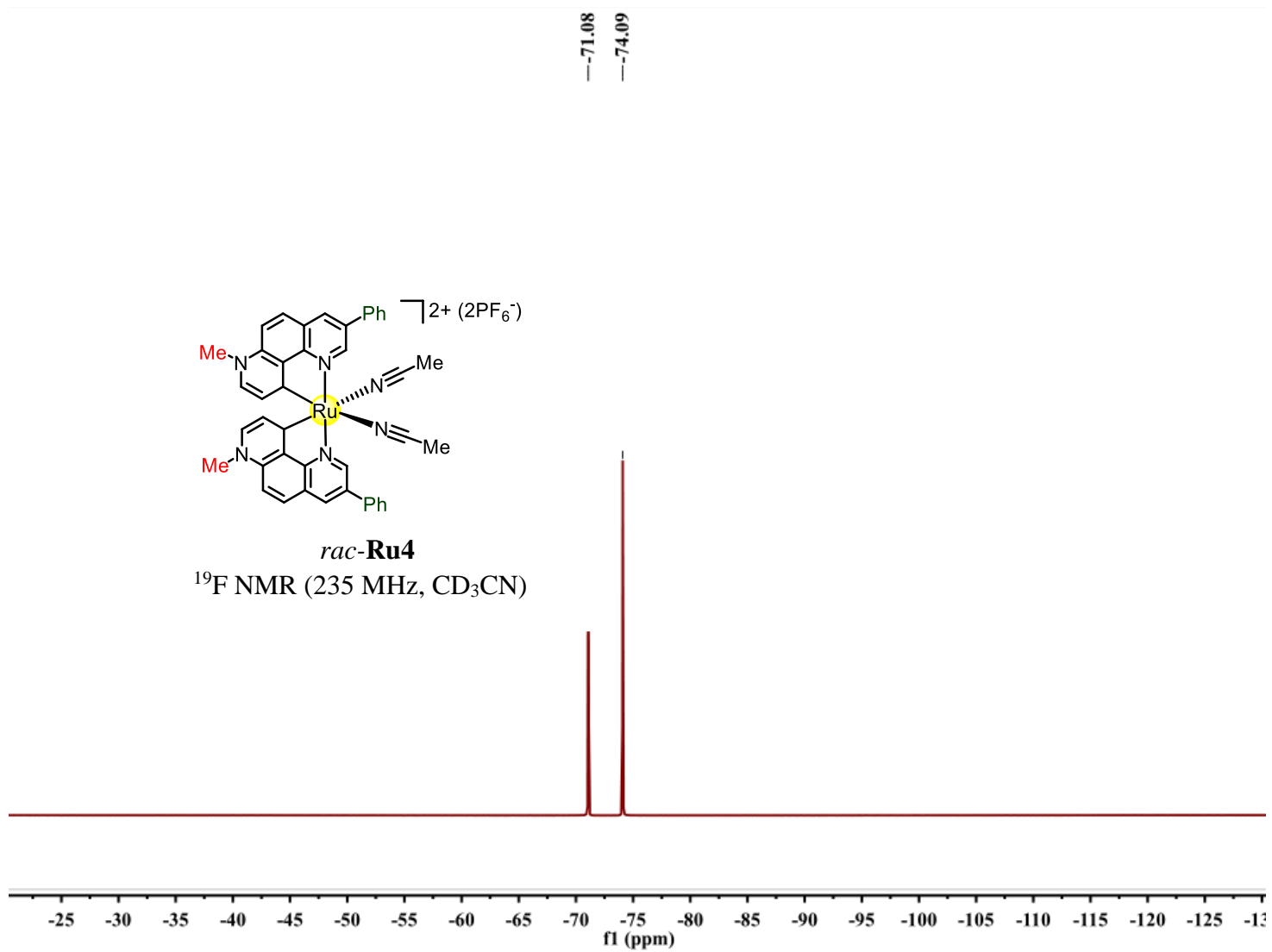


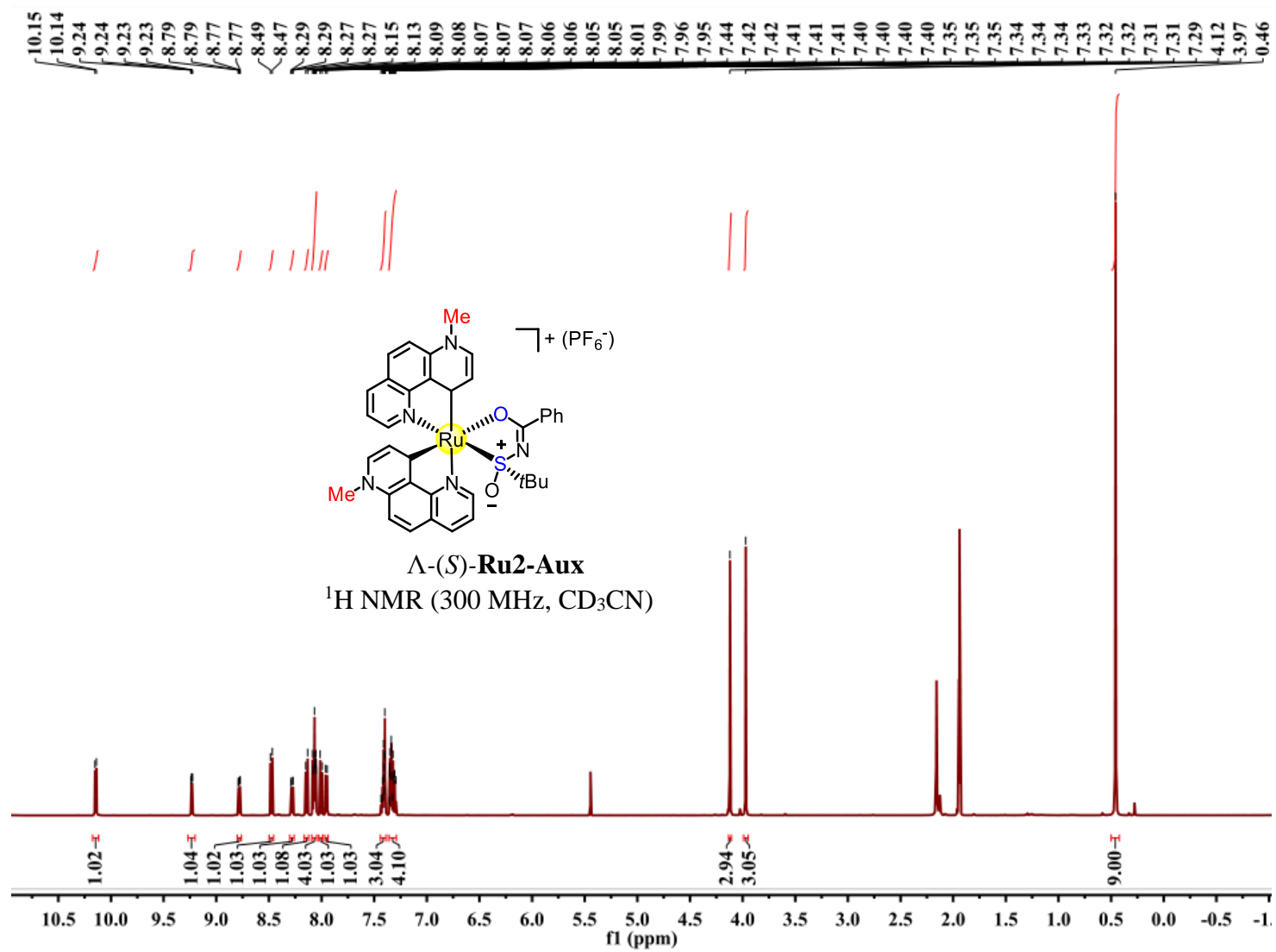


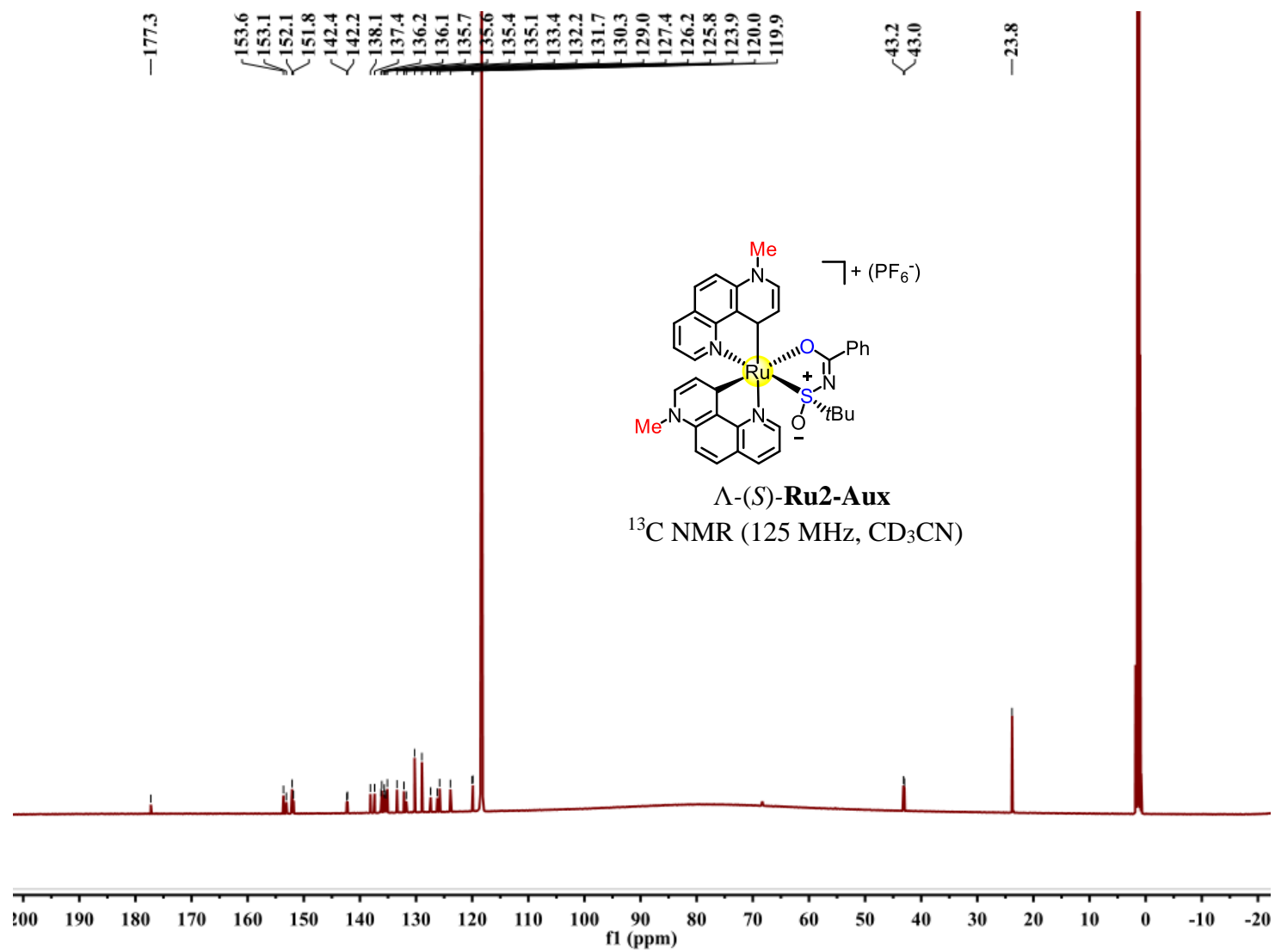


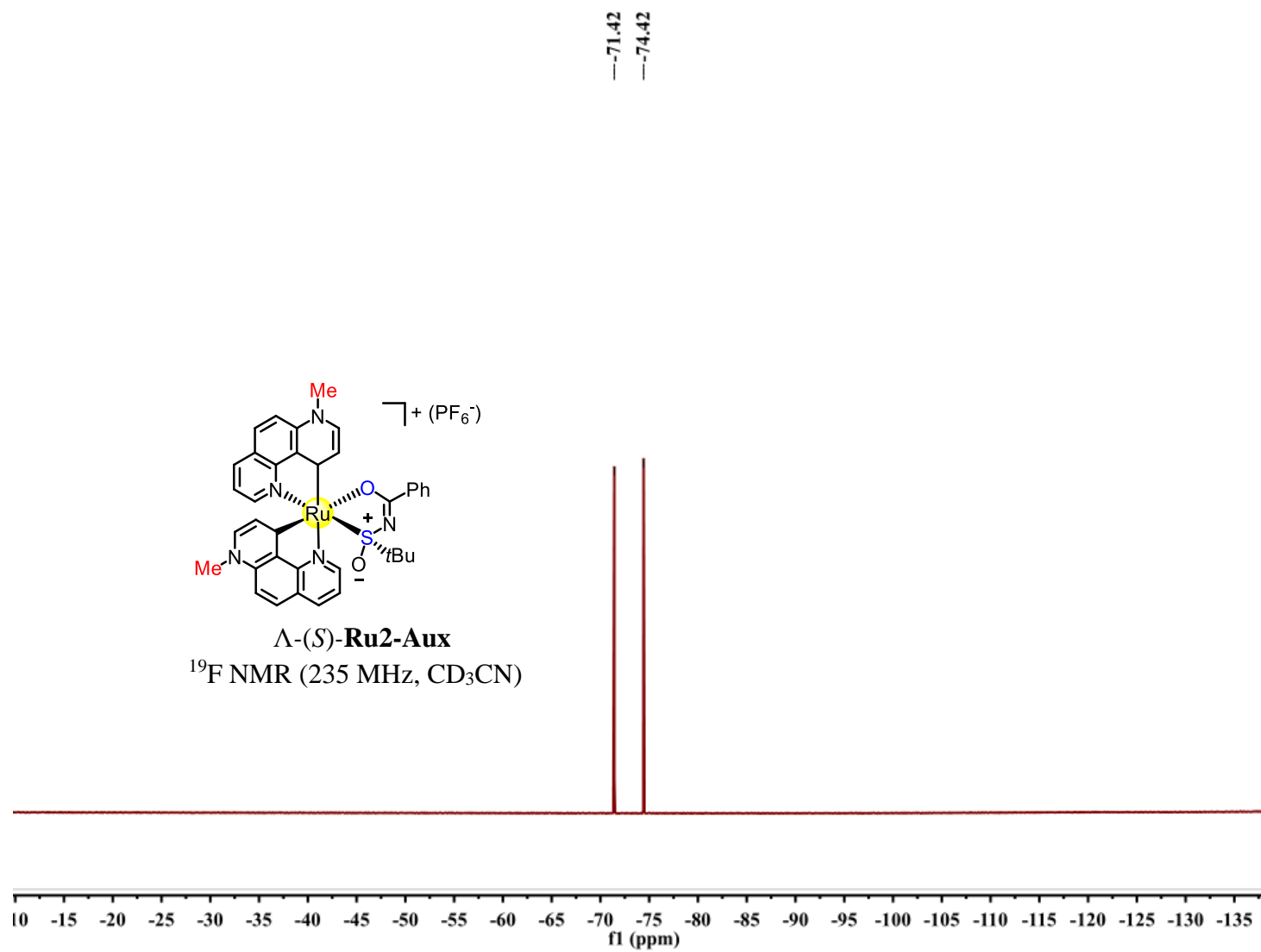


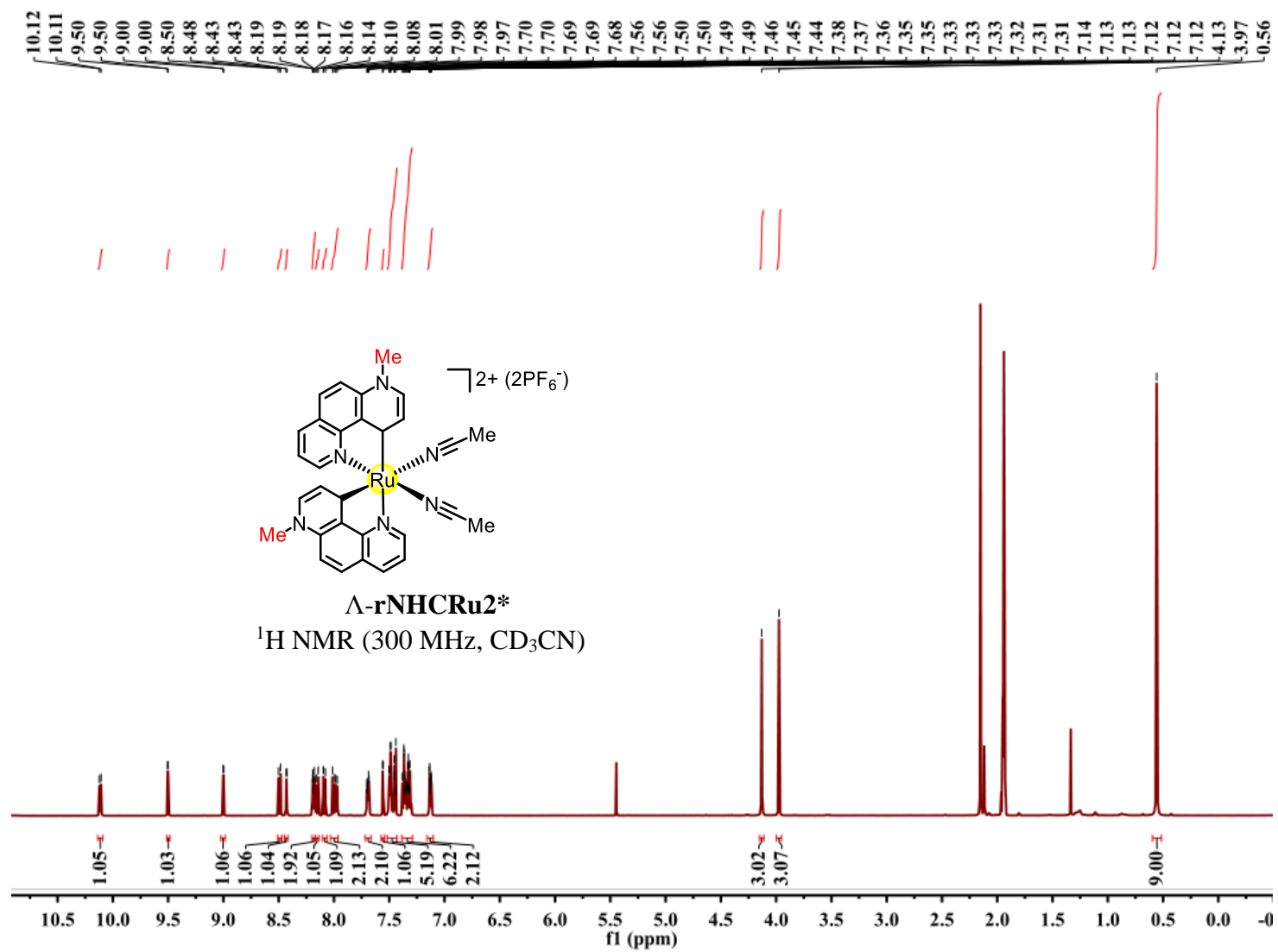


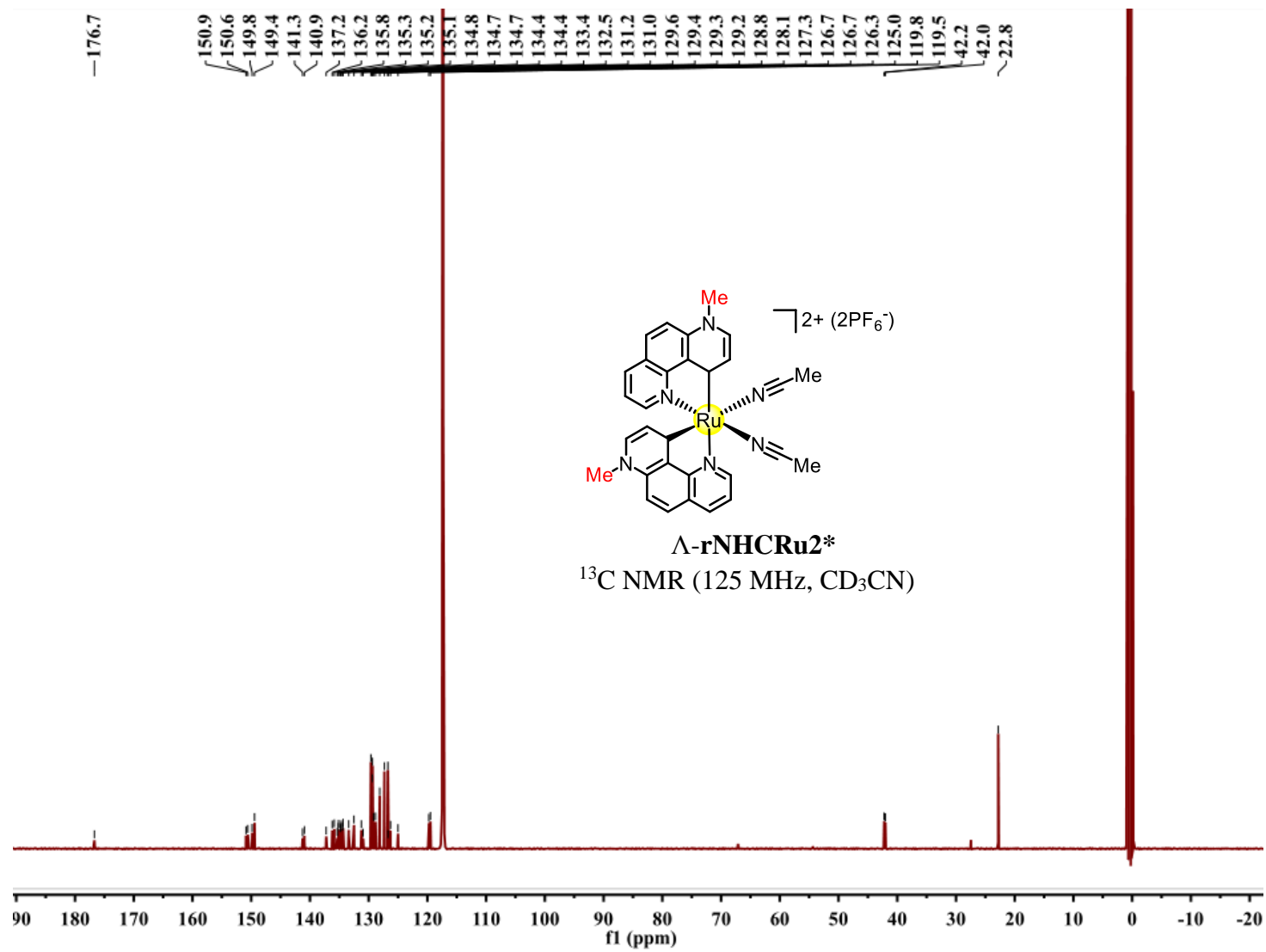


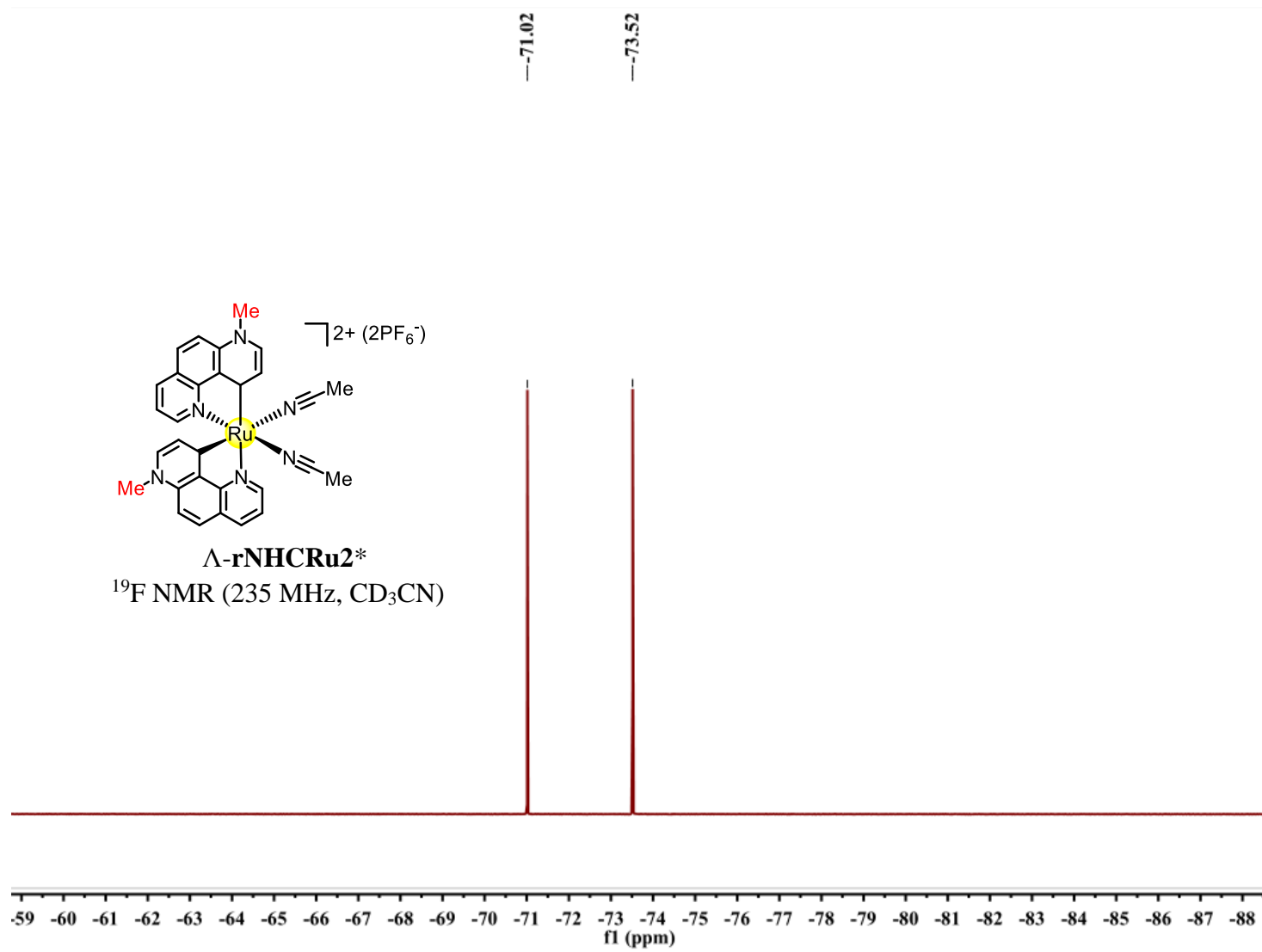


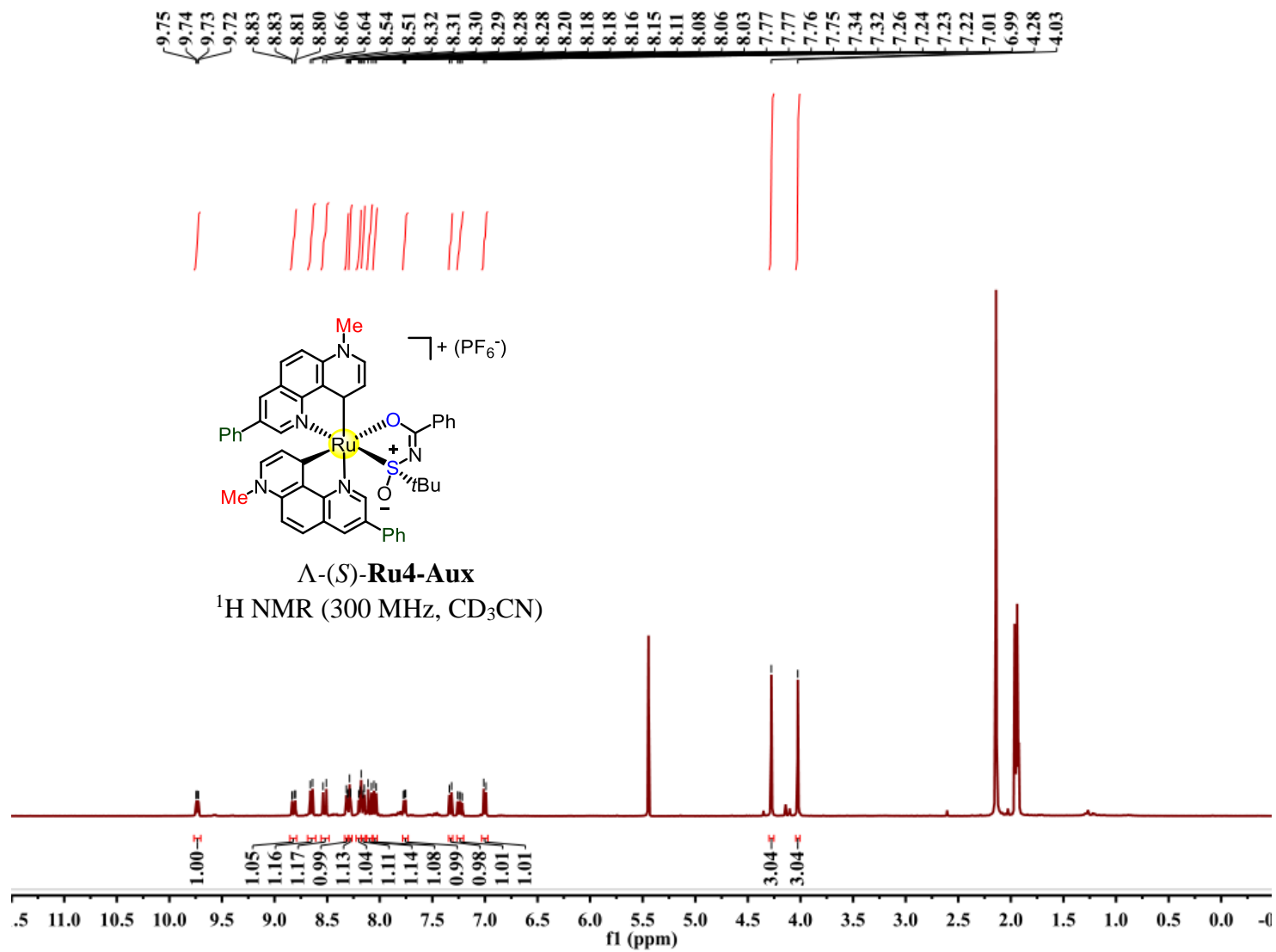


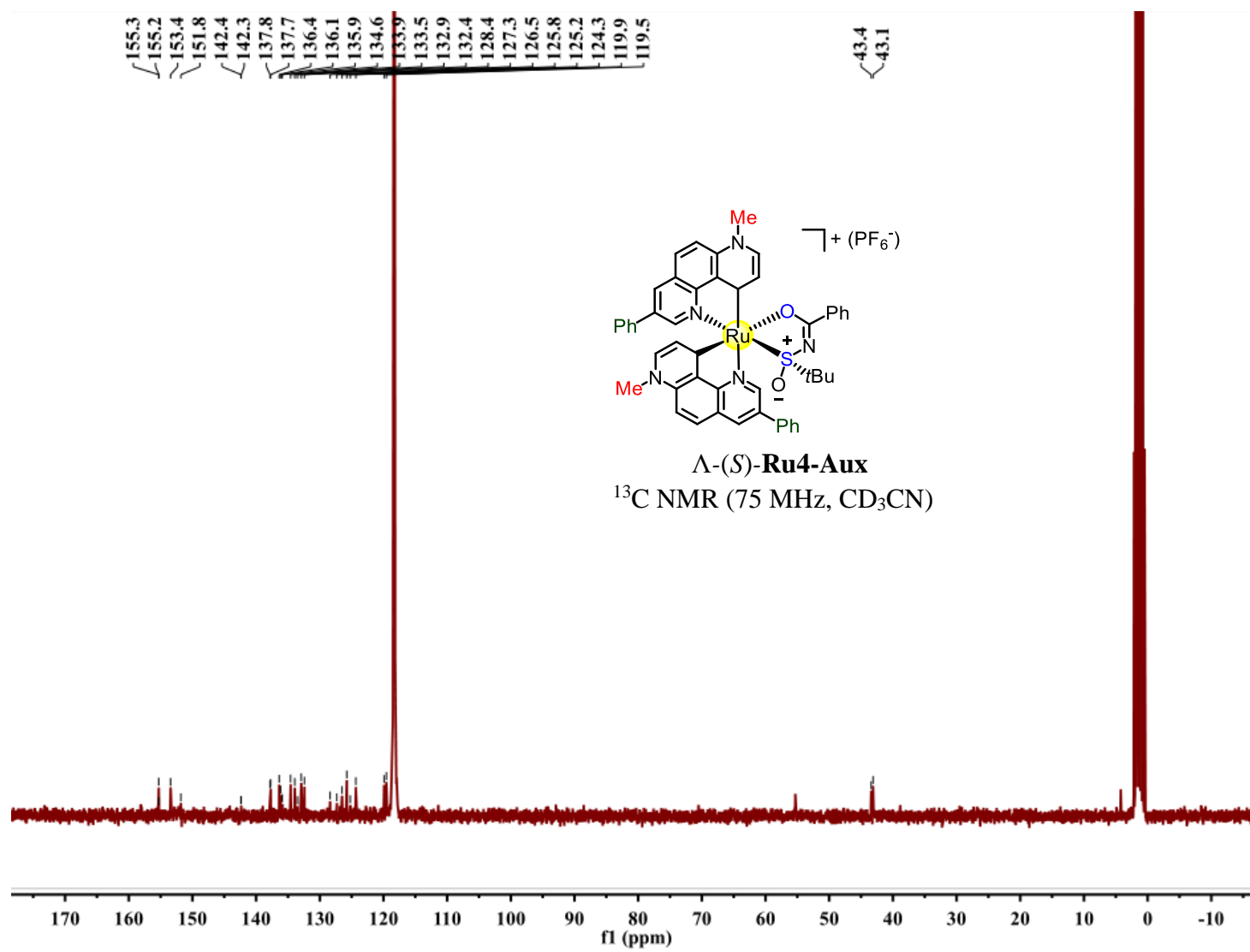


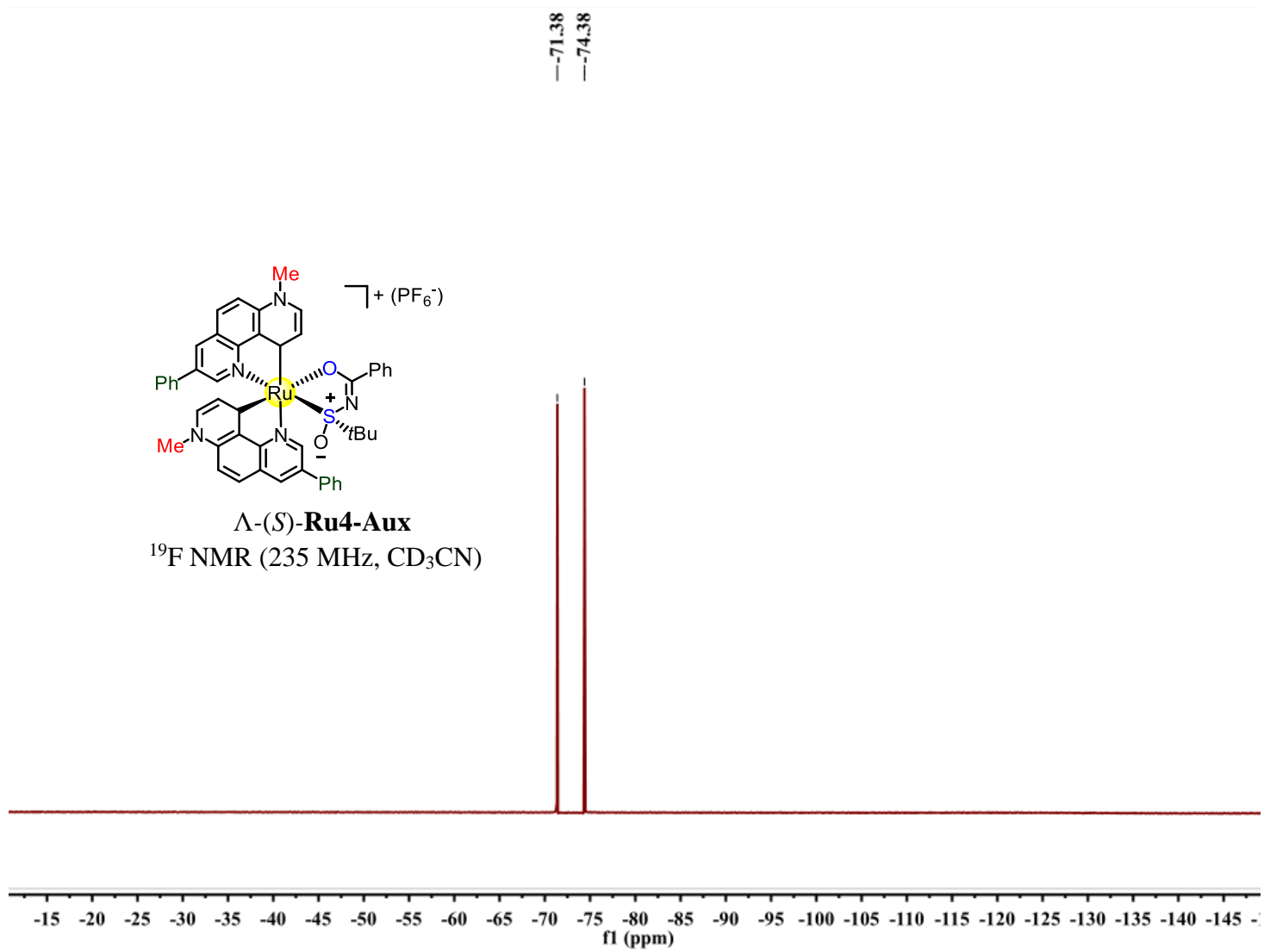


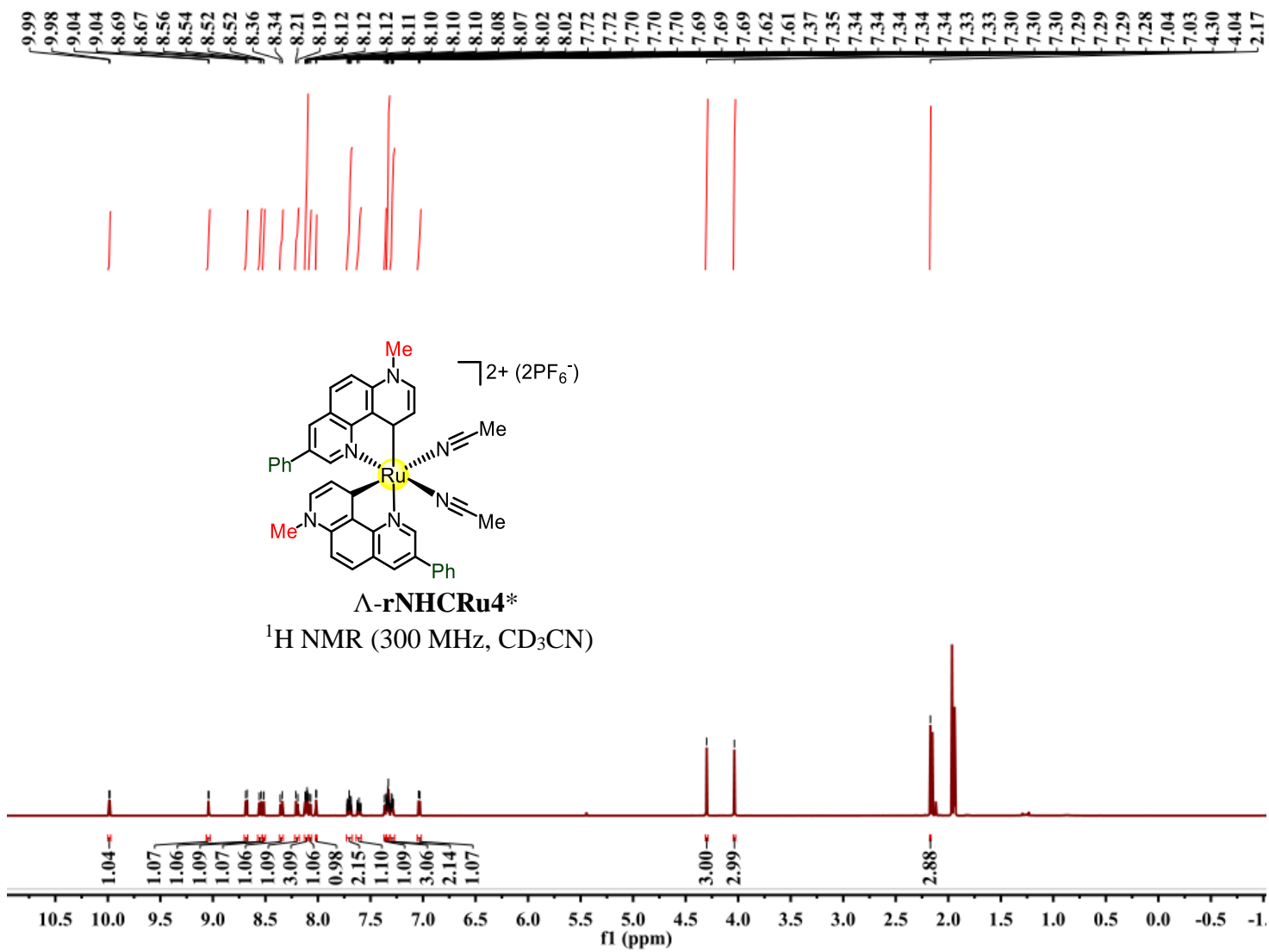


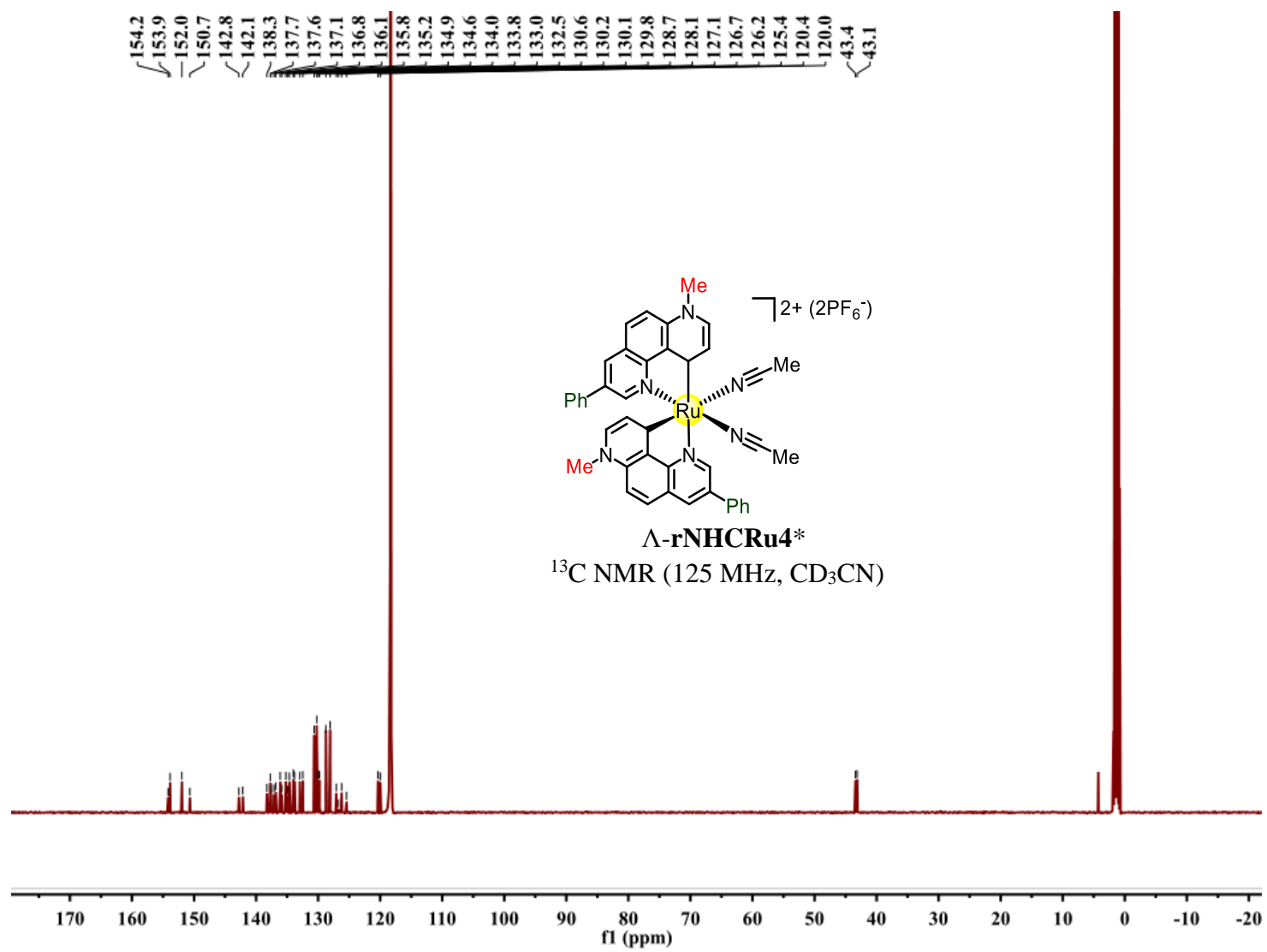


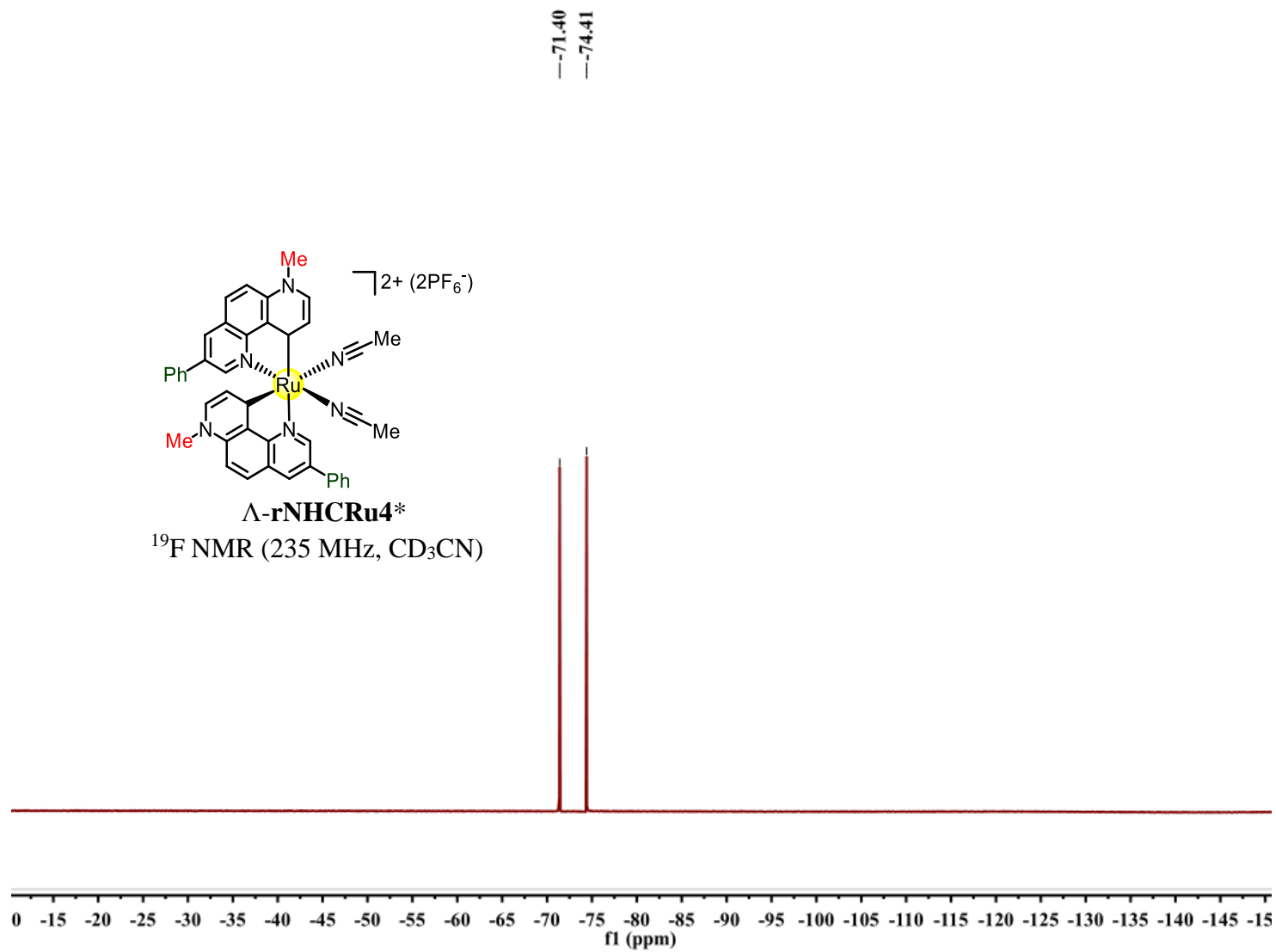


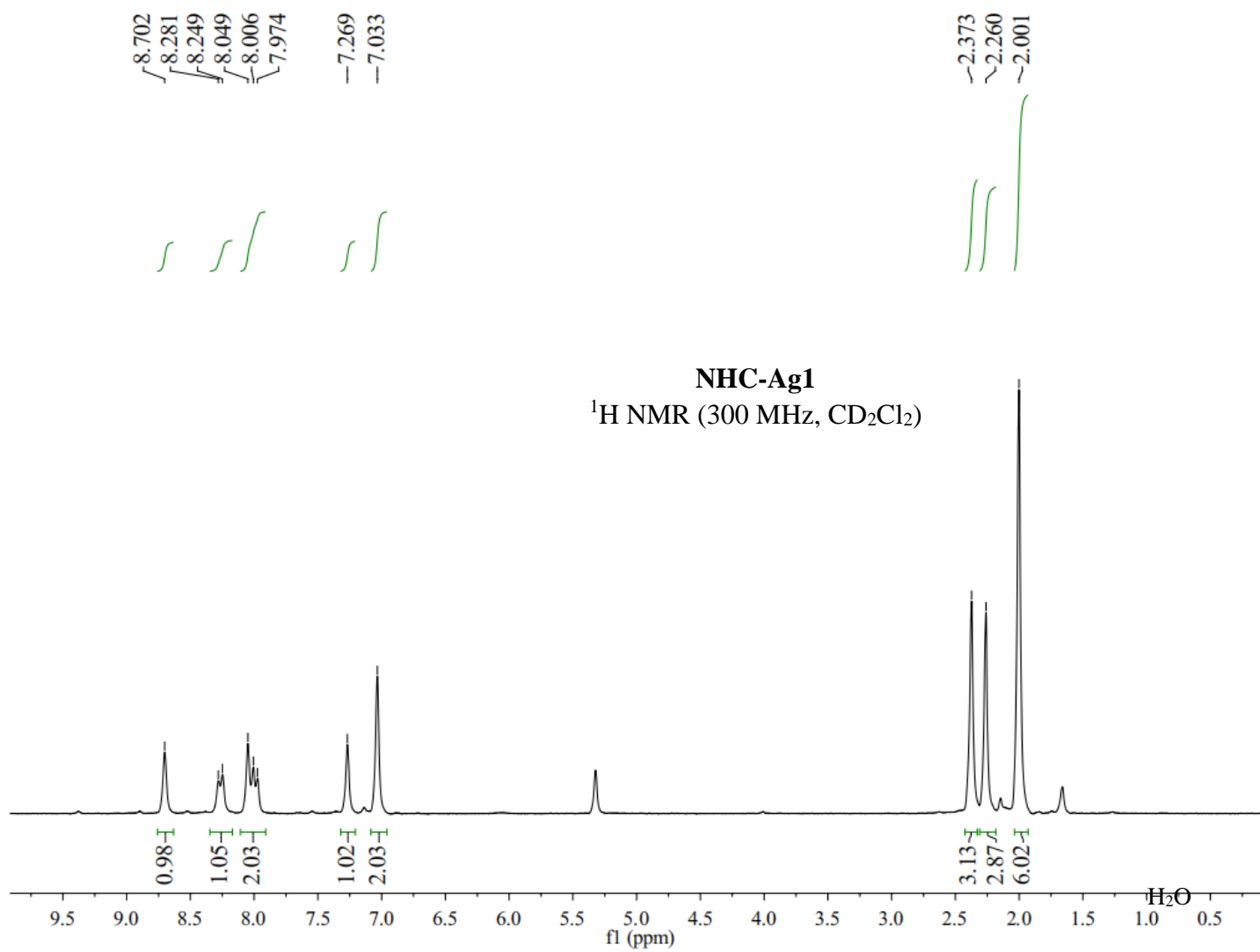


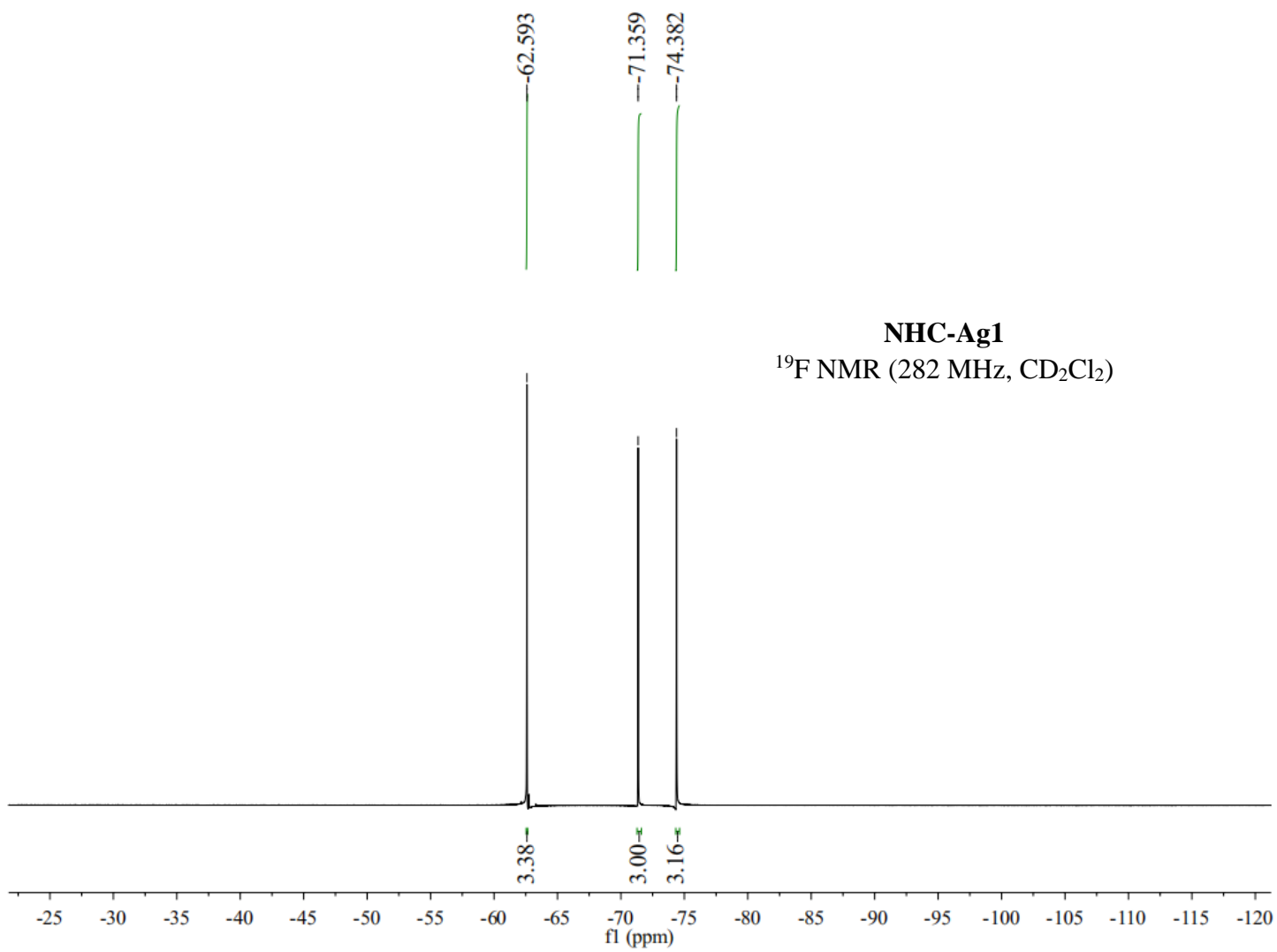


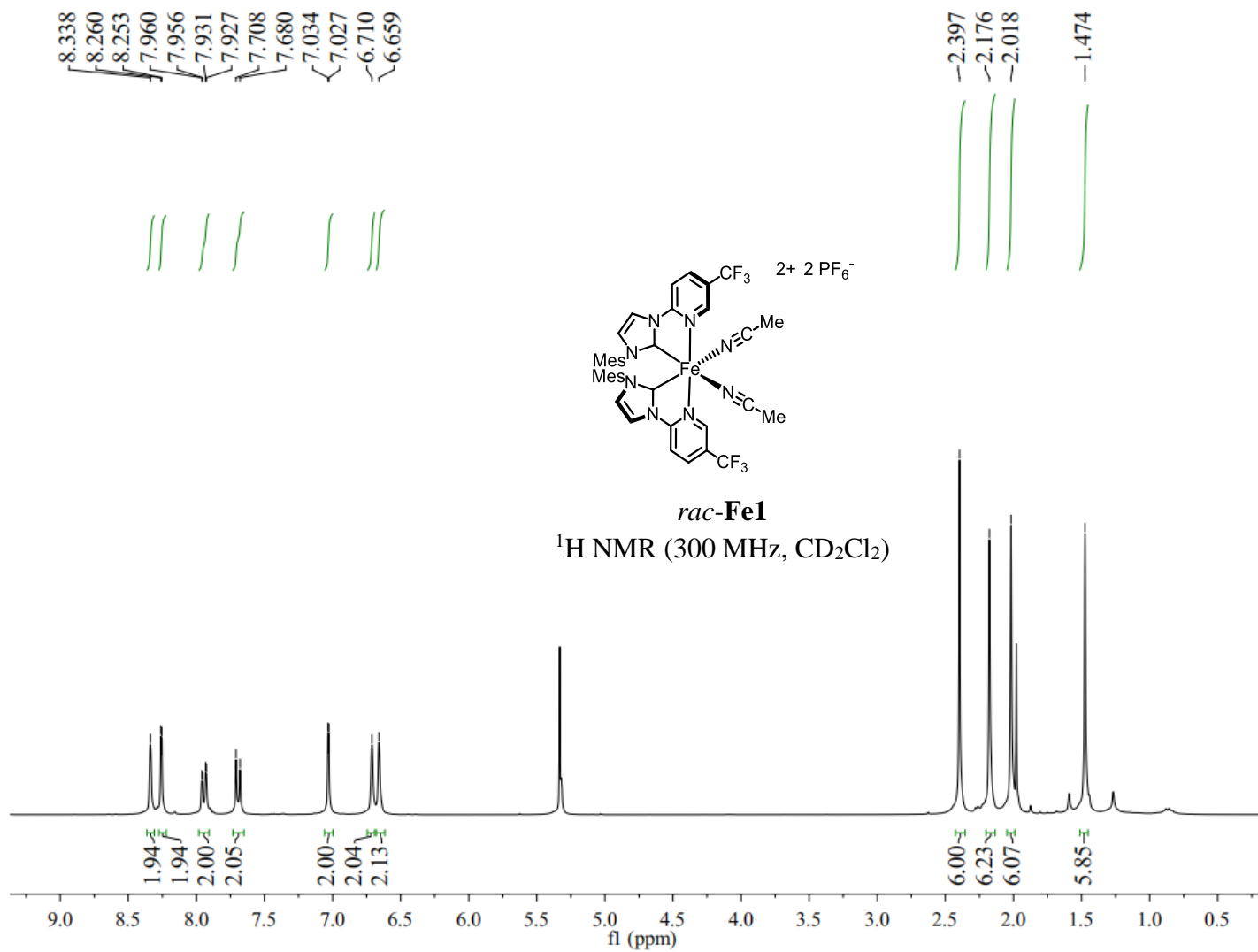


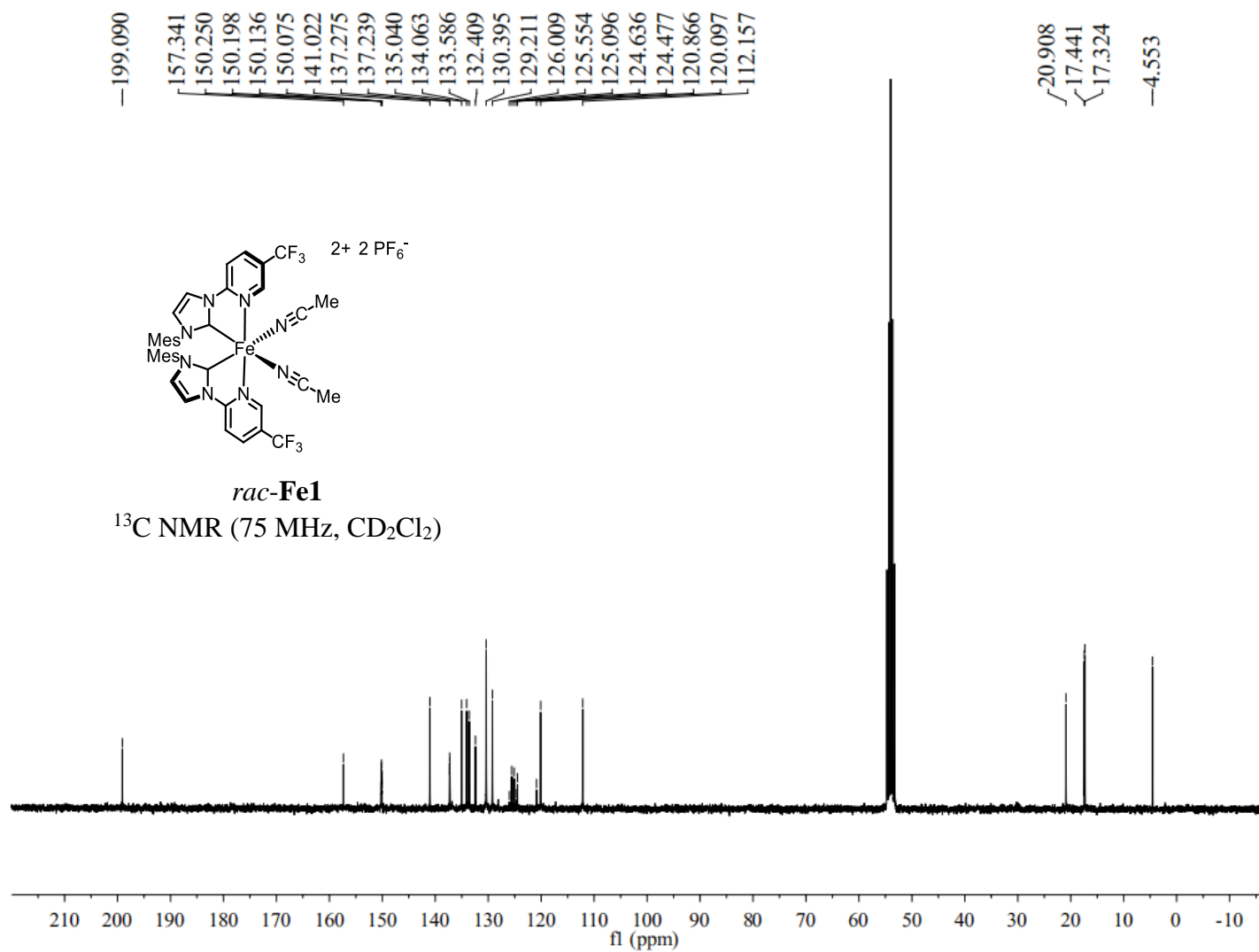


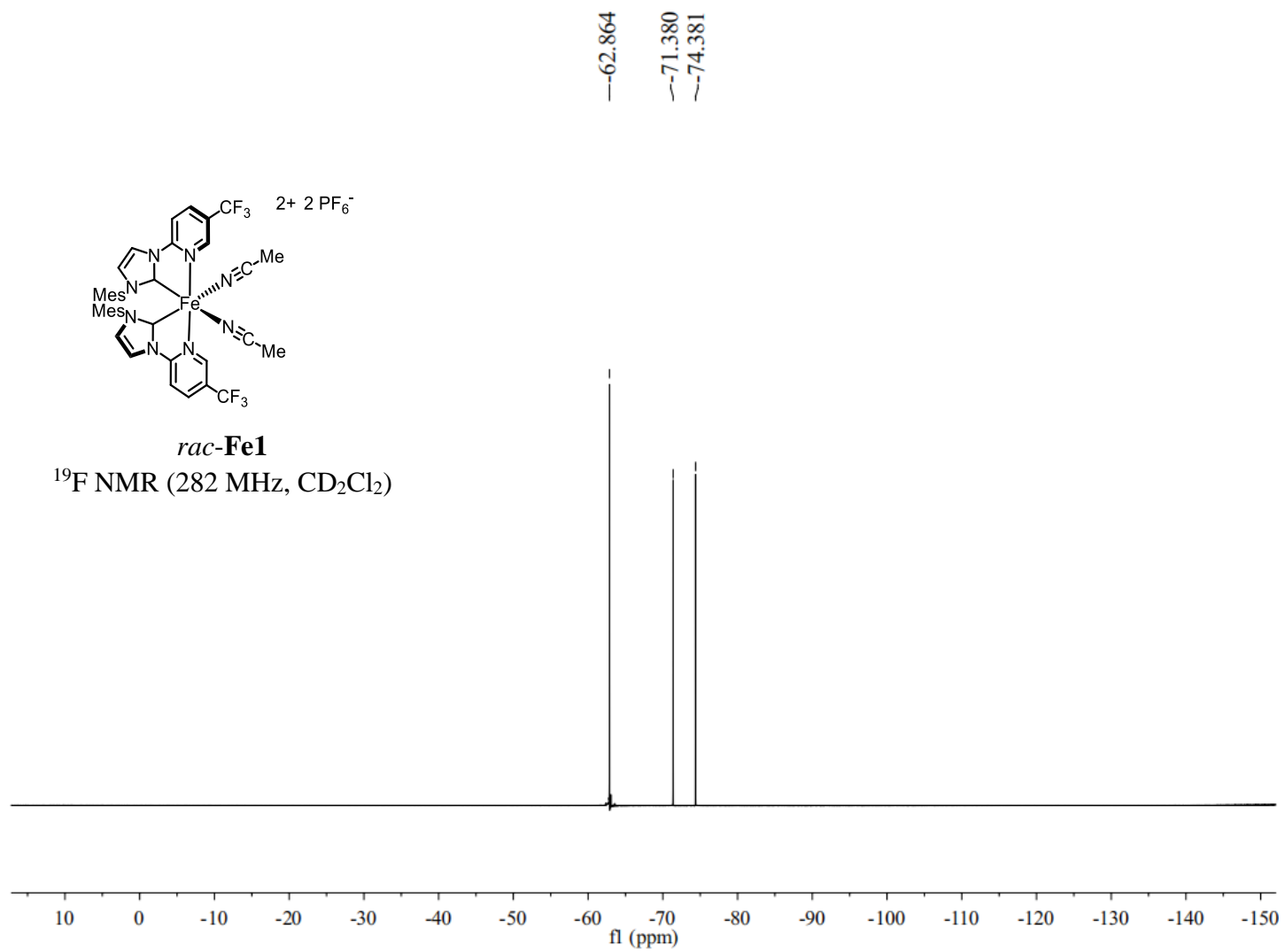


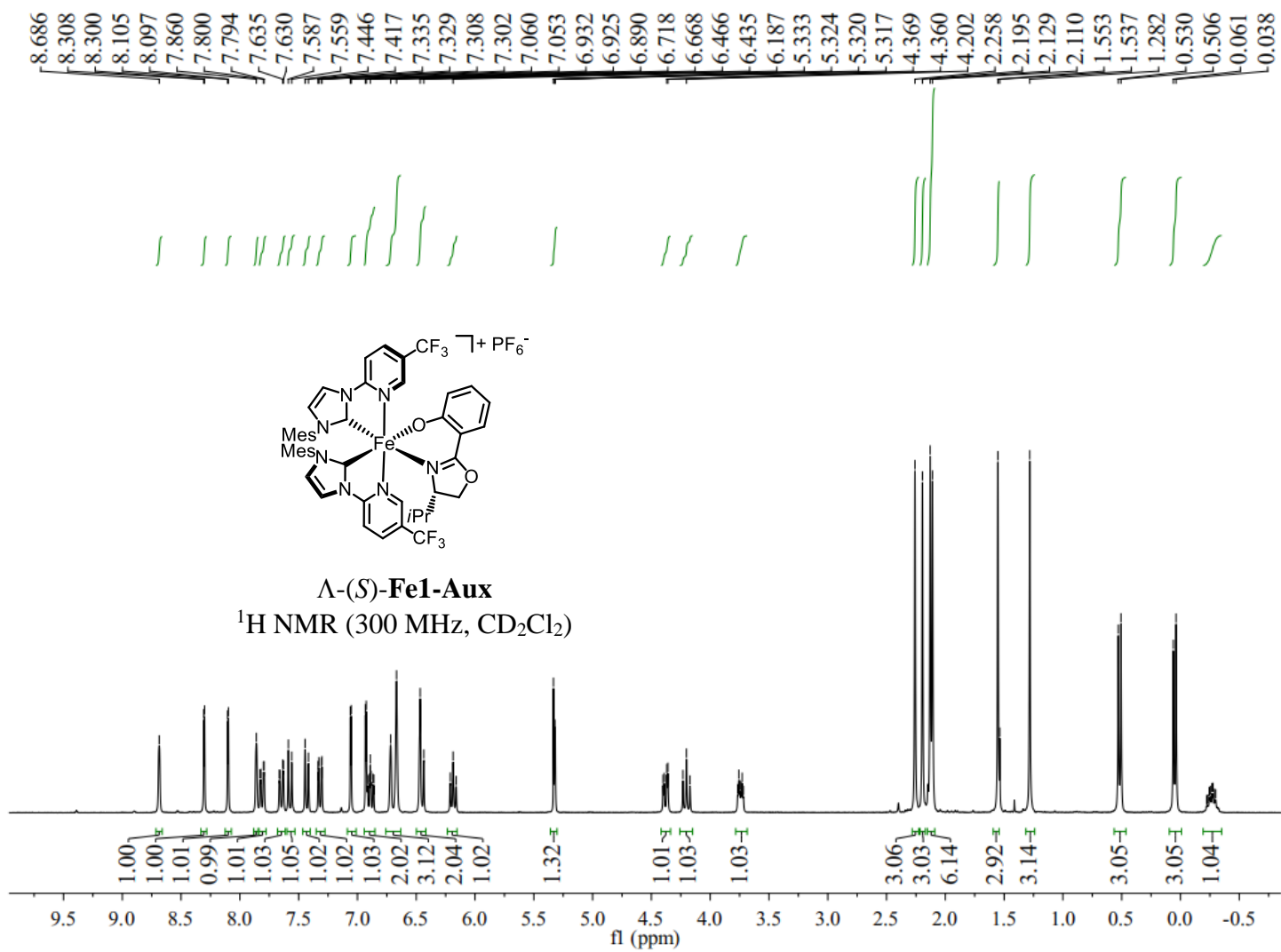


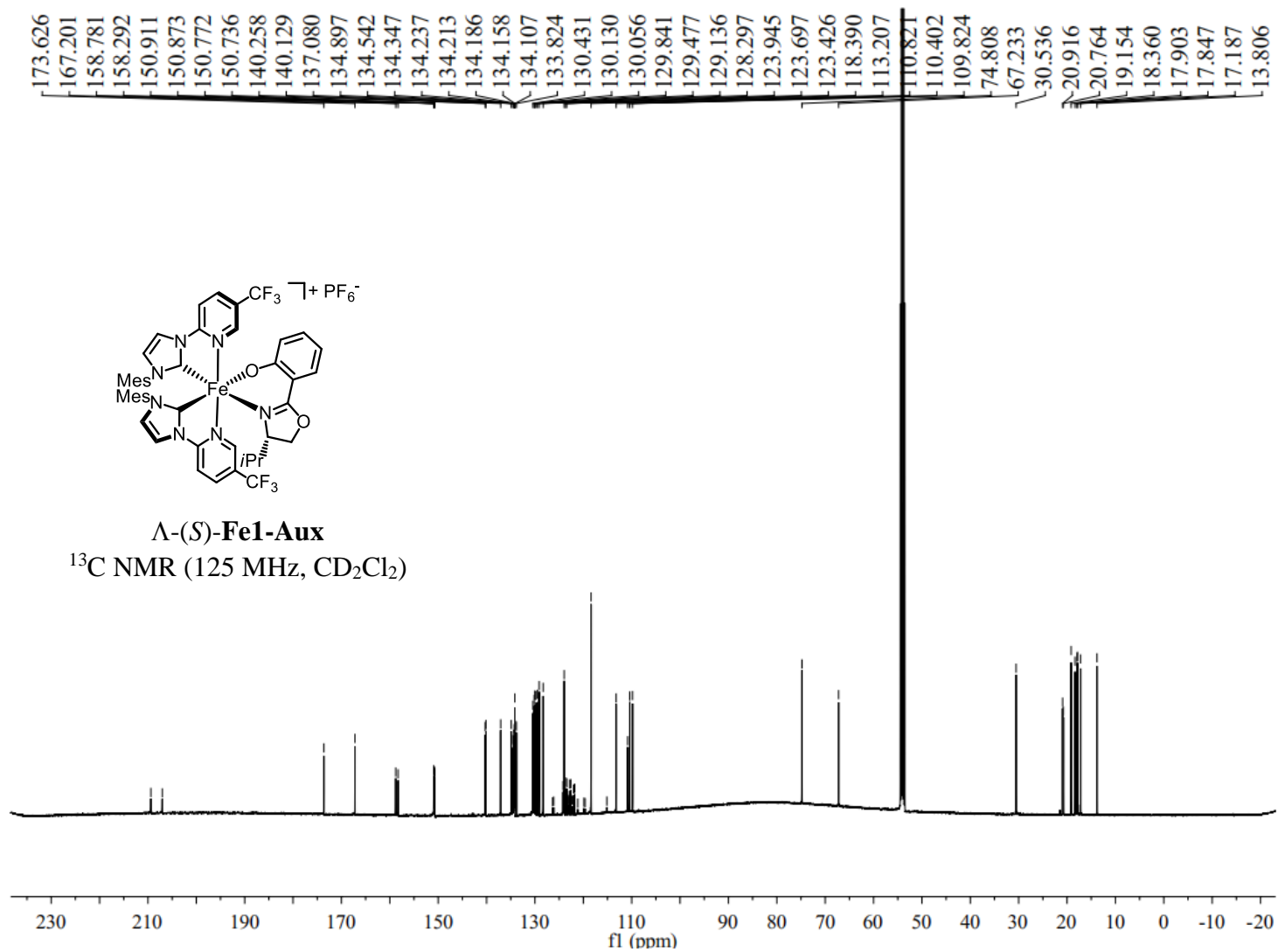


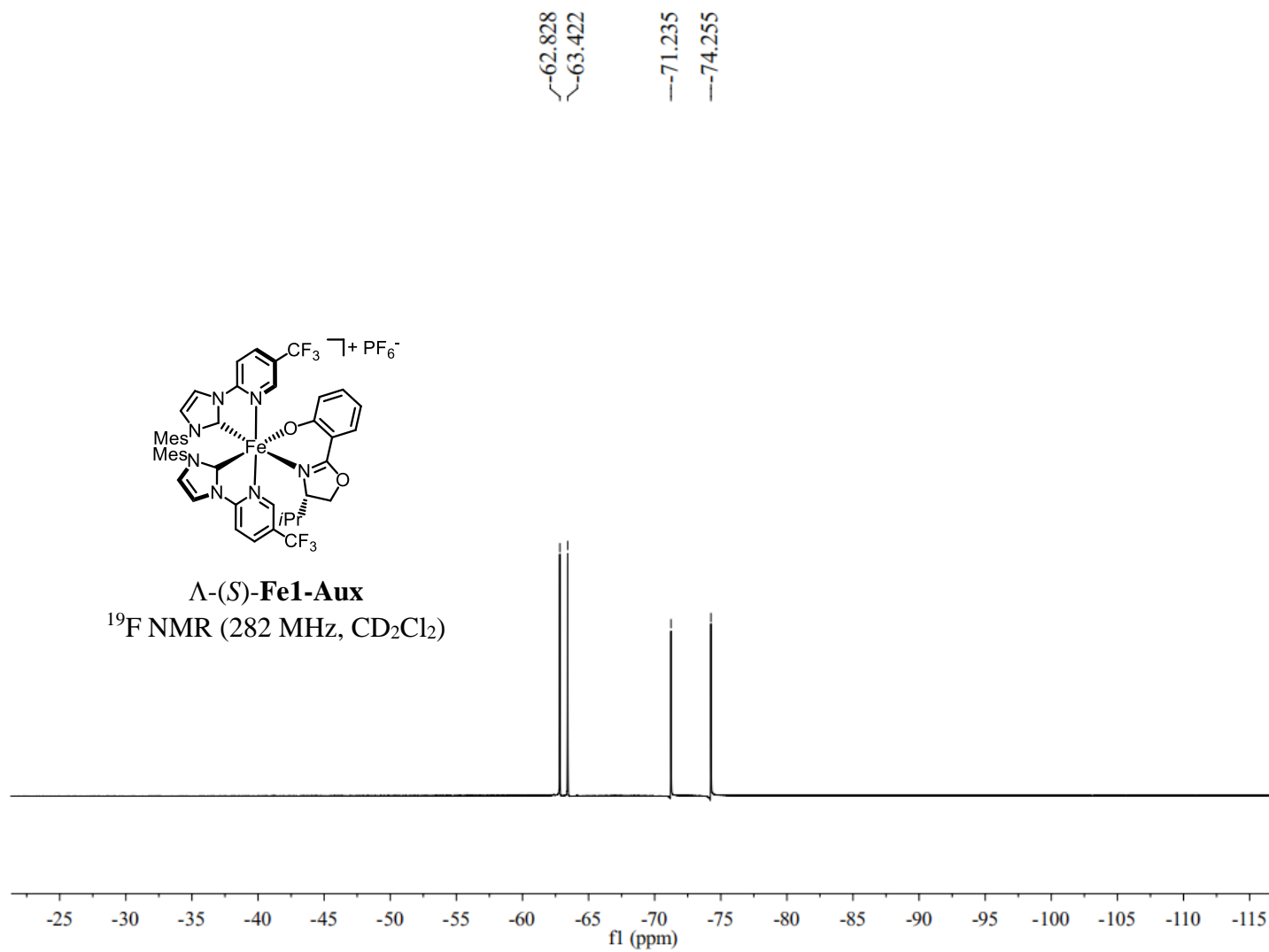


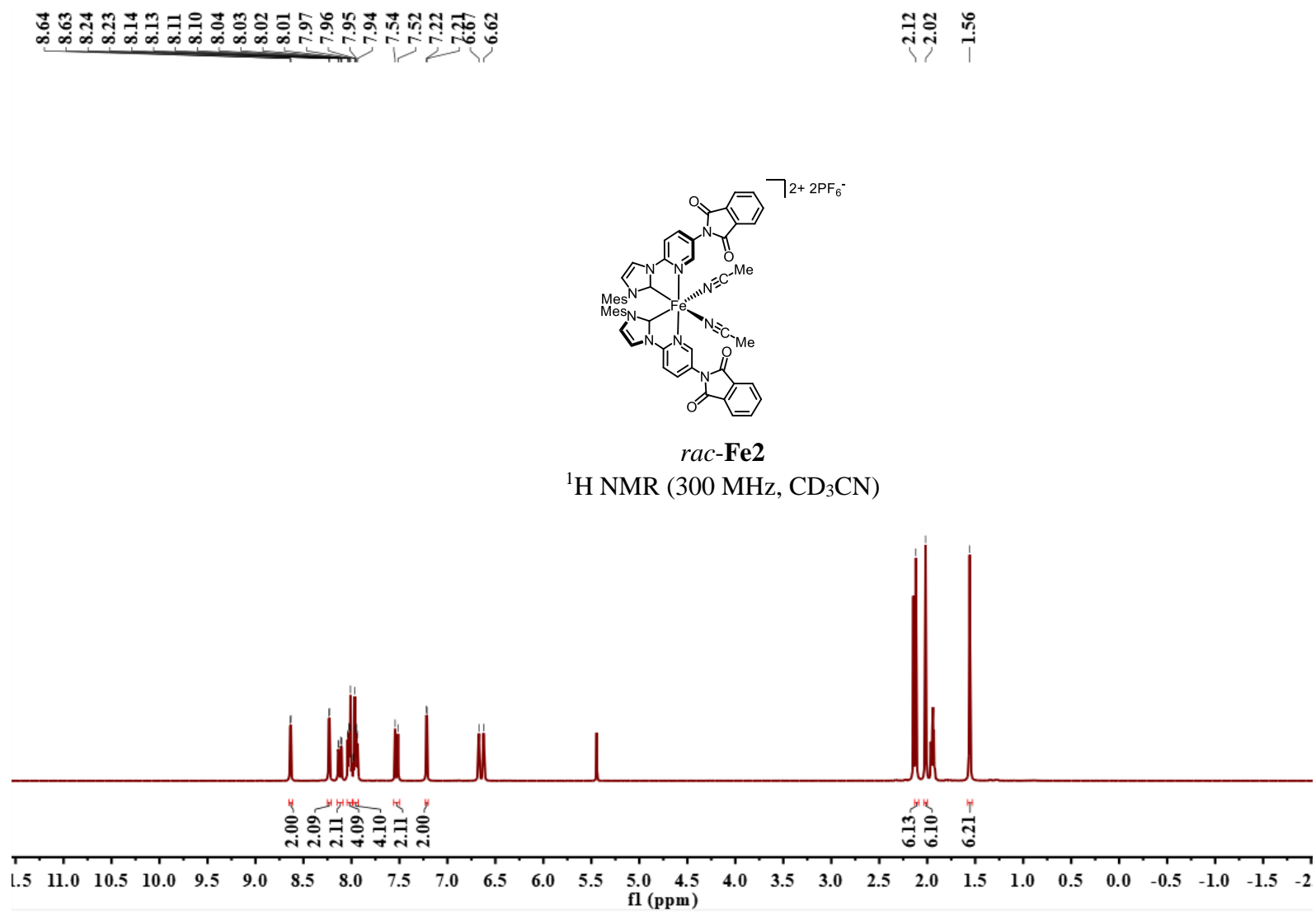


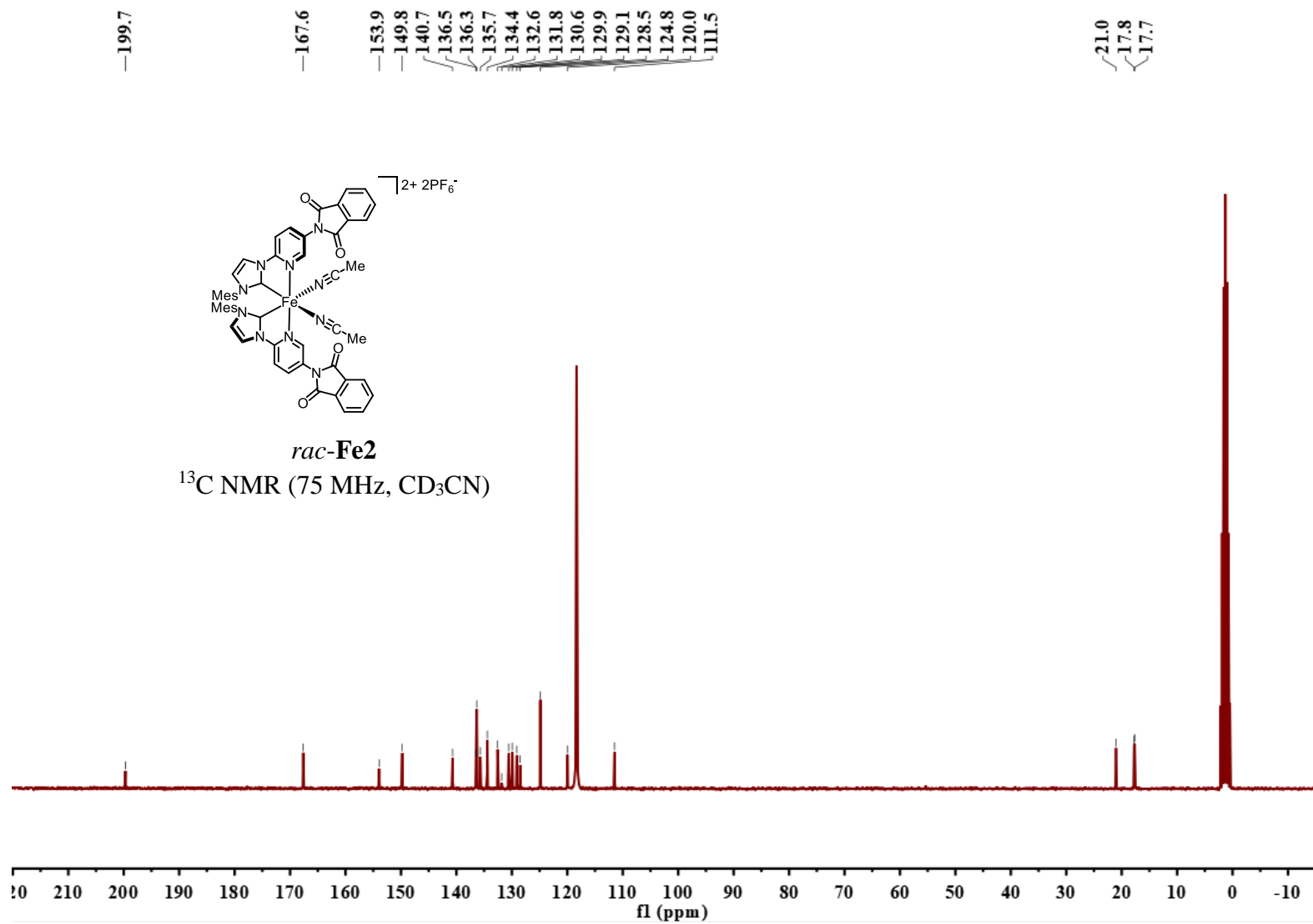


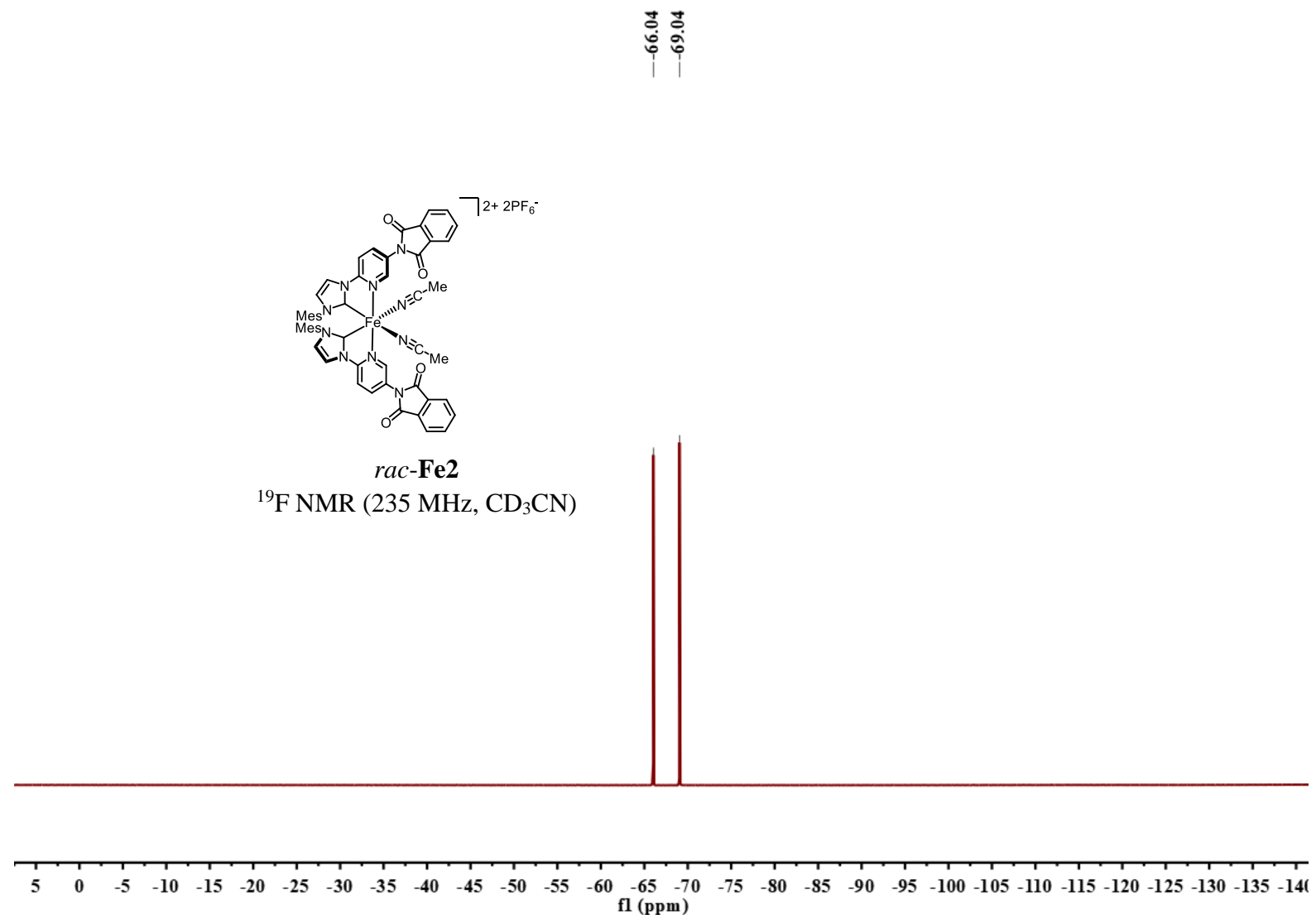


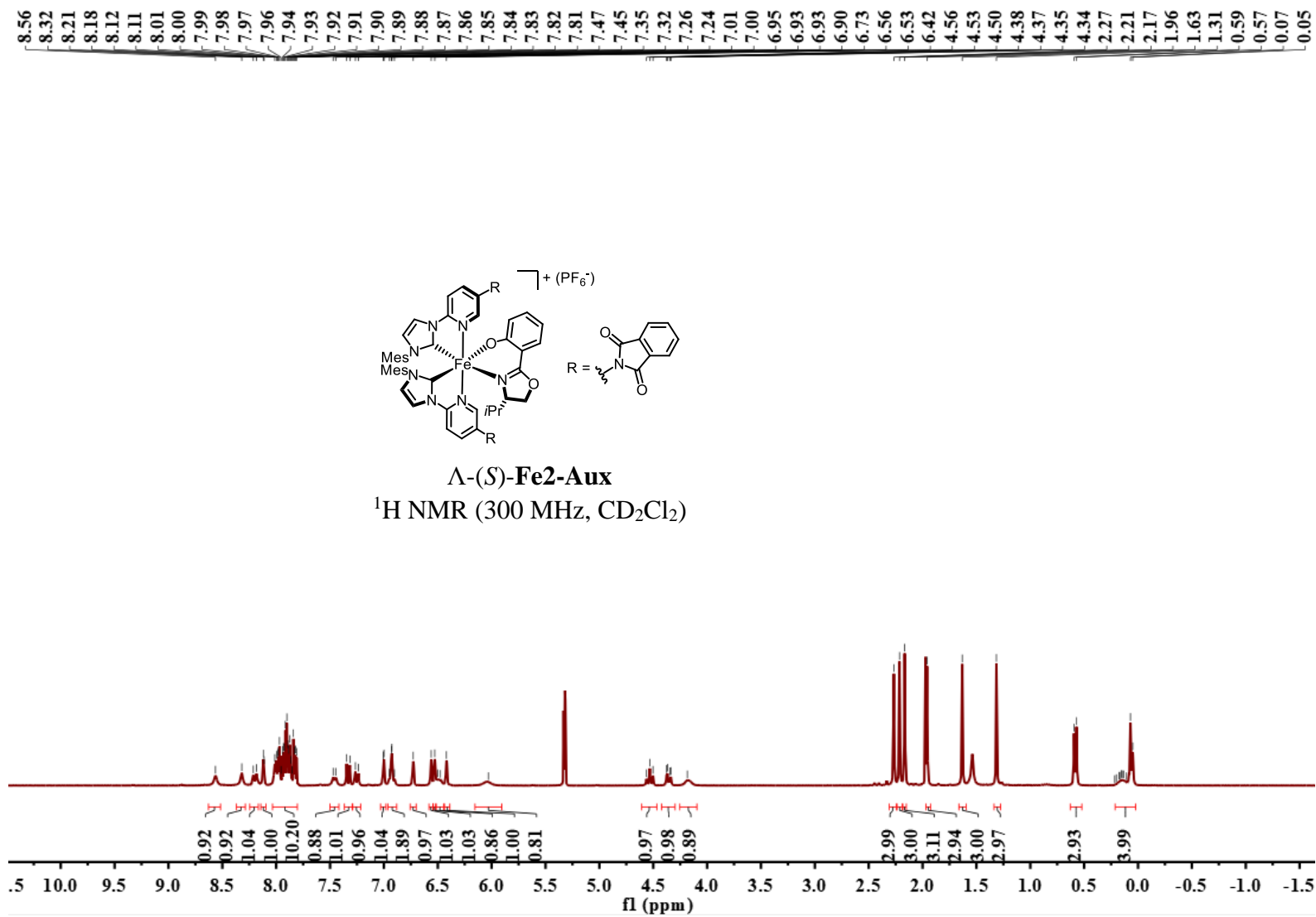


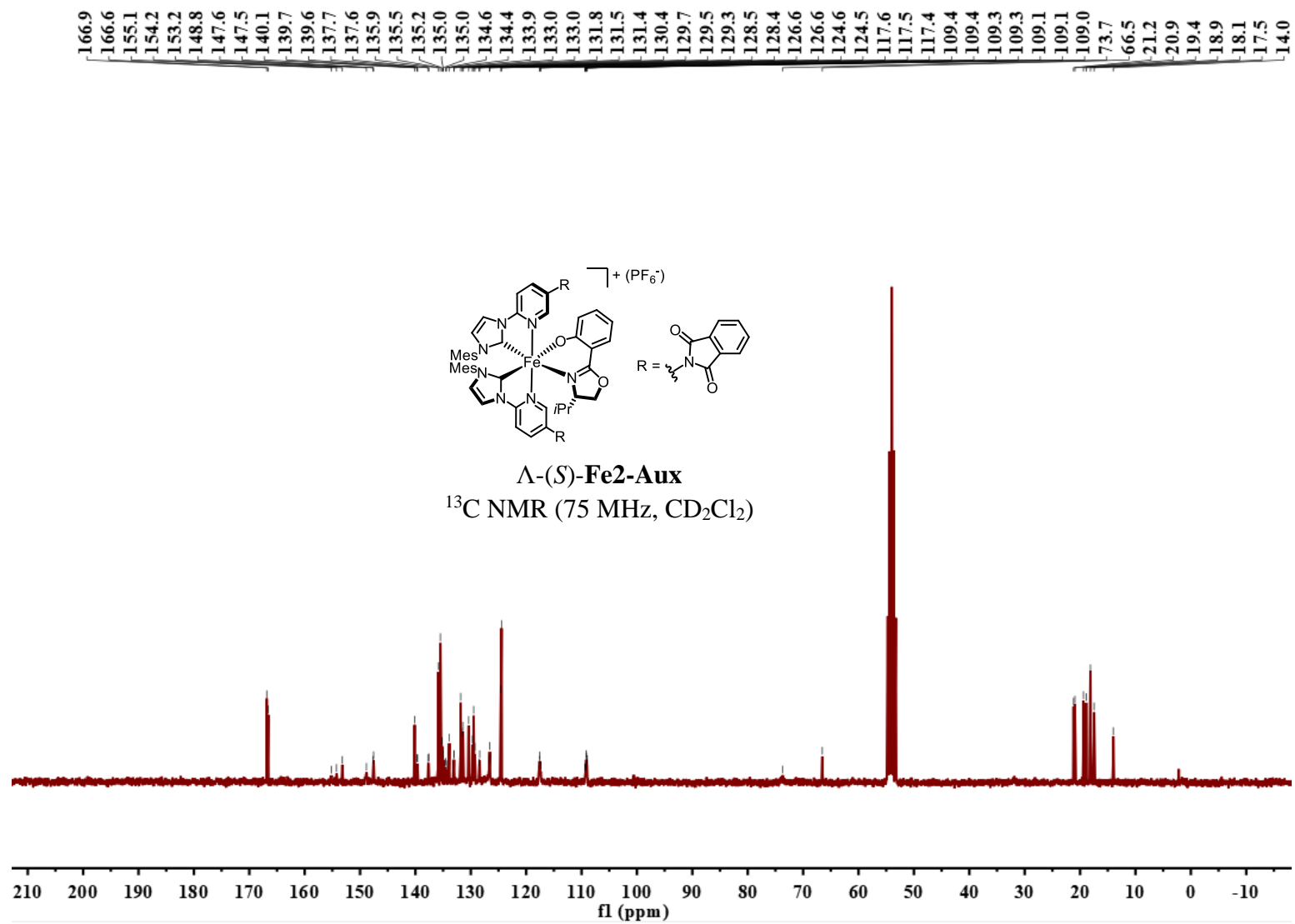


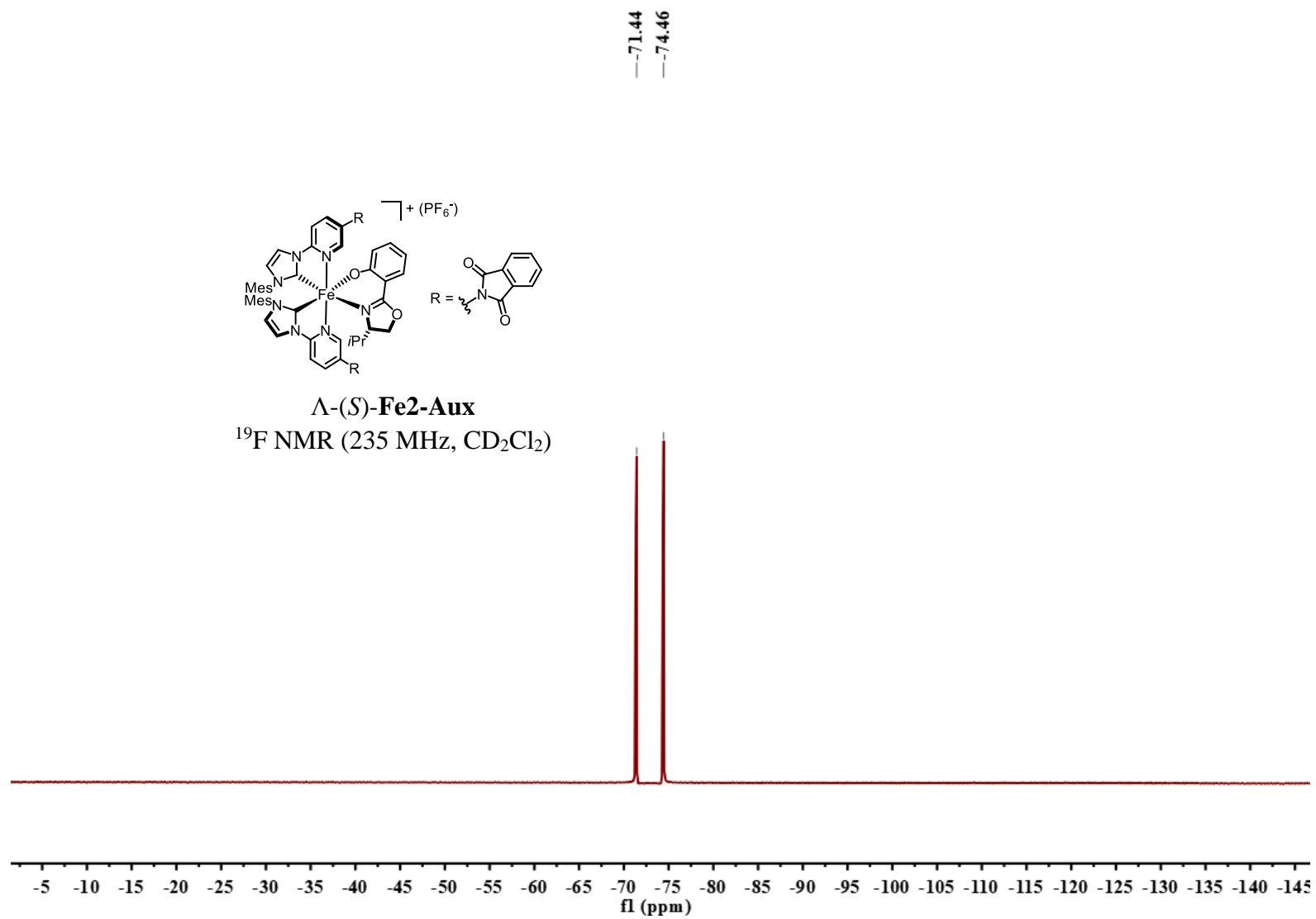


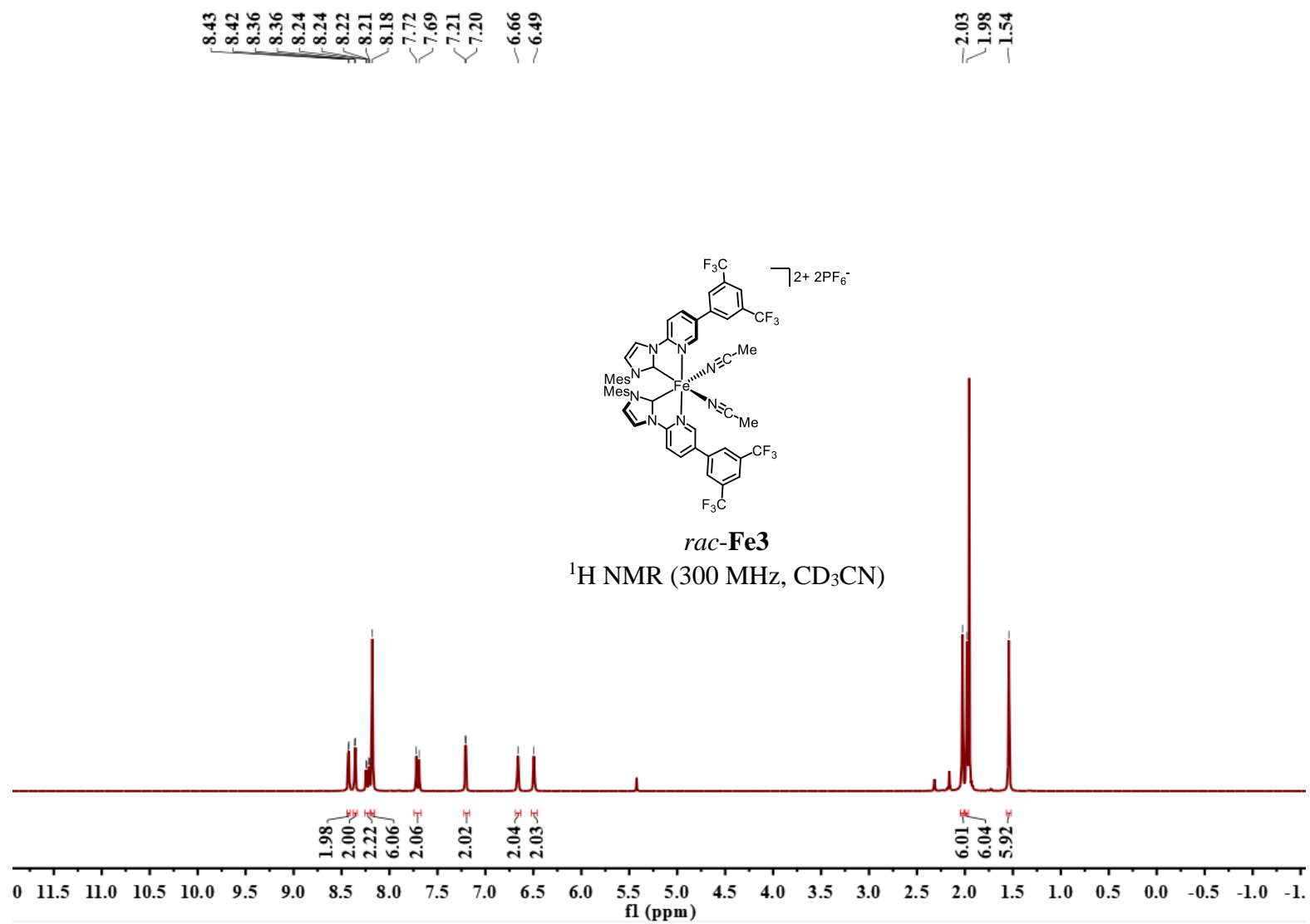


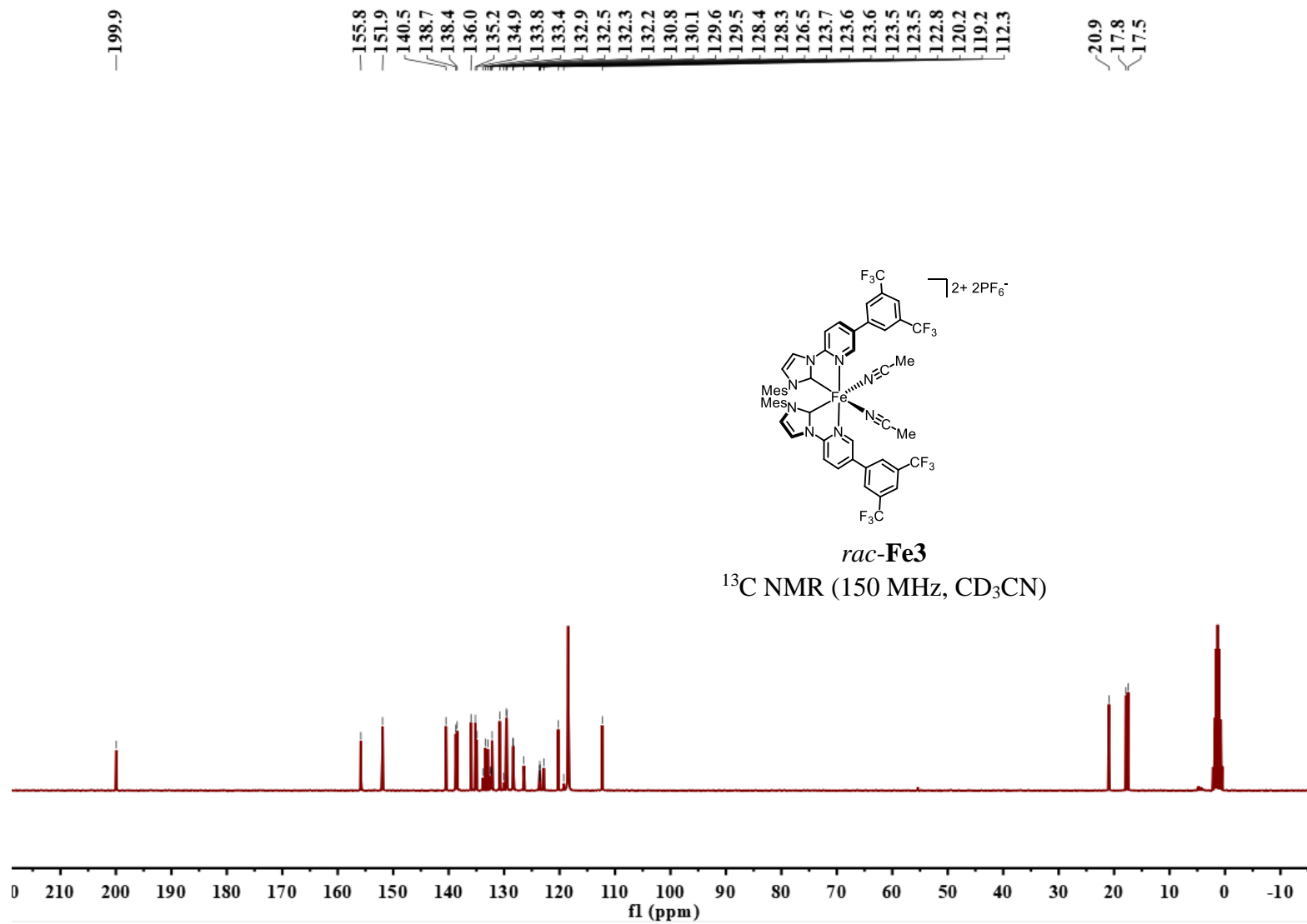


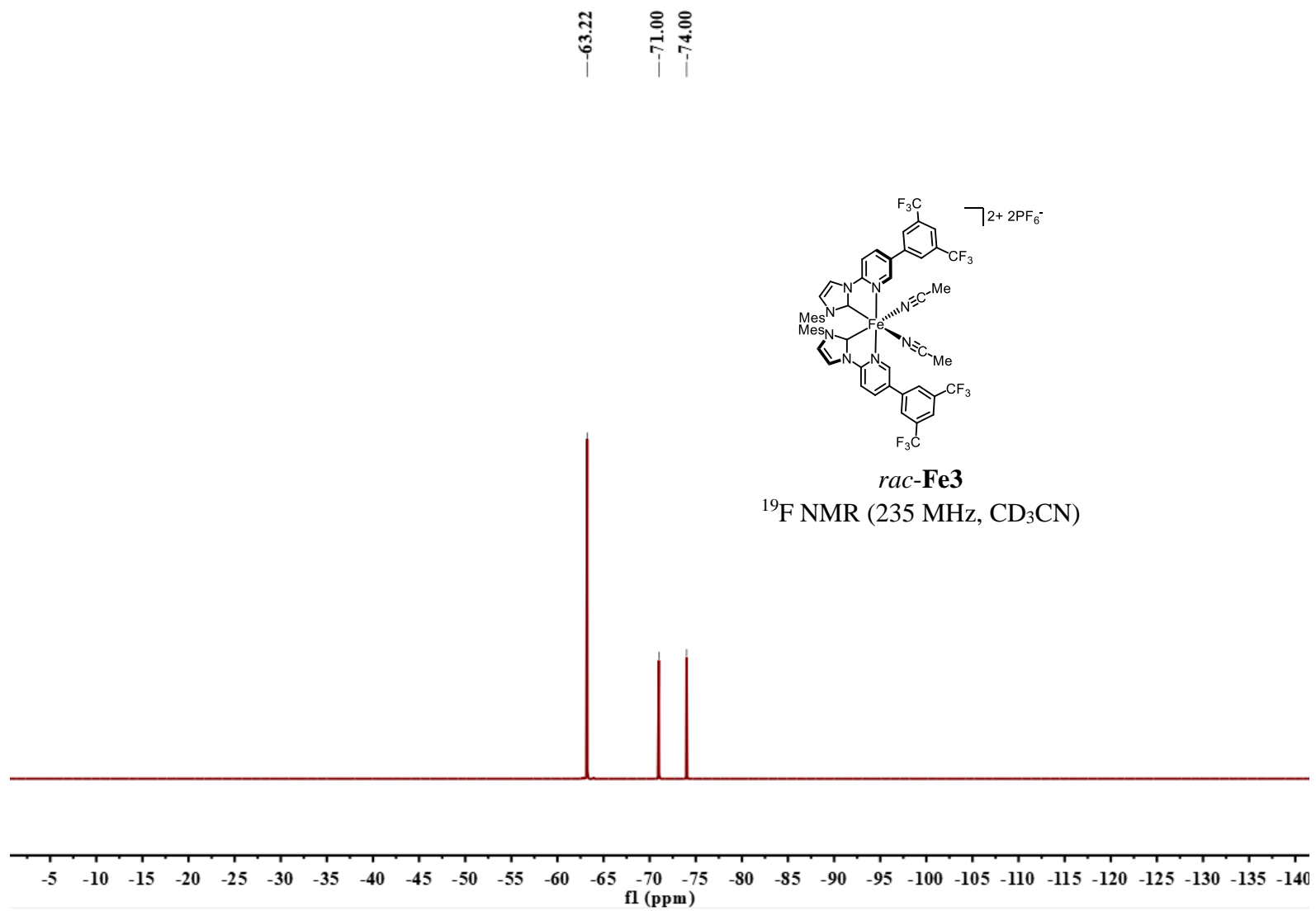


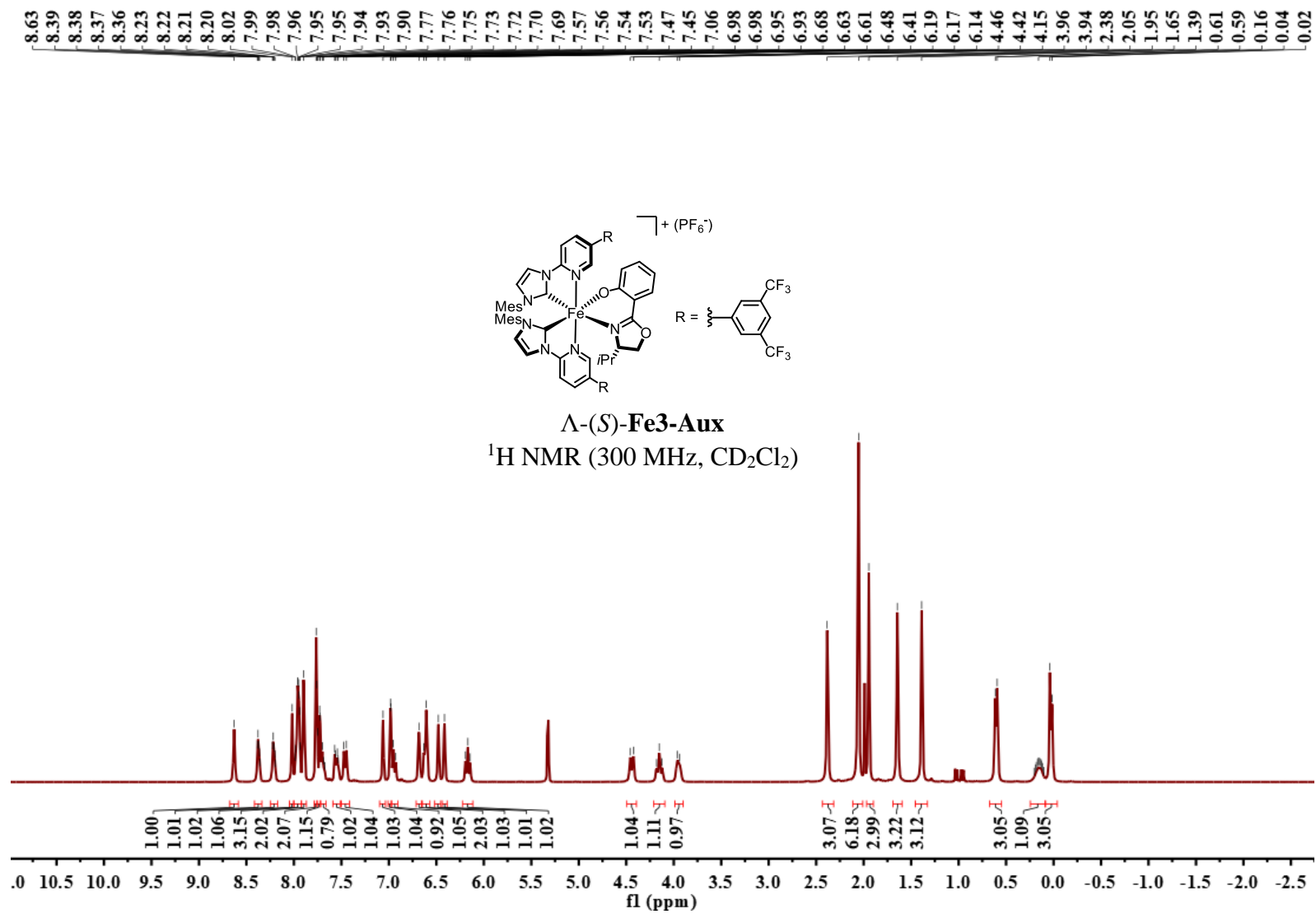


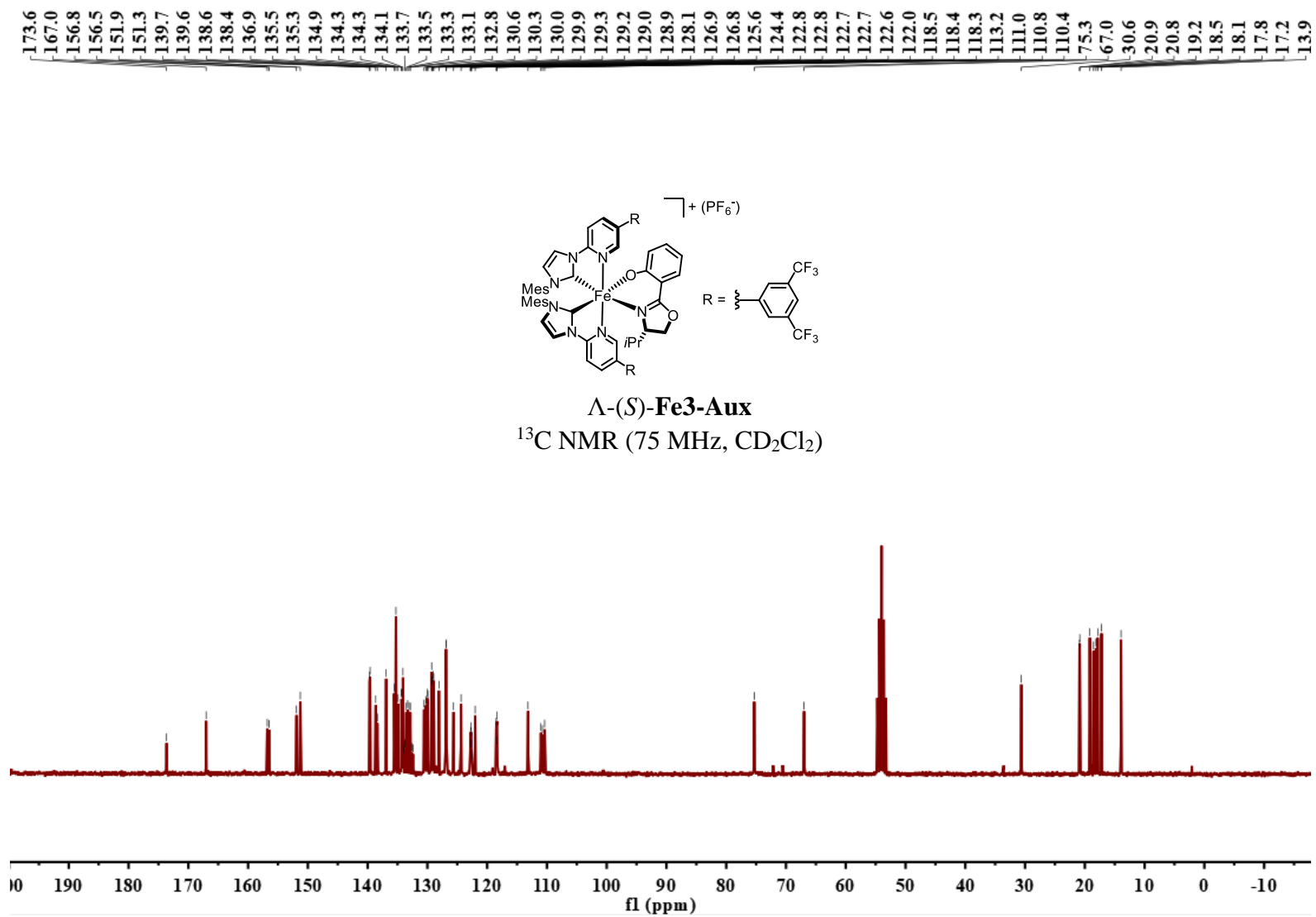




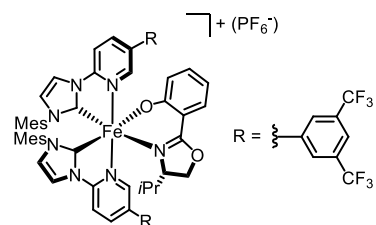






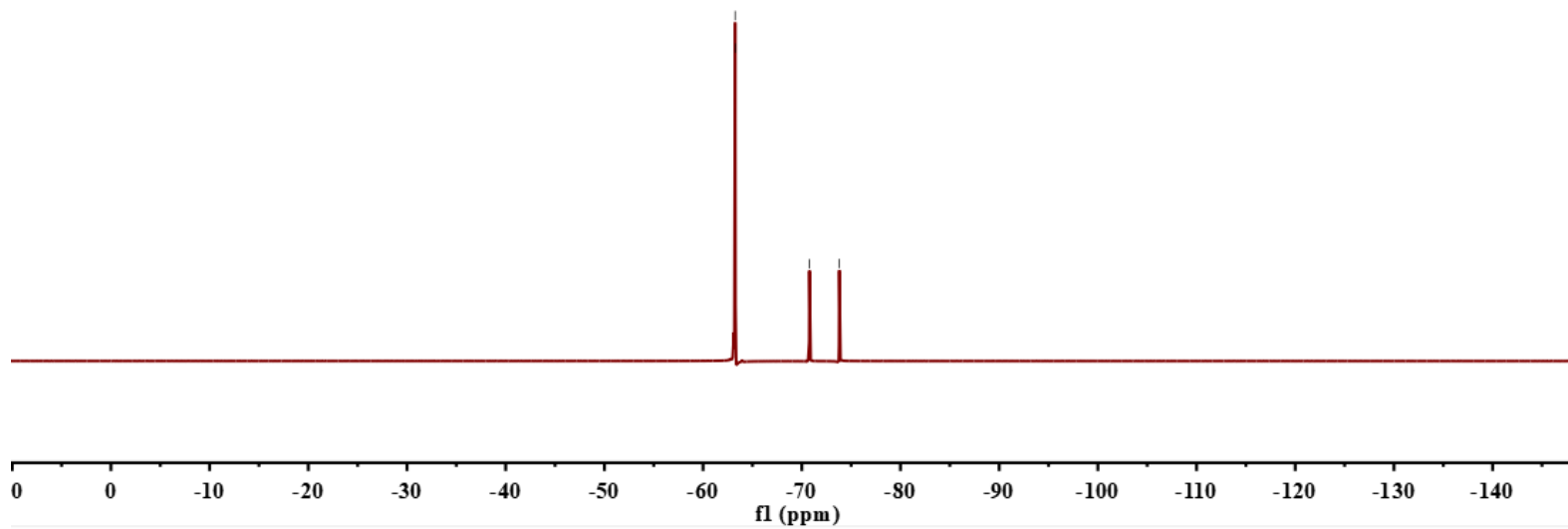


-63.25
-63.26
-70.78
-73.81



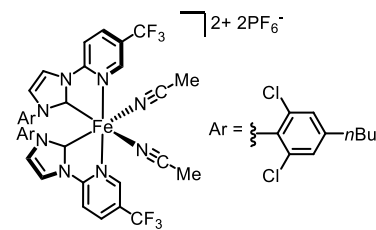
Λ -(S)-Fe3-Aux

¹⁹F NMR (235 MHz, CD₂Cl₂)



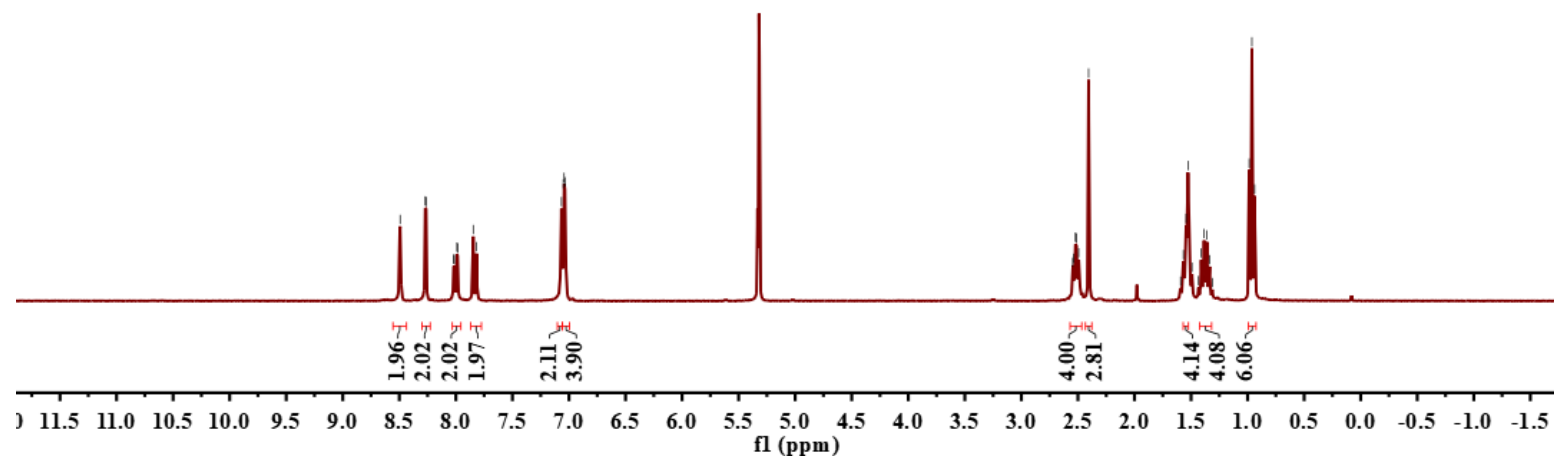
8.49
8.27
8.26
8.02
8.01
7.99
7.99
7.85
7.82
7.07
7.05
7.04
7.04

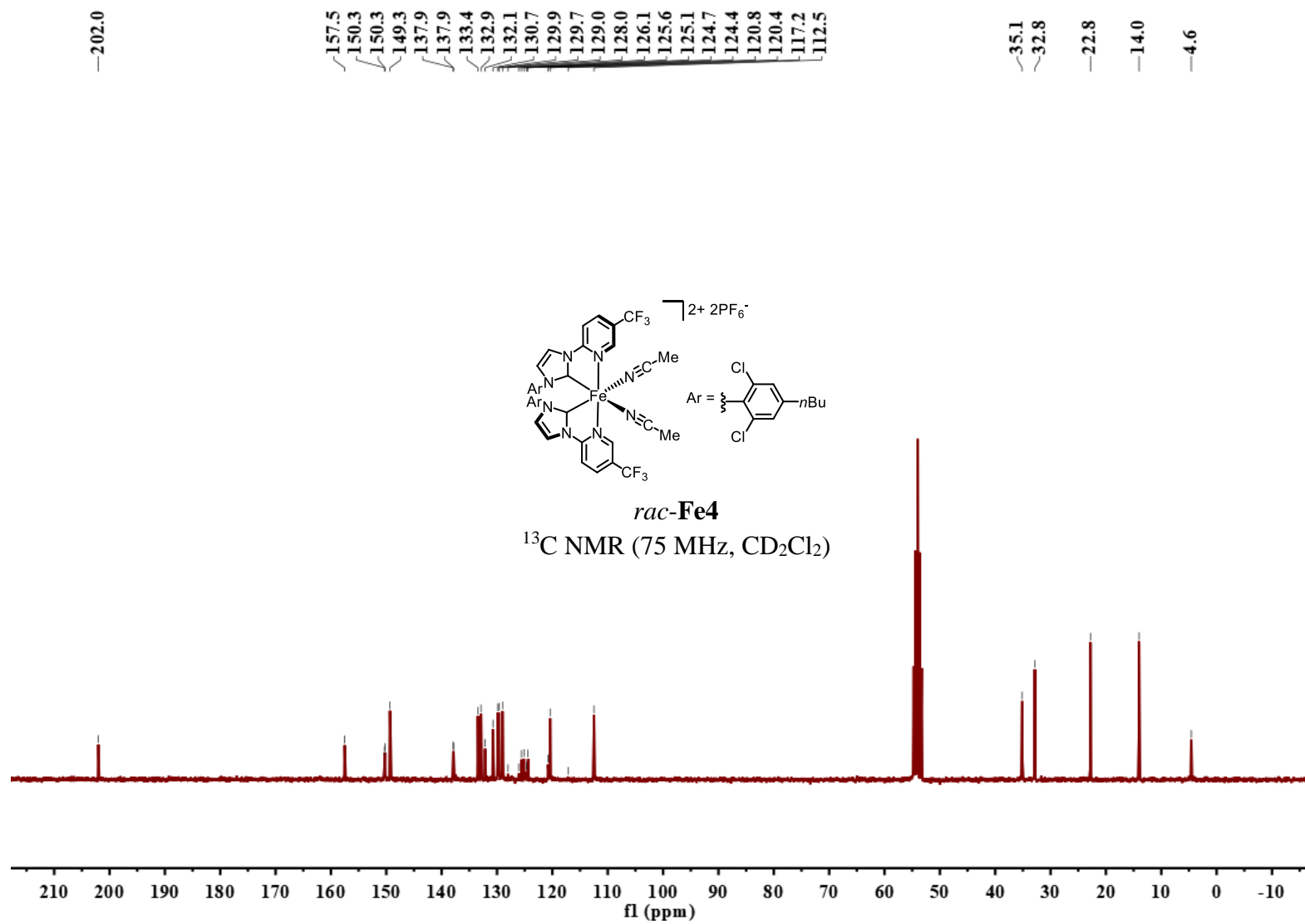
2.55
2.54
2.52
2.51
2.49
2.41
1.59
1.57
1.54
1.53
1.49
1.43
1.41
1.38
1.36
1.34
1.31
0.99
0.96



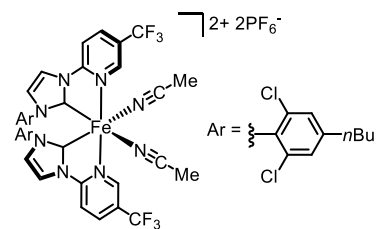
rac-Fe4

¹H NMR (300 MHz, CD₂Cl₂)



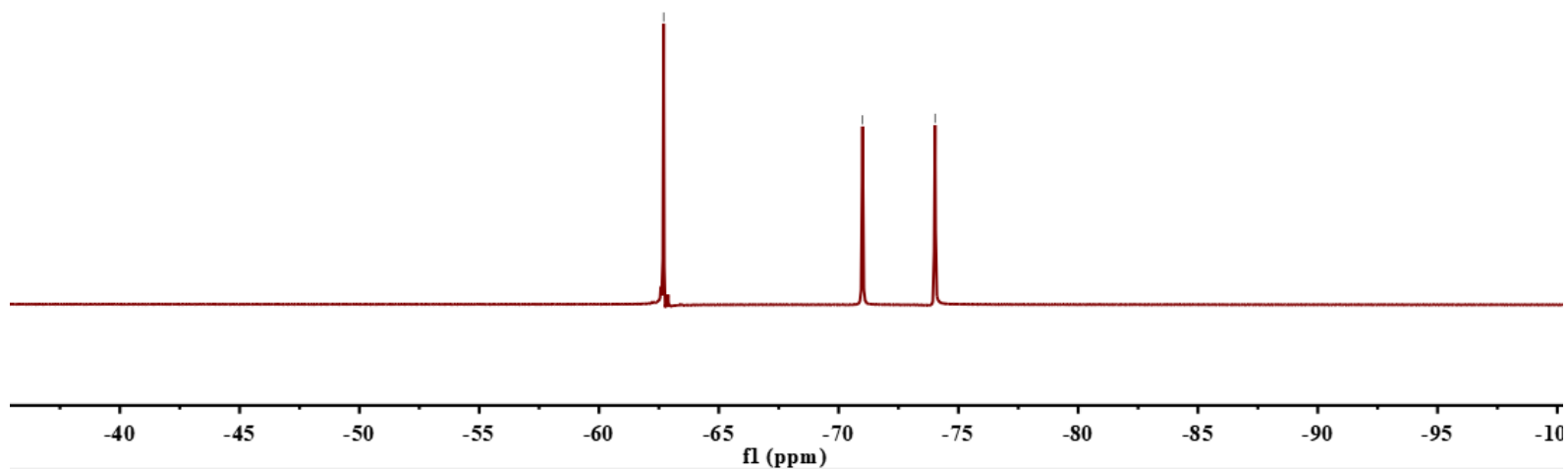


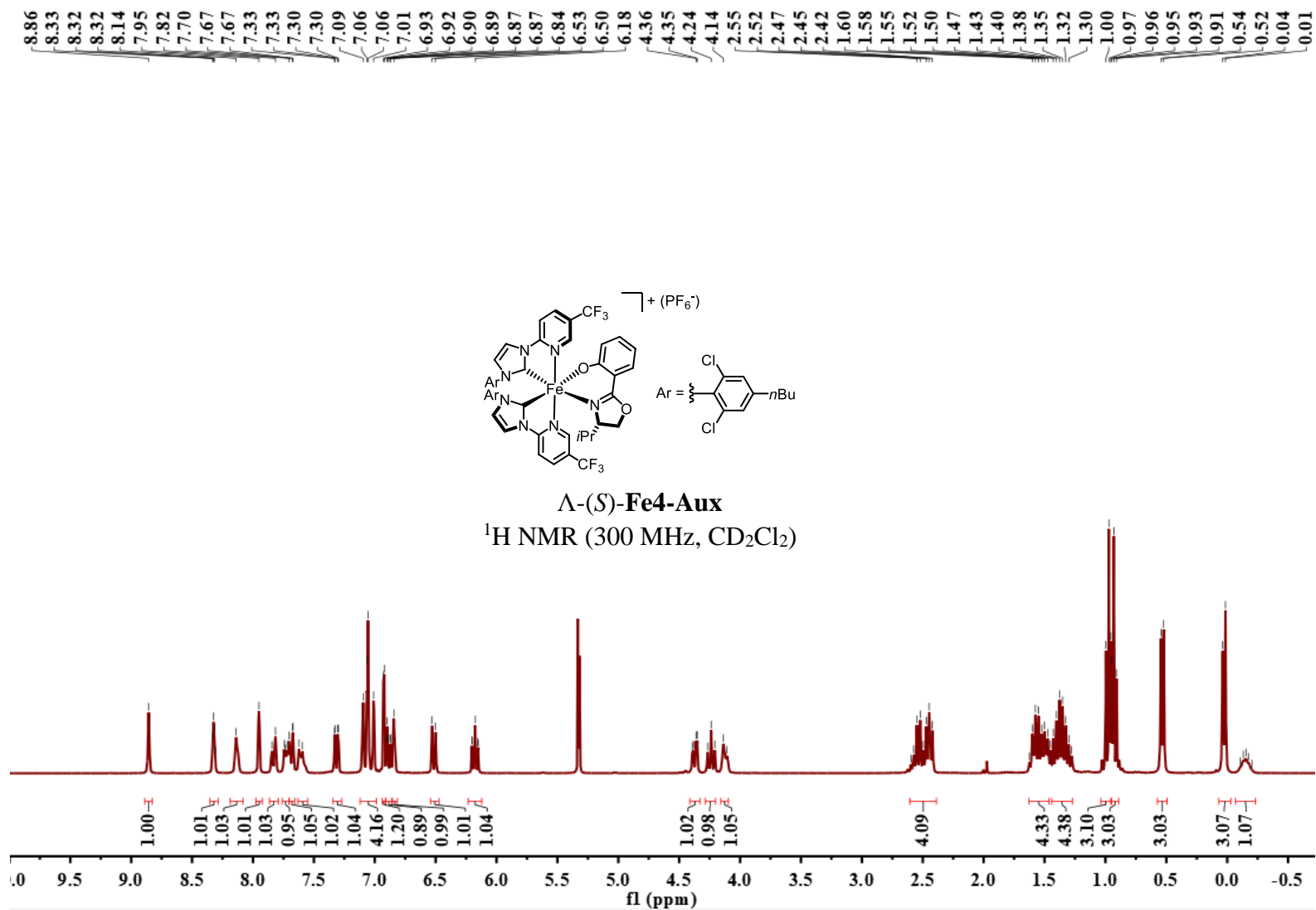
-62.70 -71.00 -74.03

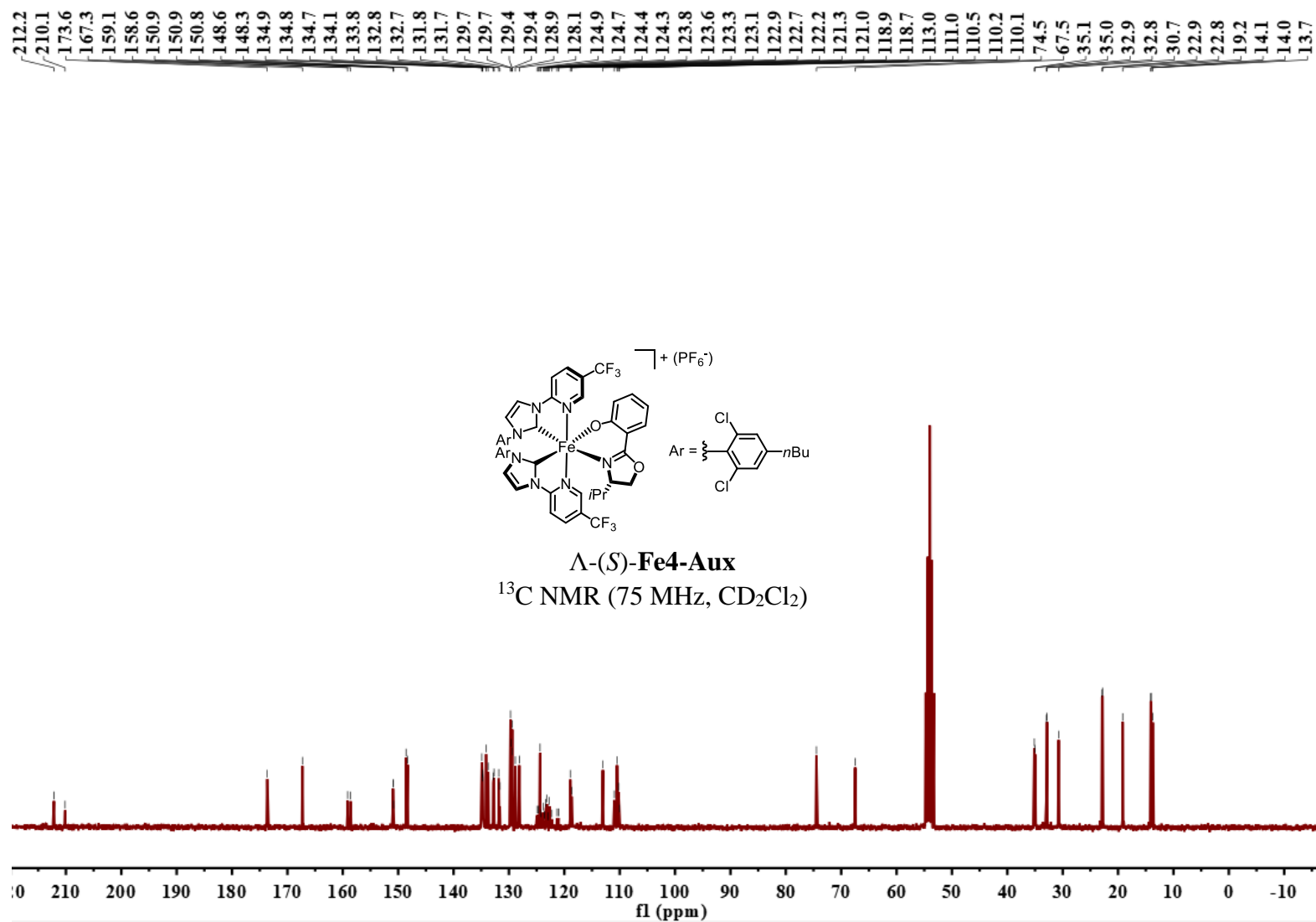


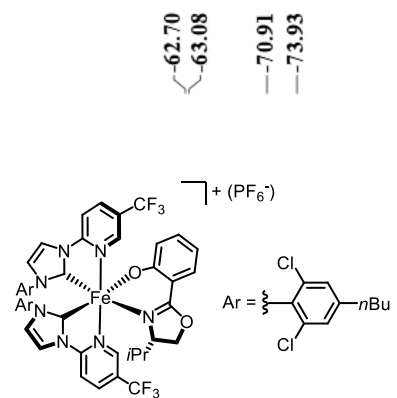
rac-Fe4

¹⁹F NMR (235 MHz, CD₂Cl₂)

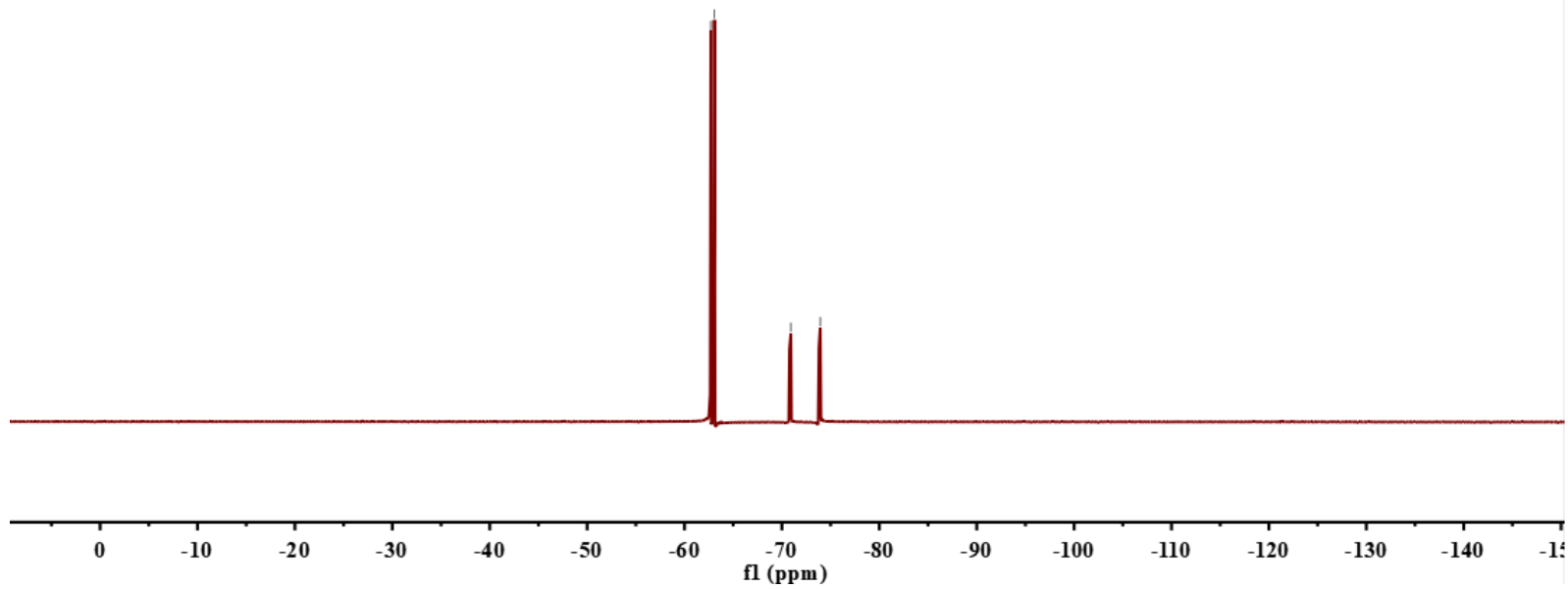






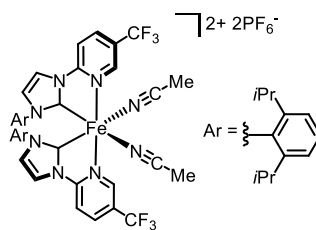


Λ -(*S*)-**Fe4-Aux**
 ^{19}F NMR (235 MHz, CD_2Cl_2)



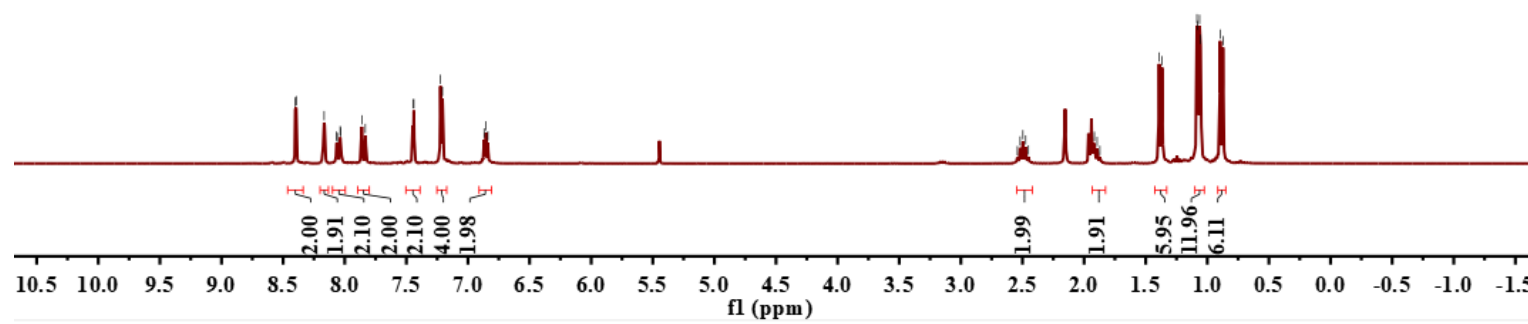
8.40
8.39
8.17
8.07
8.06
8.04
8.03
7.86
7.83
7.45
7.44
7.22
7.21
6.87
6.85
6.84

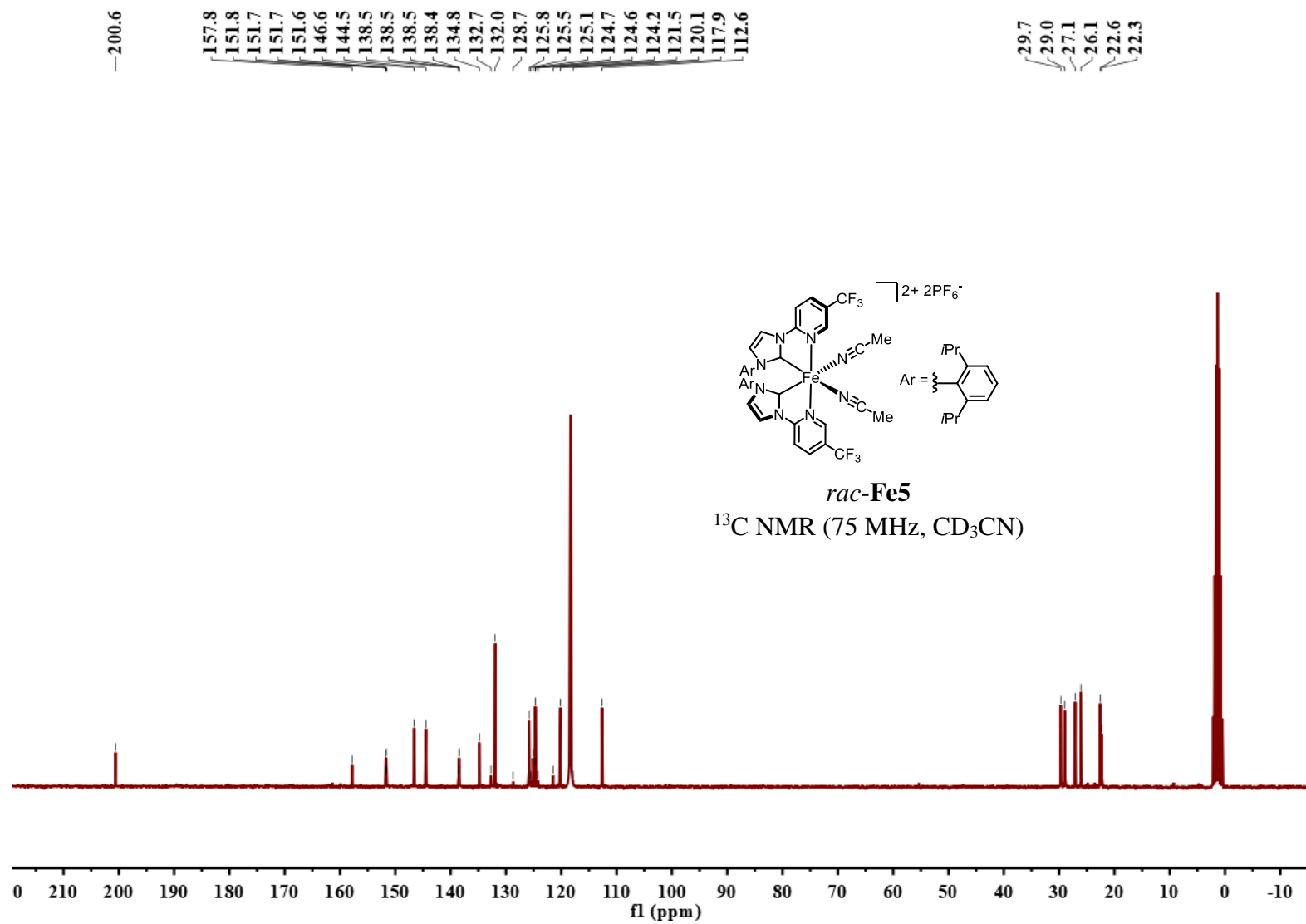
2.54
2.52
2.50
2.47
2.45
1.92
1.89
1.87
1.39
1.37
1.08
1.08
1.06
1.05
0.90
0.87

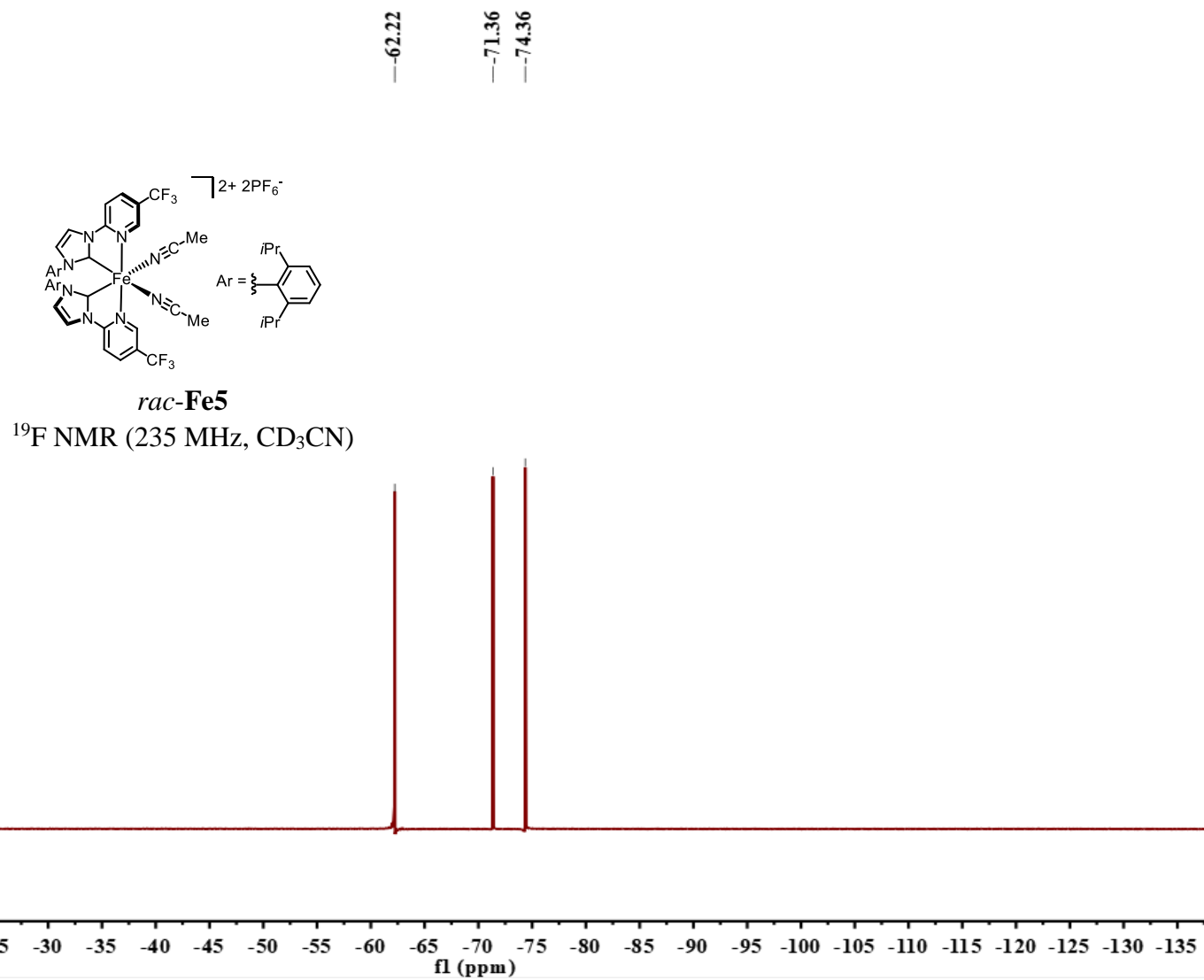


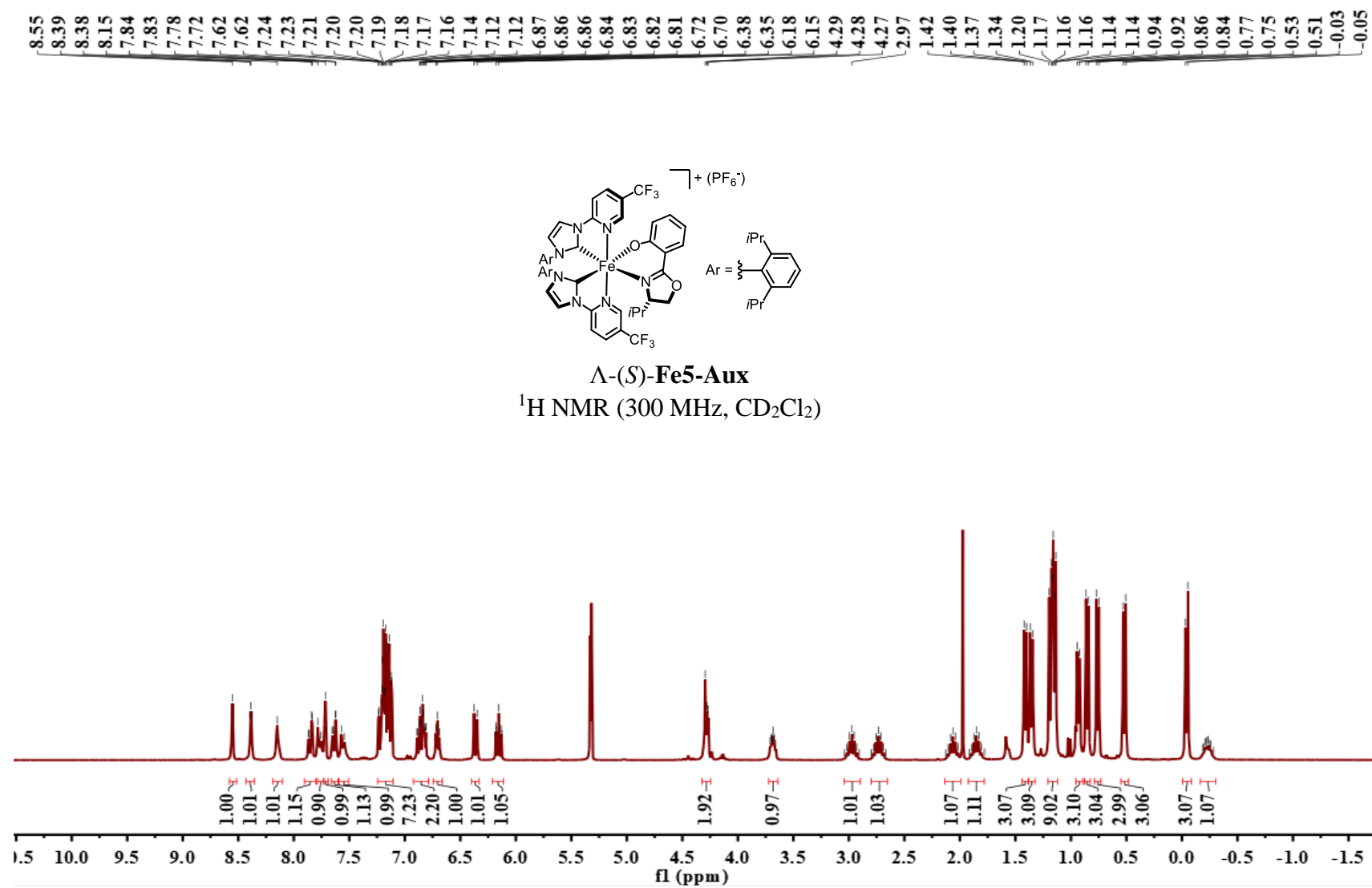
rac-Fe5

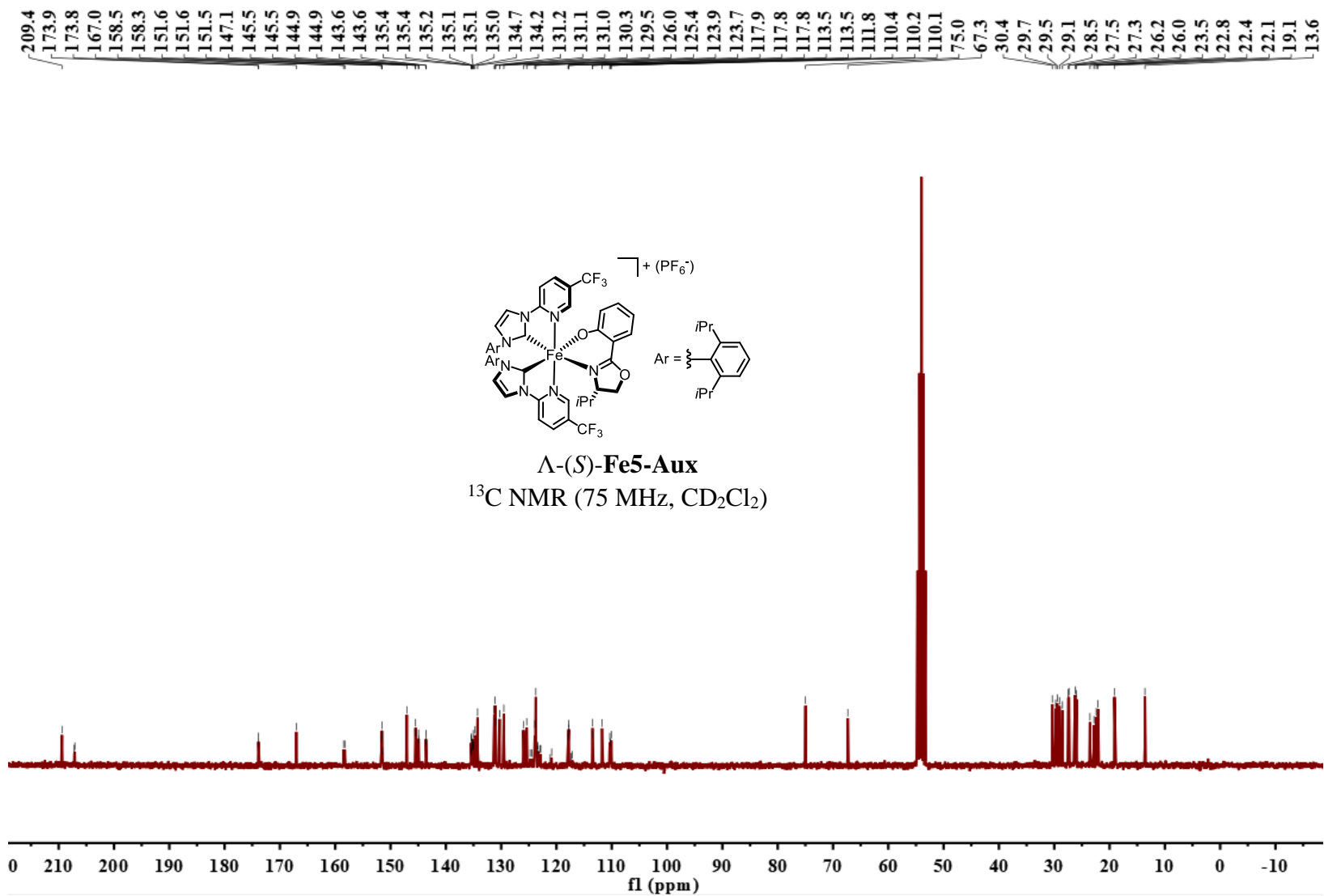
¹H NMR (300 MHz, CD₃CN)





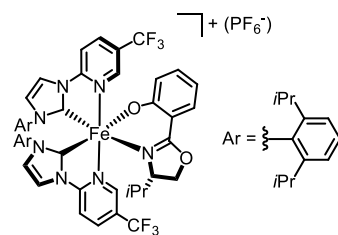






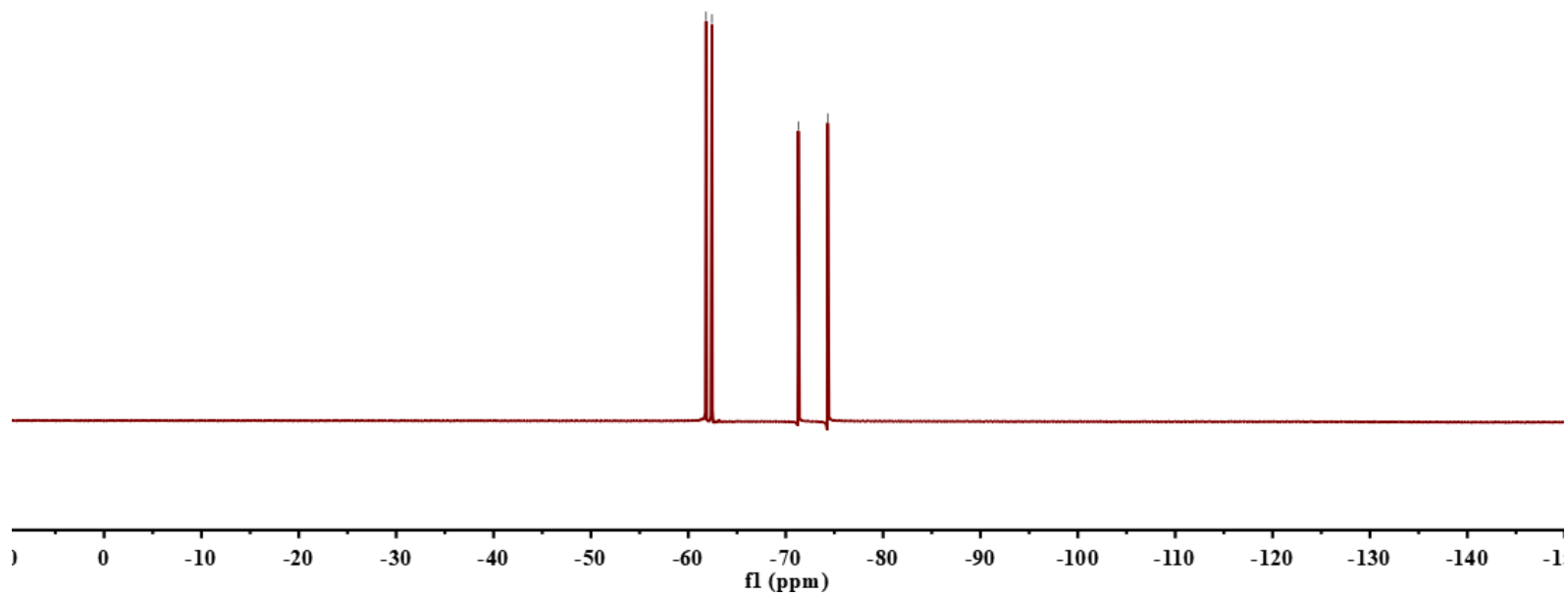
-61.82
-62.42

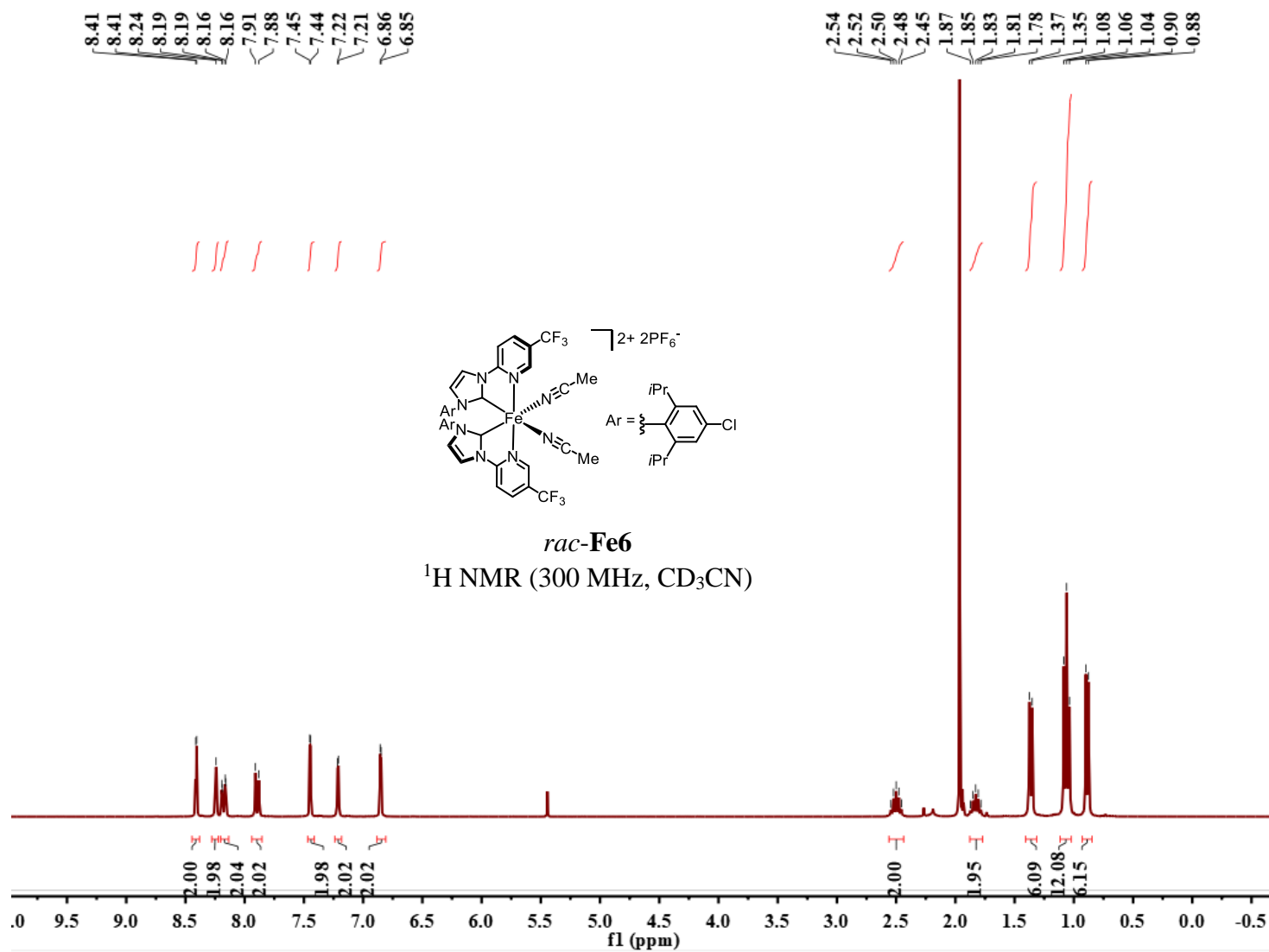
-71.29
-74.31

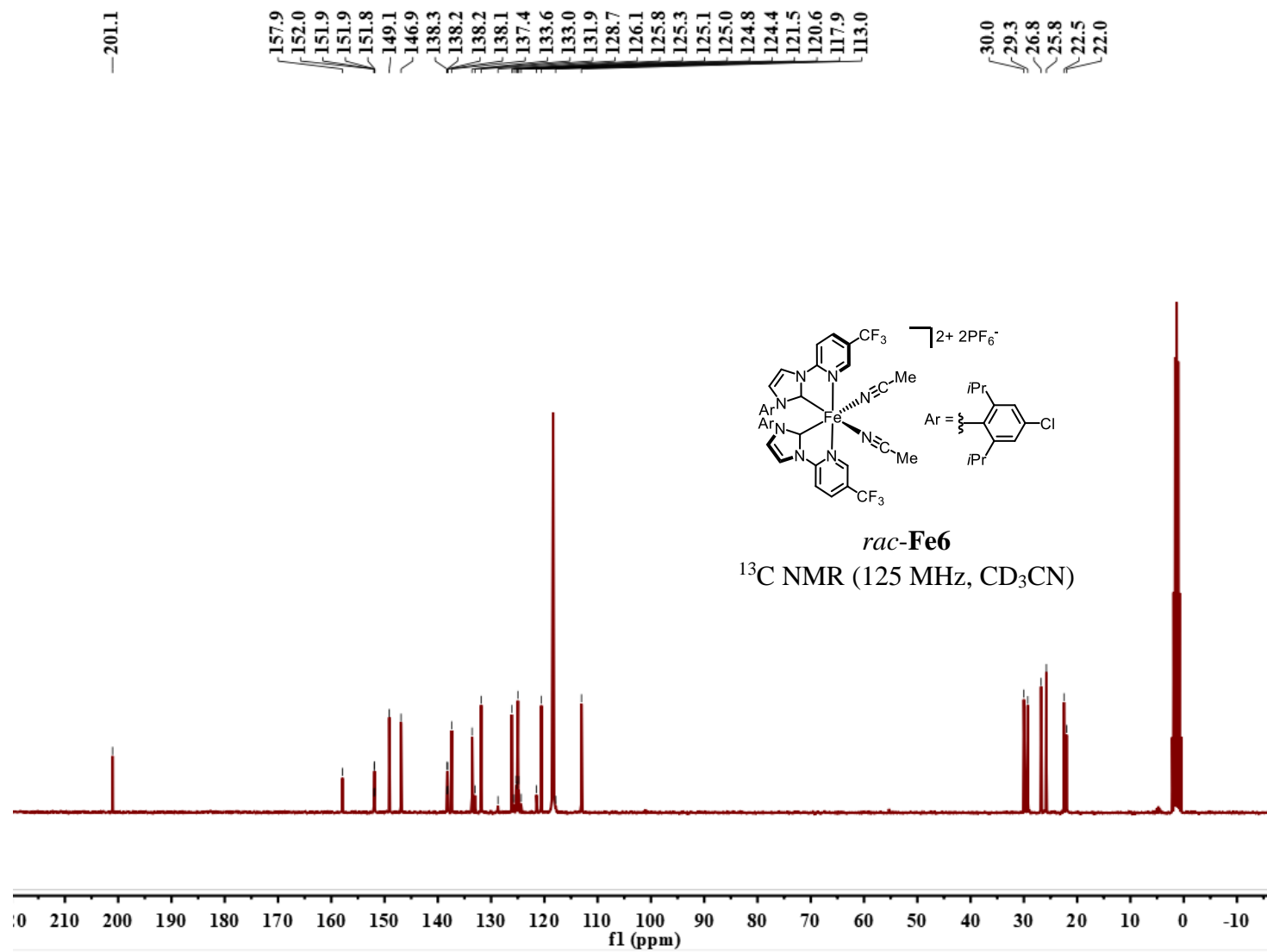


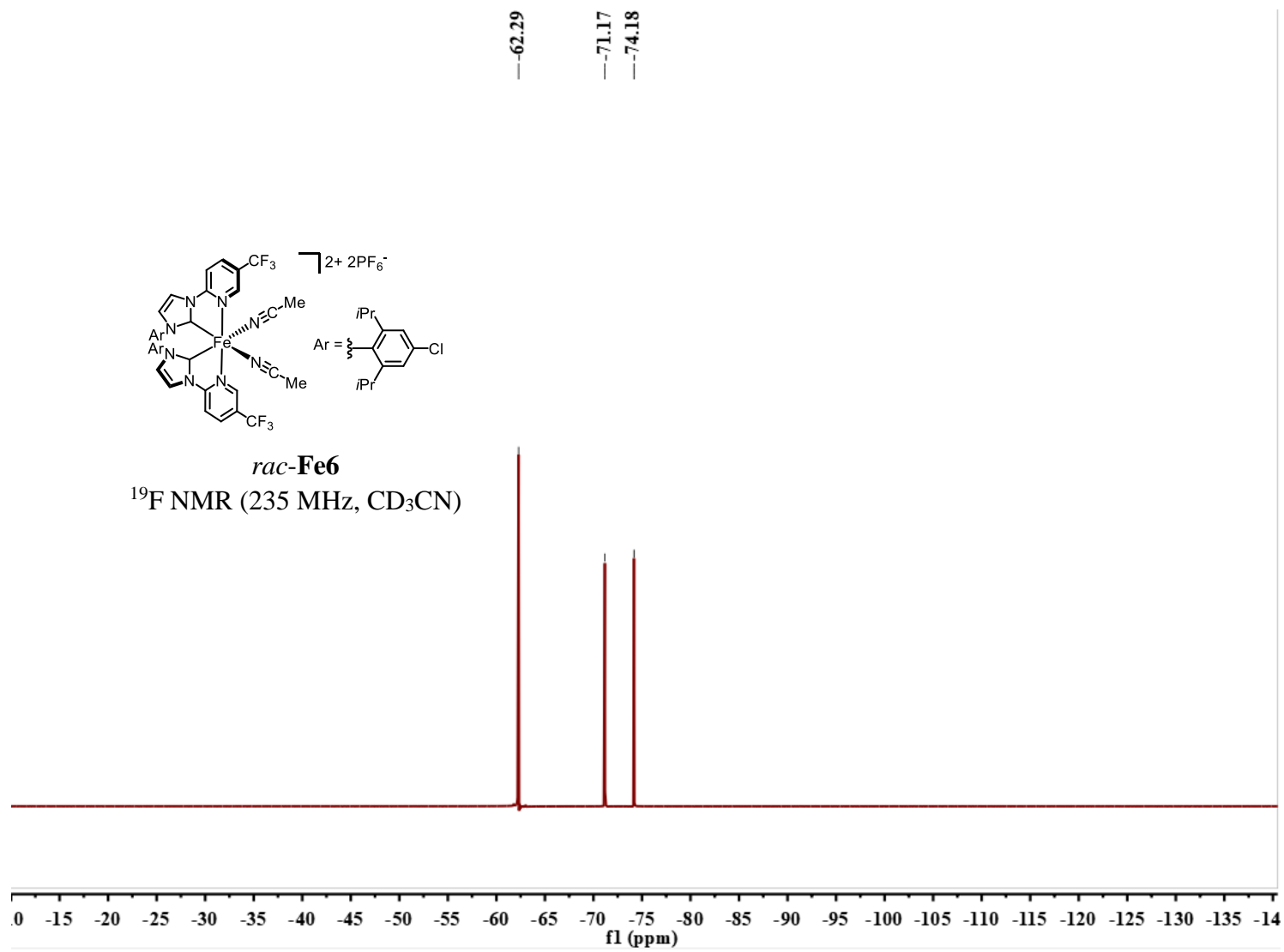
Λ-(S)-Fe5-Aux

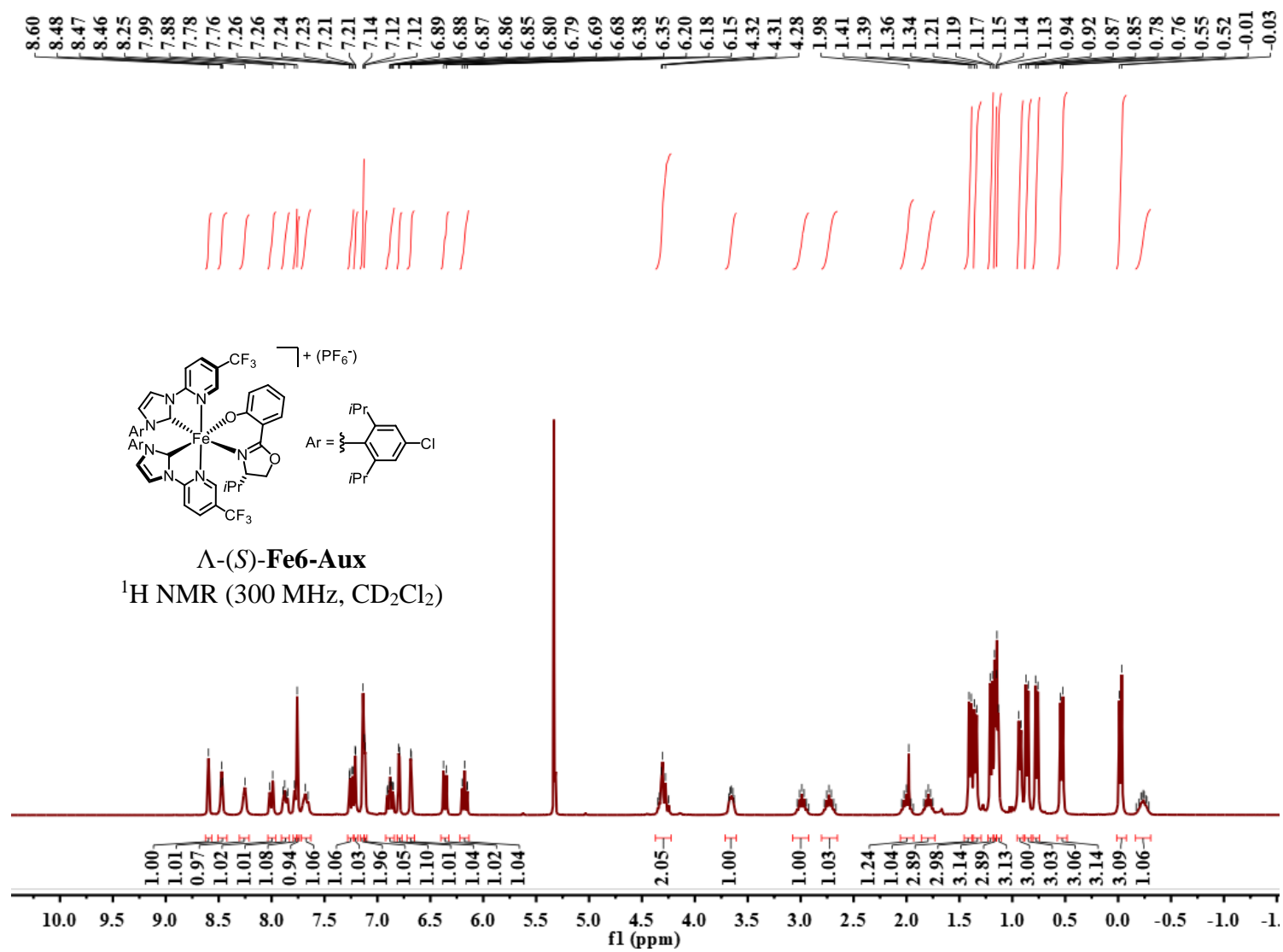
¹⁹F NMR (235 MHz, CD₂Cl₂)

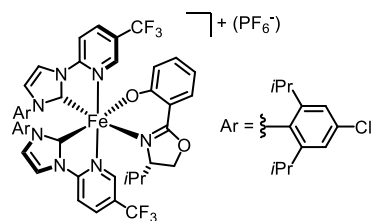
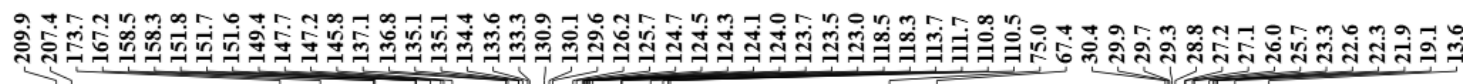






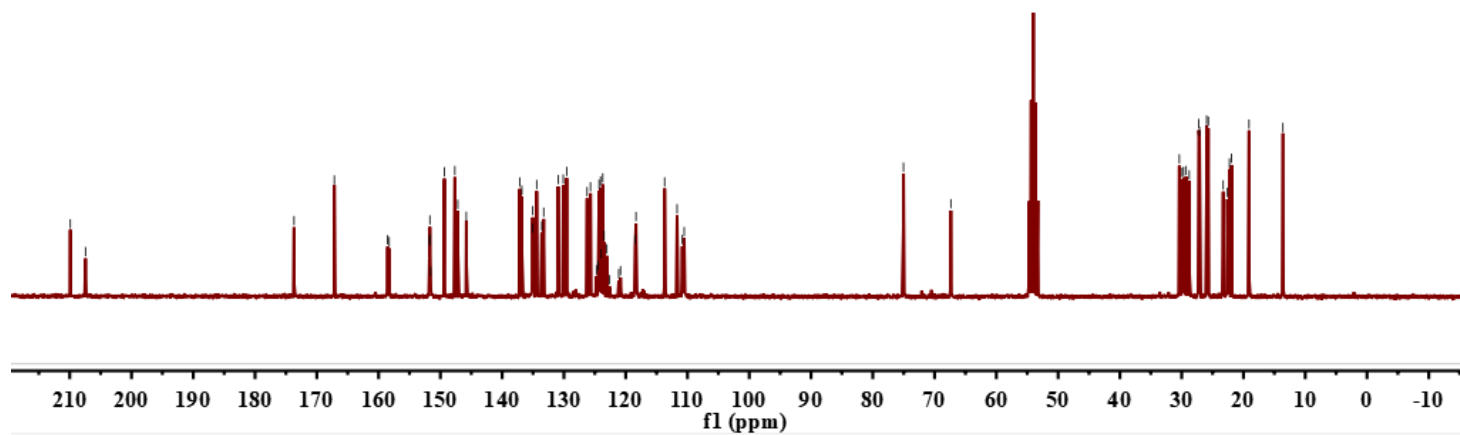


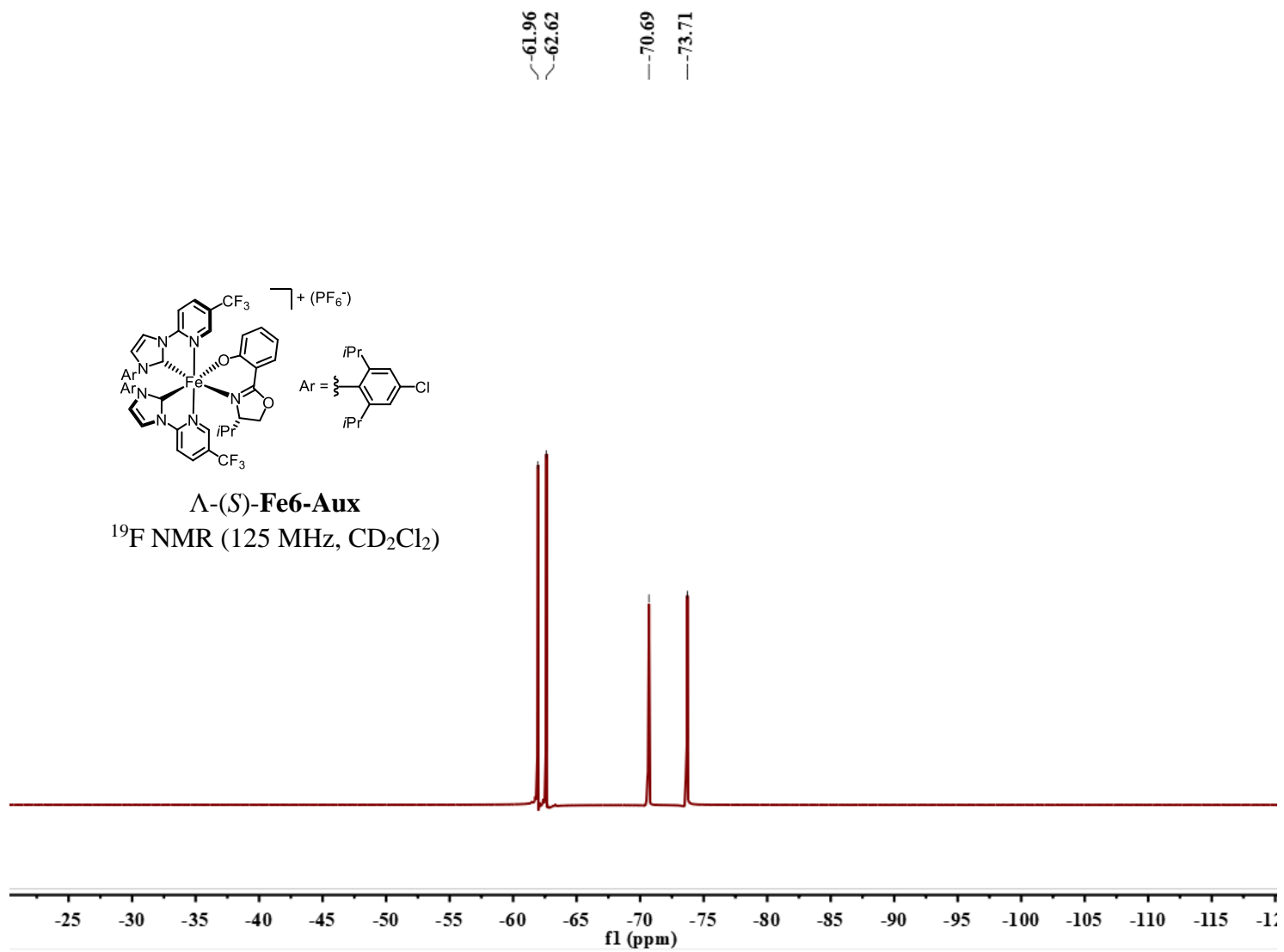




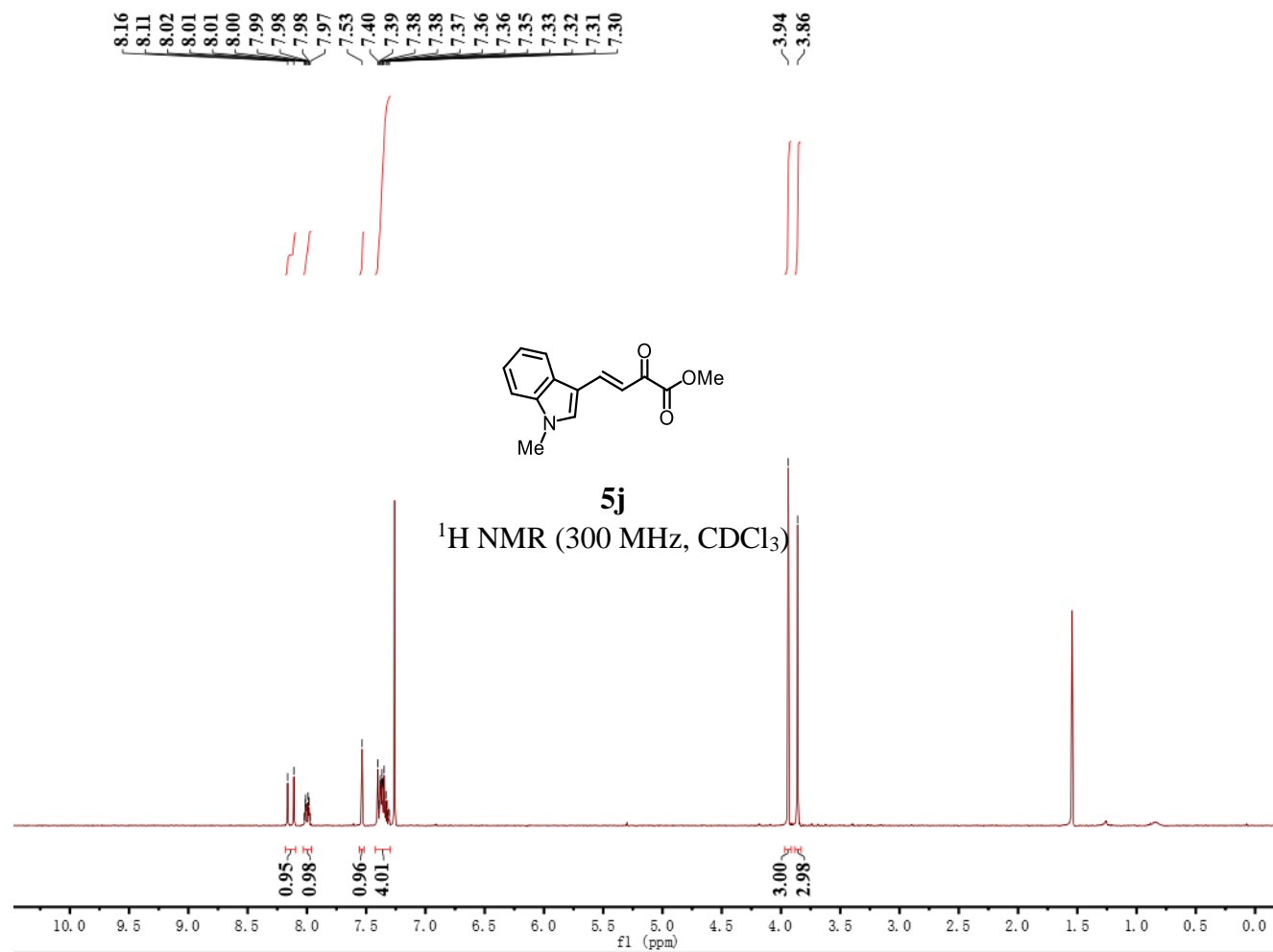
Λ -(S)-Fe6-Aux

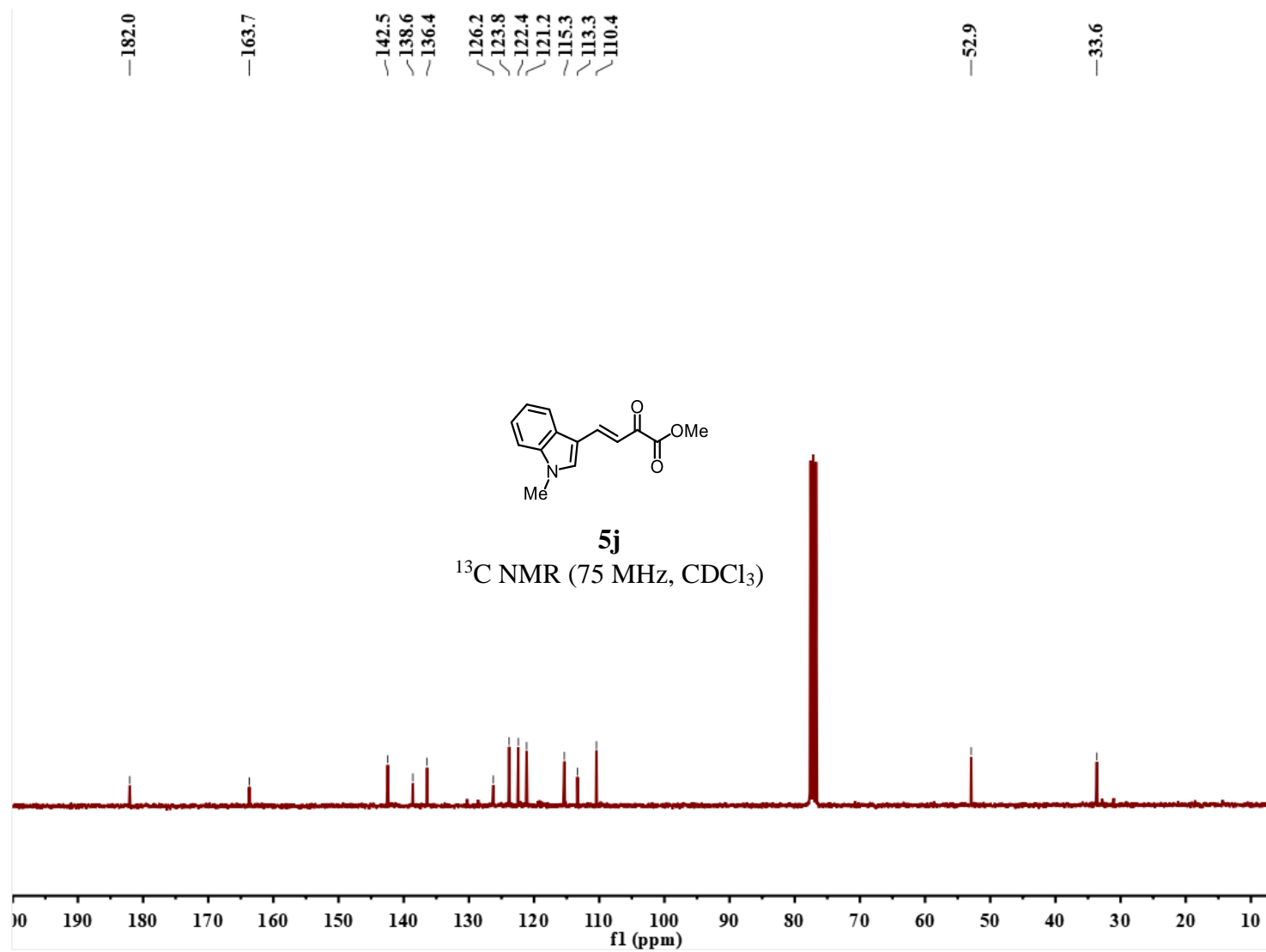
^{13}C NMR (125 MHz, CD_2Cl_2)

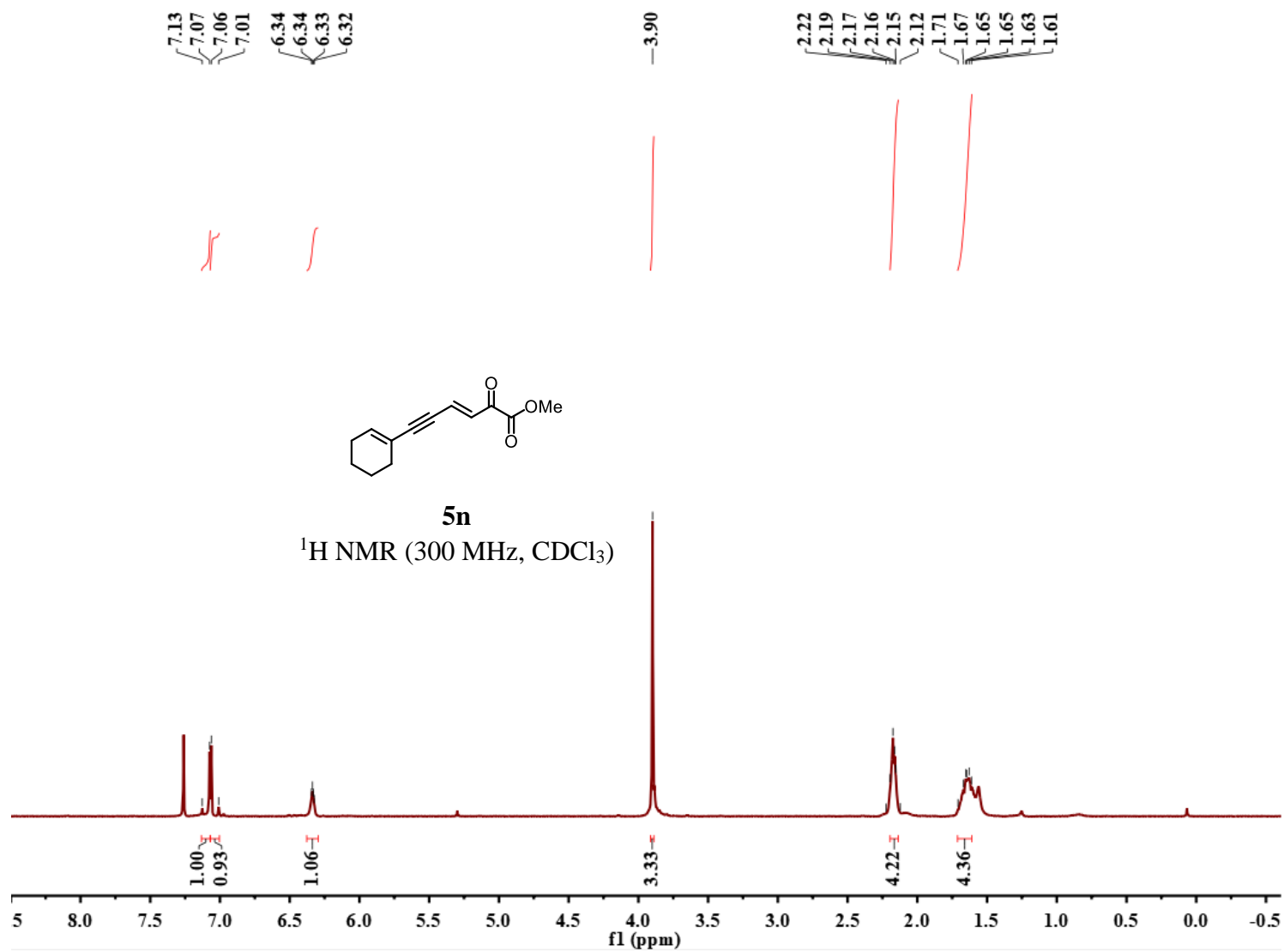


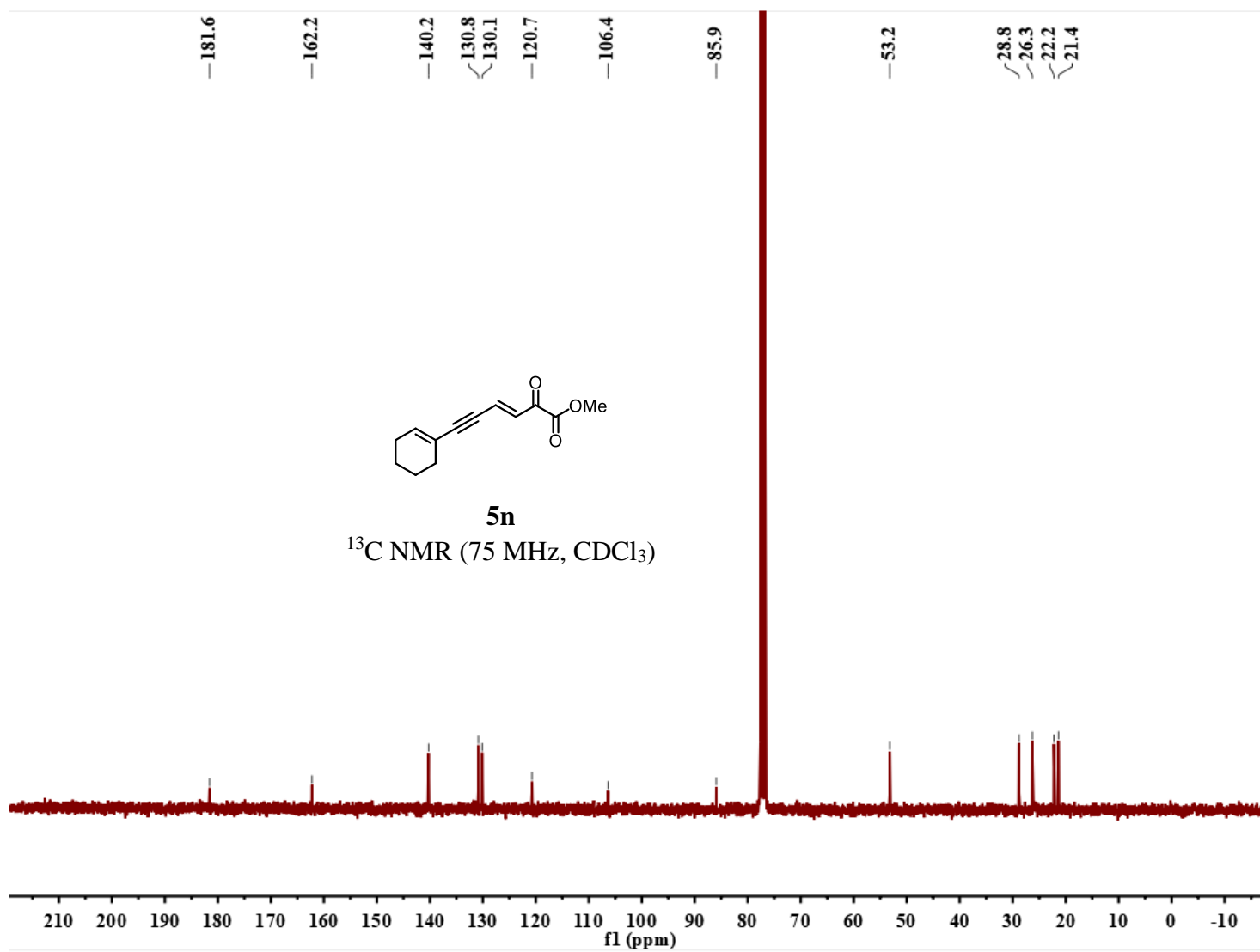


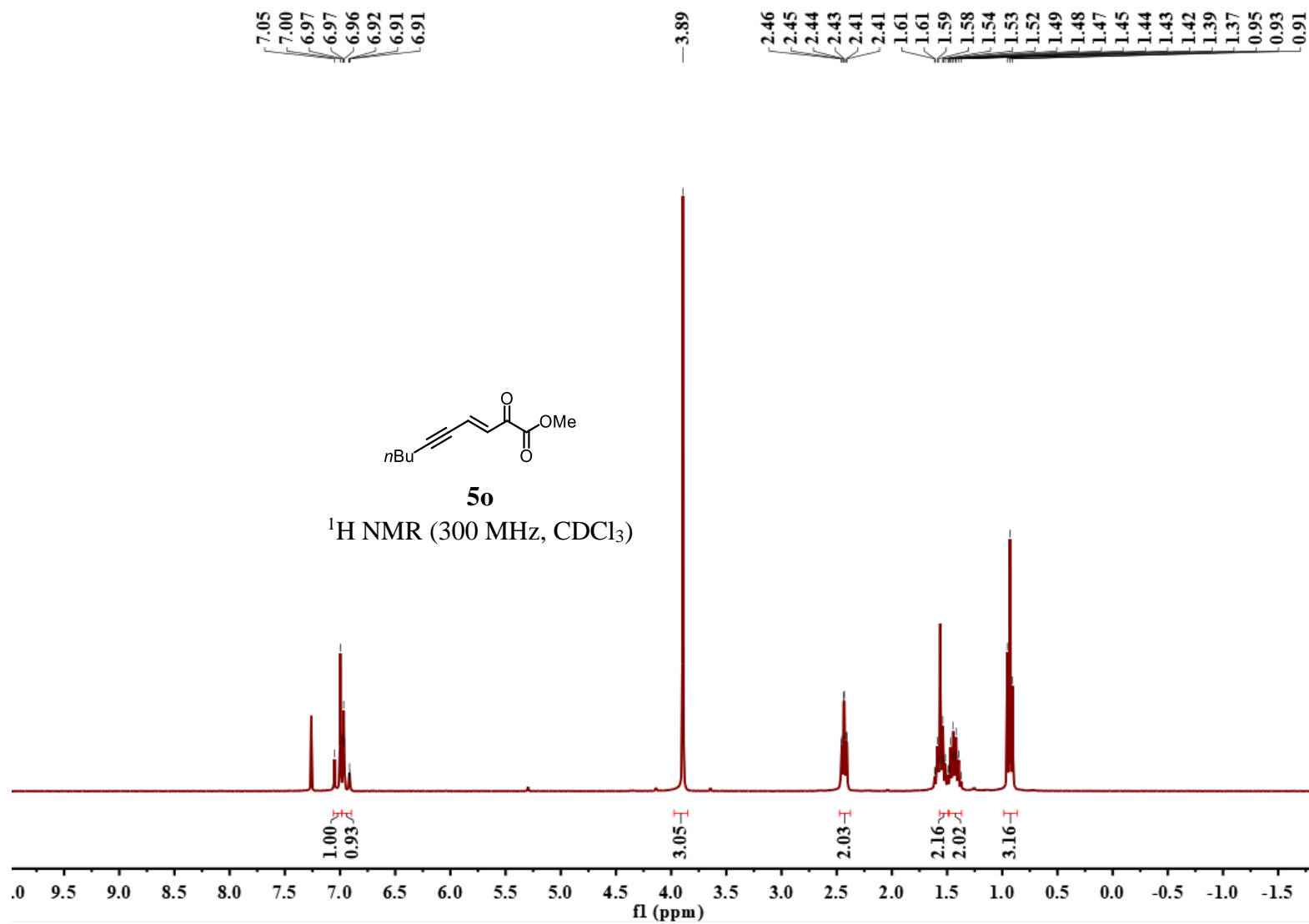
6.9 List of NMR Spectra of New Organic Compounds

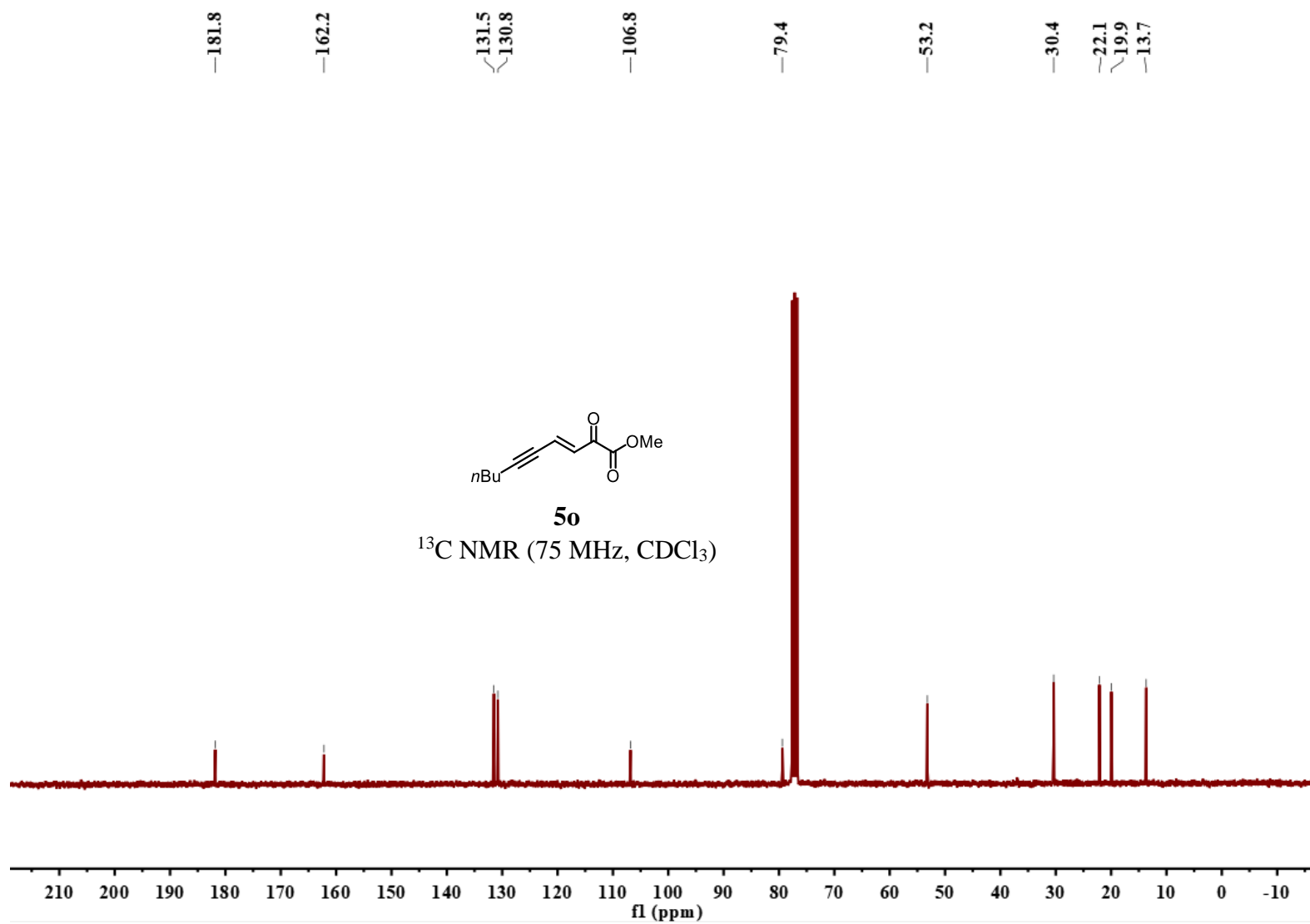


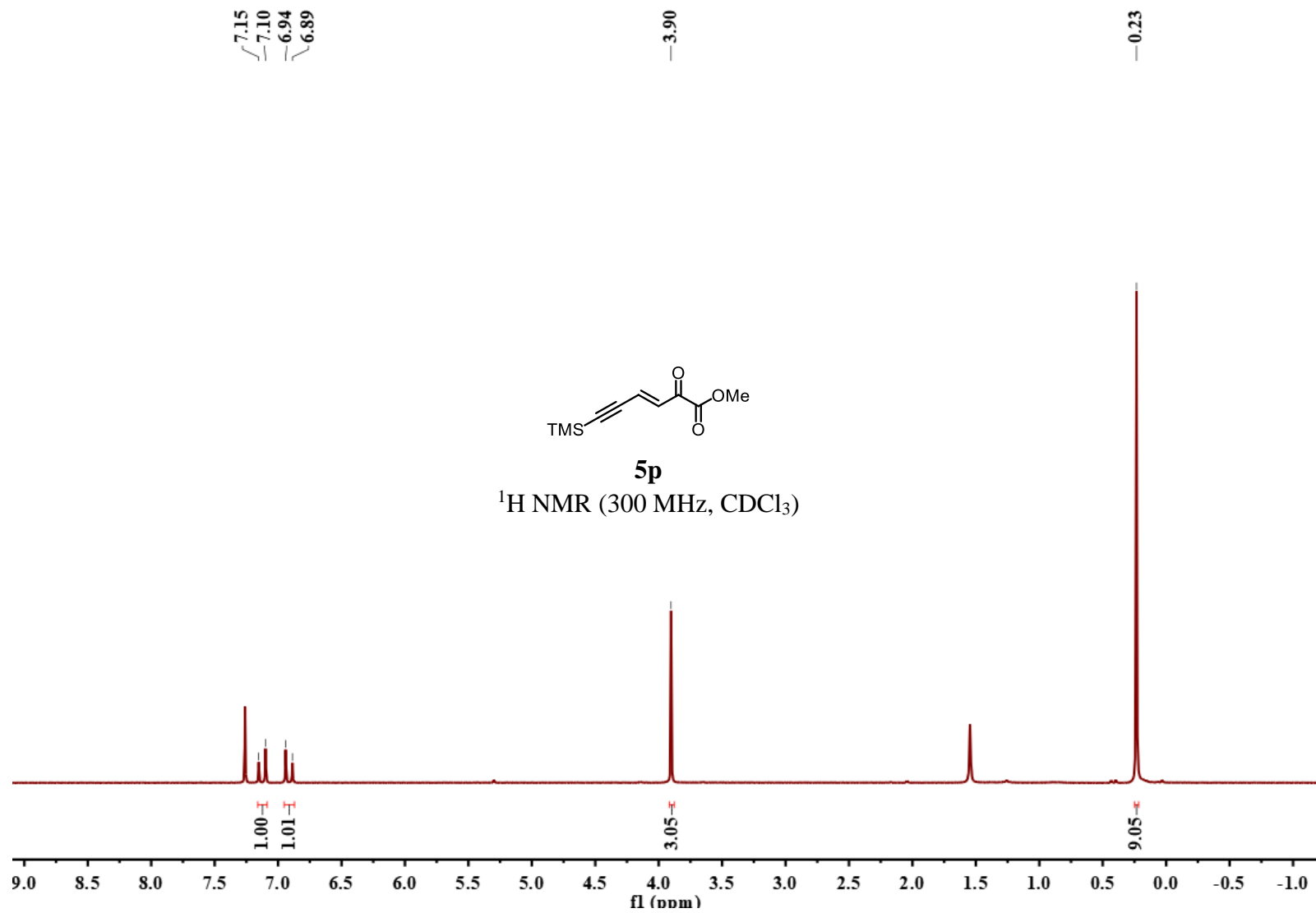


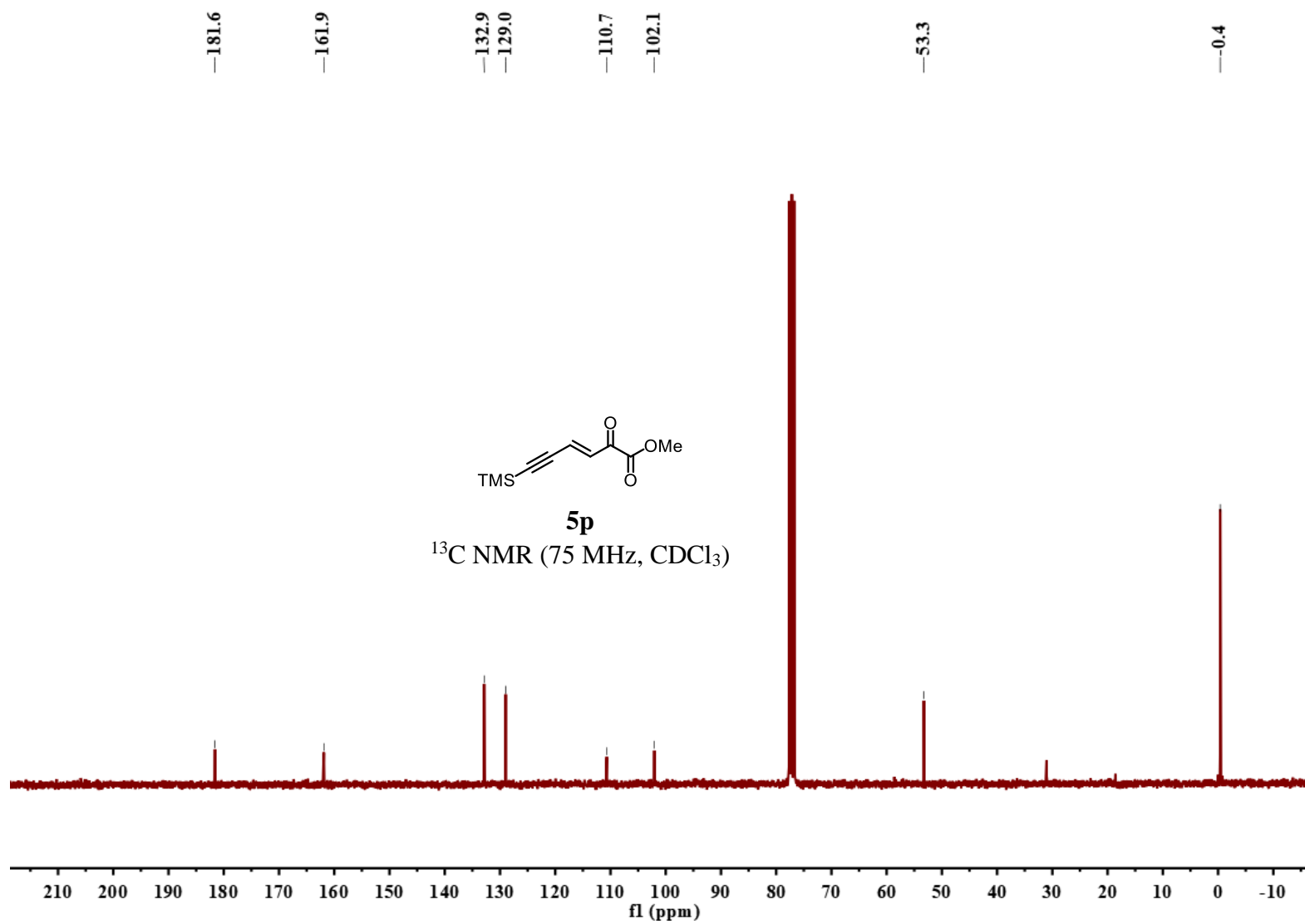


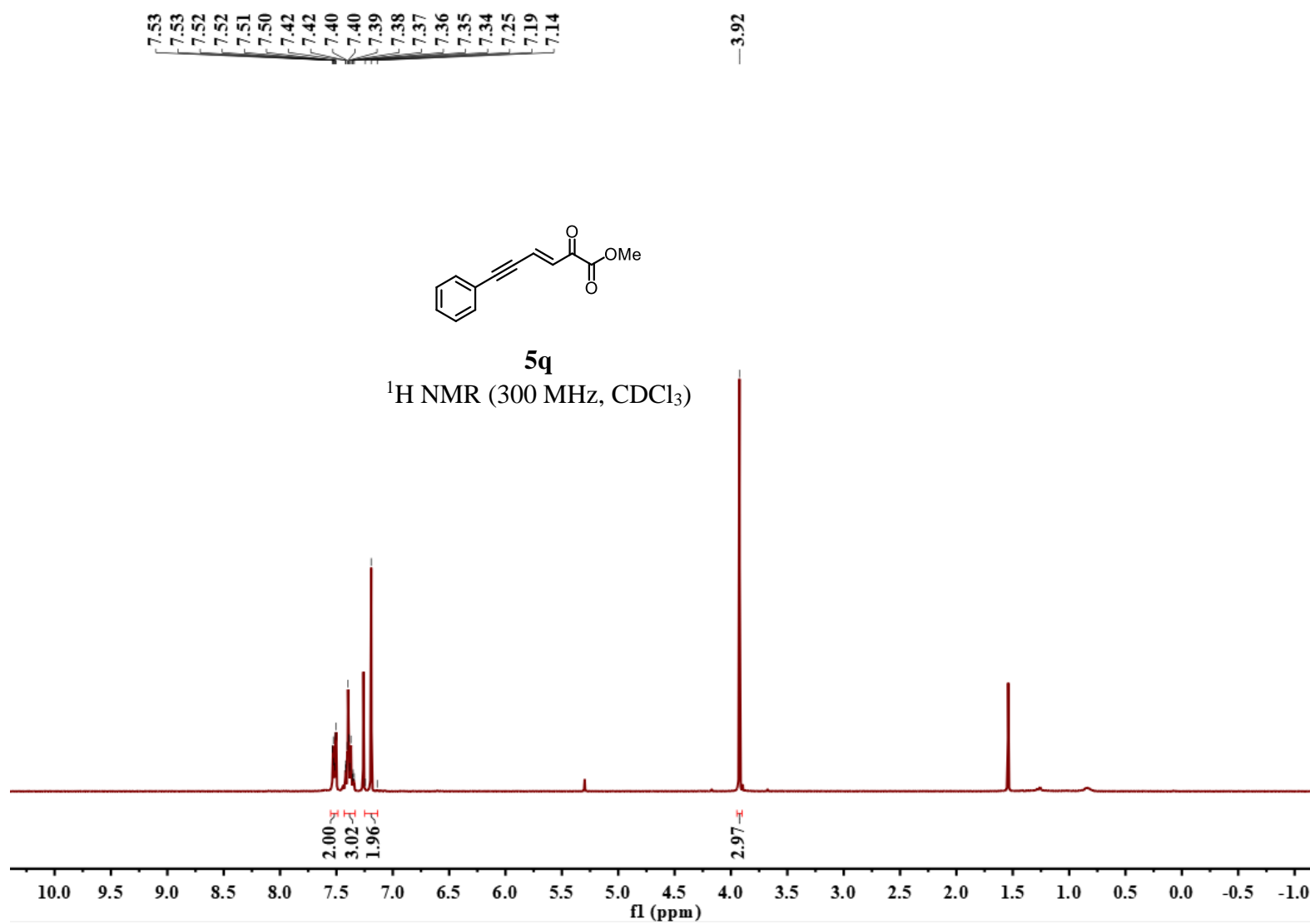


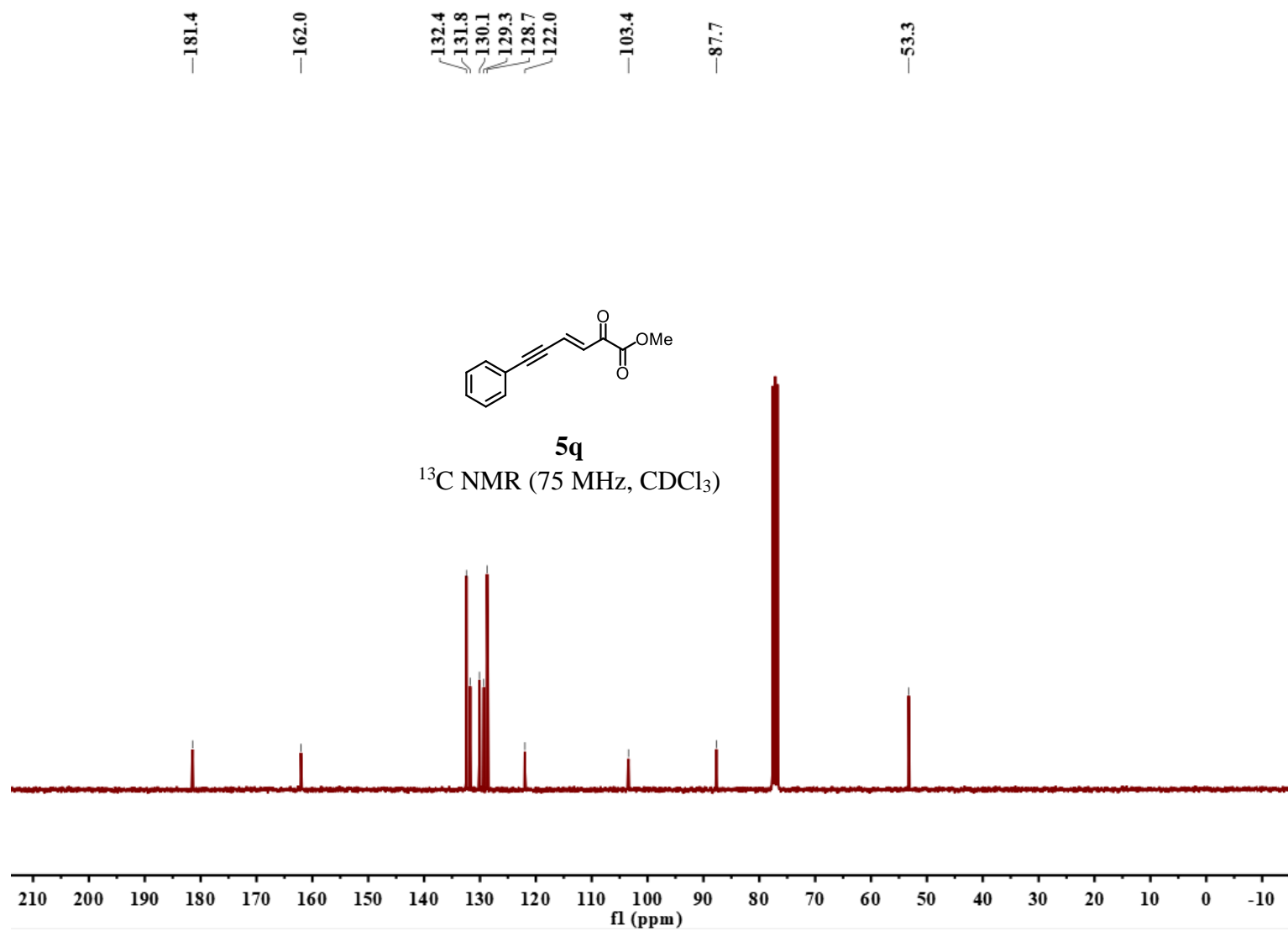


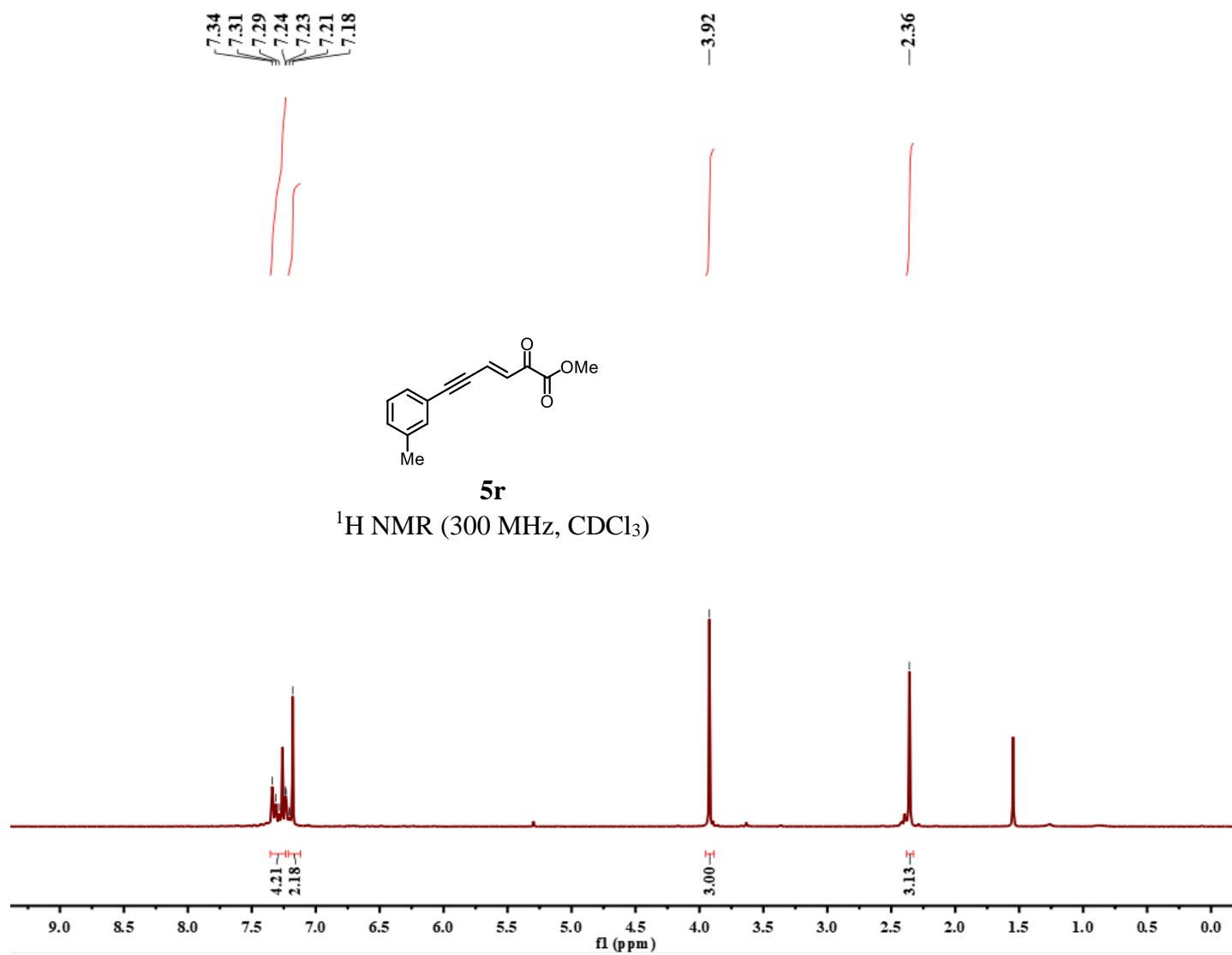


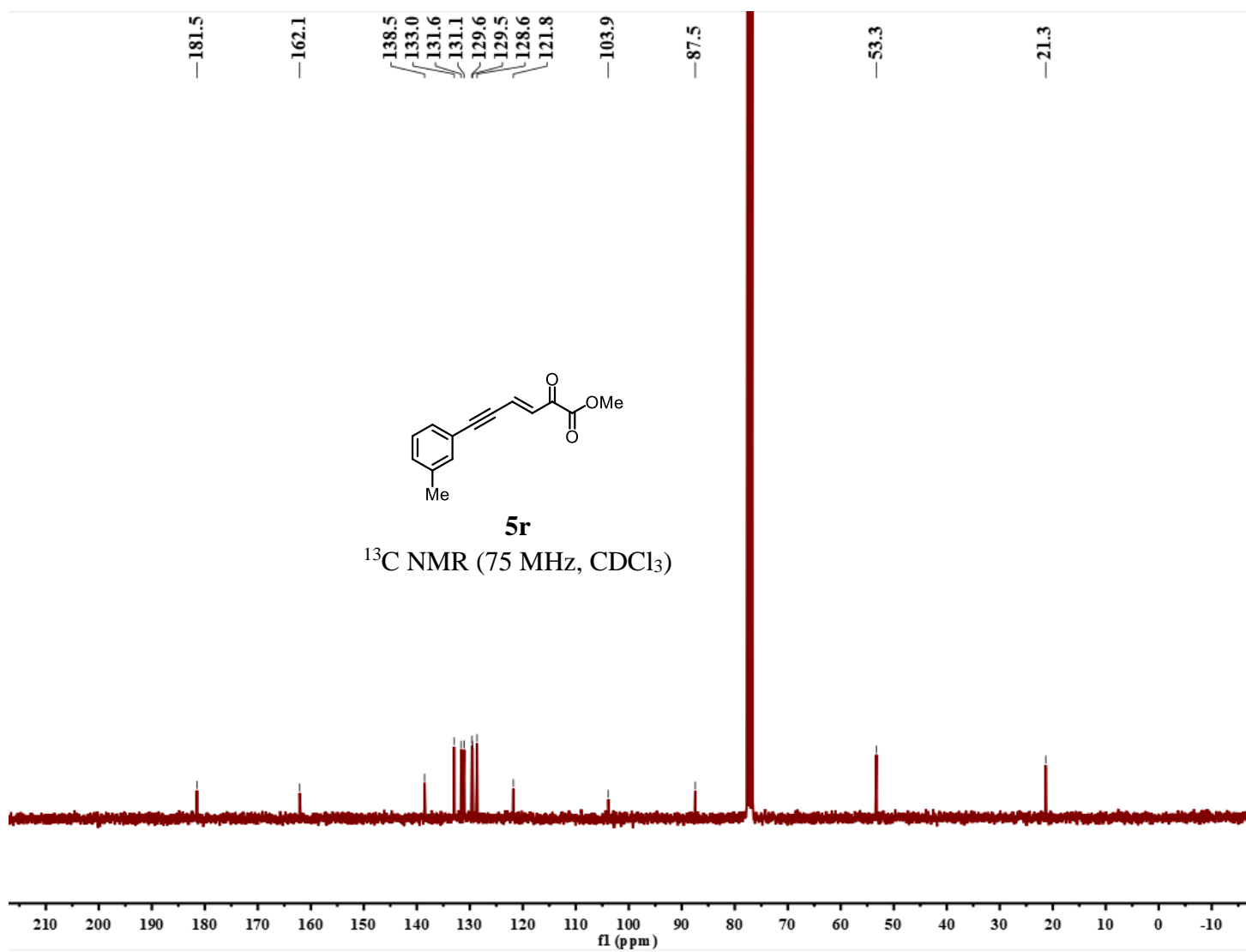


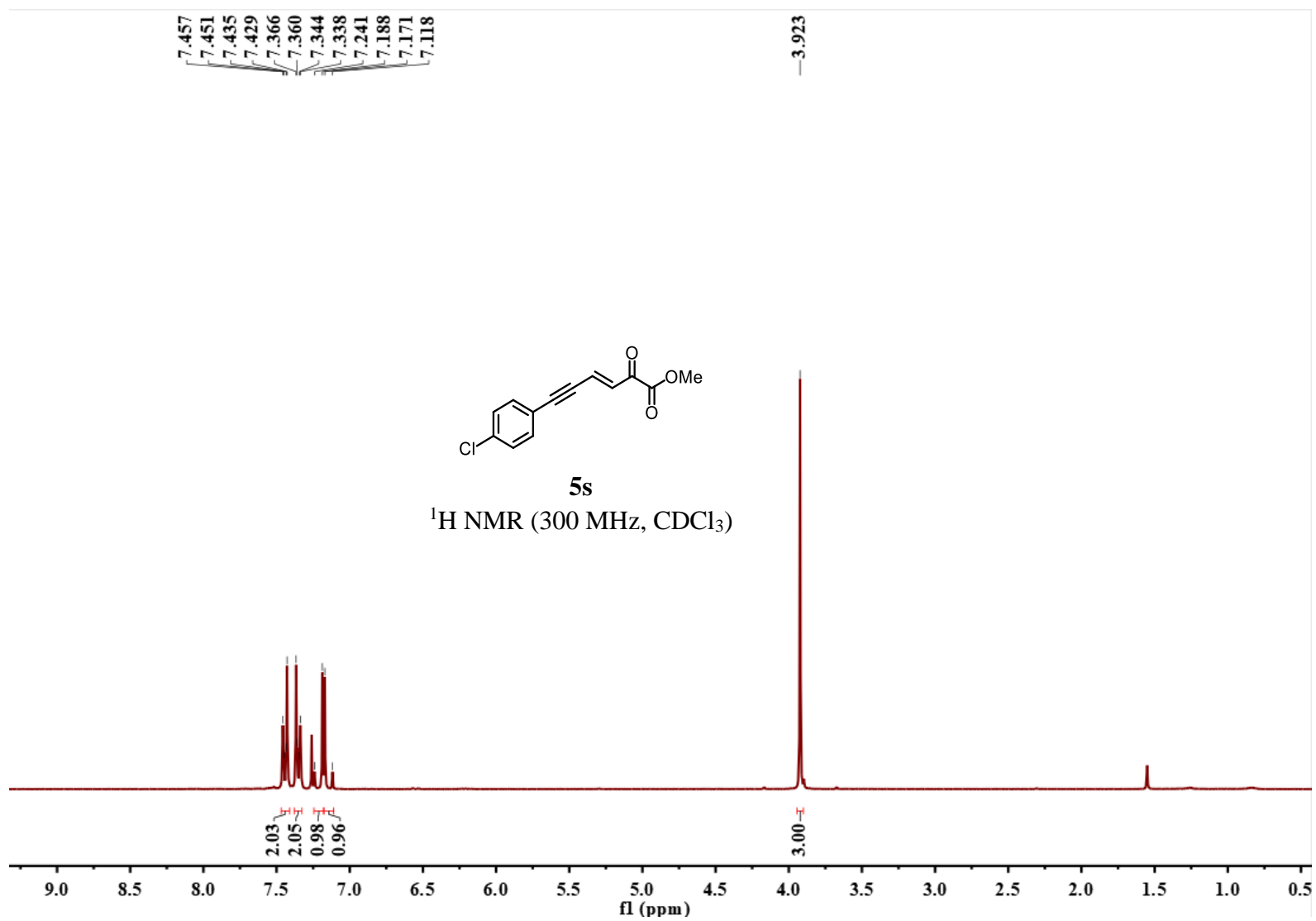


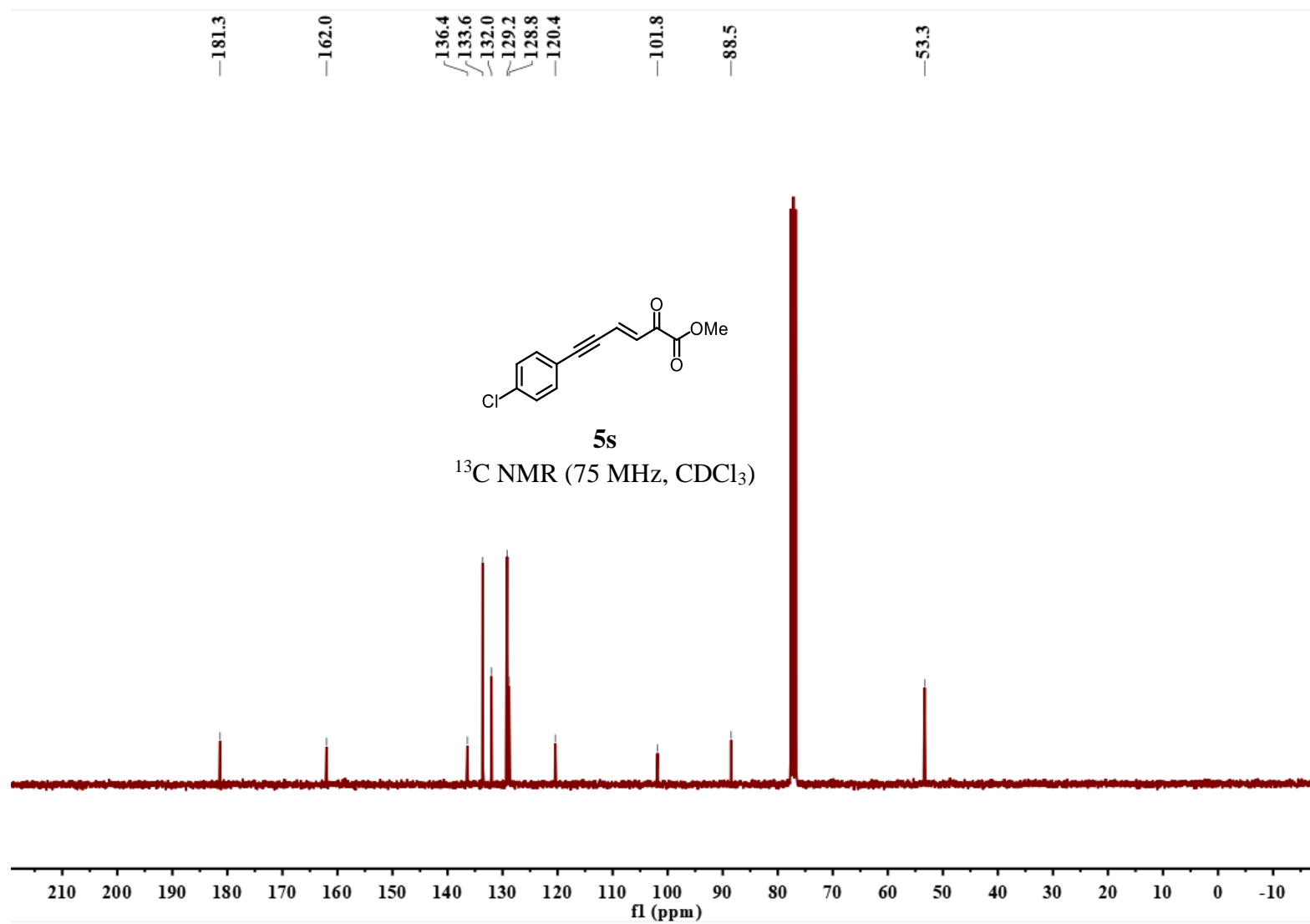


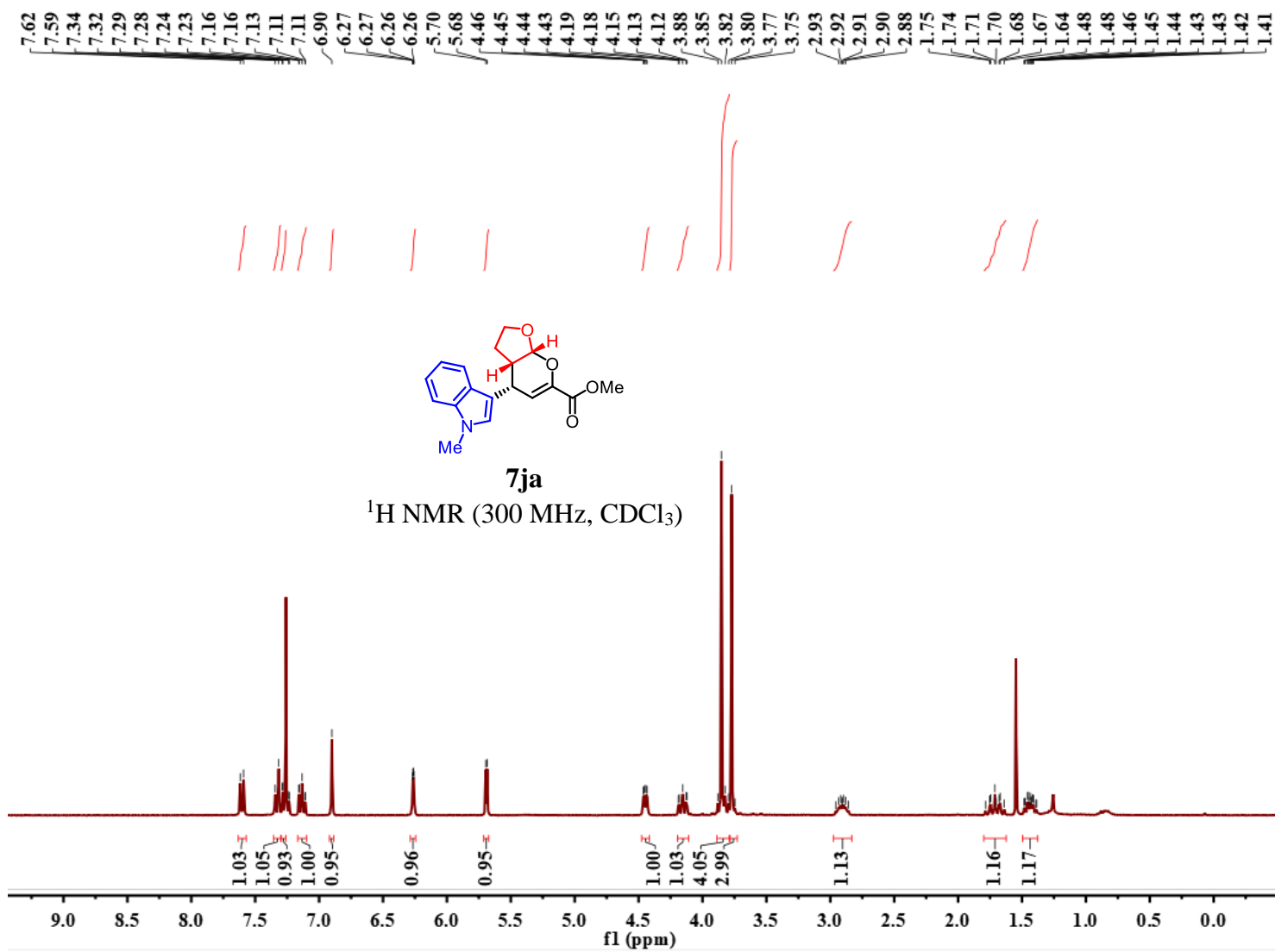


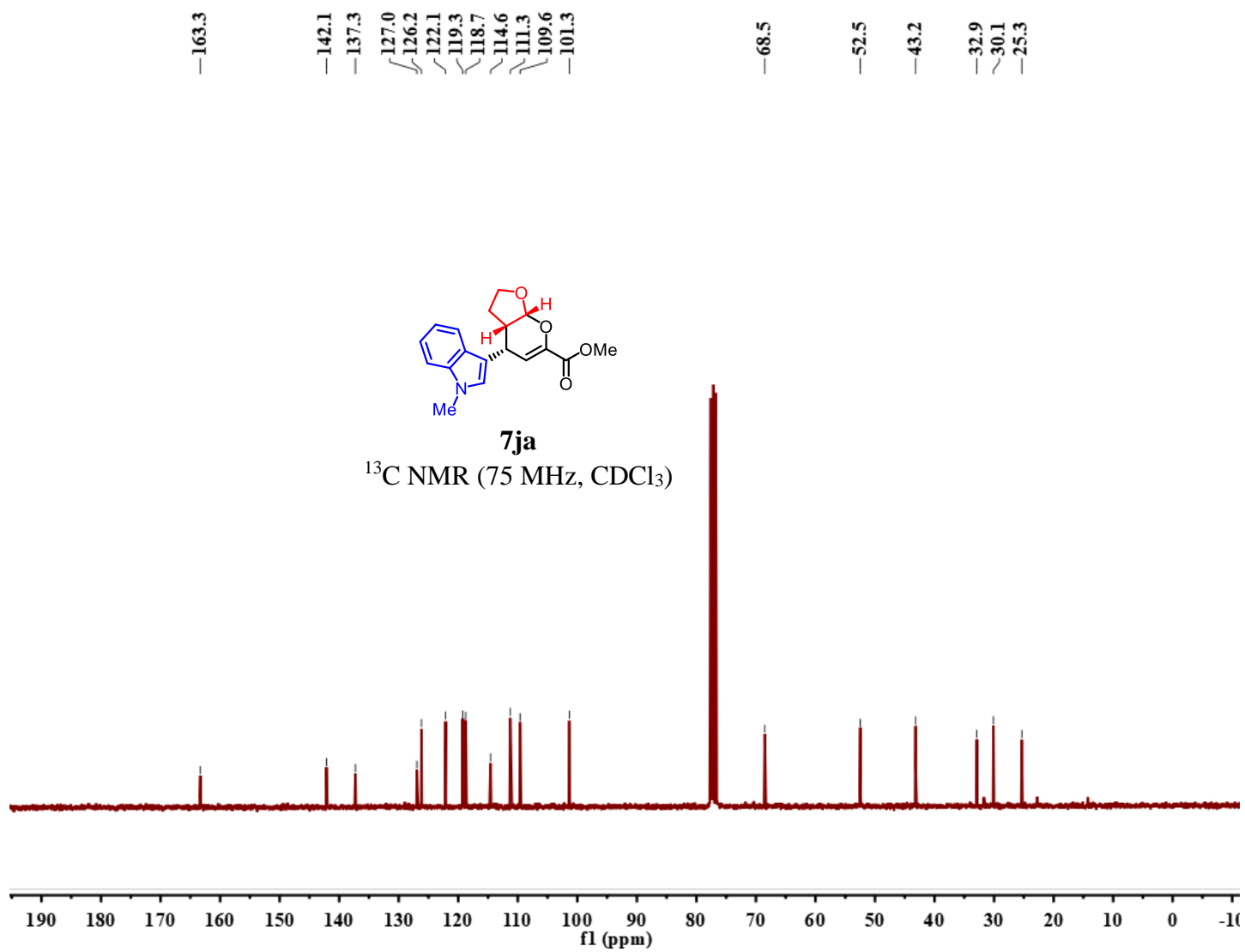


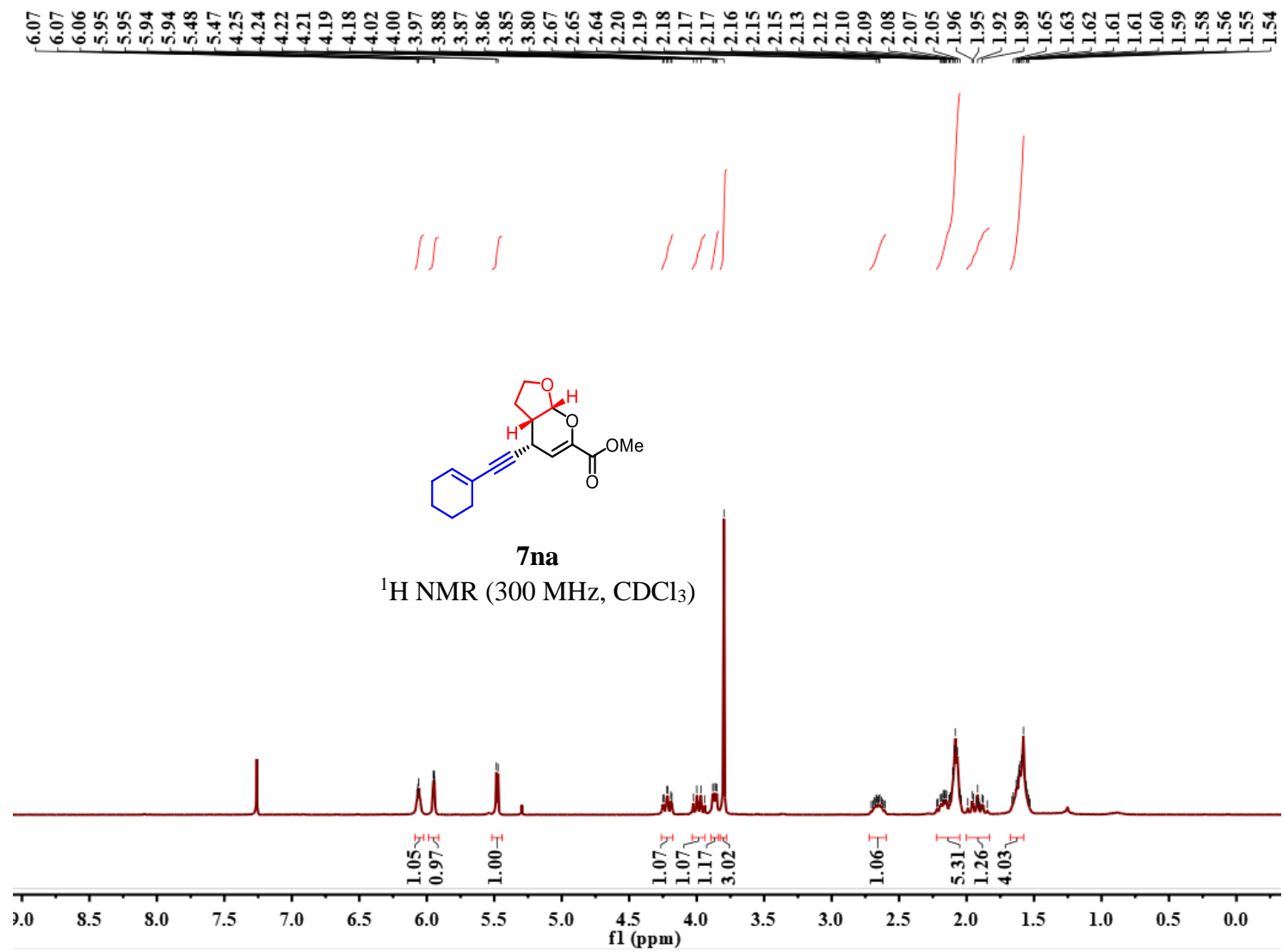


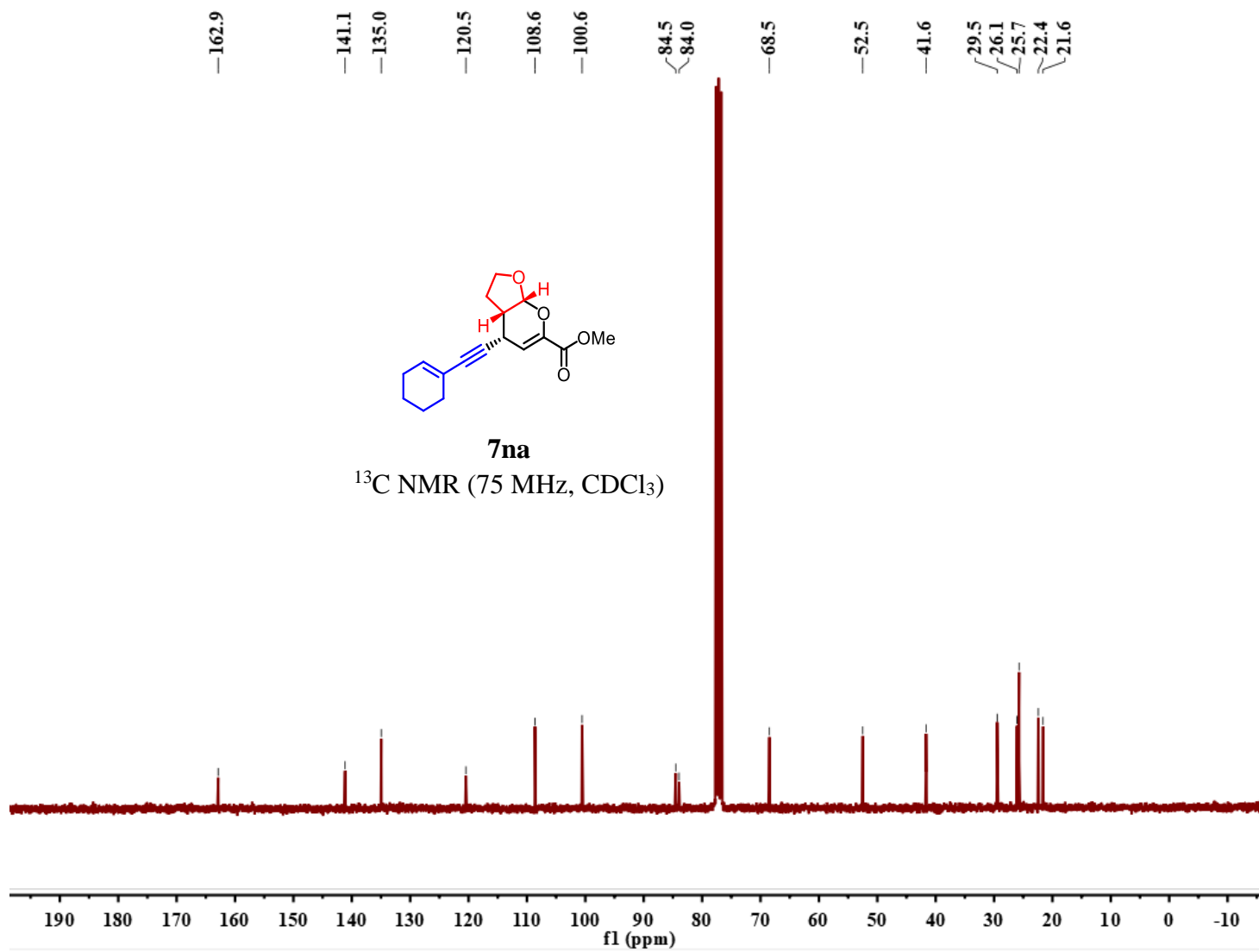


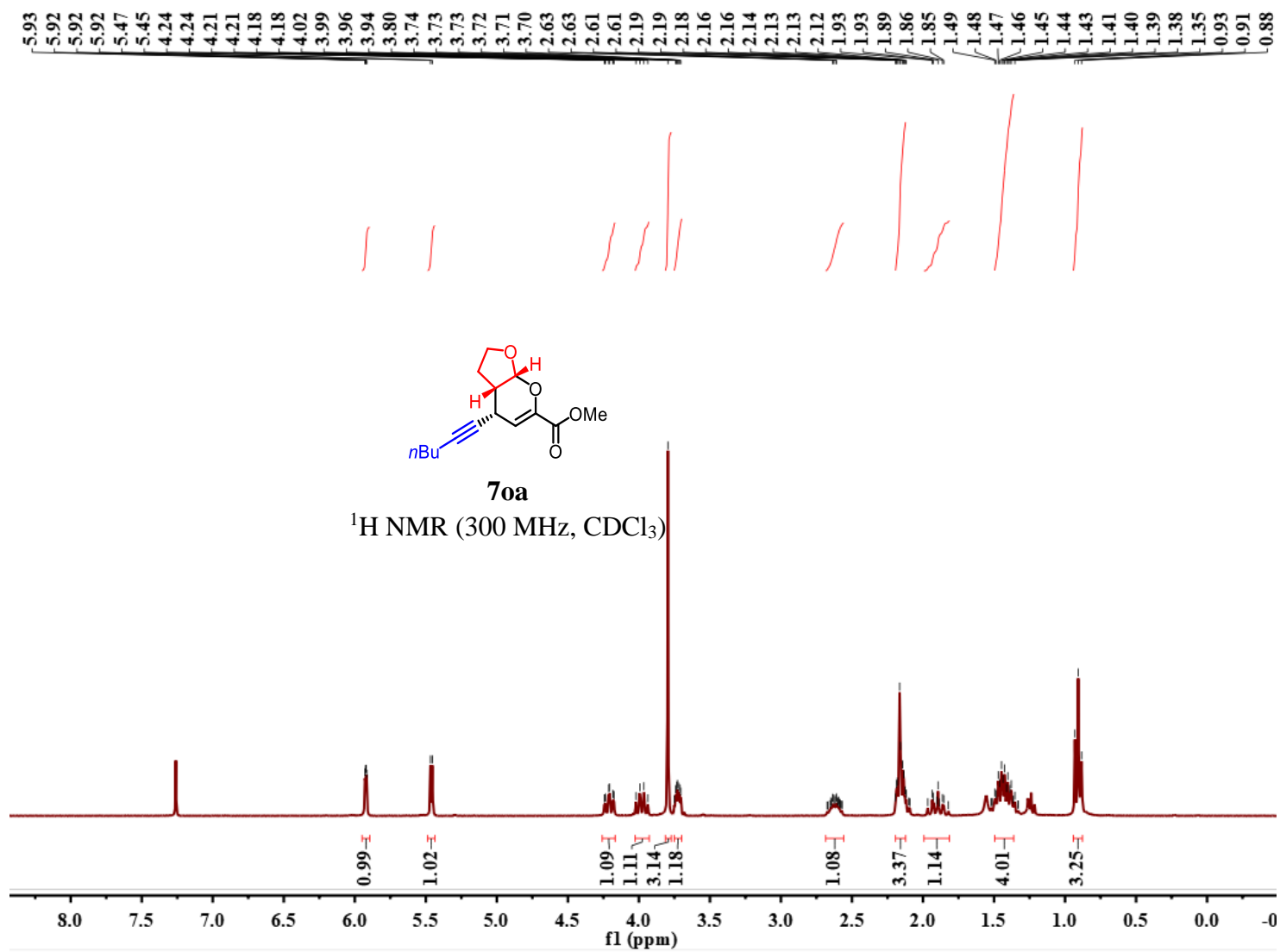


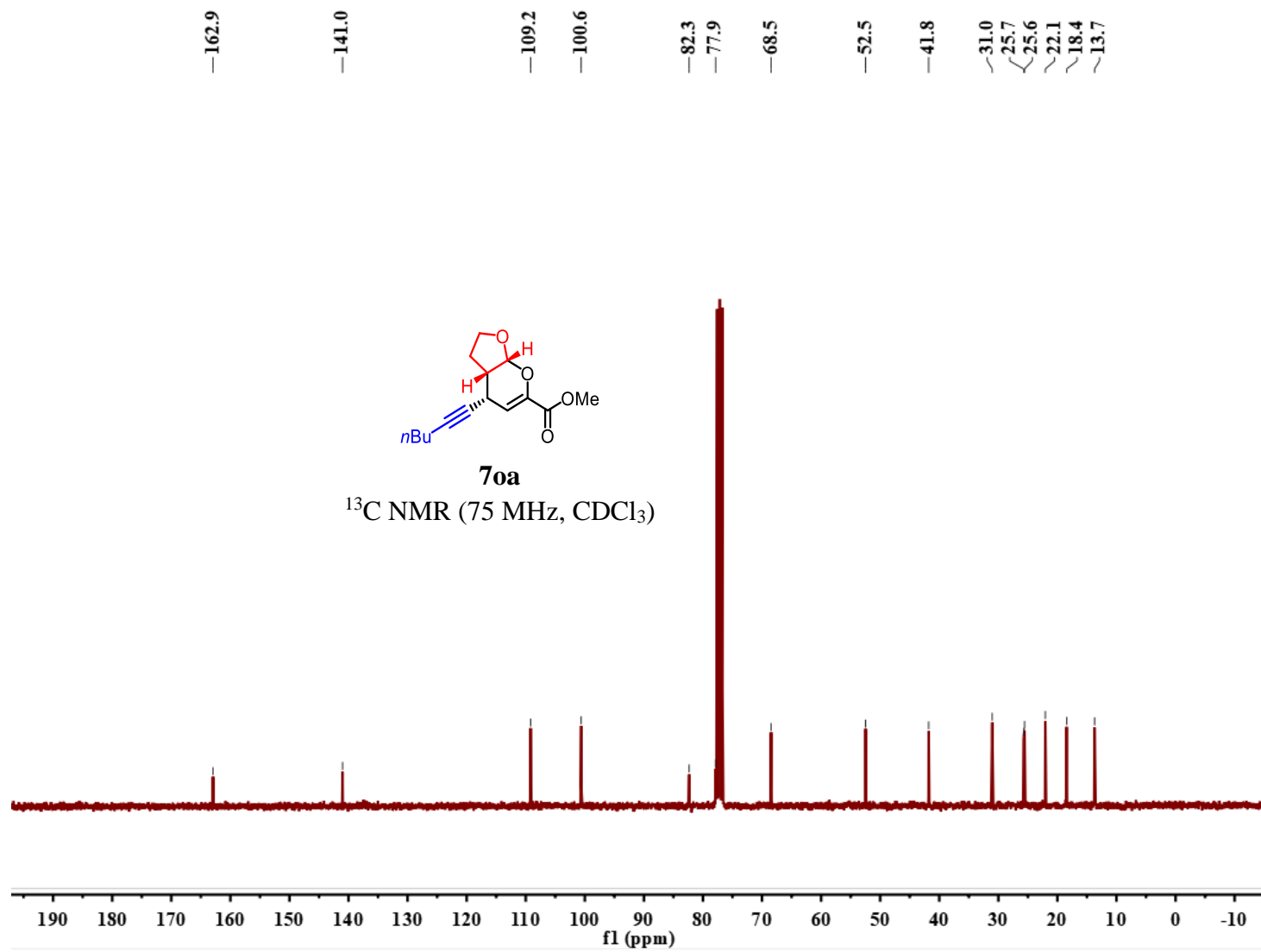


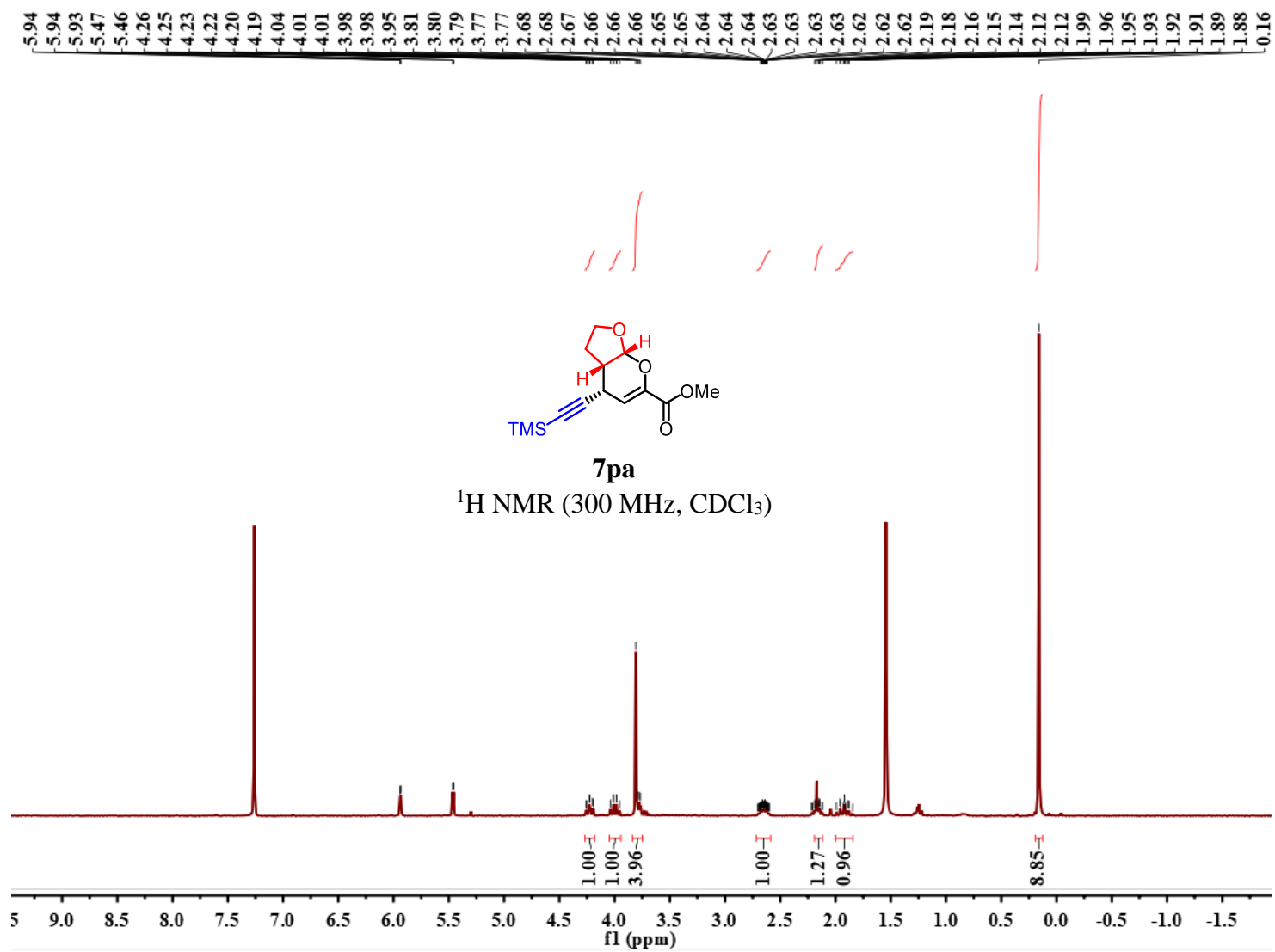


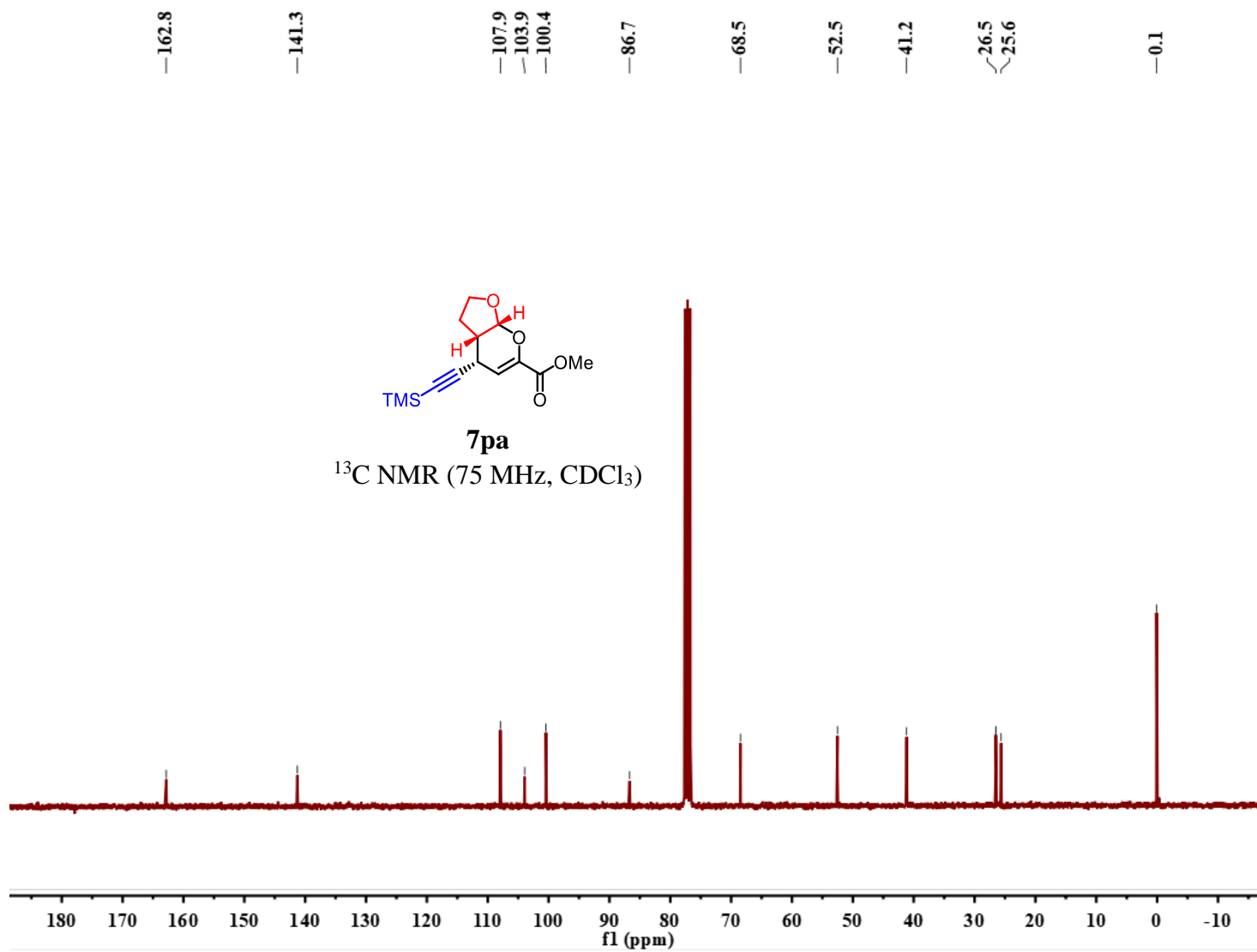


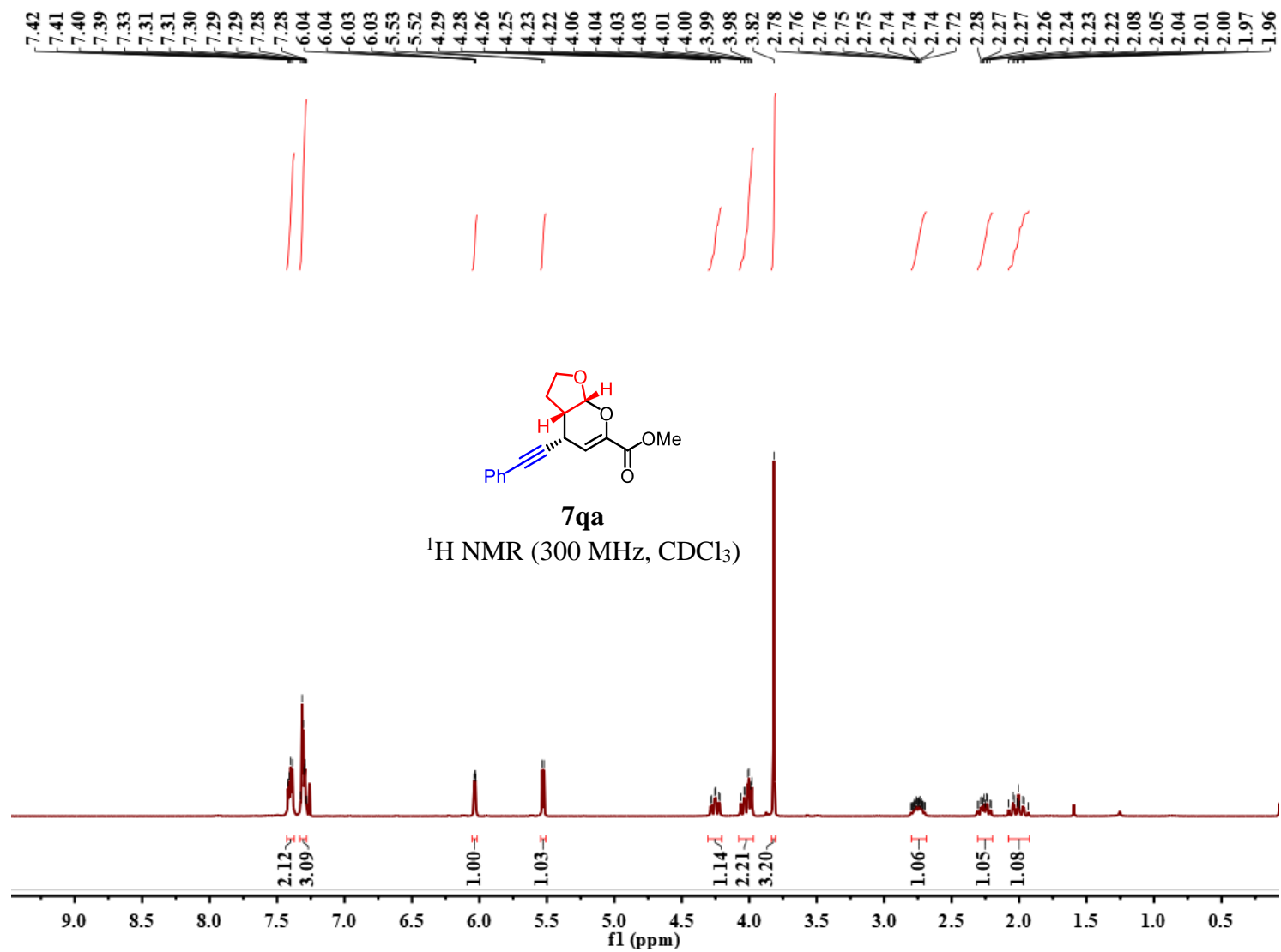


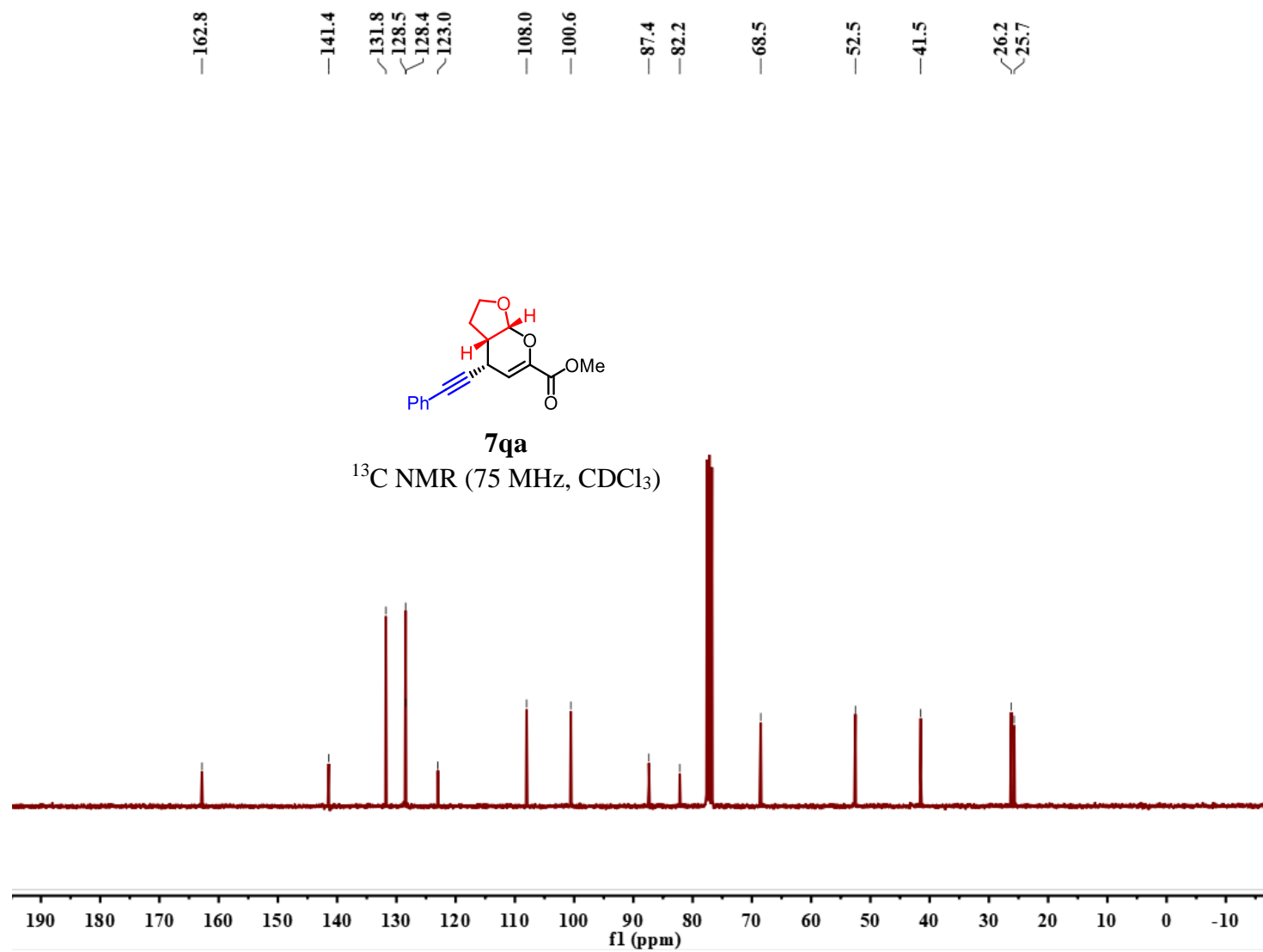


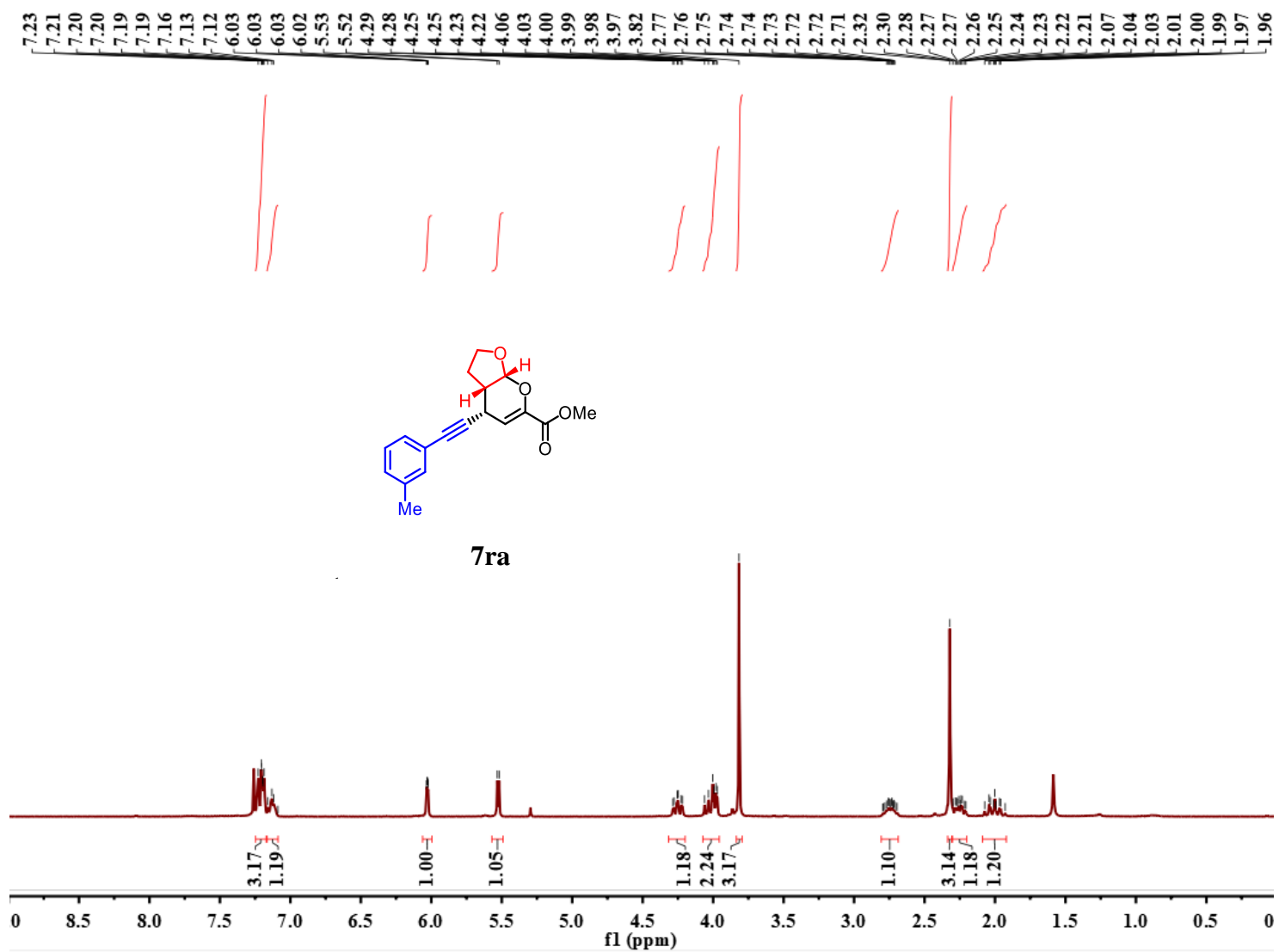


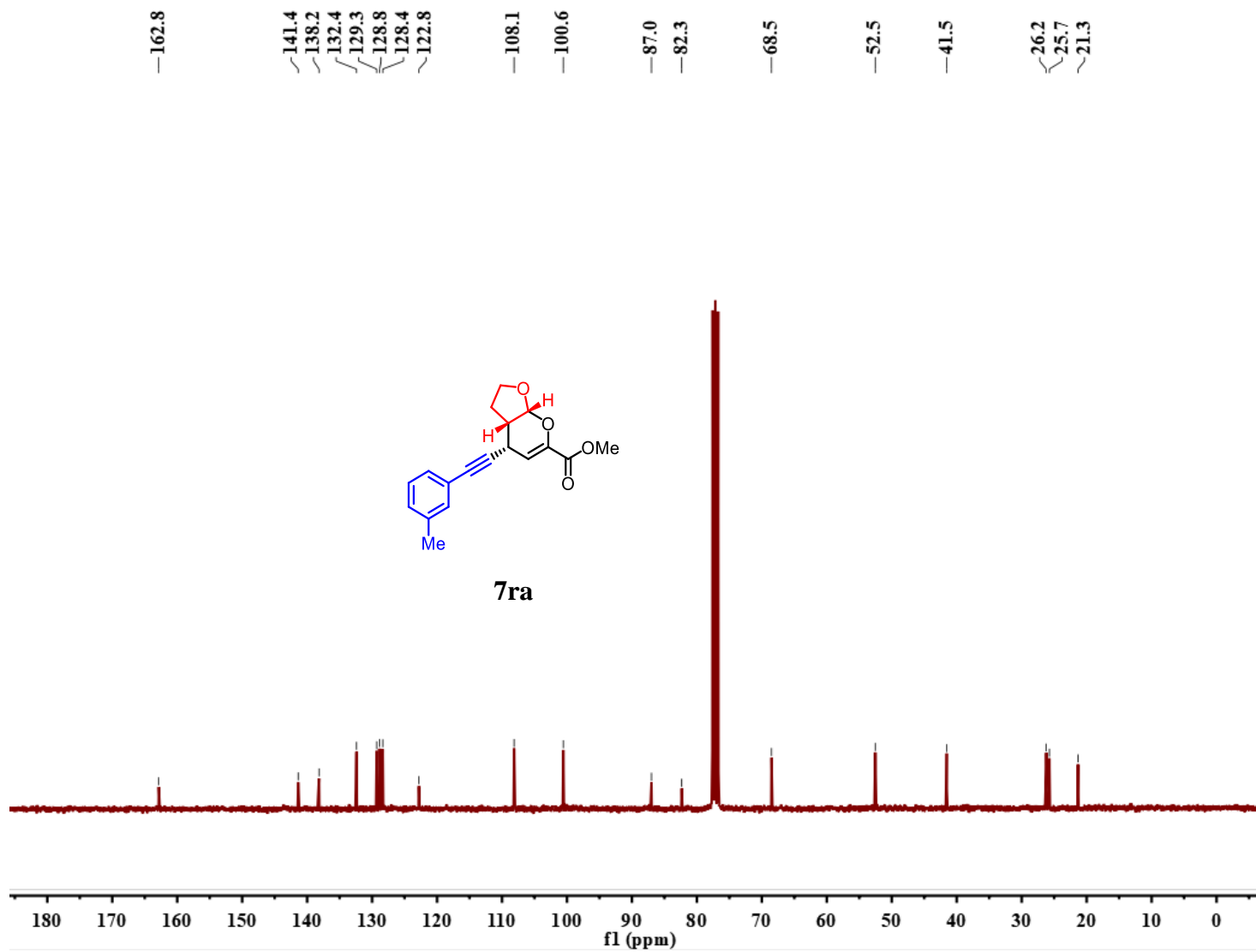


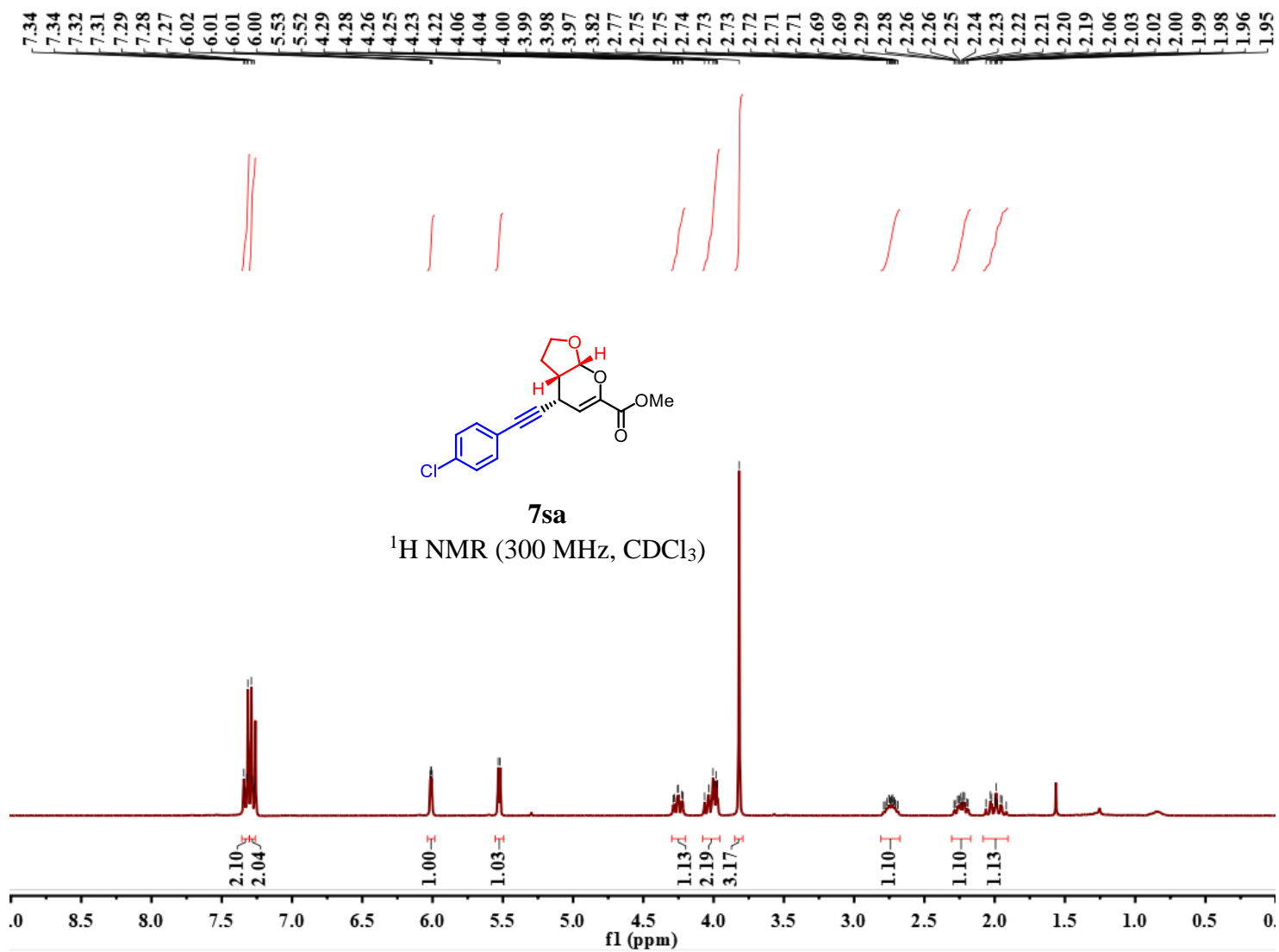


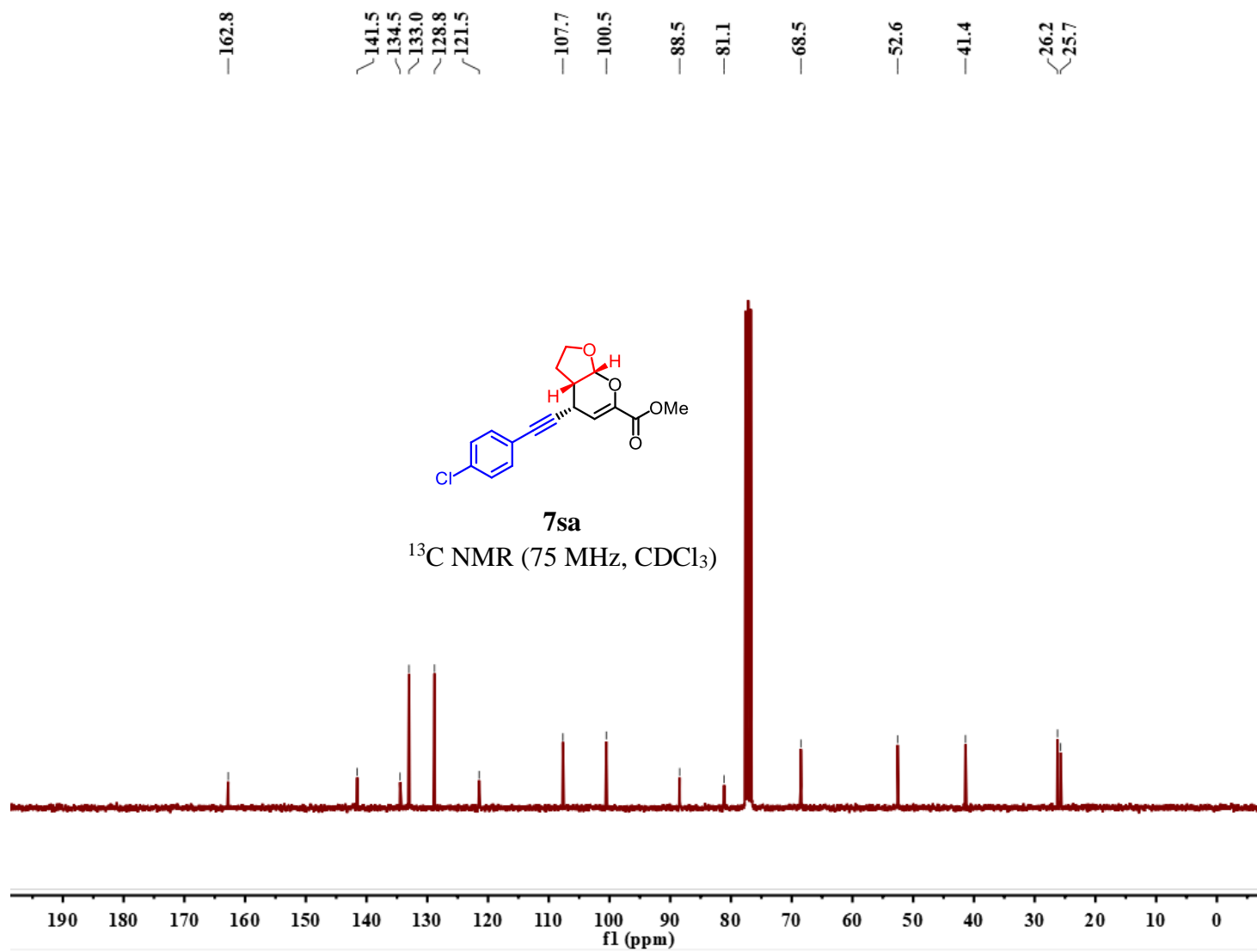


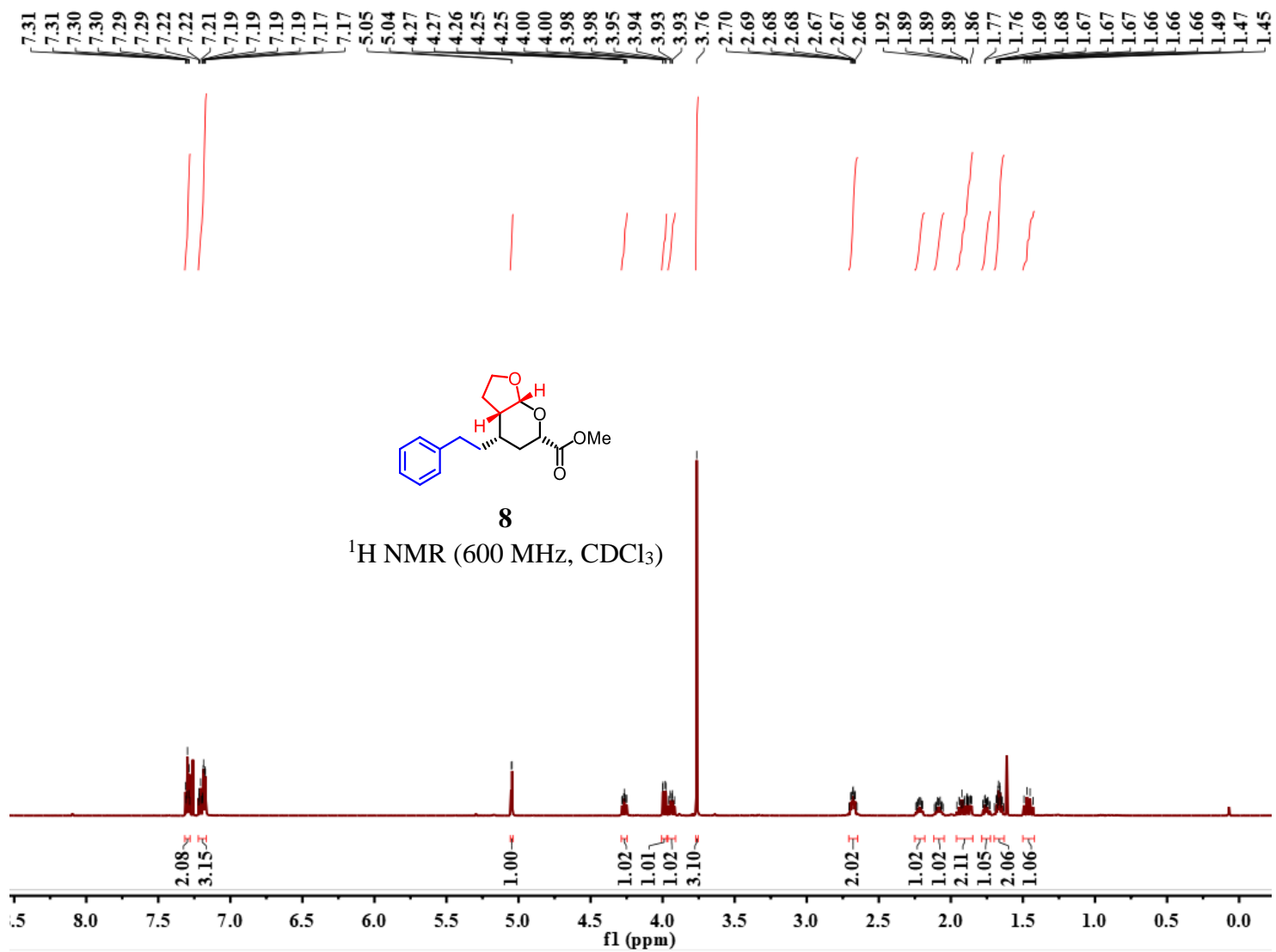












Statement

gemäß § 10, Abs. 1 der Promotionsordnung der mathematisch-naturwissenschaftlichen Fachbereiche und des Medizinischen Fachbereichs für seine mathematisch-naturwissenschaftlichen Fächer der Philipps-Universität Marburg vom 15.07.2009

Ich erkläre, dass eine Promotion noch an keiner anderen Hochschule als der Philipps-Universität Marburg, Fachbereich Chemie, versucht wurde und versichere, dass ich meine vorgelegte Dissertation

Design of Chiral-at-Ruthenium and Chiral-at-Iron Complexes for Asymmetric Catalysis

selbst und ohne fremde Hilfe verfasst, nicht andere als die in ihr angegebenen Quellen oder Hilfsmittel benutzt, alle vollständig oder sinngemäß übernommenen Zitate als solche gekennzeichnet sowie die Dissertation in der vorliegenden oder ähnlichen Form noch bei keiner anderen in- oder ausländischen Hochschule anlässlich eines Promotionsgesuchs oder zu anderen Prüfungszwecken eingereicht habe.

Yubiao Hong

Marburg, den 23.02.2021

Curriculum Vitae

Yubiao Hong

Male, born January 2, 1991 in Fujian, P. R. China

Email: hongyubiao@163.com

Education

- 12/2017–present** *Ph.D.* Organic Chemistry, University of Marburg, Germany
Advisor: Prof. Eric Meggers
- 09/2012–07/2015** *M.Sc.* Organometallic Chemistry, Soochow University, China
Advisor: Prof. Mingqiang Xue and Prof. Qi Shen
- 09/2008–07/2012** *B.S.* Chemistry, Longyan University, China

Research Experiences

Ph.D. study: Design of Chiral-at-Ruthenium and Chiral-at-Iron Complexes for Asymmetric Catalysis

Publications:

1. Y. Hong, L. Jarrige, K. Harms, E. Meggers, *J. Am. Chem. Soc.* **2019**, *141*, 4569–4572.
2. Z. Zhou, S. Chen, Y. Hong, E. Winterling, Y. Tan, M. Hemming, K. Harms, K. Houk, E. Meggers, *J. Am. Chem. Soc.* **2019**, *141*, 19048–19057.
3. Y. Grell, Y. Hong, X. Huang, T. Mochizuki, X. Xie, K. Harms, E. Meggers, *Organometallics*, **2019**, *38*, 3948–3954.
4. L. Li, F. Han, X. Nie, Y. Hong, S. Ivlev, E. Meggers, *Angew. Chem. Int. Ed.* **2020**, *59*, 12392–12395.
5. Y. Tan, Z. Zhou, Y. Hong, S. Ivlev, S. M. Chen, K. N. Houk, E. Meggers, *Angew. Chem. Int. Ed.* **2020**, *139*, 4322–4325.

M.Sc. study: Synthesis and Characterization of β -diketiminato Lanthanide(II) Borohydrides and Phenylene-bridged β -diketiminato Dilanthanide(III) Aryloxides and Their Catalytic Activity

Publications:

1. Y. Hong, Y. Zheng, M. Xue, Y. Yao, Y. Zhang, Q. Shen, *Z. Anorg. Allg. Chem.* **2015**, *641*, 1230–1237.